ТЕОРИЯ ХИМИЧЕСКОГО СТРОЕНИЯ И РЕАКЦИОННОЙ СПОСОБНОСТИ ПОВЕРХНОСТИ. МОДЕЛИРОВАНИЕ ПРОЦЕССОВ НА ПОВЕРХНОСТИ

PACS: 31.15.A-; 31.15.bu; 31.15.E-; 31.70.Dk; 36.40.-c; 61.43.Gt; 68.03.-g; 68.43.-h; 81.40.Ef 10. doi: 15407/Surface.2019.11.003

INTERFACIAL PHENOMENA AT A SURFACE OF INDIVIDUAL AND COMPLEX FUMED NANOOXIDES

V.M. Gun'ko, V.V. Turov, O.V. Goncharuk, E.M. Pakhlov, O.K. Matkovsky

Chuiko Institute of Surface Chemistry, 17 General Naumov Street, 03164 Kyiv, Ukraine, e-mail: vlad_gunko@ukr.net

The aim of this review paper was to analyze investigation results on interfacial and temperature behaviors of nonpolar and polar adsorbates interacting with individual and complex fumed metal or metalloid oxides (FMO), initial and subjected to various treatments or chemical functionalization and compared to such porous adsorbents as silica gels, precipitated silica, mesoporous ordered silicas, and polymeric composites. Note that the particulate morphology of FMO depends strongly not only the flame reaction conditions but also on the types and amounts of reagents, as well their distribution in the flame. Therefore, complex nanooxides can include core-shell nanoparticles, (CSNP) of 50-200 nm in size with titania or alumina cores and silica or alumina shells in contrast to simple and smaller nanoparticles of individual FMO. CSNP could be destroyed under high-pressure cryogelation (HPCG) or mechanochemical activation (MCA). These treatments as well simple hydrocompaction (controlled wetting-drying) affect the structure of aggregates of nanoparticles and agglomerates of aggregates, resulting in their becoming more compacted. The analysis shows that complex FMO could be more sensitive to external actions than simple nanooxides such as fumed silica. Any treatment of 'soft' FMO affects the interfacial and temperature behaviors of polar and nonpolar adsorbates. Rearrangement of secondary particles and surface functionalization affect the freezing-melting point depression of adsorbates. For some adsorbates, open hysteresis loops became readily apparent in adsorption-desorption isotherms. Clustering of adsorbates bound in pores causes reduced changes in enthalpy during phase transitions (freezing, fusion). Freezing point depression and melting point elevation cause significant hysteresis freezing-melting effects for adsorbates bound to initial and treated FMO in textural pores (voids between nanoparticles in secondary structures). Relaxation phenomena for both low- and high-molecular weight adsorbates or of filled polymeric composites are affected by the morphology of primary particles, structural organization of secondary particles of differently treated or functionalized FMO, content of adsorbates, co-adsorption order, and temperature.

Keywords: nanosilica, complex nanooxides, interfacial phenomena, adsorption, evaporation, confined space effects.

Introduction

Particulate morphology of FMO

Fumed (or pyrogenic) metal and metalloid oxides, FMO (alumina, silica, titania, zirconia, germania, *etc.*) are widely used in industry, medicine, and agriculture as individual powder materials or components of composite materials such as filled polymers, powder or monolith solids, suspensions, *etc.* [1-12]. Flame ($H_2/O_2/N_2$) synthesis at 1000-1500 ^oC using MCl_x or MR_x or $MCl_{x1}R_{x2}$ (M is a metal, and R is an organic functionality, *e.g.*, OCH_3, CH_3, etc.) as precursors leads to certain general characteristics of FMO much of it related to their nano-particulate morphology corresponding to the formation of nonporous nanoparticles (NPNP), which form

aggregates (< 1 μm in size) and agglomerates of aggregates (> 1 μm) forming a loose powder with low bulk density ($\rho_b \approx 0.05\text{-}0.15$ g/cm^3 dependent on composition) [13-30]. There is also silica fume (microsilica) analogous to fumed silica that is a by-product of the silicon and ferrosilicon alloy production, and it consists of spherical-like particles with an average particle diameter of 150 nm. Silica fume is mainly used as pozzolanic material for high performance concrete (ASTM C1240, standard specification for silica fume used in cementitious mixtures, http://astm.or). Typically, FMO are composed of roughly spherical-like nonporous nanoparticles (NPNP) sized in the 5-100 nm range (Figs. 1-11) that determines their relatively large values of the specific surface area (Table 1, S_{BET}). For silica fume, the primary particle size distribution (PPSD) is typically broader than that of FMO studied (Fig. 1).

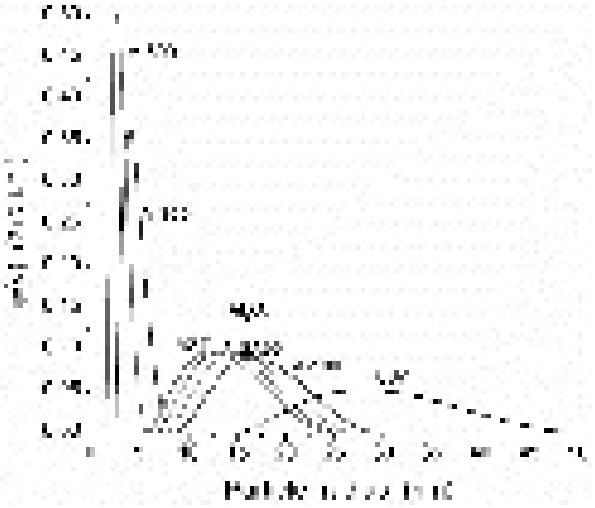

Fig. 1. Particle size distributions of FMO estimated from nitrogen adsorption data using the Vφ/SCR method.

High resolution transmission electron microscopy (HRTEM) images recorded for individual, binary and ternary FMO initial and differently treated [25-33] show (Figs. 1-11) that the shape of nanoparticles could be varied from nearly ideal spherical one to irregular one, and with very weak contacts between adjacent nanoparticles (especially of spherical shape) or more strongly adherent nanoparticles (especially of irregular shape).

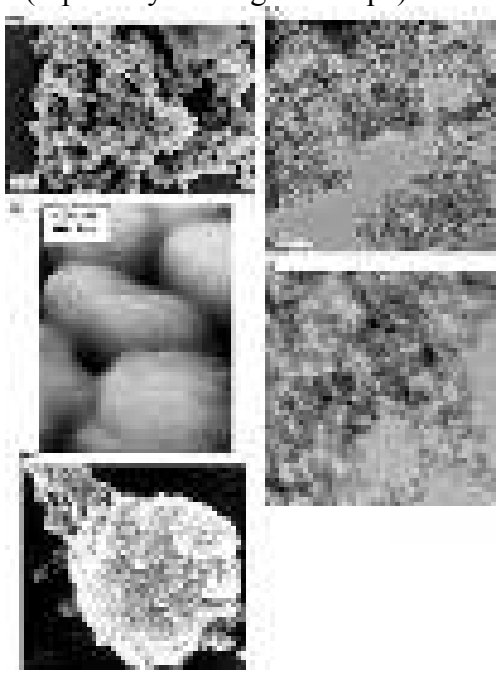

Fig. 2. (a) SEM image of initial fumed silica A-300 and (b) its TEM image after cryogelation at high pressure (~1000 atm); (c) AFM image of zirconium-containing mesoporous MCM-41 type silica [34]; (d) TEM image of a mechanical mixture (1:1) of fumed silica A-300 and fumed alumina; and (e) SEM image of fumed silica A-300 wetted and dried.

Note that nanoparticles in silica gels or ordered mesoporous silicas (see, *e.g.*, Fig. 2c) are very strongly adherent in secondary structures (such as hard microglobules or beads) in contrast to FMO composed of 'soft' agglomerates of aggregates of primary nanoparticles. This difference in the nano- and micro-particulate morphology and hierarchy leads to differences in various characteristics and properties of highly disperse FMO and granulated materials that will be analyzed below.

The FMO materials are frequently called nanooxides due to the morphology of primary nanosized particles. FMO with primary nanoparticles forming aggregates and less dense agglomerates of aggregates are typically characterized by a small portion of the solid fraction in the powder ~2-5% (Fig. 2). The nano-particulate morphology of FMO provides these materials with characteristics useful for fillers of polymers, drug carriers, pigments, and thickeners due to easy distribution of nanoparticles in polymeric or other matrices [3-5,35-45]. Additionally, these morphological features enhance a role of the interfacial phenomena in the characteristics of the materials applied in different media.

The properties of FMO depend not only on their composition but also on treatment conditions and the history of the materials because of facile rearrangement of the secondary structures with nanoparticles bonding by electrostatic and van der Waals forces with one another in 'soft' powder. Note that chemical bonds between nanoparticles are practically absent in fresh FMO powders. In contrast to individual FMO, complex (binary and ternary) nanooxides could include not only simple uniform primary nanoparticles but also core-shell nanoparticles (CSNP) (Figs. 3, 4, 7-11) [17,46,47]. Strong external actions (*e.g.*, high-pressure cryogelation, HPCG, in cryo-bombs at approximately 1000 atm) could lead to decomposition of CSNP [46,47] (Fig. 4) that caused significant changes in the textural and other characteristics of strongly treated FMO.

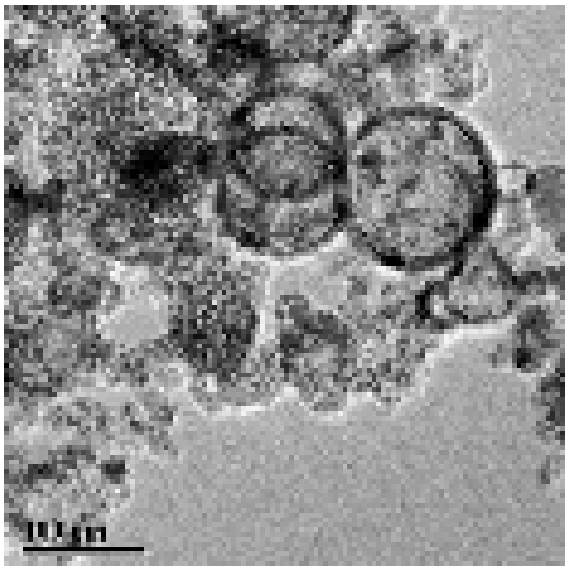

Fig. 3. TEM image of CSNP with alumina/silica/titania (AST1).

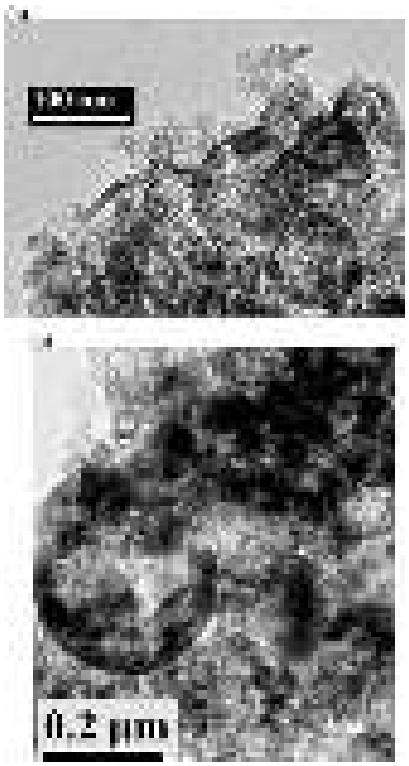

Fig. 4. HRTEM images of decomposed CSNP of AST1.

The formation of CSNP can occur when one component of a binary or ternary FMO tends to be in a crystalline form with practically pure individual oxide (*e.g.,* titania or alumina). However, conditions during the flame synthesis (high temperature, flame turbulence, high velocity of molecules, radicals, ions, protoparticles, and nanoparticles [1-23]) may prevent the formation of large crystallites [1-8]. Small crystallites (protoparticles) could form dense aggregates

(polycrystalline cores), which are then covered by some oxide layers in the flame to form CSNP. Another reason for the formation of complex CSNP is the difference in reactivity of the precursors of different oxides, and the difference in the conditions of their appearance in the flame. For example, $SiCl_4$ or $TiCl_4$ (liquids at standard conditions) are volatile and reactive compounds, but $AlCl_3$ dimerizes to Al_2Cl_6 forming a solid compound, which should be sublimated to be added to the flame. Al_2Cl_6 is less reactive than $SiCl_4$ or $TiCl_4$. Similar differences are characteristic for other precursors containing various metals. Therefore, distributions of different precursors in the flame (a relatively long jet used is characterized by certain gradients of temperature and concentration of reactants and active particles) could be nonuniform. This leads to different rates of the formation of nuclei, protoparticles, and layers with different oxides. Additionally, the formation of M_1-O-M_1 or M_2-O-M_2 bonds (where $M_1 \neq M_2$) could be preferable to the formation of M_1-O-M_2 bonds at the surface of nuclei of some phases, especially if they tend to be crystalline [27-49]. This leads to the formation of protoparticles with a nearly pure single phase (especially nanocrystallites such as titania or alumina in which other oxides, *e.g.*, silica, could be present as low-content impurities) present in complex FMO. Note that the formation of asymmetric bridges M_1-O-M_2 could affect the catalytic properties of materials [50-52], as well as aggregation of nanoparticles and agglomeration of the aggregates [53] that play an important role in applications of these materials [1-12,54-56].

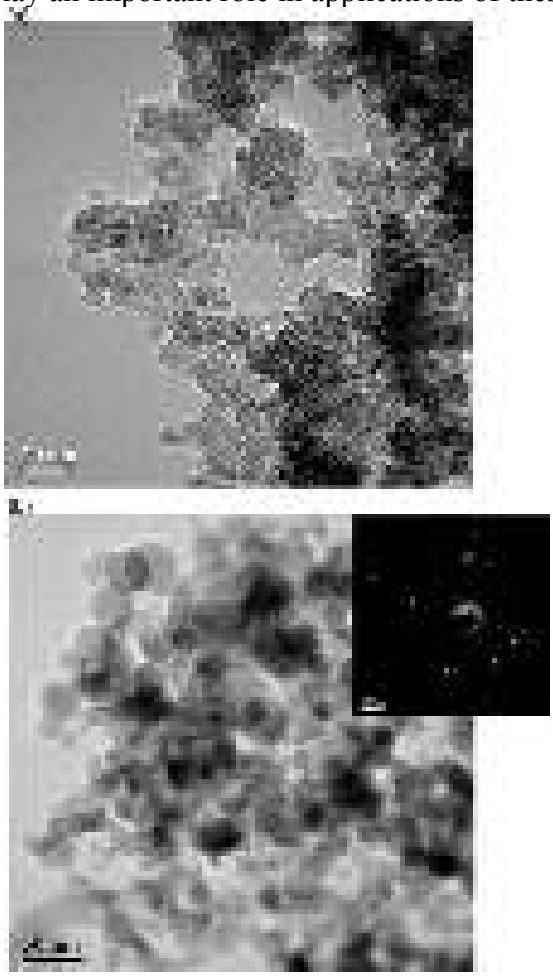

Fig. 5. HRTEM images of individual fumed oxides (a) A-300 and (b) alumina and electron diffraction pattern (insert).

For FMO, the toxicity (an important consideration in applications of these materials) of nanomaterials depends on the surface chemistry and PPSD, as well as on the behavior of aggregates and agglomerates in aqueous media or in the gas phase [37-40,57,58]. Some treatments and surface modifications could reduce the toxicity of FMO [39,40,53], as well as their dusting. Applications of FMO could give significant advantages in comparison with materials composed of much larger particles due to high activity of mobile NPNP characterized by a significant value of the specific surface area (up to 500 m^2/g). FMO applications generate additional problems [57-60],

which, however, could be solved using treatment or modification of nanomaterials. Some properties of FMO are sensitive to relatively gentle external actions (*e.g.*, treatment using a grinder, microbreaker, ball-mill, or even hand pressing) [48,49,53]. For example, several minute treatments of fumed alumina or silica/alumina in a grinder (using powder matter under vibrations of a ball (0.5-1 cm in diameter) in a cylinder, both with stainless steel) could result in changes in the phase composition of alumina nanocrystallites [48,49] and reduce dusting of the material. Clearly, these effects changing the FMO properties could alter their behavior in certain applications in liquid, gaseous, or polymeric media.

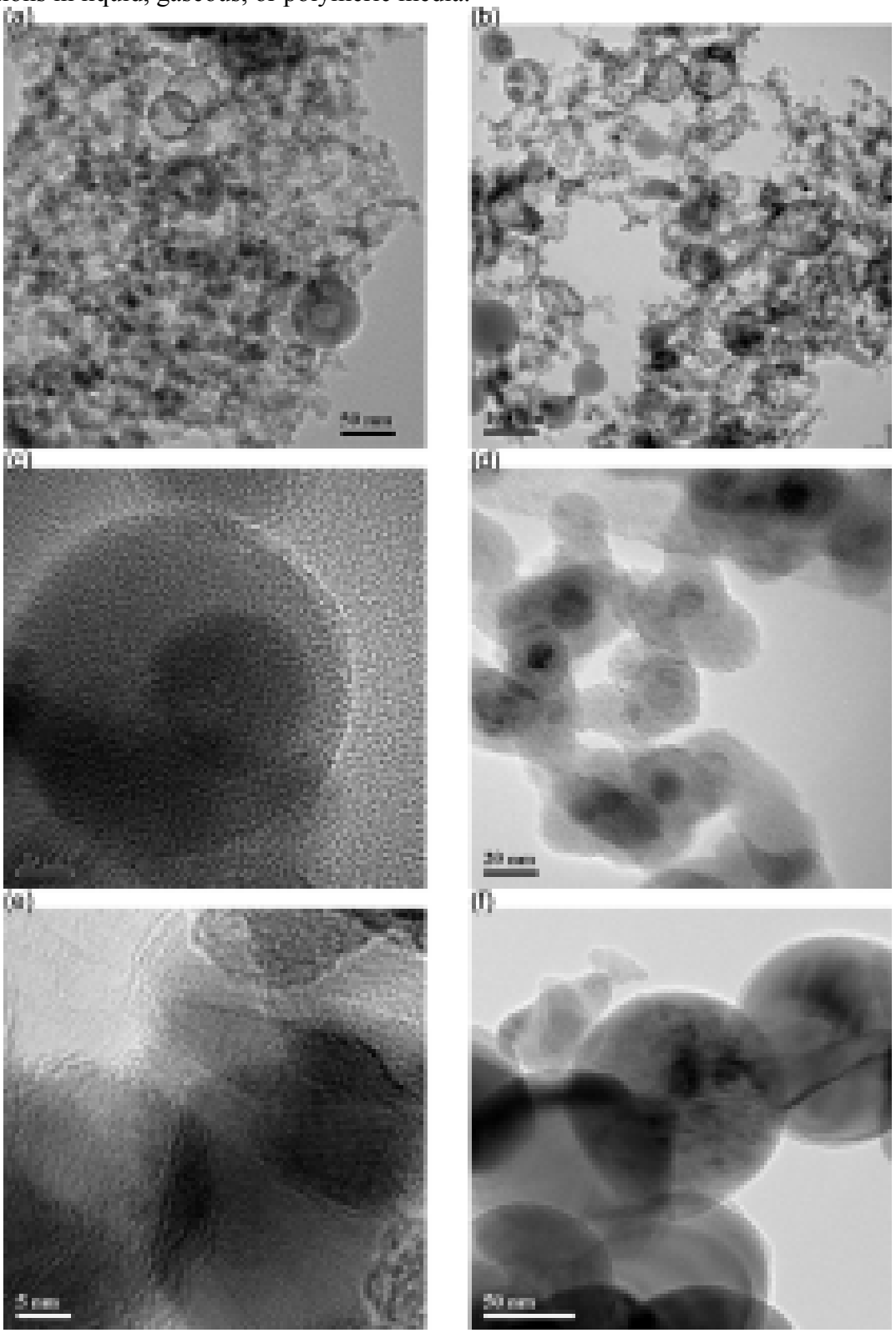

Fig. 6. HRTEM images of fumed complex oxides (a) SA23, (b, d) ST20, (c) SA96, (e) ST63, and (f) AST50.

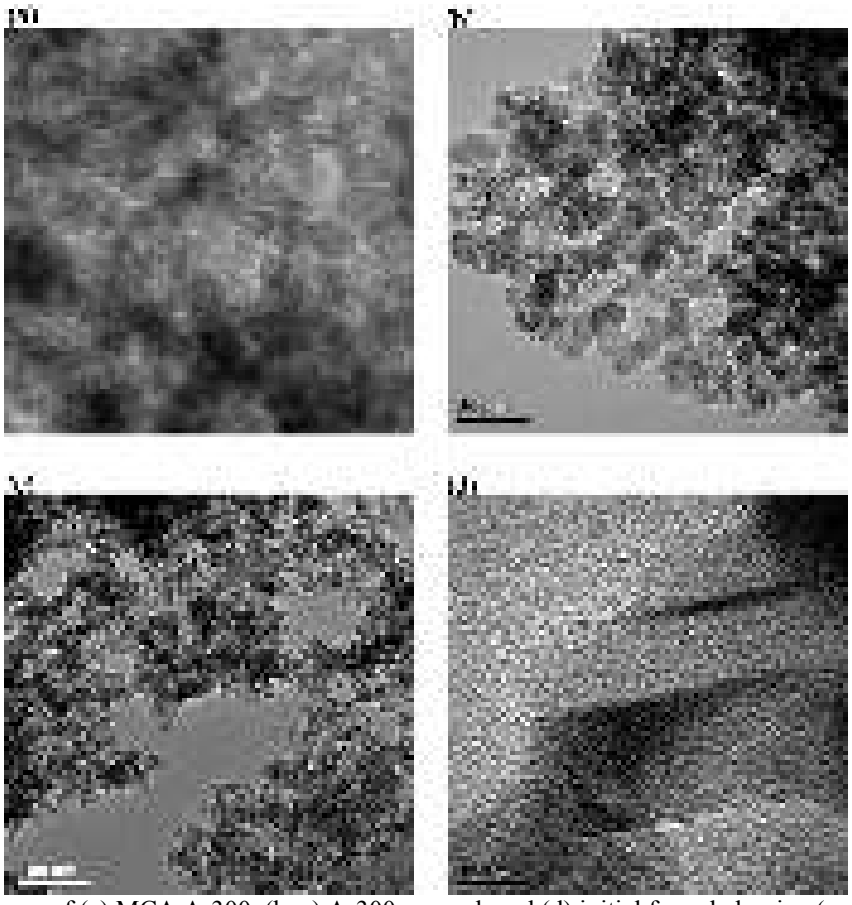

Fig. 7. HRTEM images of (a) MCA A-300, (b, c) A-300 cryogel, and (d) initial fumed alumina (scale bar 20, 50, 100, and 10 nm, respectively).

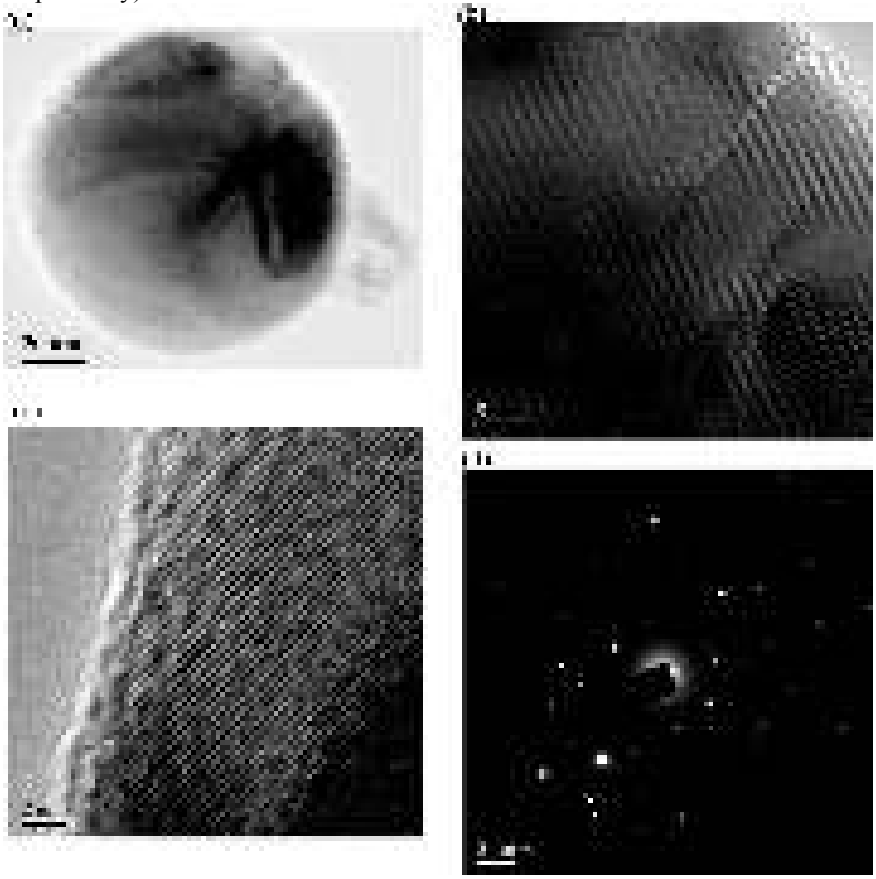

Fig. 8. HRTEM images of initial AST50 at different magnifications at scale bar of (a) 20 nm, (b) 5 nm, and (c) 2 nm, and (d) electron diffraction pattern showing the presence of titania crystallites.

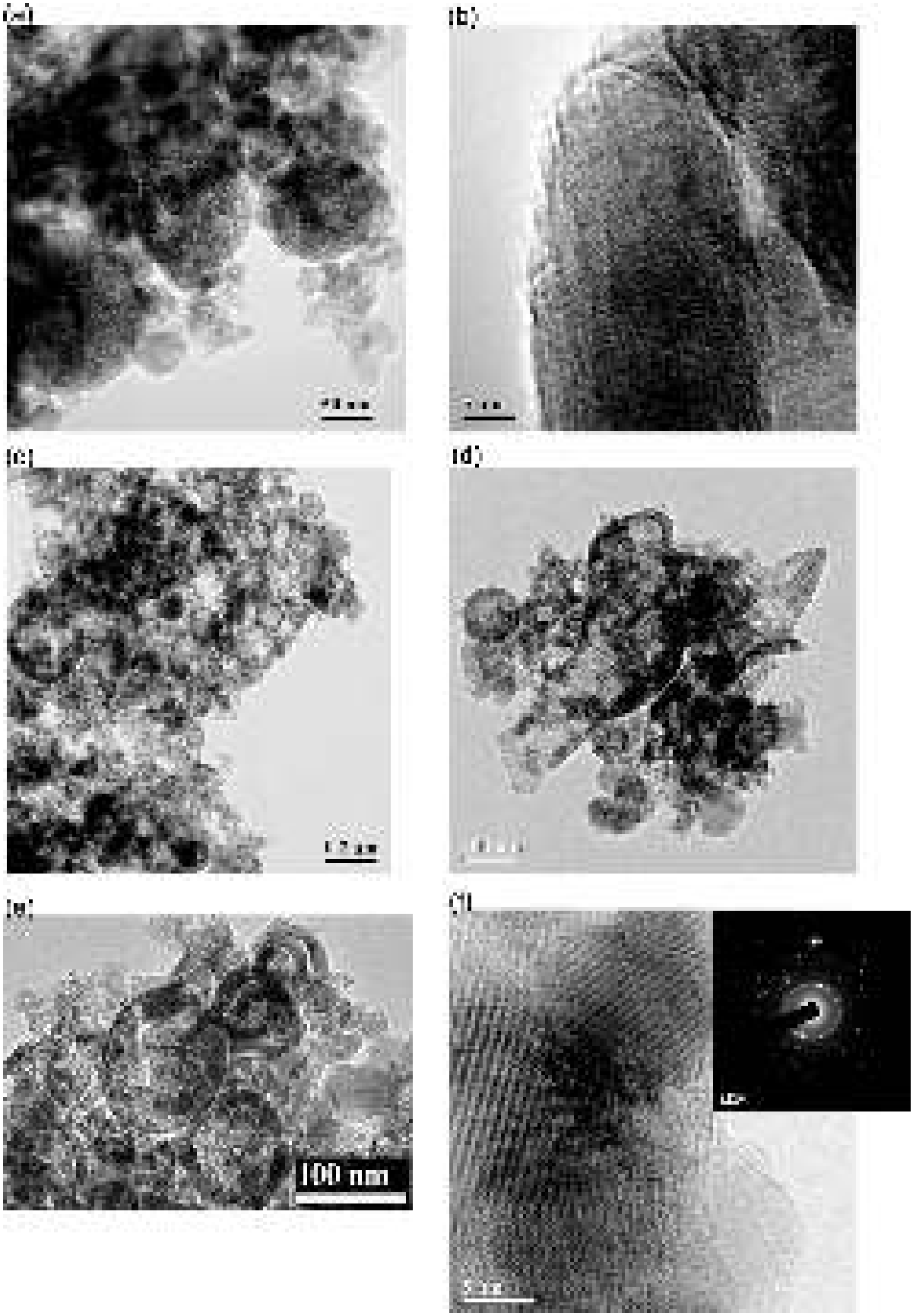

Fig. 9. HRTEM images of (a-e) AST1 (a, b) initial (scale bar 50 and 5 nm) and (c, d, e) cryogel (scale bar 200 and 100 nm), and (f) initial AST71 (scale bar 5 nm) and electron diffraction pattern (insert) showing the presence of both crystalline and amorphous phases.

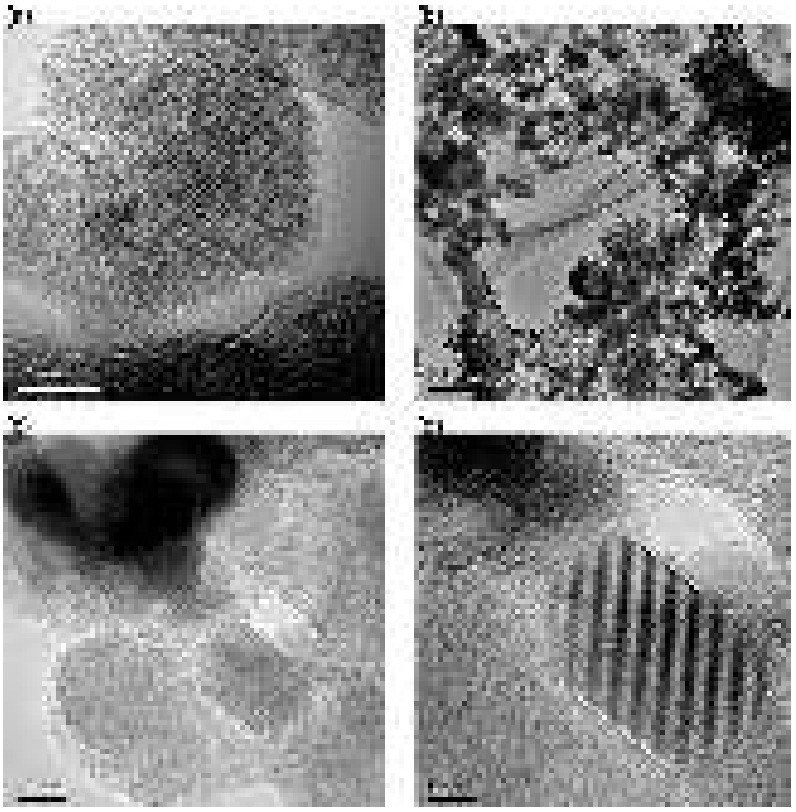

Fig. 10. HRTEM images of initial (a) ST20 (scale bar 10 nm) and (b-d) ST63 at different magnifications at scale bar of (b) 500 nm, (c) 10 nm, and (d) 5 nm.

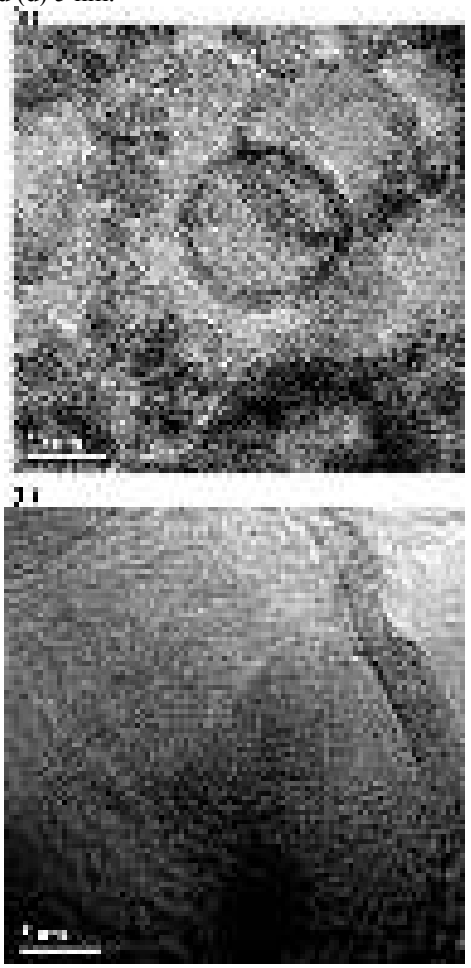

Fig. 11. HRTEM images of initial (a) SA23 and (b) SA75 (scale bar 20 and 5 nm, respectively).

Table 1. Composition, specific surface area (S_{BET}) and pore volume (V_p) of fresh fumed oxides (SCV/SCR method for individual FMO and VCV/SCR for complex FMO) and silica gels (cylindrical pore model).

Sample	C_{SiO_2} (wt%)	C_{TiO_2} (wt%)	$C_{Al_2O_3}$ (wt%)	S_{BET} (m^2/g)	V_p (cm^3/g)
A-50	99.8			52	0.126
A-100	99.8			92	0.155
A-200	99.8			206	0.463
A-300	99.8			294	0.524
A-400	99.8			409	0.859
A-500	99.8			492	0.874
SA1	98.7		1.3	203	0.416
SA3	97		3	185	0.405
SA8	92		8	303	0.688
SA23	77		23	347	0.788
SA30	70		30	238	0.643
SA75	25		75	118	0.320
Al_2O_3			100	125	0.262
ST2	98	2		77	0.263
ST9	91	9		235	0.580
ST14	86	14		156	0.386
ST20	80	20		84	0.174
ST40	60	40		148	0.333
ST63	33	63		84	0.215
ST65	35	65		34	0.080
ST94	6	94		30	0.100
TiO_2		100		42	0.117
AST50	28	50	22	37	0.095
AST71	8	71	21	74	0.127
AST82	6	82	12	39	0.150
AST87	4	87	9	42	0.148
AST88	8	88	4	39	0.123
Si-40	99.9			742	0.636
Si-60	99.9			456	0.822
Si-100	99.9			349	1.225

The presence of CSNP in complex FMO could lead to non-monotonic changes in the surface content of one of the components, *e.g.*, alumina in silica/alumina and alumina/silica/titania [26,27]. Changes in the surface content of an active component (*e.g.*, alumina or titania in binary or ternary FMO based on silica) in complex FMO could strongly affect the interfacial behavior of adsorbates of low and high-molecular weights as well as other important properties [53]. The non-monotonic changes in the surface composition could influence the properties of the final materials (FMO filled polymers, nanocomposites, aqueous suspensions, *etc.*). Therefore, deeper insight into such relationships as properties *vs*. bulk/surface composition of complex FMO (silica/alumina, silica/titania, alumina/silica/titania and other compositions) *vs*. interfacial phenomena, in comparison with related individual FMO affected by certain additional material treatments, is of interest from both theoretical and practical points of view. Many of publications analyzed here were based on investigations of individual fumed oxides (silica and alumina), binary FMO silica/titania (*e.g.*, ST20 and ST63) and silica/alumina (SA23, SA75, and SA96), and ternary alumina/silica/titania AST (AST1, AST50, and AST71) (Table 1) used as the initial powder materials [25-30]. Binary and ternary fumed oxides were prepared by simultaneous high-temperature hydrolysis of the corresponding metal chlorides ($SiCl_4$, $AlCl_3$, $TiCl_4$) [25-30,46-49,53]. Cab-O-Sil HS-5 (Cabot Corporation) was used as the initial material to prepare cryogel and suspended-dried samples.

To prepare high-pressure cryogels with FMO, aqueous suspensions of nanooxides with doubly distilled water or NaCl solution sonicated were frozen at 260 K (for 12 or 24 h) or 208 K (for 12 h) or 77.4 K (for 4 h) in thick-walled stainless-steel reactors at pressures of up to 1050 atm

[46,47]. This high pressure was caused by ice crystallites formed in the frozen suspensions (~10–15 mL) placed in the strongly restricted volume of cryo-bombs. The pressure of ice (~1000 atm) in the cryo-bombs was estimated [46,47] according to [61,62]. Cryonanooxides (CNO) were dried in air at room temperature to air-dry state. The same suspensions prepared at standard conditions were kept at room temperature or 255-260 K for 24 h and 1 atm to prepare gelled or cryogelled samples and then dried to air-dry state. All the final materials studied were prepared in the powder state [46,47].

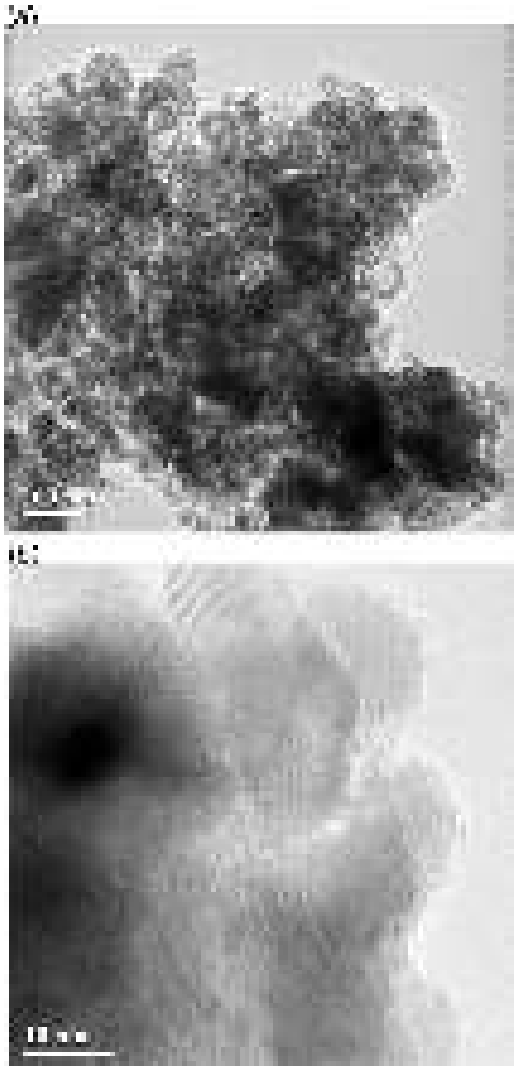

Fig. 12. HRTEM images of fumed complex oxides (a) AST1 and (b) AST71.

Features of nano-particulate morphology of various FMO (Figs. 1-16) depend specifically on the nature, composition and amounts of different oxide components, which could be both crystalline and amorphous (*e.g.,* titania, alumina) or only amorphous (silica). The main feature of FMO containing alumina and/or titania is the formation of core-shell nanoparticles, which clearly manifest as dense alumina aggregates (mono- or polycrystalline cores) with thin silica or alumina shells in SA (Figs. 6a and 11a) and AST (Figs. 3, 4, 9, and 12a) or titania cores (frequently monocrystalline) with a relatively thick silica shell (Figs. 6c,d and 10). Additionally, a decrease in the specific surface area (*i.e.* an increase in the average diameter (*d*) of primary nanoparticles since $S_{BET} \sim 1/d$) of FMO leads to a broadening of the size distribution of primary nanoparticles (Figs. 1-16) [25-30,46-49,53,63]. For SA materials, relatively large CSNP (50 nm in diameter (*d*) or larger) were observed even for SA23 (Figs. 6a and 11a), which exhibits a large S_{BET} value (Table 1) that corresponded to a small average nanoparticle size (for SA23, d_{av} = 6.9 nm).

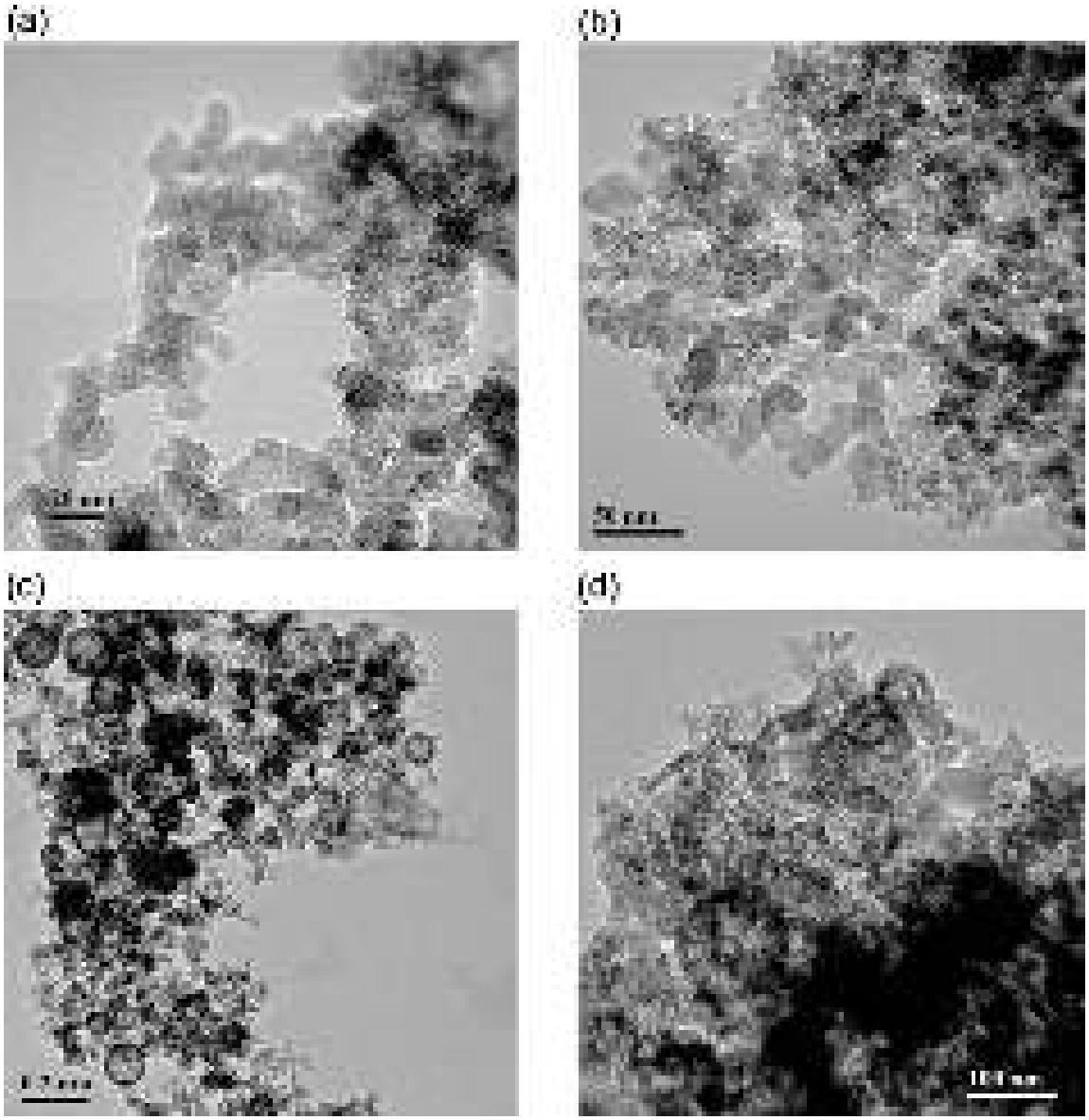

Fig. 13. HRTEM images of A-300 (a) initial and (b) cryogel, and AST1 (c) initial and cryogel.

For AST materials with lower S_{BET} values, CSNP could be 50-200 nm in size, while smaller simple nanoparticles could be also found in these FMO (Figs. 6-13). FMO nanoparticles with titania cores and silica shells are also clearly visible in AST (Figs. 2c,d, 8 and 10). However, complex ST nanoparticles (or AST at high TiO_2 amounts) frequently include only one titania crystallite (anatase/rutile) core with a silica shell (Figs. 14-16). Titania polycrystalline cores were less frequently observed than polycrystalline alumina cores. This difference could be explained by features of the pyrogenic synthesis of complex FMO prepared using such precursors as $TiCl_4$, $SiCl_4$, and Al_2Cl_6 with different properties and reactivity [25-28,64-67].

In our works analyzed here, X-ray diffraction (XRD) patterns (Figs. 14-16) were recorded over 2θ = 10-70° range using a DRON-4-07 (Burevestnik, St. Petersburg) diffractometer with Cu K_α (λ = 0.15418 nm) radiation and a Ni filter. Analysis of the crystalline structure of alumina was carried out using the JCPDS Database (International Center for Diffraction Data, PA, 2001) for γ-Al_2O_3 (JCPDS#29-0063) and α-Al_2O_3 (JCPDS#46-1212).

The crystallinity of complex FMO (Figs. 14-16) increased with decreasing silica content and increasing temperature during the synthesis or treatment [25-30,53,68]. Additionally, silica in complex FMO could delay the phase transition of anatase to rutile or low-temperature aluminas to corundum [53]. The crystallinity of titania in FMO is greater than that of alumina, and silica is

totally amorphous (Figs. 14 and 16); however, preheating of A-300 at 1400 ^{o}C resulted in crystallization of silica to α-cristobalite (Fig. 14d). The mentioned difference in titania and alumina could be explained by the higher reactivity of $TiCl_4$ compared with Al_2Cl_6. The higher reactivity resulted in titania nuclei, protoparticles and nanoparticles growing faster in the flame than alumina nanostructures. These differences appeared in the ^{29}Si and ^{27}Al NMR spectra (Figs. 17 and 18, Table 3), as well as in the surface content of alumina and titania *vs*. their total content in FMO (Fig. 19). The latter is nearly monotonic for titania and non-monotonic for alumina. At low silica content (~5 wt.%) in complex FMO (*e.g.,* ST94, SA96, AST82), silica formed a solid solution in the main phase (titania or alumina). This was indicated by ^{29}Si NMR signals of silica structures with Si-O-Si bonds absent in the spectra.

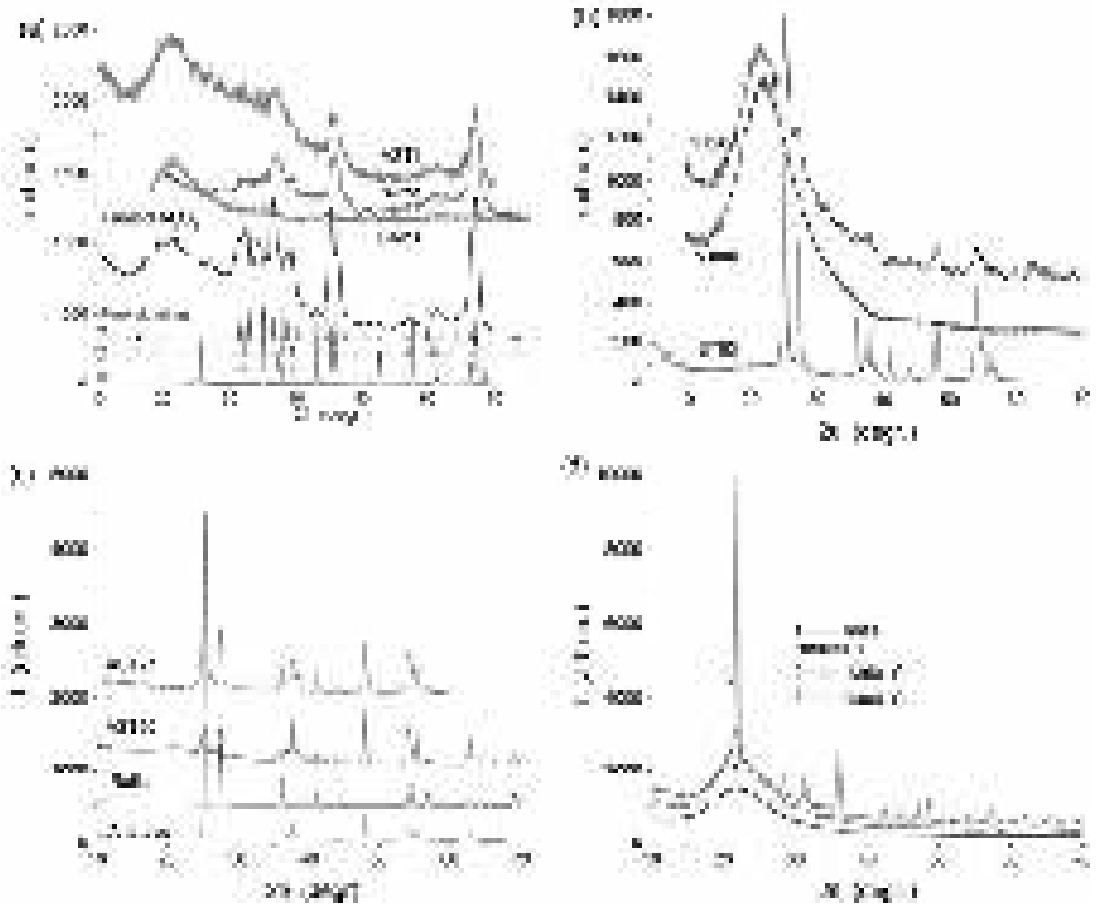

Fig. 14. XRD patterns of FMO: (a) alumina, SA, AST1, (b) ST and A-300, (c) AST and pure anatase and rutile; and (d) initial and heated A-300.

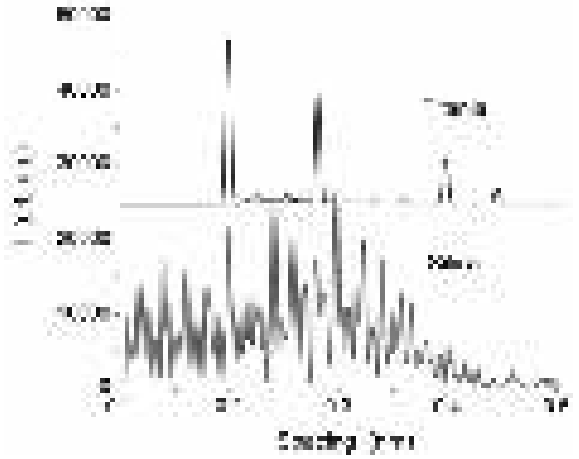

Fig. 15. Spacing distribution function for fumed silica (amorphous) and titania (crystalline) calculated from HRTEM images of A-200 and fumed titania using Fiji software (http://fiji.sc/Fiji).

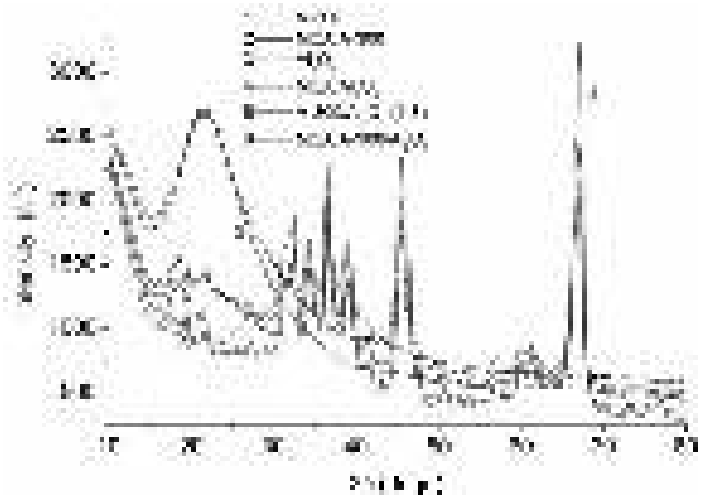

Fig. 16. XRD patterns of initial and MCA silica A-300 and alumina and their blend (1:3) initial and MCA.

Table 2. Textural characteristics of FMO initial and differently treated [46,47,53].

Sample	S_{BET} (m^2/g)	S_{nano} (m^2/g)	S_{meso} (m^2/g)	S_{macro} (m^2/g)	V_p (cm^3/g)	V_{nano} (cm^3/g)	V_{meso} (cm^3/g)	V_{macro} (cm^3/g)
Initial A-300	330	29	288	13	0.826	0.012	0.621	0.193
MCA 6 h A-300	328	85	223	20	1.325	0.019	0.978	0.327
A-300 (II)	303	94	200	10	0.735	0.035	0.523	0.176
A-300 (II) HPCG	297	38	258	2	0.826	0.012	0.798	0.017
Alumina	70	16	51	3	0.181	0.007	0.118	0.056
SA23	347	93	238	15	0.815	0.024	0.526	0.265
SA75	118	13	99	6	0.320	0.002	0.200	0.017
ST20	84	5	76	3	0.179	0.001	0.128	0.050
ST63	84	11	68	5	0.215	0.002	0.123	0.090
Initial AST1	78	12	62	4	0.234	0.006	0.156	0.072
MCA 30 min AST1	60	6	50	4	0.308	0.003	0.237	0.068
ATS1 HPCG	143	49	92	2	0.594	0.016	0.544	0.034
AST50	37	7	29	1	0.084	0.001	0.054	0.029
AST71	74	12	60	2	0.127	0.002	0.076	0.049
Initial A-300/AST1 (1/1)	184	19	158	7	0.481	0.005	0.366	0.110
MCA 30 min A-300/AST1	142	17	118	7	0.456	0.004	0.324	0.128
A-300/AST1 HPCG	145	41	53	51	1.077	0.010	0.190	0.877

Note. The V_{nano} and S_{nano} values were calculated by integration of the $f_V(R)$ and $f_S(R)$ function, respectively, at 0.35 nm < R < 1 nm, V_{meso} and S_{meso} at 1 nm < R < 25 nm, and V_{macro} and S_{macro} at 25 nm < R < 100 nm. Cryogels with A-300 and A-300/AST1 were prepared (20 wt.% and 14 wt.% suspensions, respectively) at 208 K and ~1000 atm for 12 h. AST1 cryogel was prepared (sonicated 20 wt.% suspension) in a cryo-bomb at 260 K for 24 h and 77.4 K for 4 h at ~1000 atm.

The surface chemistry of the silica powders was further characterized via solid state ^{29}Si NMR analysis using a 400 MHz Bruker Avance FT-NMR spectrometer (Bruker Corporation, Billerica, MA, USA). Cross polarization and magic angle spinning (CP/MAS) were utilized to increase ^{29}Si signal intensity and to overcome signal broadening associated with solid state NMR. A 4 mm probe was used, the number of scans was 16,384 (a run time of about 14 hours), the sweep width was 30 kHz (380 ppm), the delay time between scans was 3.00 seconds and the CP contact time was 6 ms. The transmitter frequency (SFO1) for the Si nucleus was 79.4886563 MHz, while the transmitter frequency used for the ^{1}H nucleus was 400.1314005 MHz. Solid-state ^{1}H MAS NMR spectra were recorded at a spin speed of 10 kHz and a recycle delay of 1 s, and adamantane was used as a reference. For complex FMO, the ^{29}Si (resonance frequency 59.595 MHz) cross-polarization spinning at the magic angle (CP/MAS) NMR spectra and the ^{27}Al (resonance frequency 78.172 MHz) MAS NMR spectra (program ZG) of complex oxides were recorded by a Bruker Avance™ 300 NMR spectrometer (magnetic field of 7.046 Tesla, a spinning rate of 8 kHz of 4 mm zirconia rotor). Chemical shifts of ^{29}Si and ^{27}Al were referenced to

tetramethylsilane and an $Al(NO_3)_3$ aqueous solution respectively; i.e., the resonance of $Si(CH_3)_4$ and $Al(H_2O)_6^{3+}$ was set to 0 ppm (Fig. 18, Table 3).

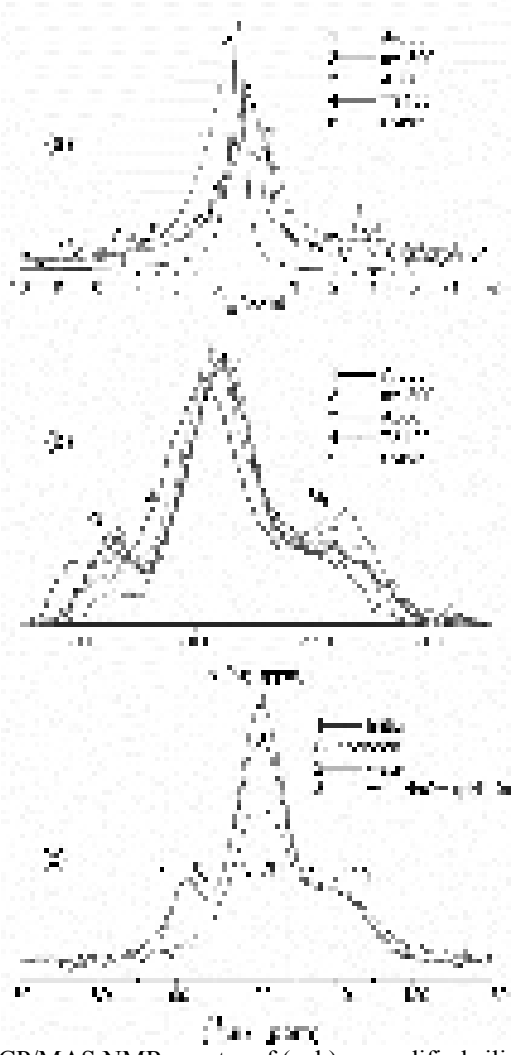

Fig. 17. (a) ^{1}H MAS and (b, c) ^{29}Si CP/MAS NMR spectra of (a, b) unmodified silicas and (c) initial Cab-O-Sil HS-5, suspended-dried and suspended in NAOH solution (pH 10) and dried. $=Si(OH)_2$, $\equiv SiOH$, and $Si(OSi\equiv)_4$ correspond to Q^2_{Si}, Q^3_{Si} and Q^4_{Si} sites at –91, –100, and –110 ppm, respectively. Silicas: fumed silica A-300 (Pilot plant of Chuiko Institute of Surface Chemistry, Kalush, Ukraine) preheated at 450 °C for 2 h; preheated A-300 hydro-compacted with water (1:2 w/w), stirred for 10 min, and then heated at 105 °C for 8 h (cA-300); fumed silica A300 (Evonik) preheated at 450 °C for 2 h; silica TS 100 (Evonik Ind.); Syloid® 244 (precipitated silica, Grace Davidson), and Cab-O-Sil HS-5 (Cabot Corporation).

Table 3. Contributions (in %) of different centers with Si and Al in SA, ST and AST samples determined as relative integral intensity of the bands obtained on deconvolution of the ^{29}Si CP/MAS and ^{27}Al MAS NMR spectra.

Sample	Q^4_{Si}	Q^3_{Si}	Q^2_{Si}	$Q_{Al(VI)}$	$Q_{Al(V)}$	$Q_{Al(IV)}$
SA1	45.7	33.3	21.0	60.3		39.7
SA3	31.1	52.6	14.2	77.9	1	21.1
SA8	48.0	45.0	7.0	73.4		26.6
SA23	45.5	33.4	21.1	55.9	3.5	40.6
SA30	28.8	50.7	20.5	51.0	4.2	44.8
ST9	33.6	44.7	21.7			
ST14	44.0	31.8	24.2			
ST20	29.1	54.6	16.3			
ST63	57.3	16.6	26.1			
ST65	64.9	19.5	15.6			
AST50	68.1	23.6	8.3	86.2		13.8
AST82				94.1	3.4	2.5

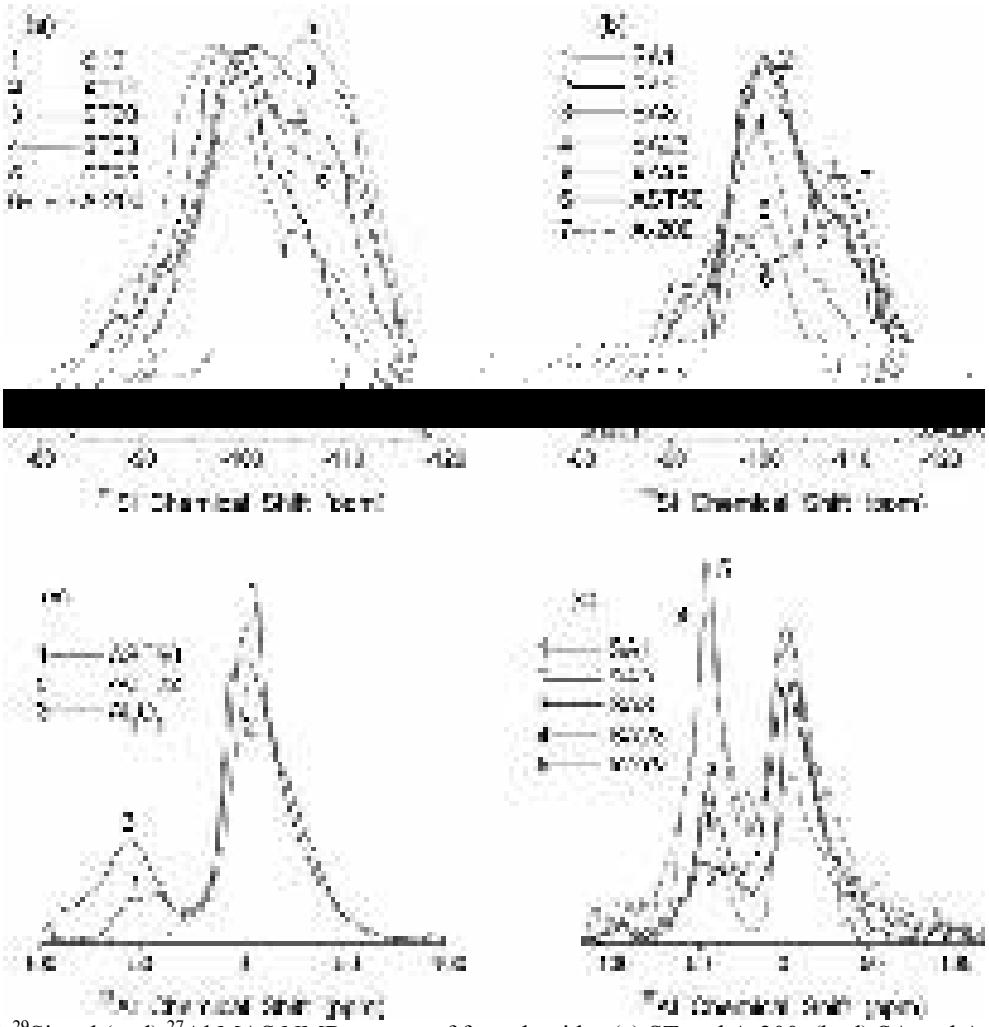

Fig. 18. (a, b) ^{29}Si and (c, d) ^{27}Al MAS NMR spectra of fumed oxides (a) ST and A-200, (b, d) SA and A-200, and (c) AST and Al_2O_3 samples.

The properties of FMO could be easily changed by modification of a nanoparticle surface using functionalization by various silanes or other reagents [69-73], treatment in plasma [74], mechano-chemical activation [75,76] or by grafting of another oxide (*e.g.*, titania, zirconia, iron oxide) onto silica matrices [53,77-82]. Note that similar nanomaterials could be synthesized at low temperature in liquid media [83], *e.g.*, precipitated silica or complex oxides. All these modifications of FMO change morphological, structural, and textural characteristics of the materials, and, therefore, the interfacial behavior of adsorbates [53].

Total chemical composition of complex oxides (Fig. 19) was analyzed by XRF (Canberra, USA) spectrophotometer with a ^{55}Fe (or ^{109}Cd) radioactive source and an amplitude analyzer (Canberra) coupled with a computer with the AXIL program. The titania phase in titania-containing samples (at $C_{TiO_2} \geq 50$ wt.%) consists of a blend of anatase and rutile at $C_{\text{anatase}}/C_{\text{rutile}}$ between 7.3 (AST50) and 0.84 (ST65). In the case of low amounts of titania in ST, the titania phase consists of a major portion of anatase with a minor contribution of amorphous oxide distributed in the silica matrix. All silica samples as well as silica and alumina in complex oxides are amorphous. Initial fumed alumina is mainly amorphous with approximately 20% of a crystalline (γ-Al_2O_3) phase (impurities 0.5 wt.% of metal oxides, mainly Fe_2O_3 (< 0.25 wt.%) and TiO_2 (< 0.16%)).

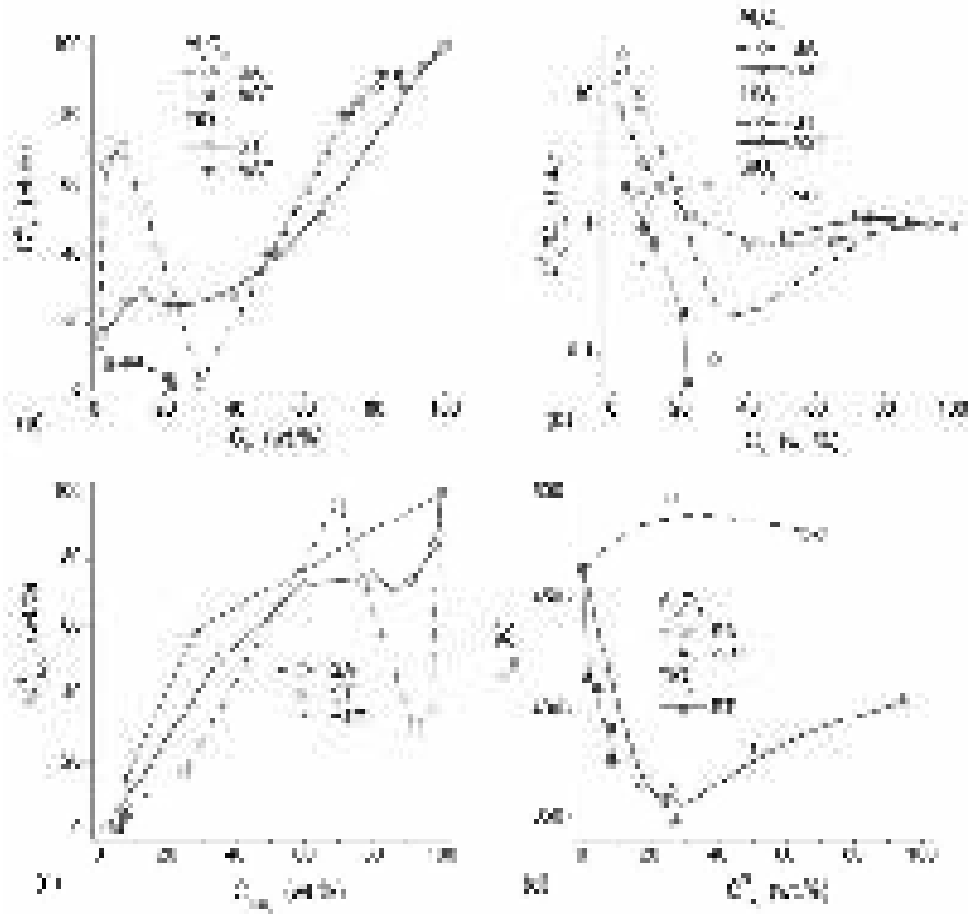

Fig. 19. Relationships between total C_X and surface content C_X^S of (a) alumina and titania, (c) silica in SA, ST and AST samples; (b) relationship between ratio C_X^S/C_X and the total content of the second phases, and (d) relationship between the surface content of alumina or titania and the peak temperature of TPD MS thermograms of desorbed water.

Surface content of aluminum (at%) in SA and AST and titanium in ST and AST (Fig. 19) was determined by Auger electron spectra (AES) recorded by a JAMP-10S (JEOL) spectrometer. The nanooxide powders were prepared with an indium/carbon matrix to avoid the charge buildup on the dielectric samples. The spectra with minimum intensity of the indium and carbon lines were selected for subsequent analysis. Sample regions most characteristic and optimum for the AES studies were determined by the electron scanning microscopy (energy of electron beam 5 keV, beam current 2×10^{-10} A, beam diameter 0.05-0.1 μm). The differential Auger electron spectra $E\times dN(E)/dE$ were recorded with an energy analyzer such as a "cylindrical mirror" with the energy resolution of $\Delta E/E$ = 0.007, a step of 1 eV, modulation amplitude of voltage on the energy analyzer 4 V, circuit voltage 2.5 kV, and the time constant of the amplification circuit of 1 s. The surface Si and Al contents were determined by the analysis of the LVV lines, and the surface titanium content was estimated using the LMM line.

The NMR spectra show that the state of the Si atoms depends more strongly on the treatment of silica (Fig. 17c) or the presence of another phase (Fig. 18) than on a type of initial silica (Fig. 17b). Additionally, nonuniform distribution of the various phases in FMO NPNP (Fig. 19) can strongly affect the properties of the materials (e.g. Fig. 19d).

Textural characteristics of FMO

To analyze the textural characteristics of nanooxides (typically degassed at 373-473 K for several hours, Table 1), low-temperature (77.4 K) nitrogen adsorption–desorption isotherms were recorded using Micromeritics ASAP 2405N or ASAP 2420 adsorption analyzers, Quantachrome Autosorb adsorption analyzers or other apparatuses [25-30,46-49,53,63-83]. The specific surface

area (S_{BET}) was calculated according to the standard BET method [84]. The total pore volume V_p was evaluated from the nitrogen adsorption at $p/p_0 \approx 0.99$, where p and p_0 denote the equilibrium and saturation pressure of nitrogen at 77.4 K, respectively [85]. The nitrogen desorption data were used to compute the pore size distributions (PSD, differential $f_V(R) \sim dV_p/dR$ and $f_S(R) \sim dS/dR$) using DFT method or a self-consistent regularization (SCR) procedure [86] under non-negativity condition ($f_V(R) \geq 0$ at any pore radius R) at a fixed regularization parameter $\alpha = 0.01$ using a complex pore model applied with slit-shaped (S) and cylindrical (C) pores and voids (V) between spherical nonporous nanoparticles packed in ordered or random aggregates (SCV/SCR for individual FMO or VCV/SCR for complex FMO) [86]

$$A = \int_{r_{min}}^{r_k(p)} f(R_p)dR_p + \int_{r_k(p)}^{r_{max}} \frac{w}{R_p} t(p,R_p) f(R_p)dR_p \tag{1}$$

where r_{min} and r_{max} are the minimal and maximal half-width or pore radius, respectively; $w = 1$ (slit-like pores), 2 (cylindrical pores) and 1.36 (voids between spherical particles packed in a cubic lattice);

$$r_k(p) = t(p,R_p) + \frac{2\gamma v_m \cos\theta}{R_g T \ln(p_0/p)} \tag{2}$$

$$t(p,R_p) = \frac{a_m}{S_{BET}} \frac{cz}{(1-z)} \frac{[1+(nb/2-n/2)z^{n-1} - (nb+1)z^n + (nb/2+n/2)z^{n+1}]}{[1+(c-1)z+(cb/2-c/2)z^n - (cb/2+c/2)z^{n+1}]} \tag{3}$$

$b = exp(\Delta\varepsilon/R_gT)$; $\Delta\varepsilon$ is the excess of the evaporation heat due to the interference of the layering on the opposite wall of pores (determined as a varied parameter using local isotherm approximation, LIA); $t(p,R_p)$ is the statistical thickness of adsorbed layer; a_m is the BET monolayer capacity; $c = c_s \exp((Q_p - Q_s)/R_gT)$; c_s is the BET coefficient for adsorption on flat surface (calculated using LIA); Q_s and Q_p are the adsorption heat on flat surface and in pores, respectively; $z = p/p_0$; $n = R_p/t_m$ is the number (noninteger) of statistical monolayers of adsorbate molecules. Desorption data were utilized to compute the $f(R_p)$ distribution with Eq. (1) using a regularization procedure under non-negativity condition ($f_V(R_p) \geq 0$ at any R_p), at a fixed regularization parameter $\alpha = 0.01$. A model of a pore mixture with slitshaped and cylindrical pores and voids between spherical nanoparticles packed in random aggregates (SCV model, MND method) was developed [86] because the standard pore models with slitshaped or cylindrical pores are inappropriate to describe the textural porosity of nanosilicas. The self-consistent regularization (SCR) procedure was used to calculate the PSDs and to determine contributions of different types of pores to the pore volume. The $f_V(R_p)$ functions linked to pore volume can be transformed to the $f_S(R_p)$ distribution functions with respect to surface area using the corresponding pore models

$$f_S(R_p) = \frac{w}{R_p}(f_V(R_p) - \frac{V_p}{R_p}) \tag{4}$$

where $w = 1$, 2, 3, and 1.36 for slitlike, cylindrical, spherical pores and gaps between spherical particles packed in the cubic lattice. The $f_V(R_p)$ and $f_S(R_p)$ functions were used to calculate contributions of nanopores (V_{nano} and S_{nano} at the pore radius $R_p < 1$ nm), mesopores (V_{meso} and S_{meso} at 1 nm $\leq R_p \leq$ 25 nm), and macropores (V_{macro} and S_{macro} at $R_p > 25$ nm) to the total pore volume and the specific surface area. The values of S_{nano}, S_{meso}, and S_{macro} were corrected that $S_{nano} + S_{meso} + S_{macro} = S_{BET}$. For estimation of deviation of the pore shape from the model, a criterion $\Delta w = S_{BET}/S_{sum} - 1$ where

$$S_{sum} = \sum_j c_j \int_{R_{min}}^{R_{max}} f_{S,j}(R_p)dR_p = \sum_j c_j \int_{R_{min}}^{R_{max}} \frac{w_j}{R_p}(f_{V,j}(R_p) - \frac{V_{p,j}}{R_p})dR_p\ , \tag{5}$$

c_j is the weight coefficient, $R_{min} = 0.3$ nm, $R_{max} = 100$ nm, j denotes a pore model, $f_{S,j}(R_p)$ is the differential distribution function with respect to the specific surface area of pores of the j-th type. The integral adsorption equation (1) may be re-written as follows

$$A_{\Sigma}(p) = \sum_j c_j A_j(p) = \sum_j c_j \left[\int_{r_{\min}}^{r_{k,j}(p)} f_{V,j}(R)dR + \int_{r_{k,j}(p)}^{r_{\max,j}} \frac{w_j}{R - \sigma_{sf}/2} t_j(p, R, \varphi(a)) f_{V,j}(R)dR \right], \quad (6)$$

where $f_{V,j}(R)$ is the PSD for the j-th type of pores, w_j is the pore type formfactor (1 for slit, 2 for cylindrical, 1.36 for voids between spherical particles packed in a cubic lattice), $c_j = c_{slit}$, c_{cyl}, and c_{void} are the weight constants ($c_{slit} + c_{cyl} + c_{void} = 1$) determining contributions of slitshaped and cylindrical pores and voids between spherical particles to the volume filled by adsorbate at pressure p ($A_{\Sigma}(p)$); $r_{k,j}$ is the half-width of slit pores, the radius of cylindrical pores or meniscus radius for voids determined through modified Kelvin equation including the thickness of the adsorbate layer t_j. In the case of the presence of nanoparticles ($c_j = c_{void}$) characterized by the size distribution function φ(a), Eq. (6) can be re-written with additional integral in the second term (Vφ/SCR method)

$$\int_{r_{k,j}(p)}^{r_{\max,j}} \frac{w_j}{R - \sigma_{sf}/2} f_{V,j}(R) \int_{a_{\min}}^{a_{\max}} t_j(p, R, a)\varphi(a)da \quad (7)$$

which is due to a certain distribution function of nanoparticle sizes becoming broader with decreasing S_{BET} value of fumed oxides. The c_j values were determined for the best fitting of the experimental isotherms using self-consisting regularization procedure with several steps in solution of the sum of integral equations. $\sigma_{sf} = (\sigma_s + \sigma_f)/2$ is the average collision diameter of surface and fluid atoms; $r_{k,j}$ is determined through modified Kelvin equation including the thickness of the adsorbate layer t_j. Lennard–Jones potential was used for slitshaped and cylindrical pores and gaps between spherical particles. This method gives better results than that used previously for complex adsorbents with one distribution function for all the pore shape models because of the use of independent $f_{V,j}(R_p)$ functions for each pore type. For a pictorial presentation of the pore size distributions, the $f_V(R_p)$ functions were re-calculated to incremental PSDs (IPSDs)

$$\Phi_V(R_{p,i}) = 0.5(f_V(R_{p,i}) + f_V(R_{p,i-1}))(R_{p,i} - R_{p,i-1}). \quad (8)$$

Additionally, $f_S(R)$ was used to estimate the deviation (Δw) of the pore shape from the model using a self-consisting (to better fit the nitrogen adsorption isotherms) regularization in the case of the use of a complex model of the pore shape

$$\Delta w = \frac{S_{BET}}{\int_{R_{\min}}^{R_{\max}} f_S(R)dR} - 1 \quad (9)$$

where $R_{\max}$ and $R_{\min}$ are the maximal and minimal pore radii respectively. The S^*_{nano}, S^*_{meso} and S^*_{macro} values were corrected by multiplication by (Δw+1) that gives $S^*(\Delta w + 1) = S_{sum} = S_{nano} + S_{meso} + S_{macro} = S_{BET}$. The effective w value (w_{ef}) can be estimated with equation

$$w_{ef} = \frac{S_{BET}}{V_p} \frac{\int_{R_{\min}}^{R_{\max}} R f_V(R)dR}{\int_{R_{\min}}^{R_{\max}} f_V(R)dR} \quad (10)$$

The specific surface area (S_{φ}) of materials composed of spherical nanoparticles characterized by the particle size distribution φ(a) (calculated using the self-consisting regularization for $f_V(R)$ and $\varphi(a)$ with the model of voids between spherical particles) can be calculated with equation

$$S_{\varphi} = \int_{a_{\min}}^{a_{\max}} \frac{3}{2a^3\rho} \left[2(a+t)^2 + Nr_m \arcsin\left(\frac{a}{A}\right)\sqrt{A^2 - a^2} - N(a+t)\left(\frac{ar_m}{A} + t\right) \right] \varphi(a)da \quad (11)$$

where $A = a + t + r_m$, a is the particle radius, ρ the density of material, N the average coordination number of nanoparticles in aggregates, t the thickness of an adsorbed nitrogen layer, and r_m is the

meniscus radius determined at $0.05 < p/p_0 < 0.2$ corresponding to the effective radius R of voids between spherical particles. Condition $S_\varphi = S_{BET}$ can be used to estimate the N value. An additional criterion $|<S_\varphi> - S_{BET}| < 1$ m^2/g was used to determine the a_{min} and a_{max} values for the $\varphi(a)$ distributions calculated at $p/p_0 < 0.5$ (*i.e.* before capillary condensation starts) with

$$< S_\varphi >= \frac{\iint S_\varphi(r_m, t)dtdr_m}{\iint dtdr_m}. \quad (12)$$

The values of $<R_V>$ and $<R_S>$ as the average pore radii calculated as a ratio of the first moment of $f_V(R)$ or $f_S(R)$ to the zero moment

$$<R> = \int f(R)RdR/\int f(R)dR \quad (13)$$

The $f_V(R)$ and $f_S(R)$ functions were also used to calculate contributions of nanopores (V_{nano} and S_{nano} at 0.35 nm < R < 1 nm), mesopores (V_{meso} and S_{meso} at 1 nm < R < 25 nm), and macropores (V_{macro} and S_{macro} at 25 nm < R < 100 nm) [86]. The morphology of primary nanoparticles as well as of particles of higher hierarchic levels is typical and nearly the same for all individual and complex fumed oxides [53,63-83]. However, the difference in the structure of active surface sites of acidic or basic characters could affect the interfacial behavior of adsorbates, even nonpolar such as nitrogen. For example, the interaction energy is higher on the adsorption of nitrogen molecules on titania than on silica or alumina due to stronger dispersive, electrostatic (–13.3, –9.5, and –5.4 kJ/mol) and charge transfer (–5.2, –2.9, and –1.6 kJ/mol) interactions in complexes –O–H···N≡N with TiO(H)Ti, SiO(H)Al and SiOH groups, respectively [53], according to the Kitaura-Morokuma analysis of these complexes using the GAMESS program suit with the 6-31G(d,p) basis set [87,88]. Both structural and energetic factors caused a small difference in the nitrogen adsorption at very low pressures $p/p_0 < 10^{-4}$ (Fig. 20a) [88]. This resulted in the same shape of normalized adsorption isotherms $\Theta(p/p_0)$ (Fig. 20a) despite the difference in the particle size distributions (PaSD) as well as in the values of S_{BET} of FMO. This similarity is better seen for derivatives $d\Theta/d(p/p_0)$ (Fig. 20b). However, there is some difference in the nitrogen adsorption energy distributions for these FMO (Fig. 20c) because of the effects of the chemical structure of silica, alumina, titania and related binary and ternary systems possessing different types and amounts of terminal and bridging hydroxyls of different acidity. Notice that these factors could more strongly affect the adsorption/desorption of water because of its more specific interactions with FMO [53].

Heating of nanosilica at different temperatures (over the 473-1173 K range) for different time (10 min – 5 h) weakly affected the morphology of particles (Fig. 21a,b) [88]. However, heating of nanosilica to 1673 K led to formation of α-cristobalite (Fig. 14d). In contrast to the nitrogen adsorption on various FMO when their difference appeared at low pressures (Fig. 20) heating of nanosilicas led to a larger difference in the adsorption at higher pressures. This was due to changes in the characteristics of both primary and secondary particles that are well seen for PSD (Fig. 21c) more sensitive to heating than the normalized isotherms because these changes were over the total range of the pore size caused by associative desorption of water from both surface and bulk of primary particles. Therefore, the specific surface area depended on treatment conditions (Fig. 22) since the $|\Delta S_{BET}/S_{BET}|$ values change over a wide range up to ~0.3 on heating at 1173 K for 2 h [88]. It should be noted that both $\Theta(p/p_0)$ and $d\Theta/d(p/p_0)$ functions are sensitive to changes in the particle morphology. This is well seen for a set of silicas: fumed silicas – silica gels – mesoporous ordered silicas (Fig. 23) [88]. However, these differences appear mainly at $p/p_0 > 0.4$ when capillary condensation starts in mesopores of various shapes, and this effect depend on PSD and topology of pores. Additionally, the $d\Theta/d(p/p_0)$ curve shapes differ at $p/p_0 < 0.02$ for porous and fumed silicas (Fig. 23c) due to the presence of narrow pores in the first one in contrast to nanosilicas loosely composed with nonporous primary nanoparticles practically without the formation of nanopores (R < 1 nm) between them.

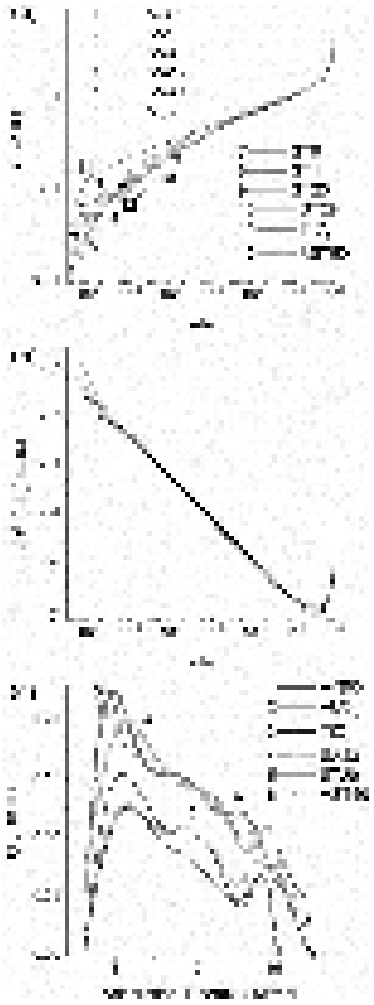

Fig. 20. (a) Relative adsorption of nitrogen ($\Theta = a/a_m$) and (b) derivatives $d\Theta/d(p/p_0)$ as function of relative pressure; and (c) adsorption energy distributions $f(E)$ for set of fumed oxides (A-300, Al_2O_3, TiO_2, SA1, SA3, SA23, SA30, ST9, ST14, ST20, ST29, AST50).

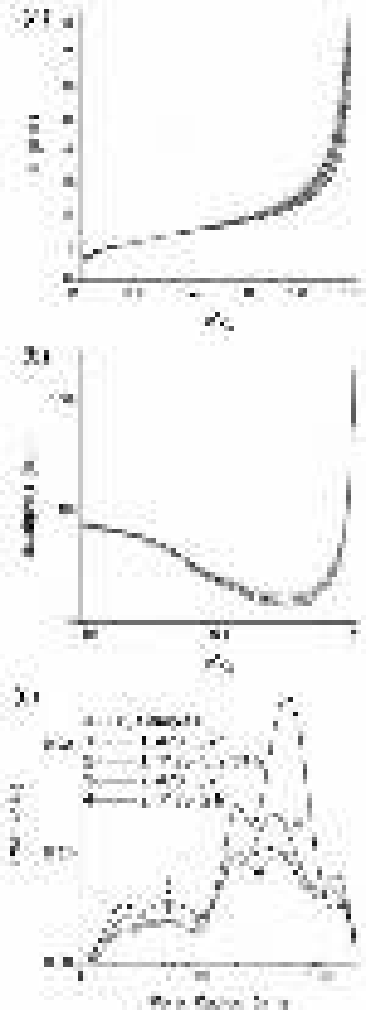

Fig. 21. (a) Relative adsorption of nitrogen ($\Theta = a/a_m$) and (b) derivatives $d\Theta/d(p/p_0)$ as function of relative pressure; and (c) DFT IPSD (model of voids between spherical particles) for two samples of A-300 (weight loss of 3.2 and 1.3 wt.% on heating to 1173 K and bulk density of 0.024 and 0.028 g/dm^3, respectively) heated at different temperatures (473, 573, 873, and 1173 K) for different time (from 10 min to 5 h).

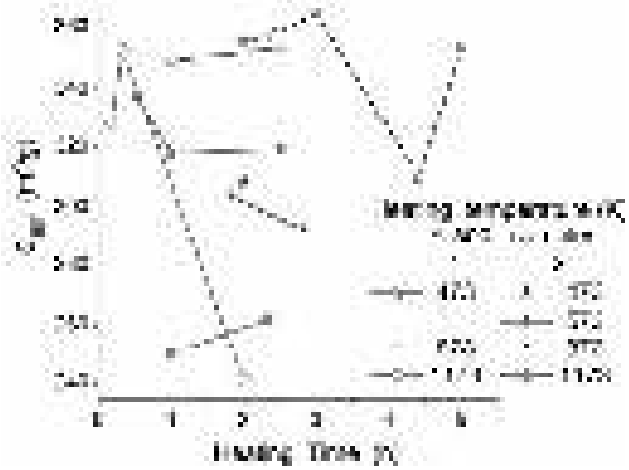

Fig. 22. Changes in the specific surface area of two samples A-300 heated at different temperatures.

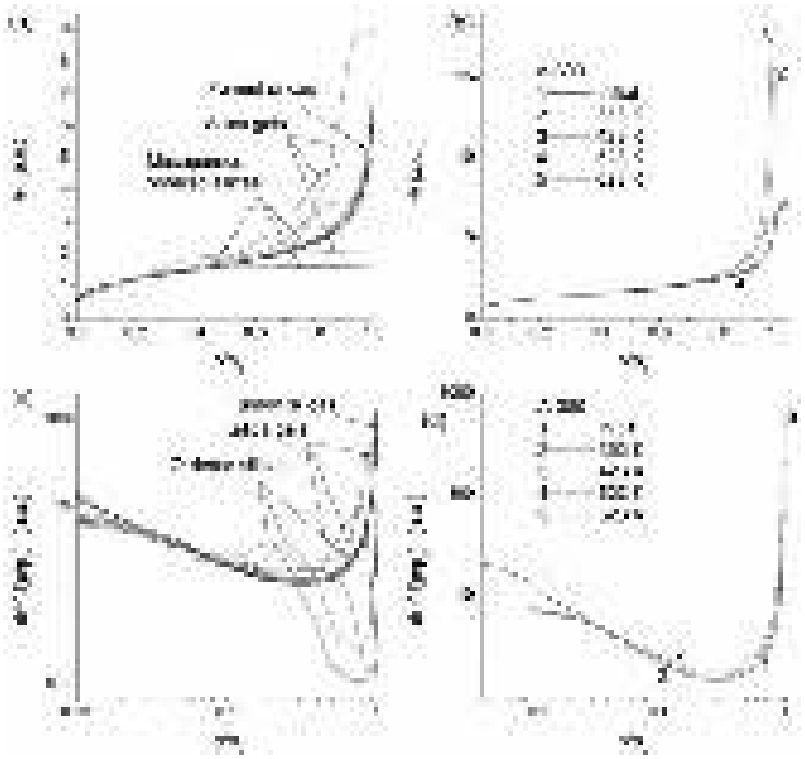

Fig. 23. (a, b) Relative adsorption of nitrogen ($\Theta = a/a_m$) and (c, d) derivatives $d\Theta/d(p/p_0)$ as function of relative pressure for (a, c) fumed silicas (A-50, A-100, A-200, A-300, A-400, and A-500), silica gels (Si-40, Si-60, and Si-100) and mesoporous ordered silicas (MCM-41, MCM-48 and SBA-15); and (b, d) A-300 initial (1), wetted-dried (2), and dried after hydrothermal treatment at different temperatures (curves 3-5).

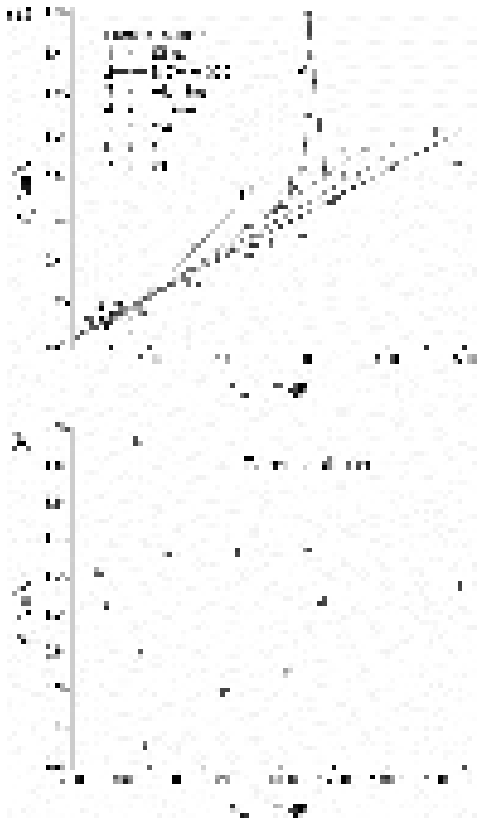

Fig. 24. Relationship between the specific surface area (S_{BET}) and the pore volume (V_p) for (a) initial various individual (silica, alumina, and titania), binary (silica/alumina, SA, and silica/titania, ST) and ternary (alumina/silica/titania, AST) fumed oxides and MCA A-300; and (b) porous silica gels (Si-40, Si-60, and Si-100) and mesoporous ordered silicas (MCM-41, MCM-48, and SBA-15) [53].

The presence of pores with a narrow PSD in ordered silicas or silica gels causes appearance of a maximum in the $d\Theta/d(p/p_0)$ curves at $0.2 < p/p_0 < 0.85$ depending on the size of these pores, since the narrower the pores, the lower the pressure of this maximum [88]. Fumed oxides do not have ordered structure of pores; therefore, a similar $d\Theta/d(p/p_0)$ maximum is absent. A similar maximum was absent after hydrothermal treatments of fumed silica A-300 at different temperatures (Fig. 23d) despite significant re-arrangement of primary particles and changes in their size [53,89]. Additionally, a similar maximum was absent on suspending of nanosilica ($C_{A\text{-}300}$ = 1-20 wt.%), sonication, drying on air, and heating at 473 K for 2 h [53]. Consequently, fumed oxides are morphologically relatively stable with respect to primary nanoparticles, but secondary structures are 'soft' and could be easily rearranged.

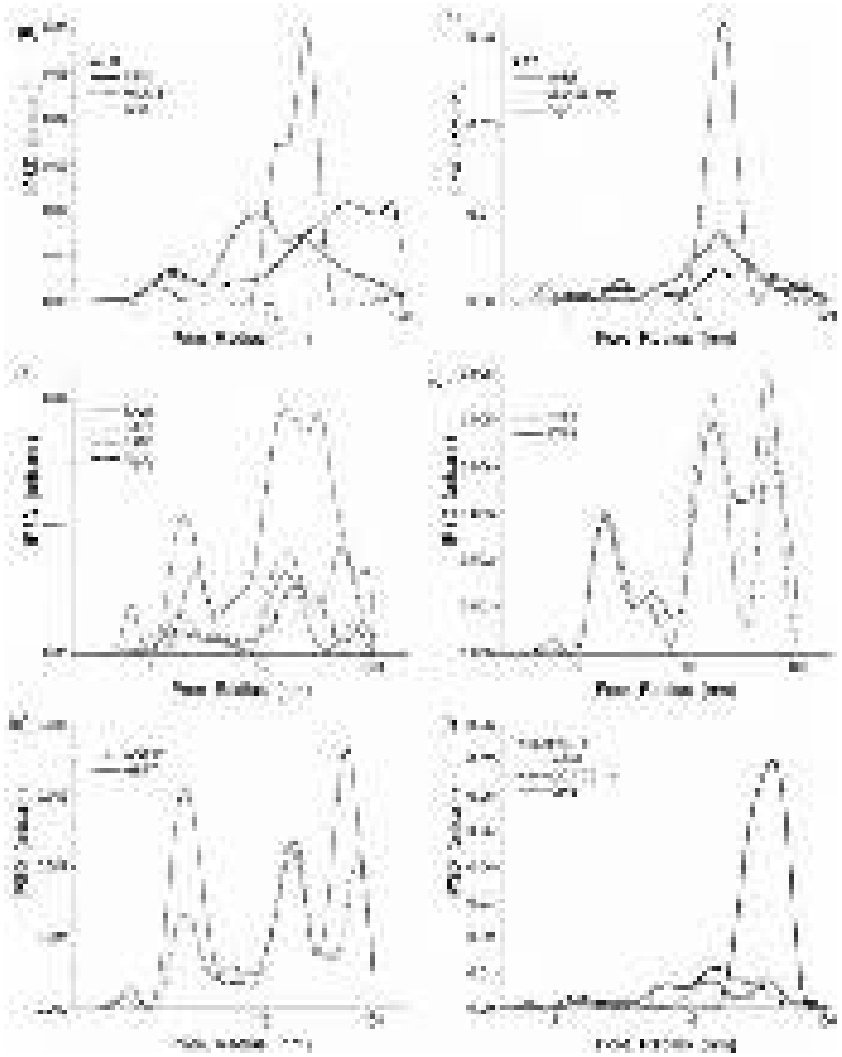

Fig. 25. Pore size distributions (SCV/SCR) of initial and differently treated FMO (a) A-300 initial, ball-milled for 6 h and cryogel prepared in a cryo-bomb (using sonicated 20 wt.% aqueous suspension) at 208 K and ~1000 atm for 12 h, (b) AST1 initial, MCA in a microbreaker for 30 min and cryogel using sonicated 20 wt.% aqueous suspension frozen in a cryo-bomb at 260 K for 24 h and 77.4 K for 4 h at ~1000 atm, (c) initial SA and alumina, (d) initial ST, (e) initial AST, and (f) A-300/AST1 (1:1) initial, MCA in a microbreaker for 30 min and cryogel (using sonicated 14 wt.% aqueous suspension) prepared in a cryo-bomb at 208 K and ~1000 atm for 12 h.

The adsorption isotherms of nitrogen could be used to determine not only the values of S_{BET} and V_p and the PSD functions but also the primary particle size distributions (PPSD) using pair integral equations related to PSD and PPSD and solved with the self-consistent regularization procedure [86,88]. Heating of nanooxides causes several processes (such as dehydration of the surface and the bulk of primary particles, chemical binding of adjacent nanoparticles due to

condensation of hydroxyls, rearrangement of secondary and ternary particles) that result in structural changes of nanooxides depending on the heating temperature. As a whole the morphology of primary nanoparticles of fumed oxides is stable on different treatments in contrast to the structure of secondary particles and especially higher level particles [53,88,89].

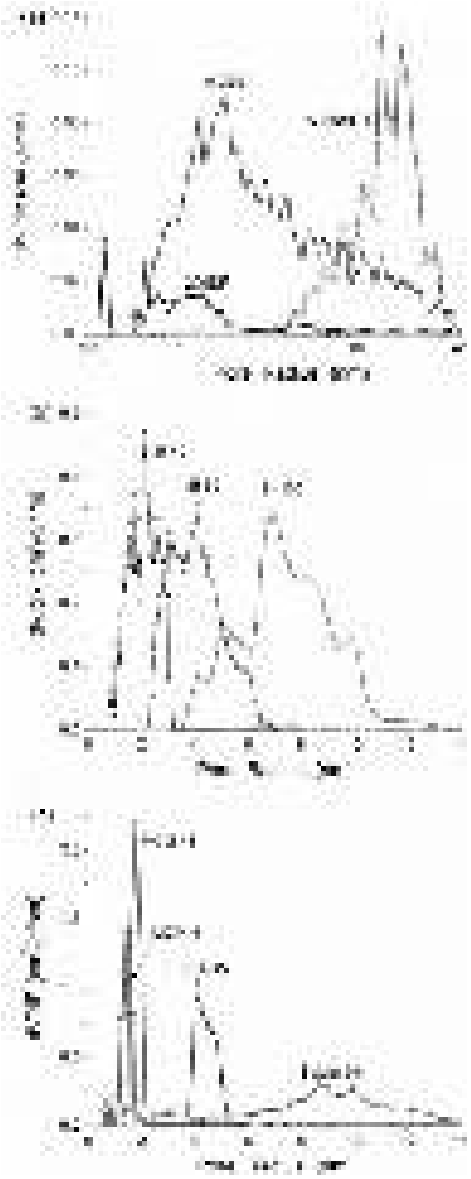

Fig. **26.** NLDFT pore size distributions of (a) fumed silica A-380 initial and after hydrothermal treatment at 150 °C (A-380HTT) and silica gel 200DF Gasil; (b) silica gels Si-40, Si-60, and Si-100; and (c) precipitated silica Syloid 244 and mesoporous ordered silicas MCM-41, MCM-48 and SBA-15.

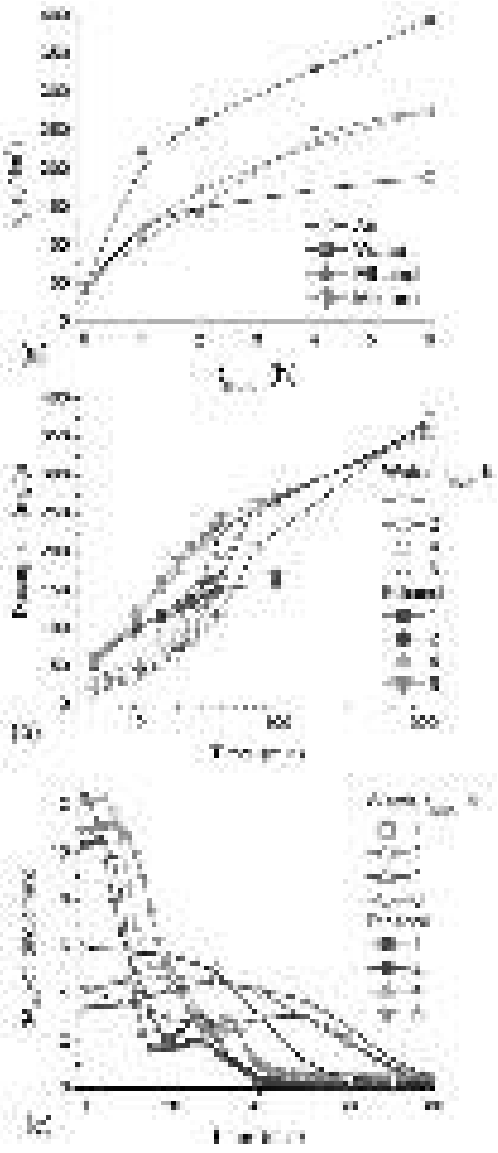

Fig. 27. (a) Bulk density of the silica powders (dried in air for 24 h) treated in different media (air and water, ethanol or water/ethanol ~0.5 g per gram of dry silica) as a function of MCA time; (b) desorption (in air at room temperature) of water or ethanol from MCA-treated silicas, and (c) corresponding desorption rate as a function of time at the initial fast stage of the desorption.

Typically, FMO with increasing S_{BET} value (*i.e.*, with decreasing size of primary particles) are characterized by increased pore volume (V_p) due to enhanced agglomeration of nanoparticles of smaller sizes (Fig. 24). The empty volume in the FMO powders can be about 95% [53]. For example, ρ_b = 0.045 and 0.13 g/cm^3 for A-300 and A-50, respectively, that correspond to V_{em} = 21.8 and 7.2 cm^3/g; however, the V_p values are much lower (0.524 and 0.126 cm^3/g, Table 1).

Voids between nonporous nanoparticles in secondary structures determine the textural porosity of the powders.

These are several types of voids between nanoparticles in FMO. Voids between adjacent nanoparticles contribute nanopores at R < 1 nm, and narrow mesopores at 1 nm < R < 3-5 nm. Neighboring nanoparticles in the same aggregate give narrow mesopores, while distant nanoparticles in the same aggregate, or from neighboring aggregates, contribute to broader mesopores or macropores. Larger voids between nanoparticles from neighboring aggregates in agglomerates give rise to macropores. Voids between agglomerates correspond to large macropores, which remained practically empty during adsorption of nitrogen even at p/p_0 close to 1. All these voids give 4-6 peaks in the PSD (Fig. 14) [90]. Practically any treatment led to an increase in the bulk density of the FMO powders [53]. The secondary structures (aggregates of primary nanoparticles and agglomerates of aggregates) became denser and the PSD profiles changed (Figs. 25a,b,f and 26a). This led to an increase in V_p despite a decrease in V_{em}. All of these effects are clearly visible in changes in the PSD calculated using the SCV/SCR or VCV/SCR methods [86], taking into account the presence of silica, alumina and titania in complex FMO (Fig. 25). Large changes in the PSD were observed for high-pressure cryogels of A-300 (Fig. 25a), AST1 (Fig. 25b) and a mixture of A-300 and AST1 (Fig. 25f). MCA of FMO in a ball mill (Fig. 25a) or a microbreaker (Fig. 25b,f) have smaller effects than HPCG [46,47,63,90]. MCA shifts the main PSD peaks toward smaller pore size with a reduction in S_{BET} (mainly due to decrease in S_{meso}), and could either increase V_p (A-300, AST1) or decrease V_p (A-300/AST1 mixture). HPCG increased the value of S_{BET} of AST1 due to decomposition of core-shell nanoparticles [46,47]. However, it did not affect S_{BET} of A-300, and decrease of S_{BET} for A-300/AST1, since the aggregates became denser (*i.e.* accessibility of nanopores decreased for nitrogen molecules). The V_p value increased for all samples due to cryogelation. Note that normal-pressure cryogelation is frequently used for structuring metal oxide materials [92-99]; however, HPCG could cause much larger changes in the texture of these materials [46,47,63]. Hydrothermal treatment (HTT) of fumed oxides [89] caused strong changes in PSD (Fig. 26a), which became similar to those of porous silicas (Fig. 26b,c).

Note that intensive MCA could strongly change the properties of treated materials. For example, changes of gibbsite and fumed silica mixture during MCA investigated using XRD, MAS-NMR and XPS [100] were observed for crystallinity and other intrinsic structural characteristics. Formation of new Al–O–Si chemical bonds was detected by the changes in Al coordination number of gibbsite in the mixture during milling, and the appearance of new resonance in ^{29}Si NMR spectrum of the ground mixture. The presence of Al–O units in silica framework was demonstrated by the increase of Al 2p binding energy and the decrease of Si 2p binding energy [100].

Mesopores (1 nm < R < 25 nm) are the main contributors to porosity and specific surface area of various FMO [53]. Wetting, suspending-drying, MCA, and HPCG of FMO resulted in an increase in mesoporosity and sometimes macroporosity of treated materials [46,47,53,63,90]. These effects could be explained by the origin of the textural porosity of FMO that is caused by voids between nanoparticles in secondary structures. Note that the empty volume V_{em} = 10-25 cm^3/g in the FMO powders is much greater than the value of V_p (0.1 – 1.3 cm^3/g, Table 1) determined from nitrogen adsorption because the adsorption of nitrogen in large macropores is too small (the molecules do not sense the oxide surface far from pore walls).

Solvents (*e.g.*, water, alcohol) in the amounts of 30-50 wt.% in respect to the FMO amount could form a multilayer coverage of all primary particles in the wetted powders. The water or ethanol molecules could penetrate in contact area between adjacent nanoparticles in aggregates. The water molecules (half smaller in volume than ethanol molecules) could penetrate in narrower voids and strongly decompose the particle-particle linkages in the aggregates. Contrariwise, water clusters could be bridges between nanoparticles from neighboring aggregates that caused diminishing voids between these aggregates in the wetted-dried powders. Primary particles in the initial silica practically do not have the siloxane bonds with neighboring particles. They were

attached one to others by the hydrogen bonds and electrostatic and dispersion interactions [53]. The solvent molecules (especially water) could break these inter-particle bonds and increase the mobility of nanoparticles during MCA treatment or sonication. The solvents in the used small amounts provide essential plasticizing effects on the wetted silica powders. The MCA treatment of water-wetted silica gave the powder with a larger bulk density (~0.4 g/cm^3, Fig. 27a) due to better packing of primary particles than that after the MCA in the dry or ethanol atmosphere [75]. However, this maximal ρ_b value corresponded to approximately 35% of dense and ordered-packed silica spheres of the same size ($d = 6/(\rho_0 S_{BET})$ = 8.26 nm at ρ_0 = 2.2 g/cm^3 and S_{BET} = 330 m^2/g) that in a cubic lattice corresponded to $\rho_b \approx 1.15$ g/cm^3. This difference could be explained by, at least, two factors: (i) primary particles of nanosilica have different sizes; and (ii) certain amounts of non-decomposed aggregates could remained after the MCA. Both factors, as well as a random structure of initial aggregates, prevent the ordered packing of silica nanoparticles in secondary particles upon MCA treatment. However, compaction of primary particles became stronger with increasing MCA time (t_{MCA}) under the plasticizing effect of a solvent because of much deeper rearrangement of agglomerates and aggregates [75].

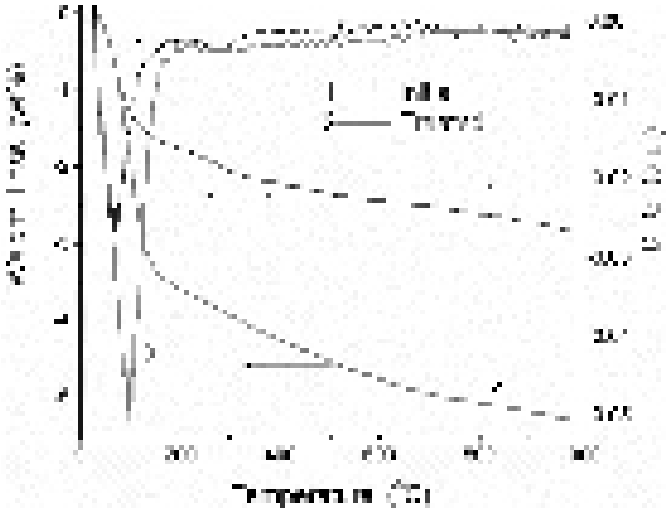

Fig. 28. Thermogravimetric (TG) and differential TG (DTG) curves of weight loss on heating of initial silica (curves 1) and water-wetted MCA-sample treated for 6 h (curves 2).

The particle compaction can affect the desorption rate of water or ethanol on evaporation at room temperature in air (Fig. 27b). However, this dependence is complex, as well as changes in the PSD of FMO affecting this process. The pore (voids between spherical nanoparticles could be considered as textural pores) size distributions depended on t_{MCA} [75].

On heating, desorption of both intact water (T < 150 ^{o}C) and associatively desorbed water (or water desorbed from the inner volume of primary particles at T > 150 ^{o}C) increased after the MCA treatment (Figs. 27b and 28) [75]. The difference in the amounts of water desorbed from initial and MCA-treated silica slightly increased with heating temperature to 900 ^{o}C. This could be explained by larger amounts of water molecules and OH groups inside silica nanoparticles treated with 0.5 g of water per gram of silica (added into the ball-mill) for 6 h, as well as retardation of water desorption from narrower pores in denser secondary structures. Thus, a variety of treatments could be used to change the characteristics of FMO as relatively soft materials. The changes in the structure – property relationships could be analyzed using XRD, Raman, UV-vis, FTIR, NMR, DSC, and other methods [25-30,46-49,53,71-91]. Note that FMO are more sensitive to various treatments in aqueous media than in organics and the effects depend on the content of nanooxide in the suspension. The adsorption and interfacial and temperature behaviors of nonpolar and polar compounds interacting with FMO at different temperatures are very sensitive to the morphological, structural and textural changes of the materials caused by the mentioned treatments [53].

Structural features of FMO

The crystallinity of simple and complex nanooxides depend on the crystallinity of titania or alumina since silica is always amorphous in initial FMO (Figs. 14-16 and 29) [30,53]. Individual titania includes both anatase and rutile (Figs. 29b,d). For other titania-containing FMO, the titania phase is composed mainly of anatase. This is of importance because the crystallinity and type of titania phases could influence the adsorption, catalytic, and other important characteristics of the materials [53].

The UV-vis DRS spectra (Fig. 29) recorded at room temperature in the wavelength range of 200–900 nm (using ZnO as a reference material) show the MCA or HPCG effects on the structure of treated FMO [90]. The differences in the nature and morphology of FMO caused differences in adsorption and other properties of the materials [53]. Note that many properties of fine powder of FMO depend on material history because their 'soft' nature due to easy rearrangement of secondary particles upon pressing, MCA, wetting or suspending and drying, and high temperature treatments [25-30,46-49,53,63-68,101-103].

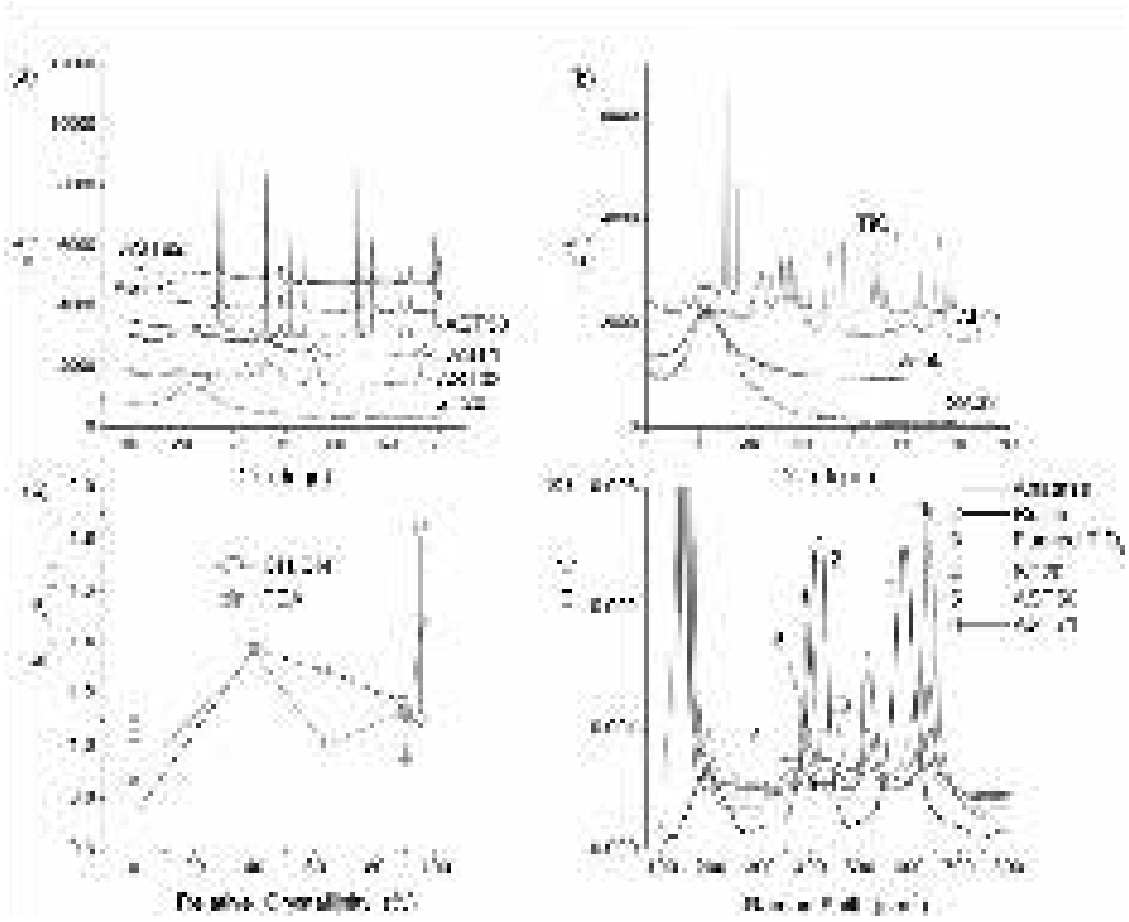

Fig. 29. (a, b) XRD patterns of nanooxides; (c) changes in the $S_{BET,X}/S_{BET,N_2}$ value as function of relative crystallinity of nanooxides determined from the XRD data; and (d) Raman spectra of some oxides containing.

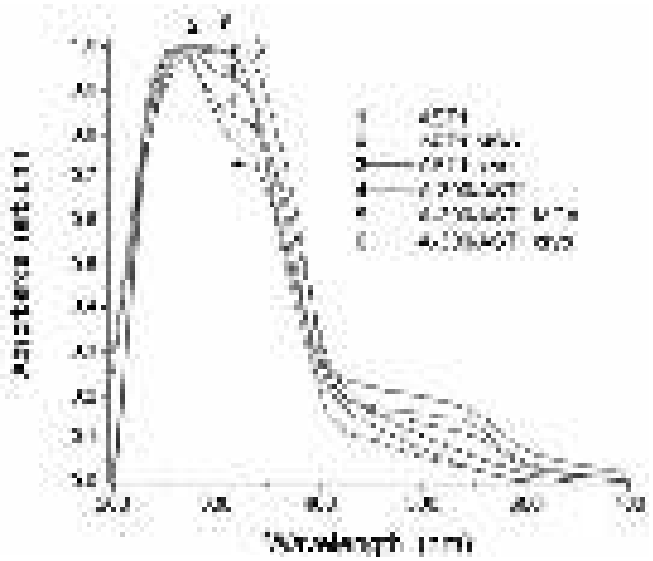

Fig. 30. UV/visible spectra (Jasco UV/vis spectrometer) of samples containing AST1 or A-300/AST1 initial, MCA 30 min in a microbreaker (label 'MCA'), or high-pressure cryogels (label 'cryo').

In addition to rearrangement of the secondary particles during MCA or high-pressure cryogelation, changes in the chemical structure of nanoparticles could also occur. Such chemical changes could be seen in UV-vis spectra of treated samples in the 300-600 nm range (Fig. 30). High-pressure cryogels with AST1 and MCA-treated AST1 or A-300/AST1 change color from white to beige of different tints. The color centers correspond to defects formed in the lattices of titania and alumina (*e.g.,* oxygen vacancies) during MCA or high-pressure gelation. Note that MCA and HPCG gave different effects in the 300-400 nm (or 4.1-3.1 eV) range. For example, A-300 damped the high-pressure effects on AST1 during HPCG, but this influence of A-300 decreased during MCA (Fig. 30) [90]. There were patterns in how FMO properties, characteristics and behavior were affected by different media, depending on their composition and history [53]. First, typically FMO containing titania and alumina were characterized by smaller S_{BET} values (*i.e.* larger nanoparticles) and pore volumes, (V_p, Table S1) because aggregation of nanoparticles decreased with increasing size. Contributions of nanopores at $R < 1$ nm (*i.e.* voids between adjacent nanoparticles in their aggregates) decreased with decreasing value of S_{BET} [53].

The infrared (IR) spectra of FMO with bound adsorbates give useful information on the structure of the interfacial layer, especially for silica because of appropriate sensitivity of the O-H stretching vibrations of surface silanols toward types and amounts of adsorbates [37,38,53]. It was of interest to compare the FTIR spectra of FMO (nanosilica) and silica gel (*e.g.*, 200DF with S_{BET} = 540 m^2/g, V_p = 0.34 cm^3/g) [104]. The FTIR spectra of nanosilicas A-300 and A-380 with adsorbed water (from air) and water/methane co-adsorbed in the spectral cell (Fig. 31a,b) were characterized by a broad band at 2500-3700 cm^{-1} which could be assigned to the OH-stretching vibrations of adsorbed water and disturbed surface silanols [38,53]. A narrow band at 3750-3747 cm^{-1} linked to free silanols [38,105] was observed for nanosilicas (more readily observed for A-300 than A-380) but not for silica 200DF (Fig. 31a). This result could be explained by clustering of water adsorbed on nanosilicas (*i.e.*, a continuous layer of adsorbed water was absent), in contrast to porous silica 200DF whose narrow pores (Fig. 26a) were practically entirely filled by water adsorbed from air.

Gaseous methane alone and adsorbed onto nanosilica was characterized by an intensive narrow band at ν_{CH} = 3016 cm^{-1} and a set of low-intensive satellite bands split due to vibrational-rotational motions of methane molecules in the vapor phase in the FTIR cell. A small quantity of methane adsorbed on nanosilica was observed after purging the cell with air (Fig. 31b, curve 2) [104]. The adsorption of methane did not lead to significant changes in the band intensity of free silanols because of the weak interaction of nonpolar CH_4 molecules with the silica surface [104]. However, calculations of the free surface area (S_{IR}) on the basis of the integral intensity of free

silanols at ν_{OH} = 3747 cm^{-1} (as a surface characteristic) and a band at 1870 cm^{-1} (as a bulk Si–O combination mode used as an internal standard related to the nanoparticle volume), according to a method described elsewhere [106], give S_{IR} = 263.3 m^2/g for A-300 alone (with adsorbed water from air) and 266.9 and 265.9 m^2/g for silica with methane adsorbed for 1 and 7 min, respectively. An increase in the S_{IR} value was due to partial desorption of water resulting from methane flow in the cell. It should be noted that the value of S_{IR} could be considered as a part of the surface area free from adsorbates, since it was determined from the band of free silanols at 3747 cm^{-1}, and it was close the value of S_{BET} for dehydrated silicas [53,104,106]. According to the values of S_{IR} and S_{BET}, adsorbed water ($h \approx 0.1$ g/g) disturbed about 22% of surface silanols. According to the values of S_{IR} after exposure to methane for 1 and 7 min, methane disturbed about 0.4 % of surface silanols free from adsorbed water. Comparing these results with the changes caused by known amounts of water it is possible to estimate the amount of adsorbed methane that give 1.8 % CH_4 with respect to adsorbed water (*i.e.* ~0.2 wt.% with respect to silica since $h \approx 0.1$ g/g) at 288 K. This value was smaller than that obtained from ^{1}H NMR spectral measurements (discussed below), giving a greater ratio of adsorbed methane and water as 0.116 : 1, but at a slightly lower temperature (280 K) [104].

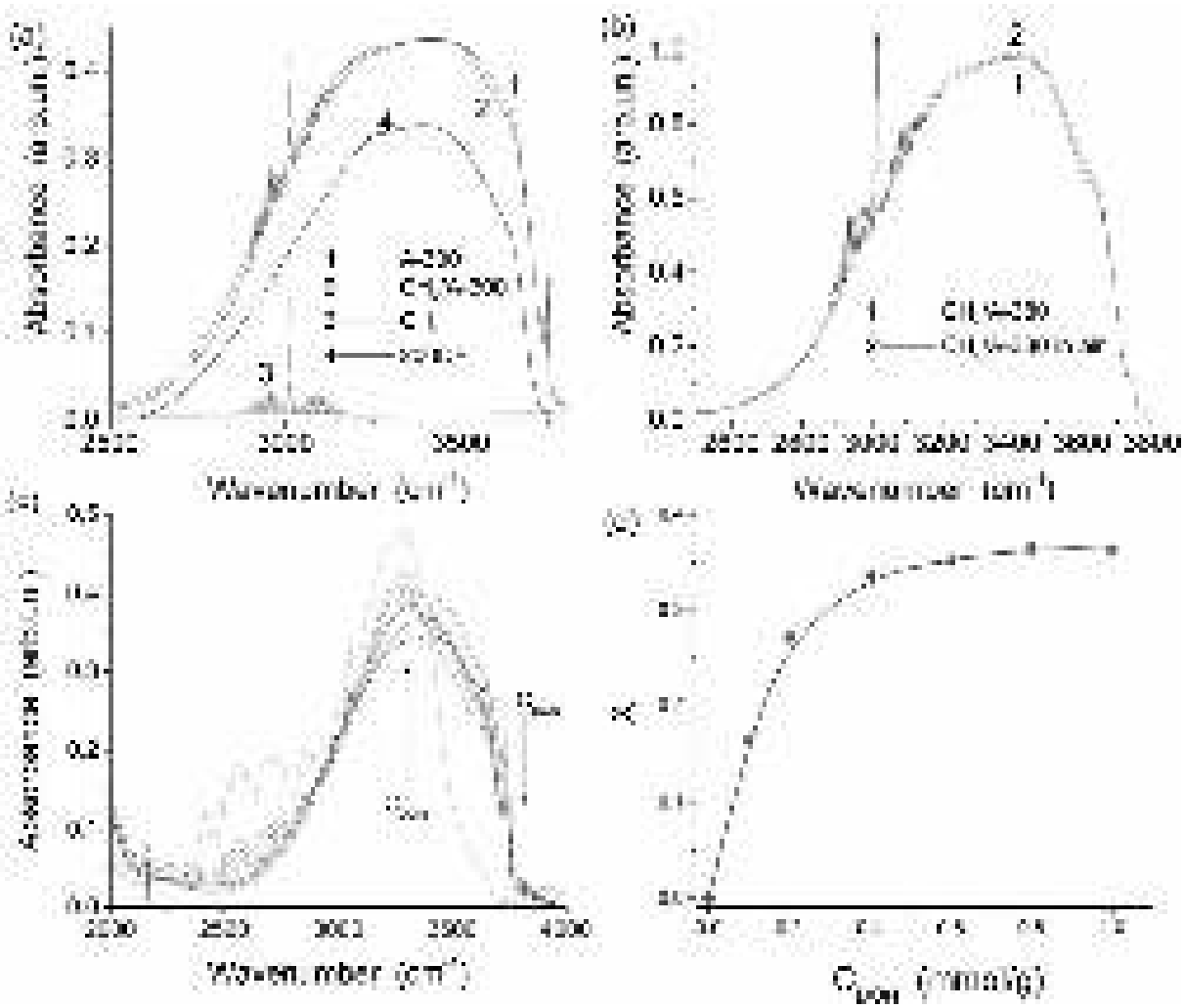

Fig. 31. FTIR spectra over the OH-stretching vibrations range for (a) silica A-300 with adsorbed water (from air) (curve 1), after blowing by methane (2), methane alone (3), and silica 200DF with water adsorbed from air (4); and (b) A-380 with co-adsorbed water and methane (1) and after blowing by air (2); (c) FTIR spectra (in a transmission mode) of nanosilica with adsorbed DON (1,5-dioxinaphthalene) at C_{DON} = 0 (1), 0.1 (2), 0.2 (3), 0.4 (4), 0.6 (5), 0.8 (6) 1.0 (7) and 1.5 mmol/g (8); (d) degree (X) of distortion of surface silanols (ν_{OH} = 3748 cm^{-1}) as a function of the adsorbed amount of DON.

Nanosilica A-380 is more aggregated and has a larger textural porosity than A-300, since the pore volume determined from the nitrogen adsorption isotherm is V_p = 0.943 and 0.714 cm^3/g, respectively [104]. Therefore, nanosilica A-380 could adsorb larger amounts of water from air. This results in a much lower intensity of the band at 3747 cm^{-1} (Fig. 31) and much smaller free surface area S_{IR} = 186 m^2/g at S_{BET} = 378 m^2/g (50.8 % reduction) than that for A-300. Purging this sample with methane gave S_{IR} = 194 m^2/g because of partial desorption of water, as seen with A-300. Subsequent purging with air led to diminution of the S_{IR} value to 183 m^2/g, because of co-adsorption of water and residual methane. Assuming that water displaced adsorbed methane, one could estimate the value of free surface area occupied by methane as 1.8 %, which is higher than that observed for A-300, due to stronger aggregation of silica nanoparticles of A-380. Notice that these estimations were not exact due to features of the used calculation methods but clearly showed tendency of the influence of pre-adsorbed water on the adsorption of methane and *vice versa*. Silica 200DF included both micro- and narrow mesopores in contrast to nanosilicas characterized by broader textural pores (Fig. 26). Therefore, silica 200DF could adsorb larger amounts of water from air than nanosilicas. Thus, the confined space effects in pores of different types, and the influence of pre-adsorbed water on the adsorption of methane, significantly differ for nanosilicas and 200DF [104].

The FTIR spectra of nanosilica A-300 impregnated by 0.2-1.0 mmol/g of 1,5-dioxinaphthalene (DON) from water-ethanol solution and dried (using tablets with a mixture with KBr (1:5)) showed interaction of DON with a surface of nanosilica. It was estimated by changes in the FTIR spectra related to the OH-stretching vibrations of free surface silanols (ν_{OH} at 3748 cm^{-1}) depending on the DON amounts (Fig. 31c). The IR bands of stretching and deformation vibrations of bonds in adsorbed DON molecules as well as the ν_{OH} vibrations of surface silanols could be identified in the spectra. The intensity of the ν_{OH} band of free silanols decreased with increasing amounts of adsorbed DON (C_{DON}) because of the hydrogen bonding of these molecules to the silanols. A sharp increase in the degree of distortion of free silanols by the DON molecules was observed at C_{DON} < 0.5 mmol/g (Fig. 31d). Notice that the values of S_{IR} for DON/A-300 were relatively high (300-338 m^2/g) that were in agreement with a relatively low degree of distortion of surface silanols (Fig. 31d). This result could be explained by the adsorption of DON in the form of clusters but not in the form of individual molecules. This is characteristic for polyaromatic compounds because of great energy of dispersion interactions upon their clustered adsorption [53].

Suspending-drying of FMO as 'soft' materials led to rearrangement of secondary structures [53,107]. AFM images of a dried solid residual of treated silica A-300 alone showed (Fig. 32) that repulsive particle-particle interactions caused by negative charging of the silica surface at pH 12 resulted in a reduction of the size of aggregates of primary nanoparticles. However, changes in silica concentration in aqueous suspension sonicated at native pH value (close to 5 with only slight negative charging of the silica surface [53]) weakly affected the aggregate structure in the dried solid residual (Fig. 32a,c). This result was confirmed by small variations in the structural characteristics (pore volume V_p = 1.42-1.58 cm^3/g, specific surface area S_{BET} = 220-239 m^2/g) and pore size distributions (Fig. 33) of these systems. However, the V_p values differ quite a bit from the initial A-300 powder, in contrast to the S_{BET} values (Fig. 34), because primary particles were not changed but their packing was changed. Similar results with respect to the morphology of secondary FMO particles were observed for the dry silica powder and dried solid residual of treated A-50, A-300, and A-380 [53]. Primary particles (30-100 nm in diameter) and their relatively small aggregates (< 300 nm) were observed for silica A-50. Mainly aggregates (< 200 nm) were observed for A-300 (primary particles were 6-18 nm in diameter) and A-380 (5-15 nm primary particles).

Rearrangement of aggregates of primary particles, due to sonication of aqueous suspensions and drying of the solid residual, led to significant changes in the shape of PSD in comparison with the initial dry A-300 powder (Fig. 33) [107]. The contributions of pores of different sizes to the total porosity and specific surface area demonstrated a concentration-dependent character (Fig. 34). The interfacial Gibbs free energy of sonicated or ball-milled

aqueous suspensions of A-300 alone has a maximum at $C_{A\text{-}300} \approx 12$ wt.% [53], as well as the $\Delta S/S(C_{A\text{-}300})$ and $\Delta V/V(C_{A\text{-}300})$ functions for the dried residual (Fig. 34). This content of silica corresponded to a critical value because the sonicated aqueous suspension could transform into a gel-like state at this or higher values of $C_{A\text{-}300}$ after 1-3 days (depending on $C_{A\text{-}300}$). A continuous cluster of silica particles formed at these concentrations. However, at lower concentrations ($C_{A\text{-}300} < 10$ wt.%) the aqueous suspension did not transform into the gel-like state even over a period of several years. Changes in the PSD shape of the solid residual slightly depended on silica concentration in the aqueous suspension (Fig. 33b), because particle packing rearrangement depended on many-particle interactions which is a function of concentration in the suspension. However, the position of the main one-two meso- and macropore peaks in the PSD did not depend on silica content, but it depended on the silica type. This suggested that the rearrangement of secondary particles resulting from the applied treatments was a function of PaSD. The process of suspending-sonication-drying led to a significant increase in the bulk density of treated silica (0.41 g/cm^3 for dried solid residual of the suspension at $C_{A\text{-}300} = 16.7$ wt.%) in comparison with the initial powder (0.05-0.06 g/cm^3), or the dry powder ball-milled for 24 h (0.3 g/cm^3), or after hydrothermal treatment of fumed silica A-300 (0.2 g/cm^3) [53,89,107].

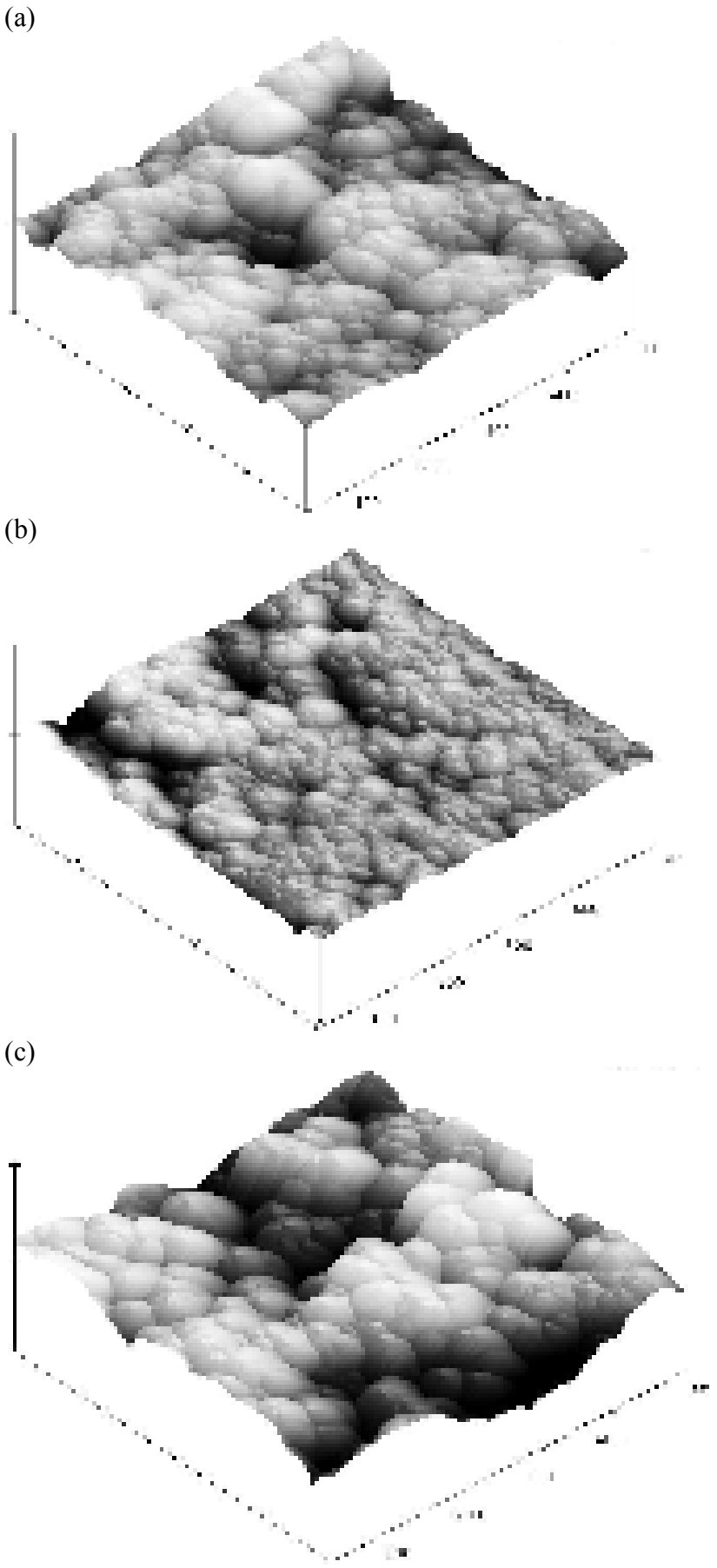

Fig. 32. AFM images of dried solid residual of aqueous suspension with A-300 (a) $C_{A\text{-}300}$ = 1 wt.% (without NaOH), (b) 1 wt.%, pH 12 (adjusted by NaOH), and (c) 20 wt.% (without NaOH) [53].

Drying of the solid residual from the aqueous suspension (16.7 wt.%) led to an approximately 3-fold reduction of the size of the continuous cluster. Despite this effect, there was no loss in the specific surface area (ΔS_{BET} was close to zero) for suspended-sonicated-dried nanosilica (Fig. 34), in contrast to the dried solid residual of the ball-milled suspensions or ball-milled dry powders (ΔS_{BET} was between −50 and −160 m^2/g for these samples) [53,107].

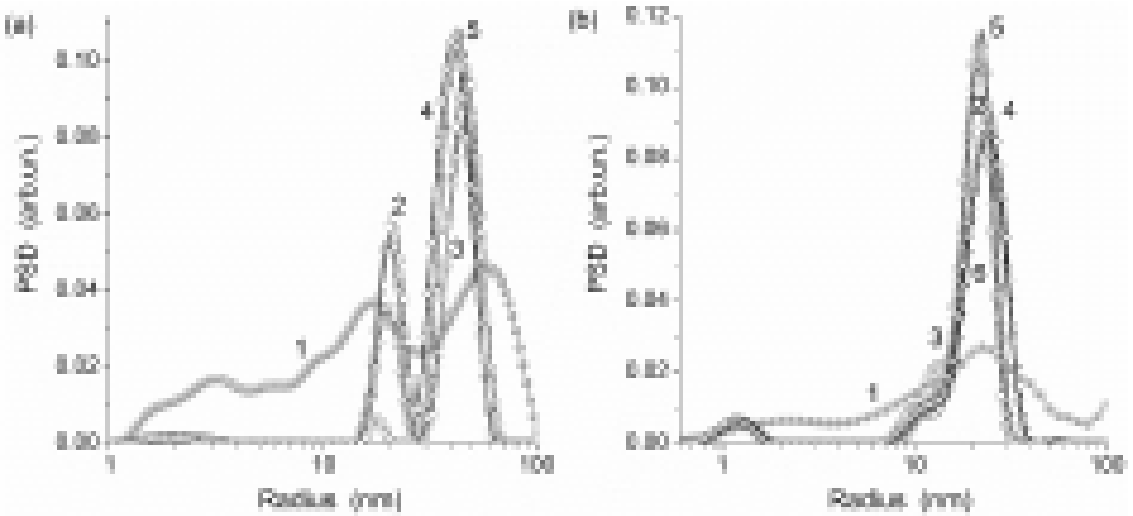

Fig. 33. $IPSD_V$ of (a) initial dry A-300 powder (curve 1) and dried residual of aqueous suspensions of A-300 (1 wt.%) (2), with addition of 0.9 wt.% of NaCl (3), pH 12 (4), and 20 wt.% + 0.9 wt.% of NaCl (5) with a model of pores as voids between spherical particles; and (b) initial dry A-300 powder (curve 1), dried residual of aqueous suspensions of A-300 at $C_{A\text{-}300}$ = 7.4 (2), 9.9 (3), 12.3 (4), 14.5 (5) and 16.7 (6) wt.% with a model of cylindrical pores.

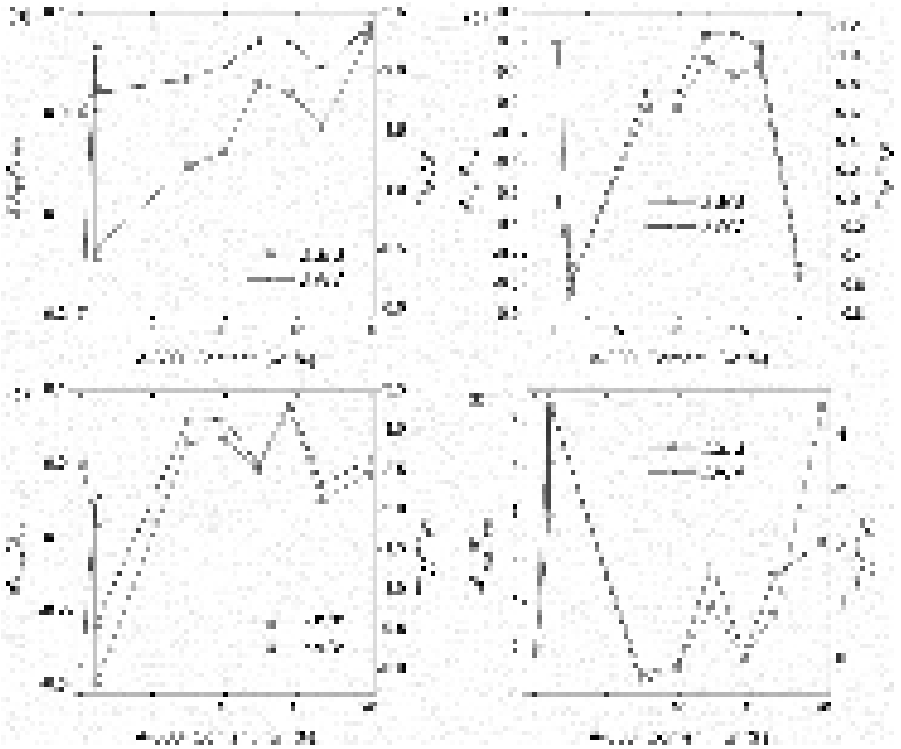

Fig. 34. Relative changes in the specific surface area and porosity: (a) total, (b) nanopores, (c) mesopores, and (d) macropores for suspended-sonicated A-300 and then dried as a function of concentration.

(Dimethylamino)azobenzene (DMAAB, pK_a = 3.3) was chosen as a color indicator to study the active site distributions on the nanooxide surfaces using the optical spectroscopy. The diffuse reflection spectra of adsorbed DMAAB (Fig. 35) were recorded using a SF-18 (LOMO, St.-Petersburg) spectrophotometer, and then converted to absorption spectra according to the Kubelka-Munk formula.

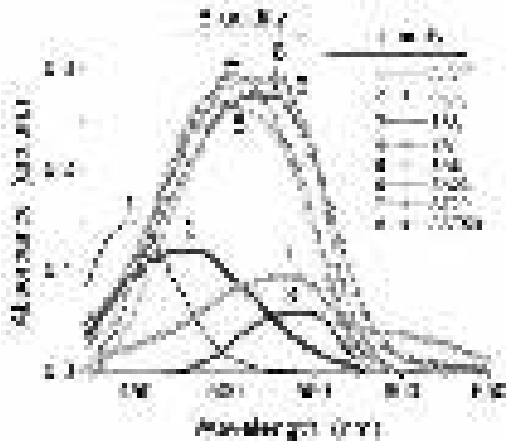

Fig. 35. Optical spectra of DMAAB adsorbed onto different fumed oxides (sample weight was selected to provide close surface area of all samples).

The DMAAB adsorption from the gas phase onto samples previously evacuated to 10^{-4} Torr, then heated in special optical glass vessels at defined temperatures for 1 h and hermetically sealed, was carried out at 338±5 K for 2-4 h. The doses by weight of samples were different to maintain a constant surface area in all measurements. The assignment of the DMAAB absorption bands was done by analogy to the spectra for this substance in neutral and acidic solutions. Four absorption bands of DMAAB adsorbed on the complex oxide surface can be detected: (a) λ = 430-470 nm, physisorbed DMAAB through dispersion interaction, (b) 470-490 nm, hydrogen-bonded DMAAB, (c) 490-545 nm, complexes with H^+ transferring from the Brønsted (B) sites to DMAAB, and (d) 550-560 nm, DMAAB complexes with Lewis (L) acid sites.

Wetting-drying and cryogelation effects depend on FMO content in the treated suspensions that is shown using fumed silica Cab-O-Sil HS-5 (Tables 4 and 5, Figs. 36-38). All these processes result mainly in compaction of the secondary structures (NPNP aggregates and agglomerates of aggregates) that affect the PSD. However, the specific surface area insignificantly changes with one exception of a sample treated at pH 10 with NaOH.

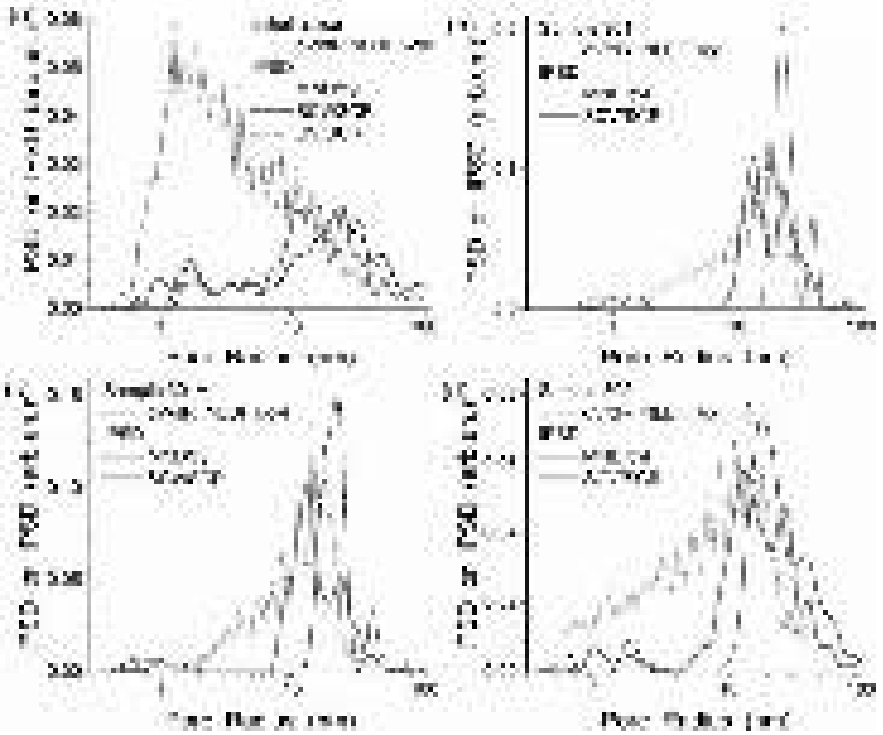

Fig. 36. Pore size distributions calculated using NLDFT (cylindrical pores), MND (cylindrical pores) and SCV/SCR methods for (a) initial silica Sab-O-Sil HS-5, and treated samples: (b) 301, (c) 301A, and (d) 302 (see Tables 4 and 5).

Table 4. Samples based on fumed silica Cab-O-Sil HS-5.

Sample number	Processing parameter	Sample number	Processing parameter
301	Normal 3 wt% slurry	406	stirred 48 hours
301 A	Frozen 72 hours	407	Silica heated 650 C 12 hrs prior to slurry making, freezing and freeze drying
302	3 wt% frozen 11 days	501	normal 5 wt %
401	Normal 4 wt% slurry	502	not frozen or freeze dried
402	sonicated 5 mins (~30 kHz in a bath sonicator)	502 crushed	crushed up chunks before TGA
403	sonicated 25 mins	503	briefly frozen and freeze dried
404	pH 4.3, not adjusted	504	frozen 48 hrs and air dried
405	Adjusted pH 10 with NaOH	1001	10 wt%
Bare	plain fumed silica		

Table 5. Textural characteristics of silicas based on Cab-O-Sil HS-5.

Sample	ρ_b (g/cm^3)	S_{BET} (m^2/g)	V_p (cm^3/g)	S_{nano} (m^2/g)	S_{meso} (m^2/g)	S_{macro} (m^2/g)	V_{nano} (cm^3/g)	V_{meso} (cm^3/g)	V_{macro} (cm^3/g)
Initial	0.045	272	0.689	66	198	8	0.031	0.535	0.123
301	0.294	284	1.677	77	183	24	0.036	1.291	0.350
301A	0.256	265	1.449	70	184	11	0.033	1.241	0.175
302	0.179	281	1.329	78	184	19	0.035	0.979	0.315
401	0.228	288	1.530	78	176	33	0.034	1.011	0.485
402	0.197	286	1.611	76	156	54	0.033	0.649	0.929
403	0.191	281	1.152	13	244	24	0.003	0.778	0.371
404	0.176	282	0.913	69	195	17	0.033	0.643	0.237
405	0.227	171	1.153	43	90	39	0.019	0.501	0.633
406	0.211	255	1.240	61	156	38	0.027	0.635	0.577
407	0.120	241	0.914	54	167	20	0.024	0.605	0.284
501	0.241	276	1.486	66	168	42	0.026	0.857	0.602
502	0.344	267	1.510	60	183	24	0.022	1.186	0.301
503	0.176	268	1.319	33	192	44	0.010	0.627	0.682
504	0.328	277	1.442	66	198	12	0.026	1.271	0.145

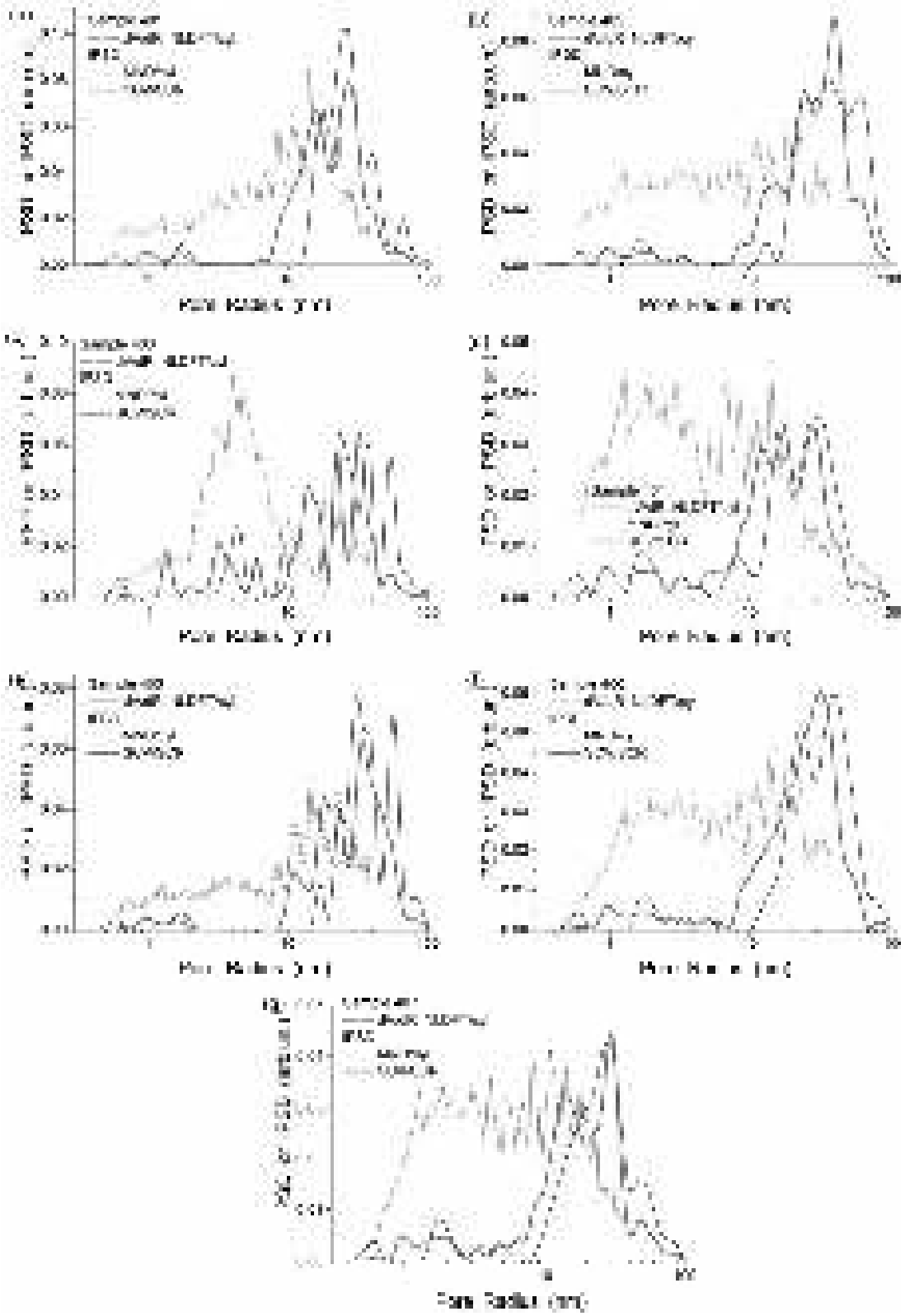

Fig. 37. Pore size distributions calculated using NLDFT (cylindrical pores), MND (cylindrical pores) and SCV/SCR methods for treated samples: (a) 401, (b) 402, (c) 403, (d) 404, (e) 405, (f) 406, and (g) 407 (see Tables 4 and 5).

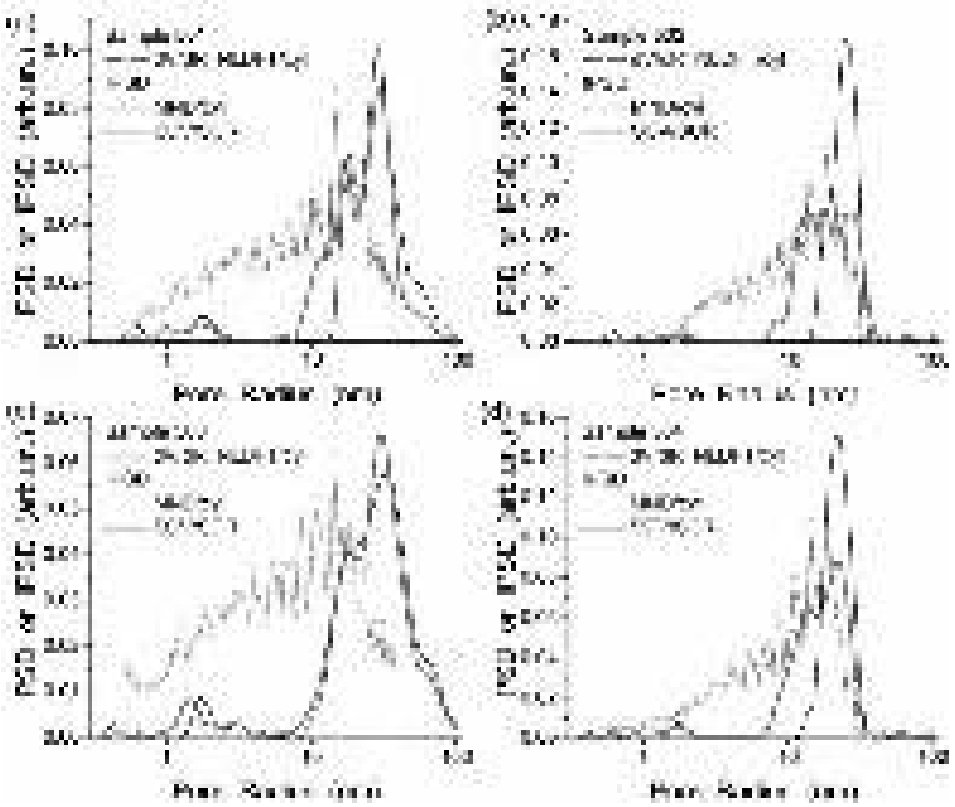

Fig. 38. Pore size distributions calculated using NLDFT (cylindrical pores), MND (cylindrical pores) and SCV/SCR methods for treated samples: (a) 501, (b) 502, (c) 503, and (d) 504 (see Tables 4 and 5).

Described above structural features of FMO can affect adsorption and other interfacial phenomena occurring in both gaseous and liquid dispersion media [53] that will be analyzed below.

Interfacial phenomena

Individual adsorption of low-molecular weight compounds

To analyze the adsorptive characteristics of a variety of initial and treated FMO (Tables 1 and 6), the adsorption of water, *n*-hexane and other low-molecular weight adsorbates was studied using an adsorption apparatus with a McBain–Bark quartz scale at 293 K [28,30,53]. Samples were evacuated at 10^{-3} Torr and 473 K for several hours to a constant weight, then cooled to 293±0.2 K, and the adsorption of water, hexane and other adsorbates was studied at varied relative pressures p/p_s [28,30]. For all studied FMO [30], the nitrogen adsorption-desorption isotherms were characterized by narrow hysteresis loops (Figs. 39-41) and could be assigned to the type II of IUPAC classification [84,85]. This regularity was due to a spherical-like (but non-ideal) shape of nonporous primary particles (average diameter d_{av} = 6.9-52.5 nm for various FMO, Tables 1 and 6, and Figs. 2-10) forming aggregates (secondary particles of 50-1000 nm in size) and looser agglomerates of aggregates (ternary particles > 1 μm in size). Voids in secondary and ternary particles provided the textural porosity of the materials but with virtually no contribution from nanopores (Fig. 42). Notice that the adsorption isotherms of various adsorbates (Figs. 39-41) could also be assigned to the type II [84,85] because of textural features of FMO. The empty volume in loose nanooxide powders was very great $V_{em} = 1/\rho_b - 1/\rho_0$ = 10-30 cm^3/g (where ρ_b = 0.03-0.10 g/cm^3 is the bulk density of the dry powders).

Table 6. Structural characteristics of nanooxide powders [28,30,53].

Sample	C_{SiO_2} (wt.%)	C_{TiO_2} (wt.%)	$C_{Al_2O_3}$ (wt.%)	$C^s_{SiO_2}$ (wt.%)	$C^s_{TiO_2}$ (wt.%)	$C^s_{Al_2O_3}$ (wt.%)	d_{av} (nm)	Δw	S_{BET,N_2} (m^2/g)	V_{p,N_2} (m^2/g)	$S_{BET,ac}$ (m^2/g)	$S_{BET,hex}$ (m^2/g)	$S_{BET,DEA}$ (m^2/g)	$S_{BET,TEA}$ (m^2/g)
SA8	92		8	29.5		70.5	8.6	0.33	303	0.68	223	207	271	265
SA23	77		23	73.6		26.4	6.9	0.23	347	0.82	362	247	434	384
ST20	80	20		75.6	24.4		27.9	0.40	84	0.18	116	80	97	115
AST03	2.7	0.3	97.0				13.9	0.30	125	0.31	162	101	114	126
AST1	10.0	1.0	89.0				18.0	0.33	99	0.25	180	99	113	117
AST50	28	50	22	58.7	40.0	1.3	47.9	0.31	37	0.08	44	31	44	42
AST71	8	71	21	5.0	80.4	4.6	21.6	0.43	74	0.13	83	63	60	70
AST82	6	82	12	0	91.2	8.8	40.2	0.27	39	0.11	43	48	46	58
A-50	>99.8			>99.8			52.5	0.38	52	0.13	42	77		
A-200	>99.8			>99.8			11.9	0.31	230	0.48	232	187		
A-300	>99.8		0	>99.8			9.2	0.17	295	0.52		261		
Al_2O_3			>99.8			>99.8	12.9	0.16	133	0.45	246	187	205	238
Al_2O_3			>99.8			>99.8	19.3	0.35	89	0.13	95	90		
TiO_2		>99.8			>99.8		35.7	0.32	42	0.09	58	43		

Note. C^s is the surface content of oxides, and Δw is relative error of the model of voids between spherical particles packed in random aggregates.

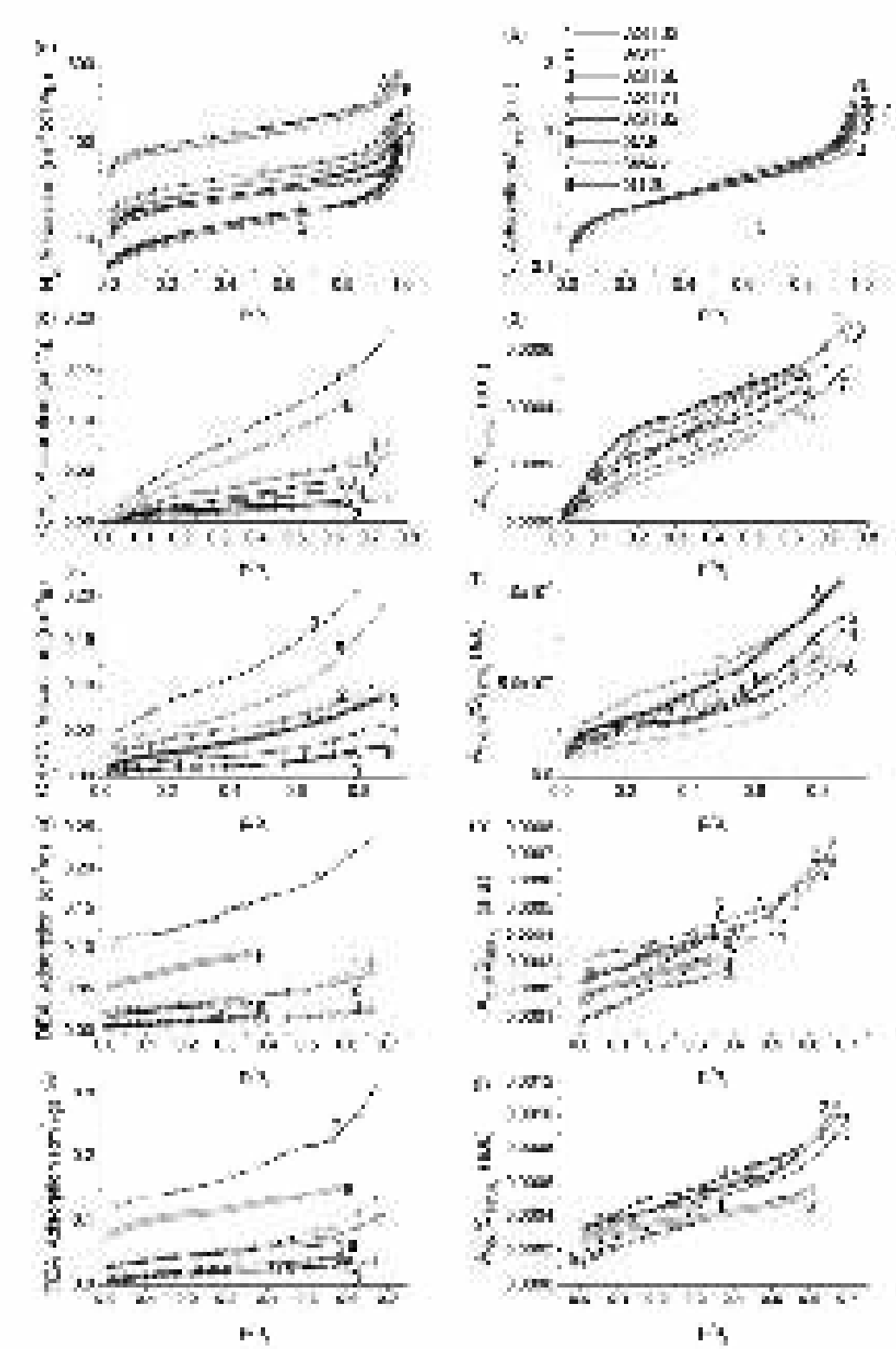

Fig. 39. Adsorption isotherms of (a, b) nitrogen, (c, d) hexane, (e, f) acetonitrile, (g, h) diethylamine, DEA, and (i, j) trimethylamine, TEA (left - initial and right - normalized by $S_{BET,N2}$) onto different oxides (1) AST03, (2) AST1, (3) AST50, (4) AST71, (5) AST82, (6) SA8, (7) SA23 and (8) ST20 degassed at 200 ^{o}C.

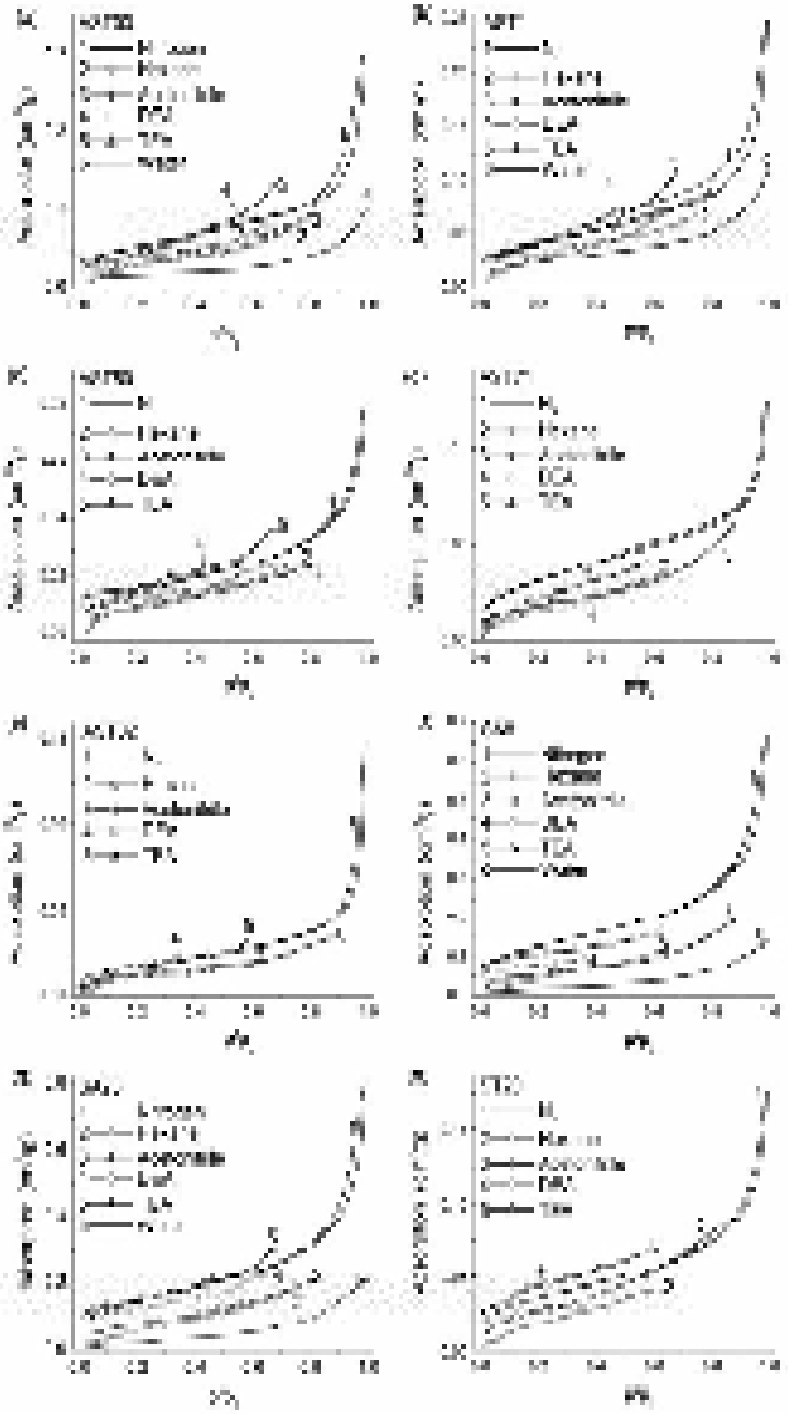

Fig. 40. Comparison of adsorption of different adsorbates (1) nitrogen, (2) hexane, (3) acetonitrile, (4) DEA, (5) TEA, and (6) water onto (a) AST03, (b) AST1, (c) AST50, (d) AST71, (e) AST82, (f) SA8, (g) SA23 and (h) ST20 degassed at 200 ^{o}C.

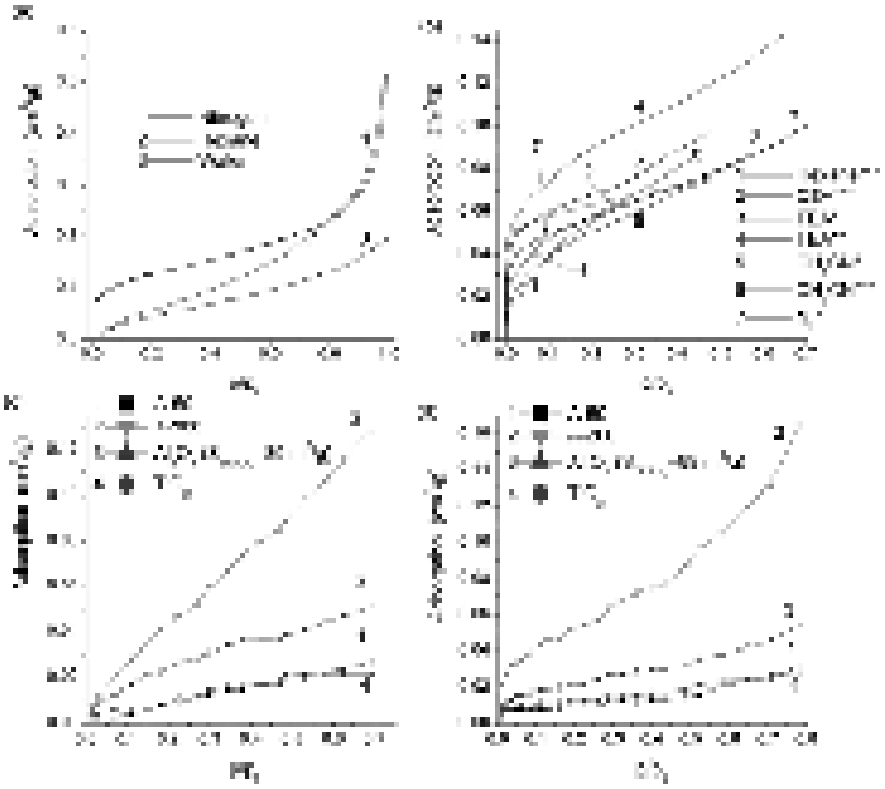

Fig. 41. Adsorption of different adsorbates onto (a) A-300 degassed at 200 °C; (b) fumed alumina (S_{BET,N_2} = 133 m^2/g) degassed at * 200, ** 600 and *** 900 °C; and adsorption of (c) hexane and (d) acetonitrile onto A-50, A-200, alumina (S_{BET,N_2} = 89 m^2/g) and titania.

A major contribution of broad voids (macropores) (Fig. 42) in secondary (aggregates) and ternary (agglomerates) particles, and thermodynamically unfavorable condensation of gases or vapors in macropores [84,85] resulted in ineffectively filling of them by any gaseous or vapor adsorbates even at p/p_0 = 0.98-0.99. For instance, the maximal V_{p,N_2} value among studied oxides was 0.82 cm^3/g for SA23 (Tables 1 and 6) (possessing the maximal S_{BET,N_2} value) which corresponded to about 3% of the V_{em} value (ρ_b = 0.036 g/cm^3). Another effect appearing due to the textural porosity was that the nitrogen adsorption was proportional to the S_{BET,N_2} value at p/p_0 up to 0.5-0.6 (Fig. 39a,b) because of weak capillary condensation and insignificant volume filling of broad voids. The S_{BET,N_2} values were calculated using the standard range of adsorption at $0.05 < p/p_0 < 0.3$ [84,85]. This did not give large errors in estimation of the S_{BET,N_2} values because of similar results of adsorption linearization in the BET coordinates for narrow and broad p/p_0 ranges. For instance, S_{BET,N_2} = 318 and 35 m^2/g for SA23 and AST50 (with the largest and smallest S_{BET,N_2} values) at $0.05 < p/p_0 < 0.5$, respectively, that were close to the S_{BET,N_2} values calculated at $0.05 < p/p_0 < 0.3$ (Table 6). Additionally, the average area occupied by a N_2 molecule could be varied (e.g., 0.162 nm^2 for carbons and nitrogen molecules located parallel to the surface or 0.137 nm^2 for silica due to changes in the orientation of the N_2 molecules around surface hydroxyls) [53].

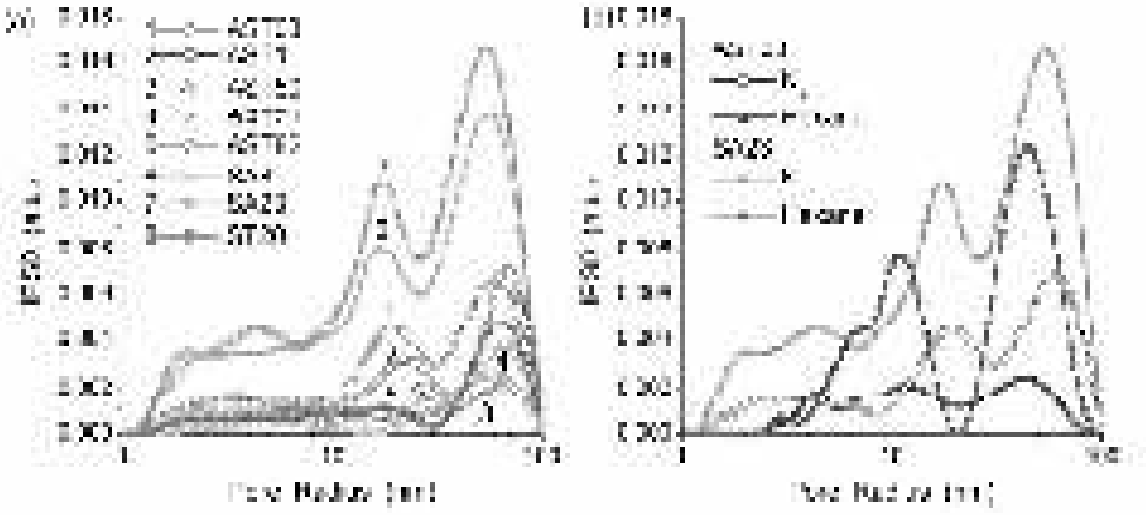

Fig. 42. Pore size distributions for studied complex oxides calculated on the basis of (a) nitrogen desorption, and (b) hexane adsorption with the model of voids between spherical particles.

Thus, despite a certain difference in the normalized (divided by S_{BET,N_2}) nitrogen adsorption at $p/p_0 > 0.5$ (Fig. 39b) caused by variations in the PSD and packing of primary particles in secondary and ternary structures [30,53], the nanooxides morphology could be assumed as roughly the same for all FMO studied. This was due to the flame synthesis of them at high temperatures $T > 1200$ °C; *i.e.*, primary particles could be in state close to liquid one in the flame [2-4] to form nano-beads. However, the studied oxide powders strongly differed in the specific surface area (Tables 1 and 6, S_{BET}), PSD and the aggregation degree of particles (V_p) that, as well as the difference in the nature of oxide surfaces, could affect the adsorption of any adsorbates. The analysis of these aspects could be undertaken by comparison of the structural characteristics (S, V) calculated from the adsorption isotherms of different adsorbates [30].

Greater differences in the adsorption on the same oxide were observed for more complex and polar adsorbates (diethylamine (DEA), trimethylamine (TEA), CH_3CN, H_2O) than for nitrogen (Figs. 39 and 40) [30]. These effects were caused by stronger bonding of stronger electron-donor and polar adsorbates to Brønsted (bridging hydroxyls) and Lewis (incompletely O-coordinated Al or Ti atoms appeared due to degassing at relatively high temperature) acid sites and other active sites (*e.g.*, terminal hydroxyls). However, there was a clear tendency toward a decrease in the adsorption of all adsorbates with decreasing S_{BET} value, despite the difference in their polarity, electron-donor properties, and molecular size. Clearly, the specific surface area and textural features of adsorbents could play an important role on the adsorption of various adsorbates. The strong influence of the value of S_{BET} on the adsorption of any adsorbates onto FMO could be explained by the fact that a significant contribution to the adsorbed amounts was due to the first monolayer [30,53] with insignificant capillary condensation of adsorbates in broad but short voids between neighboring nanoparticles in their aggregates and agglomerates. Note that some isotherms were recorded up to $p/p_0 = 0.62$-0.75 due to certain difficulties in the measurements caused by the behavior of the adsorbates studied at higher p/p_0 values [30]. Additional effects were due to the difference in the nature and content of active surface sites (terminal (≡MOH) and bridging (≡M'O(H)M"≡) hydroxyls and others) responsible for the formation of strong adsorption complexes with electron-donor and proton-donor molecules [30,53].

The degassing temperature of FMO can play an important role on measurements of the adsorption and, therefore, estimation of the structural characteristics from the adsorption isotherms. However, morphological changes in fumed alumina or titania were much smaller upon heating than that of silica [30,53]. This effect was due to the difference in the types of hydroxyls

(only terminal for silica and terminal and bridging for alumina and titania) and the O-coordinating numbers of Si (only fourfold O-coordinated) and Al (from fourfold to sixfold) or Ti (five- and sixfold O-coordinated) atoms. Therefore, associative desorption of water from a silica surface led to stronger changes in the lattice structure than for other FMO [53].

Alumina (S_{BET,N_2} = 133 m^2/g) degassed at 600 or 900 ^oC and cooled to room temperature (without contact to air) adsorbed greater amounts of acetonitrile and especially TEA than alumina degassed at 200 ^oC (Fig. 41b). This result as well as the maximal $S_{BET,X}/S_{BET,N_2}$ values (Fig. 43, Table 6) could be caused by enhancement of donor-acceptor interactions between the N atoms of adsorbates and surface Lewis acid sites (effectively formed upon strong dehydration of alumina at high temperatures) and certain diminution of the size of primary particles on thermoevacuation [30,53]. Additionally, calcination at 900 ^oC could increase the crystallinity degree of alumina that could also influence the adsorption of electron-donor compounds. Notice that the first portion of adsorbates (especially water) could dissociatively adsorb onto strained bonds appearing at the FMO surfaces degassed at high temperatures [30,53].

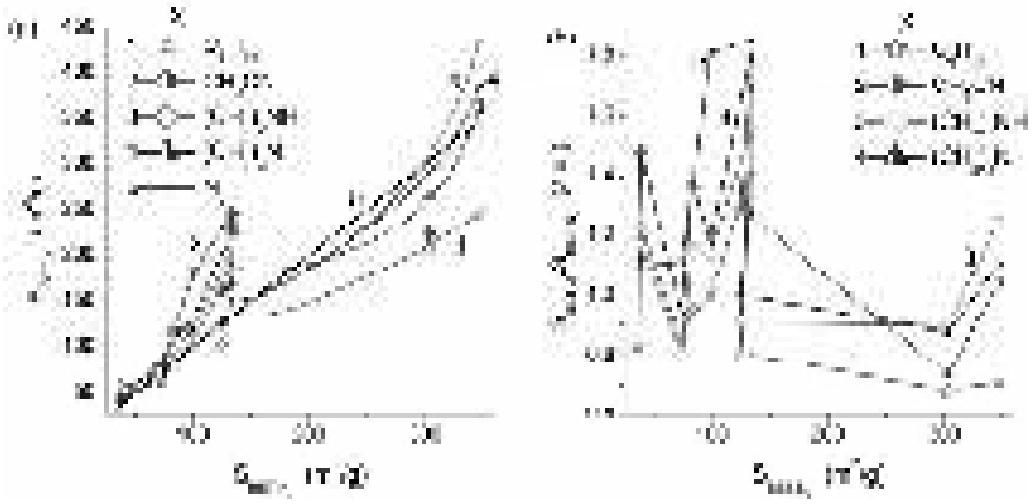

Fig. 43. Relationships between the S_{BET,N_2} and (a) $S_{BET,X}$ or (b) $S_{BET,X}/S_{BET,N_2}$ values.

The degree of aggregation of the primary particles (affecting V_p), which depended on treatment conditions, can play a certain role in the adsorption and changes in the $S_{BET,X}/S_{BET,N_2}$ values [30]. For example, for two samples of alumina, the ratio $S_{BET,X}/S_{BET,N_2}$ was greater for a sample with a larger value of V_p (Table 6) because the adsorption was greater for FMO with more aggregated nanoparticles. Additionally, variations in orientation of adsorbed molecules at a surface affected the surface area occupied by each molecule (σ) and, therefore, the $S_{BET,X}/S_{BET,N_2}$ ratio [30,53].

A minimal adsorption onto FMO degassed at 200 ^oC was observed for water (Figs. 40 and 41), despite the fact that it could form strong hydrogen bonds with surface hydroxyls [30]. This low adsorption was due to several reasons. First, saturated vapor of water has low pressure (17.5 mmHg at 293 K). Second, water adsorption was clustered rather than monolayered, *e.g.*, the surface was incompletely covered by water molecules even at C_w = 15-20 wt.% corresponding to several statistical monolayers [30,53,84,85]. Third, nanopores were practically absent in FMO and the contribution of narrow mesopores was low in the powders (Fig. 42). Among the adsorbates studied [30] only water adsorbed in the form of clusters. Even during single molecule adsorption, it tends to form two hydrogen bonds with neighboring surface hydroxyls. Therefore, nanopores and narrow mesopores were more appropriate for effective clustered or nanodomain adsorption of water than broad mesopores and macropores. In the latter, the formation of 3D structures totally

filling voids needed very large amounts of adsorbed water [53]. However, the adsorption of great amounts of water in broad pores at $p/p_0 < 0.98$ was thermodynamically unfavorable as well as for other studied adsorbates [30,53]. All the factors mentioned could play a certain role on the adsorption of organic adsorbates. However, thermodynamic conditions of their adsorption differ from that of water. This led to greater adsorption of organic adsorbates onto FMO in comparison with water (Figs. 40 and 41) at the same temperature (~20 ^oC).

Nonpolar hexane and weakly polar acetonitrile adsorbed onto FMO better than water but worse than polar DEA and TEA [30]. This was due to strong hydrogen bonding of the amines to the surface hydroxyls and Lewis acid sites. The adsorption of TEA was typically greater or close to that of nitrogen (at the same p/p_0 values), despite a large difference in the adsorption temperatures (293-297 K and 77.4 K, respectively). Temperature determines the average kinetic energy of molecules. Elevating temperature leads to diminution of the adsorption in voids between nonporous spherical nanoparticles where the steric effects are absent. For AST71, the nitrogen adsorption was much higher than that of TEA. This could be caused by dense packing of primary AST71 particles since the N_2 hysteresis loop was long. This loop started at $p/p_0 = 0.4$ for AST71 and AST1, but for other samples, it began at $p/p_0 \geq 0.7$. Consequently, capillary condensation of nitrogen began on AST71 (or AST1) at lower pressures than for other FMO that enhanced the adsorption [30].

In contrast to dispersion interactions of hexane and nitrogen, specific interactions of acetonitrile and amines with surface active sites (mainly various hydroxyls) could cause an overestimation of the $S_{BET,X}$ value in comparison with the values of S_{BET,N_2} or $S_{BET,hex}$ (Fig. 43, Table 6) [30]. This was due to several effects linked to features of orientation and packing of molecules in the first adsorbed layer. Orientation of adsorbed molecules interacting with surface hydroxyls, especially bridging ones, could corresponded to their non-maximal projection onto the surface. Therefore, the effective σ value could be smaller than the maximal value estimated from the molecular geometry of the adsorbates. This overestimation was maximal for acetonitrile. Its adsorption complexes mainly corresponded to non-lengthwise orientation of the molecules that caused a significant diminution of the effective σ value. However, the σ value for acetonitrile used for estimation of $S_{BET,ac}$ (Table 6) corresponded to the average projection area of a molecule to a surface [30].

The $S_{BET,X}$ overestimation for TEA was greater than that for DEA for FMO at $S_{BET,N_2} \leq 125$ m^2/g, significant crystallinity and surface roughness (Table 6, Δw) [30]. However, for SA8 and SA23 with large values of S_{BET,N_2} and amorphous silica and crystalline alumina phases, this effect was greater for DEA (Fig. 43). These results could be caused by different changes in the packing of adsorbed molecules of DEA and TEA in the first monolayer at the surface of smaller nanoparticles more strongly aggregated in secondary ones because the steric factor was lower for smaller DEA molecules than for TEA. This factor was greater for FMO with larger values of S_{BET} because they were characterized by enhanced aggregation of nanoparticles. For hexane, the overestimation of $S_{BET,hex}$ was observed for A-50, AST82, and alumina degassed at 200 and 900^oC, respectively, that could be explained by, at least, two factors [30]. First, a low S_{BET} value for both AST82 and A-50 with large primary nanoparticles (Table 6, d_{av}) weakly aggregated (Fig. 40g, loop beginning at $p/p_0 > 0.8$) provided better accessibility of the surface for relatively large C_6H_{14} molecules in comparison with other oxides with larger S_{BET} values and more strongly aggregated nanoparticles (Fig. 42). Second, a significant surface content of titania in AST82 (Table 6) enhanced dispersive interactions of hexane molecules with nanoparticles. For alumina degassed at 900 ^oC, there were additional factors such as diminution of sizes of nanoparticles (due to dehydration and crystallization without sintering), increased crystallinity and dissociative adsorption of a portion of the molecules [30].

An increase in the values of Δw (Table 6), *i.e.* enhancement of the surface roughness of nanoparticles and deviation of their shape from spherical, corresponded to increasing

$S_{BET,X}/S_{BET,N_2}$ ratio for, *e.g.*, X = acetonitrile. This correlation for acetonitrile was clear for ten FMO samples from fourteen ones studied. In other words, it was not strong correlation because many structural and other effects overlap here [30].

The hydrophilicity of FMO was analyzed using calorimetry (oxides were degassed at 473 K at low pressures for several hours) and ^{1}H NMR spectroscopy (oxides were equilibrated in air) methods applied to samples after different pre-treatments [30,53]. This characteristic was linked to the possibility of the formation of strong hydrogen and donor-acceptor bonds or/and dissociative adsorption of water. The treatments before the calorimetric measurements resulted in desorption of intact water and a portion of dissociatively adsorbed water (≡MOH, ≡M'O(H)M"≡, where M = Si, Al or Ti) from both surface and volume of oxide nanoparticles [53]. However, for the NMR measurements, surface and volume water was re-adsorbed from air. Therefore, one could expect that the heat effects on the adsorption of water on the calorimetric measurements should be stronger than that on the NMR measurements. This was typically observed for the samples studied with the exception of SA8 and ST20 [30,53]. There was a tendency for an increase in the difference between the Q_w and γ_S values with increasing size of primary particles. It was minimal (and the hydrophilicity coefficient $K = Q_w/Q_d < 1$) for amorphous SA23 (d_{av} = 6.9 nm, Δw = 0.23) and maximal for AST50 (d_{av} = 49.7 nm, Δw = 0.31, *i.e.*, roughness AST50 > SA23) with crystallinity > 90% (K = 1.83). However, this ratio depended on the particle composition, *e.g.*, AST50 (crystalline) and A-50 (amorphous, Δw = 0.38) had close d_{av} values but the reverse relationships between the Q_w and γ_S values; however, their γ_S values were close. These results could be caused by stronger heat effects on the water adsorption onto degassed samples composed of larger primary particles but depending on silica content and surface structure. Larger particles could adsorb greater amounts of water in the volume because the V/S ratio increased (especially for silica) as well as the ratio of volume and surface amounts of adsorbed water. Similar effects observed for different silicas resulted in a significant overestimation of the S_{BET,H_2O} value for heated and degassed FMO and $S_{BET,H_2O} \approx S_{BET,N_2}$ for samples equilibrated in air [30,53]. Notice that FMO studied with maximal S_{BET,N_2} values were characterized by minimal hydrophilicity. The K_h value, determined as the ratio of the heats of immersion in water and decane $K_h = Q_w/Q_d$, was low (< 1) for SA23 [53], and this nanooxide had the maximal S_{BET,N_2} value (*i.e.*, smallest nanoparticles) among the SA samples studied. Titania-containing samples (typically with small S_{BET,N_2} values) had larger K values than samples with alumina/silica, alumina or silica [30,53].

To analyze the effects of specific (hydrogen bonding) and nonspecific (dispersive) interactions of adsorbates with different surface sites, a variety of adsorption complexes was calculated by the *ab initio* method with the 6-31G(d,p) basis set appropriate to study the hydrogen bonding. For the adsorption of nonpolar hexane and nitrogen molecules, the interaction energy ($-\Delta E_{HF}$) was much smaller than that for weakly polar acetonitrile and polar DEA, TEA, and water molecules. This was due to the electrostatic interactions giving the main contribution to the ΔE_{HF} value for the hydrogen bonds (Table 7, ΔE_{el}), and this contribution was much larger than the dispersive interactions. Therefore, for weakly polar acetonitrile, the $-\Delta E_{HF}$ value was smaller than that for more polar adsorbates (TEA, DEA, H_2O). The formation of two intermolecular (hydrogen) bonds between an adsorbed molecule and neighboring hydroxyls in the oxide clusters led to greater $-\Delta E_{HF}$ values up to 65-93 kJ/mol (Table 7). Notice that the DFT calculations (with the B3LYP/6-31G(d,p), the HF/6-31G(d,p) geometry and consideration for the BSSE [30]) of the two-hydrogen-bonding complexes of H_2O and NH_3 with the silica cluster give slightly smaller values $-\Delta E_{DFT,BSSE}$ = 41.6 and 52.2 kJ/mol, respectively, than $-\Delta E_{HF}$. On the formation of two bonds, each of them could be weaker than an individual strong hydrogen bond. Diminution of the wavenumber of the O–H stretching vibrations ($\Delta\nu_{OH}$) (strongly linked to ΔE) upon the hydrogen bonding for individual bond O–H···N(H)$(CH_2CH_3)_3$ for SiO(H)Al was larger (1444 cm^{-1}) by two times than that for similar complex with TiO(H)Al (731 cm^{-1}). However, the $-\Delta E_{HF}$ values were

56 and 93 kJ/mol, respectively. Notice that the calculated $\Delta\nu_{OH}$ values could be underestimated due to the cluster approach and harmonic approximation used [30]. According to the experimental data $\Delta\nu_{OH}$ = 45, 305 and 975 cm^{-1} for hexane, acetonitrile and TEA, respectively, adsorbed onto silica, but the calculations gave 4, 130, and 496 cm^{-1}, respectively. Therefore, the $\Delta\nu_{OH}$ values calculated could be used only for qualitative analysis of certain tendencies in interactions between polar and nonpolar adsorbates with different surface sites of FMO [30,53].

Table 7. Interaction energy between Brønsted acid site =(HO)SiO(H)Al(OH)= and an adsorbate molecule calculated using the Kitaura-Morokuma method (6-31G(d,p) basis set) [30,53].

Adsorbate	$-\Delta E_{HF}$ (kJ/mol)	$-\Delta E_{BSSE}$ (kJ/mol)	$-\Delta E_{el}$ (kJ/mol)
H_2O	69.6	56.5	108.9
NH_3	75.5	65.2	121.0
CH_3CN	40.5	36.0	52.5
N_2	7.9	5.1	9.2
C_6H_{14}	4.7	1.7	1.7

Note. ΔE is the changes in the total energy on the bonding, ΔE_{BSSE} is the ΔE value with consideration for the basis set superposition error (BSSE) and $-\Delta E_{HF} > -\Delta E_{BSSE}$, and ΔE_{el} is the electrostatic component of ΔE.

Quantum chemical calculations of amorphous (cluster approach) and crystalline (periodic boundary conditions) SA and ST oxides showed that crystalline systems have stronger Brønsted acid sites [53], which could form stronger hydrogen bonds. There was a tendency, however, for a non-monotonic increase in the ratio $S_{BET,X}/S_{BET,N_2}$ with increasing crystallinity of FMO (Fig. 29c) [30].

Thus, according to the calculation results, the interaction energy depended not only on the type of surface sites but also on the structure of neighboring sites, especially for adsorbates tending to form several intermolecular bonds (per a molecule) with surface sites [30]. Additionally, the electron-donor properties of adsorbates can play an important role. Therefore, the maximal $\Delta\nu_{OH}$ values observed for TEA and DEA interacting with the Brønsted acid sites are in agreement with higher interaction energy for these amines or NH_3 (as their simple model) with the acid sites in comparison with other adsorbates. This was also due to the maximal contribution of the electrostatic component to the ΔE_{HF} values (Table 4) and higher polarizability of amines than other studied molecules. The latter was due to location of the highest occupied molecular orbital (HOMO) on the N atoms of amines (DEA, TEA) at 2-3 eV higher than the level of the HOMO localized on the O atoms in water, the N atoms in the N_2 or CH_3CN molecules or the C and H atoms in hexane [30,53].

Large values of $-\Delta E_{HF}$ could provide enough energy for certain deformations (required additional energy) of the adsorbed molecules interacting with neighboring active surface sites (depending on the pore sizes, especially in nanopores, and surface coverage). This condition obeys if the attractive interactions with the surface sites are stronger than the repulsive lateral interactions between neighboring adsorbed molecules, which could be more compacted than in the free fluid or vapor. Therefore, adsorbed molecules could occupy surface area smaller than average one calculated for the free molecules. Additionally, orientation of adsorbed molecules, which are strongly non-spherical, could be varied depending on structure of surface sites that leads to different projection area of them onto the surface. Both mentioned factors lead to overestimation of the $S_{BET,X}$ values in comparison with the S_{BET,N_2} values for the same FMO [30,53].

Investigations of the adsorption of polar, weakly polar and nonpolar adsorbates (X) onto individual and complex FMO showed that the ratio $S_{BET,X}/S_{BET,N_2}$ = 0.68-1.85 depended on the

structural characteristics of adsorbents, the nature of active surface sites, conditions of degassing, the polarity of adsorbates and their ability to form strong hydrogen (with Brønsted acid sites) or donor-acceptor (with Lewis acid sites) bonds with surface sites [30,53]. A stronger overestimation of the specific surface area $S_{BET,X}$ was found for complex oxides at S_{BET,N_2} = 100-133 m^2/g with maximal crystallinity and high roughness of nanoparticles than that at S_{BET,N_2} = 30-50 (with weakly aggregated nanoparticles) or 200-300 m^2/g with lower crystallinity (*i.e.* with lower Brønsted acidity) but strongly aggregated. Additionally, changes in the $S_{BET,X}/S_{BET,N_2}$ values correlated to changes in the oxide hydrophilicity (*i.e.*, strength and acidity of surface sites) estimated from the heat of immersion of nanooxides in water and decane [53]. The amounts of water bound to oxide nanoparticles in the aqueous suspensions were much larger than the pore volume V_{p,N_2} of the initial powders or dried solid residua of the suspension of the same materials. This was due to rearrangements of secondary and ternary particles in the strongly wetted powders or aqueous suspensions of FMO. Therefore, the rearrangement of secondary structures of FMO under action of adsorbates or/and solvents could affect their adsorption values and energetic characteristics as well as interactions of nanoparticles with their surroundings in complex liquid and polymer media. The results obtained showed that not only the specific surface area, pore volume, pore size distributions, and particle sizes but also surface composition and crystallinity of the surface phases and the surface roughness and rearrangement of FMO nanoparticles affected the adsorption of different adsorbates, as well as the adsorbed layer structure and the behavior of the interfacial layer. This influence was maximal for adsorbates forming the strong hydrogen and donor-acceptor bonds with different sites of FMO surfaces. The effects described are of importance for the optimization of nanooxide materials for a range of applications including adsorbents, fillers, and additives [53].

Treatment of FMO in aqueous media (and subsequent drying) more strongly affected the adsorption of both polar (water, DEA) and nonpolar (hexane) adsorbates than MCA of the powders (Figs. 44 and 45). This could be explained by a larger rearrangement of nanoparticles in sonicated aqueous suspensions compared to the rearrangement of them in organic solvents [47,53,90].

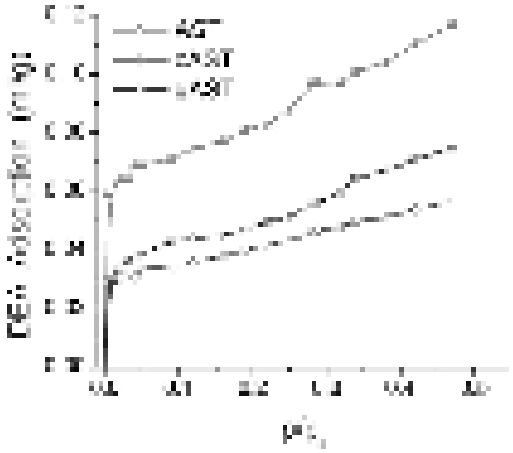

Fig. 44. Adsorption isotherms of diethylamine onto AST1 initial, cryogel (208 K for 12 h) and gel (24 h) dried and degassed.

The adsorption of water (Fig. 45a) and benzene (Fig. 45b) was similar for MCA-treated mixture with A-300/AST1. For relatively large molecules of adsorbates such as diethylamine (Fig. 45c), lower adsorption occurred after HPCG. The presence of NaCl (during HPCG and then in treated and dried samples) could reduce the compaction of aggregates, as well as silica can do in A-300/AST1 [46,47]. After HPCG, the adsorption of diethylamine onto A-300/AST1/NaCl was similar to that for suspended-dried A-300/AST1; however, the adsorption onto A-300/AST1 cryogel was much lower (Fig. 45c) [90]. The adsorption of nonpolar hexane (Fig. 45d)

demonstrated other features of the process on differently treated A-300/AST1 samples. The adsorption of hexane was largely independent on treatment type at $p/p_s < 0.4$, corresponding to mainly monolayer coverage of the FMO surface. This was in contrast to diethylamine at $p/p_s < 0.4$ where large adsorption differences were seen with treatment type. It was higher than that for initial AST1. The open hysteresis loops for the hexane isotherms, especially for the suspended-dried mixture with A-300/AST1 (Fig. 45d), could be explained by the formation of long curved pores with narrow throats in compacted secondary structures of treated FMO. With this pore geometry the desorption could be activated and, therefore, it was slow [90].

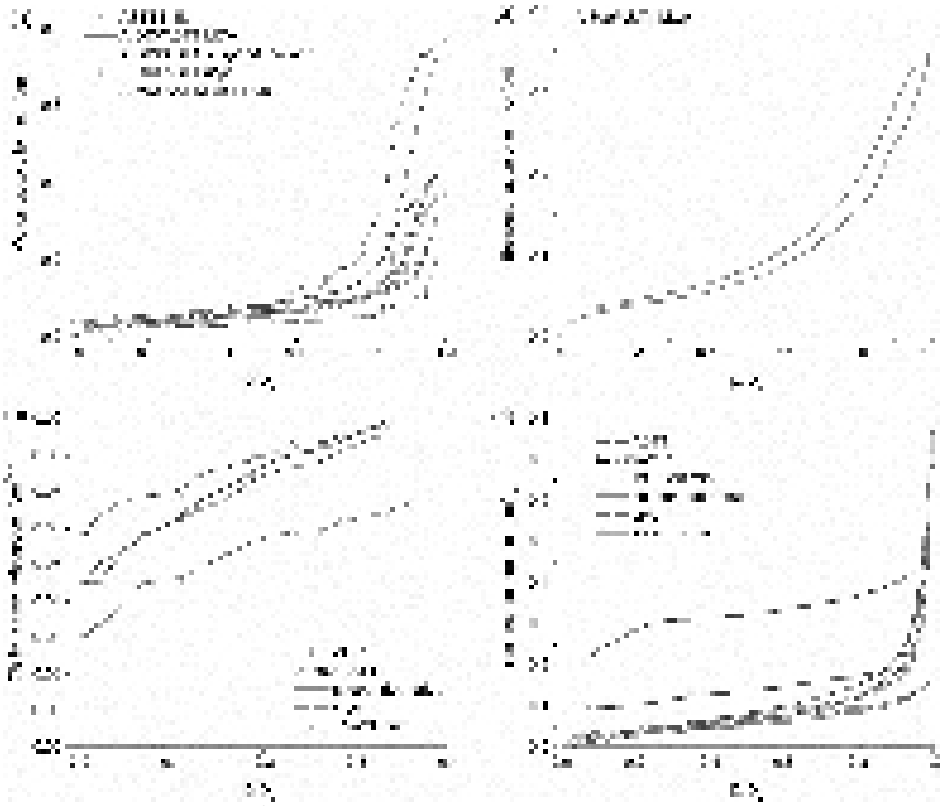

Fig. 45. Adsorption isotherms (at 20±1 °C) of (a) water, (b) benzene, (c) diethylamine, and (d) n-hexane onto AST1 or A-300/AST1 differently treated.

Surface modification of ST could lead to substitution of not only surface silanols but also Ti-OH groups [52,106]. It was believed that Ti-O-Si surface bonds were relatively easy to hydrolyze, thus the surface modified ST20 was slurred in water for 30 minutes, filtered and dried (Figs. 46 and 47). The concentration of surface C≡N was quantitatively analyzed before and after exposure to water by monitoring the CN stretching band area ratioed to the 800 cm^{-1} SiO_2 band as an internal standard. Prior to water exposure the band area ratio was 0.372 ± 0.012, and after water exposure = 0.343 ± 0.020. A paired *t*-test indicates that these values were different at the 95% confidence level, suggesting that some surface functionalized Ti-OH species were hydrolyzed upon water exposure. After this water treatment, the material was exposed to UV irradiation for 1 hour and the infrared spectrum of the dried ST20 was reacquired, with no apparent changes. Thus, the remaining surface SCN groups were stable to both hydrolysis and photocatalysis [108].

Although the differences in adsorption of methylene blue between the unmodified and surface-modified ST20 samples was evident, the differences were not as large as that of pure silica since unmodified ST20 has some strong adsorption sites that silica did not (Fig. 48) [108].

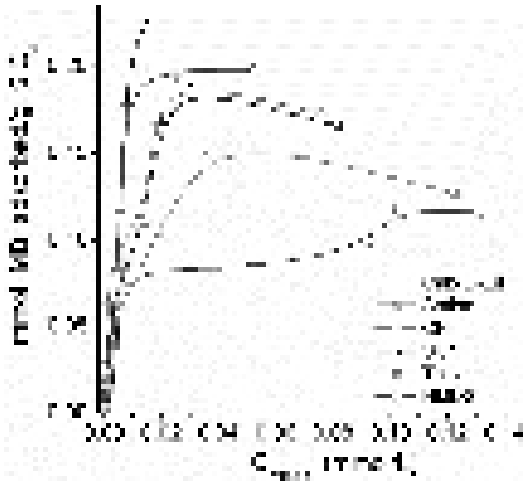

Fig. 46. Isotherms of methylene blue adsorption on unmodified and modified FMO (amine - Cab-O-Sil HS5 modified by 3-aminopropyltrimethoxysilane, CN - 3-cyanopropyltrimethoxysilane, SCN - 3-thiocyanatopropyltriethoxysilane, thiol – 3-mercaptopropyltrimethoxy silane, and HMDS - hexamethyldisilazane).

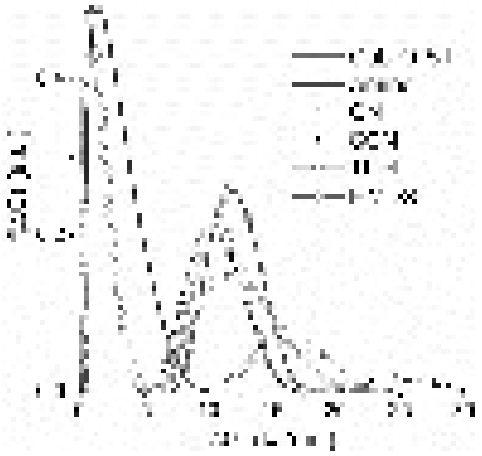

Fig. 47. Distribution functions of Gibbs free energy of methylene blue adsorption on unmodified and modified FMO.

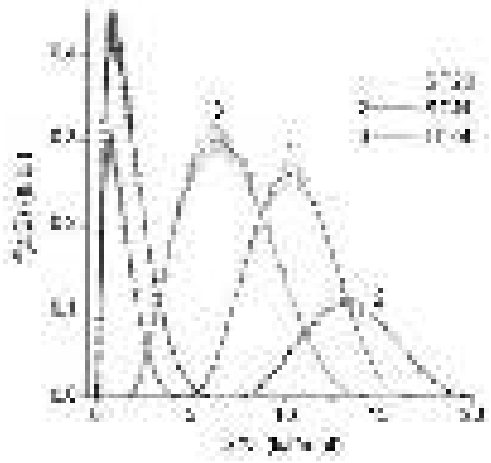

Fig. 48. Distribution functions of Gibbs free energy of methylene blue adsorption on unmodified and modified ST20 (error bar of the calculations is shown).

Complex silica/titania (ST20) more strongly affected bound water structure (Fig. 49), and was characterized by a small activation energy of dc relaxation (Table 8, $E_{a,dc}$) [109]. Residual sulfate groups affected the number and mobility of ions and, therefore, small $E_{a,dc}$ values were found for suspensions with PC-titanias (Table 8, $E_{a,dc}$), and the larger the content of sulfate groups, the smaller was the $E_{a,dc}$ value. Fumed ST20 has stronger Brønsted acid sites than titania alone; therefore, $E_{a,dc,TiO2} > E_{a,dc,ST20}$. The number of acid/base sites at a surface should not strongly affected such redox reactions as photodecomposition of methylene blue, but could affect the adsorption of MB and its electronic state, *e.g.*, MB protonation. The MB molecules adsorbed on the PC-500 surface reduced the interaction of the titania surface, with interfacial water [53,109] displaced from the surface, since the TSDC of the frozen suspension of PC-500/MB was lower than that of PC-500 at $T < 170$ K (Fig. 49c) [108,109].

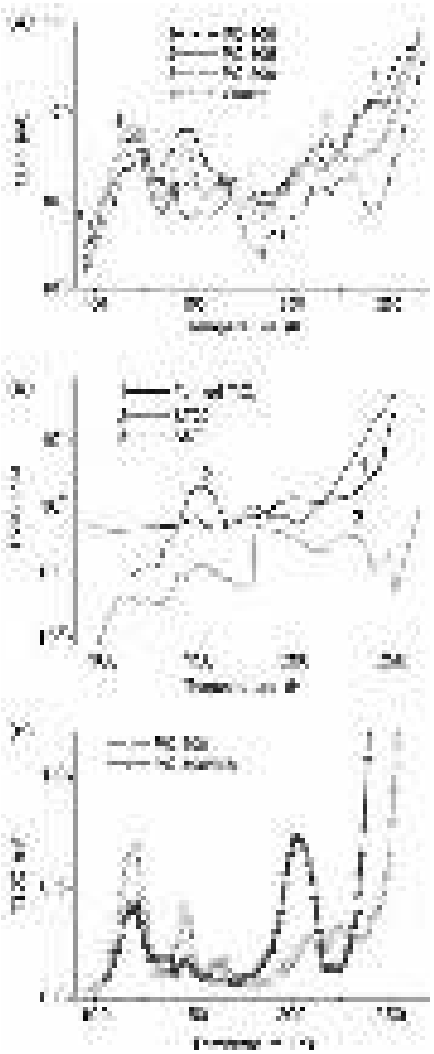

Fig. 49. TSDC thermograms for frozen 3 wt.% aqueous suspensions of (a) PC titania (and water alone) and (b) fumed oxides (thermograms were normalized to F_p = 1 MV/m).

Table 8. Structural and adsorption characteristics of nanooxides [109].

Sample	S_{BET} (m^2/g)	V_p (cm^3/g)	$\Delta H_{im,w}$ (mJ/m^2)	$\Delta H_{im,d}$ (mJ/m^2)	d_{XRD} (nm)	$E_{a,dc}$ (kJ/mol)
PC-100	89	0.358	453	157	18 (A)[a]	34.9
PC-105	78	0.356	456	147	20 (A)[a]	61.7
PC-500	207	0.375	423	137	9 (A)[a]	76.2 71.9 (MB)[c]
Fumed TiO_2	60	0.194	184		24 (A)[a] 30 (R)[b]	146.7
ST20	64	0.148	469		12 (A)[a]	45.4
AST1	99	0.253	548		-	126.4

Note. Crystallite size of [a] anatase and [b] rutile. The heat of immersion in water ($\Delta H_{im,w}$) and decane ($\Delta H_{im,d}$); [c] 0.3 wt.% MB was added to 3 wt.% PC-500 suspension.

However, polar MB molecules (both adsorbed on the titania surface and dissolved in the bulk water) strongly contribute to dipolar relaxation at $T > 170$ K. Additionally, the activation energy of dc relaxation decreased for PC-500/MB (Table 8, $E_{a,dc}$) because of the influence of MB changing the water characteristics (Fig. 49). All the mentioned effects could play an important role on photodecomposition rate since adsorbed MB molecules were most likely to be decomposed [109].

The enthalpy of phase transition of bound adsorbates (Tables 9 and 10, ΔH) is smaller by the modulus than that of bulk liquids (freezing) or solids (fusion) with one exception of *n*-decane (40% longer than *n*-hexane) bound to initial A-300/AST1. The decrease in the $|\Delta H|$ occurs due to

(i) small sizes of bound structures (clusters, nanodomains) located in voids between nanoparticles, and (ii) certain disorder of bound liquids (being in amorphous state after freezing) which are frozen at temperatures lower than the freezing point of bulk liquids [53]. Both factors cause smaller values of energy which should be spent (for melting) or realized (upon freezing) per a bound molecule of the adsorbate.

The values of the exotherms (cooling → freezing) and endotherm (heating → melting) on the DSC thermograms depend on the amounts of adsorbates and adsorbents [53]. The adsorbate amounts more strongly affect the exotherms/endotherms related to strongly (SBA) or weakly bound adsorbates (WBA). For the majority of the studied samples, the amounts of adsorbates were larger than that of adsorbents. Therefore, a significant portion of adsorbates was weakly bound that gives the sharp exotherms of freezing and the main endotherms at temperatures close to melting point of the bulk frozen compound. For better view of the effects of the types of adsorbates and adsorbents, the DSC thermograms were normalized per mg of adsorbate with subtraction of the baseline (Figs. 50-52). Relatively large amounts of adsorbates interacting with FMO lead to low intensity of melting endotherms of SBA, which are located at $T < T_m$ at $\Delta T = T - T_m > 10$ °C, in comparison with the melting endotherms of weakly bound adsorbates that is located at T close to melting point at $\Delta T < 10$ °C [53].

For aromatics (benzene, toluene), the freezing point depression is stronger than that for *n*-decane (Figs. 50-52). Melting delay (*i.e*. melting of frozen adsorbates at $T > T_m$) is observed for both nonpolar and polar adsorbates. However, it is absent for DMSO bound to initial or MCA A-300 (Fig. 50f). Note that DMSO possesses maximal donor number DN = 125 kJ/mol among studied adsorbates (*e.g*. for water DN = 75 kJ/mol) [53]. DN is a quantitative measure of Lewis basicity, *i.e*. the possibility to form strong hydrogen bonds with surface hydroxyls (Table 11). Therefore, the DMSO molecules form the hydrogen bonds with surface hydroxyls stronger than other studied adsorbates that strongly change the structure of interfacial DMSO layers in comparison with bulk liquid (and frozen DMSO). However, the acceptor number (AN) is higher for water than that for DMSO. Therefore, in contrast to other studied adsorbates, water tends to form adsorbed clusters, in which water molecules act as both proton-acceptors and proton-donors, and even at low content, water forms cyclic clusters around surface hydroxyls. For other studied adsorbates, the values of DN are much lower than those for DMSO or water, *e.g*. DN = 0 for chloroform. However, AN of chloroform is larger (by 11 kJ/mol) than that of DMSO. These features of the electronic and molecular structures of adsorbates differently affect their behavior in pores (voids between nanoparticles causing confiened space effects) such as freezing-melting point depression (or delay) *vs*. pore sizes and structures of adsorbates and pore surfaces. The observed depression is stronger for DMSO and water bound to MCA A-300 than that for initial A-300 (Figs. 50-52), because voids become narrower after MCA. This is due to the pure confined space effect, because MCA does not practically change the surface structure of nanosilica in contrast to AST1 more strongly affected by MCA (due to destroy of large core-shell nanoparticles) till to change the sample color. The HPCG more strongly affects the melting thermograms of adsorbates bound to AST1 than the MCA of AST1 does (Fig. 51). In the A-300/AST1 blend, nanosilica plays a role of a damper during HPCG. Therefore, the difference in the melting endotherms in comparison with the initial powder can be smaller for this blend (Fig. 52) than that for AST1 initial and treated alone (Fig. 51).

For certain samples, the freezing point depression corresponds to relatively small shifts of the phase transition (melting) temperature at $|\Delta T| < 10$ °C (Tables 9 and 10, Figs. 50-52). This range of the shifts of the melting points corresponds to WBA, since condition $|\Delta T| > 10$ °C corresponds to SBA. Typically, larger structures of adsorbates (domains) located in broader voids (pores) mainly correspond to WBA, but structures located in narrow voids (i.e. relatively small clusters of adsorbates) or adsorption layers located close to the pore walls frequently represent SBA. The position of very narrow exotherms related to freezing of WBA (due to excess of adsorbates much larger than the pore volume V_p, Table 1) depends on the cooling rate (β), and the greater the value of β, the lower is the freezing point. MCA results in the shifts of the PSD peaks

toward smaller pore sizes, and high-pressure or normal-pressure cryogelation leads to compacting of the secondary particles. Therefore, these treatments can enhance the contributions of SBA. These strong effects of the treatments on the texture of the powders can result in the appearance of open hysteresis loops for even non-polar compounds adsorbed onto treated FMO (Fig. 45) [53]. This open shape of the isotherms can correspond to activated desorption or swelling of adsorbents in liquid nitrogen.

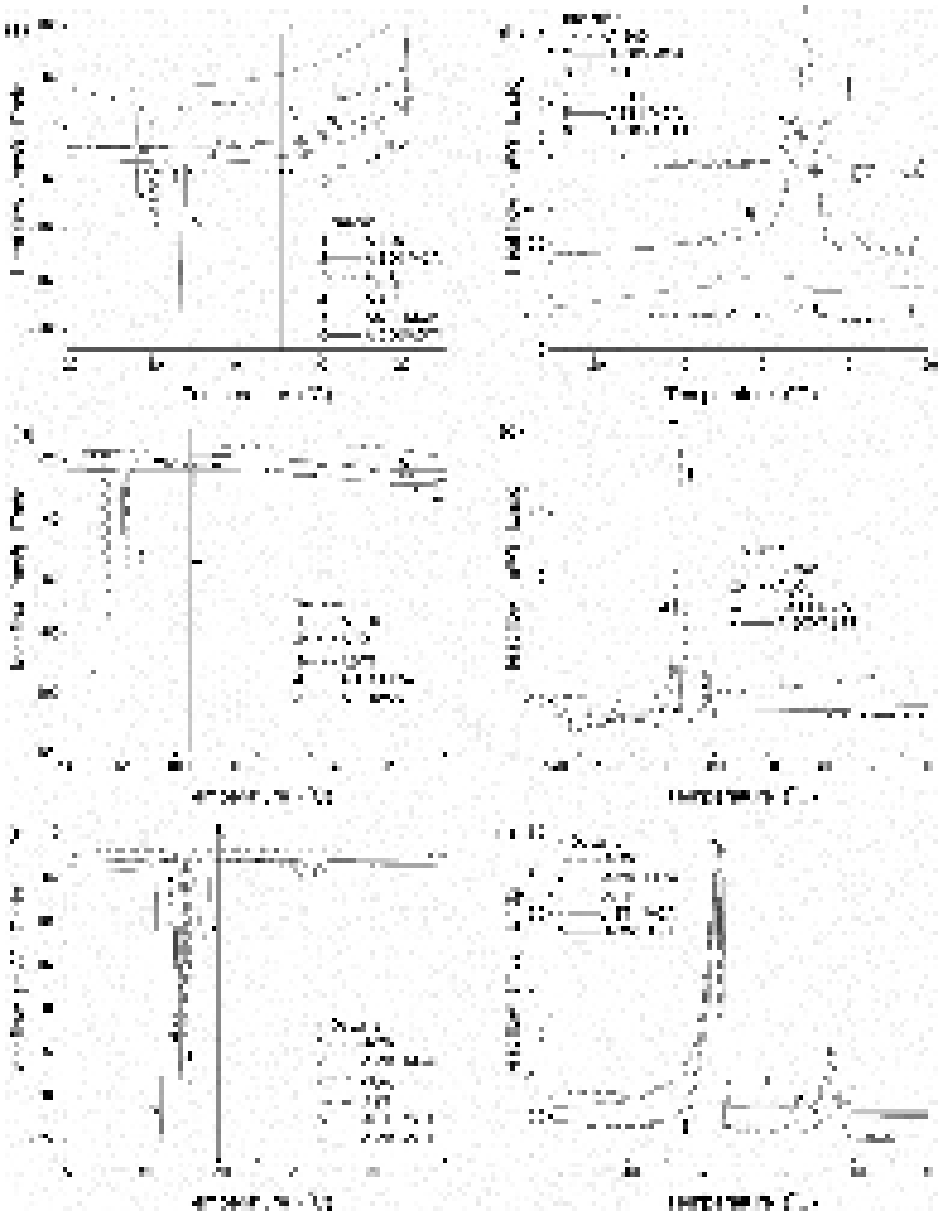

Fig. 50. DSC thermograms (cooling (a, c, e) and heating (b, d, f)) of nonpolar adsorbates bound to initial or MCA FMO: (a, b) benzene (melting point T_m = 5.53 °C, boiling point T_b = 80.1 °C), (c, d) toluene (T_m = −95 °C, T_b = 111 °C), and (e, f) n-decane (T_m from −30.5 °C to −29.2 °C, T_b from 173.8 °C to 174.4 °C). Cooling/heating rate is β = 10 °C/min for all samples with exception of toluene at β = 20 °C/min.

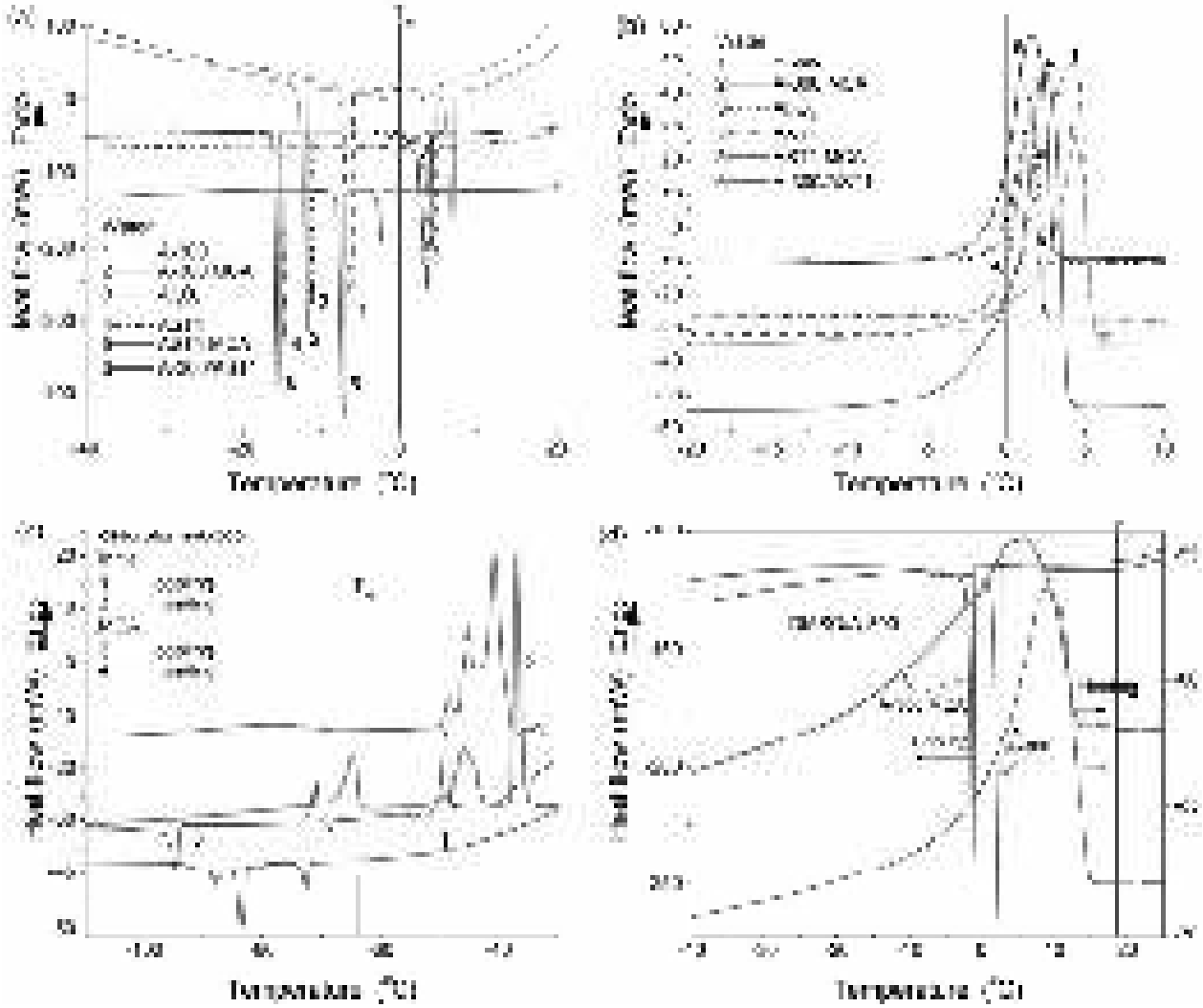

Fig. 51. DSC thermograms (cooling (a, c) and heating (b, c)) of polar adsorbates bound to initial or MCA FMO: (a, b) water (melting point T_m = 0 °C, boiling point T_b = 100 °C), (c) chloroform (T_m = −63.5 °C, T_b = 61.15 °C), and (d) DMSO (T_m = 18.5 °C, T_b = 189 °C). Cooling/heating rate is β = 10 °C/min for all samples with exception of chloroform at β = 20 °C/min.

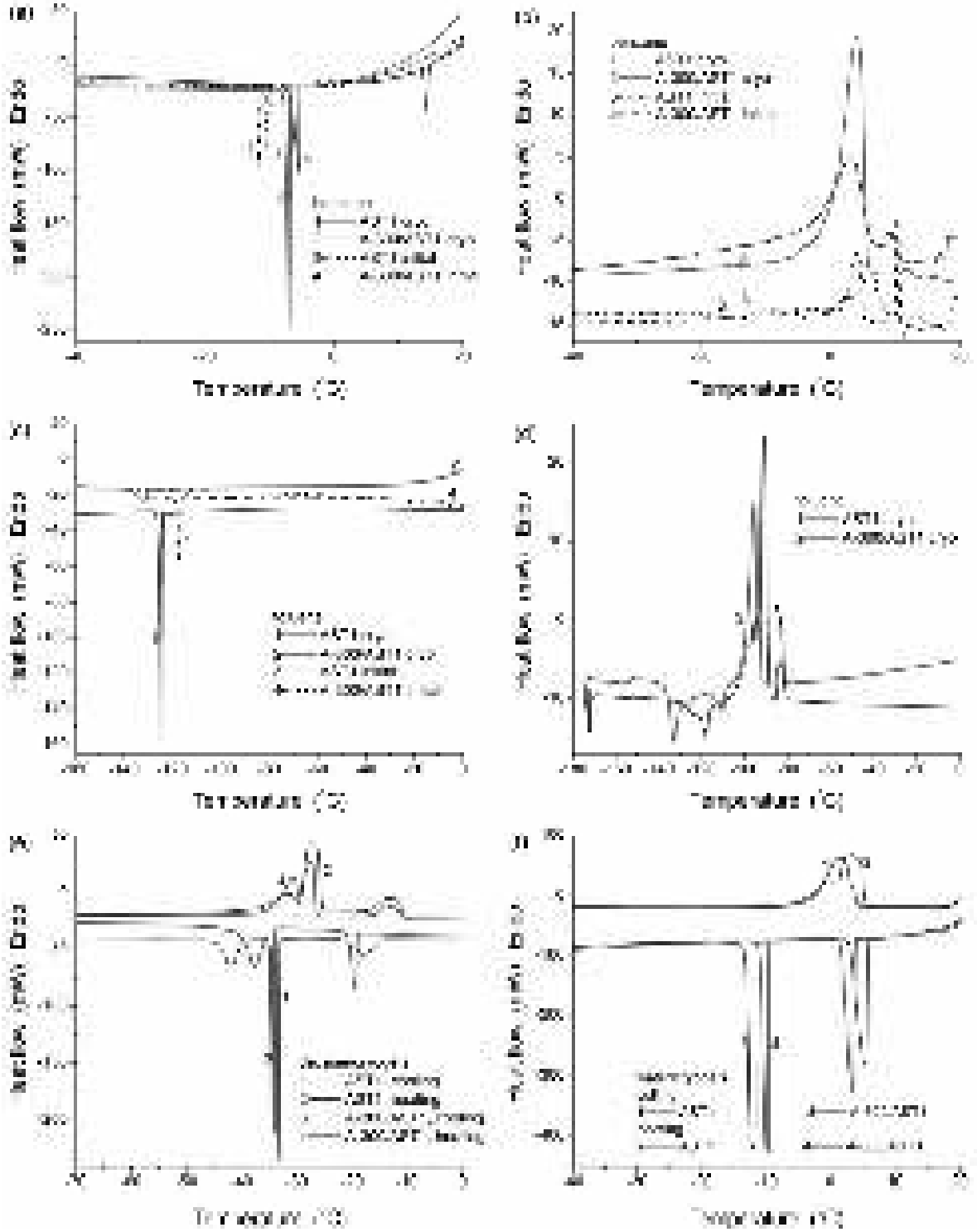

Fig. 52. DSC thermograms (cooling (a, c, e, f) and heating (b, d, e, f)) of (a, b, c) nonpolar and (d) polar adsorbates bound to FMO high-pressure cryogels: (a, b) benzene, (c, d) toluene, (e) decane, and (f) water (curves for initial FMO are also shown in (a)-(c)). Cooling/heating rate is $\beta = 10\ ^{o}C/min$ for all samples with exception of toluene at $\beta = 20\ ^{o}C/min$.

Table 9. Shifts $\Delta T = T - T_m$ (K) in peak temperatures and corresponding enthalpy ΔH (J/g) in DSC thermograms.

Sample	Process	Adsorbate															
		Water				Benzene				Toluene				n-Decane			
		ΔT	ΔH	ΔT	ΔH	ΔT	ΔH	ΔT	ΔH	ΔT	ΔH	ΔT	ΔH	ΔT	ΔH	ΔT	ΔH
A-300 initial	Cooling	–6.2	–244.3	4.4	–204.0	-15.0	–88.1	2.4	–90.1	–30.7	–37.6			–5.7	–194.9	9.7	–13.1
	Heating	4.3	233.6			0.3	89.4			3.0	47.1	12.0	4.3	1.5	200.6	19.0	12.3
A-300 MCA 30 min	Cooling	–11.7	–151.0	6.5	–108.7	–17.2	–11.8							–13.0	–14.9	–2.4	–88.5
														10.6	–12.6		
	Heating	4.3	155.7			–4.6	10.0							2.0	137.4	15.0	12.4
Alumina initial	Cooling	–11.0	–72.5	3.2	–57.9	-16.7	–6.4							–6.1	–139.0	7.6	–3.9
	Heating	–12.0	1.6	1.5	81.9	0.3	2.7										
AST1 initial	Cooling	–14.5	–149.9	3.3	–262.5	–15.7	–27.1			–22.0	–29.4			–5.0	–165.6	10.4	–18.8
	Heating	1.5	140.0			–22.3	0.9	1.9	19.1	1.9	35.1	13.5	7.3	–1.4	163.4	15.8	8.1
																18.9	3.4
AST1 MCA 30 min	Cooling	–7.3	–121.3	–2.4	–22.3	–11.9	-32.0			–24.0	–24.1			–8.0	–103.5	13.8	–15.5
	Heating	1.5	177.3			–1.0	33.4			1.9	26.8	11.5	14.1	2.1	124.8	16.1	15.7
AST1 cryo	Cooling	–12.5	–166.7	5.3	–205.0	–11.1	–31.7	9.0	–9.8	–29.8	–28.9			–11.4	–44.6	–2.9	–117.5
														12.7	–37.2		
	Heating	2.8	285.3			–2.5	34.6	4.0	0.8	3.8	34.8	11.7	5.4	–1.3	20.2	3.2	154.0
														17.7	36.0		
A-300/AST1 initial	Cooling	–15.5	–167.1	3.6	–3.1	–17.0	–67.9			–18.7	–3.6			–5.5	–250.1	11.3	–93.7
	Heating	1.6	207.0			–1.4	45.6			0.9	<1.0	12.9	<1.0	1.4	240.7	16.7	82.3
A-300/AST1 cryo	Cooling	–9.9	–249.9	3.3	–249.0	–12.3	–70.9			–36.3	–12.4			–7.3	-48.1	–3.5	–75.6
														11.0	–38.1		
	Heating	1.3	275.9			–1.5	94.9	6.0	1.5	-0.5	45.0	13.6	4.1	0.3	41.6	3.2	59.0
														16.7	34.9		

Note. Enthalpy of fusion at freezing point is 333.5 (water), 126.3 (benzene), 71.8 (toluene), 73.7 (chloroform), 183.9 (DMSO), and 201.82 (n-decane) J/g. Values of $\Delta H < 0$ and $\Delta H > 0$ correspond to exotherms and endotherms, respectively.

Table 10. Shifts $\Delta T = T - T_m$ (K) in peak temperatures and corresponding enthalpy ΔH (J/g) in DSC thermograms.

Sample	Process	Adsorbate					
		DMSO		Chloroform			
		ΔT	ΔH	ΔT	ΔH	ΔT	ΔH
A-300 initial	Cooling	–16.3	–74.1	–9.4 –25.1	–3.5 –5.6	–20.5	–44.9
	Heating	–9.9	110.5	-1.6 26.2	17.0 35.0	17.2	26.3
A-300 MCA 30 min	Cooling	–19.8	–51.6	–31.6	–6.0		
	Heating	–13.0	82.2	–16.3	8.8	22.5	44.3

Table 11. Energy of molecules of adsorbates in the gaseous and liquid state (methods ωB97XD/cc-pVDZ (gas phase) and SMD/ωB97XD/cc-pVDZ (liquid phase)).

Compound	$-E_{t,g}$ (Ha)	$-E_{t,l}$ (Ha)	$-\Delta E_s$ (kJ/mol)	E_{CDS} (kJ/mol)
Benzene	232.180344228	232.188434255	21.2	-15.1
Toluene	271.487909798	271.496489581	22.5	-15.8
n-Decane	394.239040751	394.248132818	23.9	-21.9
n-Hexane	237.020340834	237.026503668	16.2	-14.8
Chloroform	1419.28566524	1419.29329148	20.0	-12.6
DMSO	553.134547788	553.145496094	28.7	0.0
Water	76.3996333120	76.4109660870	29.8	6.1

Note. $E_{t,g}$ and $E_{t,l}$ are total energy of a molecule in the gas and liquid states, respectively. ΔE_s is the solvation energy. E_{CDS} is the non-electrostatic components of the solvation energy.

Evaporation of liquids and condensation of vapors or gases *vs*. temperature are important interfacial phenomena occurring in nature, agriculture, industry, and medicine. These processes can be affected by a type of liquid or vapor/gas, structure of liquids, surroundings (free bulk, droplets or pore-confined liquids, characteristics of adsorbents, i.e. confined space effects), presence of solutes (co-adsorbates), gas and liquid flow parameters, pressure, and they depend exponentially on temperature as activated ones [53,101,110-124]. Confined space effects lead to deceleration of evaporation, especially from long and narrow pores, despite changes in the surface tension (as well as some other characteristics such as density, critical temperature, *etc.*) of liquids located in pores. The stronger the intermolecular interactions between molecules of a liquid and solutes or between them and active surface sites of pore walls, the slower is the evaporation, especially from the depth of narrow pores [110-124]. These effects could enhance condensation of vapors or gases upon adsorption in porous media [84]. Adsorbates could form layers [53,125], *e.g.,* upon adsorption of plane molecules (*e.g.,* benzene) in slit-shaped pores of activated carbons, exfoliated graphite, graphenes, clays, *etc.* that lead to changes in their properties in comparison with bulk liquids free of layered structures. Free bulk and bound waters form clustered structures, which depend on confined space effects [53]. The properties of liquids (surface tension, boiling and critical temperatures, density, diffusivity, mobility, *etc.*, see Table S8 in SI) in strongly confined space could significantly differ from those of bulk liquids [53,126,127]. These effects become stronger in narrower pores depending on the pore wall nature (chemical structure) and shape. However, in mesopores at radius $R_p > 10t$ (where t is the adsorbate monolayer thickness), the mentioned above changes in the properties of adsorbates could be relatively small [53,127].

Experimental techniques based on evaporation (such as thermogravimetry (TG), temperature-programmed desorption (TPD) of adsorbates) [128-130] or condensation (used in recording of adsorption/desorption isotherms of gases or vapors) [84,85] give information on features of interactions between adsorbates and adsorbents depending on the nature of both ones, the texture and morphology of adsorbents [53]. Polarity, features of intermolecular interactions, molecular weight and size of adsorbates could strongly affect their temperature and interfacial behaviors [53,84]. The evaporation rate and evaporation / accommodation coefficients give

important information for deep insight into the phenomena affected by confined space effects [53,84,110-115,122-124].

Theoretical and experimental investigations of spreading of liquid droplets on solid surfaces and their evaporation were discussed for pure liquids and solutions [131]. Evaporation of complete wetting and partial wetting liquids into a nonsaturated vapor atmosphere were considered in this work. The main attention was focused on partial wetting characterized by the hysteresis of static contact angle. For complete wetting, spreading/evaporation proceeded in two stages that was theoretically described with a good agreement with experimental data. For partial wetting, the spreading/evaporation of a sessile droplet of pure liquid could occur through four subsequent stages [131]. The initial one, spreading, could be relatively short (1–2 min) and, therefore, evaporation could be neglected during this stage. During the initial stage, the contact angle reaches the value of advancing contact angle and the radius of the droplet base reaches its maximum value. The first stage of evaporation is characterized by the constant value of the radius of the droplet base. The value of the contact angle during this stage decreases from static advancing angle to static receding contact angle. During the second stage of evaporation, the contact angle remained constant and equal to its receding value, while the radius of the droplet base decreased. At the third stage of evaporation both the contact angle and the radius of the droplet base decrease until the drop completely disappears. It has been shown theoretically and confirmed experimentally that during the first and second stages of evaporation the volume of droplet to power 2/3 decreased linearly with time [131]. The universal dependence of the contact angle during the first stage and of the radius of the droplet base during the second stage on the reduced time has been derived theoretically and confirmed experimentally. The theory developed for pure liquids is applicable to nanofluids, where a good agreement with the available experimental data could be found. However, for evaporation of surfactant solutions the process deviates from the theoretical predictions for pure liquids at concentration below critical wetting concentration and it is in agreement with the theoretical predictions at concentrations above it. Thus, the theoretical models of evaporation of free and sessile droplets have been well developed [115,123,131].

For similar processes occurred for droplets in the gaseous phase or upon location of liquids in pores [101], quantum chemical (QC) calculations related to evaporation of polar and nonpolar liquids were carried out with density functional theory (DFT) methods using a hybrid functional ωB97X-D [132-134] (labelled as wB97XD in Gaussian 09) and various basis sets (aug-cc-pVQZ, aug-cc-pVTZ, cc-pVTZ, and cc-pVDZ) with the Gaussian 09 program suit [132]. The solvation effects (for molecule alone or in adsorbed state on a silica cluster in a medium with this compound or in the gas phase) were analyzed using the solvation model SMD [135] implemented in Gaussian 09. To compute the Gibbs free energy of solvation (subscript s), it was assumed that $\Delta G_s = G_l - G_g$, where G_l and G_g were the Gibbs free energies of a molecule free or bound to silica cluster in the liquid (subscript l) and gas (g) media, respectively. The calculations were performed taking into account zero-point and thermal corrections to the Gibbs free energy in the gas phase and for solved molecules and silica clusters using the geometry optimized using HF/cc-pVDZ, ωB97X-D/cc-pVDZ, ωB97X-D/cc-pVTZ or ωB97X-D/aug-cc-pVQZ (last basis was used only for water) [132-136]. The solvation effects were analyzed for the silica clusters with 8 and 22 tetrahedrons alone and with an adsorbed molecule (see SI). Note that functional ωB97X-D introduces empirical damped atom-pairwise dispersion terms into the functional containing range-separated Hartree-Fock exchange for better description of van-der-Waals (vdW) interactions [132-136]. Therefore, this functional was selected to obtain more adequate results for the gas and liquid (SMD) phases. For linear molecules of 1-butanol or *n*-hexane, four conformers free or bound to a silica cluster were taken into account. The effect of conformerization of *n*-hexane and 1-butanol molecules, resulting in conformation-dependent changes in the Gibbs free energy of the molecules in both phases, and the evaporation/condensation processes depended on the population of conformer states [138,139].

Silica surface was modelled by clusters with eight $SiO_{4/2}$ tetrahedrons and eight hydroxyls or 22 tetrahedrons with 16 OH. Interactions of molecules H_2O, C_6H_6, *n*-C_6H_{14}, $H_3C(CH_2)_3OH$,

$(CH_3)_2CO$, and CCl_4 with the silica cluster were analyzed using ωB97X-D/cc-pVDZ with complete optimization of the geometry using ωB97X-D/cc-pVDZ (smaller silica cluster) and HF/cc-pVDZ (larger cluster) [101].

The effect of conformerization of molecules, resulting in conformation-dependent changes in the Gibbs free energy of the molecules in the gas and liquid phases, was studied for 1-butanol and *n*-hexane considering linear and strongly bent conformers (see SI). The geometry of free conformers and their complexes with the small silica clusters was completely optimized using ωB97X-D/cc-pVDZ. In complexes with the larger cluster, only linear conformers were used [101].

The Gibbs free energy of an ensemble of conformers could be determined by formula [137]

$$G_N = -RT \ln \sum_{j=1}^{N} \exp(-G_j / k_B T), \quad (14)$$

N is the number of conformers, R is the universal gas constant, k_B is the Boltzmann constant, and T is the temperature in the gas or liquid phase. To estimate the average changes in the Gibbs free energy upon evaporation of a molecule, a formula could be used [101,138,139]

$$\left\langle \Delta G_{l\to g} \right\rangle = (G_{N,g} - G_{N,l}) / N, \quad (15)$$

where subscripts l and g corresponded to molecules in the liquid and gas phase, respectively. Besides the conformerization of *n*-hexane and 1-butanol, this approach was used to study interaction of the molecules with the silica clusters. The solvation effects were computed for the corresponding complexes of the molecules with the silica clusters. In this case Eq. (15) was corrected

$$\left\langle \Delta G_{l\to g} \right\rangle = \left[(G_{N,g} - G_{N,l}) + (G_{cl,g} - G_{cl,l}) \right] / 2N, \quad (16)$$

where $G_{cl,g}$ and $G_{cl,l}$ were the Gibbs free energies of the pure silica cluster in the gas and liquid phases, respectively. Thus, several processes should be considered such as evaporation of molecules (i) adsorbed onto pore walls at the gas/solid interface, (ii) located at the gas/liquid interface, (iii) adsorbed onto pore wall in liquid/solid interface and transferred toward gas/liquid of gas/solid interfaces [101,138-144].

For simplicity, one could assume that the Gibbs free energy of evaporation $\Delta G_{ev} \approx \Delta G_{l\to g}$ [139,140]. The evaporation enthalpy ($Q_{ev}(T) > 0$) contributing to $\Delta G_{ev}(T)$ could be estimated for liquids as [143]

$$Q_{ev}(T) = q(1 - T / T_c)^m, \quad (17)$$

where q and m are the constants, and T_c is the critical temperature, to estimate changes in ΔG_{ev} as [139,140]

$$\Delta G_{ev}(T) = \Delta G_{l\to g}(T_0) Q_{ev}(T) / Q_{ev}(T_0), \quad (18)$$

where $\Delta G_{l\to g} = -\Delta G_s = G_g - G_l$, $T_0 = 298.15$ K. The estimation of $\Delta G_{ev}(T)$ based on Eq. (18) is more reliable than direct QC calculation of $\Delta G_{ev}(T)$ at high temperatures [101,144] using ωB97X-D/cc-pVTZ and SMD/ωB97X-D/cc-pVTZ. Eq. (18) could overestimate a decrease in ΔG_{ev} with temperature due to different changes in the entropy with temperature for different conformers in the gas and liquid phases.

The equation for the averaged (by states of N conformers) evaporation rate $\left\langle k_{i(i+j)} \right\rangle$ [101,144] of the ith-molecule (which could be in a different conformer state) from the jth cluster or nano-, micro-droplet (hereafter referred to as droplets), taking into account conformerization effects (for *n*-hexane and 1-butanol), could be re-written in the form [138,139]:

$$\left\langle k_{i(i+j)} \right\rangle = b_{ij} \frac{p}{k_B T n_0} \exp \frac{\left\langle \Delta G_{g\to l} \right\rangle}{RT}, \quad (19)$$

where b_{ij} is the collision rate of the ith molecule with the jth droplet calculated using the kinetic gas theory [101,138-144], n_0 is the initial number of molecules in a droplet (here 4 or 20 nm in diameter), p is the reference pressure (which could be estimated according to experimental

conditions). The values of $\Delta G_{g\rightarrow l}$ and $\Delta G_{l\rightarrow g}$ for adsorbed liquids (Eq. (20)) were corrected taking into account changes in the interactions of molecule-molecule and molecule-silica surface. For simplicity, the Gibbs free energy of a microdroplet with a very large n_0 was assumed to be not affected by a removal of a single molecule. The conformerization was assumed to take place not only in a certain phase but also during possible changes in conformer states when molecules transfer from liquid to gas phase and *vice versa.* This effect depends on the population of states of various conformers in both phases and could affect the values of β and k *vs*. temperature and pressure. Clearly, the evaporation rate for liquids from pores differs from the rate of free liquids. To account the effect of pores, modified equation described in detail elsewhere [101,142] was used

$$k(T) = k_0(T)\frac{4R_p^2}{L_p^2}\exp\left(-\frac{2\gamma_p(T)V_m(T)\cos\Theta}{R_gTR_p}\right), \quad (20)$$

where k_0 is the evaporation rate for free liquid with corrections of the Gibbs free energy in respect to interactions of adsorbates with a silica surface, V_m is the molar volume, R_p is the pore size, L_p is the pore length, Θ is the contact angle (assuming $\cos\Theta = 1$), and $\gamma_p(T)$ is the surface tension for liquid located in pores determined using equation for bulk liquid [143]

$$\gamma_b(T) = A(1-T/B)^m, \quad (21)$$

where A, B, and m were constants, and in pores $\gamma_p(T) = \gamma_b(T)f(R_p)$, where $f(R_p)$ is the correction function caused by confined space effects (analyzed only for water). The form-factor $\frac{R_p^2}{L_p^2}$ in Eq. (20) corresponded to the ratio of the area of pore section and the whole bead surface. To determine k_0 in Eq. (20), Eq. (19) could be used for evaporation of free droplets [101,144] of sizes corresponding to the average diameter of pores with corrected Gibbs free energy due to the interactions of a molecule with the silica surface (modelled by a cluster). For simplicity, one could suggest that $L_p = d/4 = 75$ μm, where $d = 0.3$ mm is the average diameter of silica gel beads. The value of R_p in Eq. (20) could be calculated as the ratio of the first and zero moments of the distribution function of pore sizes [53,145].

The confined space effects are very strong in narrow pores (nanopores at $R_p < 1$ nm and narrow mesopores at $R_p < 2$ nm) [46,47,53,125-127,146-149]. These effects could be ignored for mesoporous silica gels Si-60 and Si-100 and fumed silica A-300 characterized by small contribution of pores in the mentioned range. A portion of pores in Si-40 is narrower than $R_p = 2$ nm (Fig. 26); however, contribution of nanopores at $R_p < 1$ nm is small. Consequently, the errors of developed approach could be significant for the evaporation from narrow pores of Si-40 in contrast to other silicas studied. This aspect was analyzed using appropriate experimental data [101].

Large models of narrow mesopore of silica gel filled by water or *n*-hexane or two nanoparticles surrounded by a shell with water molecules were calculated using PM7 method (MOPAC 2016) [150-152]. For visualization of the fields around molecules and small silica clusters, the TorchLite program was used [153,154]. Visualization of molecular structures was performed with the help of the GaussView [155], ChemCraft [156] or UCSF Chimera [157] programs.

The evaporation of all studied compounds from narrower pores of Si-40 was slower under ambient conditions than from Si-60, Si-100 or A-300 (Fig. 53) [101]. However, a smaller volume of pores of Si-40 could provide shorter time of evaporation of adsorbed compounds under heating. A larger value of S_{BET} of Si-40 could give the opposite result due to higher interaction energy of adsorbates with a silica surface than that of molecule-molecule interactions [53,101].

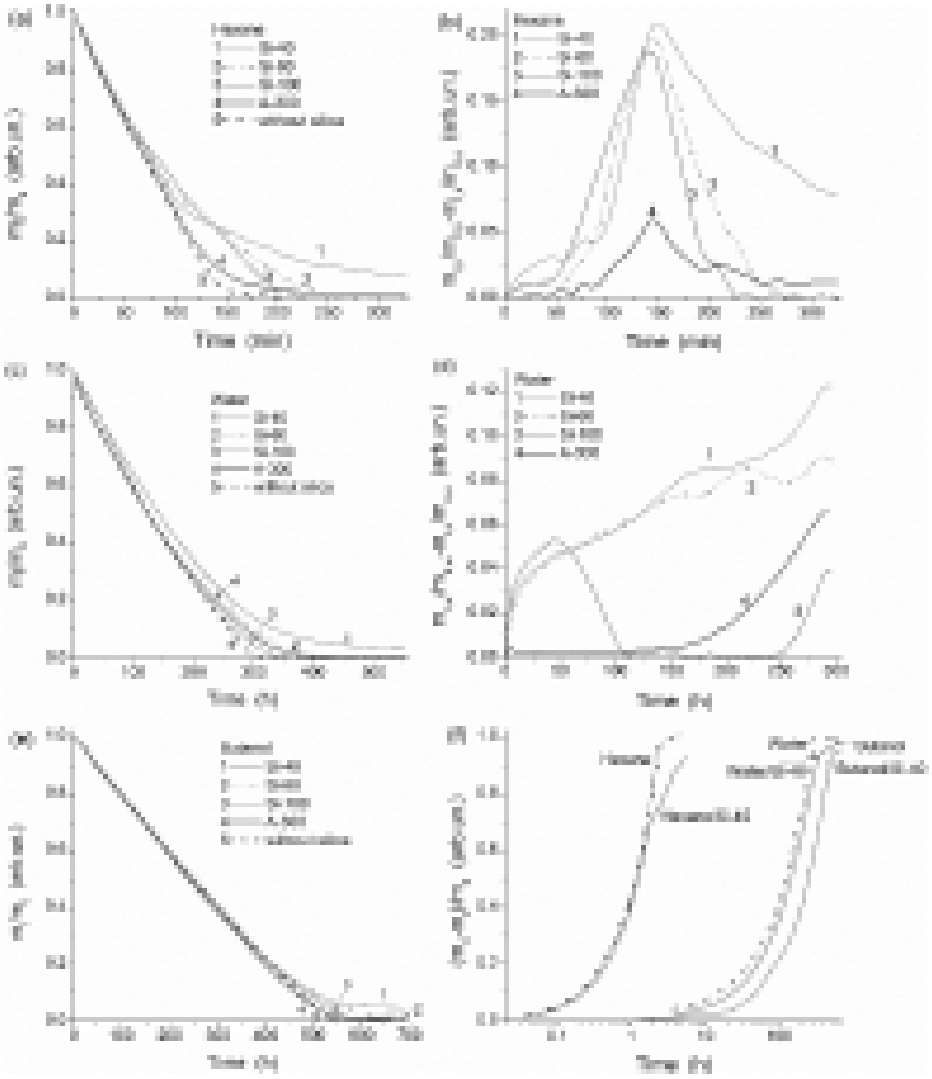

Fig. 53. Evaporation as a ratio of content of residual liquid (m_t) to initial one (m_0) of (a) hexane, (c) water, and (e) 1-butanol, difference between evaporation of liquid alone and in the presence of silicas for (b) hexane (0.1 g per 0.1 g of dry silica), and (d) water (1 g per 0.3 g of dry silica), (f) relative amounts of evaporated liquids alone or in the presence of Si-40 as a function of time.

However, in narrow pores, the surface tension of pore-confined liquid drops down that could positively affect the evaporation. In the case of an increase in the boiling temperature of adsorbate, the difference in the evaporation (at room temperature) from silicas with various pore sizes decreased from hexane (Fig. 53a,b), water (Fig. 53c,d) to butanol (Fig. 53e) that was also accompanied by increasing time of evaporation for this series (Fig. 53f). Note that the evaporation of water from Si-100 could be faster (especially from the layers located close to the surface of silica beads) than that from textural pores (voids) of A-300 (Fig. 53c,d). However, for hexane, the opposite effect was observed (Fig. 53a,b). This difference in the behavior of hexane (weakly interacting with a silica surface) and water (strongly interacting with a silica surface) in respect to Si-100 and A-300 could be explained by the difference in the particulate morphology and texture of these silicas. In contrast to total values of the interaction energies, a relative difference in the interaction energies of water-water molecules and water-silica was smaller than those for hexane [101].

The TG study of the evaporation of liquids as a function of temperature showed a role of structural, textural and morphological characteristics of adsorbents, as well as the adsorbate properties [101]. The effects of narrow pores (*i.e.* confined space effects) were stronger than that caused by the differences in the interaction energies of adsorbates with a silica surface because the evaporation of nonpolar (hexane, benzene, CCl_4) and polar (acetone, butanol, water) compounds occurred from Si-40 (possessing narrower pores) at higher temperatures than from Si-100

(possessing broader pores) at the same fraction sizes of beads (0.2-0.4 mm). This difference tends to be larger for liquids at lower boiling point. In contrast to water and 1-butanol, acetone molecule did not have proton-donor groups. Therefore, intermolecular bonds (*e.g.,* >C=O···H–C) in liquid acetone were very weak in comparison with the bonds >C=O···H–OSi≡ between acetone molecules and the silica surface. This effect and confined space effects caused the maximal difference in the evaporation *vs*. *T* for acetone desorbed from Si-40 and Si-100 (Figs. 37 and S56). Note that the effect of diminution of the value of the surface tension (γ) in narrow pores gives a small increase in the rate of evaporation from depth of long pores of Si-40 and it could be ignored for other silicas. The effect of an increase in the evaporation rate could be much stronger for liquids located around the entrances of narrow pores close to the surface of silica beads (Figs. 53 and 54), because the value of L_p (used in Eq. (20)) strongly decreased there [101].

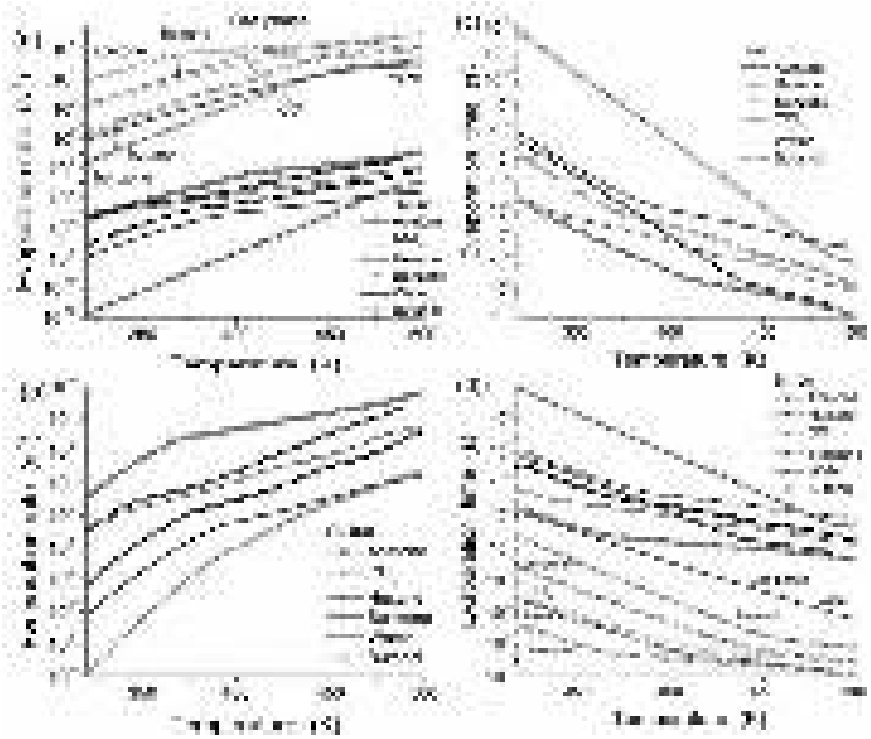

Fig. 54. (a, b) Evaporation rate *vs*. temperature for various compounds evaporated (a) in the gas phase (droplet of 20 nm in diameter) and from the depth of pores of Si-40 and (b) Si-100. (c, d) Evaporation time *vs*. temperature for different compounds evaporated from pores of (c) Si-40 (assuming d_p = 4 nm, L_p = 75 μm) and (d) Si-100 (assuming d_p = 20 nm, L_p = 75 μm) and from a droplet of 20 nm in diameter located in the gas phase.

Excess of liquids (*i.e.* the amounts of liquids were larger than the pore volume of the samples used) in the TG measurements caused a significant step in the thermograms at the boiling point of the liquids studied [101]. A part of the TG curves related to the evaporation of liquids at $T > T_b$ after evaporation of bulk liquids (located out of pores) characterizes the evaporation from pore volume and pore walls that corresponded to different ΔG values. The confined space effects for all liquids studied were more clearly observed at $T > T_b$ in the TG curves drawn *vs*. $\Delta T = T - T_b$. First, the evaporation from narrower pores of Si-40 was completed at higher temperatures but in a much narrower temperature range (429-467 K) than those for Si-100 having broader pores (Figs. 26). For the latter, the temperature of completed evaporation for liquids studied was from 347.4 K (acetone) to 468.1 K (butanol). The gap between the point of completed evaporation (T_{ev}) and the boiling point (which depended on both molecular weight of a compound and strength of intermolecular forces) $\Delta T_{ev} = T_{ev} - T_b$ was much greater for Si-40 (up to ΔT_{ev} = 118 K for CCl_4). This gap decreased for liquids having a higher value of T_b and evaporated from Si-40. It was minimal for butanol $\Delta T_{ev} \approx 55$ K that has maximal T_b = 390.81 K among studied liquids. For Si-100, minimal $\Delta T_{ev} \approx 18$ K was for acetone, and maximal $\Delta T_{ev} \approx 77$ K was for butanol [101].

The order of the values of T_b and T_c differs for studied liquids: T_b is higher for butanol than that of water but the value of T_c is higher for water. Therefore, the evaporation rate curves *vs*. T for water and butanol intersect at temperatures between the points of T_b and T_c for both free droplets and liquids evaporated from silica gels (Fig. 54). This effect could be explained by the fact that all atoms in water molecules could take part in the formation of strong hydrogen bonds in contrast to butanol molecules, in which only two atoms (from the OH group) from 15 ones could do that [101].

According to the TG data and theoretical calculations (Fig. 54) [101], the temperature ranges of evaporation of liquids from silica gels and the value orders of k and τ correlated to the values of T_b. This is due to the fact that the value of T_b (as well as evaporation features) depends on (i) the strength of intermolecular bonds that depends on the type of intermolecular bonds (hydrogen, polar, nonpolar) and confined space effects for adsorbed compounds, polarity and polarizability of molecules, that determine in total, *e.g.*, the surface tension; (ii) molecular weight and intermolecular bonds affecting molecular mobility, diffusivity, and viscosity of liquids. Of course, for the evaporation from porous media, the textural characteristics of the adsorbents play an important role. Therefore, there is a difference in the evaporation of liquids bound to silica gels and nanosilica, which are characterized by very different PSD (Fig. 26). The evaporation of a droplet with size corresponding to size of pores of Si-100 occurred much faster at the rate greater by several orders of magnitude than that observed for Si-100 upon the evaporation from the depth of pores (Fig. 54a,b). The evaporation time *vs*. temperature $\tau(T) \sim 1/k(T)$ (Fig. 54c,d) is characterized by the opposite shape and orders than values of k *vs*. T (Fig. 54a,b) for liquids evaporated from silica gels and free droplets. However, the function $\tau(T)$ demonstrates the curve shapes similar to those of the evaporation rate (Fig. 54) [101].

The porosity type of silica gel Si-100 with long cylinder-like mesopores of 4-20 nm in radius (see Fig. 26) located in millimeter-sized beads (assumed L_p = 75 μm) and fumed silica with textural pores as short voids between spherical nonporous nanoparticles (~ 8.3 nm in diameter) forming aggregates < 1 μm in size and agglomerates of aggregates > 1 μm (assumed L_p = 1 μm) strongly affected the evaporation rate (Fig. 55a) [101]. Fumed silica A-300 has a close value of S_{BET} (330 m^2/g) to that of Si-100 (314 m^2/g). However, these silicas have very different PSD affected by suspending-drying for A-300 only (Fig. 26). The curve of the water evaporation rate from A-300 (from the depth of textural pores) is located between the curves for water evaporated from Si-100 (from the depth of long pores) and a free drop (from open surface of drop) (Fig. 55a). Note that the structures of a water layer bound to nonporous silica nanoparticles or a water cluster located in narrow silica mesopore, as well as the structures of *n*-hexane clusters free or bound in narrow mesopore, significantly differ [101]. The structure of the water layer bound to the outer surface of silica nanoparticles could be less dense than the water cluster located in narrow mesopore. This is in agreement with ^{1}H NMR spectra of water bound in silica gel and fumed silica [53]. However, the *n*-hexane cluster in narrow mesopore is less dense than the free *n*-hexane cluster. These differences in the organization of interfacial water and *n*-hexane are due to the difference in intermolecular interactions between molecules *per se* and with a silica surface [101], as well as molecular and pore sizes. Similar differences in confined space effects were observed using ^{1}H NMR and calorimetry methods for water, decanol and decane bound to Si-40, Si-60 and Si-100 [158] and nanosilica [53].

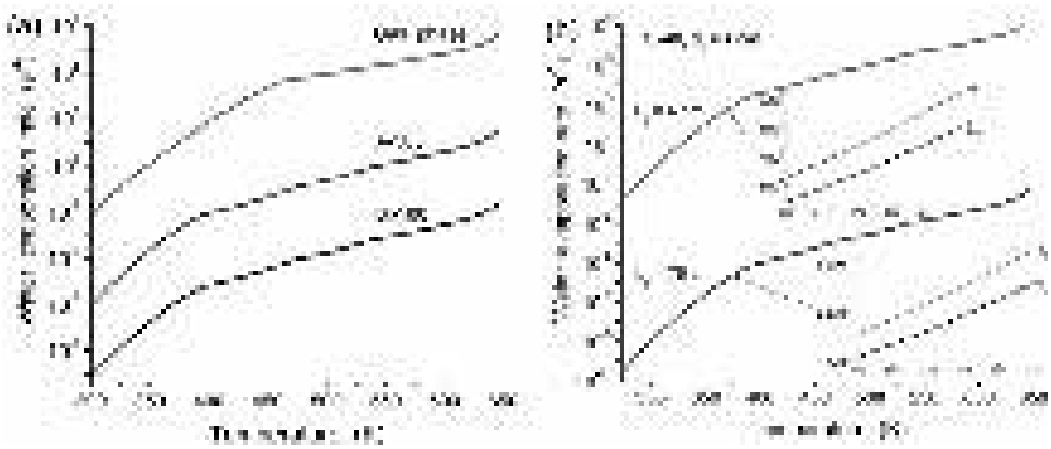

Fig. 55. Evaporation rate *vs*. temperature for water evaporated from (a) a droplet (20 nm in diameter) in the gas phase and bound in the depth of textural pores (voids between nanoparticles in their aggregates) of fumed silica A-300 (pore diameter d_p = 10 nm, pore length L_p = 1 μm in aggregates of nanoparticles) or in the depth of long mesopores of silica gel Si-100 (d_p = 20 nm, L_p = 75 μm), and (b) the effect of a decrease in the pore length and surface tension in pores on evaporation of water from short pores (L_p = 4 nm, $\gamma_p(T)$) and depth of long pores (L_p = 4 nm, $\gamma_b(T)$). Inserts showed a small portion (over 370-375 K) of evaporation curves calculated using the surface tensions of free bulk (γ_b) and pore-confined (γ_p) waters.

The confined space effects could lead to changes in the surface tension of liquids [53]. This effect was analyzed for water bound in pores of Si-40 (having the narrowest pores among silica gels studied, Fig. 26) at d_p = 4 nm (31% of water from the first monolayer affected by interactions with pore walls and 69% of water distant from the walls and having ΔG_s close to that of bulk water) [101]. An increase in the evaporation of water from the depth of long pores due to diminution of the value of γ was small (Fig. 55b, bottom insert) and could be ignored. The evaporation of water located around the entrance of the same pore at d_p = 4 nm and L_p = 4 nm was much faster than from long pore at L_p = 75 μm (Fig. 55b). The use of $\gamma_p(T)$ instead of $\gamma_b(T)$ gives a certain (relatively small) increase in the evaporation (Fig. 55b, upper insert) [101].

Thus, to calculate the average value of the evaporation rate *vs*. temperature several averaging procedures should be applied [101]: (i) by the pore length (since the evaporation of adsorbate from the entrance of pore is much faster than from the depth of the same pore); (ii) by changes in the surface tension $\gamma_p(T)$ in pores of different sizes (however, it could be ignored at $R_p > 10t$ = 3.2 nm (for water) and in the depth of long narrow pores, and this effect grows in absolute values (Fig. 55b, inserts) at the entrance of narrow pores but its relative contribution remained small); (iii) by changes in the density of liquid layered in narrow pores at the presence of specific adsorption sites [159] (changes in the values of ρ_{liq} and ρ_{gas} *vs*. temperature were taken in to account); (iv) by effects of conformerization of long linear molecules; and (v) by changes in the interaction energy with neighboring molecules (in bulk and in pores) and pore walls. Note that the first, fourth, and fifth effects are much stronger than others. All these effects result in very fast evaporation of liquids such as hexane from the outer surface of silica gel beads and the entrance of pores (in shallow depth). However, in full depth of narrow pores, liquids could remain during a long period at relatively low temperatures (Figs. 53-55). The evaporation rate is nearly exponential function of temperature (Fig. 54, linear portions in log-scale of the Y axis). Therefore, even narrow pores become empty with increasing temperature, especially at $T > T_b$ [101]. However, this process is not very rapid even at $T > T_b$. For instance, acetone was evaporated from Si-100 for approximately 4 min at $T > T_b$ [101], but it was evaporated from Si-40 for 34 min. Butanol was evaporated from both silicas for 25-30 min at $T > T_b$ similar to water. If the results shown in Fig. 38b are compared to the experimental data on the evaporation of water from Si-40 that one could conclude that the experimental time of evaporation falls approximately midway between the theoretical curves related to the evaporation from the entrance and full depth of pores. This effect could be explained by the diffusion of liquid from the depth toward the entrance of pores during a whole evaporation process. Therefore, the process could occur faster than for evaporation only from the depth of

pores, since the liquid can continually move toward the outer surface of the beads upon heating [101].

It should be noted that the values of evaporation/condensation coefficients β_V and β_g (assuming quasi-equilibrium state for gas and liquid states for free or pore-confined adsorbates at a certain temperature) [138,139,144] were typically greater for liquids evaporated from silica gels than that from free droplets with one exception for water. The values of β_V and β_g (related to the probability of condensation of molecules into droplets from the gas phase) relatively increase (at high temperatures) for compounds with a greater value of T_c in a series from acetone to water [101].

Quantum chemical calculations of interactions of adsorbate molecules with a small silica cluster with counterpoise corrections accounting the basis set superposition error (BSSE), as well as the solvation effects for the molecules (ΔG_s), cluster ($\Delta G_{s,c}$) and cluster with adsorbed molecule ($\Delta G_{s,m+c}$), showed that the values of the mentioned energies were smaller for nonpolar adsorbates (hexane, carbon tetrachloride, benzene) than those for polar adsorbates (water, acetone, butanol) [101]. This was due to the formation of strong hydrogen bonds by the latter, *i.e.* due to strong electrostatic interactions between polar molecules and silica surface. Features of interactions of water (dense coverage of the surface) and hexane (distant location of molecules from the surface) with silica were well seen from the structure of liquids in pores. The effect of stronger interactions of polar compounds with the silica surface in parallel to the effect of location of adsorbates in narrow pores of silica gels led to stronger deceleration of desorption of the polar molecules in comparison with nonpolar ones (Figs. 53-55). However, for narrow pores of Si-40, the effect of location of molecules in the depth of narrow pores was much stronger than the effect of stronger interactions of polar molecules with the silica surface at the entrance of pores (Figs. 53-55). This influences about 85-95 wt.% of adsorbates located in pores. For Si-100 possessing broader pores than Si-40 (Fig. 26), the influence of the silica surface on deceleration of desorption deals with only 15-20 wt.% of adsorbates located in pores [101]. These changes in the Gibbs free energy due to changes in the molecule location were taken into account on calculations of the evaporation rate from the depth of pores (Fig. 54). These differences could be affected by the differences in the values of both average pore diameter and specific surface area of silicas (*i.e.* the amounts of molecules located in the layer contacted to the silica surface), as well as the evaporation from depth of pores. For a small content of polar active adsorption sites (*e.g.,* carbons and silicalite), density of liquids in pores could be lower than that for bulk liquid, and air/vapor bubbles could be located in pores. This could inhibit the adsorption and accelerate the evaporation from pores, but this process was not analyzed in [101].

Note that the conformerization of molecules in the liquid and gas phases results in the appearance of additional channels of transfer of molecules evaporated from liquid to gas phase with decreased positive changes in the Gibbs free energy [101,144]. The values of $k(T)$ calculated for hexane without taking into account the conformerization could be smaller than that calculated with consideration of conformerization in bulk and bound liquids and in the gas phase (a smaller difference was at higher values of T) upon evaporation from silica gel [101]. In general, there were channels of the evaporation of different conformers both with smaller and larger values of ΔG_{ev}. However, the effects of the former could be greater if transfers through the channels with high values of ΔG_{ev} were not practically occurred. Therefore, the full effect of the conformerization could result in increasing evaporation, which, however, depend on populations of states of different conformers [101,144]. If the population of more stable conformers is greater in the liquid phase than in the gas phase that the conformerization could diminish the evaporation [101].

The results of the SMD calculations for molecules confined in narrow pores could be questionable due to some reasons [101,138,139]. For example, the structure of a solvation shell differs from that for bulk liquids, and these differences increase with decreasing size of pores. The interaction energy of studied molecules with a silica surface was typically larger (*i.e.* ΔG was lower) than that with neighboring molecules. This was taking into account (with the corresponding weighting coefficients) upon calculation of the evaporation rate and condensation/evaporation

coefficients by dividing of adsorbed compounds into three types: free bulk, bulk in pores and first monolayer of molecules bound to a silica surface using the values of S_{BET} (amounts of bound liquids in the first monolayer were estimated as tS_{BET}, where t was the monolayer thickness), and pore volume V_p (amounts of bulk liquids in pores estimated from the difference $V_p - tS_{BET}$). As a whole, for similar corrections, the experimental adsorption isotherms of studied compounds or NMR data could be used to determine the Gibbs free energy of adsorption [46,47,53,101,149].

Fig. 56. Evaporation of (a, b) hexane (at room temperature) from (a) wetted samples at amounts of hexane of 0.06-0.07 g per 0.02 g of FMO, and (b) suspensions containing FMO initial or treated (1 g of hexane per 0.05 g of FMO). To reduce the errors, only a final portion of evaporation of (a) 0.02 g or (b) 0.05 g of hexane is shown using the point at residual 0.02 or 0.05 g of hexane as $t - t_x = 0$ min at $x = 0.02$ g ($t_{0.02} \sim 70$ min) or 0.05 g ($t_{0.05} \sim 450$ min), respectively. Data shown in (a) were normalized by dividing by 0.02 g. (c) Evaporation of n-decane (1 g per 0.05 g of FMO).

For lower amounts of hexane (Fig. 56a), the rearrangement of secondary structures during wetting and evaporation was much smaller than for suspension (Fig. 56b) [90,101]. The difference in the evaporation of residual amounts (0.02 g) of hexane from different FMO was much smaller for lower amounts of hexane than evaporation of residual amounts (0.05 g) of hexane from suspended FMO. A relatively weak interaction of hexane with FMO results in slightly faster

evaporation of hexane from FMO than from pure hexane; however, this difference was very small (Fig. 56a). For suspended FMO, the evaporation of bound hexane (Fig. 56, curves 1-7) was slower than that of individual hexane (Fig. 56b, curve 8) [90,101].

Water molecules could strongly interact with oxide surfaces and other water molecules [53,90,101]. Therefore, the differences between evaporation or water alone and water bound oxide surfaces were relatively small (Fig. 57). The rearrangement of nanoparticles in aggregates or decomposition of larger core-shell nanoparticles affected the desorption of water (Fig. 57b) differently in comparison with evaporation of hexane (Fig. 56b). However, there were similar regularities for both adsorbates. For example, evaporation of them was slower from initial AST1 (Figs. 56b and 57b, curve 3) [90,101].

Despite decomposition of large CSNP and an increase in S_{BET} for AST1 cryogel, evaporation of both adsorbates was slower than that from initial AST1 [90]. However, water could be more slowly evaporated from AST1 cryogel (Fig. 57b, curve 5) than from MCA AST1 (curve 4), but for hexane, there were the opposite results (Fig. 56b). All these results could be explained by several reasons. First, hexane much weakly affected the texture of the nanooxide powder than water; *i.e.*, hexane could not change packing of nanoparticles in the secondary structures. Hexane molecules interact with oxide surfaces and other hexane molecules much weaker than water molecules. Hexane molecules were larger than water molecules. Therefore, contact surface area was smaller for hexane molecules, which could not penetrate into narrow voids between adjacent nanoparticles in contrast to water molecules [90,101].

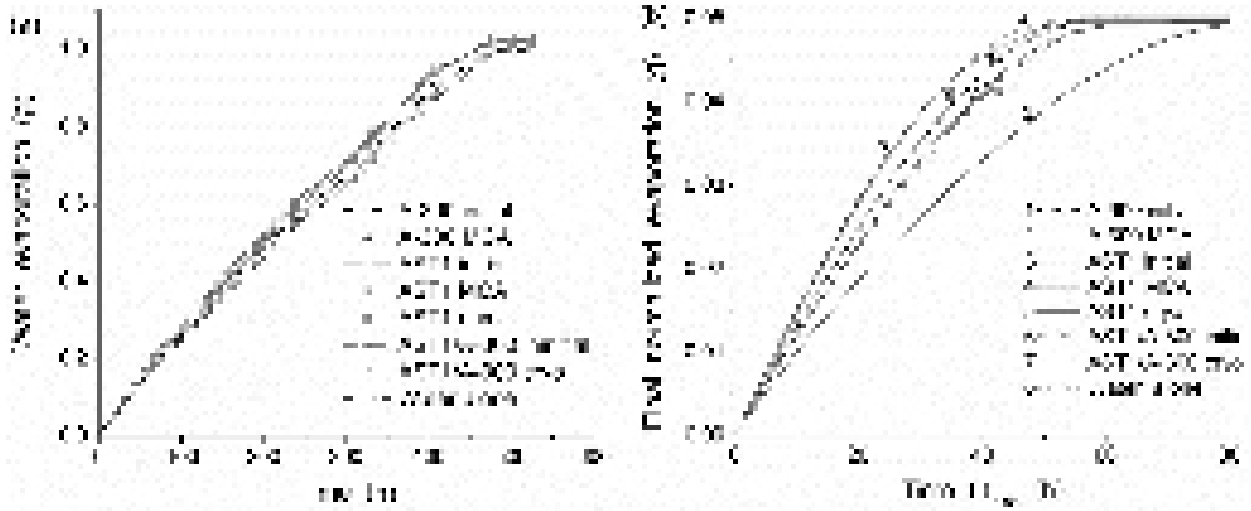

Fig. 57. Evaporation of water (at 13±1 ^{o}C) from (a) suspended samples at amounts of water of 1 g per 0.05 g of FMO, and (b) final portion of water evaporation starting at residual amounts of water of 0.05 g (*i.e.* after evaporation of 0.95 g of water).

Evaporation of *n*-decane occurred very slowly (Fig. 56c), approximately four times slower than water (Fig. 57) or two orders of magnitude than hexane (Fig. 56a). Decane alone is evaporated slower than decane disturbed in the suspensions. However, decane evaporation from the suspension of AST1/A-300 cryogel (composed of compacted particles) was similar to that for decane alone. Note that decane evaporation from AST1 cryogel occurred faster than from AST1/A-300 cryogel due to narrower pores in the latter [90].

Thus, experimental and theoretical investigations of evaporation of various liquids (polar water, acetone and 1-butanol and nonpolar *n*-hexane, benzene and carbon tetrachloride) from various silicas showed [90,101] that the evaporation rate depended on molecular properties of adsorbates (molecular weight, intermolecular bond strength, surface tension, density, boiling and critical temperatures), surface chemistry and texture of adsorbents, as well as location of molecules in depth of pores. Different orders of values of certain characteristics (*e.g.,* T_b and T_c for water and butanol) could lead to intersection of curves of evaporation rate (or time) *vs*. temperature for

different compounds. However, in general, the order (position) of curves of the rate and time of evaporation *vs.* T well correlated to the boiling point of bulk liquids and the pore diameter of adsorbents at the same values of other their characteristics and upon the evaporation from the depth of pores [90,101].

The decelerating of evaporation from the depth of pores was much stronger than that from the entrance of pores due to slower motion of the molecules toward the outer surface of adsorbent beads with decreasing size of pores [90,101]. The difference in the evaporation rate from various silica samples at a fixed temperature decreased with increasing boiling point (from hexane, water, to butanol). The effect of diminution of the surface tension in narrow pores on the evaporation of a certain adsorbate was small in the depth of pores in comparison with the effects of increasing pore length, decreasing pore diameter and increasing boiling point of adsorbates. Additionally, to estimate the time of complete evaporation of liquids from pores, one should take into account the continuous movement of adsorbate molecules along pores toward the outer surface of beads. The rate of evaporation from a surface of beads and the entrance of mesopores was close to the rate of evaporation of free droplets of similar size. However, the rate of evaporation from depth of long and narrow pores was much lower (by several orders of magnitude) than that from the surface of beads. The conformerization effects could enhance evaporation, especially if the populations of bent conformers at higher energy was significant in the liquid phase in pores (*e.g.,* due to increasing temperature) [90,101].

Developed theoretical approach used to calculate the evaporation rate and time as well as condensation/evaporation coefficients for various liquids from various porous media could be useful for deep analysis of the experimental data obtained with such techniques as thermogravimetry, temperature-programmed desorption, gas chromatography, adsorption-desorption at a fixed temperature, calorimetry, *etc.* [90,101]. Note that the averaging of the theoretical results should be performed for such characteristics as the pore diameter and length of adsorbent particles, degree of pore filling by adsorbates, surface tension $\gamma_p(T)$ of adsorbates in narrow pores (however, changes in $\gamma_p(T)$ could be ignored at $R_p > 10t \approx 3.2$ nm for water, 3.4 nm (benzene), 4.9 nm (CCl_4), *etc.*), interactions of molecule-molecule and molecule-surface, and conformerization of adsorbate molecules, especially long linear ones [90,101].

Note that the interfacial behavior of water plays a very important role in building industry (especially in respect to the properties of cement and concrete). Cement hydration led to the dissolution of alite (C_3S, $3CaO{\cdot}SiO_2$) and belite (C_2S, $2CaO{\cdot}SiO_2$) with the formation of calcium silicate hydrates (C–S–H) and calcium hydroxide (C-H) [160-166]. While calcium hydroxide is a very well-known crystalline phase [160,161]; however, the C–S–H structure, chemical composition, density and morphology remained uncertain [162]. C–S–H is a highly disordered nanoscale material containing a significant amount of bound water (Fig. 58). There were a few techniques (*e.g.*, NMR spectroscopy (Fig. 59), relaxometry, and cryoporometry) able to characterize C–S–H without removing the bound water (Figs. 58 and 59). Note that dehydration could damage the nanoscale structures of the material. The C–S–H precipitate characteristics depended on the chemical and physical conditions in which the hydration takes place [163–166]. Note that silica fume (an industrial solid waste formed as a byproduct during the production of alusil alloy or metallurgy grade silicon, and having pozzolanic properties and phase minerals comprising major silica components (95.1%) in the amorphous form, with traces of alumina, alkaline metal oxides, and transition metal oxides [167]) was used in preparation of cement and concrete. The particle size distribution of silica fume is very wide, and primary particles were from several nanometers up to 200-300 nm in diameter [167].

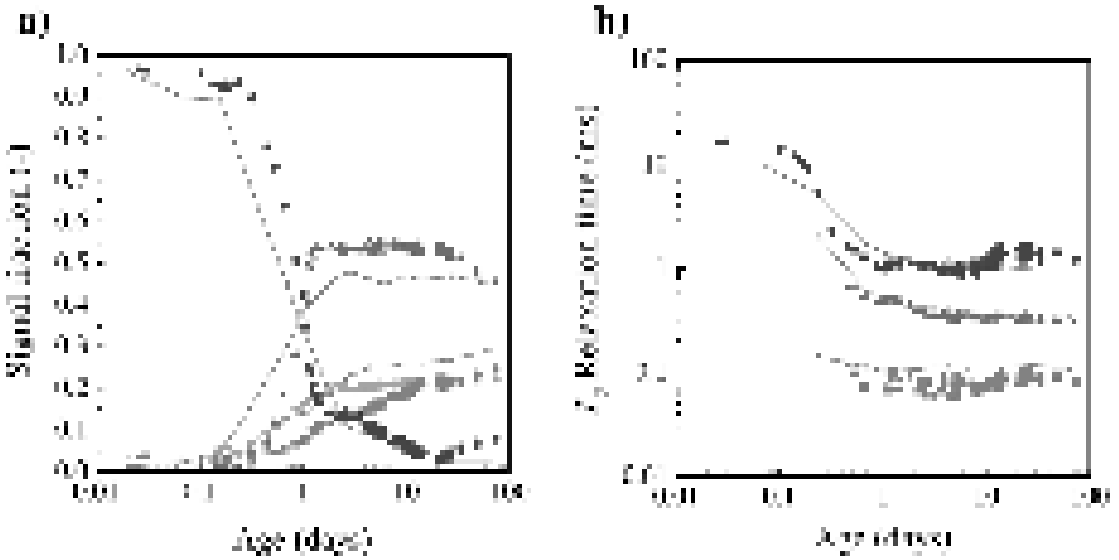

Fig. 58. (a) Evolution of the different water populations as a function of hydration time for white cement with 10% silica fume (colors), all at w/b = 0.4 (diamonds were solid signals, I_{solid}, squares were C–S–H interlayer water, I_{CSH}, triangles were C–S–H gel pore water, I_{gel}, and solid circles were "free water", I_{cap}, becoming interhydrate water. The solid signal for the plain white cement mix was not displayed. (b) Evolution of the associated T_2 relaxation times for the different water populations. The grey lines were the equivalent of the mobile fractions and T_2 relaxation times for the plain white cement.

A surface of FMO nanoparticles is practically open because FMO nanoparticles are nonporous [1-12,53]. Therefore, low-molecular weight polar or charged adsorbates or metal ions were poorly adsorbed onto unmodified surface of FMO [53,168-173] because the desolvation energy for bound adsorbate could be greater than the solvation energy of this adsorbate in the bulk solution. These properties could be changed due to adsorption of polymers [174-183] or chemical functionalization of the FMO surface [184,185]. Complex FMO or FMO matrices modified by deposion of catalytically active phase (*e.g.*, anatase) could be used as effective catalysts, especially photocatalysts because nanoparticulate structure of FMO is appropriate for excitation of electrons under UV emission and interactions with bound compounds [108,109,186].

A variety of experimental and computational techniques including macro- to meso- and microscale approaches, pivotal applications, defines the most important interfacial quantities and their experimental investigations, providing theoretical background and detailed solutions [187]. In this work, vital techniques used in interfacial flow problems, such as modern meshless numerical methods and conventional computational fluid dynamics methods were described. The technicalities of correctly using the computational methods developed for interfacial flows, as well as the simulation of interesting interfacial flow physics were discussed. This work offers an authoritative and state-of-the-art overview of computational methodologies and simulation techniques for the quantification of interfacial quantities [187].

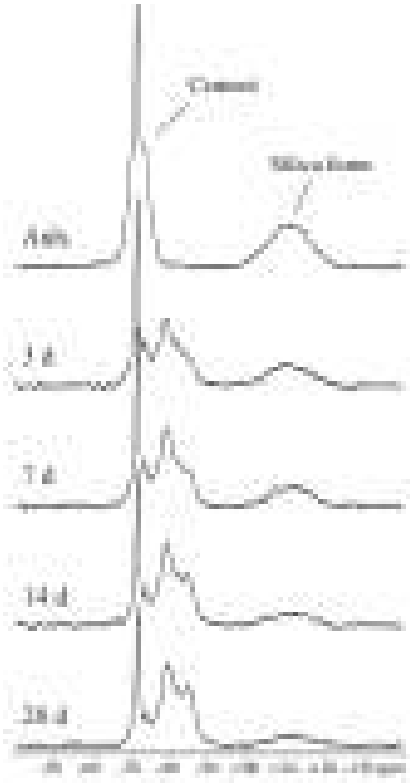

Fig. 59. ^{29}Si MAS NMR spectra (9.4 T, ν_R = 6.0 kHz) of the anhydrous white cement with silica fume and of the blend after hydration for 3, 7, 14, and 28 days.

Catalytic effects

It is difficult to expect that FMO could be good selective catalysts for fine organic synthesis because flame (pyrogenic) synthesis leads to poorly controlled structure of complex oxides. However, individual fumed titania (such as Degussa P25, Fig. 60) or titania doped by a small amount of another oxide (not more than several percent) giving a solid solution in the main phase could be effective photocatalysts for deep decomposition of organics under UV or visible light. Besides titania some other fumed oxides (e.g., containing ceria, zirconia, ZnO, *etc*.) can be used as catalysts and photocatalysts. Titania (anatase) initial or doped by various metal oxides as well as titania/silica composites possess significant catalytic activity [188-193]. Catalytic activity for the photodecomposition of methylene blue, MB (selected as representative aromatics for photocatalytic decomposition) was found as greatest (per gram of TiO_2) for non-treated ultrafine titania PC-500, which has the largest S_{BET} value and smallest particle size of the titania-containing materials studied [186]. However, this activity calculated per m^2 is higher for PC-105, possessing a much smaller value of S_{BET} than PC-500. The activity per unit surface area of titania is greatest for the fumed silica-titania complex oxide ST20, possibly due to enhanced adsorption properties of this material [53]. Calcination of PC-500 at 650 ^oC led to enhancement of anatase content and catalytic activity, but heating at 800 and 900 ^oC lowers the anatase content (since rutile appears) and diminishes catalytic activity, as well as the specific surface area because of nanoparticle sintering [186].

Nano-sized particle TiO_2-doped SiO_2 gels demonstrated the dependence of the structural and other characteristics on content of silica and a method of material preparation (Fig. 60) [194]. The concentration of TiO_2 loading, the particle size, and the surface characteristics were shown to relate to the degree of UV absorption and the measured energy bandgap (E_g) of the composites (Fig. 60a). Note that the value of E_g is one of the main characteristics of photocatalysts since the lower this value, the effective is the catalysts and it can operate even under visible light if this value is appropriately small.

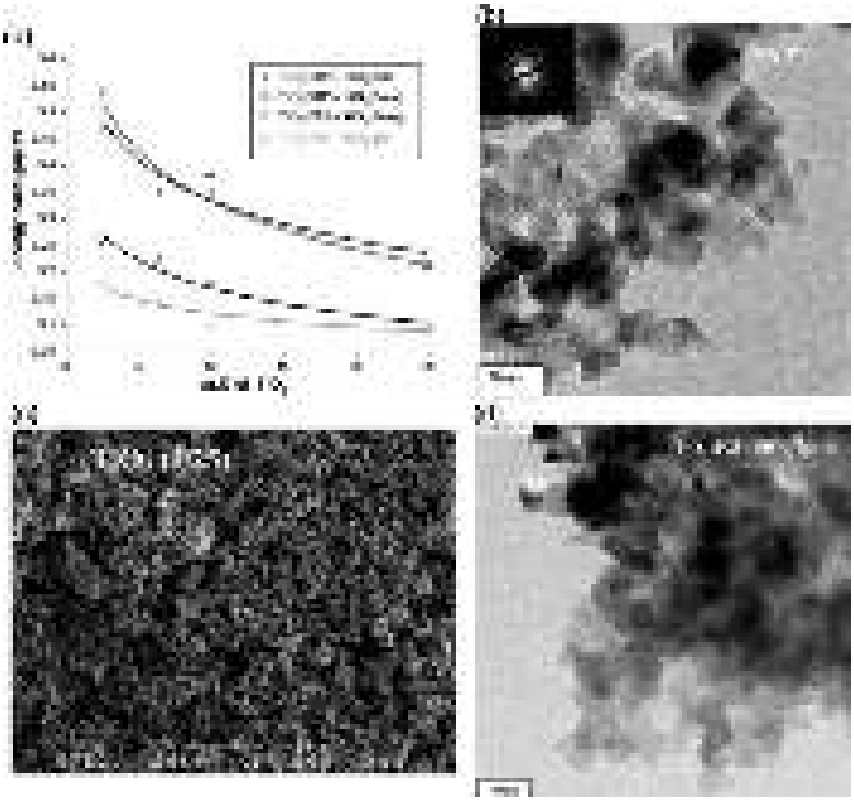

Fig. 60. (a) The energy bandgap (E_g) of TiO_2 (synthesized using titanium (IV) isopropoxide, TIP) – SiO_2 gel, TiO_2 (TIP) – fumed SiO_2, TiO_2 (Degussa P25)–SiO_2 gel and TiO_2 (P25) – fumed SiO_2 versus wt.% TiO_2 present; HRTEM image of (b) TiO_2 (P25) and mixture with TiO_2 (P25) (10 wt.%) and fumed silica Aerosil 200 (Degussa); and (c) SEM image of TiO_2 (P25).

The reaction rate constant of catalytic photodecomposition of MB could be considered as a distribution function due to the effects of surface heterogeneity, titania particle size distribution (*i.e.* band gap distribution), and other structural and energetic factors. Therefore, the concentration of MB in solution (with catalyst suspension) as a function of time of UV emission could be written as follows using a simple equation [186]

$$C_e(t) = \int_{k_{\min}}^{k_{\max}} \frac{C_0}{kC_0 t + 1} f(k)dk \tag{22}$$

Calculations of the $f(k)$ function were carried out using a regularization procedure with unfixed regularization parameter and nonnegativity condition [195]. More complex experimental $C_e(t)$ graphs were observed for some systems. Therefore, the kernel in the integral equation was modified to include additional terms related to diffusion and decomposition of MB [108,109,186,193].

$$C_e(t) = \int_{k_{\min}}^{k_{\max}} C_0[\frac{1}{a_1 z + a_2 z^{\alpha} + 1} + a_3 \exp(-\beta z)] f(k)dk \tag{23}$$

where $z = kC_0t$; a_1, a_2, a_3, α and β were the equation parameters determined by minimization of the functional

$$\Phi(k, a_i, \alpha, \beta) = \int_0^{t_{\max}} \left\{ spline(C_e(t)) - C_0[\frac{1}{a_1 z + a_2 z^{\alpha} + 1} + a_3 \exp(-\beta z)] \right\}^2 dt \to \min \tag{24}$$

The effectiveness of photodecomposition at a titania surface (Figs. 44 and 45) depended on many factors such as (i) anatase/rutile ratio and amorphous phase content (since rutile and amorphous phases generally have lower catalytic activity than anatase); (ii) specific surface area (*i.e.* contact area for adsorbed reactant); (iii) PSD, particle morphology (e.g., PaSD), and particle aggregation (accessibility of the titania surface to reactant because hindered diffusion could be in

very narrow pores, and reduced UV radiation transmitted into narrow, deep and long pores); (iv) the presence of surface functionalities (*e.g.*, sulfate) which could act as a catalyst poison, electron trap, mediator of nanoparticle aggregation, *etc.* [10,15,53,188-192]. To elucidate some of these effects the catalytic activity of PC titanias, fumed titania and ST20 was compared for the photodecomposition of MB (Fig. 61) [109]. The main results were: (i) PC-500 composed of the smallest anatase particles and with few sulfate groups possesses the largest catalytic activity per gram of oxide. PC-100 (with more sulfate groups than PC-105) is less active than PC-105, despite a larger S_{BET} value. Fumed titania, composed of anatase and rutile and having a lower S_{BET} value than PC-100 or PC-105, as well as reduced hydrophilicity potentially resulting in nanoparticle aggregation, exhibited a smaller photocatalytic effect. Finally, ST20, with 80 wt.% silica, not surprisingly was the least catalytically active as measured per gram of oxide [109,186].

Re-calculation of the photocatalytic activity as $A = (C_{MB,0} - C_{MB})/C_{MB,0}/S_{BET}$ (*i.e.* normalized to surface area) (Fig. 61b) showed that PC-500, PC-105 and fumed titania exhibited high activity at short times $t < 6$ min [109]. With time $t > 6$ min, PC-105 and fumed titania, possessing low S_{BET} values, exhibited the greatest activity per m^2. Taking into account the surface content of titania in ST20 (24 wt.% TiO_2) one could assume that surface anatase in this sample is the most active (per m^2) because of stronger and/or a greater number of adsorption complexes formed with MB [109], and due to the Langmuir-Hinshelwood reaction mechanism [196]. The latter was supported by the fact that the initial MB concentration (~20 ppm), and the equilibrium MB concentration after 20 minutes of stirring in the absence of UV light (sufficient time for equilibrium to be achieved), was nearly identical for PC titanias and fumed titania. However, the MB solution concentration exhibits a significant reduction with ST20 to 13 ppm, indicating MB adsorption was much greater for ST20 than the other materials [109].

Calculations of the distribution functions of effective MB decomposition rate were performed with Eqs. (22)-(24) using the data shown in Fig. 44a. Both integral equations give similar results with respect to $f(k)$ peak position (Fig. 62). However, the model equation with a more complex kernel in Eq. (10) gives narrower distributions, and splits $f(k)$ into two peaks for ST20. PC-500 exhibits a broader distribution than the other titania samples (Fig. 62b). This was possibly due to the more complex textural properties of PC-500 [109], and the difference in the reaction rate for MB adsorbed at the outer surface of aggregates of primary particles and in voids between primary particles in aggregates (*i.e.* in pores).

Heating of titania strongly affected its catalytic activity because of changes in the anatase-to-rutile ratio and amorphous-to-crystalline phase transformation, as well as sintering of nanoparticles resulting in significant reduction of the value of S_{BET}. The results of this influence were readily observed for PC-500 [109]. The greatest catalytic activity for MB photodecomposition was observed for titania treated at 650 ^oC, when the anatase-to-rutile transformation was not yet occurred, but the amorphous-to-crystalline phase transformation had [109]. Taking into account the 5-fold reduction of the S_{BET} value for PC-500 resulting from 650 ^oC heat treatment, the enhancement of the activity (per m^2) was substantial. This sample was more active (per m^2) than titania Degussa P25 (frequently used as a reference photocatalyst) at $t > 20$ min (Fig. 61b). Calcination at higher temperatures (800 and 900 ^oC) results in loss of titania catalytic activity due to at least two factors: i) anatase-to-rutile transformation and, ii) sintering of nanoparticles since the d_{XRD} value grows for all calcined PC titanias [109]. Additionally, it may be that certain treatments of sulfate-containing PC titanias (produced by liquid phase synthesis) could provide reduction of the band gap, because of embedding of S atoms in the lattice instead of O atoms and, therefore, the photoexcitation threshold [197,198].

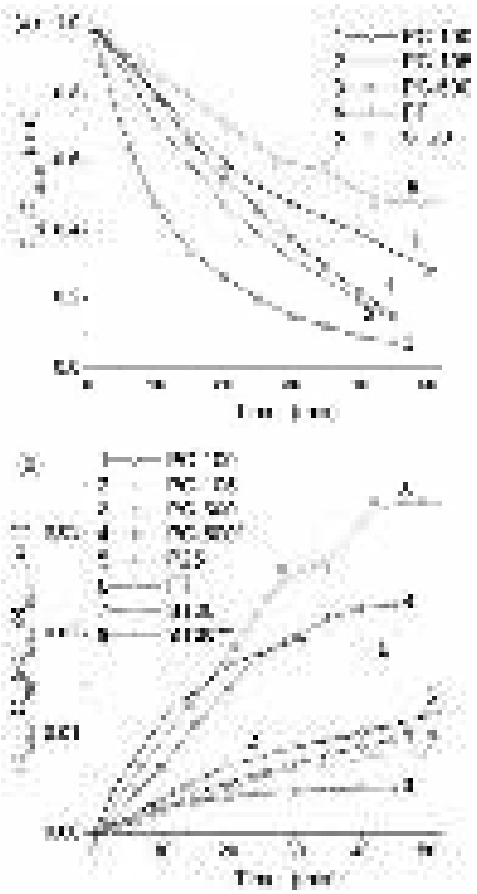

Fig. 61. (a) Relative diminution of residual concentration of MB in solution as a function of UV emission with 0.2 g of oxides, and (b) relative activity of catalysts per m^2 of their surface area; PC-500* (4) after heating at 650 ^oC; fumed titania Degussa P25 (5); and ST20** (8) with consideration for surface titania content.

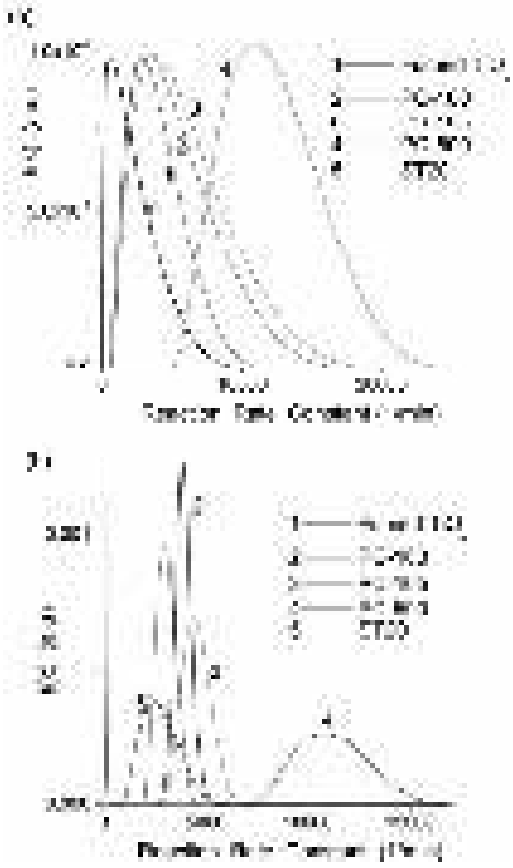

Fig. 62. (a) Normalized distribution functions of the reaction rate constant of catalytic photodecomposition of MB determined with Eq. (22); (b) distribution functions of the reaction rate constant determined using Eqs. (23) and (24).

Thus, investigations of the morphological, structural, adsorption, and catalytic characteristics of ultrafine titanias and fumed titania-containing complex nanooxides showed [109] that There were several key parameters that affected the catalytic properties: (i) accessible particle surface area and porosity of primary and secondary particles; (ii) titania nanoparticle phase composition; (iii) surface content of titania (anatase) in complex nanooxides; (iv) sintering of nanoparticles affected by calcination conditions; (v) content and type of surface hydroxyls as not only participants in photocatalysis but also as potential adsorption sites on complex nanooxides. As a whole the titania composed of the smallest anatase nanoparticles (PC-500) possesses the largest catalytic activity per gram of oxide in the photodecomposition of MB. However, estimation of the catalytic activity per m^2 of titania surface suggests that PC-105 and fumed titania, composed of larger nanoparticles than PC-500, possess a higher activity than non-heated PC-500 at reaction time t > 6 min. PC-500 calcined at 650 ^oC exhibits a striking increase of activity in MB photodecomposition (per m^2), at least comparable to fumed titania Degussa P25. The complex oxide ST20 possesses the highest catalytic activity per m^2 of titania, possibly because of enhanced adsorption of the reactant MB to the surface of this material, and the Langmuir-Hinshelwood reaction mechanism [109].

Confined space effects and interfacial phenomena

Confined space effects for various adsorbates could be analyzed using ^1H NMR, DSC, TSDC, DRS, TG and some other methods [53,199-217]. To avoid contribution of signals of water molecules from ice or other solid fractions or macromolecules, low-temperature ^1H

NMR spectra could be recorded for static samples using a narrow bandwidth (20 kHz) [53]. Changes in the Gibbs free energy (ΔG) of bound water and free surface energy (γ_S), estimated as the modulus of integrated changes of the ΔG values in the bound water layers, were determined from the temperature dependences of the amounts of unfrozen water (C_{uw} in mg of water per gram of silica) at T = 200-273 K < T_f = 273.15 K [53]. The amount of water (h) in samples was dependent on the type of the studied materials. The temperature dependence of the Gibbs free energy of ice [53,199] could be approximated as follows:

$$\Delta G_{ice} = 0.0295 - 0.0413\Delta T + 6.64369\times10^{-5}(\Delta T)^2 + 2.27708\times10^{-8}(\Delta T)^3 \text{ (kJ/mol)}, \quad (25)$$

where ΔT = 273.16 – T at 160 K < T ≤ 273.15 K. The fact that bound water may remained unfrozen at T < 273 K suggests that its structure is disturbed and due to stronger interactions with an adsorbent surface than with neighboring water molecules that results in inequality $G_w^i < G_{ice}$. Further lowering of temperature reduces this inequality until the point $T_{f,bw}$, at which a certain amount of bound water became frozen. At $T_{f,bw}$ the relationship $\Delta G_w = \Delta G_{ice}$ pertains, where $\Delta G_w^i = G_w^i(T) - G_w^0$ (G_w^0 denotes the Gibbs free energy of unperturbed bulk water at 273.15 K and superscript i stands for interfaces). It was assumed that neither G_{ice}, nor ΔG_{ice} were influenced by the solid surface. The area under the $\Delta G(C_{uw})$ curve (temperature dependences $\Delta G(T)$ and amounts of unfrozen pore water $C_{uw}(T)$ could be simply transformed into the relationship $\Delta G(C_{uw})$) determines overall changes in the Gibbs free energy of interfacial water [53]

$$\gamma_S = A \int_0^{C_{uw}^{max}} \Delta G dC_{uw}, \quad (26)$$

where C_{uw}^{max} is the total amount of unfrozen water at $T \approx 273$ K, and A is a constant dependent on the type of units used in this equation.

Water or other liquids could be frozen in narrower pores at lower temperatures, which could be described by the Gibbs-Thomson (GT) relation for the freezing point depression [53,200-205]

$$\Delta T_m = T_{m,\infty} - T_m(R) = \frac{2\sigma_{sl}T_{m,\infty}}{\Delta H_f \rho R} = \frac{k_{GT}}{R}, \quad (27)$$

where $T_m(R)$ is the melting temperature of a frozen liquid in cylindrical pores of radius R, $T_{m,\infty}$ is the bulk melting temperature, ρ the density of the solid, σ_{sl} is the energy of solid-liquid interaction, ΔH_f is the bulk enthalpy of fusion, and k_{GT} is a constant (e.g., k_{GT} = 60 K nm for water adsorbed on silicas, however, it can be varied in a wide range of 30-200 K nm depending on the type of adsorbents [53]). On the basis of this equation and the methods sensitive to transition of phase, different versions of cryoporometry, relaxometry, and thermoporometry were developed to study the interfacial phenomena, behavior of adsorbates, and structural characteristics of a variety of solid and soft materials and bioobjects [53,200-212].

Typical ^{1}H NMR spectra were observed for unfrozen water bound in wetted powder (total amount of water C_w = 11 wt.%) and aqueous suspension (C_w = 90 wt.%) of fumed silica/alumina SA8 (used as a representative sample of complex FMO) recorded at different temperatures (Fig. 63) [30]. Relative amounts of bound unfrozen water ($C_{uw,270K}/C_w$) in the suspension were much smaller (< 30 %) than that in the hydrated powder (100 %) in which practically all water ($C_{uw,270K}$) was unfrozen at 270 K. In the suspensions of AST82 and SA8, the $C_{uw,270K}$ value corresponded to 17 and 27 % of C_w, respectively (Figs. 63 and 64). The S_{BET,N_2} value of SA8 was seven and four times larger than that of AST82 and AST71, respectively (Tables 1 and 6). Therefore, the amounts of interfacial bound unfrozen water were larger for both hydrated powder and aqueous suspension of SA8 with lowering temperature than that for AST71 or AST82 (Fig. 64a). This corresponded to stronger binding of interfacial water to smaller nanoparticles of SA8 (as FMO with larger specific

surface area) than to larger particles of AST materials, and the Gibbs free energy was lower (at the same C_{uw} values) for the systems with SA8 (Fig. 64b).

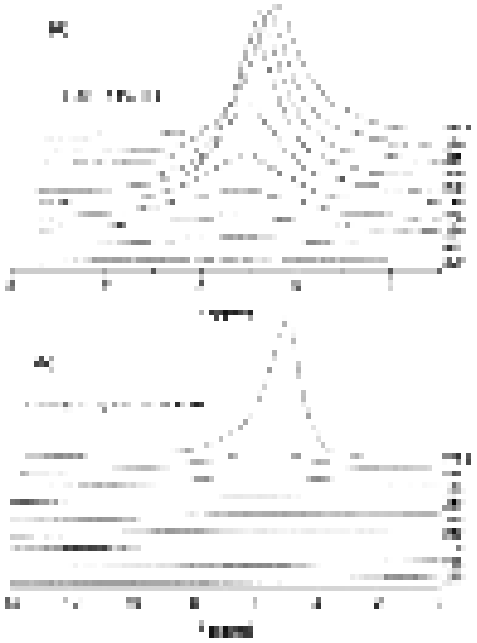

Fig. 63. ^{1}H NMR spectra of unfrozen water in (a) hydrated powder of SA8 (C_w = 11 wt.%) and (b) aqueous suspension of SA8 (C_w = 90 wt.%).

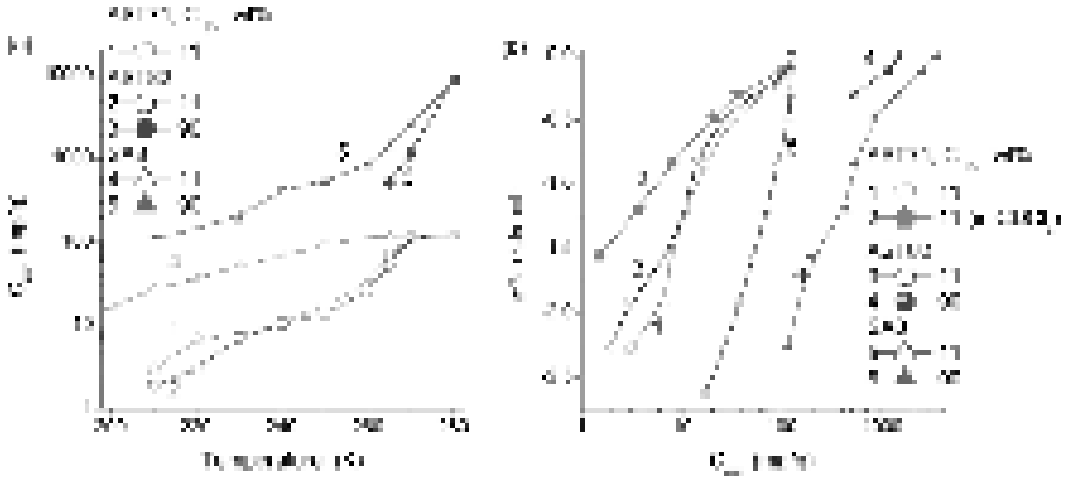

Fig. 64. (a) Temperature dependence of unfrozen water content (C_{uw}) and (b) relationships between C_{uw} and changes in the Gibbs free energy of bound water for hydrated powders (C_w = 11 wt.%) and aqueous suspensions (C_w = 90 wt.%) of different oxides.

The secondary (aggregates) and ternary (agglomerates) particles of FMO have relatively soft structure, which could be rearranged on interactions with adsorbates, especially water, other small polar molecules or polar polymers such as poly(vinyl alcohol), poly(ethylene glycol), *etc.* [53]. Similar rearrangements were revealed on comparison of the PSD (Fig. 65) calculated on the basis of the nitrogen adsorption onto dry samples and using NMR-cryoporometry (solving integral Gibbs-Thomson equation) applied to the $C_{uw}(T)$ functions for wetted samples or aqueous suspensions [30,53]. Contribution of narrow voids at $R < 3$ nm filled by structured water in wetted powder at C_w = 11 wt.% was greater than that of voids filled by nitrogen fluid in dry powder. The changes in the wetted powder could be due to several effects. Water molecules penetrating between adjacent nanoparticles (nanopore contribution grows) plasticize their contacts and contract neighboring particles in denser aggregated structures (contribution of narrow mesopores grows). Notice that these effects clearly appeared on wetting and drying of the nanooxide powders [53].

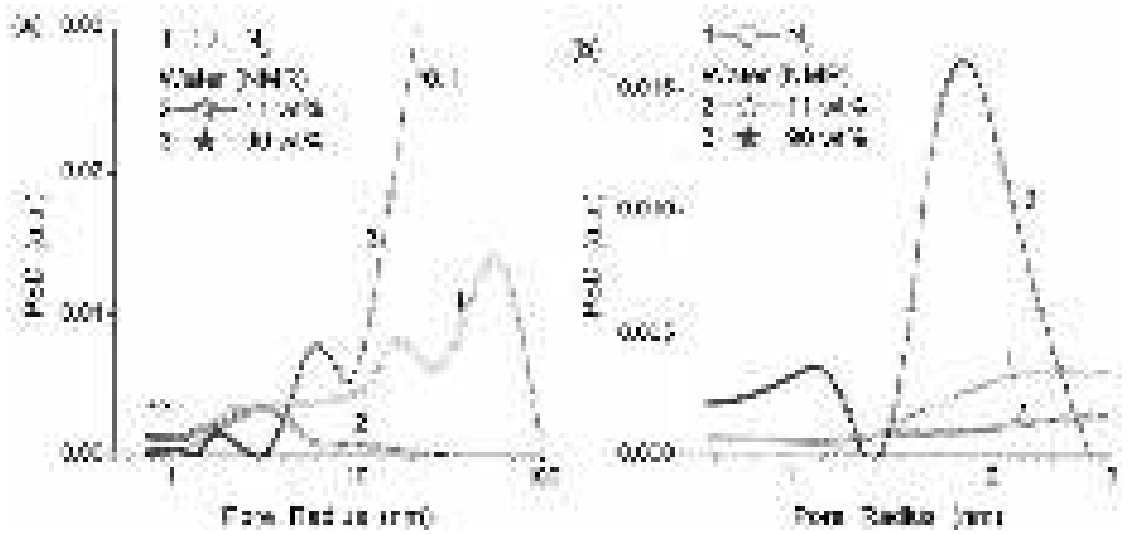

Fig. 65. PSD for SA8 calculated from the nitrogen desorption data (curves 1) and the $C_{uw}(T)$ function (NMR) for hydrated powder (2) and aqueous suspension (3) (a) with normalized curves 2 and 3, and (b) initial range of the PSD at $R < 3$ nm without the normalization of the curves.

On suspending, the rearrangements of secondary and ternary particles could be enhanced. This caused stronger textural changes in FMO after suspending-drying than after wetting-drying or interaction of the powders with organic solvents (*e.g.*, ethanol) [53]. In the suspension of SA8 (Fig. 64) C_{uw} = 2.5 g/g at 270 K, *i.e.*, the volume of bound water (V = 2.5 cm^3/g) was approximately two and four times larger than the pore volume (V_{p,N_2}) of suspended-dried SA8 (1.33 cm^3/g) and the initial powder of SA8 (0.68 cm^3/g), respectively (Tables 1 and 6). These effects were due to loosing of contacts between nanoparticles on wetting or suspending and then strong binding (up to formation of siloxane bonds) of nanoparticles one to several others on drying. These aspects of the behavior of nanooxides were of importance on treatment or use of these materials in liquid and polymer/solvents media [53].

Competitive adsorption and confined space effects

Co-adsorption of water and organic solvents onto nanooxides can lead to diminution of the water interaction with the oxide surfaces. This effect was clearly observed on suspending of wetted powder of AST71 in the $CDCl_3$ medium since the $-\Delta G$ value of bound water became smaller as well as C_{uw} (Fig. 64b, curves 1 and 2) [30,53].

Table 12. Parameters in correlation equation δ_h (ppm) = $a + bq_h$ used to estimate the δ_h values for different compounds (based on GIAO/B3LYP/6-31G(d,p)//HF/6-31G(d,p) and semiempirical calculations) [53,209,210].

Compound	Method	*a*	*b*	Probes for calibration
Water	PM3	–18.81135	92.83742	$8H_2O$-$24H_2O$
Water	PM6	–27.97889	87.56668	$16H_2O$
Water	PM7	–44.757685	131.473652	$43H_2O$
Methane	PM3	–2.33089	26.24548	$16CH_4$
Decane	PM6	3.199315	–16.632049	$C_{10}H_{22}$
Decane	PM7	9.318837	–61.145893	$C_{10}H_{22}$
PEG (CH)	PM7	10.769365	–55.335375	$C_6H_{14}O_4$
PVA (CH)	PM7	–6.929922	50.712501	$(-CH_2CH(OH)-)_4$
PDMS (CH)	PM7	–5.044178	30.462862	$H(-O-Si(CH_3)_2-)_7OH$
$H(-OP(OH)(O)-)_nOH$	PM7	–27.526046	95.608505	$H(-OP(OH)(O)-)_3OH$

For theoretical analysis of the influence of the confined space effects and surface structure of adsorbents, quantum chemical calculations were performed for relatively large models (up to 15000 atoms) using semiempirical PM3, PM6, and PM7 methods (MOPAC 2012 & 2016). To compute the values of the chemical shift of the proton resonance (δ_H), a linear correlation function

$\delta_H = aq_H + b$ linking the values of δ_H with the atomic charge (q_H) of atoms H in bound water molecules (Table 12) [53,209,210].

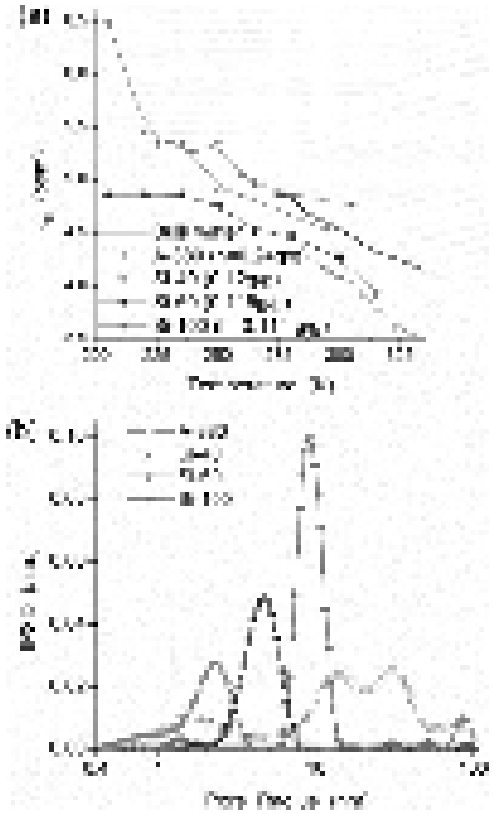

Fig. 66. (a) Chemical shift δ_H (experimental data) as a function of temperature for bulk water and hydrated silica gels (Si-40 (specific surface area S_{BET} = 732 m^2/g, pore volume V_p = 0.54 cm^3/g), Si-60 (S_{BET} = 369 m^2/g, V_p = 0.75 cm^3/g) and Si-100 (S_{BET} = 349 m^2/g, V_p = 1.23 cm^3/g)) and fumed silica A-380 (S_{BET} = 378 m^2/g, V_p = 0.94 cm^3/g), and (b) incremental pore size distributions (MND method) for these silicas [53].

The interfacial behavior of liquids depended on the type of a solid surface, *e.g.,* contents and types of hydrophilic or hydrophobic functionalities, number and density of active surface sites, particle topology and porosity of the materials [53]. The chemical shift of water interacting with a silica surface depended on the type of silica porosity (i.e., confined space effect, see Fig. 66), surface modification (*e.g.,* hydrophobization) degree of silica and presence of co-adsorbates (Fig. 67), and distribution of water in pores (silica gels) or onto the outer surface (fumed silica) of silica particles (Figs. 66-68). There were two main tendencies for the properties of water interacting with such hydrophilic adsorbents as silica gels. First, a decrease in the size of pores enhanced clusterization of water; *i.e.* average δ_H value should decrease. Second, an increase in a fraction of water directly interacting with the silica surface with increasing specific surface area (S_{BET}) enhanced the polarization of water molecules leading to a decrease in magnetic shielding of the protons; *i.e.* downfield shift should be observed [53].

Thus, these tendencies were opposite. Therefore, the $\delta_H(T)$ curve for water bound to Si-40 (possessing narrowest pores among silica gels studied, Fig. 66b) at partial filling of pores was located between the curves for water bound to Si-100 (broadest pores) and Si-60 (middle sizes of pores). Changes in the water organization at a surface of silicas depended on both temperature and pore size distribution. Thus, for silica gels with broader pores (Si-100, Si-60), the $\delta_H(T)$ curves at T < 250 K (when only mobile strongly bound water, SBW, was observed in the ^{1}H NMR spectra) demonstrate a weak dependence on T in contrast to water bound to Si-40 possessing much narrower pores than Si-100 or Si-60 that caused the strongest confined space effects [53,158,209,210].

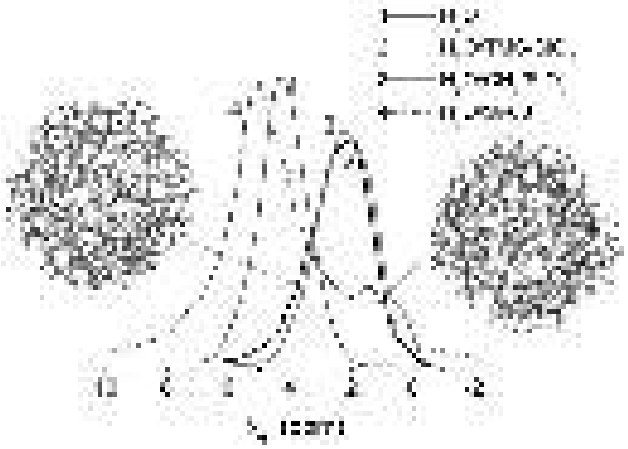

Fig. 67. ^{1}H NMR spectra of water calculated using PM6 and calibration function for 2000H_2O (curve 1) and small water clusters (mainly weakly associated water) interacting with hydrophobic silica (with trimethylsilyl (TMS) groups, curve 2) or with the presence of methane molecules (3), silica was modeled by porous particle (pore of 1.1 nm in radius), and experimental ^{1}H NMR spectrum (266 K) of water (0.24 g/g) bound to silica gel Si-60 partially modified by trimethylsilyl groups (curve 4) [209,210].

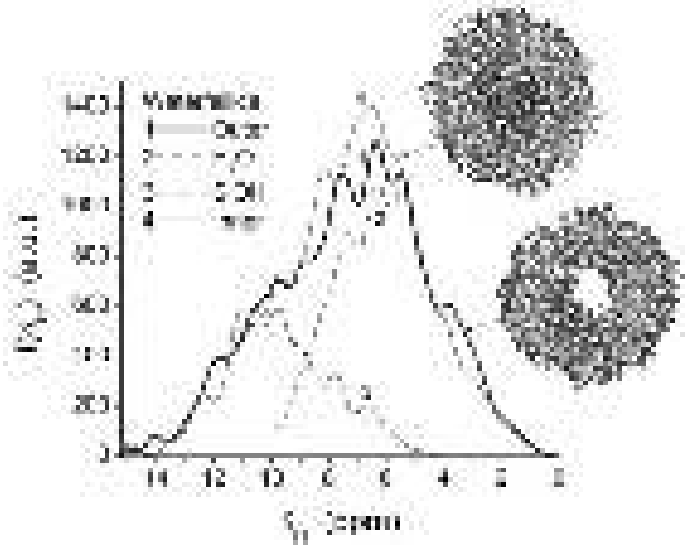

Fig. 68. ^{1}H NMR spectra of water (517H_2O) bound mainly onto outer surface or mainly in pore of silica particle (1620 atoms) calculated using PM7 method and a calibration function for water (Table 12) [209,210].

The textural features of nanosilica A-400 resulted in the formation of relatively large domains of adsorbed water even at a low hydration degree (h = 0.02 g/g) [158]. This water could be assigned to strongly associated water, SAW characterized by the chemical shift (δ_H) of approximately 5 ppm (Fig. 67a) close to that of bulk liquid water [53]. In SAW, the average number of the hydrogen bonds per a molecule was 3.5-4.0 that caused $\delta_H \approx 5$ ppm; however, $\delta_H \approx$ 7.4 ppm for ice Ih. Notice that in liquid water, a part of molecules was interstitial; *i.e.* these molecules were out of the hydrogen bond network. Therefore, the average coordination number of water molecules could be about 4.5 (*i.e.* larger than that in ice having, therefore, a lower density than liquid water) but $\delta_{H,lw} < \delta_{H,ice}$ due to thermal distortion of the hydrogen bonds (length O-H···O and angle ∠OHO were non-optimal) and the presence of interstitial water molecules [53].

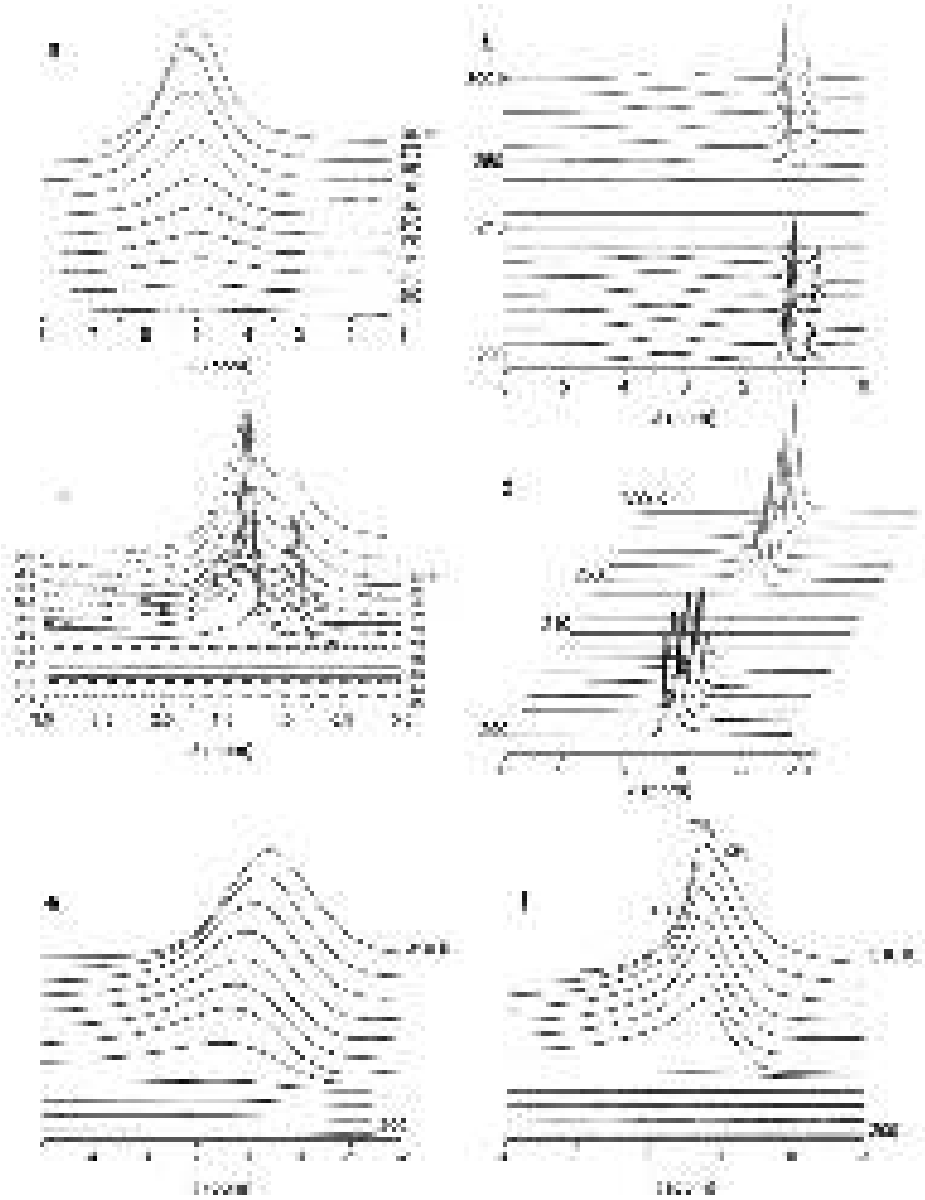

Fig. 69. ^{1}H NMR spectra (for static samples) of adsorbates bound to nanosilica A-400 (a-d) initial (ρ_b = 0.07 g/cm^3) and (e, f) compacted (ρ_b = 0.15 g/cm^3): (a) water (h = 0.02 g per gram of dry A-400); and water (h = 0.05 g/g) and n-decane of content C_d = (b) 1.5 and (c, d) 7.3 g/g, (d) with addition of polyphosphoric acid (PPA) at C_{PPA} = 0.05 g/g, (e) 0.73 and (f) 3.7 g/g; (c) A-400 initial (solid lines) and heated (dot-dashed lines) at 723 K for 10 min, loaded into the ampoule, heated at 473 K, slightly cooled, decane (7.3 g/g) was added to hot silica and boiled for 1 min.

A fraction of water bound to A-400 was unfrozen at T < 260 K, i.e., it was strongly bound water, SBW since changes in the Gibbs free energy ΔG < –0.5 kJ/mol [158]. The δ_H value (*i.e.* magnetic shielding of protons) of water depended on the average number of the hydrogen bonds per a molecule (<n_{HB}>) and the length O-H···O and angle ∠OHO of these bonds. It was equal to 7.4 ppm for single ice Ih crystals and *ca*. 1 ppm for free water molecules [53].

Despite water and decane are immiscible liquids, addition of decane (C_d = 1.5 g/g) to nanosilica A-400 weakly hydrated (h = 0.05 g/g) resulted in the upfield shift of ^{1}H NMR signal of water, since the δ_H value changed in the 3.2-3.5 ppm range (Fig. 69b) instead of 4.5-5 ppm for water adsorbed alone (Fig. 69b) with a weak dependence of the δ_H values on temperature [158]. This decrease in the δ_H value could be explained by enhanced clusterization of bound water under action of hydrophobic decane. Decane could displace water into both narrower pores (inaccessible for larger decane molecules) and larger pores (to decrease contact area between two immiscible liquids). Both displacements result in decrease in the Gibbs free energy of the system. However,

the second type of the displacements was more characteristic for the systems with greater amounts of water than h = 0.05 g/g [53,158]. Despite a relatively great amount of decane (1.5 g/g), the sample remained in the powder state; *i.e.* all decane was in bound state [158].

The ^{1}H NMR spectra (Fig. 69b,d) were recorded for both decreasing (from 290 K to 210 K) and increasing (from 210 K to 300-310 K) temperatures [158]. Adsorbed decane demonstrated two signals at 0.9 and 1.25 ppm (Fig. 69b), corresponding to methyl and methylene groups, respectively. A small shift of decane signals with temperature could be due to the temperature dependence of the magnetic susceptibility of samples and/or changes in the parameters of a resonant circuit of a sensor without stabilization of resonance conditions by using deuterons. During cooling of a sample, signal intensity of both water and *n*-decane strongly decreased at T = 220 K (Fig. 69b). During heating, intensive signals of *n*-decane (and water) appear at $T > T_f$ (Fig. 53) [158].

A sample placed in the *n*-decane dispersion medium (C_d = 7.3 g/g), stirred at 293 K, was characterized by an additional upfield shift of bound water signal to approximately 1.5 ppm (Fig. 69c), *i.e.* the water clusterization increased in comparison with the sample at C_d = 1.5 g/g [158]. Water with similarly low values of δ_H could be assigned to weakly associated water, WAW, which represents individual molecules, 1D or strongly branched 2D or 3D clusters at the boundaries of polar (*e.g.,* silica) and nonpolar (*e.g., n*-decane) media or mosaic polar-nonpolar structures [53,158]. The δ_H values for H atoms in the OH groups participating and non-participating in the hydrogen bonds as a proton-donor strongly differ because O or other electron-acceptor atoms displace the electron density from the H atoms that leads to a decrease in the magnetic shielding of the protons. Therefore, WAW is characterized by a low (< 1) average number of the hydrogen bonds per a molecule as a proton-donor. However, this WAW bound to nanosilica A-400 corresponded to strongly bound water (SBW) since its signal already appears at $T > 240$ K (*i.e.* $\Delta G < -1$ kJ/mol) when decane signal appears too. This may suggest that water (*i.e.* SBW) locates in narrow voids (pores) of A-400 corresponding to the first peak of PSD at R = 0.6-1.5 nm [158].

To analyze the influence of bound water on the behavior of bound *n*-decane, polyphosphoric acid (PPA) was added as a dehydrating agent in the amount corresponding to the amount of water (Fig. 69d) [158]. Really, water signal was not observed after addition of PPA, *i.e.* all water was bound to PPA. Signal of water/PPA could be observed at ca. 10 ppm as a very broad signal. This signal was not observed (Fig. 69d) due to features of the used measurement technique and a narrow bandwidth (20 kHz). The PPA addition led to a decrease in splitting of decane signals (compare the spectra in Fig. 69b,c,d). Thus, strong bonding of water by PPA led to enhancement of interaction of bound decane with the nanosilica surface [158].

Pretreatment of nanosilica A-400: heating at 723 K for 10 min, loading a hot sample into a NMR ampoule, heating at 473 K, slight cooling, and then addition of decane to hot silica sample and boiling in decane for 1 min, was used to reduce the silica surface hydrophilicity [158]. This treatment resulted in diminution of melting delay (Figs. 69c and 70) since signal intensity of a fraction of mobile decane increased much stronger at $T > T_f$, especially at $T > 260$ K.

This result could be explained by a better distribution of silica nanoparticles (in comparison with the initial silica) in the decane medium and stronger interaction of decane with the silica surface, which was characterized by a decreased number of surface silanols and the amount of residual water due to heating under the mentioned conditions. The stronger interaction of decane with the silica surface appears in broadening of the ^{1}H NMR bands (Fig. 69c, dot-dashed lines) similar to samples at a low content of decane located only in pores of silica [158].

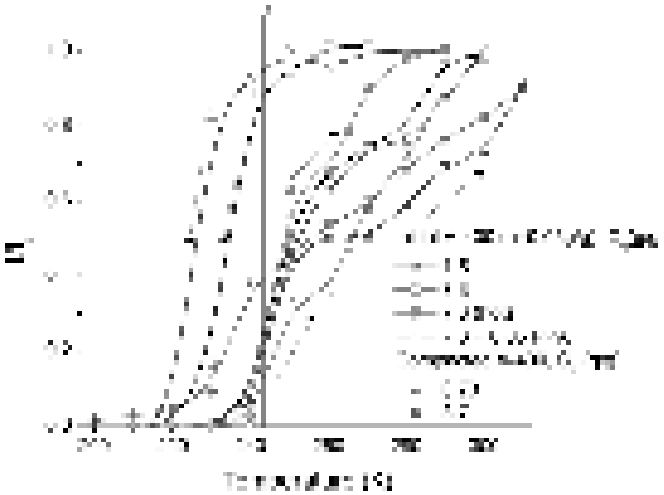

Fig. 70. Temperature behavior of signal intensity (normalized to intensity I_0 at 290-310 K) of *n*-decane bound to initial (bulk density 0.07 g/cm^3) and compacted (0.15 g/cm^3) A-400 depending on C_d and presence of PPA; curve labeled as 'hot' corresponded to A-400 heated at 723 K for 10 min, loaded into the ampoule, heated at 473 K, slightly cooled, and addition of decane to hot silica and boiling in decane for 1 min.

Freezing/melting curves, showed as relative intensity of ^{1}H NMR signals of mobile decane molecules confined in textural pores of A-400, were characterized by a broad hysteresis loop (Fig. 70) [158]. This was due to melting of solid alkane structures with a certain delay in comparison with their freezing at the same temperatures. During heating of the frozen A–400/water/decane system at C_d = 7.3 g/g, melting of a significant fraction of decane occurred at temperatures higher than the freezing point (T_f = 243.5 K) of bulk decane (Fig. 70). An increase in signal intensity was observed up to 280-310 K. Addition of PPA led to certain changes in the freezing and melting temperatures of decane. During freezing, a strong decrease in the signal intensity of decane was observed at 220-230 K, *i.e.* at $T < T_f$ (Fig. 70). This effect could be due to relatively weak interaction of a significant fraction of decane (frozen at $T > 230$ K) with the pore walls. This was clearly seen from the difference in the freezing curves at different content of decane. Since at C_d = 7.3 g/g (only ~20% decane was unfrozen at 230 K), a fraction of decane weakly bound or non-interacting with the silica surface was much greater than that at C_d = 1.5 g/g (~80% decane was unfrozen at 230 K), because decane located in pores was unfrozen at 230 K [158].

It is known that compacting of nanosilicas (*e.g.*, during MCA) could result in an increase in contribution of mesopores due to rearrangement of secondary structures with increasing bulk density from initial ρ_b = 0.04-0.07 g/cm^3 to 0.2-0.3 g/cm^3 for treated samples [53]. Therefore, confined space effects for *n*-decane could be enhanced (in comparison with initial A-400 at ρ_b = 0.07 g/cm^3) if it was bound to compacted A-400 at ρ_b = 0.15 g/cm^3 (Figs. 69 and 70) [158]. Really, at least, two effects were observed. First, in contrast to the initial nanosilica, the ^{1}H NMR spectra include broader lines without fine structures related to the CH_3 and CH_2 groups of *n*-decane (Fig. 69e,f). However, at C_d = 3.7 g/g, a certain line structure was observed (Fig. 69f) but less clearly than for *n*-decane bound to the initial silica (Fig. 69b-d). Second, the integral intensity demonstrated a smaller decrease during heating at $T > 260$ K than even at a larger C_d value for the initial A-400 sample (Fig. 70). Thus, enhanced mesoporosity of compacted A-400 led to the stronger confined space effects for bound *n*-decane and delay in melting of frozen structures diminished [158].

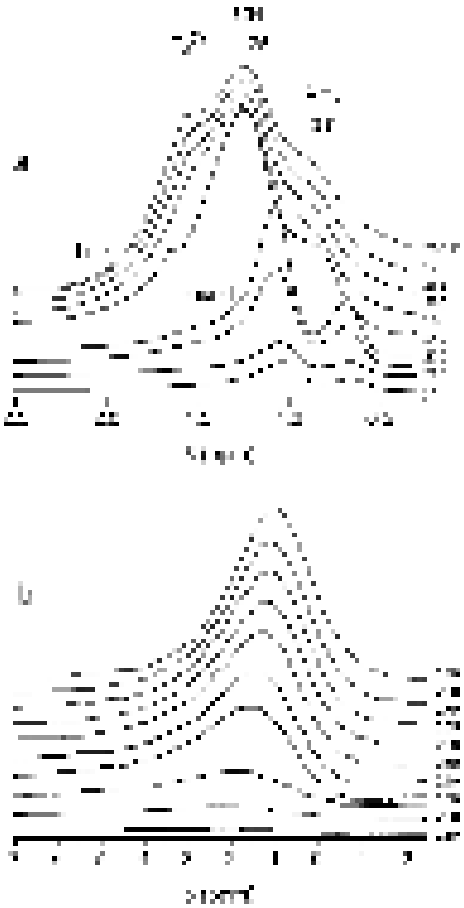

Fig. 71. ^{1}H NMR spectra (for static samples during heating) of adsorbates bound to silica gel Si-60 at decane amount C_d = (a) 3.7 g/g and (b) 0.44 g/g and residual water at $h \approx 0.005$ g/g.

As it was mentioned above, nanosilicas could be assigned to adsorbents with a 'soft' texture because adsorbates (as well as thermal, mechanical, mechanochemical, and hydrothermal treatments) could easily rearrange aggregates of primary nanoparticles and especially agglomerates of aggregates [53]. To elucidate the effects of the textural changes in A-400 due to interaction with *n*-decane (and water), silica gel Si-60 (composed of much more rigid beads than agglomerates of A-400) with the S_{BET} and V_p values similar to those of A-400 (Table 1) was used in similar ^{1}H NMR studies [158]. Notice that alkanes adsorbed onto Si-60 could not affected its textural characteristics since silica gels were rigid adsorbents in contrast to 'soft' FMO.

Samples of silica gel Si-60 were prepared with different amounts of *n*-decane (C_d = 0.44 and 3.7 g/g). Si-60 was preheated at 445 K, and then decane added to cooled silica filled a portion of pores (C_d = 0.44 g/g) or completely filled of pores and formed the dispersion medium (C_d = 3.7 g/g) [158]. The last Si-60/alkane sample was heated at 445 K for 1 min to remove air bubbles, and it was transparent after this heating. It included *ca*. 0.005 g/g of residual water (Fig. 71a). The amount 0.44 g/g of decane (liquid density 0.73 g/ml) provided filling of a major portion (0.6 cm^3/g) of pores of Si-60 (Table 1, V_p). At decane excess, the ^{1}H NMR spectra include two relatively broad signals at 1.25 and 0.9 ppm at $T > T_f \approx 243$ K (Fig. 71a). Signal of residual water appears as a shoulder at 1.5 ppm. Additionally, methylene groups linked to CH_3 groups in the decane molecule could contribute this signal. Water bound in this sample corresponded to WAW, as well as for alkane/A-400 system (Fig. 69) [158]. At $T \leq 240$ K, the signal width decreased and the upfield shift was observed due to changes in the magnetic susceptibility of the sample with a frozen fraction of decane. At C_d = 0.44 g/g when alkane molecules were located only in pores of Si-60, signals of methyl and methylene groups were broadened, overlapped and characterized by a small downfield shift with decreasing temperature (Fig. 71b). This effect was much stronger than that for decane bound to the treated nanosilica A-400 with a greater content of alkane [158]. This

difference could be explained by stronger confined space effects for decane located in narrow mesopores of rigid silica gel beads in comparison with the 'soft' A-400 powder [158].

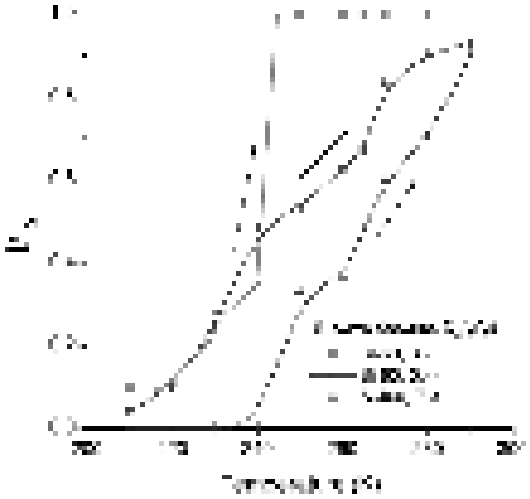

Fig. 72. Temperature behavior of signal intensity (normalized by dividing by the intensity I_0 at maximal temperature used, 290-300 K) of decane bound to Si-60 at C_d = 3.7 and 0.44 g/g or A-400 at C_d = 7.3 g/g during heating regime.

At $T < T_f$, the temperature dependences of signal intensity of decane were similar for both samples with Si-60 at C_d = 3.7 or 0.44 g/g (Fig. 72) but they were located above that of A-400 at C_d = 7.3 g/g due to a greater excess of bulk decane in the last sample [158]. This caused signal appearance only at T > 240 K during thawing of frozen decane/A-400 with significant melting delay (Fig. 72). Consequently, a greater amount of decane bound to Si-60 was unfrozen in comparison with A-400 at the same temperatures. This difference could be explained not only by the difference in the amounts of decane but also by the difference in the texture of these silicas. At C_d = 3.7 g/g, the total amount of alkane was unfrozen at $T > T_f$ during heating (Fig. 72) in contrast to the sample at a low amount of decane (0.44 g/g). This effect was due to a very small outer surface area of Si-60 beads, which could affect the temperature behavior of decane located out of pores [158]. Therefore, the effect of the silica gel on bulk alkane (melting delay) was much smaller than that for nanosilica having a much greater outer surface of aggregates of nanoparticles which affected a greater amount of nearly bulk decane and enhanced the melting delay [158]. Notice that similar structurizing effects were observed for aqueous suspensions of nanosilicas, since 10-12 wt.% of nanosilica was enough for total structurization of all water in the suspension [53]. If all decane was bound in pores of Si-60 at C_d = 0.44 g/g, its fraction was immobilized at $T > T_f$, and an increase in intensity was observed up to 280-310 K similar to that for decane/A-400 (Fig. 72); *i.e.* solid or quasi-solid decane structures did not melt due to the effect of silicas and this effect was stronger for nanosilica. In other words, the same amount of A-400 could structure a much greater amount of decane than silica gel. Thus, different morphological characteristics of A-400 and Si-60 at close S_{BET} values led to very different effects on decane located in pores and out of pores [158].

The $\delta_H(T)$ function depends on the number of possible configurations of the water molecules in the hydrogen bonds network. Considering that this number is inversely proportional to the average number of the hydrogen bonds $<n_{HB}>$, according to the entropy definition $S \approx -k_B \ln n_{HB}$ [211]. Therefore, the temperature derivative of the measured fractional chemical shift [211]

$$-\left(\frac{\partial \ln \delta(T)}{\partial T}\right)_p = -\left(\frac{\partial \ln < n_{HB} >}{\partial T}\right)_p \approx \left(\frac{\partial S}{\partial T}\right)_p \qquad (28)$$

should be proportional to the constant pressure specific heat $C_P(T)$ ($C_P = T(\partial S/\partial T)_P$). This aspect was analyzed in detail in [211]. The $T(\partial \ln\delta(T)/\partial T)_P$ functions were compared for water and decane bound to A-400 and Si-60 (Fig. 73) [158].

Heating of Si-60/decane (C_d = 0.44 g/g) frozen at 210 K led to an increase in the entropy (Fig. 73, curve 1) at T < 230 K. Then the entropy decreased (minimum is at 243 K ≈ $T_{f,decane}$) due to ordering of mobile molecules at $T < T_{f,decane}$. At $T > T_{f,decane}$, the entropy increased due to increasing disorder in a melting fraction of the adsorbate. The next minimum at *ca*. 273 K (*i.e.* at $T_{f,water}$) is due to the effects of ordering (separating) mobile water and decane (Fig. 72). Excess of decane (C_d = 3.7 g/g), when the dispersion medium for Si-60 beads was with decane, resulted in much lower entropy at $T_{f,decane}$ (Fig. 73, curve 2) due to freezing of the major portion of decane at $T < T_{f,decane}$ (Fig. 72). For adsorbed water (Fig. 73, curves 3 and 4), the entropy decreased at T close to $T_{f,water}$, and then it increased due to increasing disorder of liquid water with increasing temperature [158].

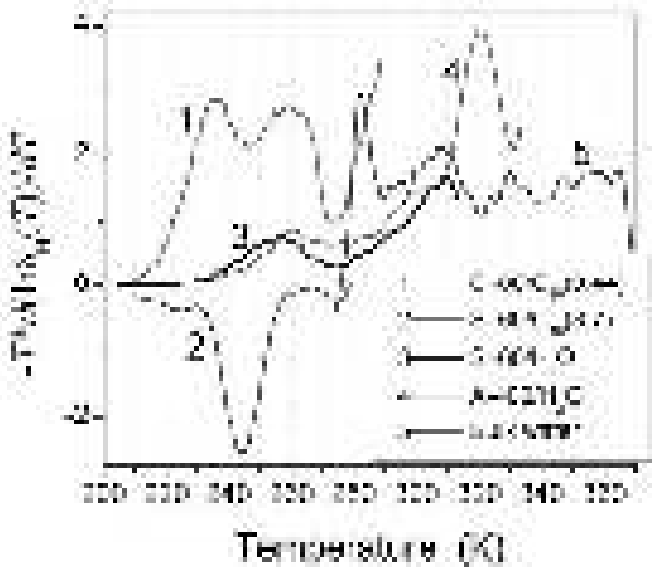

Fig. 73. Function $-T(\partial \ln\delta(T)/\partial T)_P$ *vs*. temperature for *n*-decane (C_{10}) and water bound to Si-60 or A-400 or bulk water.

Theoretical calculations of the ^{1}H NMR spectra of *n*-decane and water molecules free and bound in silica mesopore (1.1 nm in radius) or bound to a silica nanoparticle (~2.1 nm in diameter) showed (Fig. 74a) that interactions with silica resulted in downfield shift of the band maximum of decane and broadening of the spectrum (Fig. 74a, curves 3 and 4) [158]. This occurred despite weak interactions between a silica surface and nonpolar alkane molecules. The effect was stronger for decane molecules located in the narrow pore (curve 4) than that for the molecules bound to the silica nanoparticle (curve 3). Water molecules co-adsorbed with decane without formation of clusters were characterized by a band at 1-2 ppm (Fig. 74a, curve 5), *i.e.* this was WAW. These results were in agreement with the experimental data showing the WAW appearing due to co-adsorption with decane [158]. Notice that decane-decane interaction is relatively weak. The free energy of solvation of *n*-decane in the *n*-decane medium calculated using the SMD method (HF/6-31G(d,p) basis set) gives –16 kJ/mol. This was approximately 2.5 times smaller (by the modulus) that the solvation energy of silica in water. Therefore, the ^{1}H NMR spectra calculated for decane molecules free and in the decane dispersion medium were practically the same in contrast to the molecules free and interacting with the silica surface because the interaction of a decane molecule with the silica surface is stronger than that with neighboring decane molecules [158].

Interaction of water molecules with the polyphosphoric acid (PPA) fragments caused significant downfield shifts for both water molecules (compare curve 1 in Fig. 74b and curve 5 in Fig. 74a, $\Delta\delta_H$ = 3-5 ppm) and OH groups in the PPA (compare curves 2 and 3 in Fig. 74b, $\Delta\delta_H$ = 5-7 ppm) [158]. This effect is a typical downfield shift for acids interacting with water molecules due to decreasing of the electron density on the H atoms (*i.e.* decreasing magnetic shielding of protons) which tend to be de-attached as H^+ to form $H_3O^+(H_2O)_n$ (i.e. hydronium ion H_3O^+, Zundel ($H_5O_2^+$) or Eigen ($H_9O_4^+$) cations) and acidic residua both strongly affecting the water structure [53]. Notice that for the strongest hydrogen bonds of basic compounds with strongly acidic OH

groups, the chemical shift of proton resonance could reach much higher values up to 16-20 ppm [53,158].

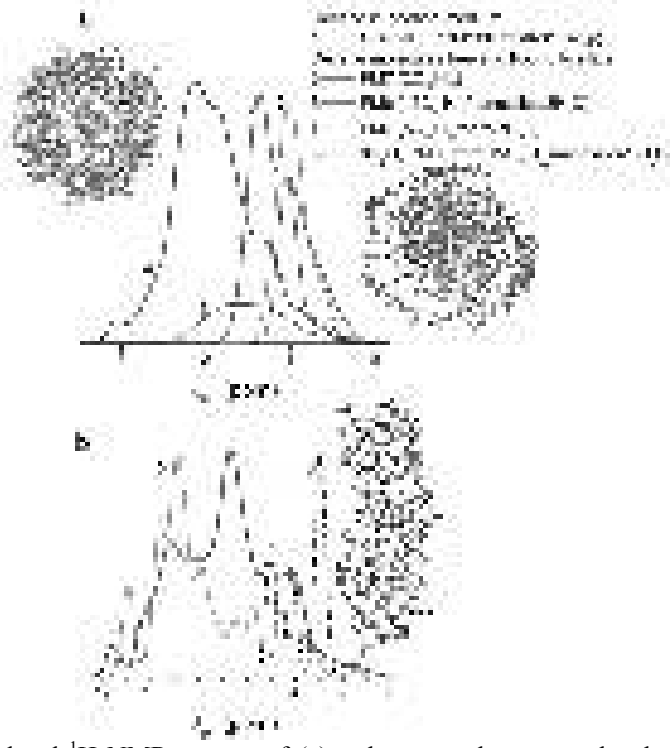

Fig. 74. Theoretically calculated ^{1}H NMR spectra of (a) *n*-decane and water molecules free (curves 1 and 2) and bound in mesopore of silica (curve 4) or to silica nanoparticle (curves 3, 5); and (b) water (curve 1, PM7) and OH groups in PPA fragments hydrated (2, PM7) and non-hydrated (3, GIAO/B3LYP/6-31G(d,p)).

The interaction energy of water or decane with silicas, measured as the heat of immersion of powder samples in liquids, increased with increasing S_{BET} of silicas (Fig. 75) [158]. The curve course is practically the same for nanosilicas and silica gels interacting with water because of the identity of the nature of their surfaces composed of the siloxane bonds and silanol groups. The latter (in contrast to the siloxane bonds) were the main adsorption sites for water [53]. In the alkane medium, the increase in the interaction energy with increasing S_{BET} was smaller than that for the aqueous medium. For silica gels, the ratio $K_h = Q_{water}/Q_{decane}$ was large (2.5-3.3), because silica gels are highly hydrophilic materials, and it increases with S_{BET} value. For nanosilicas, the K_h values were smaller (1.2-1.5) than that of silica gels due to a smaller number of surface silanols (~2OH/nm^2) than that on the silica gel surface (~5OH/nm^2). This difference is a consequence of the flame synthesis of nanosilicas at high temperatures (>1300 K) in contrast to silica gels synthesized in the liquid reaction media. This led to greater values of Q_{decane} for nanosilicas caused by stronger dispersion interactions with more open surface of nanosilicas than for silica gels with similar values of S_{BET}. Thus, nanosilicas were less hydrophilic (it adsorbs only 1-3 wt.% of water from air) than silica gels. Additionally, the surface area of nanosilicas (possessing the textural porosity caused by aggregates < 1 μm in size of nonporous nanoparticles < 10 nm in size) is more accessible for relatively large molecules of *n*-decane (Fig. 74) than that of silica gels representing rigid mesoporous particles of sizes in the millimeter range, *i.e.* possessing narrow and long mesopores.

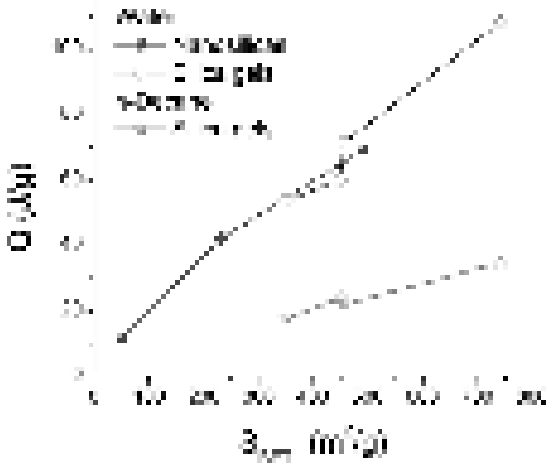

Fig. 75. The relationship between the heat of immersion of nanosilicas and silica gels in water or decane *vs*. the specific surface area (S_{BET}) of silicas.

Dispersion interactions of decane molecules with the silica surface were weaker than the hydrogen bonding of water molecules to the surface silanols (per mole of silanols), but were greater per mole of adsorbates due to a much larger size of $C_{10}H_{22}$ than H_2O [158]. Additionally, the narrowest pores of silica gels are less accessible for decane molecules larger by approximately ten times than water molecules. Adsorbed water molecules form clusters around surface hydroxyls that could reduce the effects of different numbers of surface hydroxyls per nm^2 of surface of nanosilicas and silica gels [158]. Therefore, the curves of Q_{water} *vs*. S_{BET} (Fig. 75) have similar courses for nanosilicas and silica gels. The difference in the values of K_h for these silicas is mainly due to the difference in the values of Q_{decane}. For example, Q_{decane} = 34.4 and 17.4 J/g for A-300 and Si-100, respectively, having similar values of S_{BET} (Table 1). Stronger interactions of *n*-decane with less hydrophilic nanosilicas than with more hydrophilic silica gels could explain the difference in the temperature behavior of ^1H NMR signal intensity of *n*-decane bound to nanosilica A-400 and silica gel Si-60 (Figs. 70 and 72) [158].

DSC thermograms of cooling of *n*-decane, adsorbed onto different silica gels in the amounts greater than the pore volume of silicas, demonstrate the presence of two crystallization peaks (Fig. 76) [158]. A low-temperature crystallization peak shifts toward higher temperature with increasing pore size (Fig. 76). The shift of a low-temperature melting peak with respect to a low-temperature crystallization peak depended on the pore size distribution of silica gels because melting of larger frozen structures bound in larger pores occurred at higher temperatures (Fig. 76b,c) since the heating rate of 5 K/min used was not too small to prevent certain delay observed in the melting process. Therefore, the hysteresis loop could be broader for decane located in broader pores due to the formation of larger frozen structures (quasi-crystallites). Similar effects were observed (Figs. 50-52, Tables 9 and 10) for different amounts of decane adsorbed onto the same silica because it filled only narrower pores at a lower adsorbed content. A narrow peak at T close to T_f (Fig. 76) was due to freezing of nearly bulk decane weakly bound or unbound to silica gels because decane was adsorbed in the amounts greater than the pore volume. Consequently, there was a fraction of decane weakly bound or unbound to the silica surface. The second peak, which is located at lower temperatures and broader than the first one but it depends on the pore size of silica gels, appears due to freezing of decane bound in mesopores. Melting curves of decane at $T < T_{f,d}$, *i.e.* for alkane located in pores, and water crystallites at $T < T_{f,w}$ confined in narrow pores of Si-40 were similar in shape as they demonstrate broad peaks but different in position (Fig. 76a) because these adsorbates were of very different nature and characterized by different types of intermolecular bonding affecting T_f. Water did not show the melting peak at $T \geq T_{f,w}$ (Fig. 76a, curve 4) because all water (h = 0.35 g/g) was bound in narrow pores of Si-40. During freezing of the sample (Fig. 76a, curve 3), a narrow crystallization peak was observed at *ca*. 273 K (*i.e.* there was strongly associated but weakly bound water) in addition to a broad crystallization peak at 230-250 K for water strongly bound in pores. During melting of ice bound

in pores of Si-40, the heterogeneity of adsorbent and step-by-step melting of ice in broader pores resulted in the absence of a sharp melting endotherm at temperatures close to $T_{f,w}$ (Fig. 76a, curve 4). Residual water bound to Si-60 was characterized by a small crystallization peak at 256 K (Fig. 76b, curve 1) [158].

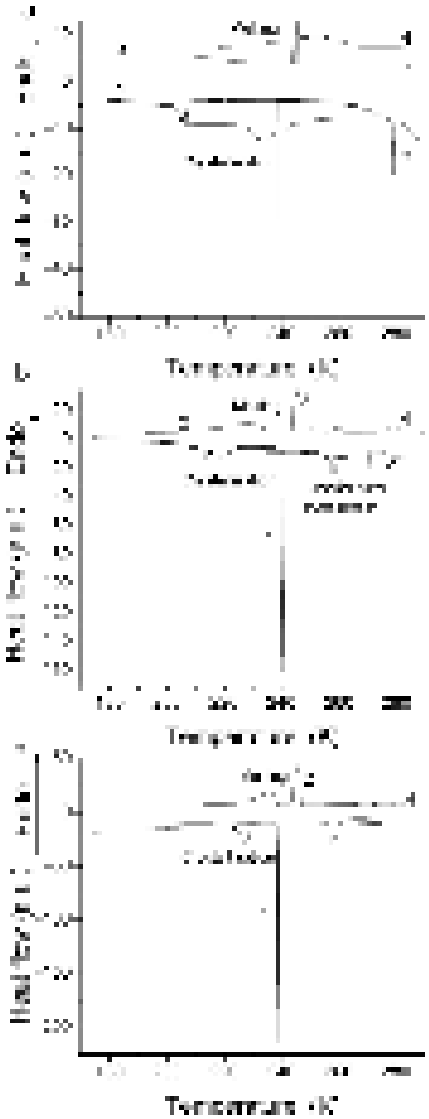

Fig. 76. DSC thermograms of cooling-heating of (a-c) *n*-decane (curves 1 and 2), (a) water (curves 3 and 4), and (b, c) 1-decanol (curves 3 and 4) bound to silica gels for (a) Si-40 (C_d = 0.61 g/g, h = 0.35 g/g), (b) Si-60 (C_d = 1.15 g/g, 1-decanol C_{dl} = 0.45 g/g), and (c) Si-100 (C_d = 1.11 g/g, C_{dl} = 1.11 g/g) at the cooling-heating rate of 5 K/min, silica sample mass was 12.8-25.6 mg.

1-Decanol ($T_{f,dl}$ = 279.5 K, less polar than water but more polar than decane) bound to Si-60 or Si-100 (Fig. 76b,c) demonstrated two freezing peaks and two melting peaks [158]. Despite a relatively low amount of decanol bound to Si-60 (0.45 g/g), a sharp freezing exotherm was observed close to its freezing point $T_{f,dl}$ (Fig. 76b). Decanol bound to Si-100 (C_{dl} = 1.11 g/g) demonstrated broader peaks than that bound to Si-60. This difference is similar to that for decane adsorbed onto these silicas [158].

Thus, there are several factors governing the temperature behavior of polar (water), weakly polar (1-decanol), and nonpolar (*n*-decane) compounds bound in pores or located out of pores of different silica gels Si-40, Si-60, and Si-100 that differs for nanosilicas. The first one is the pore size, since the temperature changes in the structure of bound liquids are more homogeneous for adsorbates located in narrower pores with a narrow PSD. The second one is the amount of adsorbate, which could be strongly or weakly bound to the surface of adsorbent or unbound (bulk), located out of pores. Additionally, the heating-cooling rate and the temperature gradient could

affect the interfacial and temperature behavior of adsorbates, especially if adsorbents have broad PSD (such as FMO) that caused the formation of inhomogeneous structures (liquid – solid) of adsorbates at different temperatures in pores of different sizes. The temperature dependence of the behavior of liquids confined in pores is the basis of several porosimetry methods, including DSC thermoporometry [53,158,212-214].

The Gibbs-Thomson equation applied to DSC melting thermograms allows one to calculate the PSD for silica gels (with the model of cylindrical pores since the errors of this model are relatively small for silica gels [158]) using melting curves at $T < T_f$, *i.e.* using the low-temperature DSC peaks. Melting curves of decane at $T < 243$ K (Fig. 76) were used to calculate the PSD with the equation $R = k_{GT}/(T_{0,m} - T_m)$ for cylindrical pore radius at $k_{GT} = 64.6$ K nm, where $T_{0,m}$ and T_m were the melting temperatures for pure bulk crystallites and confined in pores of radius R, respectively. For the freezing point depression of decane confined in pores, these calculations resulted in the PSD similar to the NLDFT PSD (Fig. 77) [158]. Notice that the DSC PSD have a simple contour than the NLDFT PSD curves because the latter were calculated using a small value of the regularization parameter fixed in the Quantachrome software. For Si-40, DSC PSD (Fig. 77, curve 1) was zero at $R = 1.0$-1.5 nm in contrast to NLDFT PSD (curve 2). This difference could be explained by two factors: (i) decane was poorly adsorbed in narrow pores at $R < 1.5$ nm due to presence of residual water and air bubbles; and (ii) the used temperature was not enough low to obtain a fraction of decane unfrozen in the narrowest pores (melting curve starts from nonzero values, Fig. 76a, curve 2). Hence, the appropriate correspondence between the NLDFT and DSC PSD for silica gels was evidence that the melting low-temperature peaks of decane were due to alkane molecules located in mesopores of silica gels [158].

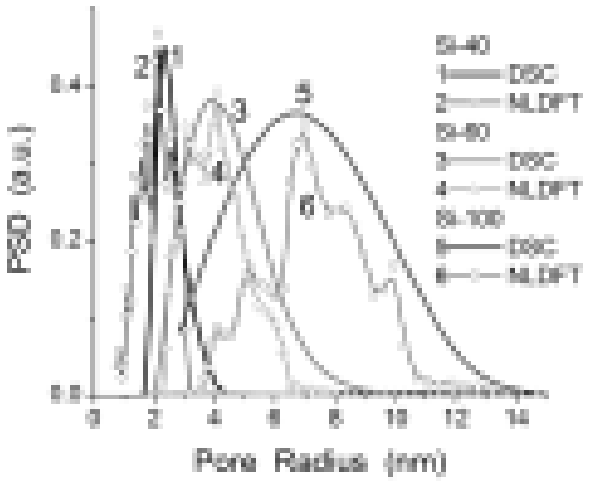

Fig. 77. Differential PSD of silica gels calculated using the NLDFT method (applied to nitrogen adsorption-desorption isotherms with the model of cylindrical pores) and the Gibbs-Thomson equation for the freezing point depression for *n*-decane confined in pores using DSC melting thermograms.

Maximal excess in the decane amount was for Si-60 ($V_d = 1.58$ cm^3/g at $V_p = 0.82$ cm^3/g) [158]. Therefore, a marked high-temperature peak at $T \approx 263$ K was observed for Si-60. However, Si-60 has narrower pores than Si-100 (Fig. 77). Therefore, decane structures confined in mesopores have maximal sizes for Si-100 but the frozen decane structures out of pores could be larger for Si-60. A minimal C_d value (slightly higher than the pore volume) was for Si-40, possessing the narrowest pores (Fig. 77) with the highest adsorption potential [158].

The differences in the PSD of silicas and the decane excess led to different hysteresis loops for integrated heat flow ($\Phi(T)$) [158]

$$\Phi(T) = \int_{T_{min}}^{T} |F(T)|\, dT\,, \tag{29}$$

during cooling (exo-effects due to crystallization) and heating (endo-effects due to melting) of decane bound to silicas (Fig. 78).

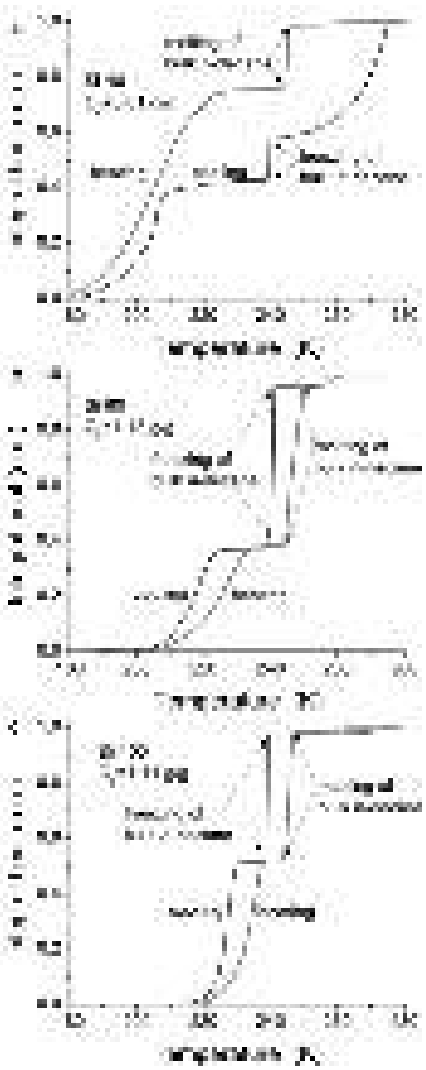

Fig. 78. Integral heat as a function of temperature Φ(*T*) (with subtraction of a nonlinear baseline and normalization to unit) for exo (cooling, crystallization) and endo (heating, melting) effects for decane confined in pores of (a) Si-40, (b) Si-60, and (c) Si-100.

For easier comparison of the Φ(*T*) graphs, the integration in Eq. (29) of both freezing and melting curves (after subtraction of a nonlinear baseline) for the modulus of the heat flow |*F*(*T*)| was carried out from a minimal temperature (~170 K) toward higher temperatures (~290 K). The Φ(*T*) curves for decane bound to Si-60 and Si-100 were similar (Fig. 78b,c) but strongly differ from that for alkane bound to Si-40 (Fig. 78a). This difference could be explained not only by the difference in the PSD of these silicas but also by the smallest amount (0.61 g/g) of decane adsorbed on Si-40. A nearly vertical step on the Φ(*T*) curve of freezing of bulk (or nearly bulk) decane at *ca*. 240-243 K was greater for Si-60 (with maximal excess of adsorbed alkane) than for Si-100 or Si-40 (Fig. 78) due to larger decane structures formed out of pores of Si-60, despite pore sizes of Si-100 were greater than that of Si-60 (Fig. 77). Larger structures of nearly bulk decane gave a greater exothermic effect during freezing, since a greater endothermic effect was observed during melting (Figs. 76-78). Notice that a certain inclination of a step around T_f was observed on the melting curves, especially for Si-60 and Si-100 (Fig. 78b,c) due to certain delay in melting of large frozen structures during heating at $T > T_f$ [158].

The DSC results allowed one to explain broad hysteresis loops for the integral ^{1}H NMR intensity for decane, both bulk and confined between silica nanoparticles of A-400 (Fig. 70), as well as for decane bound to Si-60 (Fig. 72) depending on the excess of the alkane [158]. The effect of decane excess for freezing-thawing during ^{1}H NMR measurements could result in the formation of large quasi-solid structures (quasi-crystallites) which were not observed in the ^{1}H NMR spectra

recorded at a narrow bandwidth (20 kHz) because of a relatively short time of transverse relaxation of an immovable fraction (despite appearance of a fraction of unfrozen bulk decane at $T > T_f$). For DSC measurements (Fig. 76), a relative significance of this effect was smaller (since only a small peak is at $T \approx 263$ K) due to a smaller decane excess and a certain physical difference in the phenomena studied by the NMR (changes in the molecular mobility with temperature) and DSC (release or absorption of heat with decreasing or increasing temperature) methods [53,158].

Thus, combined NMR/DSC/thermoporometry/nitrogen adsorption/quantum chemistry analysis [53,158] of the temperature and interfacial behavior of *n*-decane, water and 1-decanol bound to nanosilica and silica gels showed that a portion of decane or decanol remained frozen (quasi-solid) at temperature higher than the freezing point of bulk liquids during heating of samples. Additionally, a fraction of adsorbates remained unfrozen at temperatures below the freezing point during cooling due to the confined space effects. However, freezing and melting curves did not coincide and the hysteresis loop width depended on the NMR (or DSC) experiment conditions [158].

For *n*-decane adsorbed onto silica gels Si-40, Si-60 and Si-100, two-four freezing or melting peaks were observed on the DSC thermograms over the 170-300 K range during cooling or heating of samples that depended on the pore size distribution of silicas and the amount of decane [158]. Integrated heat flow curves *vs*. temperature demonstrated the hysteresis loops similar to the effects observed by the NMR method; however, the shapes of the hysteresis loops differed because of the difference in the observed effects: changes in molecular mobility (NMR) or absorption (melting) and release (freezing) of heat (DSC). According to ^{1}H NMR data, a portion of *n*-decane, which is in quasi-crystalline state characterized by fast molecular exchange (short transverse relaxation time) and not observed in the NMR spectra, was greater during heating of samples than a portion of decane frozen during cooling at temperature close to the freezing point of bulk liquid (T_f). A similar effect appearing in the DSC endotherms for samples heated at the same heating rate was smaller than that in the NMR measurements due to different excess in the decane amounts and the difference in the phenomena studied by the low-temperature ^{1}H NMR (changes in molecular mobility with temperature) and DSC (release or absorption of heat with decreasing or increasing temperature) methods. The enhanced confined space effects for nanosilica A-400 compacted toward twice greater bulk density (0.15 g/cm^3 instead of 0.07 g/cm^3 for the initial A-400) resulted in an increase in a portion of unfrozen *n*-decane at $T > T_f$. For a small content of water co-adsorbed with *n*-decane (of a large content > V_p), water displaced by decane into narrower pores where it could not form large structures. Therefore, this water is weakly associated water. The studied regularities in the temperature and interfacial behavior of water and *n*-decane or 1-decanol co-adsorbed onto different silicas could be used to explain features of the work and the efficiency of adsorbents applications at different temperatures and concentrations of adsorbates [53,158].

Treated FMO

Water adsorbed on the initial silica A-300 was characterized by two ^{1}H NMR signals (Fig. 79a) at δ_H = 2.8-4.8 (SAW) and 1.5 ppm (WAW) [215]. The presence of two signals suggests the difficulties in the exchange processes between the corresponding water structures. This could be explained by the formation of small clusters and nanodomains of water bound in narrow pores between adjacent particles (WAW) and broader voids between several neighboring particles in aggregates (Figs. 26 and 80), respectively, as it was described above. Similar values of δ_H were observed for water adsorbed onto porous silicas and assigned to the hydrogen-bound and non-bound protons in the water molecules [53,158]. However, it should be noted that the topology of pores in silica gels or ordered mesoporous silicas and voids in the nanosilica powders were strongly different. Therefore, conditions of water clusterization were much better for nanosilica (at low amounts of water) than for silica gels [53,213-215].

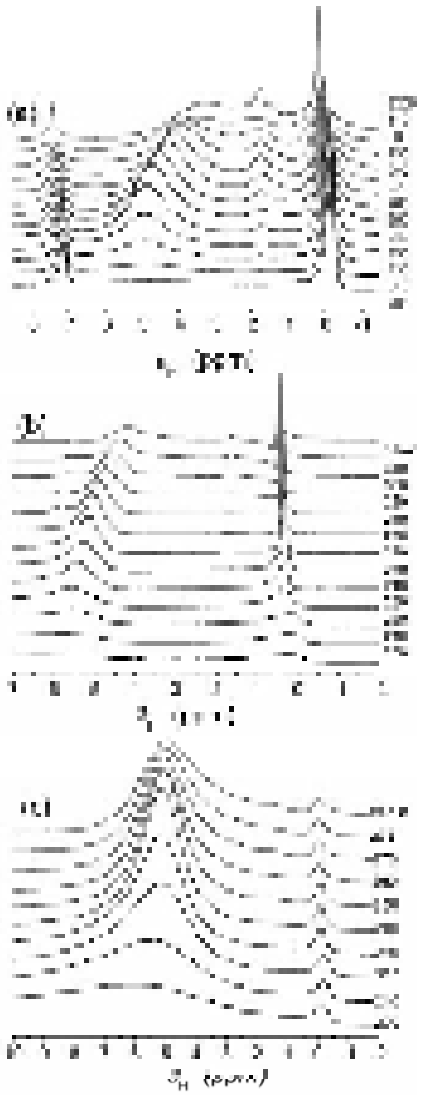

Fig. 79. ^{1}H NMR spectra recorded at different temperatures of water (5 wt.%) adsorbed on A-300 (a, b) initial and (c) MCA in (a) $CDCl_3$ and (b, c) CCl_4 media.

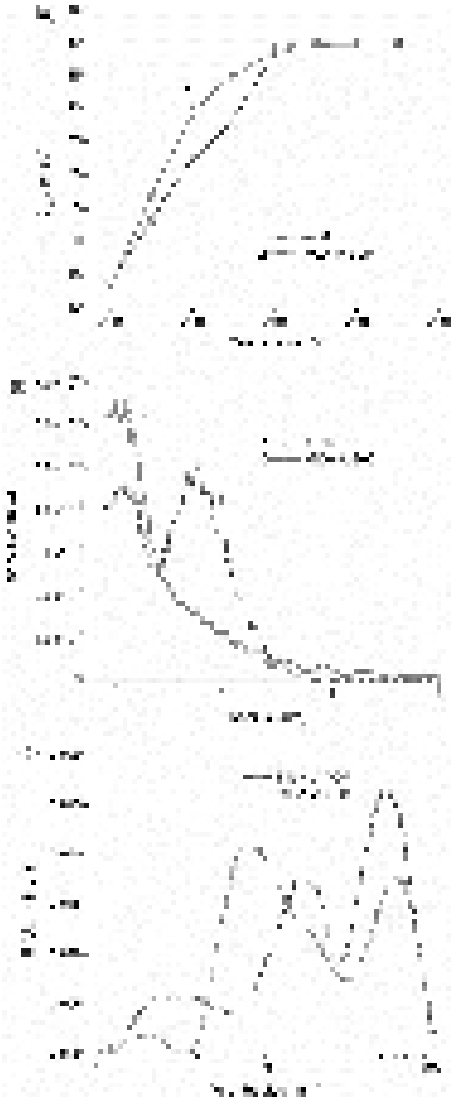

Fig. 80. (a) Temperature dependence of content of unfrozen water, C_{uw} (total water content 5 wt.%) adsorbed to initial A-300 and MCA A-300; (b) cluster size distributions of this water (CCl_4 medium); and (c) PSD (MND method) for initial and MCA treated A-300.

Signals at δ_H = 0 and 7.16 ppm were due to tetramethylsilane and $CHCl_3$ (admixture in $CDCl_3$), respectively. According to the ^{1}H NMR signal classification [53,213], observed water signals (Fig. 79a) could be assigned to strongly and weakly associated waters, respectively. The SAW signal shifted toward the strong magnetic field with increasing temperature. This could be explained by breakage of a portion of the hydrogen bonds, decomposition of large polyassociates of unfrozen water and stabilization of smaller structures of unfrozen water in narrow pores [215].

At T < 250 K the SAW signal intensity decreased due to freezing of this water with lowering temperature [215]. This process was accompanied by signal broadening because of decreased mobility of adsorbed water at lower temperatures. A certain broadening of the SAW signal at T > 250 K was due to such factors as accelerating exchange processes between SAW and WAW and an increase in nonuniform broadening due to appearance of solvent vapor babbles formed with elevating temperature. The latter could lead to a decrease in the SAW signal intensity.

The WAW signal decreasing with lowering temperature was narrower than the SAW signal (Fig. 79a) [215]. Two split signals of different intensity were observed for WAW because of nonuniformity of this water. At T > 250 K the WAW signal intensity increased due to decreased content of SAW. Two signals of WAW (Fig. 79a) could be attributed to water dissolved in

chloroform (the right signal of lower intensity) and water bound to silica nanoparticles (the left signal of greater intensity).

NMR-cryoporometry results showed the difference in the organization of water clusters adsorbed onto the initial and MCA A-300 (Fig. 80) because of the difference in the PSD of these silicas [215]. Despite an increase in contribution of smaller water clusters bound to MCA A-300, the contact surface area between water and silica (determined by integration of the $f_S(R)$ distribution functions) was larger for the initial silica (78 m^2/g) than for MCA A300 (56 m^2/g). Notice that 5wt.% H_2O was too low content to form a continuous water layer at the silica surface and to fill all textural pores. Therefore, water was strongly bound (freezing starts at $T < 250$ K, Fig. 63a) and could cover only a portion of the silica surface and filled only a small portion of pores, mainly narrow mesopores and nanopores, forming clusters of radius $R < 3$ nm (Fig. 80b) [215]. The behavior of water bound by silica initial and after the MCA of the water-wetted powder for 1 and 6 h was studied by the ^{1}H NMR spectroscopy with layer-by-layer freezing-out of bulk and bound water at $200 < T < 273$ K in different media (air, water, chloroform) (Fig. 81) [75,215].

It was shown that the longer the MCA causing narrowing voids between silica nanoparticles, the stronger bound the interfacial water and the stronger the $CDCl_3$ effects on this water [215]. For low hydration $h = 0.11$ g/g, the displacement of bound water by chloroform into larger voids became more visible at $T < 260$ K since the amounts of strongly bound water [53] frozen at $T < 260$ K decreased differently. For strongly wetted powders the ^{1}H NMR spectra of unfrozen water were observed at lower temperatures to 200 K with the single signal at chemical shift of the proton resonance $\delta_H = 4.5$-5.5 ppm close to that of bulk water [53,215]. For the aqueous suspension of the initial silica, the ^{1}H NMR signal was observed at $T \geq 220$ K [215]. Water in both cases was strongly associated [53] since the δ_H value was close to that of bulk water. A portion of adsorbed water frozen close to 273 K could be assigned to weakly bound water (WBW) at $|\Delta G| < 0.5$ kJ/mol. At $h = 0.11$ g/g, the spectra shape depended on the t_{MCA} value and medium (air or $CDCl_3$). Water adsorbed on all samples being in the air medium was strongly bound since the signal decreased only at $T < 250$ K. For the chloroform medium, a portion of adsorbed water was weakly bound since the signal strongly decreased at $T < 265$ K. The signal shifted toward the weak magnetic field with lowering temperature because of a stronger influence of the silica surface on closer located water layers frozen at lower temperatures. Additional signals at $\delta_H \approx 7$ and 0 ppm were due to H in chloroform (as an admixture in $CDCl_3$) and trimethylsilane (added to chloroform as a reference compound), respectively. A signal of weakly associated water, WAW appeared at $\delta_H = 1.0$-1.5 ppm [53,213] for the sample in $CDCl_3$ medium. This signal could be assigned to water dissolved in chloroform or forming small clusters in contact with both chloroform and the silica surface in narrow voids. The amounts of this water decreased for MCA-treated samples because of changes in the textural porosity and associativity of water molecules adsorbed in different voids. At temperatures close to 273 K the WAW signal was split into two signals due to structural nonuniformity [53] of the silica-water-chloroform system (Fig. 81) [75].

SBW (frozen at $T < 260$ K, Fig. 81) at $h = 0.11$ g/g was located in narrow voids at $R < 5$ nm between neighboring primary particles [75]. The pores filled by unfrozen water were narrower in MCA-treated samples. Chloroform could displace bound water into larger voids since this provided a smaller boundary area between larger water structures and weakly polar chloroform located in voids (note that water and chloroform are immiscible liquids in the bulk). This displacement depended on t_{MCA} since the larger the bulk density of the powder (longer MCA time), the smaller the displacement of the water. For weakly hydrated initial silica at a low hydration degree $h = 0.11$ g/g, the specific surface area determined with NMR-cryoporometry $S_{cryo} < S_{BET}$ (Table 7) because water could cover only a portion of the particle surface at $h = 0.11$ g/g [53]. This portion decreased in the $CDCl_3$ medium because of the displacement of bound water and the S_{cryo} value decreased (Table 7). For MCA-treated powders at $h = 1.2$ and 1 g/g, $S_{cryo} < S_{BET}$ was due to the same reason and possible remaining of air babbles in narrow voids. For the initial silica at $h = 40.7$ g/g, $S_{c,mes} > S_{c,mic}$ but at $h = 3$ g/g, $S_{c,mes} < S_{c,nano}$ (Table 13) because of attractive

interactions between neighboring nanoparticles through water bridges in the wetted powder and repulsive interactions between charged particles in the suspension. Therefore, DLS showed mainly individual nanoparticles for the initial silica. The $S_{c,meso}$ value was small at h = 0.11 g/g since water in the form of clusters located only in narrow voids and did not form coverage of the total surface of particles. In the suspension or strongly hydrated powder, the $S_{c,mes}$ value strongly increased, especially for the initial silica [75].

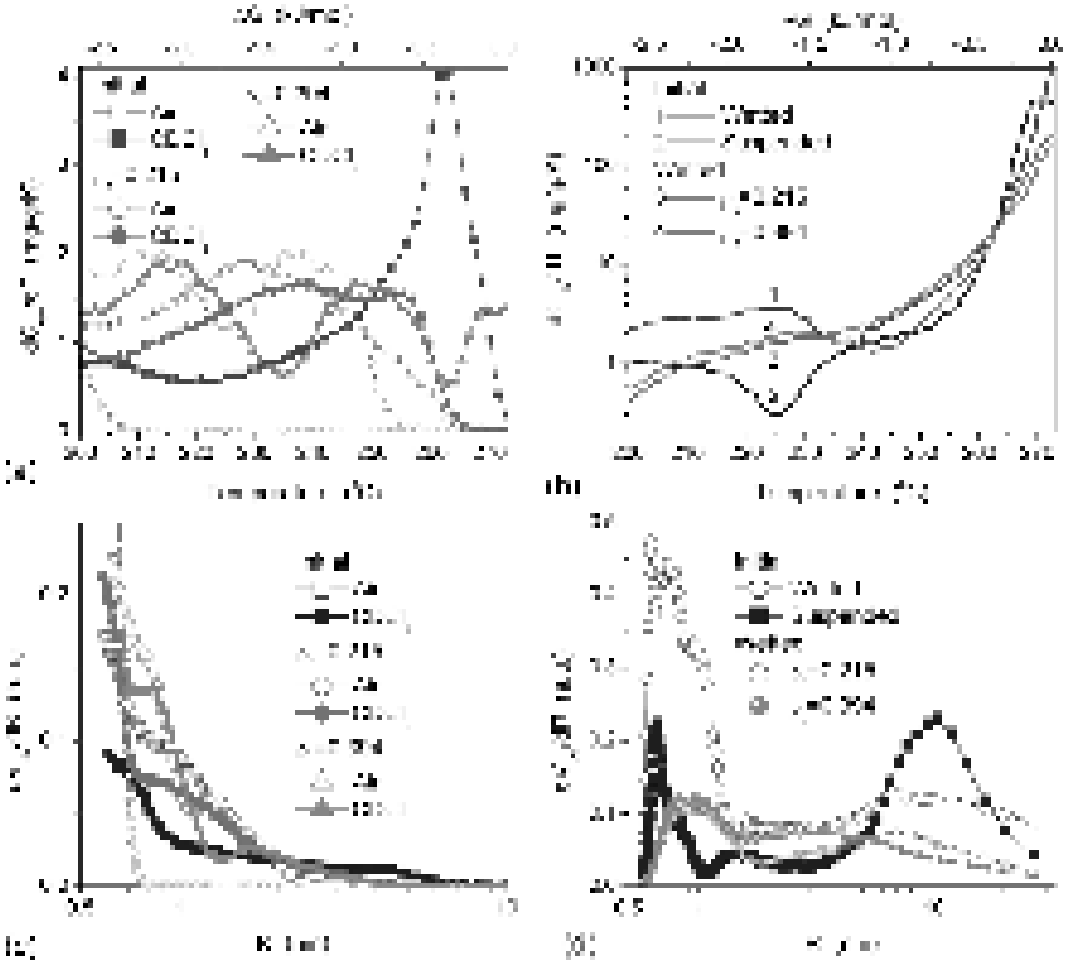

Fig. 81. Differential changes in the amounts of unfrozen water (dC_{uw}/dT) as a function of temperature (bottom x-axis) and changes in the Gibbs free energy (ΔG, top x-axis) in (a) weakly wetted samples (h = 0.11 g/g) initial (ρ_b = 0.045 g/cm^3) and treated for 1 h (ρ_b = 0.215 g/cm^3) and 6 h (ρ_b = 0.394 g/cm^3) without and with $CDCl_3$ medium and (b) strongly hydrated (h = 3, 40.7, 1.2 and 1 g/g, respectively) silicas; (c, d) differential functions with respect to the sizes of unfrozen water structures for (c) weakly and (d) strongly hydrated silicas.

Table 13. Characteristics of water unfrozen at T < 273 K and bound to initial and wet-MCA-treated A-300 nanosilica estimated by NMR-cryoporometry [75].

t_{MCA} h	ρ_b g/cm^3	h g/g	S_{cryo} m^2/g	$S_{c,nano}$ m^2/g	$S_{c,meso}$ m^2/g	$V_{c,nano}$ cm^3/g	$V_{c,mes}$ cm^3/g	γ_S J/g	$-\Delta G$ kJ/mol	Medium
0	0.045	0.11	159	111	48	0.045	0.055	10.3	3.03	Air
0	0.045	0.11	69	56	13	0.022	0.077	6.3	2.96	$CDCl_3$
0	0.045	3.0	322	207	115	0.085	1.367	32.2	3.08	H_2O
0	0.045	40.7	281	80	201	0.031	2.136	26.6	3.12	H_2O
1	0.215	0.11	188	131	57	0.053	0.076	10.8	2.87	Air
1	0.215	0.11	142	101	41	0.024	0.076	9.4	3.00	$CDCl_3$
1	0.215	1.2	123	52	71	0.022	0.772	15.6	3.21	H_2O
6	0.394	0.11	332	332	0	0.100	0	16.7	3.21	Air
6	0.394	0.11	100	94	6	0.040	0.058	8.3	2.71	$CDCl_3$
6	0.394	1.0	124	65	59	0.028	0.676	17.9	3.09	H_2O

Note. ΔG corresponds to the changes in the Gibbs free energy of a water layer closely located to the silica surface; γ_S is the modulus of overall changes in the Gibbs free energy of all bound water.

The γ_s values varied between 32.2 J/g (98 mJ/m^2) and 6.3 J/g (19 mJ/m^2) for initial silica at h = 3 and 0.11 g/g (in $CDCl_3$) were relatively small [75]. This was due to relatively small amounts of the surface silanols on fumed silica synthesized at high temperature [1-23]. Therefore, this silica can adsorb ~1.6 wt.% of water from air (desorbed at T < 150 ^{o}C), and only 7.9 % of the surface area was occupied by the adsorbed water molecules. More hydrophilic fumed silicas could adsorb 5-7 wt.% of water from air and have γ_s = 150-200 mJ/m^2 [53]. The γ_s values for MCA-treated silica were smaller than that of suspended or strongly hydrated initial silica (Table 13). This result suggested that the number of surface silanols could insignificantly change on MCA but particles were strongly aggregated that reduce total amounts of bound water since C_{uw} < h (1.2 or 1 g/g) and the number of silanols accessible for adsorbed water [75].

The low-temperature ^{1}H NMR spectroscopy used dealt with static samples to avoid signals of solid adsorbates and silanols of silica [53] that contribute the spectra recorded using the magic angle spinning (MAS) technique [216-225]. However, the difference in the MAS and non-MAS ^{1}H NMR spectra of water bound to fumed silica could be small [104].

Addition of *n*-decane to wetted precipitated silica Syloid 244 at h = 0.3 g/g resulted in the displacement of a portion of water into larger pores (Table 14 and Fig. 82) [91]. However, the associativity of water in larger pores increased that resulted in a downfield shift of the water signal [91]. Besides the water associativity effect on the value of the chemical shift of proton resonance, δ_H, stronger interactions of water with silica were observed in narrower pores [53,91,158]. For example, MCA (6 h) A-300 was characterized by increased contribution of nanopores. Therefore, the values of δ_H of water (h = 0.1 g/g) bound to MCA A-300 were greater than those of water bound to Syloid (h = 0.3 g/g) [91].

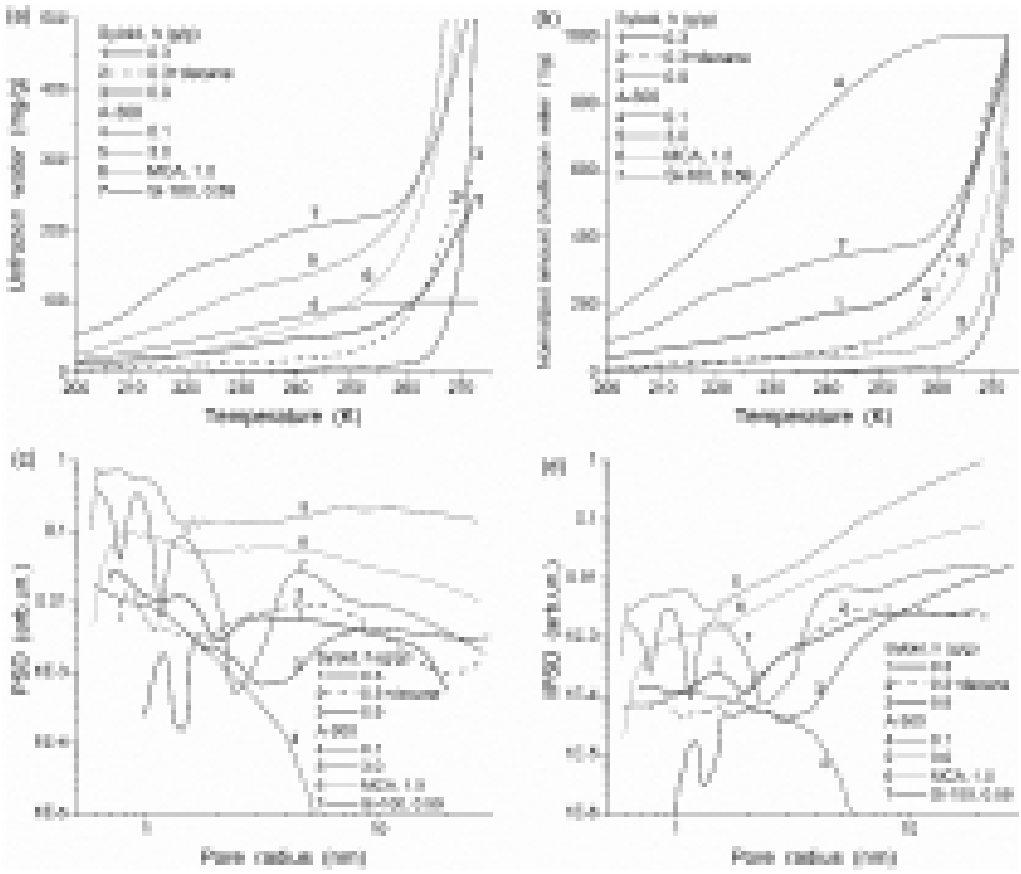

Fig. 82. (a, b) Amounts of unfrozen water vs. temperature (a) initial and (b) normalized by dividing by the total water content; (c, d) pore size distributions calculated using NMR cryoporometry (c) differential and (d) incremental PSD.

Note that partial freezing of water in pores changed the confined space effects for another fraction of water remained in unfrozen state [91]. This could lead to greater contribution of

nanopores estimated from the $C_{uw}(T)$ function than from nitrogen adsorption. This difference was well observed for Si-100 at h = 0.5 and 0.59 g/g (Table 14, Fig. 83c). The PSD from the NMR cryoporometry has peaks absent in the PSD from nitrogen adsorption (Fig. 83c). This effect was less visible for Syloid (Fig. 83a) or A-300 (Fig. 83b) having less ordered porosity with broader PSD than silica gel Si-100 has. Additionally, the secondary structures of A-300 or Syloid 244 could be more easily rearranged during interaction with water/ice than globules of Si-100 [91].

Table 14. Characteristics of water unfrozen at T < 273 K and bound to silicas studied estimated by NMR-cryoporometry [91].

Sample	h g/g	S_{uw} m^2/g	$S_{uw,nano}$ m^2/g	$S_{uw,meso}$ m^2/g	$V_{uw,nano}$ cm^3/g	$V_{uw,meso}$ cm^3/g	γ_S J/g	$-\Delta G$ kJ/mol	$<T_m>$ K
Syloid	0.3	69	47	22	0.020	0.197	9.2	3.05	252.8
Syloid (+decane)	0.3	48	19	29	0.008	0.253	7.3	2.77	259.7
Syloid	0.9	24	0.1	20	0.0	0.298	3.2	2.27	268.2
Si-100	0.5	104	58	45	0.024	0.448	17.1	3.10	255.6
Si-100	0.59	275	239	34	0.104	0.401	30.4	3.15	244.0
A-300	0.1	159	111	48	0.045	0.055	10.3	3.03	223.0
A-300	3.0	322	207	115	0.085	1.367	32.2	3.08	263.3
A-300 MCA	1.0	124	65	59	0.028	0.676	17.9	3.09	261.3

Note. h is the hydration degree of silicas (amounts of water in gram added per gram of dry silica); ΔG is the changes in the Gibbs free energy of water layer closely located to a surface of intracellular structures; γ_S is the modulus of the total changes in the Gibbs energy of bound water unfrozen at T < 273.15 K; S_{uw} is the specific surface area in contact with unfrozen water, $S_{uw,nano}$ and $V_{uw,nano}$, $S_{uw,meso}$ and $V_{uw,meso}$ were the specific surface area and pore volume of nanopores at R < 1 nm and mesopores at 1 nm < R < 25 nm, respectively, filled by unfrozen water; and $< T_m >= \int_{T_{min}}^{T_{m,0}} \frac{dC_{uw}(T)}{dT} TdT \Big/ \int_{T_{min}}^{T_{m,0}} \frac{dC_{uw}(T)}{dT} dT$ is the average melting temperature, $T_{m,0}$ is the melting temperature of individual bulk ice, T_{min} correspond to the temperature at which C_{uw} = 0 [91].

However, at h = 1 g/g, contribution of water located in nanopores decreased (Table 14, $S_{uw,nano}$ and $V_{uw,nano}$). A similar difference was observed for ^{1}H NMR spectra of water bound to silica gel (narrow PSD, greater downfield shift) and Syloid (broad PSD, smaller downfield shift) (Fig. 26) [91].

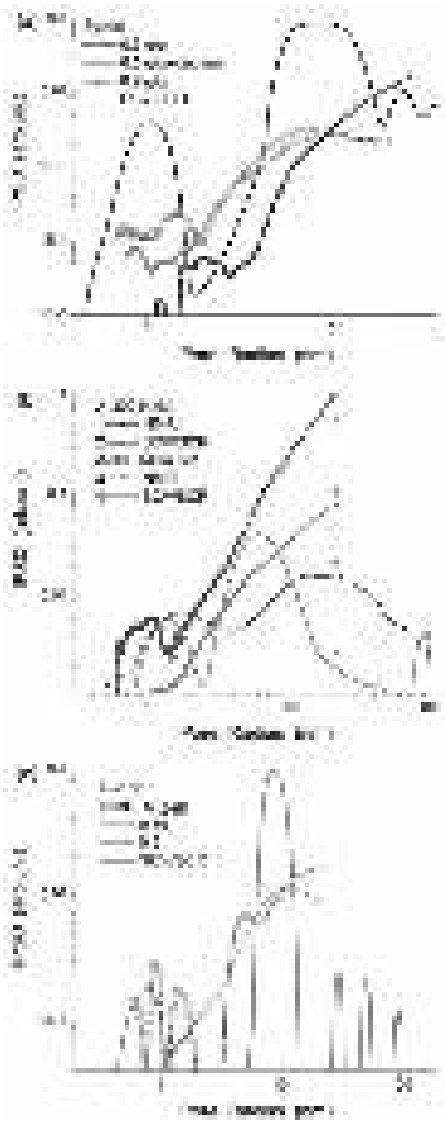

Fig. 83. Comparison of the incremental PSD calculated using the amounts of unfrozen water vs. temperature (NMR cryoporometry) and the amounts of adsorbed nitrogen vs. pressure using the SCV/SCR method for (a) Syloid 244, (b) A-300, and (c) Si-100.

Comparison of the DSC thermograms of nonpolar (benzene, toluene, decane), weakly polar (chloroform) and polar (water, DMSO) adsorbates bound to nanosilica A-300 initial and MCA 6 h and Syloid 244 showed (Fig. 84) the hysteresis effects of freezing-melting [91]. Significant differences in the temperature positions of freezing exotherms and melting endotherms were observed for both nonpolar and polar adsorbates, and the maximal values were mainly observed for Syloid (up to 70 ^{o}C for toluene, 28 ^{o}C (decane), 24 ^{o}C (benzene), 21 ^{o}C (water)). For chloroform (~50 ^{o}C) and DMSO (~6 ^{o}C), the gaps were similar for all adsorbents studied. The heat effects (Tables S15 and S16, ΔH) for both exotherms and endotherms were smaller than that for bulk liquids/solids, and the difference depended on the amounts of adsorbates. This difference increased with decreasing amounts of adsorbates due to preventing of the crystallization of liquids upon freezing in the interfacial layers and narrow pores, in which, maximal disturbance of the structure of adsorbates was provided [53]. Among the studied adsorbates, the enthalpy of fusion at the freezing point was maximal for water (333.5 J/g) and minimal for toluene (71.8 J/g), and the hysteresis effect was much greater for toluene than that for water for all FMO studied. Note that the hysteresis effect was smaller for polar DMSO and water than that for nonpolar adsorbates. This result could be explained by stronger interactions between an adsorbent surface and nonpolar adsorbates than the molecule-molecule interactions that results in stronger changes in the structure (organization) of organic liquids bound to silicas [91].

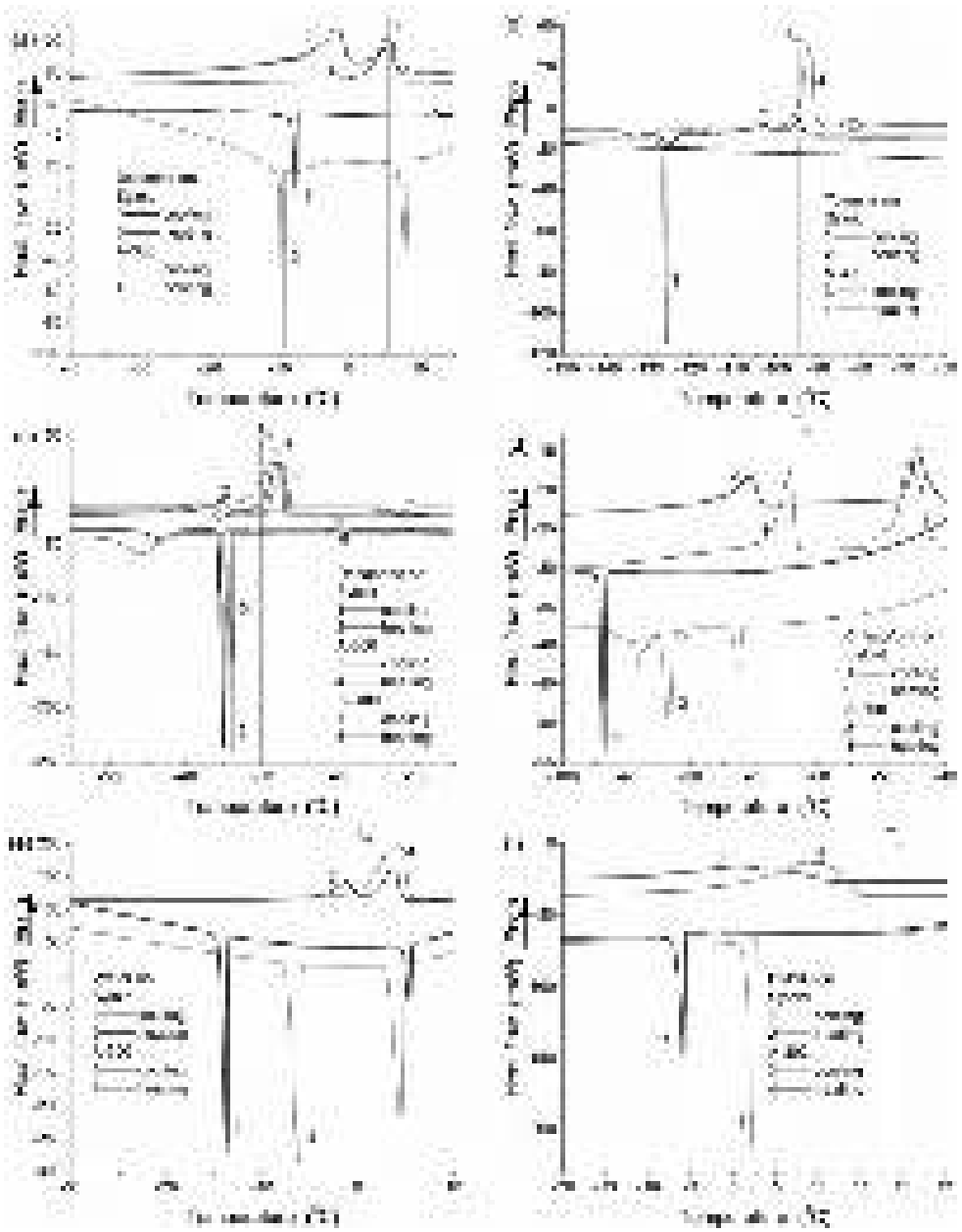

Fig. 84. DSC thermograms for (a) benzene, (b) toluene, (c) n-decane, (d) chloroform, (e) water, and (f) DMSO interacting with Syloid 244 and A-300 during cooling and heating runs at a cooling-heating rate of 20 ^{o}C/min for toluene and chloroform and 10 ^{o}C/min for other adsorbates.

Typically, the freezing exotherms were narrower than the melting endotherms (Fig. 84) [91]. However, if the amount of adsorbate was relatively small (*e.g.,* 3.878 mg of toluene per 1.834 mg of Syloid) that the freezing exotherm could be absent (Fig. 84b). For A-300, the amount of toluene was greater (8.127 mg per 1.578 mg of A-300) that resulted in a large and sharp freezing exotherm (Fig. 84b). For some adsorbates such as water (Fig. 84e), benzene (Fig. 84a), and decane (Fig. 84c), there were exotherms at $T > T_m$ that could be explained by changes in the structure of unfrozen liquids bound to silicas with temperature before the formation of a solid phase [53,91].

Rearrangement of silica nanoparticles in the secondary structures can occur due to interaction with water [53]. One of the sequences of this effect could be changes in the PSD calculated using the DSC melting thermograms for water (ice) bound to silicas in comparison with the PSD for the silica powder estimated from the nitrogen adsorption/desorption isotherms (Fig. 85) [91]. The maximal difference was observed for the initial A-300 (Fig. 85a). It was smaller for MCA (6 h) A-300 (Fig. 85b). It was minimal for precipitated silica (Fig. 85c) because of features of its synthesis. Therefore, adsorption of water could produce minimal changes in the textural

characteristics of precipitated silica. However, wetting-drying-wetting could affect the structure of Syloid too (Fig. 85c) due to swelling of particles, decomposition of a part of inter-particle bonds, and formation of new inter-particle bonds [91].

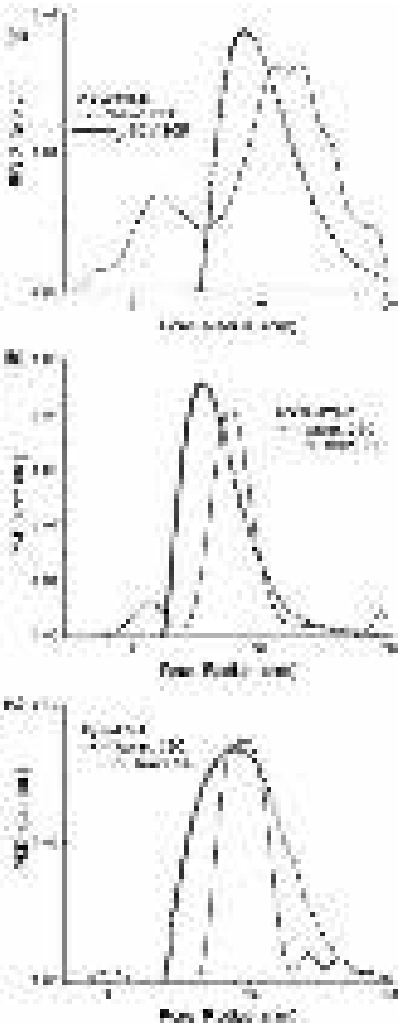

Fig. 85. Comparison of the IPSD calculated from nitrogen adsorption-desorption isotherms and the DSC melting thermograms of water (ice) bound to (a) initial A-300, (b) MCA 6 h A-300, and (c) Syloid 244.

Thus, investigations of fumed silica A-300 initial and mechanochemically activated, precipitated silica Syloid 244 and silica gel Si-100, which have a similar specific surface area (~330-350 m^2/g), using infrared spectroscopy, DSC, NMR, and adsorption methods, showed some similarities and differences in their properties appearing in different media under different conditions [91]. Mechanochemical activation of A-300 in a ball-mill or a microbreaker affected the structure of aggregates of nanoparticles and agglomerates of aggregates, which became more compacted (since the bulk density increased from 0.045 to 0.394 g/cm^3), and slightly changed the morphology of nanoparticles. The latter appeared as changes in the shape of the IR band of the Si-O stretching vibrations at 1100 cm^{-1}. Any treatment of 'soft' nanosilica affected the interfacial behavior of polar and nonpolar adsorbates because significant rearrangement of secondary particles changes the freezing-melting point depression of bound adsorbates. Precipitated silica Syloid 244 and silica gel Si-100 demonstrated higher stability of the properties than fumed silica upon interaction with water and other adsorbates in a broad range of temperatures [91].

Clusterization of adsorbates bound in pores caused diminution of the heat effects during phase transition (freezing and fusion). The freezing point depression and increasing melting point caused significant hysteresis freezing-melting effects for adsorbates bound in pores, that was larger for nonpolar compounds than for polar ones due to the differences in such interactions as molecule-molecule and molecule-silica surface affected by stronger confinement in narrower pores [91].

The study [91] showed that fumed and precipitated silicas could be more sensitive than silica gel to external actions such as wetting-drying and MCA. These effects should be considered upon applications of the materials in different media.

Cryogelation and confined space effects

For high-pressure cryogelation in cryo-bombs, fumed silica A-300 (S_{BET} = 330 m^2/g) was used as the starting material [63]. Aqueous suspensions of A-300 (5, 10, 15 and 20 wt.%) were prepared using doubly distilled water and sonicated (22 kHz) for 5 min. The resulting dispersion was then frozen at 259, 208, or 77 K in thick-walled-stainless-steel reactors at pressures from 1 to 1050 atm, caused by ice formed in the frozen suspension (~10-15 ml) for 24 h. The pressure (estimated according to [61,62]) was controlled using partial (450 atm) or complete (~1000 atm) filling of a freezing bomb with stainless steel. Then cryosilica (CS) samples were placed in a glass dish and dried in air at room temperature for 2-5 days to an air-dry state. The final materials were in the powder state [46,47,63].

Cryosilicas CS20 ($C_{A\text{-}300}$ = 20 wt.% in the aqueous suspension frozen where ice produced a pressure of 450 atm) and CS20m (prepared at ~1000 atm) were studied at different degrees of hydration (h = 0.08, 0.75, 1.1 and 5.67 g of water per gram of dry silica) [46,47,63]. Hydration levels were controlled by addition of a known amount of water to a powder sample placed into an ampoule. Samples were equilibrated at 293 K for 1 h before NMR measurements. Experiments with methane were performed at a slightly increased pressure because an ampoule was linked to a rubber vessel with methane at 1.1 atm. Liquids (*n*-decane, chloroform, dimethylsulfoxide (DMSO), acetonitrile, water, or concentrated aqueous solutions of H_2O_2, HCl or CF_3COOH) were added to fill the total volume of a NMR ampoule with hydrated silica (the weight of dry silica was ~100 mg). After addition of hydrophobic decane, the sample was heated to 320 K for 1-2 min to remove air bubbles and to completely fill free pores of hydrated silica powder [46,63].

The freezing of aqueous suspensions of nanosilica in high-pressure reactors resulted in dried powdered materials that were very different from silicas treated in vapor phase water at high pressures and temperatures [37,38,53,91,226-228], at high temperatures and normal pressure in air [90,91], or at room temperature and normal pressure followed by air drying [68,229-231]. The air-dried high-pressure cryosilicas were in the powder state with agglomerates of 1-20 μm in size (Fig. 86), which was far more compacted than in the fumed silica starting material [46,63].

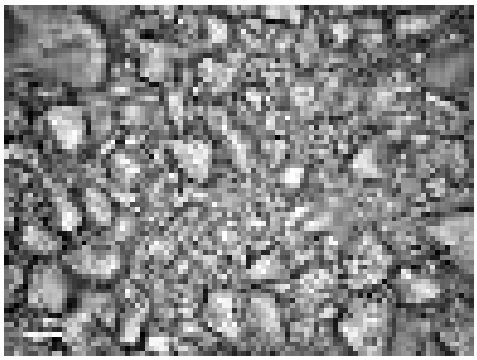

Fig. 86. Microphotograph (Primo Star optical microscope, Carl Zeiss) of CS20m powder prepared at 1000 atm (scale bar 10 μm).

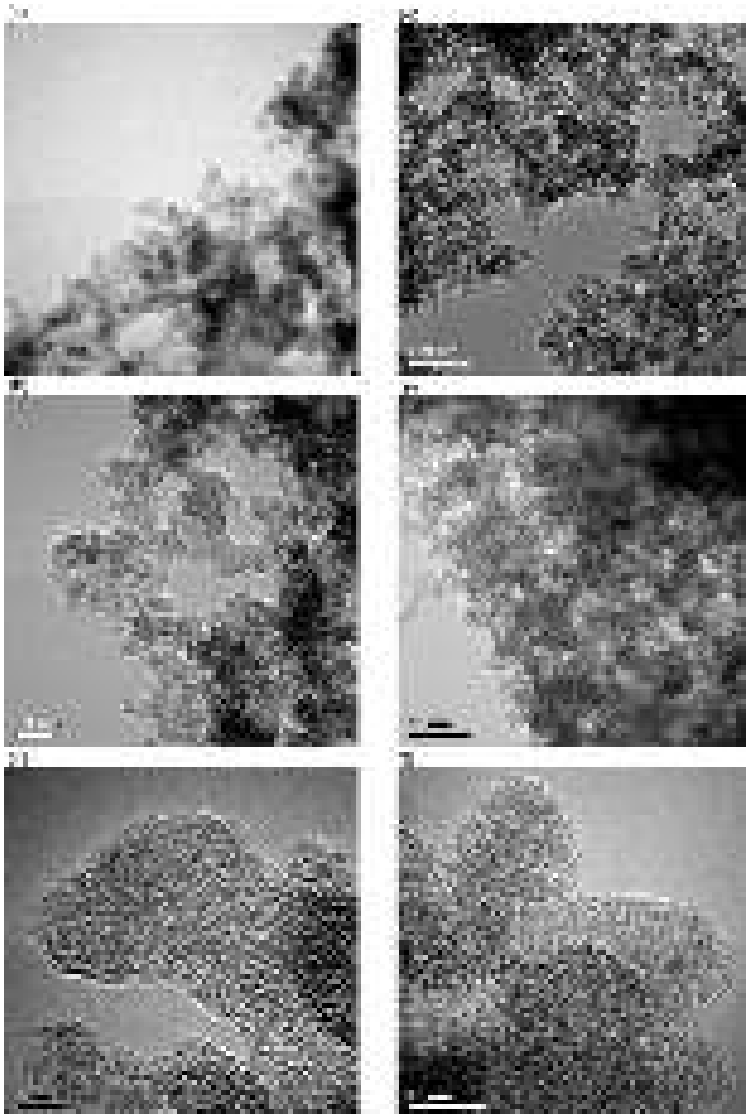

Fig. 87. HRTEM images of (a, b, c) initial A-300 and (d, e, f) CS20m at different magnifications (scale bars (d) 100 nm, (a, e) 50 nm, (b) 20 nm, (f) 10 nm, and (c) 5 nm).

The bulk density of the cryosilica powder, as well as of any suspended and dried nanosilicas, increased approximately five-fold (Table 15, ρ_b), since ρ_b = 0.045 g/cm^3 for the initial A-300 powder [63]. This was due to re-arrangement of nanoparticles in aggregates and agglomerates of aggregates during suspension and subsequent drying. Primary particles became mobile in sonicated aqueous suspensions including a large proportion of individual nanoparticles [53]. During drying of the suspensions, nanoparticles tended to form more compacted aggregates and agglomerates than those formed in the flame (flow velocity > 20 m/s) during pyrogenic synthesis. Typically, the pore volume (Table 15, V_p) determined from the adsorption of nitrogen at p/p_0 = 0.98-0.99 was much smaller than the empty volume, V_{em} of the powder. For example, for initial fumed silica (ρ_b = 0.045 g/cm^3) V_{em} = 21.8 cm^3/g, but V_p = 0.65 cm^3/g was much smaller because nitrogen could not effectively fill large pores, especially at R > 100 nm. For suspended-frozen-dried silica CS20m ρ_b = 0.31 g/cm^3 and V_{em} = 2.8 cm^3/g but V_p = 1.28 cm^3/g; *i.e.* the difference between the V_{em} and V_p values strongly decreased after cryogelation. These textural changes were readily observed in the HRTEM images (Fig. 87), IPSD (Fig. 88a-e) and nitrogen adsorption isotherms (Fig. 88f) [63].

According to HRTEM images (Fig. 87), CS20m was composed of amorphous primary particles more strongly compacted in aggregates (comp. Fig. 87a,e). These aggregates remained

porous with the textural porosity as voids between nonporous primary particles (Fig. 87d). The shape of primary particles was not ideally spherical for both initial A-300 and CS20m.

Table 15. Textural (specific surface area S_{Ar} and S_{BET}), bulk density (ρ_b) and adsorption (desorption of water in TG) characteristics of silicas *vs*. silica content in the frozen suspension ($C_{A\text{-}300}$), pressure and treatment temperature (T_{tr}) [63].

Sample	$C_{A\text{-}300}$ (wt.%)	S_{Ar}[a] (m^2/g)	S_{BET} (m^2/g)	V_p (cm^3/g)	S_{nano} (m^2/g)	S_{meso} (m^2/g)	S_{macro} (m^2/g)	V_{nano} (cm^3/g)	V_{meso} (cm^3/g)	V_{macro} (cm^3/g)	Δw
Initial			330	0.826	51	270	9	0.026	0.653	0.147	0.025
CS5	5	317	280	1.474	14	258	8	0.009	1.358	0.107	0.392
CS10	10	303	293	1.341	23	268	1	0.015	1.294	0.032	0.431
CS15	15	295	292	1.347	29	262	1	0.019	1.289	0.039	0.454
CS20	20		297	1.279	33	263	1	0.022	1.231	0.026	0.463
CS20m	20		285	1.277	31	253	1	0.021	1.220	0.037	0.458
CS5*	5	332	286	1.393	10	275	1	0.006	1.364	0.023	0.363
CS10*	10	326	289	1.298	15	272	2	0.010	1.247	0.041	0.459
CS15*	15	323	304	1.470	27	276	1	0.017	1.423	0.029	0.401
CS20*	20	306	303	1.443	20	281	2	0.013	1.402	0.028	0.404
CS5**	5	302	300	1.449	24	273	2	0.015	1.390	0.044	0.389
CS10**	10	318	303	1.445	23	278	2	0.014	1.390	0.041	0.405
CS15**	15		304	1.455	19	281	3	0.012	1.390	0.053	0.397
CS20**	20	317	296	1.408	36	257	3	0.023	1.328	0.056	0.451

Sample	ρ_b (g/cm^3)	Intact water[b] ($T < 200^oC$) (mmol/g)	Total water[c] ($T < 900^oC$) (mmol/g)	ΔW[d] ($W_{200}–W_{600}$) (mmol/g)	c_{void}	c_{cyl}	c_{slit}	Pressure (atm)	T_{tr} (^oC)
Initial	0.045	0.889	1.556	0.383	0.308	0.368	0.324	-	-
CS5	0.235	0.619	3.417	1.780	0.159	0.611	0.230	450	-14
CS10	0.208	1.238	2.600	0.744	0.197	0.387	0.416	450	-14
CS15	0.228	0.745	1.397	0.537	0.194	0.268	0.538	450	-14
CS20	0.294	5.177	6.225	0.798	0.203	0.203	0.622	450	-14
CS20m	0.309	1.556	3.103	0.962	0.209	0.171	0.620	1000	-14
CS5*	0.285	12.742	13.545	0.708	0.182	0.695	0.123	1	-14
CS10*	0.294	2.596	4.035	1.005	0.227	0.380	0.393	1	-14
CS15*	0.349	1.977	2.924	0.731	0.163	0.458	0.379	1	-14
CS20*	0.282	2.290	3.047	0.609	0.151	0.555	0.294	1	-14
S5**	0.277	1.711	3.202	1.170	0.180	0.522	0.298	1	25
S10**	0.311	1.630	3.204	1.143	0.174	0.522	0.304	1	25
S15**	0.216	2.054	3.692	1.011	0.168	0.565	0.268	1	25
S20**	0.202	1.576	5.894	1.548	0.185	0.223	0.592	1	25

Notes. [a]Samples were heated at 100 ^{o}C for 2 h before measurements of the specific surface area. The amounts of water desorbed during heating from [b]20 ^{o}C to 200 ^{o}C, [c]20 ^{o}C to 900 ^{o}C, and [d]200 ^{o}C to 600 ^{o}C [63].

However, the average value $< d >= \int df(d)\mathrm{d}d / \int f(d)\mathrm{d}d$ (*i.e.* the first moment of the distribution function) was smaller for CS20m (<*d*> = 0.3766 nm) than for initial A-300 (<*d*> = 0.3979 nm). Thus, high-pressure cryogelation resulted in not only stronger aggregation of primary particles (the bulk density ρ_b (Table 9) increased) but also in certain deformation of nanoparticles (the <*d*> value decreased). Changes in the textural porosity of treated nanosilica reflected in changes in the ρ_b value could be analyzed using the pore size distributions (Fig. 88) [63].

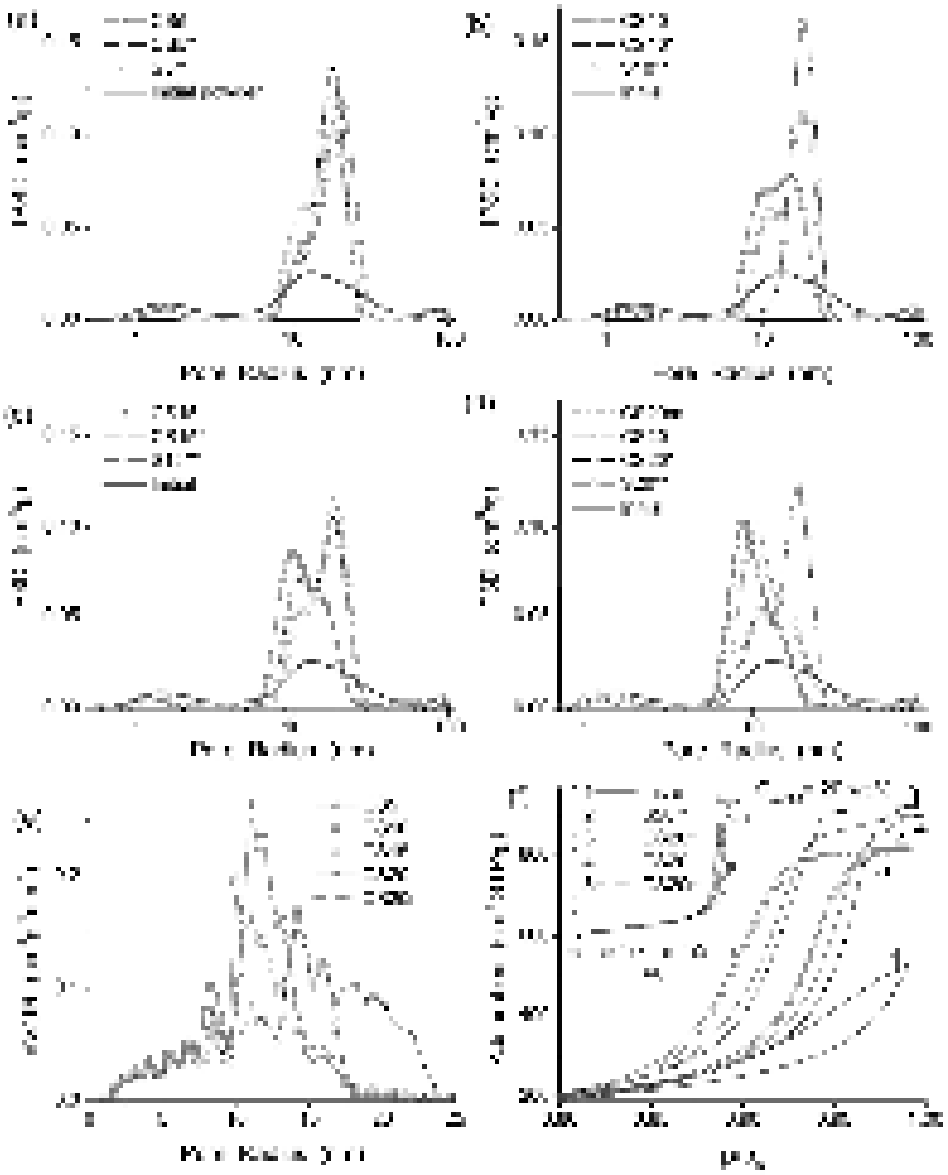

Fig. 88. Incremental PSD (SCV/SCR) for initial powder of A-300 and silicas prepared at $C_{A\text{-}300}$ = (a) 5 wt.%, (b) 10 wt.%, (c) 15 wt.% and (d) 20 wt.% in the aqueous suspensions under different conditions: frozen at high pressure (450 atm) or at maximum high pressure (1000 atm), frozen at normal pressure (*), suspended under normal conditions (**), as well as initial A-300 powder, (e) NLDFT for cryosilicas prepared from 5-20 wt.% suspensions and CS20m; (f) nitrogen adsorption-desorption isotherms for differently treated samples at $C_{A\text{-}300}$ = 20 wt.%.

For treated silica powders, contribution of nanopores and narrow mesopores decreased, while the contribution of mesopores at R = 10-30 nm increased compared with the initial fumed silica A-300 (Fig. 88, Table 15) [63]. The primary particles were not strongly changed during suspending-cryogelation-drying (Figs. 86 and 87). Therefore, the nitrogen adsorption isotherms were practically the same at $p/p_0 < 0.8$ (Fig. 88f, insert) but they characterized by different hysteresis loops at $p/p_0 > 0.8$ and different maximal adsorption at $p/p_0 \approx 0.99$ (Fig. 88f).

Table 16. Textural characteristics of initial and differently treated nanooxides.

Oxide	Medium	T_t (K)	P_t (atm)	Note	S_{BET} (m^2/g)	S_{nano} (m^2/g)	S_{meso} (m^2/g)	S_{macro} (m^2/g)	V_p (cm^3/g)	V_{nano} (cm^3/g)	V_{meso} (cm^3/g)	V_{macro} (cm^3/g)	Δw
gsPS300*	0.1M NaCl	293	1	Gel/NaCl	264	20	242	2	1.257	0.010	1.207	0.040	0.325
gswPS300*	0.1M NaCl	293	1	Gel/NaCl washed	276	24	251	1	1.313	0.012	1.263	0.038	0.331
csPS300*	0.1M NaCl	260	1000	Cryogel/NaCl	262	27	234	1	1.194	0.015	1.147	0.032	0.362
cswPS300*	0.1M NaCl	260	1000	Cryogel/NaCl washed	279	29	248	1	1.291	0.016	1.244	0.031	0.376
PS300+AST(gSAST)	water	293	1	Gel	147	57	55	36	1.029	0.017	0.374	0.638	0.042
PS300+AST(cSAST)	water	208	1000	Cryogel	147	51	62	34	1.098	0.017	0.542	0.539	0.114
PS300+AST(gsSAST)	0.1M NaCl	293	1	Gel/NaCl	155	58	62	35	1.064	0.018	0.454	0.592	0.066
PS300+AST(csSAST)	0.1M NaCl	208	1000	Cryogel/NaCl	155	58	66	31	1.142	0.018	0.608	0.515	0.123

Note. *Gelation during 24 h, gelation of all other samples was during 12 h. Labels in dried samples correspond to cryogel (c), cryogel with NaCl (cs), gelation at room temperature (gel, g) with NaCl (gs), and washed samples gelatinized with NaCl (csw or gsw).

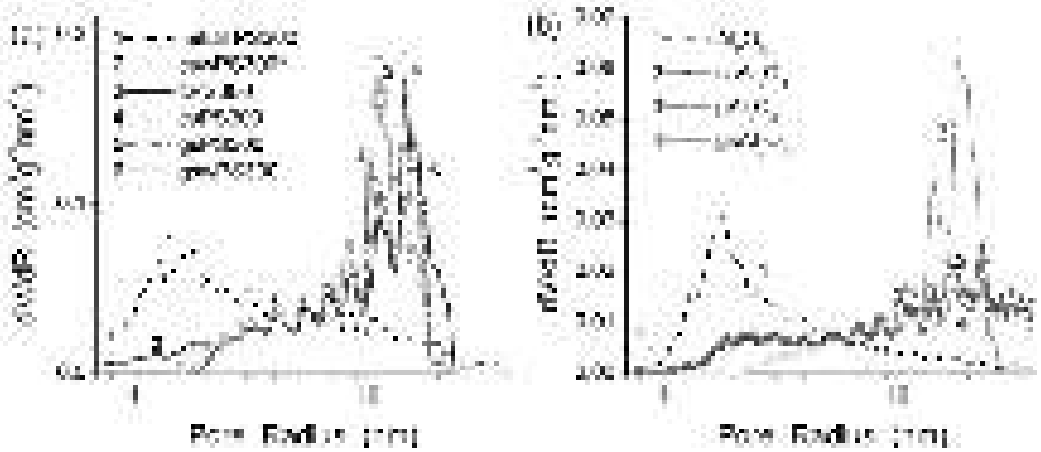

Fig. 89. NLDFT PSD for (a) silica and (b) alumina: initial powder and differently treated nanooxide cryogelation in 0.1 M NaCl solution at 208 K, suspended in water or 0.1 M NaCl solution and dried at room temperature and standard pressure and then washed (sample labels correspond to them in Table 15).

These results showed significant changes in packing of primary particles in aggregates. This packing increased with increasing pressure during cryogelation. Additionally, the effect became stronger with increasing silica content in the suspensions (comp. Fig. 88a-e) [63]. An increase in the silica content in the suspensions resulted in an increase in mesopore contribution at $R \approx 10$ nm, and in a decreased contribution of mesopores at $R \approx 20$ nm for high-pressure cryosilicas in contrast to samples prepared at standard pressure.

The main PSD peak (both IPSD and dV/dR, Fig. 88) for HP-cryosilicas shifted toward smaller R values with increasing silica content in the suspensions. Additionally, HP-cryosilicas, in contrast to silicas frozen or non-frozen at normal pressure, the contribution of pores modeled by slit-shaped pores (Table 15, c_{slit}) increased due to the high-pressure effects. This effect was due to certain changes in the shape of primary particles (Fig. 87), which were discussed above [63].

Contributions of nanopores (Figs. 88 and 89, Tables 15 and 16, S_{nano} and V_{nano}) and macropores (S_{macro} and V_{macro}) were much smaller than that of mesopores (S_{meso} and V_{meso}) for all silicas treated in the aqueous media under different conditions [63]. However, in contrast to V_{meso}, the S_{nano}, S_{macro}, V_{nano}, and V_{macro} values for treated silicas decreased in comparison with the initial silica. The S_{meso} values for high-pressure cryosilicas were smaller than that for the initial silica but the S_{meso} values for normal-pressure cryosilicas (Table 15, label *) and non-frozen suspended-dried silicas (label **) were larger than that of the initial silica. All these textural changes were due to different rearrangement of aggregates of primary nanoparticles depending on treatment conditions [53].

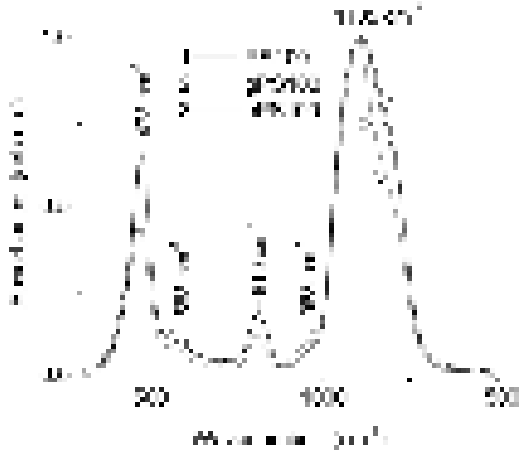

Fig. 90. IR spectra of PS100, cPS100, and gPS100 (1:100 mixture with KBr).

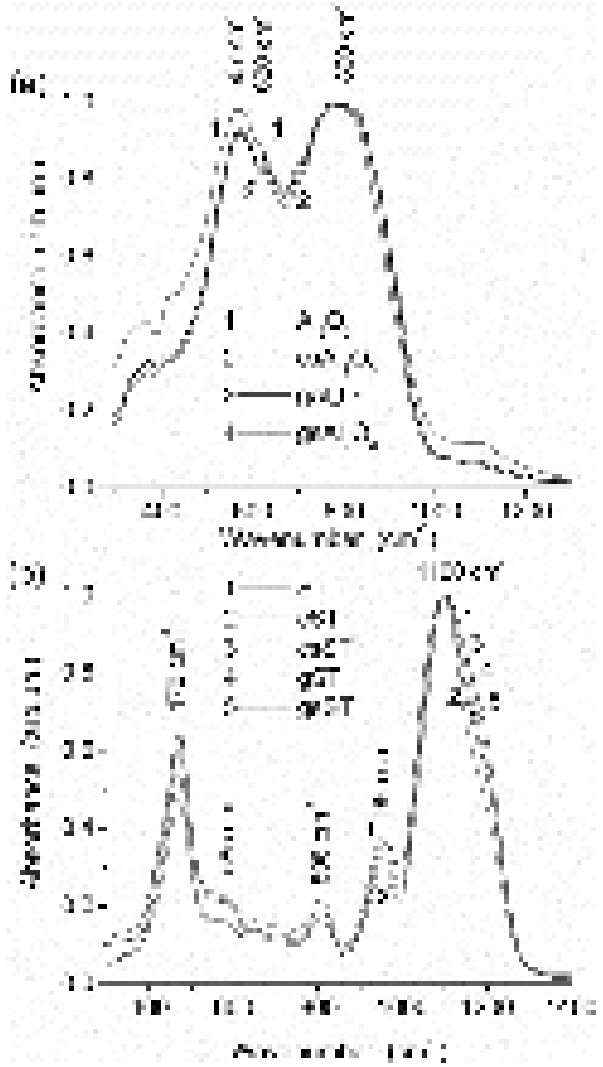

Fig. 91. IR spectra of (a) alumina samples: initial air-dry (curve 1), cAl_2O_3 (2), gAl_2O_3 (3), and $gsAl_2O_3$ (4); and (b) ST samples: initial air-dry (curve 1), cryogel prepared at 208 K and ~1000 atm pure (2) and with 0.1 M NaCl (3), gelatinized at standard conditions (4) and with addition of NaCl (5) (1:100 mixture with KBr). All spectra of ST samples were normalized to the asymmetric mode of $Si\text{-}O_{Si}$ at 1100 cm^{-1}.

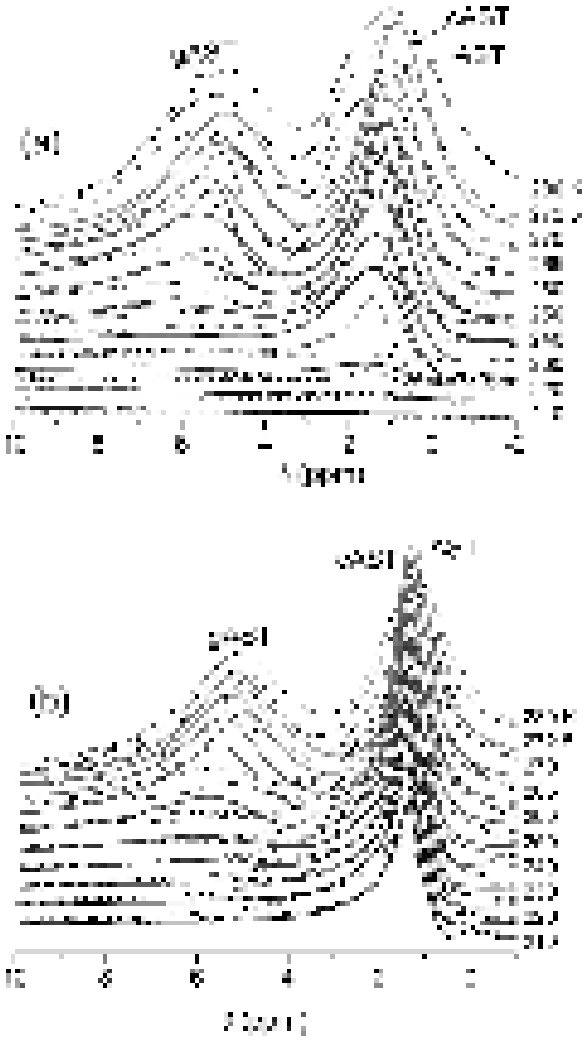

Fig. 92. ^1H NMR spectra of water (0.1 g/g) and n-decane (0.15 g/g) bound to AST (dashed lines), gAST (dot-dashed lines) and cAST (solid lines) in media (a) air and (b) $CDCl_3$ with addition of TFAA (6 : 1).

Cryogeletion affects the textural and structural characteristics of FMO. The IR spectra of the Si-O and Al-O stretching vibrations change (Figs. 90 and 91) due to particle compaction. These changes affect the behavior of bound water (Figs. 92 and 93) that is also influenced by the dispersion media (air, water, chloroform + TFAA). These effects appear in the pore size distributions those filled by unfrozen water (Figs. 94 and 95).

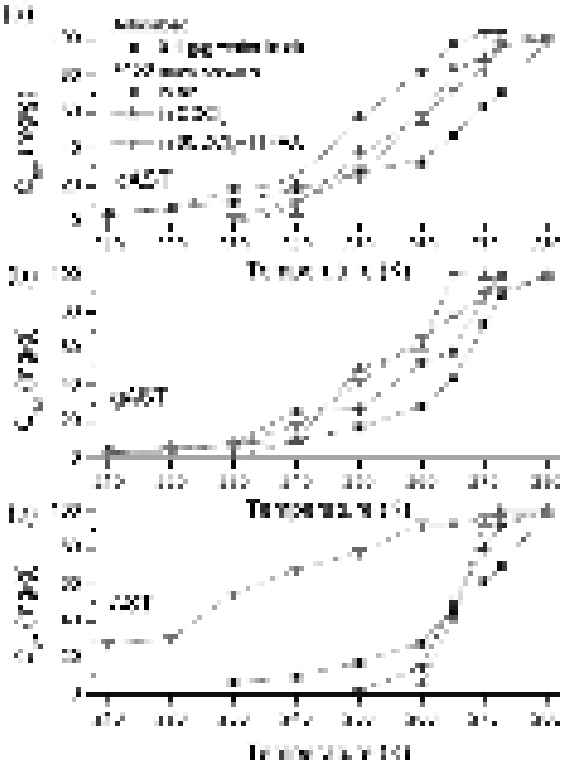

Fig. 93. Amounts of unfrozen water as a function of temperature for (a) cAST, (b) gAST, and (c) AST located in different media.

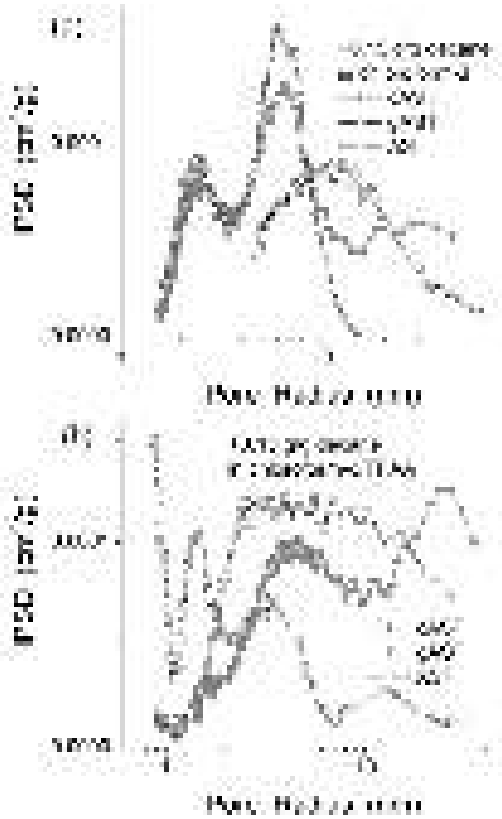

Fig. 94. Incremental PSD calculated from ^{1}H NMR spectra of water (0.1 g/g) bound to AST, gAST and cAST with addition of n-decane in media (a) $CDCl_3$ and (b) $CDCl_3$ with addition of TFAA (6:1).

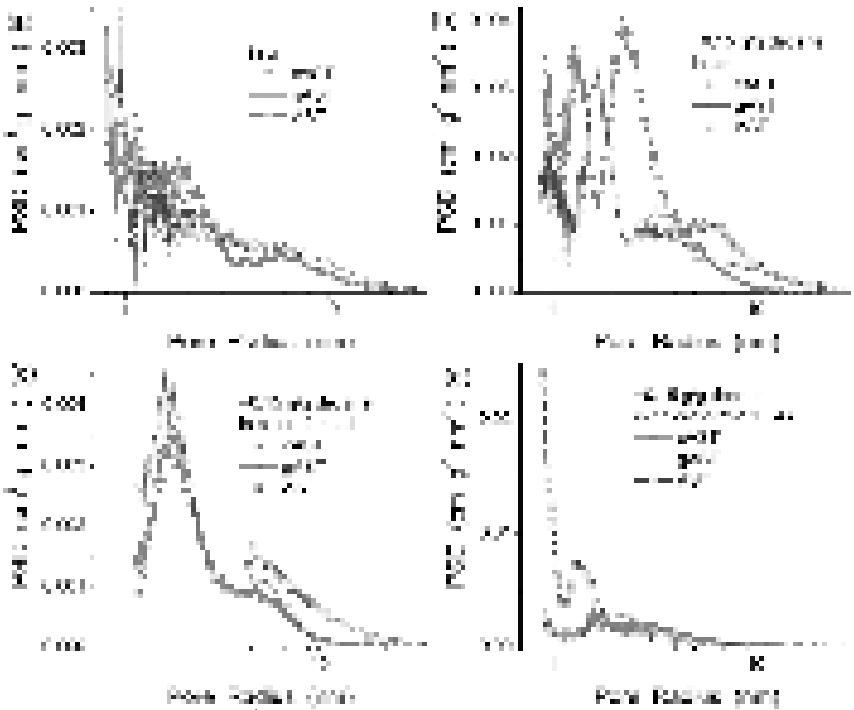

Fig. 95. Differential PSD calculated from ^{1}H NMR spectra of water (0.1 g/g) bound to AST, gAST and cAST (b-d) with addition of n-decane in media (a, b) air, (c) $CDCl_3$, and (d) $CDCl_3$ with addition of TFAA (6:1).

DFT B3LYP/6-31G(d,p) calculations of the chemical shifts of ^{1}H were performed for pure water alone (Fig. 96a, curves 1 and 3) or with NaCl (curves 2 and 4). Larger structures were calculated using the PM7 method (curves 5 and 6). These calculations show that the difference in

the $f(\delta_H)$ shapes for pure water and water with dissolved Na^+ and Cl^- ions decreases with decreasing salt content. Additionally, the presence of dissolved Na^+ and Cl^- ions results in a downfield shift (Fig. 96b, curves 4 and 5) in comparison with the system with NaCl nanocrystallites (curves 2 and 3) bound to a silica surface. The δ_H values for the SiOH groups interacting with water molecules are greater than that for water molecules (comp. curves 2 and 3 or 4 and 5, Fig. 96b). These results explain a certain difference in the spectra of water bound to PS300 without (Fig. 96a) and with NaCl (Fig. 96b).

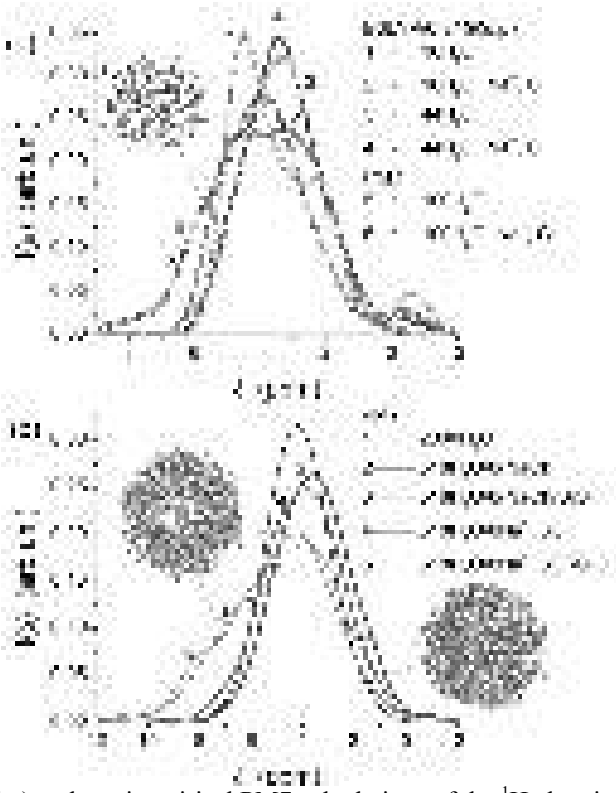

Fig. 96. DFT B3LYP/6-31G(d,p) and semiempirical PM7 calculations of the ^1H chemical shifts in pure water, water with NaCl (a) alone or (b) bound to silica surface (silica pore with 1620 atoms).

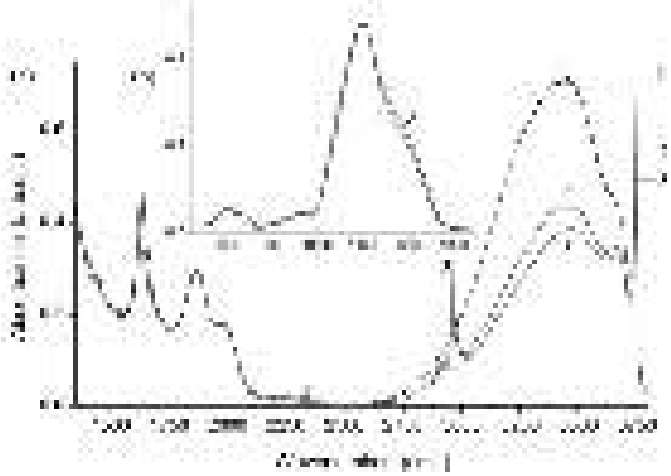

Fig. 97. IR spectra of PS300 unmodified (curve 1) and modified at Θ_{TMS} = 27.2 % (2) and 37.2 % (3); the spectra of modified silicas were normalized to the intensity of the band at (a) 1867 cm^{-1} or (b) 1100 cm^{-1} of unmodified silica.

For high-pressure cryogels, there were two tendencies: (i) a certain decrease in the specific surface area (Table 15, S_{Ar} and S_{BET}) with increasing silica content in the suspension, and (ii) nonlinear changes in the amounts of desorbed water (total water desorbed at $T < 900$ °C) with a maximum for the material prepared at $C_{A\text{-}300}$ = 5 wt.% (Table 15) [63]. Both tendencies remained

for cryogels prepared at normal pressure (Table 15, CS-X*). Thus, the desorbed water amounts (intact and total water) change with increasing silica content in the suspension. This could be explained by the formation of more compacted secondary structures with increasing $C_{A\text{-}300}$ value, changes in the sizes of pores filled by water, and the number of hydroxyls. Note that changes in the specific surface area depended on the preparation conditions (C, P, T) much less than the pore volume (V_p) and the content of desorbed water (Table 15). These results could be explained by greater changes in the organization of primary silica nanoparticles in secondary structures (Table 15, Fig. 88), with less change in nanoparticle size (Fig. 87), *e.g.*, observed during hydrothermal treatment of silicas [89].

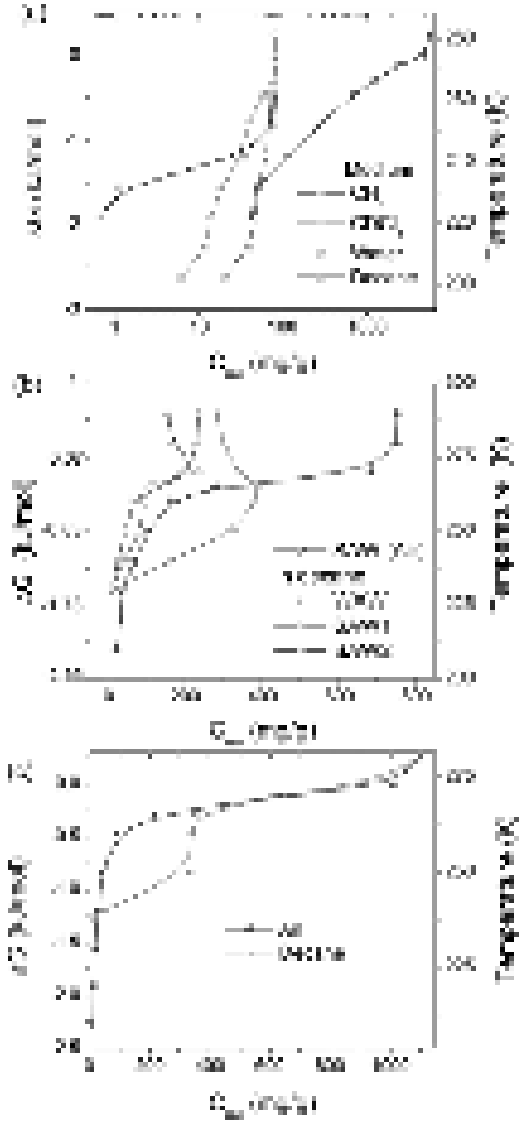

Fig. 98. Temperature dependences of the amounts of unfrozen water ($C_{uw}(T)$) and changes in the Gibbs free energy ($\Delta G(T)$) of bound water as well as relationships between C_{uw} and ΔG for CS20 in different dispersion media at (a) h = 0.08 g/g (in methane, chloroform, or decane) and 5.67 g/g (concentrated 15% suspension); (b) h = 0.75 g/g and (c) h = 1.1 g/g (in air or decane).

Since CS20 and CS20m exhibited the largest structural changes among high-pressure cryosilicas, low-temperature ^{1}H NMR spectroscopy studies focused on these materials. Water was either the sole probe compound or it was used as a co-adsorbate with different organics in various dispersion media (Figs. 98-100, Table 17) for deeper insight into the interfacial behavior of different adsorbates and co-adsorbates such as nonpolar methane and *n*-decane, weakly polar chloroform, and polar water, DMSO, acetonitrile, H_2O_2, HCl, and CF_3COOH [63]. CS20 (cryogelation at 450 atm) studied by NMR contained 0.08 g of water per gram of dry silica. To analyze the interfacial behavior of bound water, the sample was studied in different dispersion

media [63]. In the methane dispersion medium, the spectra of bound water included a single signal exhibiting a chemical shift (with respect to methane of $\delta_H = 0$ ppm), $\delta_H \approx 4$-5 ppm [63]. This was similar to the δ_H value of bulk water. Consequently, this water could be assigned to strongly associated water, SAW, with an average number of hydrogen bonds per molecule of 3-4, similar to that in bulk water [53,63].

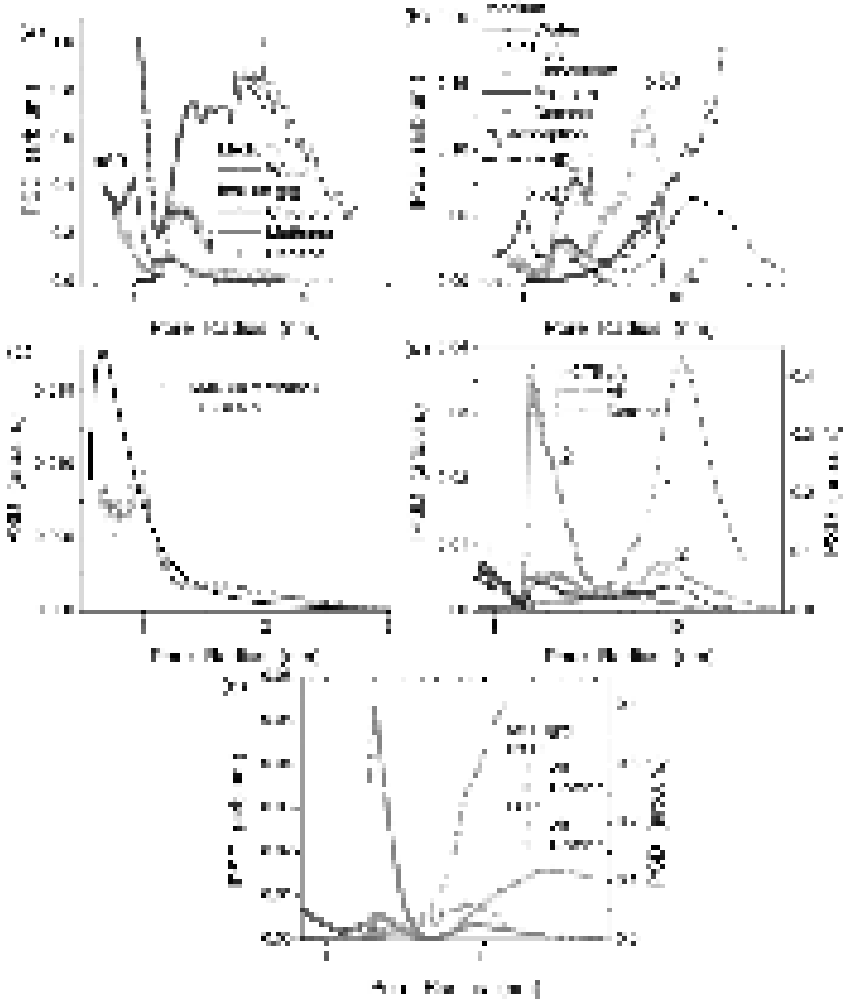

Fig. 99. Pore size distributions (a, c, d) differential and (b, d) incremental calculated using NMR cryoporometry (calculated as size distributions of water structures unfrozen in pores) (IPSD for initial A-300 was calculated using nitrogen adsorption-desorption isotherm, dot-dashed line), (c) NMR cryoporometry and TG thermoporometry curves; (d) $h = 0.75$ g/g and 1.1 g/g (air or decane dispersion media) for CS20 in different dispersion media; (a-d) CS20 and (e) CS20m samples.

Freezing of bound water occurred at low temperatures at $T < 260$ K (Fig. 98) because of the freezing point depression for liquids confined in pores [53,63]. Since freezing of bound water occurred at $T < 260$ K, all of this water could be assigned to strongly bound water, SBW. The ^{1}H NMR signal of methane at $\delta_H \approx 0$ ppm had a weak dependence on temperature [63]. From the intensity ratio of water ($h = 0.08$ g/g) and methane, the amount of adsorbed methane could be estimated as small as ~8 mg/g at 280 K. This low adsorption of CH_4 was due to filling of nanopores (voids between adjacent nanoparticles) by water (Fig. 99, Table 17), which methane could not displace. This was because methane has much weaker interactions with the silica surface compared to water [53,63].

In the $CDCl_3$ dispersion medium, bound water ($h = 0.08$ g/g) corresponded to SAW characterized by $\delta_H \approx 5$ ppm [63]. A fraction of this water became weakly bound, WBW frozen at $T > 260$ K. Additionally, at higher temperatures, a weak signal was observed at $\delta_H \approx 1.8$ ppm corresponding to weakly associated water, WAW [53]. The signal at $\delta_H \approx 0$ ppm corresponded to

tetramethylsilane used as a chemical shift standard. In contrast to methane, weakly polar chloroform diminished the interaction of water with silica: the average melting temperature (Table 17, $<T_m>$), filling of mesopores by unfrozen water (V_{meso}, S_{meso}), and changes in the Gibbs free energy of the first layer (ΔG_s) of bound water increased; while the free surface energy (γ_S), filling of nanopores (V_{nano}, S_{nano}), and the SBW content decreased. Similar effects were observed for a variety of adsorbents due to the displacement of water by weakly polar chloroform from narrow to broader pores or out of pores altogether [53]. The main driving force of these effects led to a reduction of the contact area between immiscible polar (water) and weakly polar (chloroform) or nonpolar (decane) liquids. This reduction resulted in a free energy decrease because water-water interactions are similar to water-silica interactions, but interactions of organic co-adsorbates with silica are stronger than that of organics-organics or organics-water interactions [53]. The character of re-organization of bound water under the action of chloroform was seen in changes in the PSD, and in particular the IPSD, (Fig. 99b) when compared with water bound to CS20 in the methane dispersion medium (Fig. 99a) [63].

Nonpolar *n*-decane more effectively displaced bound water than weakly polar chloroform (Figs. 98 and 99, Table 17) [63].

Table 17. Characteristics of water bound to cryosilica powder CS20 and CS20m in different media [63].

h (g/g)	Medium	C_{uw}^{s} (g/g)	C_{uw}^{w} (g/g)	$-\Delta G_s$ (kJ/mol)	$-\Delta G_w$ (kJ/mol)	γ_S (J/g)
0.08	Methane	0.08	-	3.50	-	9.1
0.08	$CDCl_3$	0.06	0.02	2.97	0.47	5.2
0.08	Decane	0.08	-	2.23	-	5.7
0.75	Air	0.30	0.45	2.91	0.50	18.9
0.75	Decane	0.14	0.61	1.88	0.35	38.3
5.67	Water	0.80	3.27	2.34	0.30	67.4
0.1#[a]	Air	0.08	0.02	2.77	0.39	7.8
0.1#[b]	Air	0.08	0.02	2.78	0.44	8.0
1.1#	Air	0.21	0.890	3.21	0.35	15.0
1.1#	Decane	0.34	0.760	1.35	0.5	24.7
h (g/g)	$<T_m>$ (K)	S_{uw} (m^2/g)	S_{nano} (m^2/g)	S_{meso} (m^2/g)	V_{nano} (cm^3/g)	V_{meso} (cm^3/g)
0.08	216.2	89	71	18	0.03	0.05
0.08	241.8	45	21	24	0.01	0.07
0.08	240.0	65	0	65	0	0.08
0.75	259.7	115	32	83	0.01	0.67
0.75	248.5	110	0	110	0	0.74
5.67	260.9	301	0	301	0	4.10
0.1#[a]	229.6	41	36	5	0.02	0.07
0.1#[b]	229.0	42	36	6	0.02	0.07
1.1#	261.0	103	23	80	0.01	0.52
1.1#	258.4	84	0	78	0	0.67

Note. #CS20m, and other samples were based on CS20; CS20m stored at [a] 298 K and [b]255 K for a week [63].

This result could be explained by much greater dispersion interactions of larger decane molecules with the silica surface than small methane or chloroform molecules. Notice that similar effects of the water displacement were observed for small but polar molecules such as acetonitrile. Adsorbed decane demonstrated two ^{1}H NMR signals at 0.9 and 1.25 ppm [63] corresponding to methyl and methylene groups, respectively. The water signal was weak due to the relatively small amount compared to the decane content, and observed at $\delta_H \approx 1.8 – 2.5$ ppm [63]. However, at h = 0.75 g/g, the water signal was much more intense but remained lower than the decane signal. The water observed was a WAW-SAW mixture, with a major contribution of SBW since it was frozen at $T < 260$ K. However, this water was more weakly bound to silica than that in either the methane or chloroform media (Fig. 98). The WBW content increased with increasing water content (Table 17, C_{uw}^{w}), this led to an increase in the $<T_m>$ value. This was because the relative content of SBW

decreased significantly from 75-100% (h = 0.08 g/g), 20-40% (h = 0.75 g/g) to 14% at (h = 5.67 g/g). Both highly hydrated powder CS20 at h = 0.75 g/g, and the concentrated (15%) aqueous suspension at h = 5.67 g/g, exhibit strongly and weakly bound water (Table 17).

Water adsorbed onto CS20 at h = 0.75 g/g could be divided into SBW and WBW, frozen at lower and higher temperatures, respectively. SAW (Table 17) was also found in the suspension [63]. This effect could be explained by the formation of clusters and domains of water (Fig. 99d) which were not spatially separated. When this sample at h = 0.75 g/g was in the decane dispersion medium, the characteristics of bound water change quite a bit (Figs. 98b and 99d, Table 17). WAW and two types of SAW appeared, and the PSD became bimodal.

Notice that even at a low adsorbed water content (h = 0.08 g/g), There was a broad PSD (Fig. 99a,b) including clusters at $1 < R < 2$ nm and domains at $2 < R < 20$ nm [63]. These structural features exhibited traces of the IPSD (determined from the nitrogen adsorption isotherm) characteristic of the initial fumed silica (Fig. 98b, dot-dashed line) which contained mesopores at $2 < R < 10$ nm. However, smaller and larger pores (voids between nonporous nanoparticles) differed because of the rearrangement of primary nanoparticles in the secondary structures due to suspending, cryogelation at high pressure (CS20 was prepared at 450 bar), and drying in air [53,63,232].

Results thus far have addressed systems using co-adsorbates that were either non- or much less polar than H_2O. It was of interest to study the systems with CS20 containing water co-adsorbed with more polar compounds such as H_2O_2, HCl, and CF_3COOH [63].

A 30% aqueous solution of H_2O_2 (0.05 g per gram of dry CS20) was added to CS20 preheated at 470 K for 15 min (to desorb residual water) and then equilibrated for 1 h [63]. For the sample in air, two signals of H_2O_2 (δ_H = 12 ppm) and H_2O (δ_H = 5 ppm) were observed at $T < 240$ K. From the intensity ratio of these signals, and the temperature behavior of the 5 ppm signal (compared with pure water), one could assume that water included a small portion of dissolved H_2O_2 (since bound water is a poor solvent [53]). Similarly, the H_2O_2 structures responsible for the signal at 12 ppm were practically free of water. In other words, not only was bound water a poor, inactive solvent, but hydrogen peroxide was also [63].

Thus, partial freezing of the solution and its cryoconcentration with decreasing temperature could cause the formation of spatially separated clusters [63] since proton exchange between H_2O and H_2O_2 was slow on the NMR timescale [53]. At $T > 240$ K, the exchange became faster and the signal width of H_2O_2 became broader and, therefore, not detected (since the bandwidth was 20 kHz). The water resonance exhibited a slightly higher chemical shift due to the interaction of water with H_2O_2. Besides the signal of SAW at 5 ppm, a weak signal of WAW was observed at 1.8 ppm, the intensity of which increased with increasing temperature due to melting. The WAW did not interact with hydrogen peroxide because of space confined effects, and the formation of spatially separated structures with WAW and hydrogen peroxide occurred [63].

The behavior of water bound to CS20m ($h \approx 100$ mg/g) was also analyzed depending on storage of the sample under different conditions (Fig. 100) [63]. The sample CS20m stored at 255 K for a week was loaded into cooled NMR ampoule, and after the NMR spectra recording, this sample was stored at 293 K for a week in air, and the spectra were recorded again. A small difference in the spectra (Fig. 74a) and the $C_{uw}(T)$ curves (Fig. 100b) could be caused by adsorption of an additional portion of water from air onto the cooled sample. This resulted in an increase in the signal intensity. Adsorbed water was located in narrow voids mainly at $R < 3$ nm (Fig. 100c). Therefore, the surface area of silicas in contact with bound water was about 40 m^2/g (Table 17, S_{uw}), and $S_{nano} > S_{meso}$; however, $V_{nano} < V_{meso}$. Therefore, the major portion of water (~80%) was strongly bound water (Table 17, C_{uw}^s). This led to the value of $\gamma_S^* = \gamma_S/h$ recalculated per gram of water (~80 J/g) greater than that for the aqueous suspension but lower than that for a sample in the methane atmosphere. As a whole, the observed changes in the behavior of water bound to CS20m stored under different conditions were small due to the stability of cryosilica properties [63].

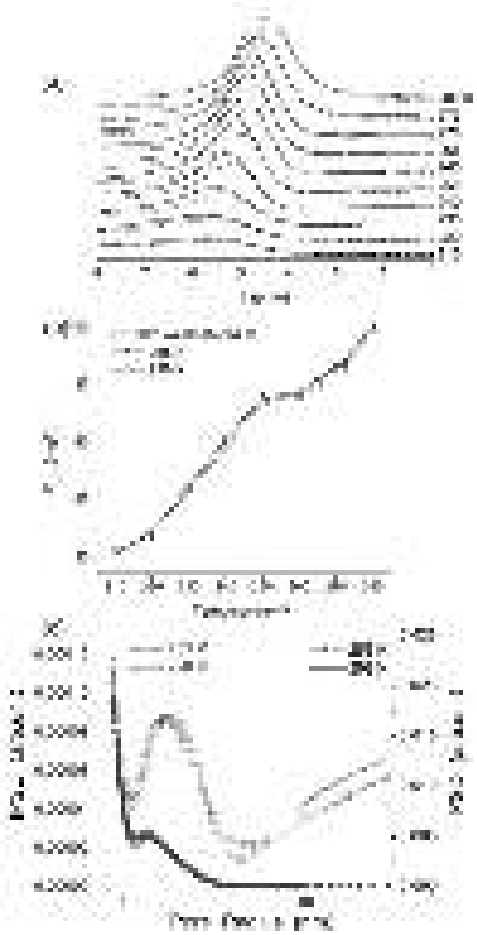

Fig. 100. (a) ^{1}HMR spectra of CS20m stored at 255 K (solid lines) for a week and then stored at 298 K (dashed lines) for a week; and the corresponding (b) $C_{uw}(T)$ dependences and (c) PSD and IPSD.

This aspect is of importance because silica samples were studied using a set of methods under very different conditions including TSDC measurements of strongly cooled samples (Fig. 101) [63]. TSDC thermograms showed dipolar relaxations at $T < 220$-220 K and direct current (dc) relaxation at $T > 210$-220 K (Fig. 101). In contrast to ^{1}H NMR showing nonzero intensity due to local mobility of molecules, the dc relaxation was due to through conductivity when There were conditions for percolation of protons or $H_3O^+(H_2O)_n$ (*i.e.*, Zundel ($H_5O_2^+$) and Eigen ($H_9O_4^+$) cations) between two electrodes [53]. Therefore, the dc relaxation could start at slightly higher temperatures than the NMR spectra appear for mobile molecules of adsorbates. The activation energy (assuming that the dc relaxation obeys the Arrhenius law) was relatively low for the system studied (54.8, 52.7, 41.3 and 55.2 kJ/mol for curves 1-4, Fig. 101, respectively). The E_a value for the CS5 suspension was smaller than that for initial 5 wt.% aqueous suspension of nanosilica [53,63].

The TSDC was higher for wetted powder of CS20m (h = 1.6 g/g) than for other samples (Fig. 101) because the relative amount of water contacted with the silica surface was greater than in other samples [63]. The high-pressure cryogelation effects appear since the TSDC intensity was much lower for 20 wt.% suspension of A-300 (nontreated at low temperature and only sonicated) than that of not only for CS20m but also for CS5m. The TSDC intensity for dipolar relaxations increased with increasing silica content from 5 wt.% to 20 wt.% for cryosilicas because water molecules were strongly polarized by the electrostatic fields near the silica surface. However, this effect depended also on the organization of silica nanoparticles in secondary structures [63].

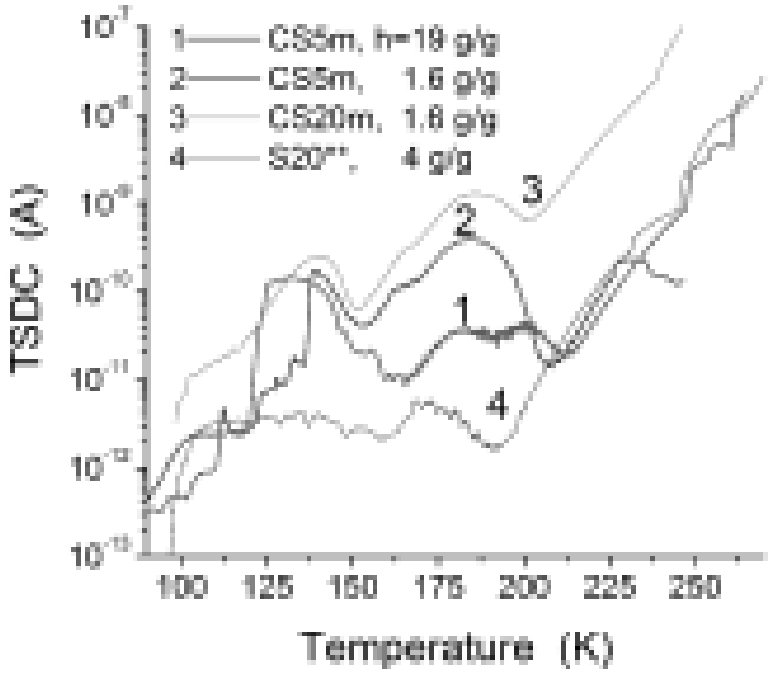

Fig. 101. TSDC thermograms (normalized to F_p = 100 V/mm) of cryosilicas CS5 and CS20m dried and hydrated at h = 1.6 g/g, thawed aqueous suspension of CS5m (1000 atm) and gel-like concentrated suspension (S20**, 20 wt.% of A-300) prepared at standard condition without freezing.

Thus, high-pressure cryogelation affected the properties of cryosilica powders and suspensions depending on the silica content in initial aqueous suspensions (5-20 wt.%) frozen-dried [46,47,53,62,63]. The largest changes were observed for CS20 and CS20m (20 wt.% suspension frozen at 450 or 1000 atm, respectively). The adsorption of water onto CS20 from air increased several-fold in comparison with CS5, CS10 or CS15. The specific surface area decreased slightly during high-pressure cryogelation. This was due to rearrangement of primary nanoparticles in the secondary structures, which were denser than the initial silica powder. However, the structure of primary particles *per se* changes only slightly according to HRTEM images. This rearrangement resulted in changes of the PSD shape and contributions of pores of different shapes (cylindrical, slit-shaped, and voids between nanoparticles) and sizes (nano-, meso-, and macropores) [63].

The morphological and textural characteristics are of importance for applications of nanooxides; therefore, changes in these characteristics of CNO were analyzed in detail (Tables 15-18, and Figs. 101 and 102) [46,47,63]. Maximal change (double increase) in the specific surface area of CNO was observed for cAST in comparison with the initial AST powder. This result could be explained by lower stability of relatively large AST particles at 50-200 nm in diameter, which represented polycrystalline particles covered by a shell, in comparison with smaller single alumina crystallites or silica nanoparticles (Fig. 102). Ternary AST particles were less uniform than binary ST (with much smaller increase in S_{BET} approximately by 3%) or pure silica and alumina with decreased S_{BET} for CNO during high-pressure cryogelation at low temperature.

Table 18. Textural characteristics of initial and differently treated nanooxides [46,47,63].

Oxide	Medium	T_t (K)	P_t (atm)	Note	S_{BET} (m^2/g)	S_{nano} (m^2/g)	S_{meso} (m^2/g)	S_{macro} (m^2/g)	V_p (cm^3/g)	V_{nano} (cm^3/g)	V_{meso} (cm^3/g)	V_{macro} (cm^3/g)	Δw
PS300	–	–	–	Initial powder	302	94	200	9	0.734	0.035	0.523	0.176	0.021
cPS300	water	208	1000	cryogel	297	38	258	2	0.827	0.012	0.798	0.017	0.749
gsPS300	0.1M NaCl	293	1	Gel/NaCl	292	27	265	1	0.826	0.009	0.807	0.010	0.741
csPS300	0.1M NaCl	208	1000	Cryogel/NaCl	283	16	266	1	1.212	0.007	1.193	0.012	0.281
PS100	–	–	–	Initial powder	84.4	32	49	3	0.206	0.012	0.124	0.070	0.290
gPS100	water	293	1	Gel	83.7	8	53	23	0.427	0.003	0.059	0.365	–0.108
cPS100	water	208	1000	Cryogel	83.8	28	43	13	0.474	0.014	0.207	0.253	–0.094
Al_2O_3	–	–	–	Initial powder	89	12	75	2	0.167	0.006	0.132	0.029	–0.227
gAl_2O_3	water	293	1	Gel	76	13	60	2	0.545	0.007	0.504	0.034	0.450
$gsAl_2O$	0.1M NaCl	293	1	Gel/NaCl	72	4	43	26	0.521	0.002	0.150	0.369	0.209
$csAl_2O$	0.1M NaCl	208	1000	Cryogel/NaCl	72	7	44	22	0.553	0.004	0.238	0.311	0.437
ST	–	–	–	Initial powder	87	27	56	4	0.228	0.012	0.144	0.072	–0.291
gST	water	293	1	Gel	90	31	49	11	0.365	0.010	0.161	0.195	–0.168
cST	water	208	1000	Cryogel	89	30	49	10	0.366	0.010	0.168	0.188	–0.182
gsST	0.1M NaCl	293	1	Gel/NaCl	86	33	39	14	0.415	0.010	0.121	0.284	–0.105
csST	0.1M NaCl	208	1000	Cryogel/NaCl	88	30	44	13	0.402	0.009	0.138	0.255	–0.100
AST	–	–	–	Initial powder	83	12	68	3	0.217	0.005	0.166	0.047	–0.164
gAST	water	293	1	Gel	74	6	46	22	0.532	0.003	0.231	0.298	0.363
cAST	water	208	1000	Cryogel	160	15	136	9	0.595	0.008	0.466	0.121	0.125
gsAST	0.1M NaCl	293	1	Gel/NaCl	120	7	100	13	0.506	0.004	0.294	0.208	–0.060
csAST	0.1M NaCl	208	1000	Cryogel/NaCl	133	9	112	13	0.508	0.005	0.305	0.199	–0.090

Note. Gelation of all other samples was during 12 h. Labels in dried samples correspond to cryogel (c), cryogel with NaCl (cs), gelation at room temperature (gel, g) with NaCl (gs).

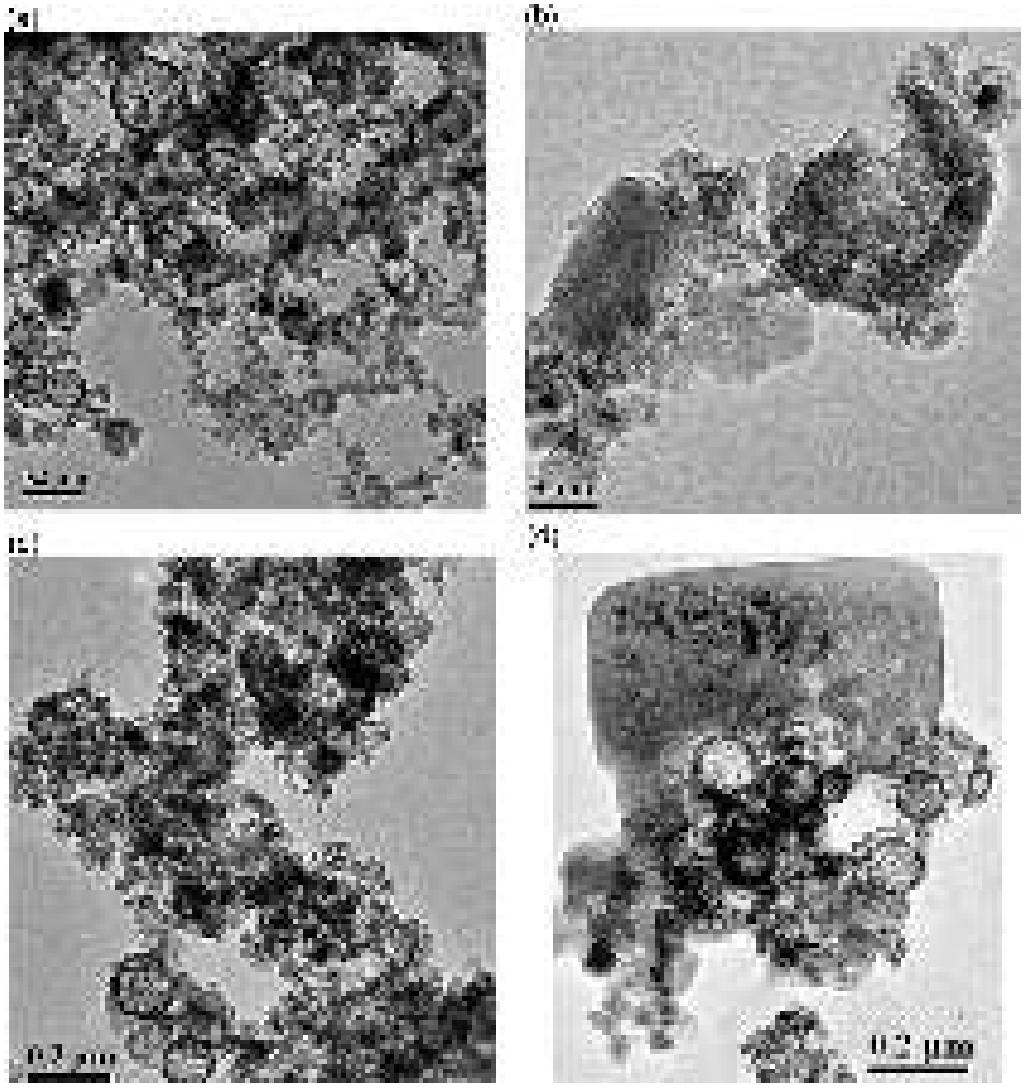

Fig. 102. HRTEM images of (a) AST, (b) cAST, and (c, d) csAST.

Among primary AST nanoparticles there near pure alumina, silica, and titania nanoparticles. In the presence of a small amount of NaCl (2.8 wt.% in dried samples due to 0.1 M NaCl in the 20 wt.% suspensions), an increase in the S_{BET} value for csAST (by 64%) and gsAST (by 45%) was smaller than that for cAST (by 93%) [45,46].

Salt crystallites formed in rigid pores could damage the materials that depended on pore sizes, as well as on content of salts and water [233]. However, occurrence of this process during cryogelation of the aqueous suspensions was less probable because oxide nanoparticles were nonporous but pores were the voids between nanoparticles in their "soft" loose aggregates. During drying of samples, salt crystallites could form in these voids; *i.e.* they fill a portion of the volume of textural pores and block a portion of the oxide surface (Fig. 102c,d). However, this effect was small since the NaCl amount was only 2.8 wt.% and NaCl crystallites were relatively large (Fig. 102d). Additionally, salt could increase the amounts of residual liquid water during cryogelation; *i.e.*, this could diminish pressure of ice crystallites onto oxide nanoparticles. Perhaps this effect can play the most important role in diminution of the S_{BET} value for csAST and gsAST in comparison with cAST, and decomposition of complex AST nanoparticles decreased (Fig. 102). For a mechanical mixture with AST and PS300 (1 : 1 w/w), after gelation or HPCG and drying the S_{BET} value decreased for mixtures without (gSAST, cSAST by 23%) and with addition of NaCl (gsSAST, csSAST, by 19%) in comparison with a non-treated blend powder having S_{BET} = 192 m^2/g. Thus, small nanoparticles of PS300 (d_{av} ≈ 9 nm) could play a role of a damper decreasing high pressure effects of ice crystallites on larger AST particles (d_{av} ≈ 30 nm). A small increase (2-3%) in the S_{BET} value was observed for binary oxide ST after cryogelation and drying. These

results for AST and ST could be due to the difference in the temperature/pressure behavior of silica, alumina and titania during extreme treatment of binary and ternary fumed oxides consisting of complex nanoparticles, since similar effects were absent for treated individual fumed silica and alumina. The S_{BET} value diminution was greater for cPS300 (by 1.7%) than that for cPS100 (by 0.7%). It also decreased for CNO with pure alumina (by ~5%). Thus, for CNO with complex ternary and binary fumed oxides, an increase in the specific surface area could be observed due to partial decomposition of complex nanoparticles characterized by much greater residual stress than such uniform fumed oxides as amorphous silica and crystalline alumina (mainly with θ-Al_2O_3 which was stable up to 1150 ^oC and then transforms into α-Al_2O_3) [46,47,63]. Therefore, the difference in the temperature behavior of silica, alumina and titania phases could lead to cracking of complex nanoparticles during HPCG. For CNO with individual oxides, S_{BET} decreased but nanoparticle sizes do not practically change after HPCG and drying. Thus, the S_{BET} value could decrease due to rearrangement (compaction) of aggregates and agglomerates of pure silica or alumina.

The pore volume (Tables 15-18, V_p), increased for all the CNO or systems suspended-dried at standard conditions [46,47,63]. This was due to the morphological features and related textural characteristics caused by the formation of loose aggregates with nonporous nanoparticles and very loose agglomerates of aggregates in the initial powders of nanooxides strongly changed during HPCG or gelation. Compaction of nanoparticles in aggregates during HPCG (or even gelation at standard conditions) and drying led to the opposite effects for V_{em} (which strongly decreased) and V_p (which increased, Tables 15-18). The gelation/drying led to an increase in the ρ_b value from 0.067 g/cm^3 (PS300) to 0.31 g/cm^3 (cPS300). Therefore, V_{em} decreased from 14.5 cm^3/g (PS300) to 2.8 cm^3/g (cPS300) due to diminution of the volume of macropores, which, however, were poorly filled by such low-molecular weight adsorbates as nitrogen, water, *etc.*, and, therefore, $V_{em} >> V_{macro}$. However, after HPCG or gelation (and compaction of aggregates) despite a decrease in V_{macro}, the V_p value increased due to a significant increase in V_{meso} (Tables 15-18). Similar effects were observed for other studied nanooxides that are, however, smaller due to their larger nanoparticles, an increase in their bulk density, and a decrease in their pore volumes over the total pore size range (Fig. 103, Tables 15-18) [46,47,63].

According to HRTEM images (Fig. S66), during HPCG and drying of cPS300, the nanoparticle morphology of nanosilica did not practically change [46,47,63]. However, the textural characteristics (Tables 15-18, Fig. 103) could significantly change because of rearrangement of CNO nanoparticles in their aggregates and agglomerates. Contribution of nanopores at $R < 1$ nm and narrow mesopores at 1 nm < R < 5–10 nm into the PSD decreased after gelation/drying due to compaction of the aggregates/agglomerates of nanoparticles. In other words, each nanoparticle could be closer to neighboring nanoparticles in CNO than in the initial powder (Fig. 103).

Contribution of large mesopores at 5–10 nm < R < 25 nm and narrow macropores at 25 nm < R < 60-100 nm into the PSD strongly increased after gelation/drying (Fig. 103) [46]. However, contribution of large macropores $R > 100$ nm decreased due to compaction of nanooxides after gelation/drying since the bulk density increased by several times. Notice that primary nanoparticles of PS300 have non-ideal spherical shape. Therefore, the SCV/SCR model errors could be relatively large (Tables 15-18, Δw) and the Δw value could increase for CNO because of certain deformation of nanoparticles and changes in the shape of the contact zones between them in aggregates. Therefore, $\Delta w = 0.021$ for the initial PS300 (*i.e.* about 2 % error in the SCV/SCR model) but it increased for cryogels and suspended/dried samples (Tables 15-18, Δw). For PS100, Δw was greater (0.29) than for PS300 (0.02) since the deviation in the particle shape from the spherical one could grow with increasing size of primary particles of fumed oxides [1-23,46,47,53].

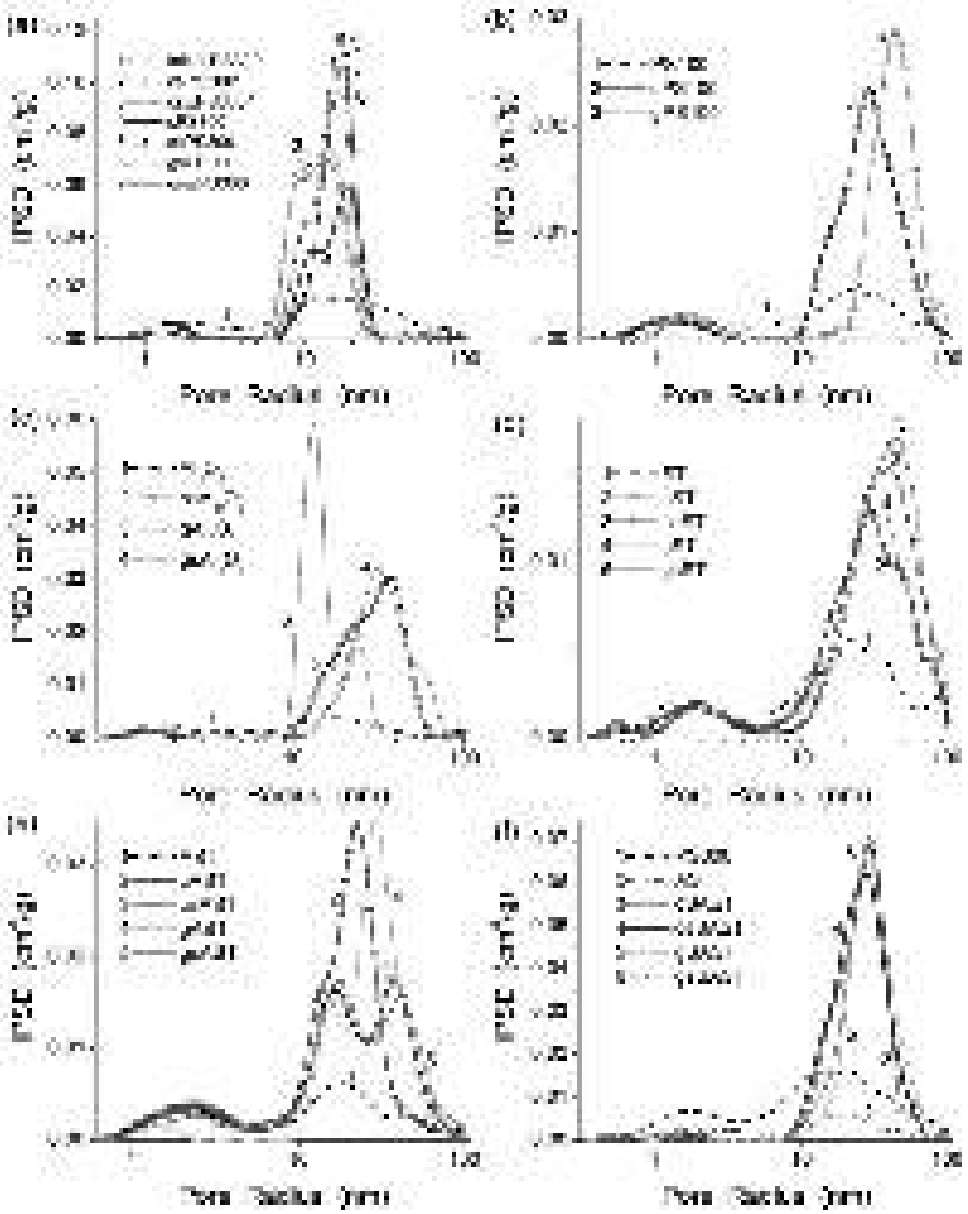

Fig. 103. Incremental SCV/SCR PSD for silicas (a) PS300 and (b) PS100, (c) alumina, (d) silica/titania, (e) alumina/silica/titania, and (f) blend PS300 + AST (1:1): initial powder and differently treated nanooxides: cryogelation in pure water at 208 K, in 0.1 M NaCl solution at 260 K or 208 K, suspended in water or 0.1 M NaCl solution and dried at room temperature and standard pressure (sample labels correspond to them in Tables 15-18).

During HPCG or gelation and drying NaCl particles could affect the PSD (Fig. 103) and other textural characteristics (Tables 15-18) [46,47,63]. This was due to several reasons. First, NaCl dissolved in water affected oxide particle-particle interactions [46,47,53,63,170] and caused an increase in the amounts of unfrozen water during HPCG due to enhanced freezing point depression also caused by confined space effects that led to a certain diminution of the pressure and reduce the nanoparticles compaction. Second, NaCl in the shape of nanocrystallites could negatively affected the interactions between adjacent oxide nanoparticles that result in decreasing compaction (including valence bonding of nanoparticles) of nanoparticles in the rearranged aggregates during drying. Third, NaCl crystallites *per se* (NaCl density of 2.16 g/cm^3 was close to the density of amorphous silica of 2.2 g/cm^3) could give a certain contribution into the textural characteristics of the materials depending on the NaCl crystallite sizes. Additionally, NaCl nanoparticles could fill voids between oxide nanoparticles that influence the S and V characteristics of the materials. However, these direct effects of NaCl crystallites on the textural

characteristics were small since the NaCl amount was low (2.8 wt.%) and crystallites were relatively large [46,47,63].

For csPS300, the presence of NaCl in the dried CNO powder caused diminution of the specific surface area (Table 18, S_{BET}, S_{nano}) but an increase in the pore volume (V_p, V_{meso}) in comparison with pure cPS300 [46]. For alumina, AST and ST, the NaCl effects differed (in general, it was smaller) from those for PS300 because of the difference in the textural characteristics, density, primary particle sizes, and the aggregation degree of these nanooxides. Minimal effects were observed for ST (Table 18, Fig. 103). This could be due to relatively uniform distribution of titania in the volume and surface of complex ST nanoparticles characterized by a maximal number of the Si–O–Ti and Si–O(H)–Ti bridges among silica/titania nanooxides [53]. This prevents cracking ST nanoparticles during HPCG.

Sample cPS300 with strongly increased bulk density (0.31 g/cm^3) and decreased contribution of nanopores and macropores (Table 18) was characterized by increased total V_p because of a significant increase in contributions of pores over the 10–30 nm range (Fig. 103a) [46,47,63]. The rearrangement of silica nanoparticles in 0.1 M NaCl suspensions frozen at 260 K and 208 K was similar (Tables 15-18). However, their PSD differ (Figs. 103) since the PSD of csPS300 shifted toward larger pore sizes. Washing of csPS300 (giving cswPS300) resulted in a certain increase in all the textural parameters (Tables 15-18) because of removal of NaCl particles filling voids between neighboring silica nanoparticles and changes in particle-particle interactions after washing-drying. Therefore, the PSD intensity of cswPS300 increased around $R \approx 10$ nm (Fig. 103a, curves 2 and 3). Similar results were observed for non-washed and washed suspended-dried samples gsPS300 and gswPS300 (Tables 15-18). However, their PSD intensity around $R \approx 10$ nm was lower than that for cryogels (Figs. 103a, curves 6 & 7 *vs*. 2 & 3) due to weaker compaction of suspended/dried but non-frozen samples.

For a mixture PS300/AST, the effects of NaCl differ from those for the corresponding individual systems PS300 and AST (Tables 15-18, Fig. 103f) [46,47,63]. For individual PS300, addition of NaCl into the aqueous media led to decreasing textural parameters of HPCG samples but for AST, the opposite results were observed. For csSAST, a smaller increase (in comparison with pair of AST and csAST) in the parameters was observed in comparison with cSAST (Tables 15-18). For alumina, NaCl enhanced contribution of macropores but the opposite effect was for mesopores and nanopores. This feature was well seen in the PSD (Figs. 103).

Not only textural and morphological characteristics of nanooxides changed due to HPCG but also the crystalline structure of samples containing alumina [46]. An intensive line at $2\theta \approx 31.7^o$ could be assigned to NaCl crystallites ($2\theta \approx 31.1^o$ for individual NaCl) bound to alumina in $csAl_2O_3$. This band was low-intensive in Al_2O_3 and gAl_2O_3 (Fig. 104). However, this line could be rather attributed to θ-Al_2O_3 having a doublet at 31.3 and 31.7^o. In other words, an increase in the crystallinity degree of alumina after HPCG could lead to an increase in the intensity of θ-Al_2O_3 lines. However, intensity of a line at 32.85^o which was higher in both pure θ-Al_2O_3 and initial fumed alumina or gAl_2O_3 was lower than that at 31.7^o in $csAl_2O_3$. The latter could be due to the effect of NaCl. Additionally, in both initial Al_2O_3 and gAl_2O_3, There was a line at 32.0^o which could be assigned to γ-Al_2O_3 and which was not observed in $csAl_2O_3$. Thus, certain but not strong changes in the crystalline structure were observed in $csAl_2O_3$ (Fig. 104). However, the hydroxide $Al(OH)_3$ lines were very weak in $csAl_2O_3$ in contrast to treated AST (Fig. 105). These insignificant changes in the crystalline structure of $csAl_2O_3$ were in agreement with relatively small changes in the S_{BET} value (≤ 19 %) of treated alumina samples in contrast to AST (≤ 93%) (Table 18) [46,47,63].

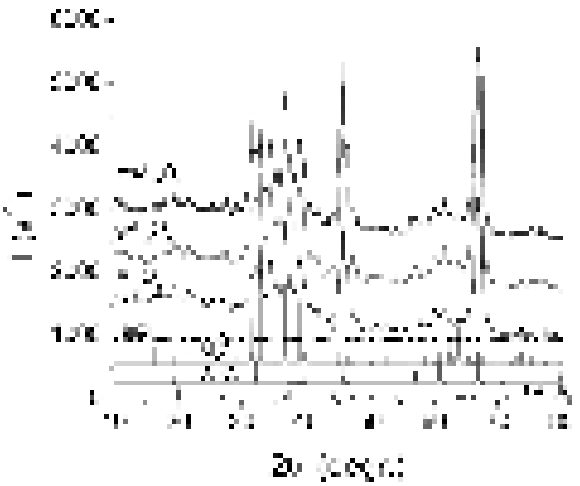

Fig. 104. XRD patterns for initial alumina (Al_2O_3), suspended/dried at standard conditions (gAl_2O_3), and cryogel prepared in 0.1 M NaCl solution at 208 K ($csAl_2O_3$) (sample labels correspond to them in Table 18), and pure crystalline NaCl and θ–Al_2O_3.

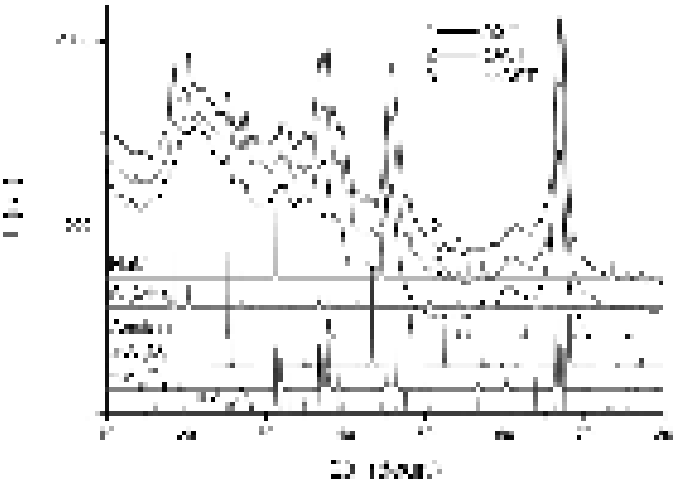

Fig. 105. XRD patterns for initial AST, and cryogel prepared in water (cAST) or 0.1 M NaCl solution at 208 K (csAST) (sample labels correspond to them in Table 18), and pure crystalline NaCl, anatase, and different crystalline alumina phases: corundum (α–Al_2O_3), γ–Al_2O_3, and θ–Al_2O_3.

Greater changes in the XRD patterns, especially at 20–40°, were observed for AST after HPCG in comparison with individual alumina (Fig. 104) [46]. From these changes, the HPCG effect on the XRD pattern of AST was stronger than the presence of NaCl (due to its low content of 2.8 wt.%). The lines of such several phases as aluminum hydroxide $Al(OH)_3$, corundum α–Al_2O_3, γ–Al_2O_3 and θ–Al_2O_3 were better observed without NaCl (cAST) than in the presence of NaCl (csAST) or in initial AST. Stronger XRD changes in treated AST (Fig. 105) than that of alumina (Fig. 104) were in agreement with greater changes in the textural characteristics of CNO with AST than alumina (Tables 15-18). The crystallinity degree of AST, csAST and cAST was 32 %, 37 and 43 %, respectively (estimated from the area of crystalline peaks and residual amorphous halo). The size of alumina crystallites was about 10 nm that was in agreement with the particle size of cAST (12 nm) estimated from the S_{BET} value but much smaller than that for the initial AST (~25 nm). The increase in the crystallinity degree of cAST and csAST was mainly due to appearance of hydroxide $Al(OH)_3$ (lines at 18.2 and 20.5°) and a certain increase in intensity of lines over the 25-70° range of several alumina phases in comparison with the initial AST (Fig. 105) [46,47,63].

The changes in the structural characteristics of treated samples studied were accompanied by changes in the surface structure. Treated silica samples studied using the IR spectroscopy were more hydrated than initial nanosilica since a broad band over 2500–3800 cm^{-1} was more intensive for them (Fig. 97). Therefore, the surface area free of water (estimated according to [106]) was 262 (PS300), 90 (cPS300), 67 (csPS300), 71 (gPS300), and 41 (gsPS300) m^2/g. This was due to compaction of silica nanoparticles in aggregates during treatment in the aqueous media and drying. Additionally, NaCl bound to silica was highly disperse since NaCl particles and adsorbed water (bound to silica and NaCl particles) strongly disturb a larger portion of the surface hydroxyls than in pure initial silica and CNO (compare the IR spectra for cPS300, gPS300 and csPS300, gsPS300) [46,47,63].

The IR spectra of AST change due to pre-heating (Fig. 106, curves 1 and 2) and gelation under different conditions (curves 3-6). There was no narrowing of the cooperative Si–O–Si asymmetric modes at 1100 cm^{-1}, as well as of the bands related to Ti–O_{Si}, Al–O_{Al}, and Al–O_{Si}. This result was in agreement with diminution of the sizes of AST particles after HPCG and some changes in the phase composition, *e.g.,* appearance of $Al(OH)_3$ (Fig. 105) [46]. Changes in intensity of the IR bands over the 900-500 cm^{-1} range could be due to dehydration of the surface on heating at 723 K and appearance of four- or fivefold O-coordinated Al atoms instead of sixfold

O-coordinated ones. This led to an increase in intensity of the bands at 800-900 cm^{-1} and decrease in intensity of the bands at 500-600 cm^{-1}. HPCG of the aqueous suspensions results in the opposite effects due to enhanced hydration (formation of the $Al(OH)_3$ phase) and O-coordination number of Al atoms [46].

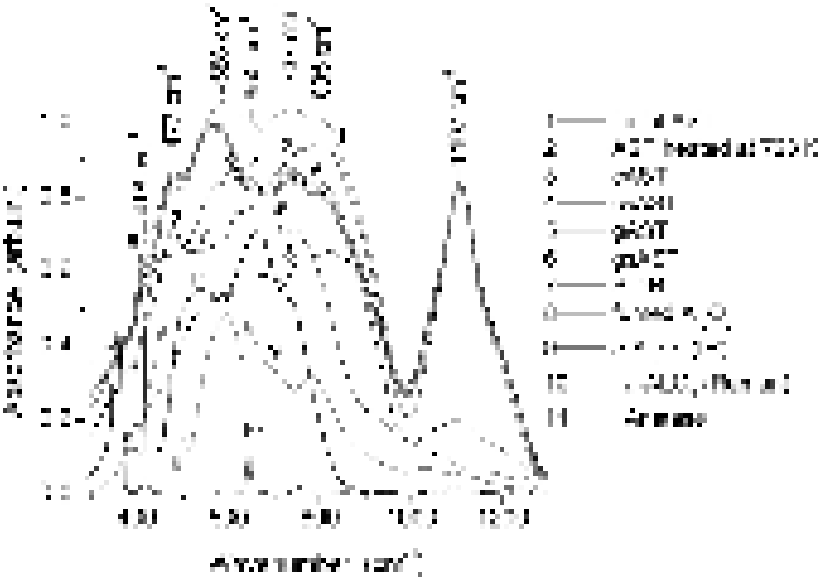

Fig. 106. IR spectra of AST (curve 1) initial and (2) preheated at 723 K for several hours, (3) cAST, (4) csAST, (5) gAST, (6) gsAST, (7) fumed ST94 with 6 wt.% SiO_2 and 94 wt.% TiO_2, (8) pure fumed alumina, corundum α-Al_2O_3 (9) IR and (10) Raman spectrum, and (11) pure anatase, (1:100 mixture with KBr). All spectra of AST samples were normalized to the asymmetric mode of Si-O_{Si} at 1100 cm^{-1}.

Adsorption energy of water or other compounds depended strongly on the content of already adsorbed amounts (Fig. 107) [53,58]. This effect caused different changes in the structure of bound water depending on the distance from the adsorbent surface. This is also reflected in the relationship of ΔG *vs.* C_{uw} *vs.* T [53].

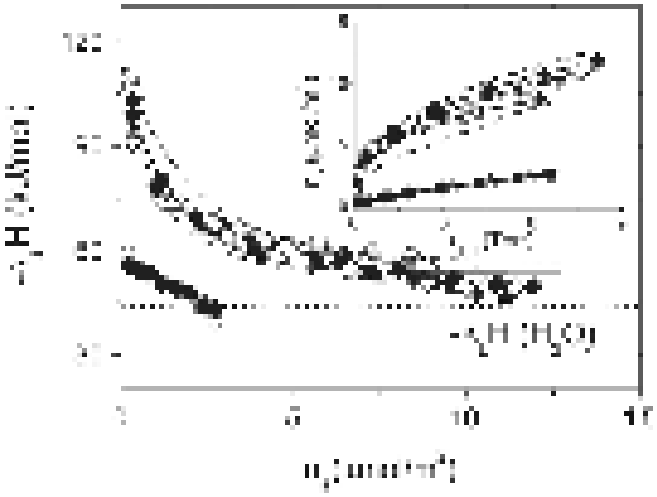

Fig. 107. Adsorption enthalpy vs. uptake for H_2O vapor adsorption (T = 303 K) on (i) silica-coated anatase (A-S: ▼,▽) and silica-coated rutile (R-S: ♦, ◊) in comparison with uncoated anatase (A8/A72, dot-dashed curves), uncoated rutile (R, dashed curves) and a plain (fumed) silica specimen (S: ●,○); (ii) alumina/dimethicone-coated rutile (R-Alu-D: ◮,◭) and a plain (fumed) alumina specimen (Alu: ◆,◇). Volumetric isotherms in the inset. Solid symbols 1st run, open symbols 2nd run of adsorption. All samples were preliminary outgassed at T = 303 K. Latent enthalpy of liquefaction of water: $-\Delta_L H(H_2O)$ = 44 kJ/mol (dotted line).

The changes in the texture and surface properties of treated samples led to significant changes in adsorption-desorption of polar water and nonpolar hexane (Fig. 108) [46,47,63]. A maximal increase in the water (Fig. 108a) and hexane (Fig. 108b) adsorption was observed for pure cryogels cPS300 and cAST, and for the latter this effect was stronger, since for the latter this

increase for water adsorption corresponded to a factor 2.5 but for the former it was 2.2. For nonpolar hexane, this effect was similar. This difference could be explained by stronger changes in the morphology of AST particles than for PS300 during cryogelation at high pressure (Table 18). Practically the same changes in the adsorption of polar water and nonpolar hexane could be explained by the effects of the textural changes in the materials but not by changes in the content of surface hydroxyls due to particle decomposition.

The presence of NaCl resulted in diminution of changes in both structural (Table 18) and adsorption (Fig. 108) properties of gAST and gsAST in comparison with cAST and csAST [46,47,63]. Changes in the texture (Fig. 103) and structure (Fig. 105) of differently treated AST samples resulted in an increase in water desorption mainly in the 350-500 K for cAST and gAST in comparison with the initial AST [46]. Compaction of the particles with their simultaneous decomposition (Fig. 75) and formation of the aluminum hydroxide in cAST caused a shift of the main peak toward higher temperatures. For gAST, desorption of water increased by several times in comparison with AST but the peak position was practically the same [46].

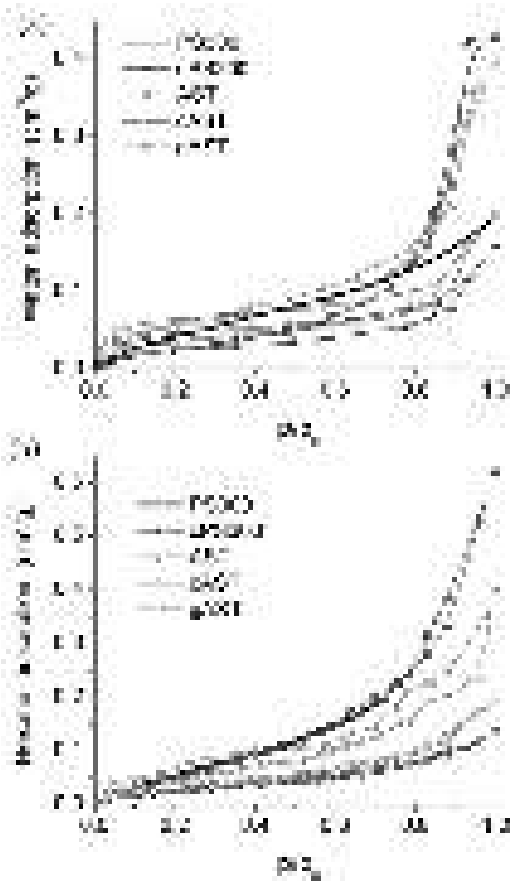

Fig. 108. Isotherms of (a) water and (b) n-hexane adsorption-desorption onto initial PS300, cryogels cPS300 and cAST (prepared at 208 K and ~1000 atm), and AST initial and gelatinized at standard conditions.

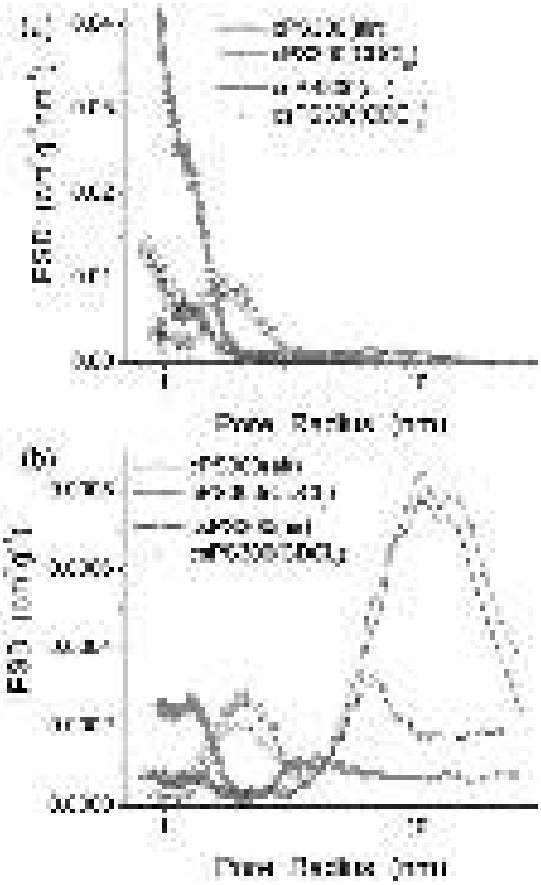

Fig. 109. Size distributions (a) differential or (b) incremental for structures of unfrozen water bound to cPS300 in different dispersion media at hydration degree h = 0.1 g/g in air or chloroform-*d* with addition of 0.15 g of *n*-decane (at cryoporometry constant 67 K nm).

To analyze the NaCl influence on the HPCG results, ^{1}H NMR study of water bound to cPS300 and csPS300 was carried out for samples being in air or chloroform-*d* media also affected by added non-polar *n*-decane (Fig. 109) [46]. The NaCl effects were stronger than the effects of $CDCl_3$ or *n*-decane [63]. Typically, hydrophobic media ($CDCl_3$ here) displace a portion of water from pores to form larger water structures in larger pores or out of pores [53]. This resulted in faster decrease in signal intensity with decreasing temperature [46]. However, addition of a small amount of *n*-decane (0.15 g/g) caused re-arrangement of water adsorbed in amounts close to the

equilibrium adsorption (0.1 g/g) at $p/p_s \approx 0.9$ for initial PS300 or at $p/p_s \approx 0.9$ for cPS300 in air medium (Fig. 108). Therefore, addition of $CDCl_3$ to *n*-decane/water/cPS300 resulted in the opposite effect, since water structures became smaller and PSD intensity increased at $R < 2$ nm (Fig. 109). For csPS300, a similar effect was weaker due to influence of NaCl crystallites on the organization of adsorbed water. In other words, strong interactions of water molecules with NaCl nanocrystallites and dissolved ions Na^+ and Cl^- led to diminution of the influence of changes in the dispersion media [46,47,63].

Significant changes in the texture and structure of cAST in comparison with AST and gAST (Tables 15-18, Figs. 102, 103e, 105, 106, and 108) led to a difference in the interfacial behavior of water alone or in the presence of decane (Figs. 110 and 111) [46,47]. Small amounts of water (0.1 g/g) and decane (0.15 g/g) were used to fill only a portion of pores of the materials (approximately V_p half of cAST and gAST, Table 18). The greatest difference in the ^{1}H spectra was observed for AST samples with water/decane in chloroform-*d* with addition of trifluoride acetic acid (TFAA) (Fig. 110b). This was due to the influence of the texture of AST (differently changed for gAST and cAST as shown above), *i.e.* confined space effects, on organization of both water and decane and dissolution of TFAA in this water. A maximal amount of TFAA was dissolved in water bound to AST since the ^{1}H NMR peak was at δ_H = 9-10 ppm. The TFAA amounts dissolved in water decrease for gAST and it was minimal for cAST [46,47,63].

For treated AST (gAST and cAST), decane displaces water into narrower voids (comp. Fig. 111a,b). Chloroform medium enhanced this trend. A minimal effect of the chloroform medium was for water bound to AST, *i.e.* water structures bound to AST were larger than those bound to gAST or cAST. Therefore, TFAA could be better dissolved in water bound to initial AST. There was apparent contradiction between this effect and the shapes of water structures. However, it was due to a fixed constant k_{GT} = 67 K nm in the Gibbs-Thomson equation [53] for all calculations with NMR-cryoporometry (Figs. 109 and 111). Clearly, this constant for pure water and water with dissolved TFAA could be different [46,53].

Weakly associated water (WAW) characterized by δ_H = 1.2-2.0 ppm appeared after addition of decane, especially for gAST [46,47,63]. There was certain content of WAW in the nanooxide systems in the chloroform media (Fig. 110). The main reason of the WAW appearing was the formation of branched 3D clusters of water located in narrow voids. Weakly polar (chloroform) or nonpolar (decane) co-adsorbates were immiscible with water and their molecular sizes were larger than that of water. Therefore, they could displace water into very narrow voids where they could not be located. The number of such narrow voids increased for cAST due to nanoparticle decomposition. Therefore, displacement effect of decane onto water was stronger for cAST than that for gAST or AST (Fig. 111b). Some theoretical calculations of the ^{1}H NMR spectra of water alone and bound to silica, pure and with NaCl analyzed in the ESI confirm this interpretation of the experimental ^{1}H NMR spectra [46,47].

High-pressure cryogelation of 20 wt.% aqueous suspensions of nanooxides (silicas PS300 and PS100, alumina, silica/titania, alumina/silica/titania) pure or with addition of 0.1 M NaCl at 208 K or 260 K led to significant changes in the textural characteristics of dried cryonanooxides and changes in the crystallinity of certain oxides [46,47,63]. Maximal changes in the specific surface area and crystalline structure were observed for high-pressure cryogels with ternary nanooxide AST. Large ternary nanoparticles (composed of nanocrystallites covered by a shell) could be decomposed during high-pressure cryogelation, the crystallinity degree increased by approximately 10 % and a new phase of aluminum hydroxide appears. Addition of PS300 to AST (mechanical blend at 1:1 w/w) led to diminution of the decomposition of AST particles during HPCG. For individual nanooxides (silica, alumina), high-pressure cryogelation caused a decrease in the specific surface area, but for ternary AST and binary ST, the specific surface area increased (much greater for ternary AST). For all treated samples, a significant increase in the volume of large mesopores (at pore radius 5–10 nm < R < 25 nm) and macropores (25 nm < R < 60–100 nm) was observed. However, contribution of nanopores (R < 1 nm) and narrow mesopores (1 nm < R < 5–10 nm) decreased after HPCG due to compaction of nanoparticles in aggregates. Thus, such

individual nanooxides as amorphous nanosilica and crystalline nanoalumina were morphologically more stable during HPCG than complex nanooxides such as ternary nanooxide with alumina (crystalline)/silica (amorphous)/titania (solid solution in alumina and silica), especially composed of nanocrystallites covered by a shell, and binary nanooxide with silica (amorphous)/titania (partially crystalline). Nanosilica PS300 with the highest S_{BET} value among studied oxides were characterized by maximal rearrangement of aggregates and agglomerates during HPCG because of the most minimal sizes of primary nanoparticles that provide maximal flexibility of secondary structures of the material [46,47].

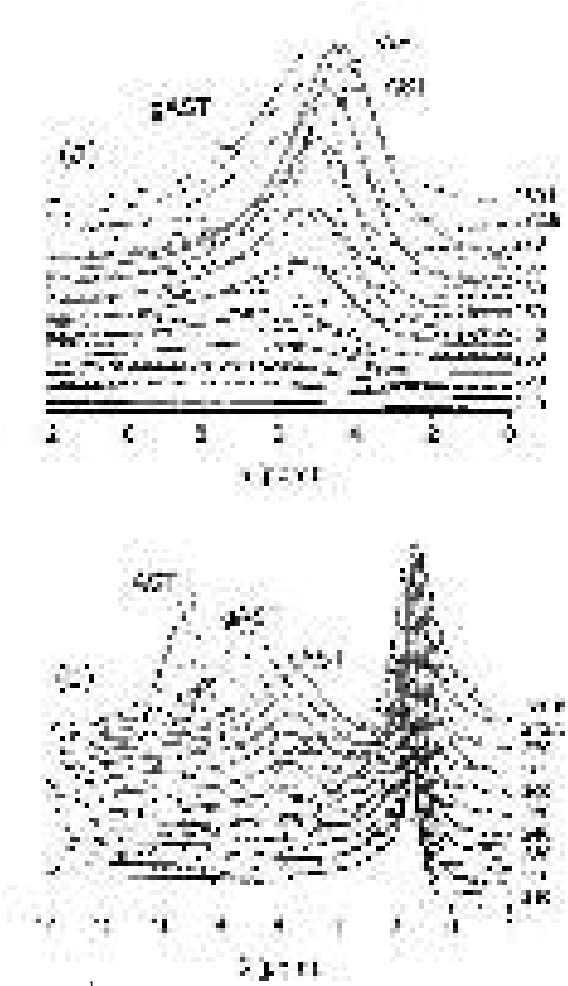

Fig. 110. ^{1}H NMR spectra of water (0.1 g/g) and (b) n-decane (0.15 g/g) bound to AST (dashed lines), gAST (dot-dashed lines) and cAST (solid lines) in media (a) air and (b) $CDCl_3$ with addition of TFAA (6 : 1).

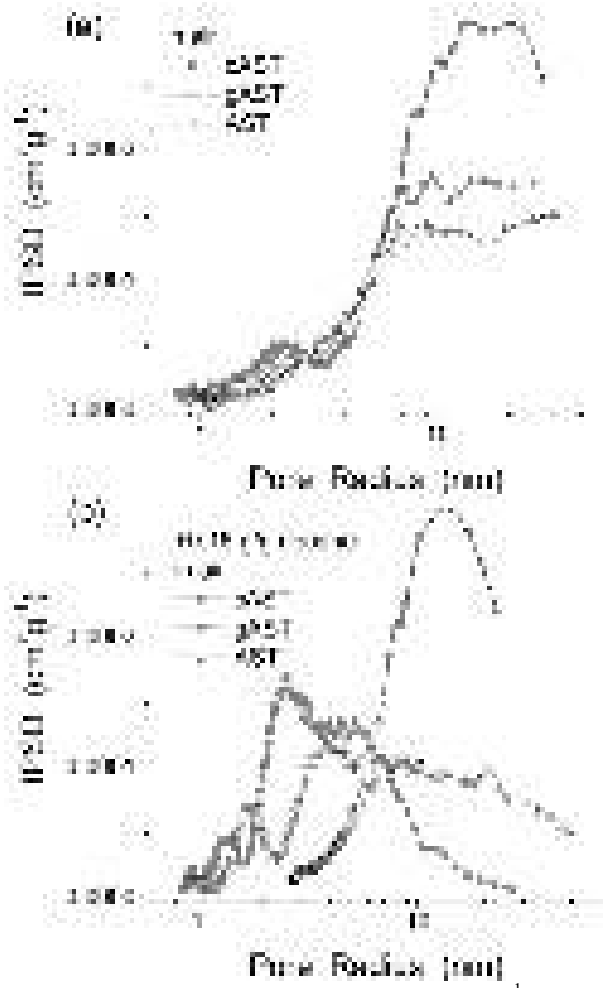

Fig. 111. Incremental PSD calculated from ^{1}H NMR spectra of water (0.1 g/g) bound to AST, gAST and cAST (b) with addition of *n*-decane in air.

Addition of NaCl (0.1M) into the aqueous suspensions of nanooxides sonicated before HPCG affected the textural and structural characteristics on the finished cryogels due to several reasons [46,47]. First, ice was much pure than water with respect to dissolved compounds. Therefore, concentrating NaCl solution occurred during HPCG that results in additional depression (besides the depression due to confined space effect) of the freezing point of interfacial water with dissolved NaCl. This could slightly reduce pressure caused by ice crystallites formed in the cryo-bombs. Second, interfacial water was characterized by lower activity as a solvent. Therefore, the formation of NaCl nanocrystallites could start during HPCG (and finish during drying of cryogels) and they could affect oxide inter-particle interactions. This could reduce the transformation of complex oxide nanoparticles, *e.g.,* cAST was composed of smaller nanoparticles than csAST due to stronger decomposition complex nanoparticles. Third, NaCl crystallites *per se* could affect the

textural characteristics of dried cryogels. However, this influence could not be strong since the amounts of NaCl were small (~2.8 wt.% in dried powders) and NaCl crystallites were relatively large up to 500 nm.

The difference between IPSD of initial powders and treated samples was smaller at $R < 2$ nm (contact zones between adjacent nanoparticles were only slightly compacted) than at $R > 10$ nm since the whole texture of aggregates and agglomerates undergoes significant rearrangement during HPCG, simple gelation or MCA in contrast to nanoparticles *per se* (Figs. 97, 103, and 112) [46,47]. MCA for 5 or 30 min gave small changes in the IR spectra in the range of the M–O (M = Si or Al) stretching vibrations in the SA13 blends (Fig. 113). These small changes of nanoparticles affected by MCA slightly touch crystalline structure of alumina (silica was amorphous) whose crystallinity increased, sizes of nanoparticles (decreased) and their electronic structure [47]. A decrease in the size of primary particles should result in increasing S_{BET}; however, enhanced contacts between adjacent nanoparticles could compensate this effect and the value of S_{BET} for MCA SA samples was smaller than that for HPCG or gelled samples [47].

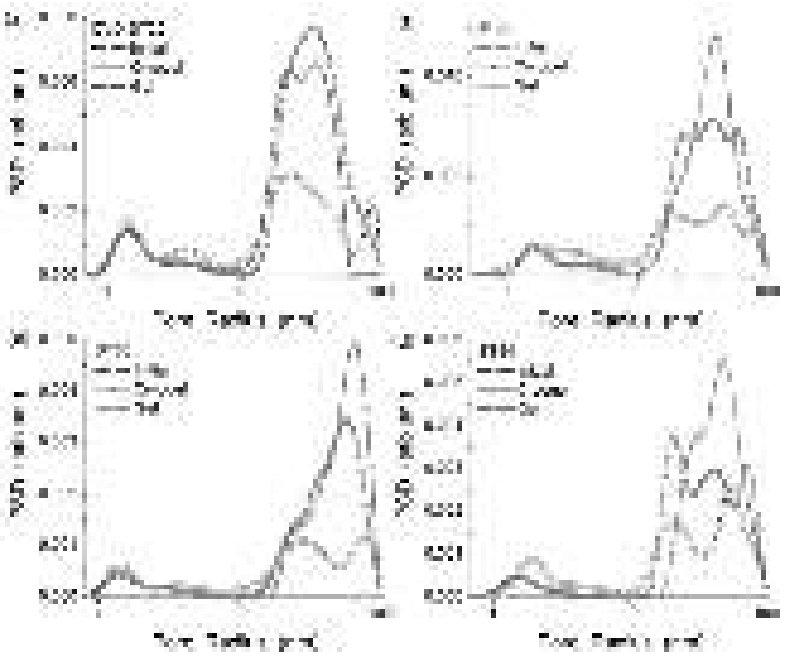

Fig. 112. Incremental pore size distributions (VCV/SCR method for silica and titania) (a) CVT-ST20 initial (curve 1), HPC (2) and gel (3), (b) ST63 initial (curve 1), HPC (2) and gel (3), (c) ST80 initial (curve 1), HPC (2) and gel (3), and (d) ST94 initial (curve 1), HPC (2) and gel (3).

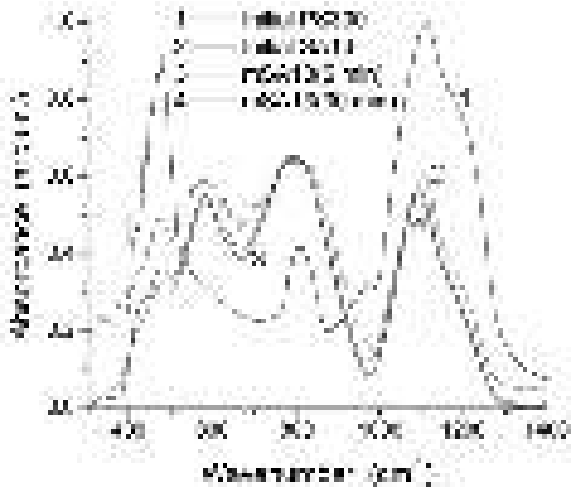

Fig. 113. Infrared spectra of initial PS300 (curve 1) and SA13 blend initial (2) and after MCA for 5 min (3) or 30 min (4).

During HPCG freezing temperature plays an important role because it could affect pressure in the freezing bombs [46,47,63]. AST sample was the most interesting among all nanooxides studied under HPCG [46,47] because it included a fraction of core-shell nanoparticles of a relatively large size (50-200 nm), which could be destroyed under HPCG. To analyze the temperature behavior of AST during HPCG, three regimes of freezing were used (Fig. 114) [47]. Two-step HPCG (sample c26077AST frozen at 260 K and then at 77.4 K) resulted in maximal compaction of AST since the hysteresis loop shifted toward smaller pressures (Fig. 114a) and the main IPSD peak shifted toward smaller pore sizes (Fig. 114b). A similar but slightly smaller effect was observed for c77AST after HPCG at 77.4 K. HPCG at 208 K (c208AST) resulted in weaker compaction of aggregates and agglomerates. However, the IPSD at $R < 5$ nm for all HPC samples were very similar (Fig. 114b). Thus, the destroying degree of the core-shell large nanoparticles was practically the same at these three temperature regimes, since the value of S_{BET} was the same for all HPCG AST samples and approximately twice larger than that of the initial AST powder [47]. However, rearrangement (compaction) of the secondary structures depended on the freezing conditions (Fig. 114) [46,47].

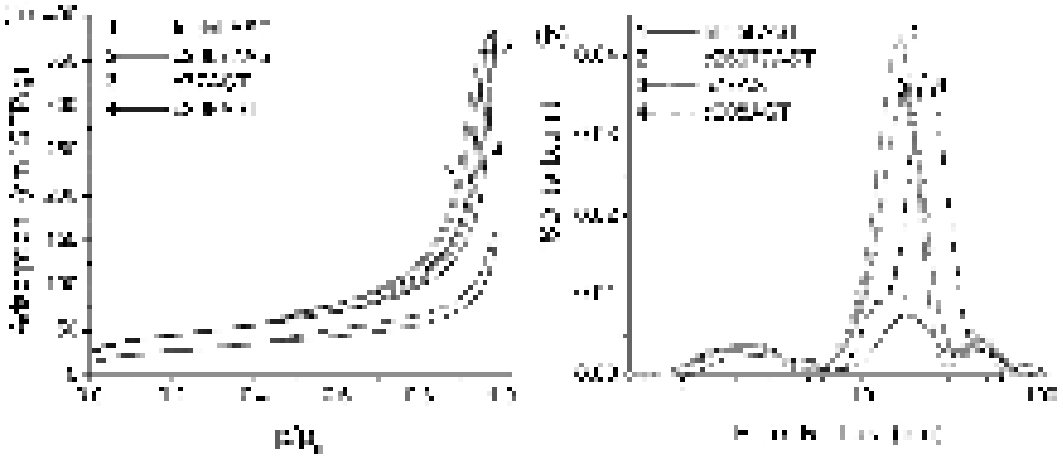

Fig. 114. (a) Nitrogen adsorption-desorption isotherms and (b) incremental pore size distributions (VCV/SCR method for alumina and silica) for initial dry powder AST (curve 1), cryogels prepared at (2) 260 K for 24 h and then 77.4 K for 4 h, (3) 77.4 K for 4 h, and 208 K for 12 h.

Unmodified and modified silicas and interfacial behavior of adsorbates

Fumed silica could be modified using a variety of reagents (e.g., a set of silanes) with different functionalities including simple hydrophobic groups (CH_3 and longer), groups with reactive bonds (C=C, N-H, etc.), polar groups (NH, COOH, CO, COH, SH, etc.) [1,11,37,38]. Typically, hydrophobicity of silica increased with increasing TMS content on the silica surface (Table 19) [53,72]. A decrease in the hydrophilicity (accompanied by an increase in intensity of the C–H stretching vibration bands of the TMS groups at 2970 and 2907 cm^{-1}) of modified silicas was accompanied by a decrease in the adsorption of water from air. This led to a reduction of intensity of the broad band of adsorbed water at 3300 cm^{-1} [72].

Table 19. Heat of immersion of unmodified and modified silicas in water and *n*-decane [72].

Θ_{TMS} (%)	Q_w (J/g)	Q_d (J/g)	$\beta = Q_w/Q_d$
0	48	22.0	2.0
27.2	39	24.5	1.6
37.2	33	24.0	1.4

Deconvolution of a broad band of the O–H stretching vibrations (into four bands for PS300 and six bands for partially hydrophobized nanosilica HS1 (Θ_{TMS} = 27.2 % substitution of SiOH by TMS groups) and HS2 (Θ_{TMS} = 37.2 %) due to the presence of two C–H bands [53]) gave integral

intensity of a band of strongly bound water or strongly disturbed silanols at 3290-3280 cm^{-1} as 68.2, 56.0, and 50.8 % for PS300, HS1, and HS2, respectively [72]. Relative contribution of slightly disturbed silanols at 3670-3680 cm^{-1} (which were poorly accessible for adsorbates) increased for modified silicas, since integral intensity of this band was 5.2, 7.8, and 8.1 % for PS300, HS1, and HS2, respectively. Notice that There was a slight broadening of a band of asymmetric Si–O stretching vibrations at 1150–1250 cm^{-1} of HS2 in comparison with PS300 (Fig. S75). This could be due to surface ≡Si–O–Si$(CH_3)_3$ groups (the spectra were normalized to the intensity of the band at 1867 cm^{-1} (which was the bulk silica overtone mode proportional to the total mass of silica probed by the IR beam and used as the inner standard) or 1100 cm^{-1} (Si–O stretching vibrations) of unmodified silica) [72]. Typically, a decrease in separation between the cooperative Si–O–Si asymmetric modes at 1100 cm^{-1} (*i.e.* band narrowing) in the IR spectra of silica was usually associated with an increase in the polymerization degree, *i.e.* an increase in the number of Si–O–Si bonds in larger particles [37,38,105,235]. However, it was difficult to suppose that silica nanoparticles' size decreased during silylation since the specific surface area of modified silica decreased. Therefore, the observed broadening could be assigned to the surface groups because their symmetric and asymmetric stretching vibrations could occur at higher frequency [72].

Calculations of the specific surface area according to the IR data [106] (using the normalized ratio of integral intensity of the bands at 1867 and 3750 cm^{-1}) give S_{IR} = 328, 296, and 250 m^2/g at Θ_{TMS} = 0 (PS300), 27.2 % (HS1), and 37.2 % (HS2), respectively. This reduction of the S_{IR} value could be due to two effects. First, real diminution of the specific surface area was due to attaching TMS groups. Second, diminution of the content surface silanols caused apparent decrease in the specific surface area since this content was used to estimate the S_{IR} value [106]. Thus, real diminution of the specific surface area was slightly smaller than the S_{IR} value showed [53]. The reduction of the specific surface area of modified silica with increasing modification degree was a typical effect [53,236,237]. Besides this surface area reduction, the adsorption potential also decreased with increasing Θ value with respect to both polar and nonpolar compounds and polymers [29]. Thus, the interfacial behavior of such co-adsorbates as methane or hydrogen and water could depend on several factors: (i) the textural characteristics *vs*. surface composition; (ii) changes in the adsorption potential; (iii) changes in clustered adsorption of water; (iv) freezing and melting points of co-adsorbates; (v) current temperature, and (vi) concentration of co-adsorbates and dispersion medium type. Some of these aspects were analyzed with low–temperature ^1H NMR measurements [72].

Partial silylation of PS300 (Θ_{TMS} = 27.2 and 37.2%) caused an increase in nanoparticle aggregation observed in the suspension with increasing Θ_{TMS} value (Fig. 115a-c). This could be explained by rearrangement of modified silica nanoparticles in aggregates to reduce the contact area between hydrophobic TMS groups and water molecules. Notice that the aggregation was higher for HS1 than for HS2 (Fig. 115). This could be explained by a greater nonuniformity of the surface at a lower degree of the silylation. Similar effects were observed for other samples [53,237,238]. However, the observed changes in aggregation were similar to typical changes in aggregation of different unmodified nanosilicas [238]; *i.e.*, they were not extensive since the silica surface was only partially hydrophobized. Changes in the zeta–potential of partially modified nanosilicas were relatively small compared to the initial silica (Fig. 115d). Only a portion of surface silanols was deprotonated in the used range of pH. The modified silica surface had enough number of silanols to provide a close value of the surface charges. Additionally, the zeta–potential was linked to average charging under slipping plane in the electrical double layer, EDL, around primary particles and their aggregates. Thus, partial silylation of the nanosilica surface led also to changes in a dense part of EDL [72].

A self-consistent electrostatic theory was used to predict disjoining pressure isotherms of aqueous thin-liquid films stabilized by non-ionic surfactants and air-water surface tensions and zeta potentials of electrolyte solutions with and without non-ionic surfactant. This model

combined specific adsorption of hydroxide ions at the interface with image charge and dispersion forces on ions in the diffuse EDL [239].

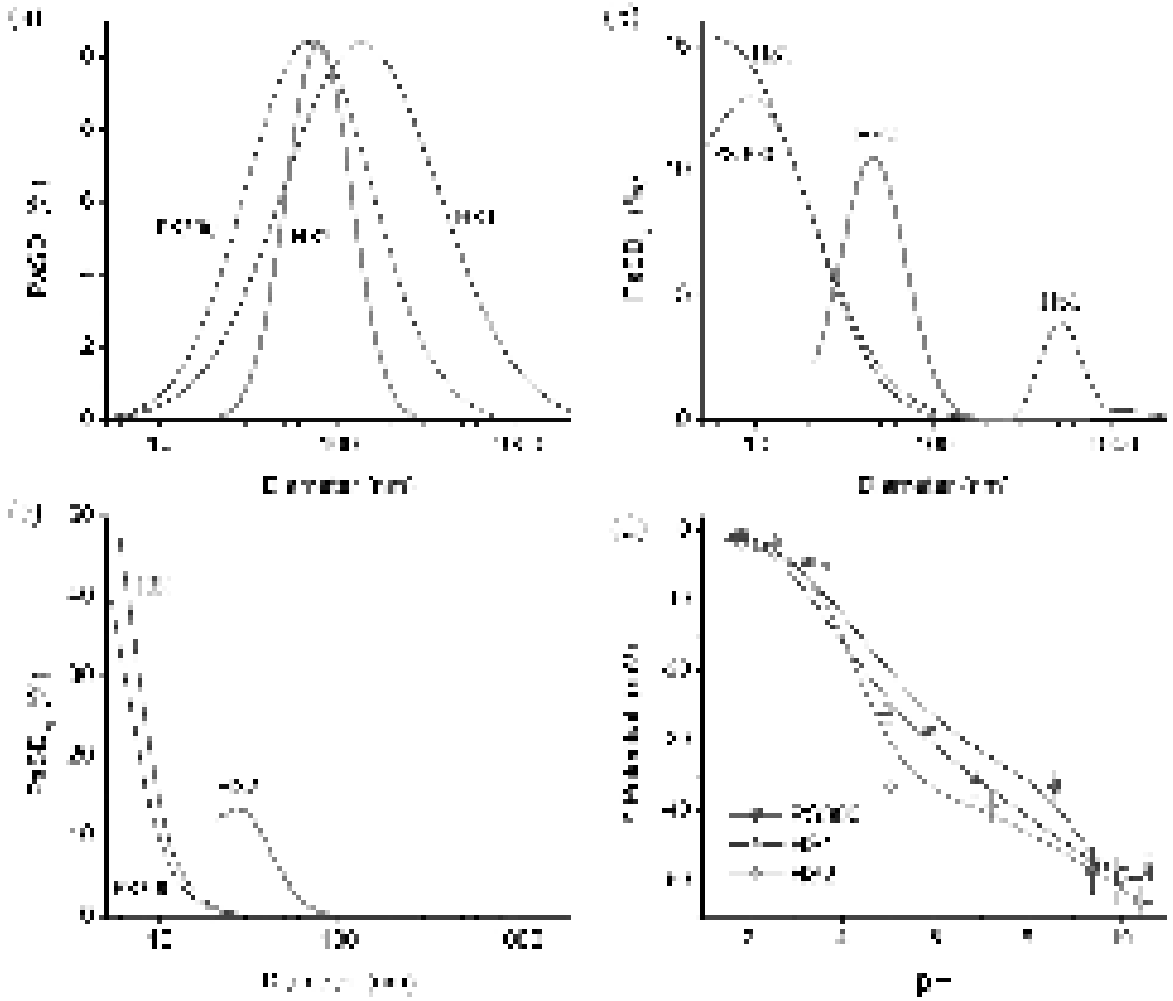

Fig. 115. Particle size distributions with respect to (a) scattered light intensity, (b) particle volume, and (c) particle numbers, and (d) zeta−potentials of PS300, HS1, and HS2 samples in the diluted (0.02 wt.%) aqueous suspensions.

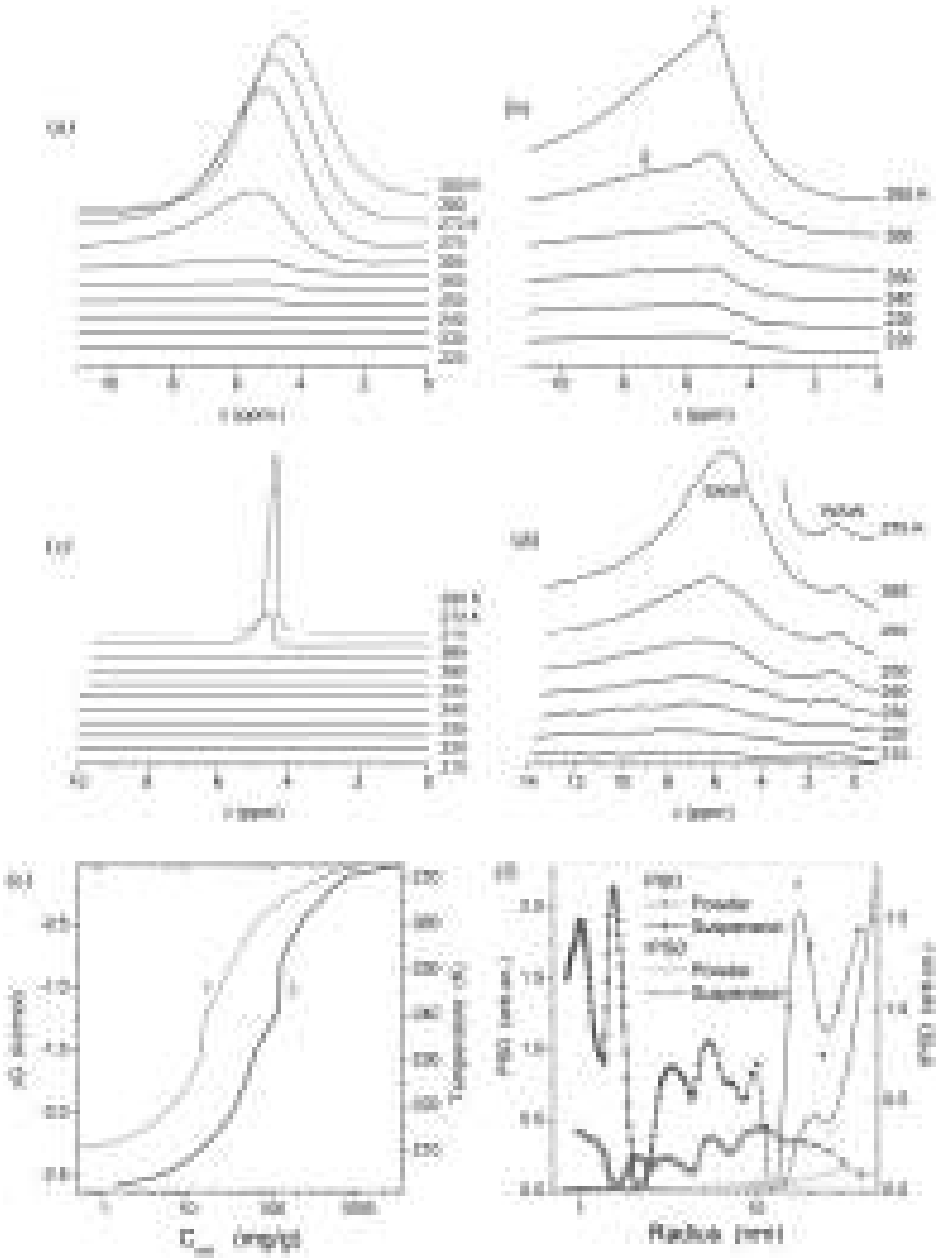

Fig. 116. ^{1}H NMR spectra recorded at different temperatures of water bound to modified PS300 (HS2, Θ = 37.2 %) for (a, b) wetted powder at h = 1.2 g/g and (c, d) aqueous suspension at h = 13 g/g, (e) amounts of unfrozen water C_{uw} *vs*. temperature and *vs*. changes in the Gibbs free energy of bound water (errors < ±10%), and (f) size distributions of unfrozen water clusters bound to silica in wetted powder and aqueous suspension (Figs. b and d correspond to subsets of Figs. a and c at low temperatures).

The mechanisms of the protonation of solid metal oxides and hydroxides in aqueous media were analyzed using theoretical approaches and experimental results [240]. The apparent acidity/basicity of each kind of surface sites of metal oxides and hydroxides in aqueous suspensions was strongly influenced by the overall surface charge of the materials and thus by the electrical potential smeared out at the interfacial region. Depending on its sign this increased or decreased the hydrogen ion concentration on the surface, thus promoting or hindering protonation. This was manifested by the shifts of the protonation peaks of the various kinds of sites with respect to the −pK values of the corresponding intrinsic protonation constants and the appearance of an extra peak in the $d[H^{+}_{cons,surf}]/dpH$ vs. pH curves. Potentiometric titrations experiments performed for four technologically important oxides showed that the proposed protonation mechanism describes indeed the protonation of polycrystalline oxides and hydroxides in aqueous media [240].

For modified nanosilicas in more concentrated aqueous suspensions, stronger aggregation could be expected than observed in [72] for the more diluted suspensions or for unmodified silicas [53,237,238]. Therefore, one could expect that the aggregation of modified silica nanoparticles could affect the interfacial behavior of water bound to a surface.

The forces acting in colloidal suspensions and affecting their stability and aggregation kinetics have been analyzed [241] and the approximations used for these forces in numerical simulations and the importance of the balanced account for both colloidal forces and hydrodynamic interactions have been discussed. Simulations were based on the Langevin equations with pairwise interaction between particles and take into account Brownian, hydrodynamic and colloidal forces. It was confirmed that the neglecting of hydrodynamic interaction results in an accelerated growth of aggregates. The results of numerical simulations of aggregation kinetics were compared with well-known analytical solutions [241].

Water adsorbed onto a surface of any adsorbent could exist in clusters due to nonuniformity of the surface (*e.g.,* mosaic coverage with surface hydroxyls) if the water amounts were relatively small (< 20 wt.% for nanosilica [53]). Additionally, bulk or bound water tends to form a maximum number of hydrogen bonds per molecule possible [53,242]. The appearance of hydrophobic TMS groups at a silica surface (with mosaic ≡Si–OH and ≡Si–O–Si$(CH_3)_3$ coverage) could affect the structure of bound water (Fig. 116, Table 20) [72]. At a relatively high hydration degree h = 1.2 g/g, water could form a continuous layer at the modified silica (HS2) surface. Therefore, the only signal observed was from strongly associated water (SAW) [53] in the ^{1}H NMR spectra (mobile at T < 273 K), identified by the chemical shift of the proton resonance δ_H = 5.0–5.5 ppm. These δ_H values were typical for hydrated silicas [53,218] and close to that of bulk liquid water. At 265 K < T < 273 K, a main fraction of this water was frozen. Therefore, it could be assigned to weakly bound water [53]. At low temperatures, two relatively weak signals were observed at 5 ppm (signal 1) and 7 ppm (signal 2) (Fig. 116b). On the basis of freezing temperatures and δ_H values, this water could be assigned to strongly bound water [53] of the SAW type. The δ_H value of signal 2 was close to that of ice. This ordering of interfacial water (similar to ice) could be caused by the effects of hydrophobic TMS groups on the water [53,242]. In the concentrated aqueous suspension at h = 13 g/g, besides the signal of SAW at δ_H = 4.5–6.0 ppm (Fig. 116c,d), a signal of weakly associated water was also observed at $\delta_H \approx 1$ ppm. This could be explained by water filling of adsorption sites at the surface in a confined space between neighboring TMS groups [72]. For wetted powder (h = 1.2 g/g), the degree of filling of adsorption sites by water is likely much lower (*i.e.*, the hydration shells of nanoparticles were nonuniform) than in the suspension. WAW corresponds to 1D, 2D or branched 3D clusters, in which a relative number of the H atoms in the hydrogen bonds was smaller than 50% [53]. The complex signal shape seen at 272.5 K and 280 K (Fig. 116c) may be due to nonuniformity of the modified silica [72].

For wetted powders, the greater the amount of adsorbed water, the smaller the fraction of strongly bound water [53]. The WBW fraction could increase with increasing water content because the amount of water distant from the adsorbent surface increased. For aqueous suspensions, three main types of water could be present: SBW, WBW and bulk (unbound water, UW) water, and one could expect that all of the water was SAW. There were two sections in the $C_{uw}(T)$ curves (Fig. 116e) corresponding to SBW (at lower Gibbs free energy, ΔG) and WBW (at higher Gibbs free energy) [72]. The amounts of SBW were 0.13 and 0.45 g/g for the wetted powder and the suspension, respectively, while the total volume of bound water was 0.965 and 4.325 cm^3/g, respectively (Table 20, V_{uw}). Contact area between bound water and the HS2 surface increased nearly five-fold in the suspension (Table 20, S_{uw}).

Table 20. Characteristics of unfrozen water bound to modified silica (HS2, Θ = 37.2%) at different conditions [72].

Sample	h (g/g)	V_{uw} (cm^3/g)	S_{uw} (m^2/g)	$S_{uw,nano}$ (m^2/g)	$S_{uw,meso}$ (m^2/g)	$S_{uw,macro}$ (m^2/g)	$V_{uw,nano}$ (cm^3/g)	$V_{uw,meso}$ (cm^3/g)	$V_{uw,macro}$ (cm^3/g)	γ_S (J/g)	$<T>$ (K)	$-\Delta G_s$ (kJ/mol)
Wetted powder	1.2	0.965	62	3	52	7	0.001	0.860	0.103	9.91±1.0	267.45	2.31±0.2
Suspension	13	4.325	287	47	143	97	0.022	2.628	1.675	34.86±3.5	267.96	2.62±0.3
Weakly wetted powder +CH_4	0.05	0.050	15	12	3	0	0.005	0.045	0	3.36±0.34	230.92	2.63±0.3
Nearly dry powder +H_2	0.005	0.005	0.3	0	0.3	0	0	0.005	0	0.12±0.01	258.33	1.63±0.2
Powder in $CDCl_3$+TFAA	0.05	0.038	19	15	4	0	0.007	0.031	0	2.49±0.25	242.27	2.63±0.3

Note. V_{uw} is the volume of bound water unfrozen at $T < 273$ K; S_{uw} is the specific area of silica in contact with unfrozen water; nano-, meso- and macro-components of S_{uw} and V_{uw} were determined by integration of the distribution functions at radius values of 0.3−1.0 nm (nano), 1−25 nm (meso), and 25−100 nm (macro); γ_S is the surface free energy (in J per gram of dry oxide); $<T>$ is the average melting temperature; and ΔG_s is changes in the Gibbs free energy of strongly bound water.

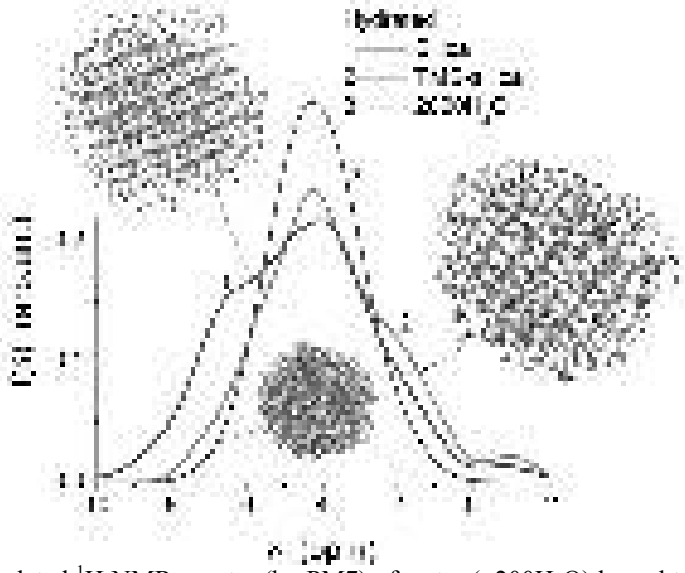

Fig. 117. Theoretically calculated ^{1}H NMR spectra (by PM7) of water (~200H_2O) bound to unmodified (curve 1, 828 atoms) or partially modified (curve 2, 1272 atoms) silica particle, and pure water with 2000H_2O (curve 3).

Therefore, contributions of structures of three types of water–filled nanopores (at radius R < 1 nm, $S_{uw,nano}$, $V_{uw,nano}$), mesopores (1 nm < R < 25 nm, $S_{uw,meso}$, $V_{uw,meso}$) and macropores (25 nm < R < 100 nm, $S_{uw,macro}$, $V_{uw,macro}$) all increased significantly. Changes in contacts between bound water and the HS2 surface caused an increase in the interaction energy. Therefore, the surface energy increased by several times (Table 13, γ_S), and the Gibbs free energy of the first adsorption layer (corresponding to SBW) decreased (ΔG_s). The γ_S values were calculated in J per gram of dry silica. Therefore, at a small content of adsorbed water these values were small (Table 20, h = 0.05 or 0.005 g/g). However, for wetted powder, the γ_S value was small despite h = 1.2 g/g that suggested weak interactions between water and HS2 [72].

The average melting temperature for water bound in the suspension was close to that for the wetted powder (Table 20, <T>) [72]. The <T> values for wetted powder and concentrated suspension suggest that WBW was predominant in both systems, in agreement with the dependences of C_{uw} *vs*. ΔG and T (Fig. 116e) showing that the major portion of bound water was WBW. This was also in agreement with the bound water cluster sizes (Fig. 116f), since water in larger clusters should be more weakly bound to the surface as their distance from the surface increased. There was a tendency of a decrease in the <T> value with decreasing hydration degree (Table 20). However, this also depended on other conditions (*e.g.,* compare systems at h = 0.05 and 0.005 g/g, Table 20).

According to theoretically calculated ^{1}H NMR spectra, water bound to nanosilica was characterized by a broader band exhibiting a larger contribution of water with downfield shift (Fig. 117, curve 1) in comparison with pure water (curve 3) [72]. Water (SAW) bound to silylated silica surface was characterized by an upfield shift with appearance of WAW at 1–2 ppm (Fig. 117, comp. curves 2 and 1) similar to experimentally observed spectra. These effects were due to enhanced clustering of water bound to TMS–silica with mosaic hydrophilic–hydrophobic patches, in comparison with water bound to an unmodified silica surface [72].

Methane molecules interacting with adsorbents due to weak van-der-Waals bonds could be effectively adsorbed only into nanopores or narrow mesopores. Therefore, methane adsorption onto nanosilica was relatively low, particularly on unmodified nanosilicas [53,72,104]. It was also shown that co-adsorbed water could increase the adsorption of methane. To increase methane adsorption, partially silylated nanosilica HS2 was used with a small amount of pre-adsorbed water (h = 0.05 g/g). This water, partially freezing at T < 273 K, could change the topography of the silica surface and the topology of voids between adjacent nanoparticles. Under these conditions, clathrate formation was impossible (clathrates only form at high pressures) and the low content of

water forming strongly clustered structures at residual silanols located between attached TMS groups [72].

HS2 with pre-adsorbed water (h = 0.05 g/g led to a larger content of SAW than WAW or SBW than WBW), various portions of which could be frozen at different temperatures, was a nonuniform adsorbent for methane (Fig. 118) [72].

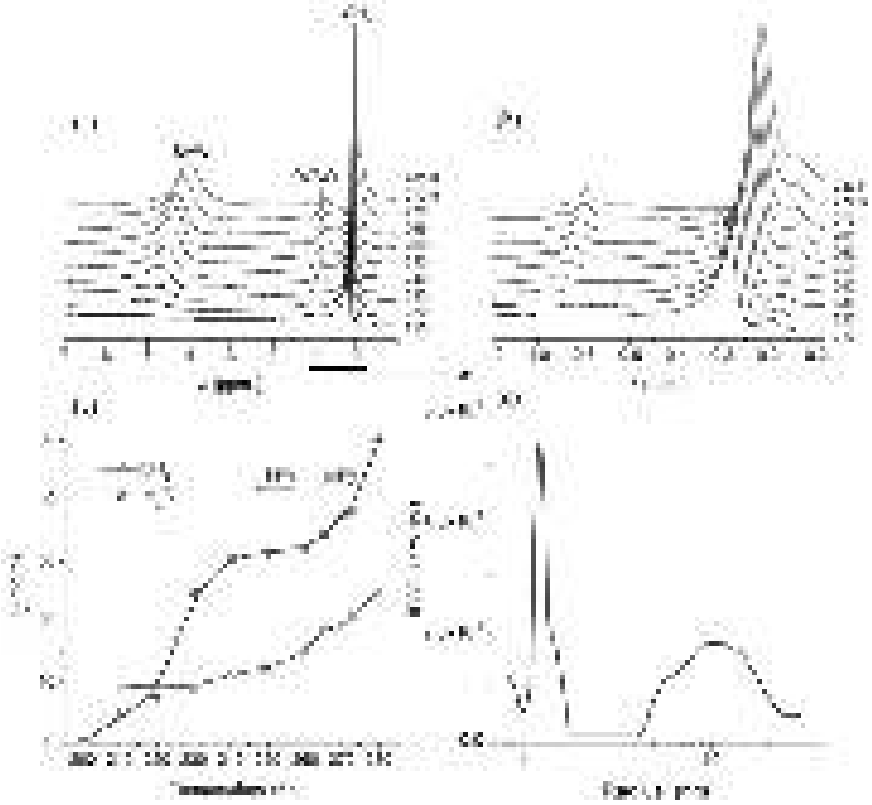

Fig. 118. (a, b) ^{1}H NMR spectra recorded at different temperatures of water and methane bound to HS2, (c) temperature dependences of concentrations bound unfrozen water and adsorbed methane (errors < ±10%), and (d) size distribution of voids filled by unfrozen water.

This nonuniformity was also observed in the distribution of unfrozen water structures filling voids between silica particles (Fig. 118d) and structural characteristics of voids filled by bound water (Table 20). Therefore, two signals of methane were observed in the ^{1}H NMR spectra at δ_H = –0.1 – 0.4 ppm (Fig. 118a,b). Signal intensity of methane increased with increasing temperature (Fig. 118a). The amounts of unfrozen water and adsorbed methane *vs*. temperature (Fig. 118c) demonstrated concerted changes at T > 240 K. This could be caused by changes in the topology of voids (pores) where melting of water occurred resulting in increased mobility of water molecules with increasing temperature. The observed downfield shift of methane signal with lowering temperature could be caused by the temperature dependence of the sample's magnetic susceptibility [243]. For weakly hydrated unmodified nanosilica (h = 0.005 g/g), methane adsorption decreased from 0.034 g/g at 200 K to 0.01 g/g at 280 K, opposite to the trend seen with the partially silylated nanosilica. With more highly hydrated unmodified nanosilicas when h = 0.045–0.15 g/g, methane adsorption was much lower (0.001–0.002 g/g) over this temperature range, again exhibiting decreasing adsorption with increasing temperature [104]. Thus, partial silylation of nanosilica caused changes in the adsorption trend of methane with temperature in comparison with the unmodified silica [72,104]. Water was adsorbed as SAW (4–5 ppm) and WAW (0.8–1.5 ppm) (Fig. 118a). The downfield shift was observed for both water types, and this shift was stronger for SAW possessing larger sizes. This occurred due to ordering of water clusters on freezing (*e.g.,* mobile water → amorphous ice → crystalline ice). Signal intensity decreased with lowering temperature due to water fraction freezing.

To study changes of confined space effects, additional water was added to the HS2 sample to form a wetted powder ($h \approx 1$ g/g), then stirred and heated at 400 K for 10 min (bulk density ~0.3 g/cm^3). The resulting sample contained a residual amount of bound water ($h = 0.005$ g/g). This water gave a broad ^{1}H NMR signal whose intensity could not be determined (Fig. 119a); therefore, the amount of adsorbed methane was given in arbitrary units (Fig. 119b). Estimation of the CH_4 signal noise level in the spectra of initial HS2 (Fig. 118a) compared to the additionally treated HS2 (Fig. 119a), suggests that the adsorption of methane onto treated HS2 was lower than on initial HS2. This may be a result of changes in the confined space effects and the amounts of co-adsorbed water located in narrow pores mostly able to bind adsorbed methane molecules. However, for the treated HS2, there was a larger temperature dependence of the adsorbed amount of methane than that for the initial HS2. This result could be caused by enhancement of confined space effects in compacted nanosilica [72].

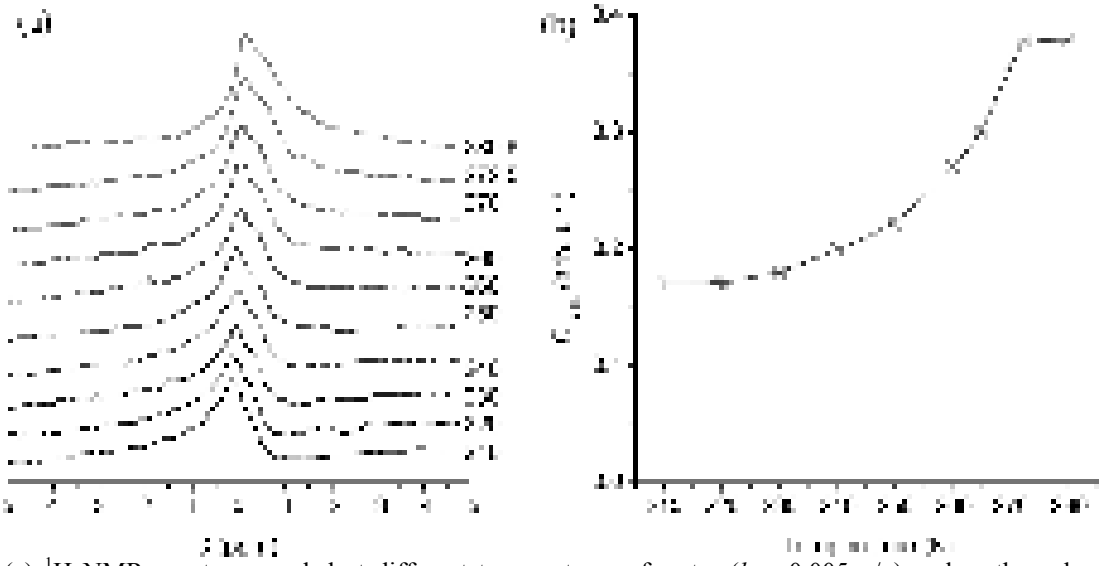

Fig. 119. (a) ^{1}H NMR spectra recorded at different temperatures of water ($h = 0.005$ g/g) and methane bound to compacted HS2, and (b) changes in the methane adsorption with temperature (errors < ±10%).

Theoretically calculated ^{1}H NMR spectra of water and methane in different structures (Fig. 120) showed that for the H atoms of methane molecules interacting with neighboring water molecules in $10CH_4@8H_2O$ (curves 4–6), There was a downfield shift of ~1 ppm. This led to a broadening of the methane band at 0–1 ppm (curves 4–6). The peaks at 3 and 5.5 ppm were linked to the water molecules from the same clusters. This splitting resulted from calculation features of clusters of restricted sizes, since experimentally there should be only one band due to fast molecular exchange. Changes in the DFT functionals (in GIAO calculations) and optimization type (DFT or HF) resulted in small differences in the spectra. Use of the PM7 method with the calibration function gave the spectrum of $10CH_4$ (Fig. 120, curve 3), which was close to that calculated using the GIAO method with B3LYP/6–31G(d,p)//HF/6–31G(d,p) (curve 2). Therefore, this approach was applied to a large system (Fig. 120, curve 7). A downfield shift for methane bound to hydrated TMS–silica nanoparticles was similar to that for $10CH_4@8H_2O$. WAW appears as a shoulder at 1–2 ppm (curve 7). SAW peak of maximum intensity was at 4 ppm, similar to the experimental data (Fig. 91a). Additionally, there was a shoulder at 6–7 ppm (Fig. 120, curve 7) similar to the experimental signal seen at low temperatures (Fig. 116b). These theoretical results confirmed interpretation of the experimental ^{1}H NMR spectra described above [72].

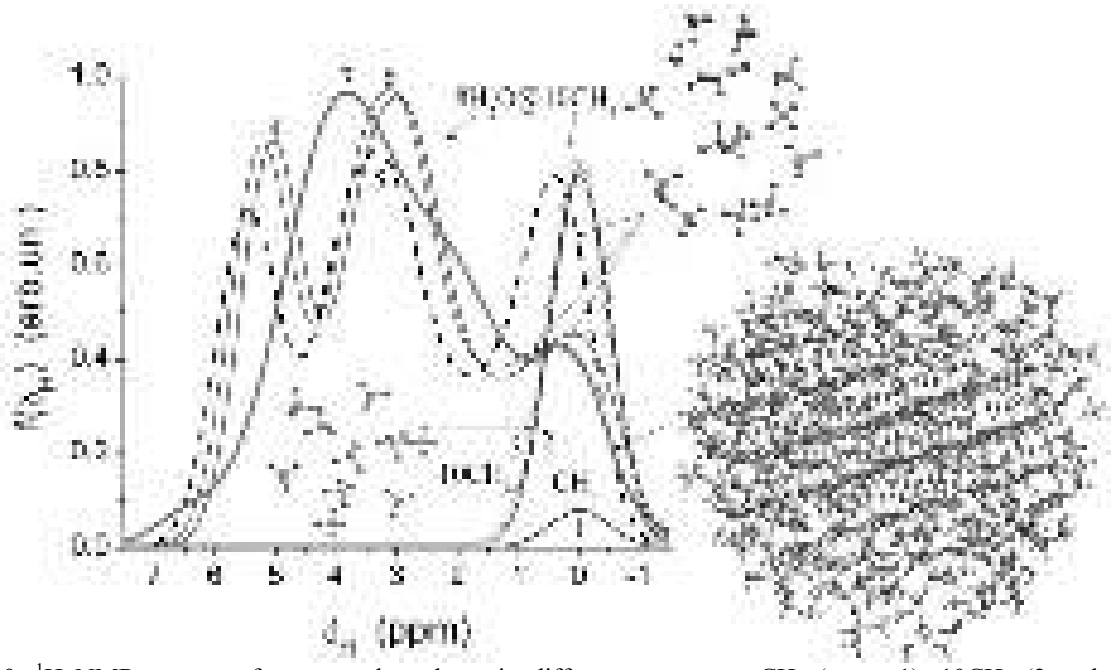

Fig. 120. ^{1}H NMR spectra of water and methane in different structures: CH_4 (curve 1), $10CH_4$ (2 and 3), and $10CH_4@8H_2O$ (curves 4–6) calculated with GIAO using B3LYP/6–31G(d,p)//HF6–31G(d,p) (curves 1, 2 (line), and 4) wB97XD//HF6–31G(d,p) (curve 5) or wB97XD (curve 6), and PM7 with a correlation function ($10CH_4$, 3 (symbols) and water molecules bound to TMS–silica nanoparticle with co-adsorbed methane molecules, curve 7).

Hydrogen is poorly adsorbed onto any adsorbent at normal pressure because of very weak van-der-Waals interactions. Nearly dry HS2 at h = 0.005 g/g was used here to study the interfacial behavior of hydrogen co-adsorbed with a small amount of pre-adsorbed water [72]. Adsorbed hydrogen was observed in the low-temperature ^{1}H NMR spectra as a broadened signal at δ_H = 4.5 ppm (Fig. 121a). This broadening suggested adsorption, since the resonance for H_2 gas would be much narrower at 4 ppm. The small upfield shift for adsorbed hydrogen was due to location of the electron density in the H_2 molecules mainly between the two protons. This led to a decrease in their magnetic shielding upon hydrogen adsorption. Residual water was observed as both SAW at δ_H = 4.0–4.5 ppm and WAW at δ_H = 1.0–1.5 ppm (Fig. 121a) [72]. Water was in a strongly clustered state, since its contact area with the HS2 surface was very small (Table 20, *S*). Additionally, there was a methane signal (added to hydrogen as a standard) at δ_H = 0 ppm. In contrast to hydrogen, water was frozen with lowering temperature that led to signal reduction at T < 260 K and its disappearance at $T \leq$ 220 K.

The adsorption of hydrogen onto HS2 was very low (≤ 0.2 mg/g) and smaller by an order of magnitude than that of methane. Hydrogen adsorption (Fig. 121b) increased with increasing temperature, similar to the behavior of adsorbed methane (Figs. 118 and 119). Notice that despite the low content of pre-adsorbed water (Table 20), it formed both smaller (~1–2 nm) and larger (10–30 nm) structures (Fig. 121c). This corresponded to known clustered adsorption of water [53] enhanced by partial silylation of the silica surface. Melting of ice nanocrystallites located in nanopores and narrow mesopores with increasing temperature, and enhanced mobility of water molecules, could free up a portion of these smaller pores. Such pores were better able to adsorb hydrogen molecules than larger mesopores. Therefore, the adsorption of hydrogen increased with temperature [72].

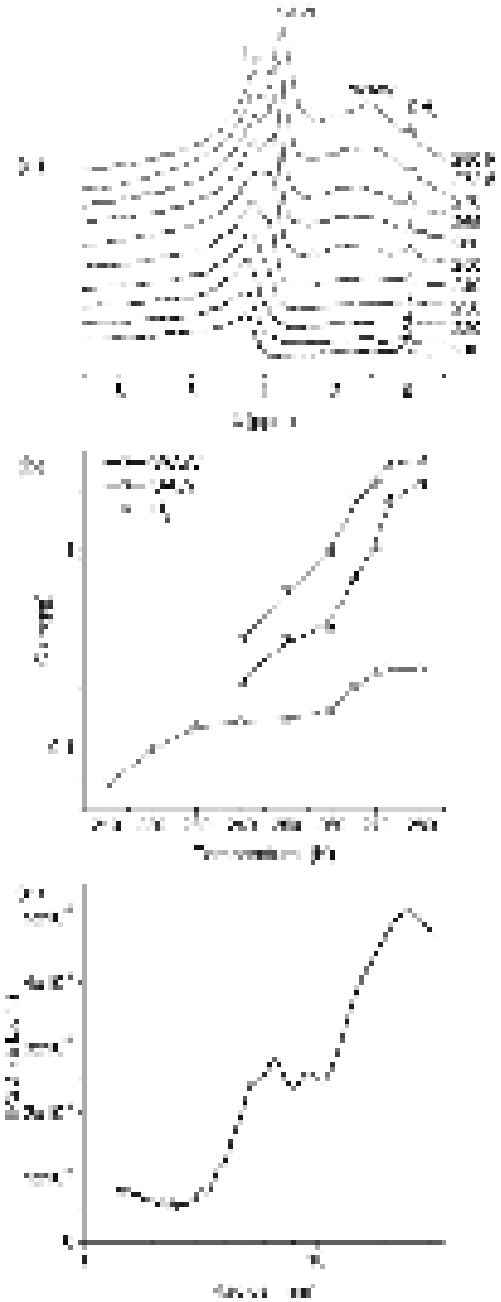

Fig. 121. (a) ^{1}H NMR spectra recorded at different temperatures of water (h = 0.005 g/g), hydrogen and methane bound to HS2, (b) amounts of WAW, SAW and hydrogen *vs*. temperature (average errors were smaller than ±10%), and (c) size distribution of pores filled by unfrozen water bound to HS2.

Nonpolar or weakly polar media could slow down molecular exchange between water molecules from different clusters and domains located at an adsorbent's surface. This could result in narrowing or even splitting of bands in the ^{1}H NMR spectra [53]. Addition of acids to the dispersion media allows one to differentiate several types of SAW, which could dissolve acids or salts differently [46,53,244]. Typically, interfacial WAW could not dissolve the acids. Here trifluoroacetic acid (TFAA) was added to chloroform-*d* medium (C_{TFAA} = 15 wt.% in $CDCl_3$). Before addition of TFAA, bound water was observed as SAW at 3.5 ppm at 280 K and 5 ppm at 210 K, as well as WAW at δ_H = 1.0–1.5 ppm (Fig. 122a,c). The intensity of the SAW signal decreased more rapidly than the WAW signal (Fig. 122c). Besides these signals of interfacial water, signals of $CHCl_3$ (as an admixture in $CDCl_3$) and tetramethylsilane (as a chemical shift standard added to $CDCl_3$) were also observed. From comparison of the ^{1}H NMR spectra of water bound to HS2 without [72] and with $CDCl_3$ (Fig. 122a), a disordering of SAW was observed due to the weakly polar liquid dispersion medium. Evidence of disordering came from δ_H values being

smaller in the presence of $CDCl_3$, and the SBW amount decreased from 0.035 g/g to 0.023 g/g. This was due to the displacement of a portion of bound water from the silica surface by $CDCl_3$ (Table 20, *S*, *V*) leading to a decrease in the γ_S value, and an increase in $<T>$. Despite the low water content (h = 0.05 g/g), several types of water structures including nanoclusters at R < 1 nm, larger clusters (R = 1–10 nm) and domains (R > 10 nm) were observed (Fig. 122d, Table 20) [72].

Addition of TFAA resulted in significant downfield shifts of SAW signals (δ_H = 12–13 ppm) due to fast proton exchange between TFAA and water molecules (Fig. 122b) [72]. At T > 240 K, two SAW signals (signals 1 and 2, Fig. 122b) corresponding to different amounts of dissolved TFAA (more dissolved TFAA for water with signal 1) were observed. Besides SAW with TFAA, a weak signal of SAW without dissolved TFAA (signal 3) was observed at 4 ppm. At 273–250 K, signal 2 decreased more than signal 1, and a downfield shift was observed for signals 1 and 2. But at T < 250 K, an upfield shift was observed in parallel to a strong decrease in signal intensity due to freezing of both TFAA and water. Besides signals of SAW, signals from WAW at 1.0–1.5 ppm were observed (Fig. 122b). The chemical shift of WAW was the same with and without TFAA suggesting that WAW did not dissolve TFAA [72].

Theoretical calculations of the ^{1}H NMR spectra (GIAO/DFT) of hydrated TFAA in molecular and ionized states (Fig. 123) suggested that signals 1 and 2 (Fig. 122b) may be caused by hydrated TFAA in similar states [72].

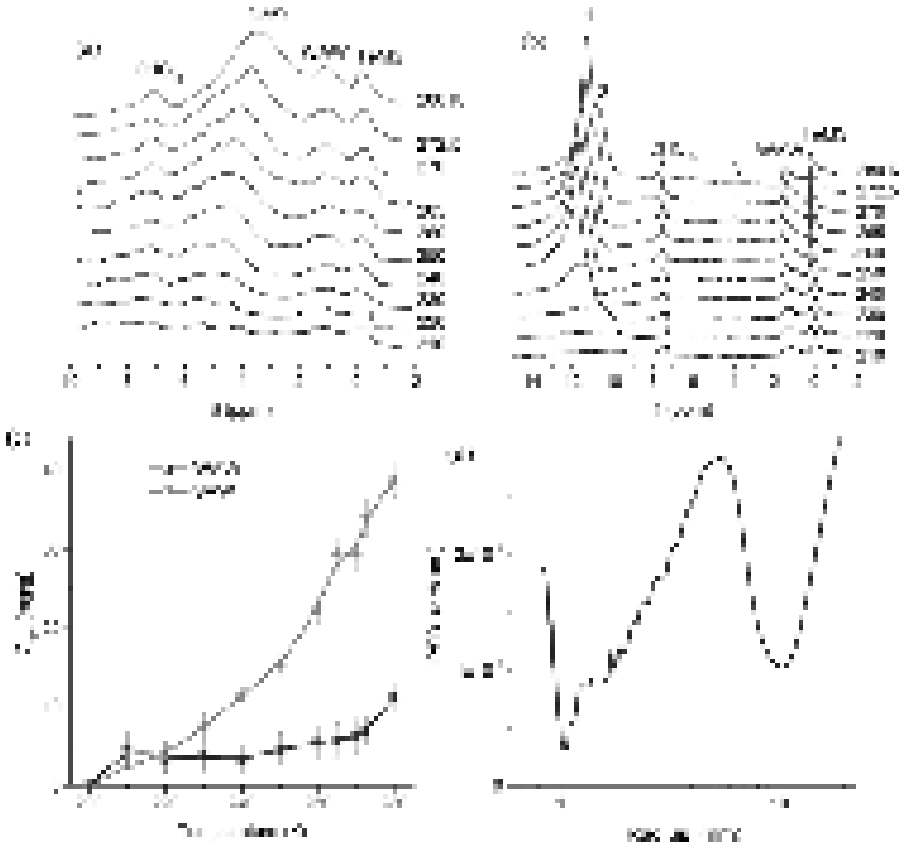

Fig. 122. ^{1}H NMR spectra recorded at different temperatures of water (h = 0.05 g/g) bound to HS2 in the $CDCl_3$ dispersion medium (a) without and (b) with addition of TFAA (15 wt.% with respect to $CDCl_3$ amount), (c) amounts of SAW and WAW *vs*. temperature without TFAA, and (d) size distribution of water structures without TFAA.

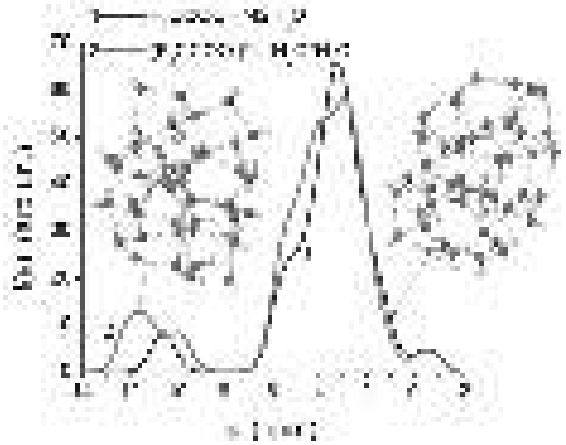

Fig. 123. ^{1}H NMR spectra of hydrated TFAA in molecular (curve 1) or ionized (curve 2) state calculated with GIAO/B3LYP/6−31G(d,p)//HF/6−31G(d,p).

Despite partial hydrophobization (heterogenization resulting in a mosaic surface with hydrophilic and hydrophobic patches) of the PS300 surface by attachment of TMS groups (Θ_{TMS} = 37.2%), modified silica could bind significant amounts of water (up to ~5 g/g) in an aqueous suspension. However, only approximately 0.5 g/g of this water was strongly bound while the major fraction of water was weakly bound. The presence of surface TMS groups caused the appearance of weakly associated water (at chemical shift δ_H = 1–2 ppm) at the interfaces, even in the aqueous suspension of TMS−silica. The adsorption of methane onto partially silylated nanosilica with pre-adsorbed water (0.05 g/g) increased with temperature in contrast to the adsorption of methane onto unmodified silica where a reduction of methane adsorption was seen with increasing temperature. It was believed that changes in both confined space effects and the temperature dependent organization of interfacial water may explain these results [72].

Changes in the organization of interfacial water were observed upon changes in the types of dispersion media and co-adsorbates [72]. In weakly polar $CDCl_3$ medium, interfacial water existed in states that were strongly (chemical shift δ_H = 4–5 ppm) and weakly (δ_H = 1–2 ppm) associated, as well as strongly (changes in the Gibbs free energy $-\Delta G$ > 0.5–0.8 kJ/mol) and weakly ($-\Delta G$ < 0.5–0.8 kJ/mol) bound [53]. Water in these different forms resulted in differences in their activity as solvents. WAW did not dissolve trifluoroacetic acid, but some SAW could dissolve TFAA. In addition, the SAW activity differs for different fraction of SAW (*e.g.,* located in narrower and broader pores). This appeared as downfield and upfield shifts of water/TFAA clusters and domains with temperature. Therefore, the increase in the adsorption of methane onto partially silylated nanosilica with increasing temperature could be explained by enhanced mobility of unfrozen water which was displaced from some narrow pores, and these pores could be occupied by methane [72].

Typically, water confined in narrower pores was characterized by a smaller average number of the hydrogen bonds per a molecule [53,245]. Therefore, the value of δ_H of confined water decreased in comparison with bulk water (Fig. 124). Notice that $\delta_H \approx 1$ ppm was observed for individual water molecules in the gas phase or dissolved in nonpolar or weakly polar organic solvents, $\delta_H \approx$ 4-5 ppm was for bulk water and $\delta_H \approx 7$ ppm was for Ih ice [53]. The hydrogen bond network structure of bound water differed from that of bulk water or ice and depended on the topology of pores and chemical composition of the pore walls affecting the energy of the hydrogen bonds (ΔE_H) [53]. The hydrogen bonds between water molecules and active surface sites (hydroxyls) of silica or other oxides were stronger ($-\Delta E_H$ = 40-50 kJ/mol) than the hydrogen bonds between water molecules ($-\Delta E_H$ = 25-28 kJ/mol) [53]. Therefore, the heat of water adsorption on hydrophilic adsorbents was greater than the latent heat of bulk water condensation (Q = 45 kJ/mol). This led to reduction of the Gibbs free energy (ΔG < 0) of interfacial water in comparison with the bulk depending on the pore size

and chemical structure of the pore walls [245].

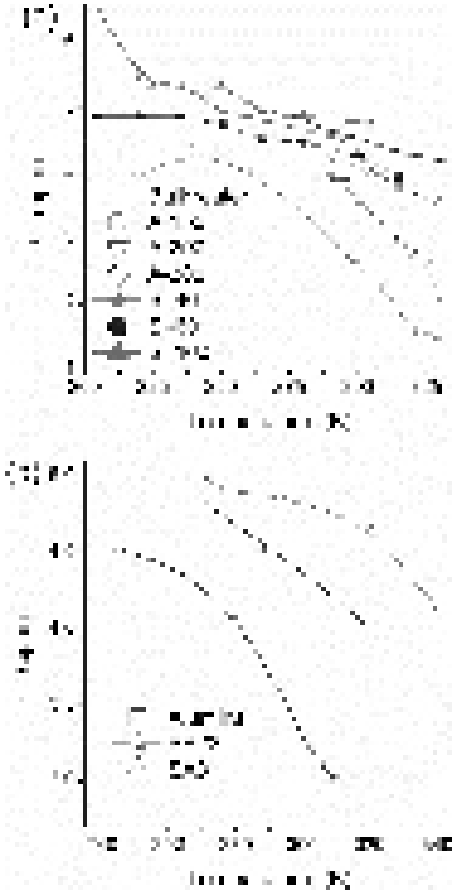

Fig. 124. Temperature dependence of the δ_H value for bulk water (line without symbols) and water adsorbed on (a) nanosilicas and silica gels at h = 0.21 (A-150), 0.163 (A-200), 0.24 (A-380), 0.12 (Si-40), 0.115 (Si-60), and 0.114 (Si-100) g/g, and (b) fumed alumina and SA at h = 0.2 (Al_2O_3), 0.37 (SA3) and 0.223 (SA23) g/g.

The δ_H values of bound water characterize both topological and surface nature effects on this water (Fig. 124) [53,245]. The values of δ_H were larger for water adsorbed on mesoporous silica gels than on fumed silica, alumina and SA composed of nonporous primary nanoparticles forming aggregates and agglomerates of aggregates [245].

Features of the primary particle size distribution ($\varphi(a)$) and their aggregation in secondary particles (*i.e.* textural porosity characteristics) influence the diffusion of water molecules in concentrated aqueous suspensions of nanosilicas [53]. Therefore transverse relaxation time (T_2) was two-three times longer (*i.e.* the molecular mobility was higher) for water in the aqueous suspensions of A-50 (average diameter of primary particles $d \approx 52$ nm) than that for A-300 ($d \approx 9.3$ nm) at the same silica concentrations. Additionally, the temperature effects were stronger for the A-50 suspension. In other words, at the same weight concentration of nanosilicas, water was more strongly bound in the suspension with smaller particles (A-300) because of larger amounts of the interfacial water in the suspension of A-300 (by several times) because this silica had much larger S_{BET} value and more strongly aggregated primary particles than A-50. The ^{1}H NMR spectroscopy investigations of a variety of nanosilicas and other oxides showed that concentrations of surface hydroxyls and their acidity could strongly influence the amounts and characteristics of bound water in the aqueous suspensions [53]. Therefore, not only the morphology, the $\varphi(a)$ distributions, and the S_{BET} values but also the surface structure of nanoparticles could affect the molecular mobility, the dipolar and direct current (dc) relaxations and other dynamic processes in interfacial water [245].

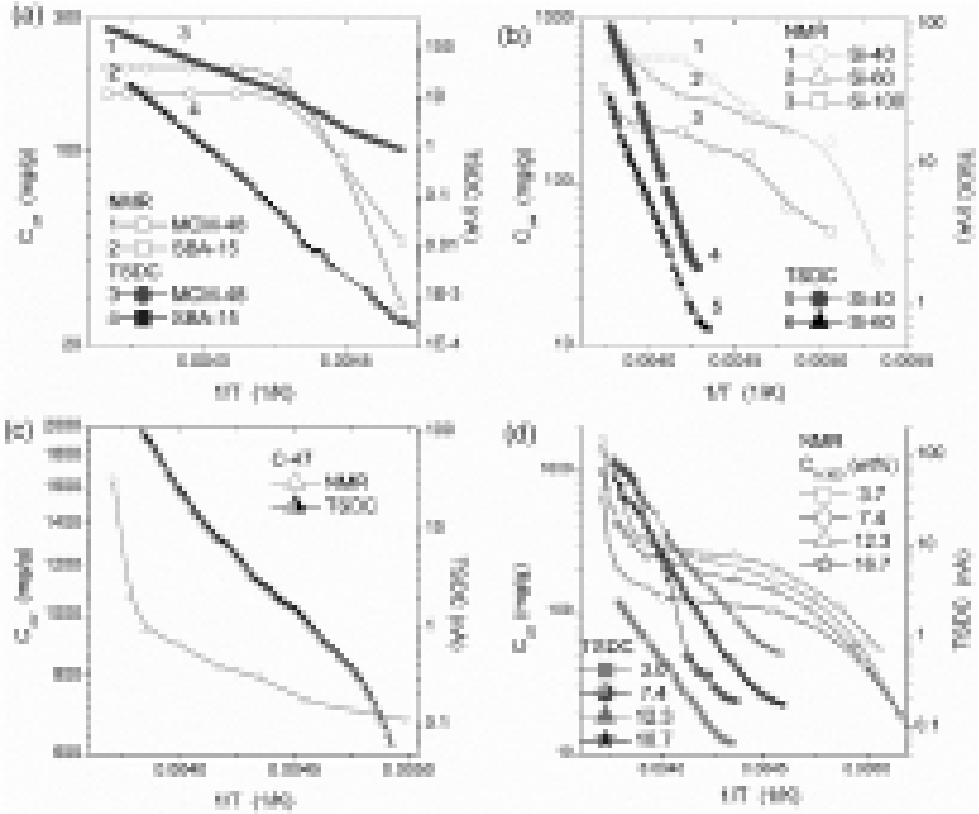

Fig. 125. Temperature dependences of the amounts of unfrozen water (C_{uw}) and TSD current (dc) on the adsorption of water on (a) ordered mesoporous silicas MCM-48 (hydration h = 0.25 (NMR) and 5 g/g (TSDC)) and SBA-15 (0.19 (NMR) and 5 g/g (TSDC), (b) silica gels Si-40, Si-60 and Si-100 (h = 19 (NMR) and 5 g/g (TSDC)), (c) activated carbon C-47 (h = 4.71 (NMR) and 13.3 g/g (TSDC)); and (d) nanosilica A-300 at $C_{A\text{-}300}$ = 3.0 (TSDC, $h \approx$ 32.3 g/g), 3.7 (NMR, $h \approx$ 26.0), 7.4 ($h \approx$ 12.5), 12.3 ($h \approx$ 7.1) and 16.7 wt.% ($h \approx$ 5.0 g/g).

The ^{1}H NMR spectra were linked to mobile water molecules [53] but the dc relaxation (TSDC) [214] was caused by mobile protons and other ions when condition of throughout percolation of ions (between two electrodes in a TSDC cell) was achieved on heating of a frozen system [53,245]. Both dynamic phenomena were temperature dependent (Fig. 125). For all samples, a linear dependence of ln(I_{TSDC}) versus 1/T was observed for the dc relaxation; *i.e.* it obeys the Arrhenius law. The mobility of water molecules (NMR) demonstrated more complex character caused by non-Arrhenius or several Arrhenius processes since two-three linear portions were observed for the curves of ln($C_{uw}(T)$) versus 1/T [245]. This effect could be explained by the presence of several types of interfacial water (*i.e.*, SAW, WAW, SBW and WBW) located in different pores at different distances from the oxide surfaces [53] and responsible for different local molecular mobility of interfacial water observed at different temperatures (due to layer-by-layer freezing-out of confined water with lowering temperature). Additionally, certain cooperative effects could be observed in water bound in nanopores or interacting with surface functionalities because of a clustered structure of bound water characterized by a dense hydrogen bond network that led to cooperative relaxations of water clusters or nanodomains [53,214]. Typically, a more complex and broader PSD led to a more complex lnC_{uw}(1/T) function (Fig. 125) [245].

The complexity of the behavior of interfacial water reflecting in complex temperature dependences of the molecular mobility and related characteristics reflected in a broad distribution of the activation energy of the local molecular mobility (LMM) at E_{LMM} = 5-83 kJ/mol (NMR) and the dc relaxation at E_{dc} = 46-98 kJ/mol (TSDC) calculated assuming that the processes obey the Arrhenius law, and typically $E_{LMM} < E_{dc}$ for the same systems [245]. The E_{LMM} values were greater for the suspensions with A-300 (maximal values E_{LMM} = 46 and 52 kJ/mol at h = 7.1 and 5 g/g, respectively) than E_{LMM} for porous silicas: 40 (MCM-48), 25

(SBA-15), 34 (Si-100), 18 (Si-60) and 21 kJ/mol (Si-40) [245]. These results could be due to larger S_{BET} values of porous silicas than that of nanosilicas and stronger confined space effects in narrower pores. These effects led to diminution of the average number of the hydrogen bonds per a molecule that diminish the E_{LMM} values. Calculations of the distribution functions of activation energy ($f(E)$) of the local mobility (NMR) [53] and the dipolar and dc relaxations (TSDC) [6] in the interfacial water at a surface of polymer adsorbent LiChrolut EN [214] (Fig. 126) and nanosilica A-300 (as representative samples with high nanoporosity (C-47) or textural porosity (A-300)) revealed the presence of several dynamic processes in bound water studied by both methods. The dipolar relaxation (TSDC) [214] was observed at temperatures (90 K < T < 210-220 K) lower than that characteristic for appearance of the local molecular mobility (NMR) [245].

The throughout molecular mobility causing the dc relaxation (TSDC) appeared at higher temperatures (T > 210-230 K) than local molecular mobility (NMR) and both processes depended (but differently) on the confined space effects [245]. These results were due to the influence of surface electrostatic fields on the structure of the hydrogen bond network in interfacial water (*i.e.*, the average number of these bonds per a molecule and their strength) and due to additional conditions necessary for the dc relaxation (ion percolation) in comparison with the local molecular mobility. An increase in the content of an adsorbent (and therefore contribution of interfacial water) led to diminution of the low-temperature (LT) peak of the dipolar relaxation at 120 K characteristic for bulk water and related to the dipolar relaxations of OH groups in small clusters (without the cooperative effects) and the relaxation of interstitial water molecules (without the hydrogen bonds and $\delta_H \approx 1$ ppm) [53,245].

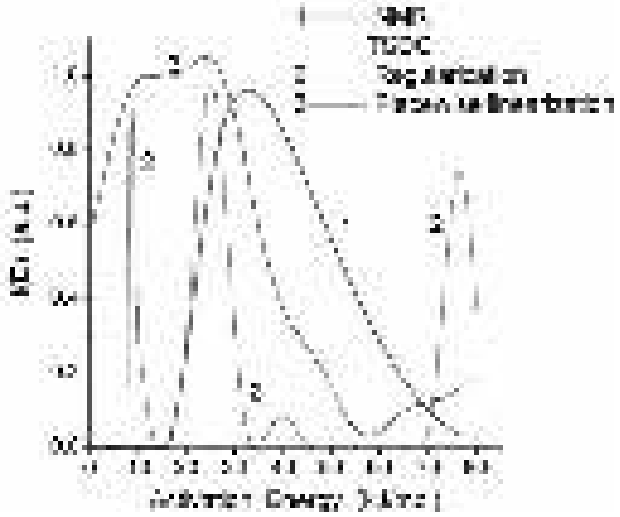

Fig. 126. Distribution functions of the activation energy of the mobility of water molecules at a surface of polymer LiChrolut EN adsorbent calculated on the basis of the ^{1}H NMR data (curve 1, hydration h = 2 g/g) and dipolar and dc relaxation (TSDC, curves 2 (regularization) and 3 (piecewise linearization), h = 5.4 g/g).

Complex nanooxides (silica/alumina and silica/titania) have strong Brønsted acid sites (≡SiO(H)M≡ where M = Al or Ti) and a set of weaker sites (bridging (≡MO(H)M≡) and terminal (≡MOH, ≡SiOH) hydroxyls, Lewis acid sites, *etc.*) that affected the behavior of interfacial water (Fig. 97) [53,245]. The chemical nonuniformity of the SA, ST or AST surfaces could cause a stronger non-Arrhenius character of the dc relaxation and the molecular mobility in the aqueous suspension (Fig. 127) in comparison with nanosilica [245]. The molecular mobility of interfacial water appears in the aqueous suspensions of SA at lower temperatures than that for nanosilica (Fig. 100). However, the dc relaxation began at temperatures close to that for nanosilica. Consequently, changes in the local structures in interfacial water and the temperature behavior of this water (NMR) more strongly depended on the oxide surface structure than the ion percolation effects (TSDC) depended on the composition of oxide particles and their aggregation in the suspensions [245].

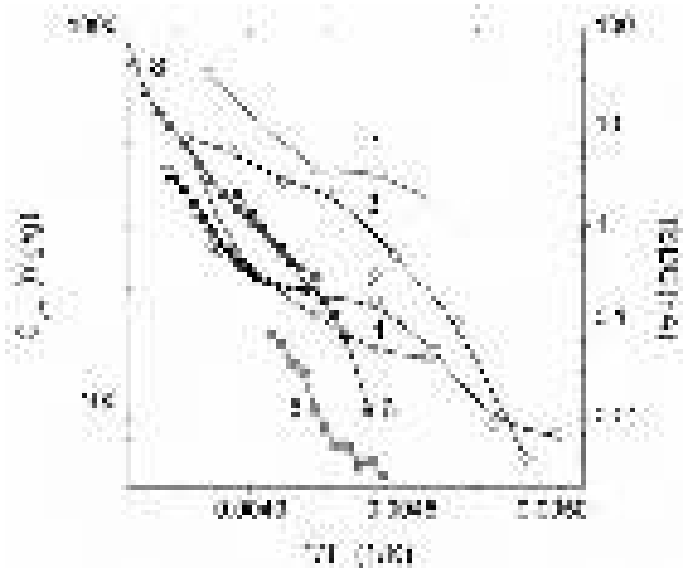

Fig. 127. Amounts of unfrozen water (NMR, curves 1-4) and dc relaxation (TSDC, curves 5-8) as functions of reciprocal temperature for fumed Al_2O_3 (curves 1 and 5), SA1 (2 and 6), SA3 (3 and 7) and SA23 (4 and 8) at C_{ox} = 5 wt.% (1-4) and 3 wt.% (5-8).

Comparative investigations of water confined in pores of solid materials and bioobjects using the ^{1}H NMR, TSDC and microcalorimetry methods showed that the difference in temperature of transition from the local molecular mobility of water bound at the pore walls or intracellular functionalities to ion percolation effects (throughout conductivity) could be 10-40 K [245]. This value depended on several factors such as the morphology of particles, textural and structural characteristics of adsorbents, chemical structure of the surfaces, concentrations of components, the presence of dissolved salts (*e.g.*, NaCl) and other compounds. There were four types of water confined in solid adsorbents and bioobjects such as strongly ($\Delta G < -1$ kJ/mol) and weakly ($\Delta G > -1$ kJ/mol) bound and strongly (δ_H = 4-5 ppm) and weakly (δ_H = 1-2 ppm) associated waters. At low amounts of adsorbed water (much smaller than the pore volume) typically all water was strongly bound. A portion of this water could be weakly associated if the pore walls were mosaic and composed with hydrophilic and hydrophobic patches, *e.g.*, for partial silylation of silica surface. The local molecular mobility of bound water depicted a non-Arrhenius character or included several Arrhenius-type processes characterized by different activation energies because the corresponding water was differently clustered and bound to different structures at the interfaces. Therefore, the dynamic characteristics of these types of bound water could significantly differ. The temperature dependence of ion percolation in bound water has the Arrhenius character for relatively uniform systems such as the aqueous suspensions of nanosilica or mesoporous silicas. However, for complex materials (*e.g.*, complex nanooxides) or adsorbents possessing both broad and very narrow pores (*e.g.*, activated carbons) certain deviations from the Arrhenius behavior were observed on the dc relaxation. The behavior of interfacial water depended strongly on the presence of nonpolar or polar organic solvents which could displace a portion of water from narrow pores into larger ones, change the associativity of bound water and its interaction energy with solid surfaces or intracellular functionalities. Water and polar organics confined in narrow pores were much poorly complex than in the bulk that led to enhanced clusterization of water bound to the mosaic surfaces [53,245].

The ^{1}H NMR spectra of mobile water and water/methane at $T < 273$ K were recorded without the use of the MAS technique [53,104]. The spectral bandwidth (non-MAS) of surface silanols and OH groups from ice was much broader than mobile water. However, immobile OH structures could affect the baseline of the spectra of mobile water bound to silicas characterized by different PSD (Fig. 128). The values of δ_H of free unbound silanols was 1.5-2.0 ppm (Fig. 129, rotor frequency f_r = 9 kHz, curve 2) [218-222]. This band was absent for A-300 at h = 0.05 (Fig.

129, curve 1, f_r = 0 kHz) and 0.08 g/g [104]. However, the O-H stretching vibrations of free silanols were observed at 3747 cm^{-1} in the FTIR spectra of A-300 at a similar h value, because free silanols could be observed at the nanosilica surface at $h < 0.2$ g/g due to clustered adsorption of water [53]. The bands at δ_H = 1-2 ppm (*i.e.* in the range of free silanols observed in the ^{1}H MAS NMR spectra of silica (Fig. 129) [218-222]) were observed for silica 200DF at $h \approx 0.005$ g/g [104]. However, intensity of these bands decreased with lowering temperature and they were not observed at 210 K. This behavior was more characteristic of weakly associated but strongly bound water than for free silanols [53]. Additionally, the O-H stretching vibrations of free silanols were not observed for silica 200DF; *i.e.* all the SiOH groups were hydrogen bonded [104]. Notice that a small portion of water could be dissolved in chloroform and contribute to the spectra at $\delta_H \approx 1.2$ ppm. The band at δ_H = 3-4 ppm, which was not observed at $T < 240$ K, could be assigned to strongly associated water with a major fraction of weakly bound water (frozen at $T > 260$ K). As a whole clustering of water adsorbed on nanosilica diminishes with increasing amounts of water; *i.e.* it became more strongly associated [53]. Therefore ^{1}H NMR signal intensity decreased faster with lowering temperature for A-300 than 200DF with a greater amount of adsorbed water, which was readily seen at $T \leq 240$ K. Thus, this NMR technique allowed one to observe the ^{1}H NMR spectra of mobile water, in contrast to the ^{1}H MAS NMR technique giving the spectra of all OH structures (silanols, bulk and adsorbed liquid and frozen water). This technique, with layer-by-layer freezing-out of bound water at 200-280 K, could give detailed information on co-adsorption of methane and water on the studied silicas [104].

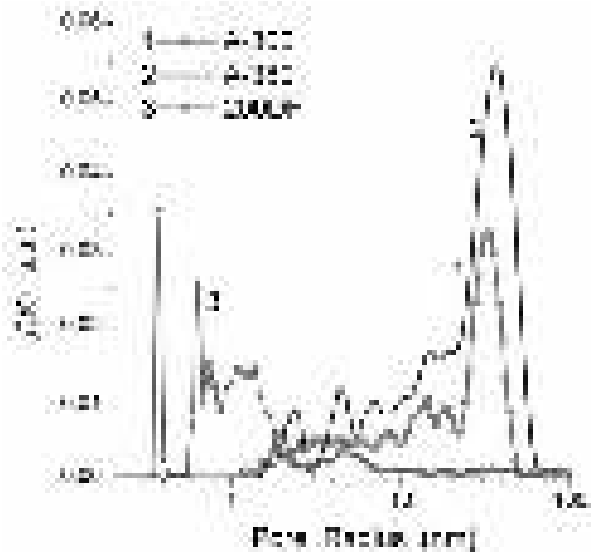

Fig. 128. Incremental pore size distributions of silicas A-300 (1), A-380 (2) and 200DF (3) calculated from the nitrogen adsorption/desorption isotherms (77.4 K) using the DFT method. A model of cylindrical pores was used for 200DF, and a model of pores as voids between spherical nonporous primary particles forming aggregates of random structures for nanosilicas was employed.

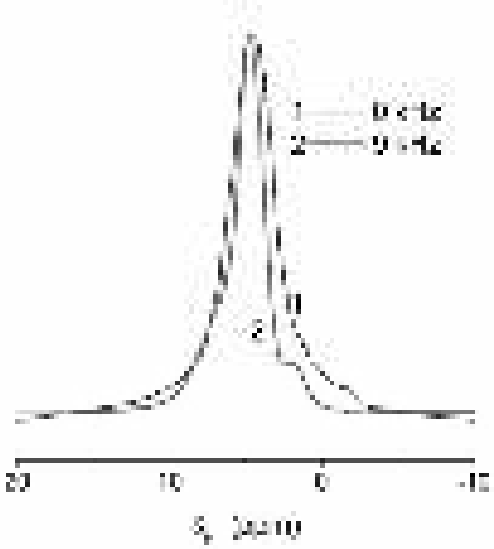

Fig. 129. ^{1}H NMR spectra of initial A-300 (h ≈ 50 mg/g) recorded at 293 K using the MAS technique (rotor frequency f_r = 0 (1) and 9 (2) kHz).

The ^{1}H NMR spectra of water and methane co-adsorbed on nanosilica A-300 at different hydration levels were recorded over the 200-280 K range [104]. These spectra include a single or weakly-split signal of methane at δ_H = 0.0-0.3 ppm. This signal slightly increased with lower temperature due to increasing adsorption of methane, and an enhanced interaction with the silica surface. Water was responsible for two signals at $\delta_H \approx 1$ and 4-5 ppm corresponding to weakly associated water (WAW) with a significant portion of unbound H atoms, and strongly associated water (SAW), with dipolar coupled molecules due to O–H···O hydrogen bonds, respectively. The presence of several ^{1}H NMR signals of an adsorbate suggests slow (on the NMR timescale) molecular exchange between the corresponding states [53,243]. The signal intensity of SAW at $\delta_H \approx$ 4-5 ppm decreased, but the δ_H value increased, with lower temperature because of layer-by-layer freezing-out of fractions of more weakly bound SAW and WAW. However, complete freezing of WAW was observed only at h = 0.005 g/g and T < 220 K, and at h > 0.03 g/g only a certain portion of WAW was frozen at 200 K. Equilibration of the water/A-300 system for a week led to several important effects [104]: (i) the adsorption of methane decreased for the equilibrated compared with the non-equilibrated system at the same h values; (ii) water became more strongly associated due to equilibration, *i.e.* it became less clustered with a greater number of hydrogen bonds per molecule; (iii) this latter effect was stronger with increasing hydration of nanosilica as well as silica 200DF (Fig. 130). For the latter clustered adsorption of water was observed only at minimal hydration h = 0.005 g/g (shoulder at δ_H = 1-2 ppm). At greater amounts of water adsorbed onto silica gel 200DF only SAW was observed at δ_H 4-6 ppm. This led to strong diminution of the adsorption of methane with increasing amounts of pre-adsorbed water [104].

When h < 0.3 g/g all water was strongly bound to the nanosilica surface because it freezes at T < 260 K, and changes in the Gibbs free energy ΔG < –0.5 kJ/mol (Figs. 130 - 132) [104]. Four of six non-equilibrated A-300/H_2O/CH_4 samples (with the exception of samples at h = 0.005 and 0.1 g/g), showed an increase of WAW with lower temperature (Fig. 130b). The most methane adsorption was observed at h = 0.1 g/g (Fig. 130c) when the amount of WAW was largest and the system was non-equilibrated (Fig. 130b). Equilibration of this system for 7 days caused significant diminution of the adsorption of methane. However, this effect was much smaller at lower hydration (Fig. 130c) because adsorbed water was more clustered at smaller amounts despite the long equilibration time. Notice that changes in the ΔG and γ_S values after equilibration were relatively small (Fig. 131); however, changes in contributions of SAW (Fig. 130a) and WAW (Fig. 131b) were significant. Consequently, changes in the adsorption of methane after pre-equilibration of the A-300/water system were more influenced by structural changes in adsorbed water (*e.g.*,

increase in the associativity and the size of adsorbed water structures) than because of changes in its energetic characteristics [104].

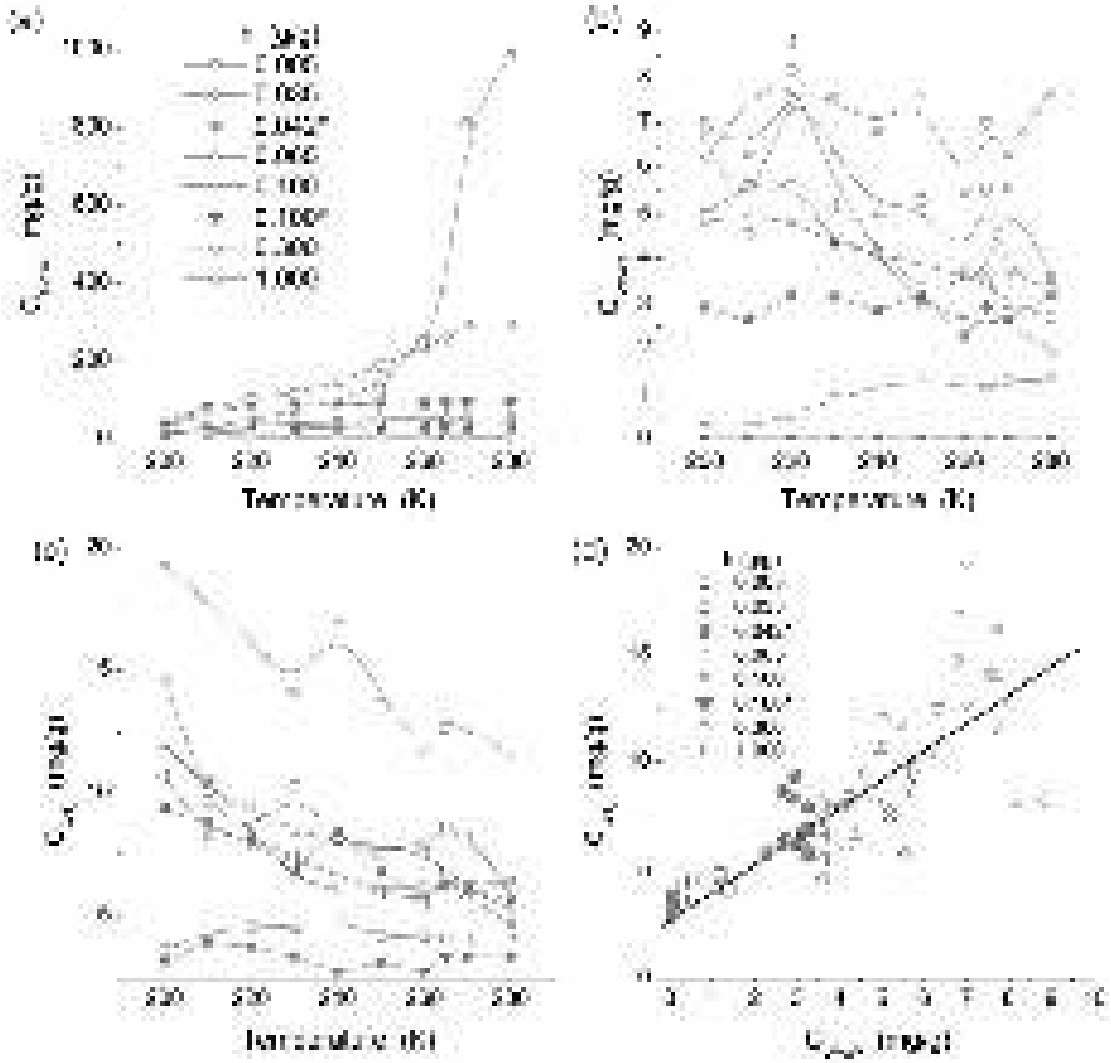

Fig. 130. Temperature dependences of concentration of (a) SAW, (b) WAW and (c) methane co-adsorbed on nanosilica A-300 and (d) relationship between concentrations of methane and WAW.

There was a correlation between the amount of adsorbed methane and WAW (Fig. 130d). Lower amounts of adsorbed methane were observed for samples at minimal (h = 0.005 g/g) and maximal (1 g/g) hydration of silica [104]. The former included too little water to form effective nanoporosity (between the surface of adjacent silica nanoparticles, clusters and domains of unfrozen water and ice nanocrystallites), and the latter included too much water which could form a nearly continuous surface SAW film (Fig. 130a), and bound water was less clustered. Strong clustering of bound water was a necessary condition for the maximal adsorption of methane onto nanosilica [104].

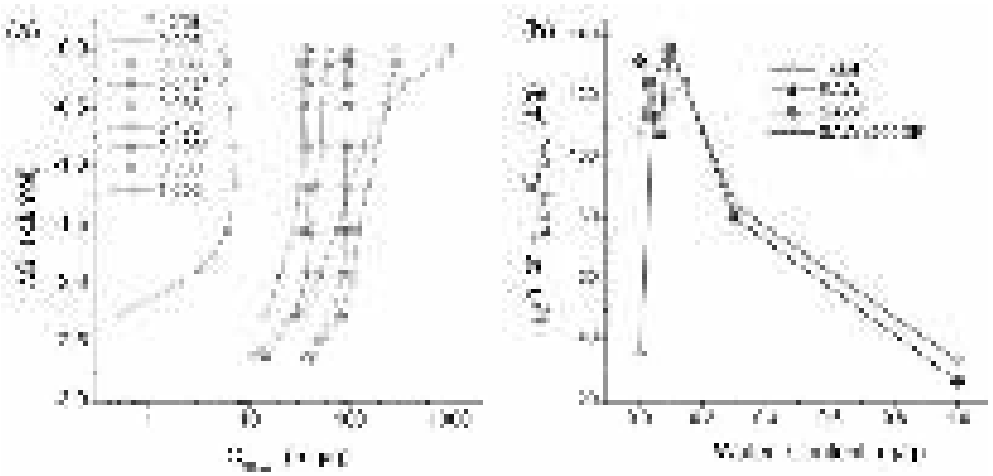

Fig. 131. (a) Relationship between changes in the Gibbs free energy and the SAW amounts on co-adsorption of water and methane onto nanosilica A-300, and (b) normalized interfacial energy (γ_s/h or $\gamma_{s,SAW}/C_{SAW}$) as a function of water content (SAW* corresponds to samples equilibrated for a week) for A-300 and 200DF.

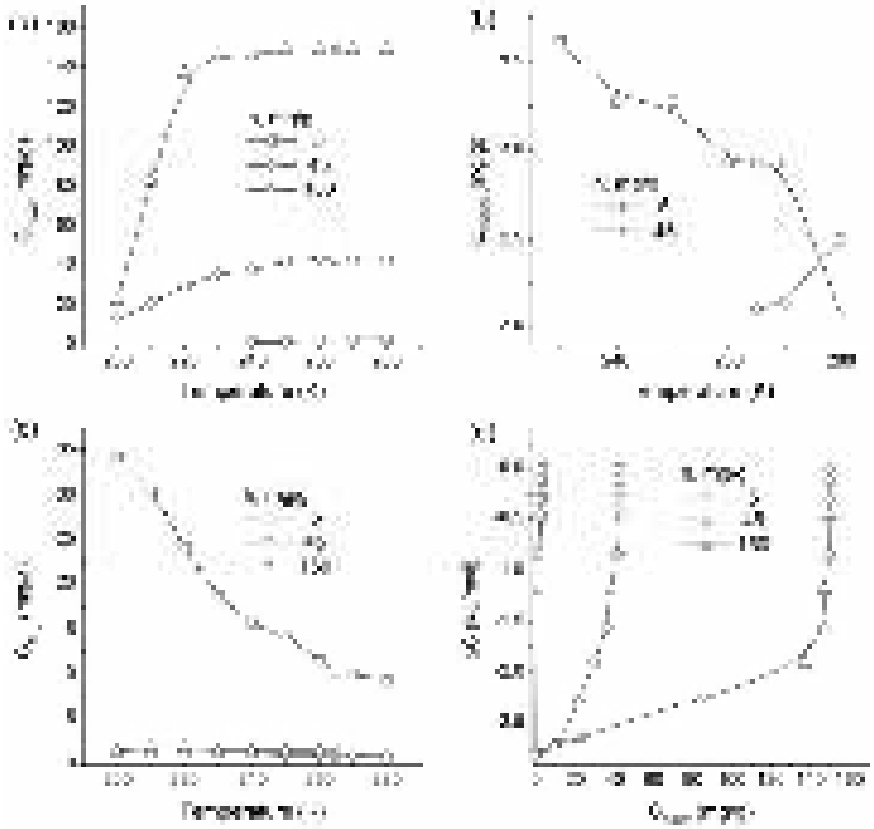

Fig. 132. Temperature dependence of the concentration of (a) SAW, (b) WAW and (c) methane co-adsorbed on silica 200DF and (d) relationship between concentration of SAW and changes in Gibbs free energy of bound water.

The value of interfacial energy (γ_s), determined as the modulus of the total decrease in the Gibbs free energy of the adsorbent-adsorbate system [53], increased with increasing water content [104]. However, normalized interfacial energy ($\gamma_{s,SAW}/C_{SAW}$ for SAW and γ_s/h for all bound water) decreased at h = 0.3 and 1.0 g/g (Fig. 131b), because the influence of the silica surface decreased for distant layers of bound water. For a sample at h = 0.1 g/g the γ_s/h and $\gamma_{s,SAW}/C_{SAW}$ curves have a maximum. This was due to the equilibrium state of intact sample (with water adsorbed from air and equilibrated for long periods) compared to the incomplete equilibration of heated (at 150 ^{o}C to h = 0.005 g/g) and subsequently wetted samples. Complete equilibration of treated and wetted nanosilica required several days due to the slow penetration of water molecules into the particle

volume [37,38,53]. Notice that the γ_s/h and $\gamma_{s,SAW}/C_{SAW}$ maxima at h = 0.1 g/g corresponded to the largest contribution of WAW and greatest adsorption of methane [104].

The relative contribution of WAW of total bound water was maximal (up to 20%) at the smallest hydration (0.005 g/g) of silica, and minimal (< 1 %) at the largest hydration (1.0 g/g) [104]. Consequently, the characteristics of bound water strongly corresponded to the characteristics of SAW, the major contributor of bound water. There were four-three types of SAW structures (Figs. 133 and 134); *e.g.*, clusters, nanodomains and microdomains. These SAW structures became frozen at different temperatures depending on the strength of their interactions with the silica surface, reflecting changes in the relationship between ΔG and C_{SAW} (Fig. 131a). A displacement of the dC_{SAW}/dT maxima toward higher temperatures with increasing h value (Fig. 133) was seen because of the reduced interaction of SAW fractions with the silica surface with growing hydration. This results in the appearance of weakly bound water (characterized by $\Delta G >$ –0.5 kJ/mol and frozen at $T > 260$ K) at $h \geq 0.3$ g/g (Figs. 130 and 131), due to the formation of relatively large water structures. These water structure sizes were determined by the Gibbs-Thomson (GT) relation for the freezing point depression of confined liquids [53], were relatively large (Fig. 134), and frozen at $T > 260$ K (Fig. 133). Notice that the relative contribution of nanopores was largest at h = 0.1 g/g; however, absolute values were larger at h = 0.3 g/g. At h = 1 g/g the S_{nano} and V_{nano} values strongly decreased but the S_{meso} and V_{meso} values strongly increased. These results corresponded to significant enhancement of water associativity with increasing h value [104].

For weakly hydrated samples at $h \leq 0.1$ g/g, the maximal contributions of dC/dT and $f(R)$ (Figs. 134 and 135) were for structures with strongly bound water frozen at $T < 230$ K with sizes $R < 3$ nm [104]. These water structures, attributed to clusters at $R < 1$ nm and nanodomains at R = 1-3 nm, corresponded to nanopores and narrow mesopores, respectively. Water partially filling narrow pores at $R < 10$ nm between primary silica nanoparticles provided enhancement of effective nanoporosity at $R < 1$ nm. This results in an increase in the adsorption of methane, especially at h = 0.1 g/g, when the contribution of small water structures at $R \leq 1$ nm was maximal as the relative contribution of nanopores filled by bound unfrozen water [104].

The molecular mobility of water could appear in different structures where water molecules have different numbers of hydrogen bonds (per molecule) of different strength. Therefore, the distribution functions of the activation energy ($f(E)$) of the molecular mobility (calculated using the temperature dependences of $dC_{SAW}(T)/dT$ assuming that this process obeys the Arrhenius law) [53,245] were relatively broad over the 15-85 kJ/mol range (Fig. 136a) [104]. This range of E values corresponded to the motion of water molecules having from one to four hydrogen bonds per molecule.

The activation energy of the molecular motion of methane (determined from the temperature dependences of dC_{CH4}/dT) was 1-10 kJ/mol for a minimally hydrated sample (Fig. 136b). However, for more strongly hydrated silica (h = 0.1 and 1.0 g/g) the values of E increased by several times. This could be explained by several reasons. First, enhanced nanoporosity formed by water clusters, nanodomains and ice nanocrystallites, partly or completely frozen with lowering temperature, enhanced the barriers for methane motion. Second, complex water/methane structures could demonstrate cooperative motion; therefore, the activation energy of the methane motion depended on the water motion. Thus, co-adsorbed water and methane were not individual phases independent from one another. This was also confirmed by the correlation between the amounts of adsorbed methane and WAW (Fig. 131d) [104].

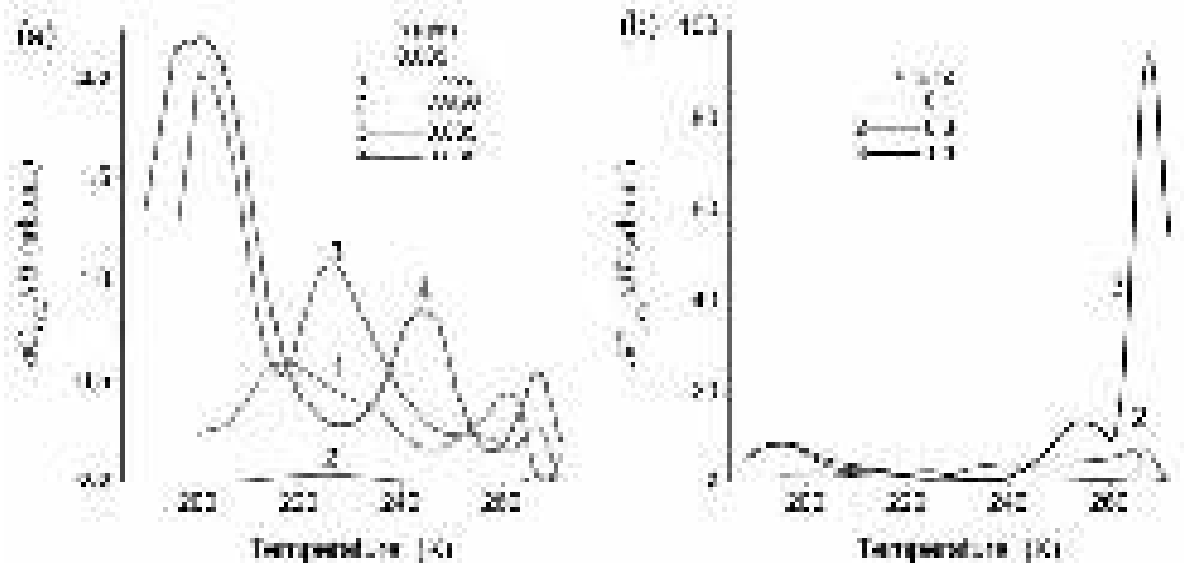

Fig. 133. Temperature derivatives of the SAW content for (a) weakly and (b) strongly hydrated samples; dC_{WAW}/dT was shown for a sample at h = 0.005 g/g (a, curve 2).

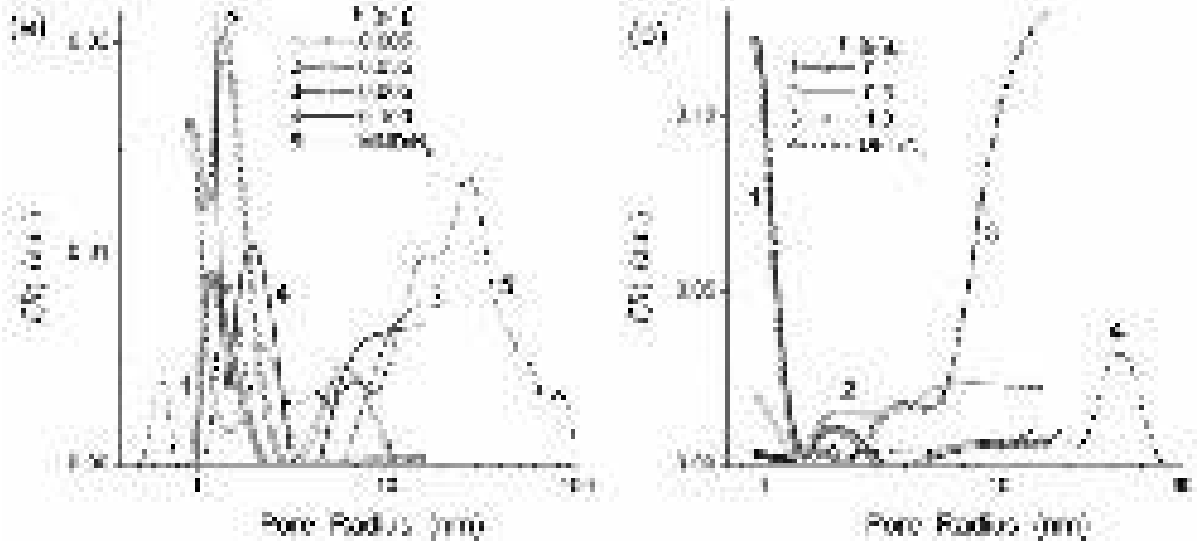

Fig. 134. Distribution functions of sizes of unfrozen bound water structures at (a) low and (b) high hydration and the pore size distribution of A-300 calculated using modified Nguyen-Do equation with the model of cylindrical pores (a, curve 5) and DFT method with the model of voids between spherical particles (b, curve 4).

The adsorption of methane onto nanosilica A-300, composed of nonporous primary nanoparticles (average diameter 8.1 nm) at standard pressure, was a function of temperature and silica hydration. The silica hydration dependence was nonlinear, and maximal adsorption of methane (1.9-1.2 wt.% at 200-280 K) was observed at hydration h = 0.1 g/g for intact silica. A decrease (on heating) and increase (on wetting) of the silica hydration both led to a reduction of methane adsorption. Co-adsorption of methane and water led to the appearance of a ^{1}H NMR signal from weakly associated water at $\delta_H \approx 1$ ppm. The amount of this water correlated to concentration of adsorbed methane, because weakly associated bound water was most clustered at the surface of nanosilica composed of nonporous primary nanoparticles. The adsorption of methane on micro/mesoporous silica 200DF decreased with increasing amount of pre-adsorbed water characterized by significant associativity ($\delta_H \approx 5$ ppm) at $h \geq 0.005$ g/g [104].

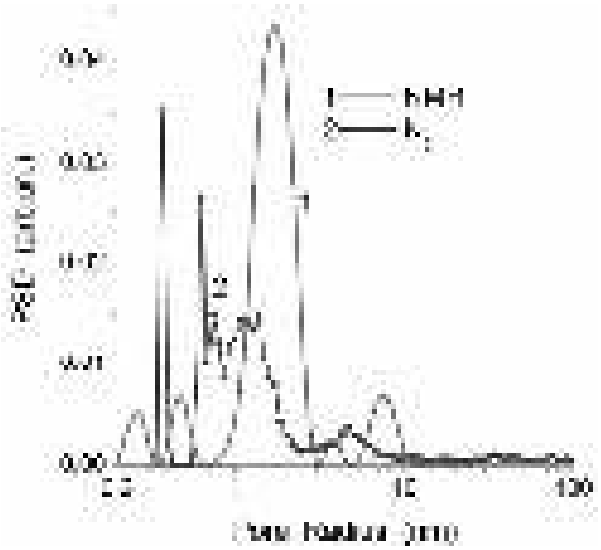

Fig. 135. Distribution function of sizes of unfrozen water structures (curve 1, h = 0.15 g/g) and pore size distribution of silica 200DF (2).

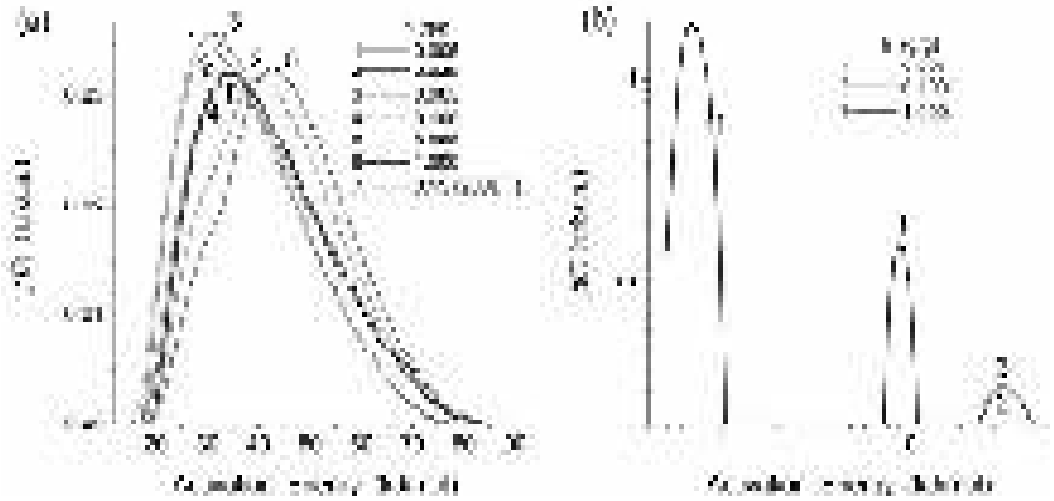

Fig. 136. Activation energy of molecular motion of unfrozen water at T < 273 K and different hydration of A-300 and 200DF with co-adsorbed methane.

Thus, to enhance the adsorption of methane onto adsorbents with pre-adsorbed water at standard pressure and T < 280 K, this water should exhibit maximal clustering. The amount of clustered water should be equal to a value characteristic for a given adsorbent, to maximize the contribution of narrow nanopores appropriate for the adsorption of methane [104].

Dry powder of A-380 could be characterized by certain structural hierarchy of particles starting from primary particles (5-15 nm in size, average diameter 7.2 nm), aggregates of primary particles and agglomerates of aggregates [53,246]. Adsorbed water at low amounts (< 20 wt.%) localized mainly in the zone of contacts between adjacent nanoparticles. At higher amounts, adsorbed water could form continuous layers covering whole nanoparticles [53]. Consequently, for two samples at h = 0.5 and 1 g/g continuous water layers should be formed but for other samples at h = 0.07, 0.08, and 0.15 g/g island adsorption of water could be to form only partial coverage of the surface. Despite this structural difference, water bound to nanosilica gives a single ^{1}H NMR signal at δ_H = 4-5 ppm, *i.e.* it was SAW, whose intensity decreased with lowering temperature at T < 250 K due to partial freezing of water. The δ_H value decreased with elevating temperature because of the influence of thermal motion of water molecules on the hydrogen bond network structure. There were fractions of SBW and WBW but WAW was absent. Addition of organic solvents to A-380/water slightly affected the shape and the position of the water signal. A weak signal of the CHD_2 groups of admixtures in CD_3CN and DMSO was observed at δ_H = 2-2.5 ppm.

Co-adsorbed DMSO (in a mixture with $CDCl_3$) more strongly affected freezing-out of water since even at 210 K an intensive signal of unfrozen water was observed [246].

Table 21. Characteristics of bound water in hydrated powders of nanosilica A-380 with the presence of organic solvents [53,246].

h (g/g)	Organics (g/g)	C_{SBW} (mg/g)	C_{WBW} (mg/g)	□-ΔG^S (kJ/mol)	γ_S (J/g)	S_{uw} (m^2/g)	S_{nano} (m^2/g)	S_{meso} (m^2/g)	S_{macro} (m^2/g)	V_{nano} (cm^3/g)	V_{meso} (cm^3/g)	V_{macro} (cm^3/g)
1	-	250	750	2.52	30.2	116	14	102	0.4	0.007	0.976	0.007
	1 $CDCl_3$	150	850	2.87	23.0	150	35	115	0.5	0.016	0.966	0.008
	2 $CDCl_3$	170	830	2.37	27.0	130	0	130	0.1	0	0.996	0.002
	6 $CDCl_3$	30	970	2.57	21.6	121	6	115	0.3	0.003	0.985	0.005
0.5	-	125	375	2.84	16.5	87	43	43	0.5	0.020	0.451	0.007
	2 $CDCl_3$	100	400	2.59	15.8	56	23	32	0.8	0.011	0.449	0.014
	8 $CDCl_3$	75	425	3.16	15.2	53	19	34	0.7	0.009	0.458	0.011
0.15	-	100	50	2.78	11.1	78	67	11	0.1	0.029	0.117	0.001
	3 $CDCl_3$	100	50	2.43	9.3	40	28	12	0.1	0.013	0.134	0.001
	6 $CDCl_3$	100	50	2.70	8.8	10	0	10	0.1	0	0.145	0.002
	0.5 DMSO	100	50	3.37	14.7	181	177	4	0.4	0.073	0.055	0.006
	0.5DMSO+1.5$CDCl_3$	145	5	3.35	21.4	227	221	6	0	0.094	0.056	0
0.08	-	60	20	3.48	7.8	75	71	4	0.2	0.029	0.043	0.002
	2.0 $CDCl_3$	55	25	2.47	4.6	5	1	4	0.1	0	0.074	0.002
	1.0 DMSO	70	10	3.92	12.3	178	177	1	0	0.065	0.013	0
	1 DMSO+2 $CDCl_3$	70	10	3.76	10.7	116	114	2	0	0.046	0.029	0
0.07	1 CD_3CN+0.5 $CDCl_3$	35	35	2.32	3.1	15	0	15	0	0	0.054	0
	1 CD_3CN+1 $CDCl_3$	35	35	2.42	3.3	17	0	17	0	0	0.059	0
	1 CD_3CN+2 $CDCl_3$	30	40	2.14	2.9	15	0	15	0	0	0.056	0

Note. S_{uw}, S_{nano}, S_{meso} and S_{macro} were the surface area total, nano- (radius $R < 1$ nm), meso- ($1 < R < 25$ nm) and macropores ($R > 25$ nm), respectively, of silica in contact with unfrozen water; V_{nano}, V_{meso}, and V_{macro} were the pore volume of nano-, meso-, and macropores, respectively [53,246].

To study features of the influence of organic solvents on the characteristics of bound water localizing in voids between adjacent silica nanoparticles in their aggregates on the basis of the temperature dependences of changes in the integral intensities of the signals of unfrozen water, the relationships between changes in Gibbs free energy on water adsorption and the amounts of unfrozen bound water were determined (Fig. 137). At relatively high level of hydration the influence of organic solvents was weaker than that at low hydration. For the former, There were near vertical (related to SBW) and horizontal (WBW) sections in the $\Delta G(C_{uw})$ graphs. The maximal amount of SBW was 250 mg/g which corresponded to approximately third volume of pores (voids between adjacent primary particles in aggregates) filled by nitrogen at 77.4 K. Addition of chloroform alone or in a mixture with DMSO led to stronger changes in the characteristics of bound water at lower hydration (Table 21, Fig. 137). The effects of chloroform in a mixture with acetonitrile were smaller than that of $CDCl_3$+DMSO. These effects could be explained by the difference in the solubility of water in these organics individual and in mixtures. Co-adsorbed chloroform decreased the interfacial energy (γ_S) of bound water at different hydration (Table 21) [246].

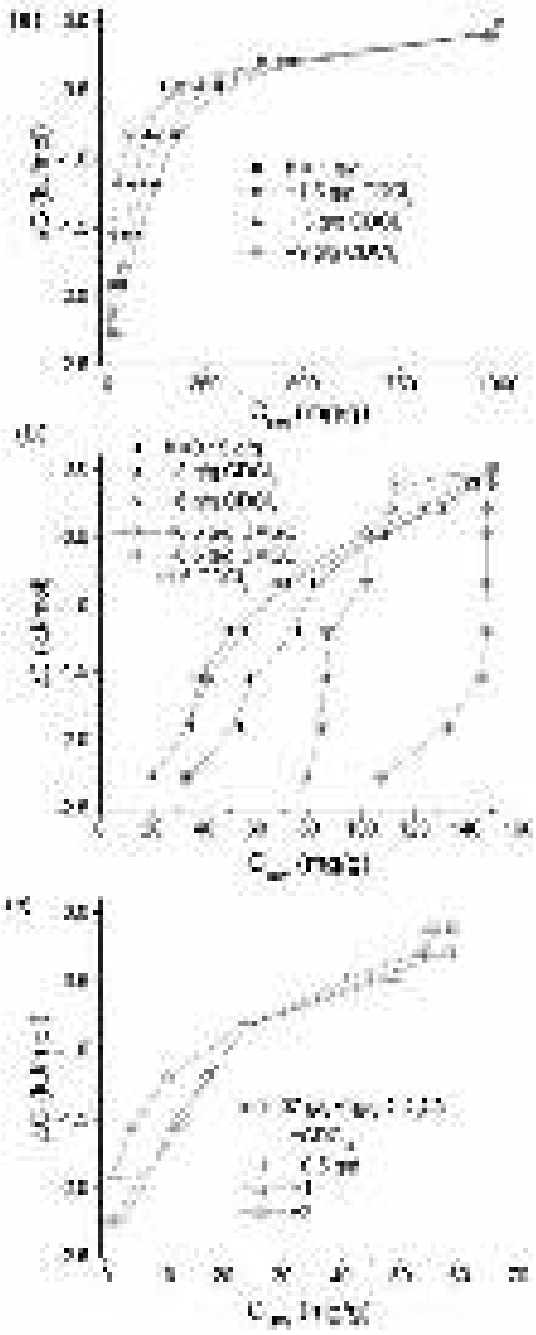

Fig. 137. Relationships between content of unfrozen water and changes in the Gibbs free energy of unfrozen water in differently hydrated powders of nanosilica A-380 at h = (a) 1, (b) 0.15, (c) 0.07 and different amounts of organic solvents [246].

The interfacial energy normalized to h = 1 g/g as $\gamma_S^* = \gamma_S/h$ increased with decreasing h value because of a decrease in the amounts of WBW. There was tendency of a decrease in the γ_S^* value with increasing content of chloroform. This could be explained by the displacement of a portion of water from narrow voids to broader ones, and this effect was stronger at lower hydration (Fig. 137) when bound water did not form continuous adsorption layers and co-adsorbed organics could easily contact the silica surface. Such electron-donor solvents as CD_3CN and DMSO were well dissolved in water and chloroform. However, chloroform-DMSO (CD_3CN) mixtures could stratify on addition of a small quantity of water to form layers enriched by chloroform and an electron-donor. To avoid this effect such quantities of mixtures were added to the silica powder to prevent the formation of a liquid phase. CD_3CN and DMSO differently affected the interaction of water with the silica surface (Table 21, Fig. 138) since CD_3CN enhanced but DMSO diminishes the interfacial energy value of bound water [246].

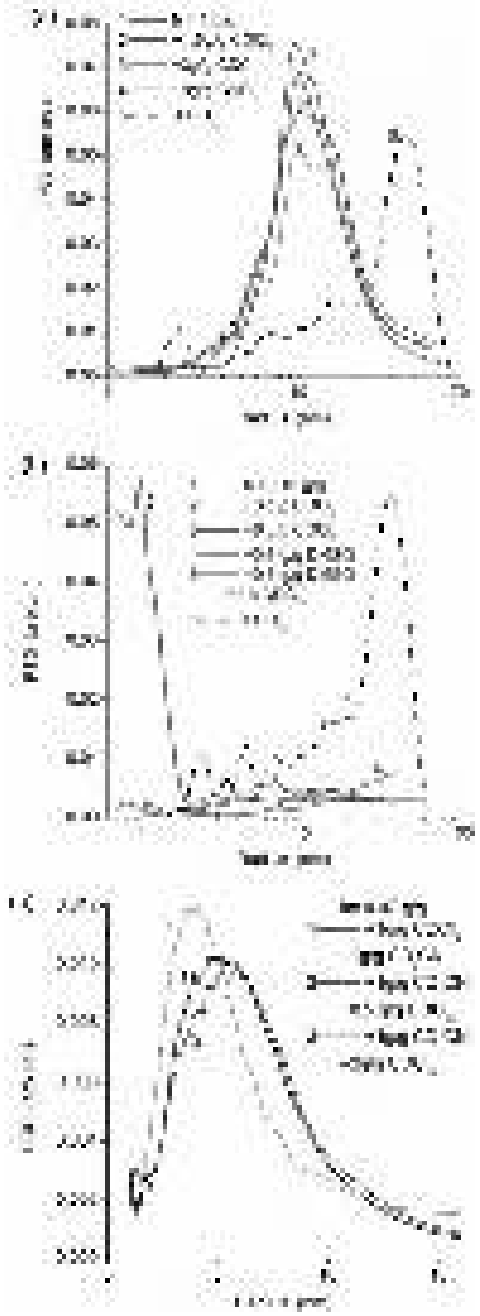

Fig. 138. Size distribution of unfrozen water structures for hydrated A-380 powder at h = (a) 1, (b) 0.15, (c) 0.07 and different amounts of organic solvents [246].

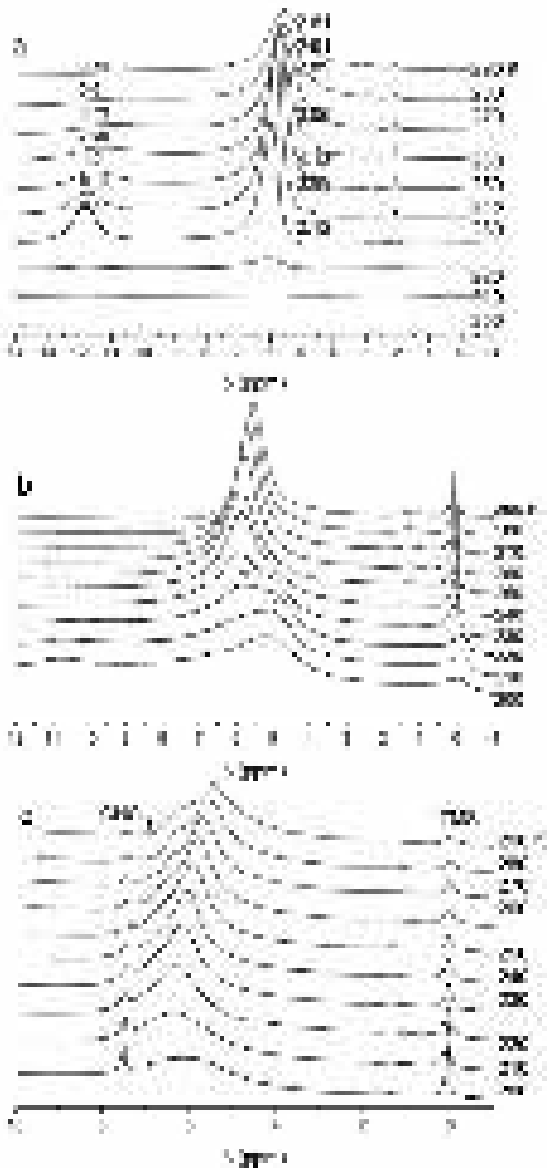

Fig. 139. ^{1}H NMR spectra of aqueous 30% solution of H_2O_2 (a) bulk and adsorbed (10 wt.%) onto A-400 being in (b) CCl_4 and (c) $CDCl_3$ media.

On the co-adsorption of water and studied organics, there were several factors affecting changes in the structure (clusterization) of bound water. If only weakly polar chloroform was co-adsorbed with water that the phase boundary tends to be minimal. Therefore, if pre-adsorbed water formed a continuous coverage of the silica surface that the effects of chloroform were minimal. These effects increased if the island coverage with pre-adsorbed water was realized (Fig. 137). Chloroform in a mixture with polar organics could be mixed with bound water because DMSO effectively interacting with both polar water and nonpolar chloroform could separate water and chloroform clusters. There was no tendency to decrease the contact area between water and chloroform at the silica surface because they contact only with DMSO and the silica surface. This was well seen from the structural characteristics of bound water (Table 21) since maximal specific surface area (total and of nanopores) of unfrozen water structures was observed for the DMSO+$CDCl_3$ (or DMSO alone). However, even for these cases these values were much smaller than the S_{BET} value of silica A-380. Notice that $S < S_{BET}$ on the adsorption of water alone at h =1 g/g. This could be explained by structural nonuniformity of bound water (*i.e.* its clusterization, formation of nanodomains (Fig. 138) and absence uniform continuous water layers covering silica nanoparticles) and the absence of contacts between total surface area of silica particles and water [246].

Water bound to nanosilica did not form uniform layers even at relatively high hydration (1 g of water per 1 g of dry silica). Co-adsorption of water with weakly polar chloroform alone or in a mixture with polar DMSO or acetonitrile more strongly affected the structure of water bound to nanosilica A-380 at lower hydration when significant portion of silica surface remained uncovered by water. Maximal clusterization of bound water was observed on the co-adsorption with chloroform/DMSO mixture because DMSO could effectively interact with both nonpolar (through dispersion interactions of chloroform with CH_3 groups) and polar (water interaction with S=O) structures [246].

The aqueous solution of hydrogen peroxide was characterized by two ^{1}H NMR signals at $\delta_H \approx 6$ (H_2O) and 12 (H_2O_2) ppm (Fig. 139a) [247]. The signal width increased with increasing temperature but stronger for H_2O_2 due to enhancement of the proton exchange $H_2O \leftrightarrow H_2O_2$. A weak signal at $\delta_H \approx 2$ ppm could be assigned to methyl groups of acetone added as a standard for determination of the chemical shift. The chemical shift of water interacting with H_2O_2 was 1-1.5 ppm larger than that for bulk liquid water. Symbols at the peaks (Fig. 139a) showed the integral intensity of these peaks. At $T < 230$ K the intensity drops down because of water and hydrogen peroxide freezing. Complete melting of the frozen components occurred at $T_m = 250$ K. The ratio of the integral intensity of the signals was 4:1 that was close to that of their molar fractions. A decrease in the intensity at $T > T_m$ was due to changes in nuclear level population (Curie law) [243]. Additionally, H_2O_2 could decompose with elimination of oxygen, which solving in water could provide additional channel (paramagnetic centers) of relaxation of the nuclear magnetization. It was possible that the presence of dissolved oxygen in the H_2O_2 solution could be a reason of a stronger manifestation of the Curie law in comparison with other similar heterogeneous systems [53]. The intensity of the H_2O_2 signal (Fig. 139a) decreased with increasing temperature much stronger than that of water. This could be explained by changes in the component clusterization (due to cryoconcentration) which decreased with increasing temperature. There were two states of H_2O_2 characterized by slow and fast proton exchange (in NMR time scale) and the contribution of the latter increased with increasing temperature.

According to clustered structure of water, liquid water is composed of clusters and nanodomains, state of which could be changed due to external actions, solutes, co-solvents, confined space effects, etc. [53,242]. For such miscible liquids as water and hydrogen peroxide, more clustered structure could be formed at lower temperatures (Fig. 140, right picture) [247]. This clustered structure could be destroyed with increasing temperature due to enhanced motion of the molecules forming random structure (Fig. 140, left picture). The latter was characterized by broadened ^{1}H NMR spectrum theoretically calculated (Fig. 140). For the solution, the water peak shifted toward weak magnetic field (curves 2w and 3w) due to interaction of water molecules with hydrogen peroxide molecules [247].

At $T < 250$ K water (SAW) mixed with H_2O_2 was partially unfrozen but characterized by lower activity as a solvent worse dissolving H_2O_2. Therefore, the latter tends to be more clustered (as shown in Fig. 140, right picture). Greater δ_H values for water than that for pure liquid water was due to the hydrogen bonding of water molecules with H_2O_2 molecules. With increasing temperature, the solubility of H_2O_2 in SAW increased that resulted in enhancement of the proton exchange between water and hydrogen peroxide. One could expect the appearance of broad but non-split signal of the H_2O-H_2O_2 mixture shifted toward weak magnetic field in comparison with water. However, this effect was absent since the separated signals of water and hydrogen peroxide were observed at $T > 250$ K (Fig. 139a). This effect could be explained by the existence of the clustered H_2O_2 structure even at 280-290 K [247].

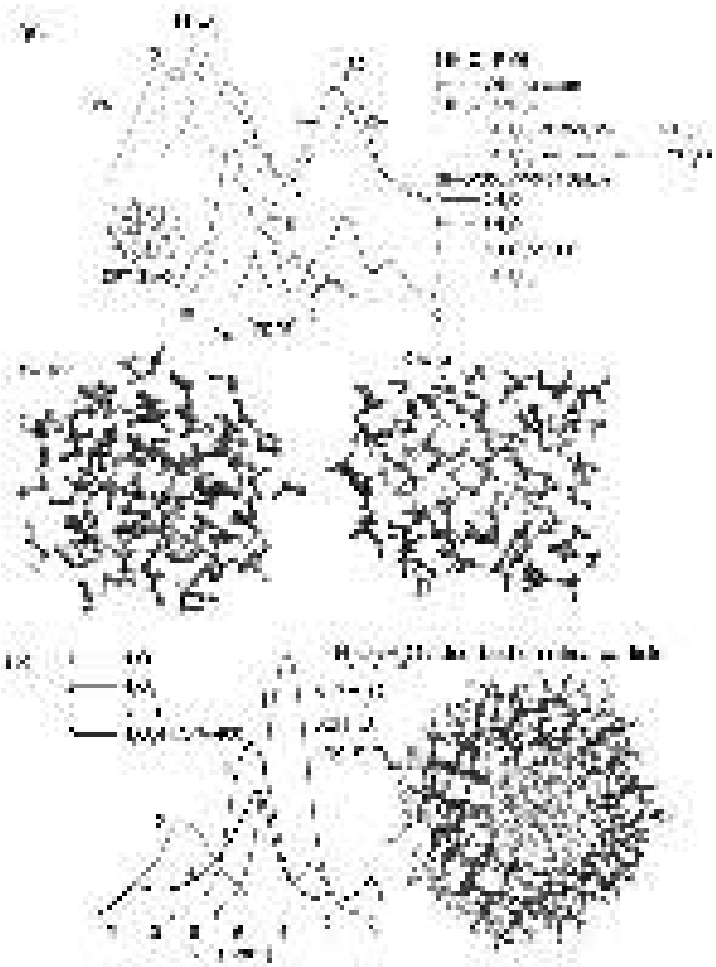

Fig. 140. ^{1}H NMR spectra of clusters calculated using PM6 method and the correlation functions for water and hydrogen peroxide based on the GIAO/DFT and PM6 calculations of the same systems (a, curves 1-3, and b), GIAO/B3LYP/6-31G(d,p) (a, curves 4-6) and GIAO/IEFPCM/B3LYP/6-31G(d,p) (a, curve 7) with (a) hydrogen peroxide alone or with water molecules; two types of the mixtures were shown with pure solution (curves 3) and clustered (curves 2) structures; and (b) $317H_2O*32H_2O_2$ adsorbed onto silica particles (199 tetrahedrons) and experimental ^{1}H NMR spectrum of H_2O_2/H_2O/A-400 (10 wt.% of 30 wt.% H_2O_2 solution in water) recorded at 200 K (curve 4).

For interaction of the aqueous solution of H_2O_2 with nanosilica (dehydrated before mixing with the solution) being in nonpolar (CCl_4) or weakly polar ($CDCl_3$) solvents, the temperature behavior of the ^{1}H NMR signals differed from that for the pure solution (Fig. 139) [247]. Several signals were in the spectra: WAW ($\delta_H \approx 1$ ppm), two signals of SAW with different amounts of dissolved H_2O_2 ($\delta_H \approx 5$-6.5 ppm). Additionally, in the CCl_4 medium, separated signal of hydrogen peroxide was observed at $\delta_H \approx 11$ ppm. Freezing temperature of CCl_4 was 240 K. The dispersion medium freezing (Fig. 139b) resulted in broadening of TMS signal at $\delta_H = 0$ ppm. Near freezing temperature of CCl_4 transition of SAW from state 1 at $\delta_H \approx 5$ ppm into state 2 at $\delta_H \approx 6$ ppm was observed. Both signals were observed at 210-240 K. The H_2O_2 signal decreased with temperature and it disappeared at $T > 240$ K [247].

In weakly polar $CDCl_3$ medium (Fig. 139b) the δ_H value of SAW increased [247]. Splitting of the SAW peak into 1 and 2 states occurred at $T > 250$ K. Signal 2 shifts toward strong magnetic field with increasing temperature because of decreasing clusterization of the solution. This effect for signal 1 was much smaller. Silica A-400 as a nanostructured material affected the clusterization of the solution located in narrow nano- and mesopores (voids between silica nanoparticles). This process was also dependent on cryoconcentration, *i.e.* relative concentration of H_2O_2 in certain structures increased due to partial freezing of water [247].

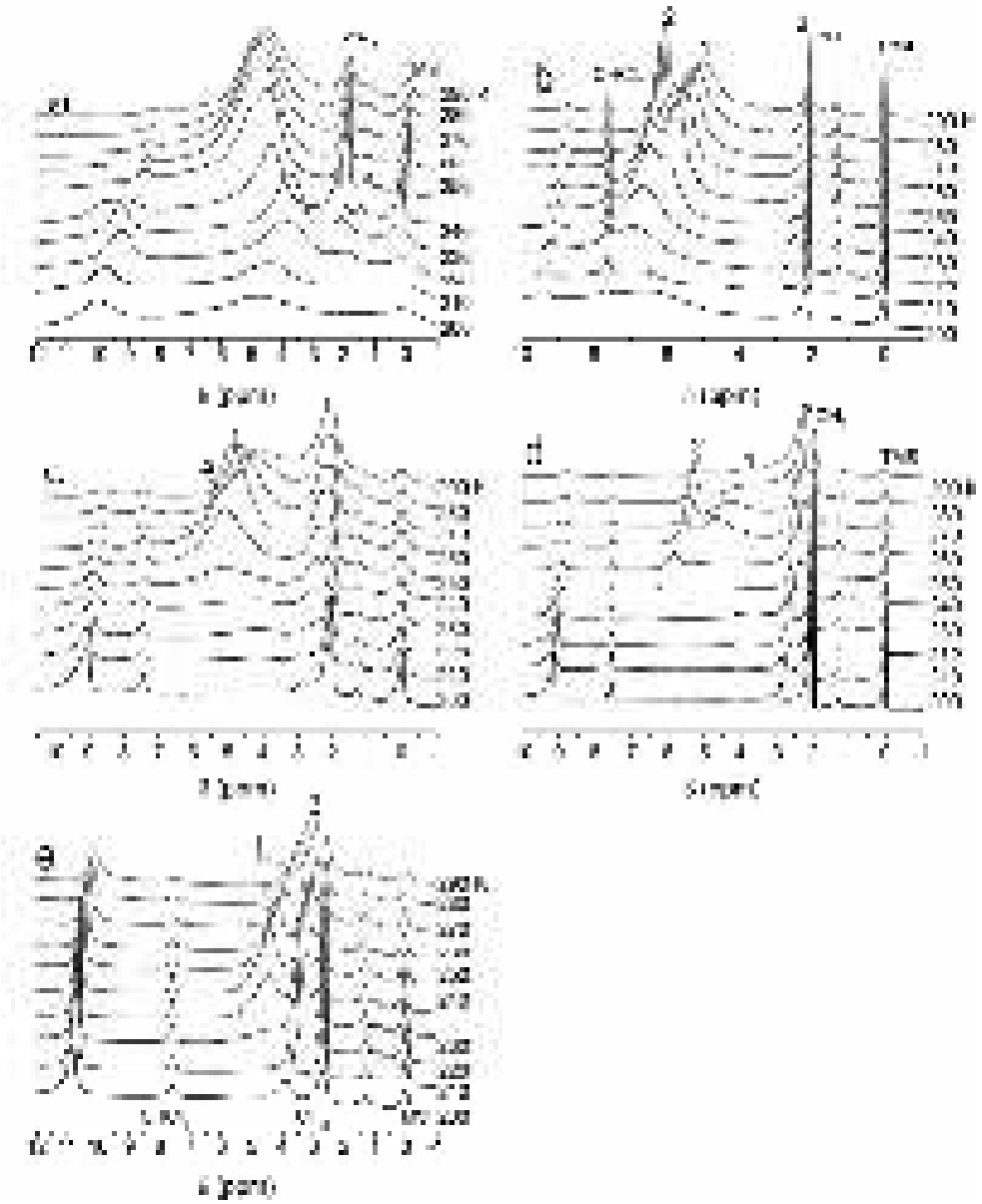

Fig. 141. ^{1}H NMR spectra of aqueous 30% solution of H_2O_2 adsorbed (10 wt.%) onto A-400 being in (a) CCl_4 + 8 % CD_3CN, (b) $CDCl_3$ + 8 % CD_3CN, (c) $CDCl_3$ + 15 % CD_3CN, (d) $CDCl_3$ + 22 % CD_3CN, (e) $CDCl_3$ + 8 % DMSO media.

The ^{1}H NMR spectra of the H_2O/H_2O_2 mixture adsorbed onto nanosilica being in different mixtures of nonpolar (CCl_4) or weakly ($CDCl_3$) solvent with addition of polar solvents (CD_3CN, $(CD_3)_2SO$) (Fig. 141) demonstrated complex temperature behavior [247]. Besides signals of water, H_2O_2 and TMS, signals of methyl groups of CH_3CN (as admixture in CD_3CN) at δ_H = 2.2 ppm and $(CH_3)_2SO$ (admixture in $(CD_3)_2SO$) at δ_H = 2.5 ppm were observed. In frozen CCl_4 medium (T < 240 K) signals of SAW and H_2O_2 were observed separately (Fig. 141a). The SAW signal shifted toward strong magnetic field with increasing temperature and minimal value δ_H = 3.5 ppm was observed at 230 K and then it shifted toward weak magnetic field. At 240 K two signals of H_2O_2 in the adsorbed solution were observed at δ_H = 10 and 8.5 ppm. However, at higher temperatures only one weak signal was observed and its δ_H value decreased with temperature. Since the δ_H value of this signal was lower than that of pure H_2O_2 one could assume that the H_2O_2 molecules form clusters with water and acetonitrile molecules [247]. After melting of CCl_4 (T > 240 K) a major portion of H_2O_2 dissolved in the SAW nanodomains (that resulted in increasing δ_H value of SAW) or formed the adsorption complexes with surface silanols groups. Their signal could be

absent in the spectra due to the proton exchange SiOH↔HOH causing significant shortening of the relaxation time [247].

In the $CDCl_3$ with addition of CD_3CN (Fig. 141b), a weak signal of H_2O_2 was observed at $\delta_H \approx 9$ ppm. It could be due to the formation of clusters with the participation of H_2O_2, H_2O and $CDCl_3$ or CD_3CN molecules (as well as in the system shown in Fig. 141a). SAW was observed as one ($T < 240$ K) or two signals (signals 1 and 2) which shift toward strong magnetic field with increasing temperature. Signal 1 shifts stronger than signal 2. The maximal δ_H value for SAW was 7 ppm at 220 K. At lower temperatures, the signal intensity and its δ_H value decreased due to partial freezing of water and H_2O_2. Weak signal of water (signal 3) was also observed at $\delta_H = 2.2$-2.4 ppm (to the left from the signal of methyl groups of acetonitrile). This δ_H value was intermediate between the values of WAW (1-1.5 ppm) and water bound to acetonitrile molecules (3 ppm). This signal intensity increased with increasing concentration of acetonitrile in the mixture with CD_3Cl (Fig. 141b-d). It was possible that it could be caused by clusters with CD_3Cl-CD_3CN-H_2O bound to the A-400 surface in narrow voids. The H_2O_2 signal intensity at $\delta_H \approx 9$ ppm increased with increasing CD_3CN concentration (Fig. 141b-d). The minimal δ_H value of SAW decreased to 4 ppm. Signals 1 and 2 were observed separately only at $T > 270$ K. Signal 3 was the most intensive at 22% CD_3CN in mixture with CD_3Cl. It intensity increased with increasing temperature but intensity of signal 1 decreased. For a $CDCl_3$ mixture with DMSO (Fig. 141e), the δ_H value of hydrogen peroxide increased to 11 ppm. Significant changes in the intensity of signals 3 and 1 (similar to that at 22% CD_3CN) were already observed at 5% DMSO added to CD_3Cl [247].

Observed patterns of relationship of the ^1H NMR signals of aqueous 30% solution of hydrogen peroxide bound to nanosilica A-400 being in solvents of different polarity and hydrophobicity could be interpreted in terms of the formation of clusters and nanodomains in voids between spherical silica nanoparticles, and these clusters contain different amounts of H_2O_2 [247]. At low temperatures the confined space effects increased due to partial freezing of components forming crystallites in voids between silica nanoparticles. This led to cryoconcentration of certain components. In the hydrophobic nonpolar medium, the solution of H_2O_2 became inhomogeneous and formed two types of structures with strongly associated water with different content of hydrogen peroxide. The content of weakly associated water was much smaller than for similar samples with water without H_2O_2. For the H_2O/H_2O_2 mixtures in weakly polar CD_3Cl with addition of polar CD_3CN or strongly polar DMSO, three types of clusters and domains were formed at the silica surface: (i) clusters with concentrated H_2O_2 at $\delta_H = 9$-11 ppm; (ii) clusters with concentrated water and dissolved certain amounts of co-solvents; and (iii) clusters with organic solvents containing certain amount of water and H_2O_2. The activity of solvents increased with increasing temperature and the cryoconcentration effects decreased that result in the formation of more homogeneous interfacial solutions including organic solvents. Hydrogen peroxide formed clusters with water molecules which could slowly exchange by protons with the clustered SAW and WAW. Significant amounts of WAW were observed only for CD_3Cl/DMSO medium [247].

Effects of salts in free media and confined space

The presence of dissolved salts in the aqueous media can affect the value of the chemical shift δ_H (Fig. 142) [53,210]. These effects depended on the salt type and content (Figs. 142 and 143). Frequently, a diminution of the water structure order due to dissolved salts results in a decrease in the values of δ_H. However, for some salts (e.g., KCN), the opposite effects were observed. These results could be explained by kosmotropic and chaotropic properties of ions [242].

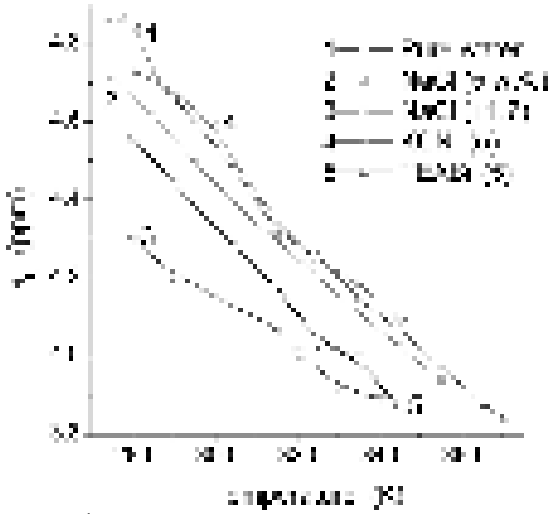

Fig. 142. Temperature dependence of the ^{1}H NMR chemical shift δ_H for pure water or concentrated solutions of different salts (experimental data) [53,210].

During grinding salt (KCl was selected as a color representative) with strongly hydrated PMS at h = 9 g/g (Fig. 144a,b) or more weakly hydrated nanosilica at h = 0.1 g/g (Fig. 144c,d) KCl microcrystallites were observed. A low content of water could not allow the dissolution of salts. Their sizes were smaller in KCl/PS300 ($d \leq 5$ μm) than KCl/PMS ($d \leq 20$ μm) because of an abrasive effect of nanosilica which was much harder than the polymer used. Additionally, the KCl/PS300 has uniform color that suggests a uniform distribution of KCl particles in the mixture [53,210].

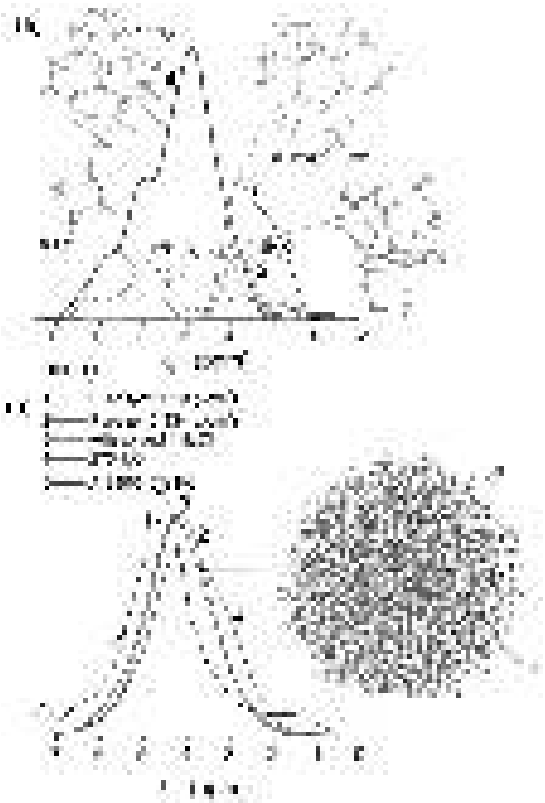

Fig. 143. ^{1}H NMR spectra of (a) small clusters of water (8-43 molecules) and water/DMSO calculated using GIAO/B3LYP/6-31G(d,p) used for calculation of calibration functions for (b) water clusters with 275 and 2000 molecules (pure and dissolved ions $4Na^+ + 4Cl^-$) calculated by the PM6 method, and experimental ^{1}H NMR spectrum of water in 3.6 % solution (0.44 g/g) of KCl bound to nanosilica A-380. [53,210].

Water bound to NaCl with the presence of *n*-decane showed a broad signal at $\delta_H \approx 4.5$ ppm at 280 K (Fig. 145a, dash-dotted lines) [248]. At 270 K, its intensity became much lower and it

disappears at 265 K due to freezing of water. This suggests that all water was weakly bound because it was frozen close to the freezing point of bulk water. This water was strongly associated since δ_H was close to that of bulk water. Decane gave two signals at δ_H = 0.95 ppm (CH_3 groups) and 1.25 ppm (CH_2) (Fig. 145a). At low temperatures, a weak signal at 1.5-2.0 ppm could be assigned to weakly associated water. Addition of a certain amount of TFAA to chloroform (1 : 9) led to a downfield shift of signal of TFAA/water toward 7-8 ppm. It was broad at high temperatures and shifts toward 10 ppm with decreasing temperature close to that for bulk TFAA solution (~11 ppm) [248].

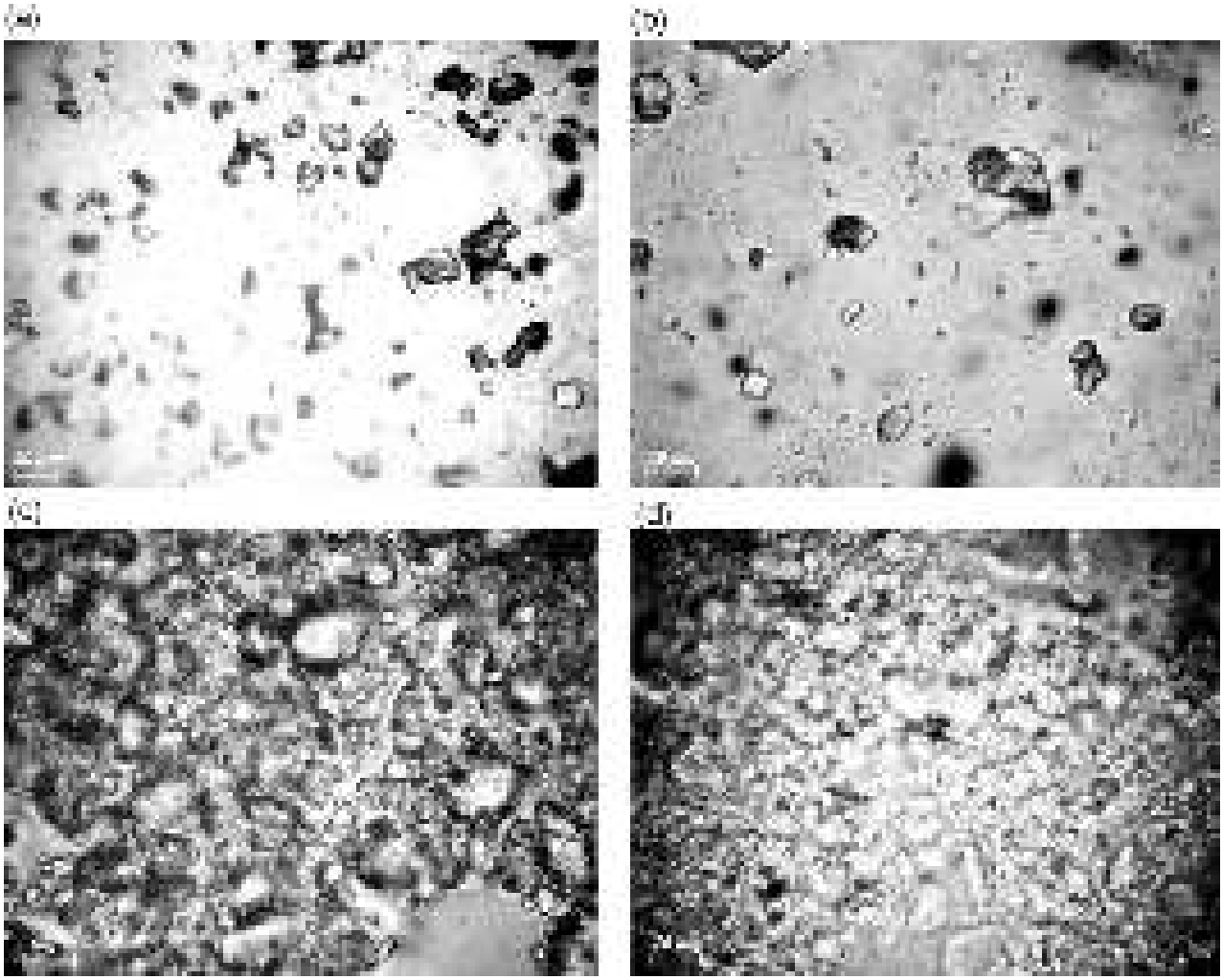

Fig. 144. Microphotographs (Primo Star optical microscope, Carl Zeiss) of grinded samples (during 10 min) (a, b) hydrated PMS (h = 9 g/g) with KCl (1 : 3 w/w) and (c, d) KCl/PS300 (1:6) at h = 0.1 g/g in (c) air and (d) silicone oil (scale bar 20 μm (a), and 10 μm (b, c, d)) [248].

Fig. 145. ^{1}H NMR spectra recorded at different temperatures of water and *n*-decane bound to the NaCl powder in (a) $CDCl_3$ (dash-dotted lines) and $CDCl_3$/TFAA (9:1) (solid lines) at 0.1 g/g of water and 0.1 g/g of decane; (b) a mixture of hydrated PMS (h = 9 g/g) with decane (1 : 1) (dash-dotted lines) and a mixture with hydrated PMS/KCl (1 : 3) at h = 9 g/g and decane (4 : 1) (solid lines) [248].

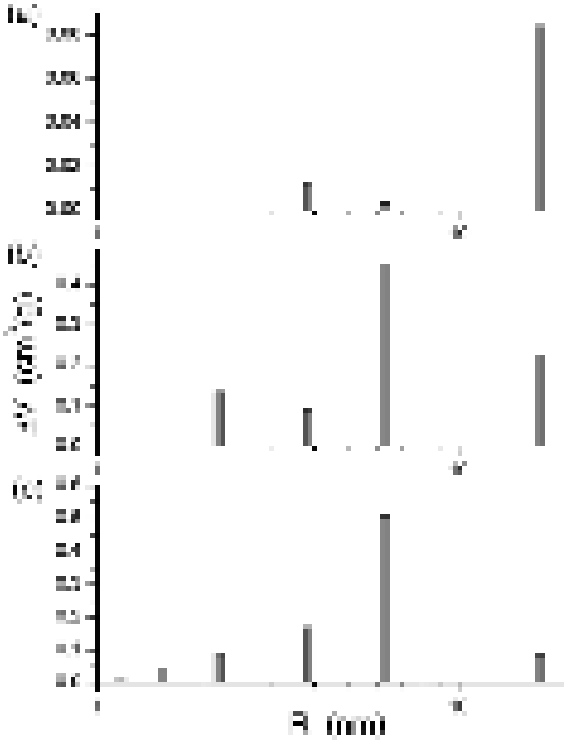

Fig. 146. Size distributions of unfrozen water structures in (a) NaCl powder with 0.1 g/g of water and 0.1 g/g decane in $CDCl_3$ medium; (b) hydrated PMS (90 wt.% water) with decane (1 : 1); and (c) a mixture with hydrated PMS/KCl (1 : 3) and decane (4 : 1) [248].

A decrease in the content of decane and addition of KCl to hydrated PMS resulted in unexpected upfield shift of water signal from 5-6 ppm (dash-dotted lines) toward 4.5-5.0 ppm (solid lines, Fig. 145b) [248]. This result could be explained by diminution of sizes of bound water structures after addition of KCl (Fig. 146b,c). In contrast to the systems with NaCl (Fig. 145a), signals of water and decane were not observed at $T < T_{f,d}$ = 243.5 K (freezing point of bulk *n*-decane) (Fig. 145b). However, in the presence of KCl signal of water was observed at 250-260 K. Thus, a small fraction of SAW was strongly bound, and signal of WAW disappears at low temperatures even at $T < T_{f,d}$. Certain broadening of decane signal could be due to nonuniformity of magnetic susceptibility of samples including relatively large solid particles of salts [248].

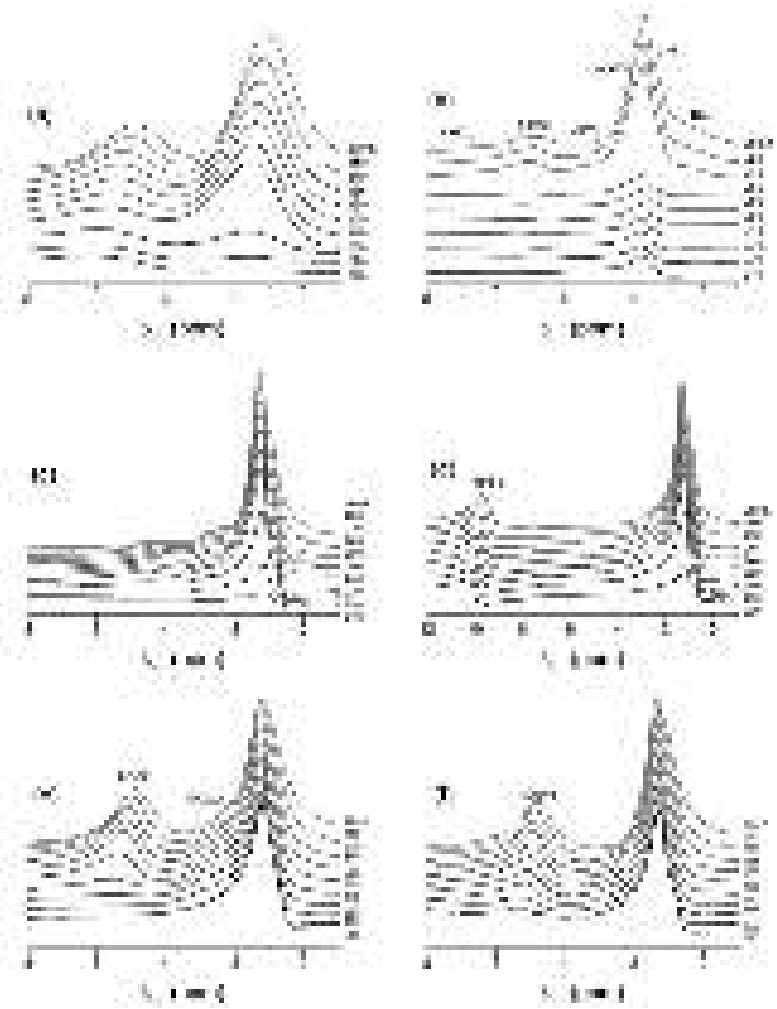

Fig. 147. ^{1}H NMR spectra recorded at different temperatures of water and *n*-decane bound to (a) PS300/KCl (6 : 1) at h = 0.1 g/g and C_d = 0.2 g/g in air; (b) PS300/KCl (6 : 1) at h = 0.1 g/g in a mixture with $CDCl_3/C_{10}H_{22}$ (7 : 1); (c) PS300/NaCl (6 : 1) at h = 0.1 g/g and C_d = 0.15 g/g in a mixture $CDCl_3/CD_3CN$ (4:1) medium; (d) PS300/NaCl (6 : 1) at h = 0.1 g/g and C_d = 0.15 g/g in a mixture $CDCl_3/CD_3CN$/TFAA (4:1:1) medium (e) PS300/KCl (6 : 1) at h = 0.1 g/g and C_d = 0.2 g/g in $CDCl_3$ medium; and (f) PS300/LiCl (1 : 1) at h = 0.1 g/g and C_d = 0.15 g/g in $CDCl_3$ medium [248].

Despite a relatively small amount of water (insufficient to dissolve NaCl in the studied samples) bound to NaCl particles, water formed relatively large structures at R > 3 nm in radius (Fig. 146a). They corresponded to SAW but WBW, since surface area of relatively large NaCl crystallites was small [248]. Water bound to PMS, which was characterized by developed surface area ~200 m^2/g [53,69], formed much smaller structures (Fig. 146b,c), which corresponded to both SBW and WBW, as well as SAW and WAW (Fig. 118b). Addition of KCl led to diminution of sizes of these structures (Fig. 146c) [248].

In a mixture of PS300 nanoparticles with small KCl particles being in air, the freezing point depression was observed for both bound water and decane (Fig. 147a) [248]. Unfrozen water was observed even at 210 K and decane at 220 K. Water formed relatively small structures (Fig. 148a) in narrow voids between silica and salt particles. In $CDCl_3$ medium, lines became narrower (due to diminution of molecular exchange effects) (Fig. 147b). A portion of water was displaced from pores. This led to differentiation of signals, since two signals of SAW were observed at δ_H = 5 ppm (SAW1) and 3.5 ppm (SAW2), as well as WAW at δ_H = 1.7-2.0 ppm. Addition of CD_3CN to this mixture (Fig. 147c) caused an upfield shift of water signals and a relative increase in the amounts of SAW2 and a decrease in the content of SAW1. This suggested decreasing associativity of bound water molecules. Addition of TFAA (Fig. 147d) resulted in simplification and averaging of the spectra due to fast proton exchange between molecules of water and TFAA. Intensive signal of the aqueous solution of TFAA was observed at 10 ppm. Replace of NaCl by KCl (Fig. 147e) or

LiCl (Fig. 147f) led to enhancement of SAW1, including both SBW and WBW. Appearance of these waters corresponded to the formation of relatively small structures (Fig. 148c, d) [248].

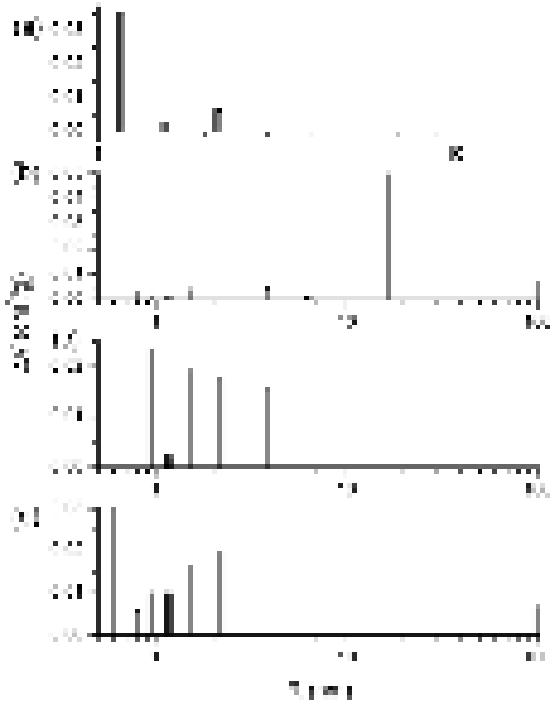

Fig. 148. Size distributions of unfrozen water structures in (a) PS300/KCl (6:1) in air; (b) PS300/NaCl (6:1) in $CDCl_3$; (c) PS300/KCl (6:1) in $CDCl_3$; and (d) PS300/LiCl (1:1) in $CDCl_3$ [248].

The interfacial behavior of bound decane depended on the type of adsorbents (silica PS300 and HPS300, PMS, salts), the presence of water, and the type of dispersion medium [248]. All these features reflect in the changes in the amounts of unfrozen decane *vs*. temperature recorded at increasing temperature from 210 K to 290 K (Fig. 149). At $I/I_0 = 0$, all decane was in solid-like state (freezing point $T_{f,d} = 243.5$ K), and at $I/I_0 = 1$, all decane was liquid. The I/I_0 curves for decane bound to PMS (Fig. 149a, curves 3 and 4) showed a weak influence of hydrated PMS on the temperature behavior of decane that was similar to bulk decane. Consequently, decane could not displace water from the PMS surface, since the confined space effects for decane were practically absent. For all other systems, the confined space effects were observed because a fraction of unfrozen decane was observed at $T < T_{f,d}$. There was another effect of inhibition of melting a fraction of solid-like decane at $T > T_{f,d}$. This effect was maximal for decane bound to PS300/NaCl located in the $CDCl_3$ medium (Fig. 149b, curve 1). This immobilization of bound decane could be maximal effective in mesopores of appropriate sizes. PS300 possesses textural mesopores and macropores. During any treatment (grinding, suspending/drying, gelation, mechanochemical activation) of PS300, it became more compacted and its bulk density strongly increased (up to 0.3 g/cm^3), and this led to increase in contributions of textural mesopores [53,248]. A fraction of solid-like structures of decane formed in mesopores could remained during heating at $T > T_{f,d}$ because the heating rate was relatively high. This led to delay in melting of bound structures. Notice that the I/I_0 curves for the systems with $CDCl_3$ dispersion medium were located lower than that for the systems in air (Fig. 149). In both air and $CDCl_3$ medium at $T \approx T_{f,d}$, approximately 70 % of decane was in a liquid state. This showed a strong colligative effect of solvents with lower freezing point than that of solutes [53,248].

Table 22. Sample characteristics and integrated changes in the temperature range of phase transition of *n*-decane [248].

Solids	h (g/g)	C_d (g/g)	Medium	ψ_- (K)	ψ_+ (K)	I/I_0 $T = T_f$
NaCl	0.15	0.1	$CDCl_3$	–17.8	5.1	0.73
NaCl	0.15	0.1	$5CDCl_3$+1TFAA	–17.8	9.0	0.71
PMS	9.0	1.0	Air	–1.7	4.2	0.40
1PMS/3KCl	9.0	0.23	Air	–1.5	3.4	0.35
6PS300/1KCl	0.1	0.20	Air	–7.9	6.5	0.73
6PS300/1NaCl	0.1	0.15	$CDCl_3$	–3.7	20.8	0.11
6PS300/1NaCl	0.1	0.15	$4CDCl_3$+$1CD_3CN$+1TFAA	–12.7	8.7	0.77
6PS300/1KCl	0.1	0.20	$CDCl_3$	–21.3	7.3	0.68
PS300/LiCl	0.1	0.15	$CDCl_3$	–14.8	5.6	0.65
HPS300/KCl	0.1	0.10	CCl_4	–18.9	2.9	0.83

Note. $\psi_- = \int_{T_{min}}^{T_f} I(T)/I_0 dT$ and $\psi_+ = \int_{T_f}^{T_{max}} \frac{I_0 - I(T)}{I_0} dT$.

Fig. 149. Relative intensity in the ^{1}H NMR spectra of decane (I_0 corresponds to intensity at 290 K) bound to (a) NaCl at C_d =0.1 g/g and h = 0.1 g/g in $CDCl_3$ (curve 1), with added TFAA as $CDCl_3$/TFAA = 5 : 1 (2); PMS/KCl (1 : 3) at C_d =0.225 g/g and h = 9 g/g (3); PMS at C_d =1 g/g and h = 9 g/g (4); and PS300/KCl (6:1) at C_d =0.2 g/g and h = 0.1 g/g in air (5); (b) PS300/NaCl (6:1) at C_d =0.15 g/g and h = 0.1 g/g in $CDCl_3$ (curve 1); HPS300/KCl (1:1) at C_d =0.1 g/g and h = 0.1 g/g in CCl_4 (2); PS300/NaCl (6:1) at C_d =0.15 g/g and h = 0.1 g/g in $CDCl_3$/CD_3CN/TFAA (4:1:1) (3); PS300/LiCl (1:1) at C_d =0.15 g/g and h = 0.1 g/g in $CDCl_3$ (4); and PS300/KCl (6:1) at C_d =0.2 g/g and h = 0.1 g/g in $CDCl_3$ (5) [248].

Minimal integrated effects on melting of decane were observed for the poly(methylsiloxane) (PMS) systems (Table 22, ψ) [248]. This due to filling of pores by water (h = 9 g/g), relative hydrophilicity of PMS due to the presence of a number of residual silanols [39], and relatively large sizes of KCl crystallites. Notice that the maximal difference in changes in the

Gibbs free energy of solvation of non-dissociated was for LiCl. Calculations with SMD/B3LYP/6-31G(d,p) clusters $M_{10}Cl_{10}$ (M = Li, Na) and K_8Cl_8 with the geometry optimized using the HF/6-31G(d,p) method gave for solvation in water and *n*-decane, respectively: –41.3 and –34.9 kJ/mol ($Li_{10}Cl_{10}$), –28.2 and –24.9 kJ/mol ($Na_{10}Cl_{10}$), and –22.5 and –18.2 kJ/mol (K_8Cl_8). Thus, the difference for KCl particles in solvation by water and decane added a reason to form of large decane structures (bound to PMS/KCl) with the properties close to that of bulk decane. A significant decrease in the amounts of water from h = 9 g/g bound to PMS to 0.1-0.15 g/g bound to silica with salts or individual NaCl led to enhancement of the interfacial effects on decane (Table 22, ψ). In many cases, the freezing point depression effects (*i.e.* ψ_-) were stronger than the melting delay effects (*i.e.* ψ_+). Both effects depended more strongly on the textural characteristics and the amounts of water (*i.e.* filling of pores by water) than the types of silica and salts. The latter could be explained by relatively weak effects of salt crystallites or dissolved ions on the ^{1}H NMR spectra of water without of adsorbents (Fig. 150) or bound to silica (Fig. 151) because all the spectra were characterized by a signal at 4-5 ppm typically observed for bound SAW or bulk water [53]. The spectrum of hydrated LiCl nanoparticles was slightly different due to partial dissolution of LiCl and formation of charged particles including H_3O^+ and OH^-. Anions Cl^- were chaotropes but cations Li^+ were kosmotropes, which differently affected the water structure, especially at a surface of polar nanoparticles. The dissolution effects were much weaker for NaCl nanoparticles (Fig. 150, curve 2). However, some separated fragments were formed.

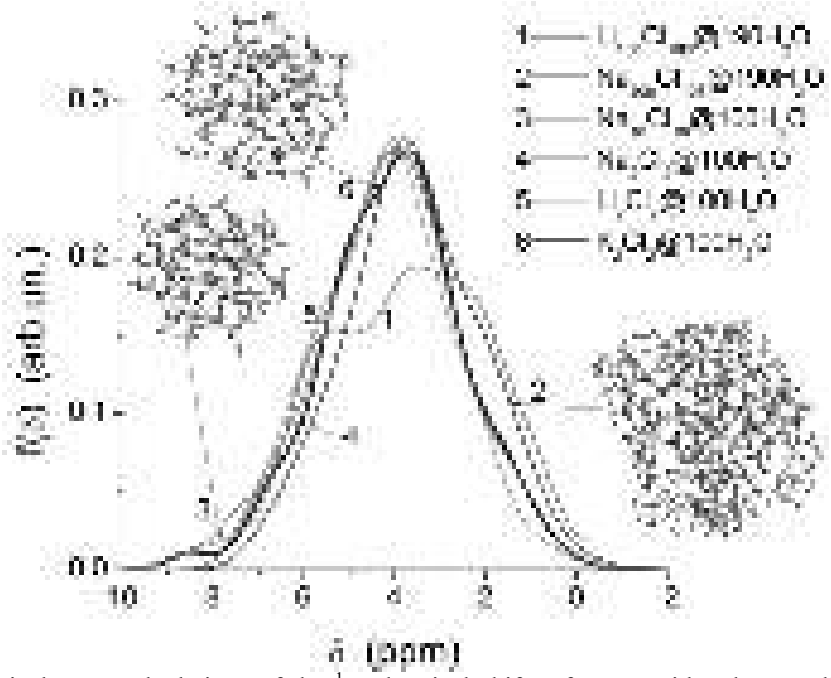

Fig. 150. Semiempirical PM7 calculations of the ^{1}H chemical shifts of water with salt crystallites (curves 1-3) or dissolved ions (curves 4-6) [210].

The interfacial and temperature behavior of mixed water and *n*-decane depended on such several factors as the texture and surface nature of adsorbents, the presence and content of microparticles or nanoparticles of salts, the amounts of components [53,210,248]. If water completely fills pores of poly(methylsiloxane), which contains both non-polar Si-CH_3 and polar Si-OH groups, that decane co-adsorbed onto already hydrated PMS practically did not sense the confined space effects and its freezing/melting occurred near the freezing point of bulk decane. If co-adsorbed water and decane fills only a portion of pores that their interfacial and temperature behavior depended on the texture of the adsorbents and amounts of salt crystallites. This led to broadening of the temperature range of melting of decane in both sides from the freezing point of bulk decane. Typically, the freezing point depression due to confined space effects resulted in stronger changes in the temperature behavior of adsorbed decane than the effects of melting delay

due to both kinetic suppression and immobilization of solid-like structures of decane in mesopores of adsorbents. The dispersion media (nonpolar CCl_4, weakly polar $CDCl_3$, polar CD_3CN and TFAA) influence the interfacial and temperature behavior of co-adsorbed water and *n*-decane because decane could be easily dissolved in non-polar or weakly polar solvents but water could strongly interact with polar solvents. This caused additional differentiation of the interfacial structures with water (including its four types SAW & WAW, SBW & WBW) and decane [53,210,248].

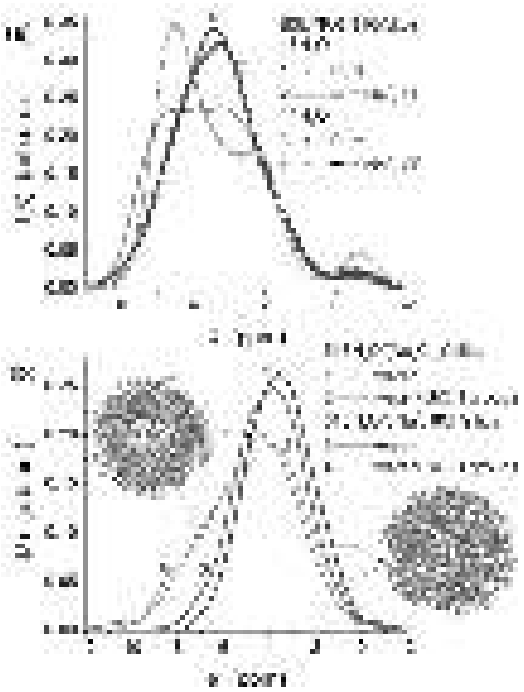

Fig. 151. (a) DFT B3LYP/6-31G(d,p) and (b) semiempirical PM7 calculations of the ^1H chemical shifts in pure water, water with NaCl (a) alone or (b) bound to silica surface [210].

Acidic solutions in confined space

Interfacial water at a small content could form large clusters interacting with silica with the presence of hydrophobic or weakly polar surroundings [53]; however, practically all water remained strongly bound [53,215] and did not form the phase separated from silica. Similar regularities in the temperature dependences were observed for adsorbed aqueous solution of HCl (Fig. 152). Pure liquid hydrochloric acid (36 wt.%) has the signal at δ_H = 8.8-9.4 ppm increasing with lowering temperature (Fig. 152a). Hydrated complexes of HCl with a dissolved fraction (Fig. 152b, signal 1) and SAW (signal 2) bound by nanosilica differ in their temperature dependence. The δ_H value and intensity of signal 1 depended weakly on temperature in contrast to signal 2 which increased and shifts toward the strong magnetic field with increasing temperature. Signal 2 was not observed at T < 240 K. Addition of hydrochloric acid (Fig. 152b) led to diminution of the signal of WAW interacting with silica (δ_H = 1.5-2 ppm) in comparison with the A-300-water system (Fig. 152a). However the signal of water dissolved in chloroform (δ_H = 1 ppm at very low amount of this water) did not depend on the presence of hydrochloric acid [215].

The spectra shape of SAW bound in samples placed in the CCl_4 medium changed weakly (Fig. 152c); however, the difference in the chemical shift of two signals of SAW decreased [215]. The difference between signals 1 and 2 decreased with increasing HCl concentration since relative intensity of signal 1 increased. A decrease in the intensity of signal 2 was observed at T < 240 K (Fig. 152).

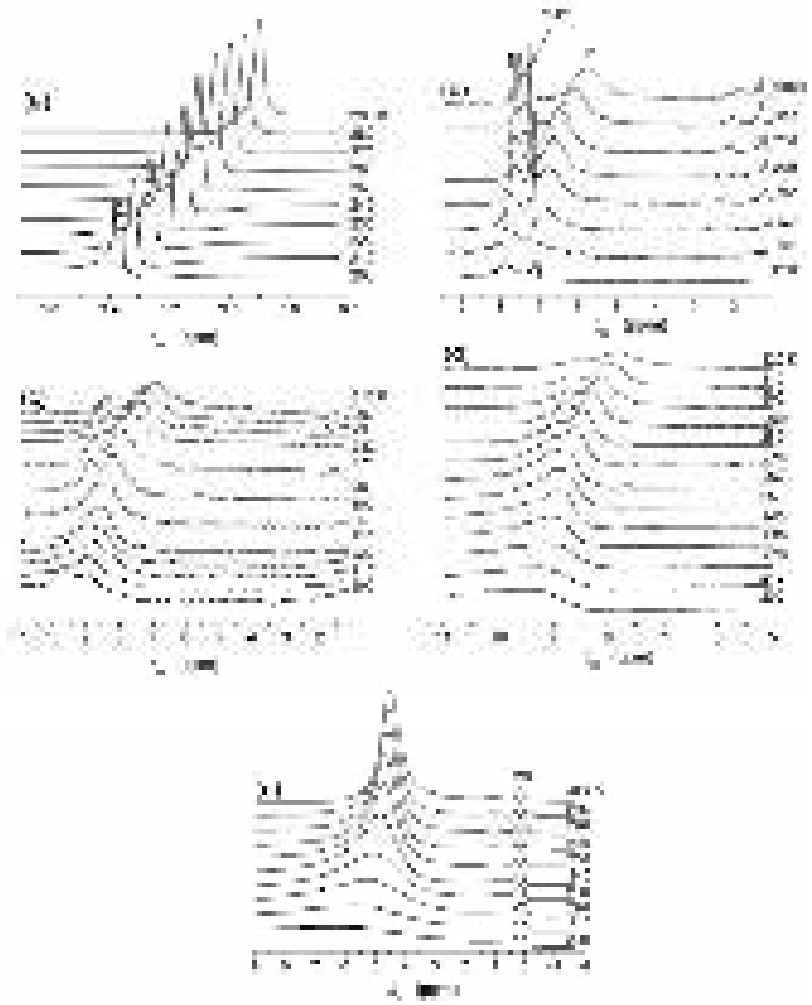

Fig. 152. ^{1}H NMR spectra at different temperatures of (a) 36% hydrochloric acid, and hydrochloric acid and water adsorbed to (b)-(d) initial and (e) MCA A-300 in (b) $CDCl_3$ or (c)-(e) CCl_4; (b, c, e) 38 mg/g H_2O and 44 mg/g HCl, (d) 140 mg/g H_2O and 120 mg/g HCl.

In 36% hydrochloric acid used six water molecules were per HCl molecule. This solution was frozen at $T < 200$ K (Fig. 152a) with simultaneous freezing of water and HCl. Freezing of the HCl solutions was possible at higher temperatures if the HCl concentration decreased. Consequently, the results shown in Fig. 152b-d could be interpreted as the formation of two types of HCl/water structures with different concentrations of HCl (C_{HCl} was smaller in structures corresponding to signal 2 at a lower δ_H value and these structures include mainly non-dissociated HCl molecules) [215]. The chemical shift of signal 1 was close to that of individual HCl solution, *i.e.* the structures corresponding to signal 1 have the properties similar to that of the bulk HCl solution with significant contribution of dissociated HCl molecules [215].

For water/HCl adsorbed onto MCA A-300 the ^{1}H NMR spectra (Fig. 152e) were similar to that of water adsorbed on MCA A-300. Freezing of the adsorbates in these systems occurred at similar temperatures. Water in confined space of smaller voids in MCA A-300 could have a lower activity as a solvent. Therefore, water clusters adsorbed on MCA A-300 include a lower amount of dissolved HCl molecules. Quantum chemical calculations of the An anhydrous cluster with 16HCl but calculated with consideration of the solvation effects (GIAO/IEFPCM/B3LYP/6-31G(d,p)) was characterized by a narrow $f(\delta_H)$ distribution function (Fig. 153) because all the HCl molecules remained non-dissociated.

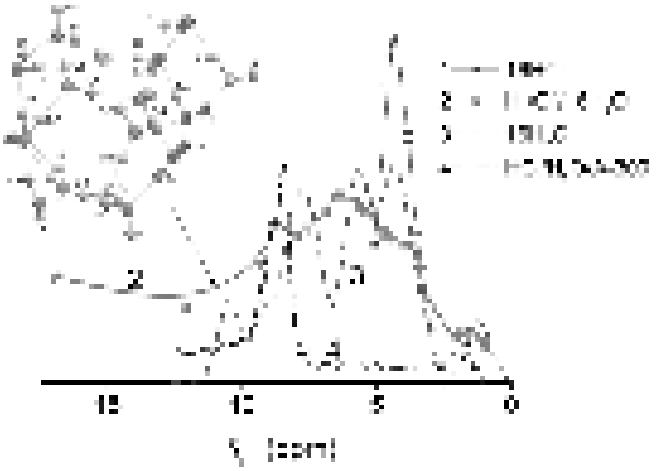

Fig. 153. The distribution function of the δ_H values for clusters with $16H_2O$, 16HCl and dissociated HCl interacting with $16H_2O$ (geometry was optimized using IEFPCM/B3LYP/6-31G(d,p) and the NMR spectra were calculated using GIAO with consideration of the solvation effects), and experimental ^{1}H NMR spectrum of water/HCl/A-300 (concentrated solution of HCl) recorded at 280 K (curve 4) [210,215].

The ^{1}H NMR spectra of the anhydrous cluster with 16HCl and of the water cluster with dissociated HCl strongly differ (Fig. 153). The latter had characterized by greater δ_H values up to 17 ppm. These calculations showed that the position of the observed resonance (signal 2, Fig. 152b) could be affected by the presence of non-dissociated HCl. Zundel and Eigen cations located far from Cl^- ions [249] provide signals at higher δ_H values (signal 1, Fig. 152b) [215].

Adsorption of a homogeneous HCl/water mixture onto nanosilica A-300 initial or mechanochemically activated resulted in diminution of HCl dissolution in water (at a low content of water in the system), especially for MCA silica with narrower voids between nonporous nanoparticles [215]. This effect appeared as changes in the ^{1}H NMR spectra of the HCl solution characterized by signals at the δ_H values corresponding to both dissociated and non-dissociated HCl molecules. Obtained results showed that the use of nanosilica as an oral sorbent could change the characteristics of gastric juice with the HCl solution. The concentration of dissociated HCl molecules could be smaller in voids between silica nanoparticles in their aggregates. These changes could depend on the type of nanosilica, *e.g.*, initial or MCA silica. For the latter the mentioned effect was stronger because of diminution of the size of voids between silica nanoparticles [53,215].

The ^{1}H NMR spectra of fresh 30% solution of phosphonic acid in D_2O demonstrate the main signal of the protons in the PO-H groups (and H_2O or HDO due to H-D exchange reactions between PO-H and D_2O) with δ_H = 6 ppm (290 K) increased to 9.8 ppm (200 K) with decreasing temperature [244]. The signal intensity decreased with lowering temperature and its width increased because of freezing of a portion of water and acid as well as concentrating of the acid solution with decreasing temperature. Notice that for a similarly concentrated HCl solution, δ_H = 9.0-9.4 ppm at 290-200 K [215] because the dissociation degree of HCl is much higher than that of POA. Two signals of lower intensity were observed at weaker and stronger fields than the main signal. The difference between their δ_H values was approximately 2.1 ppm. These δ_H values depended weakly on temperature; however, the intensity sharply increased at $T \geq 260$ K but the width increased at $T < 260$ K. This occurred due to freezing of a portion of POA. After boiling of the sample and its storage at 290 K for a week, the intensity of the H_P doublet signals decreased because of the H_P-D_{D2O} exchange reaction. The ^{1}H NMR spectra of solid phosphonic acid with a low content of water (50 mg per gram of solid POA) in CCl_4 medium include three signals at δ_H = 6 (signal 1), 5 (weak signal as a shoulder of signal 1) and 3.5 (signal 2) ppm at 290 K (Fig. 154a). The shape of signal 1 was asymmetrical. Its intensity decreased with decreasing temperature (Fig. 127a), as well as the δ_H value decreased to 5 ppm at 200 K (in contrast to the behavior of the signal in the concentrated POA solution). The δ_H values for other two signals depended weaker on

temperature than signal 1. Addition of water to 70 mg/g results in an increase in the signal intensity and width (Fig. 154b). However, the temperature behavior of the spectra was similar to that at C_{H2O} = 50 mg/g [244].

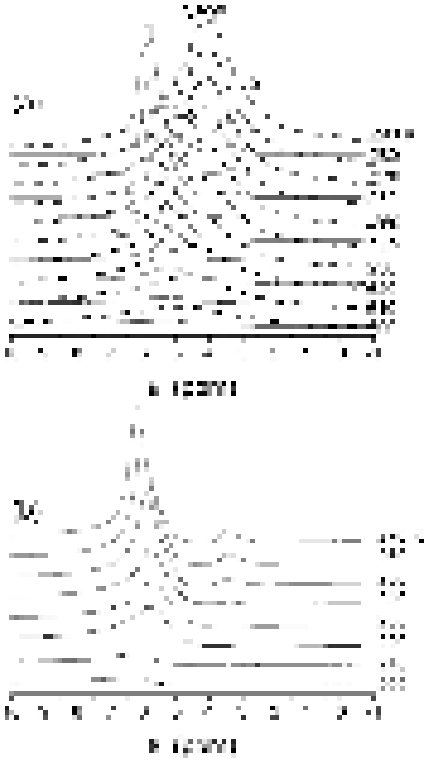

Fig. 154. ^{1}H NMR spectra recorded at different temperatures of weakly hydrated solid phosphonic acid (a, b) alone and (a, dashed lines) adsorbed onto nanosilica at A-300/POA = 4/1 at *h* = (a) 50, (b) 70 and (a, dashed lines) 100 mg/g in CCl_4 medium.

The displacement of signal 1 toward the weak magnetic field with increasing temperature suggests that contribution of protons in water with dissolved acid increased with temperature (Fig. 154) because increased solubility of H_3PO_3. Contribution of hydrated protons (*i.e.* dissociated POA) was small at small content of water (Fig. 154a) because the δ_H value decreased with decreasing temperature in contrast to that for the concentrated POA solution. The spectra shape showed that structures with water/dissolved H_3PO_3 were nonuniform since several signals could be found. Signal 2 at 3.5 ppm could be attributed to water molecules with one hydrogen bond as a proton-donor and PO-H without the hydrogen bonding (see quantum chemical calculation results) [244].

Dried suspension with 16 wt.% of silica and 4 wt.% H_3PO_3 as a powder with approximately 10 wt.% of water was characterized by the ^{1}H NMR spectra with only one relatively broad signal at 4-4.5 ppm (Fig. 154) [244]. Similarly hydrated nanosilica A-300 modified by phosphonic acid obtained by hydrolysis of adsorbed PCl_3 was characterized by larger values δ_H = 6.5-10.5 ppm [53]. During drying of the concentrated suspension with silica and POA, solution supersaturation results in formation of acid crystallites. Additionally, residual water bound by nanosilica has low activity as a solvent. Therefore, according to the ^{1}H NMR spectra (Fig. 154), bound water could dissolve a low amount of H_3PO_3 since the δ_H value depended weakly on temperature as well as the signal shape [244].

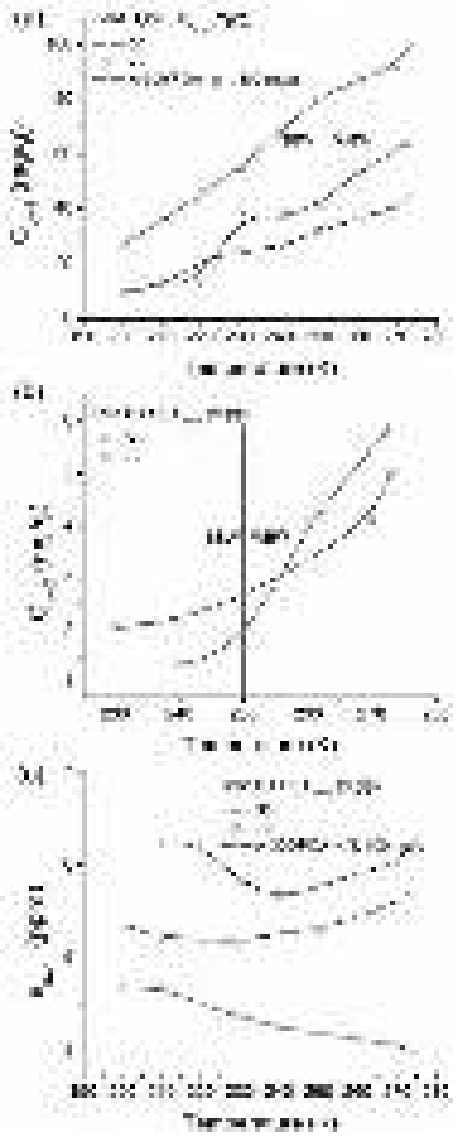

Fig. 155. Temperature dependences of concentration of unfrozen water responsible for signal (a) 1 and (b) 2 and (c) chemical shift of signal 1 for weakly hydrated solid H_3PO_3 (C_{H2O} = 50 or 70 mg/g) and A-300/H_3PO_3 = 4/1 (C_{H2O} = 100 mg/g) in CCl_4 medium.

Water unfrozen at T < 273 K due to bonding to solid POA or dried A-300/POA powder (Fig. 155a) could be attributed to strongly (SBW unfrozen at T < 250 K) and weakly (WBW frozen at T < 250 K) bound water. However, there was not a clear boundary between SBW and WBW because of changes in the concentration of dissolved POA. A major fraction of water responsible for signal 1 ($C_{uw1}(T)$) (Fig. 155a) corresponded to SBW but a major fraction of water giving signal 2 corresponded to WBW (Fig. 155b) [244].

The δ_H value of sample with 50 mg H_2O per gram of acid depended weakly on temperature (Fig. 155c) [244]. It slightly increased at T > 230 K. An increase in the water content to 70 mg/g gives an increase in the δ_H value with a minimum at 240 K. For the dried A-300/H_3PO_3 powder, the δ_H value decreased with increasing temperature (Fig. 155c). These results were caused by two competitive processes such as diminution of associativity of water molecules (δ_H decreased) and increase of concentration of dissolved acid (δ_H increased) with temperature [244]. During freezing of the solution, pure ice and acid crystallites (which do not contribute the ^{1}H NMR spectra here) form separately. However, interfacial water could be frozen at lower temperature than acid that affected the concentration of acid dissolved in the interfacial water and the chemical shift δ_H decreased with lowering temperature. However, signal of the concentrated acid solution was absent in weakly hydrated A-300/H_3PO_3 powder because water bound to the silica surface did not

dissolve the acid which formed crystallites weakly bound to silica surface, according to the FTIR spectra [244].

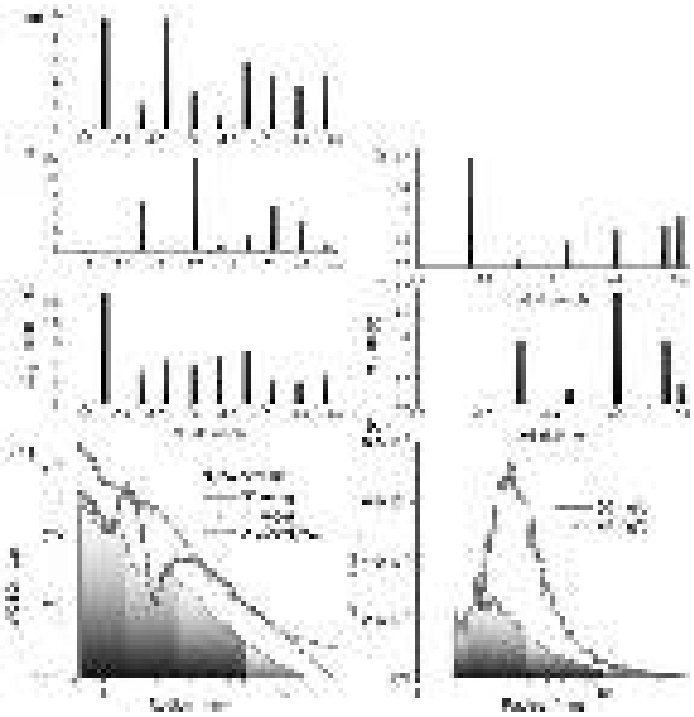

Fig. 156. Changes in the Gibbs free energy of bound water in weakly hydrated solid H_3PO_3 in CCl_4 medium at C_{H2O} = (a, e) 50 or (b, f) 70 mg/g and (c) A-300/POA at C_{H2O} = 100 mg/g and (d, g) water cluster size distributions (WCSD) with respect to signals (d) 1 and (g) 2.

Water bound to solid POA or silica/POA powders was energetically and structurally nonuniform (Fig. 156) because of spatial restrictions dependent on void size distribution between nanoparticles and the difference in the surface effects on water layers nearest to the surface and located in the next layers [53,244]. As a whole, at low content of adsorbed water (50-100 mg/g) it tended to form small clusters (Fig. 156d) characterized by relatively large changes in the Gibbs free energy (Fig. 156a-c) of bound water with the cluster size distributions (WCSD) over 0.6-10 nm in radius (Fig. 156d). Water responsible for signal 2 was nonuniform too but it did not form nanoclusters at R < 1 nm (Fig. 156g). Its nanodomains weaker interacted with solid POA (Fig. 156e,f) than water responsible for signal 1 [244].

Melting of anhydrous H_3PO_4 occurred at 290 K; however, the aqueous solution of the acid could be frozen at much lower temperature because of colligative properties of the aqueous solutions [53,242,244]. Initial sample OX-50/H_3PO_4 at C_{H2O} = 5 mg/g has only a weak ^{1}H NMR signal at δ_H = 4 ppm. Its intensity decreased with lowering temperature because of freezing of water which was weakly bound. Signal at 0 ppm was due to tetramethylsilane (0.2 wt.%) used as a reference compound. For dried OX-50/POA powder at C_{H2O} = 45 mg/g, the values of all the structural characteristics were much lower than those of A-300/POA at C_{H2O} = 50 mg/g because OX-50 has the S_{BET} value six times smaller than that of A-300. However, the difference in the S_{uw} values was smaller than that in the S_{BET} values because of contributions of POA nanocrystallites. Very large values of the structural characteristics of unfrozen water were observed for the concentrated suspension of OX-50/POA. In other words, water in this suspension was strongly clustered (vide infra) due to interactions with POA molecules and oligomers [244].

There was a significant difference in the solubility of POA in bulk and bound water because of decreased activity of the interfacial water [244]. Low-temperature ^{1}H NMR spectroscopy investigations of water bound by phosphoric and phosphonic acids solid alone or adsorbed onto nanosilicas OX-50 or A-300 showed that concentrated solutions or weakly hydrated solid POA or dried silica/POA powders being in CCl_4 medium were characterized by different

temperature dependences of the δ_H values because of only partial dissociation of the PO-H bonds. The δ_H values depended strongly on water amounts, silica type and temperature. NMR cryoporometry showed that small water clusters (< 1 nm) and nanodomains (up to 20 nm in size) were present at the interfaces of hydrated solid POA and silica/POA powders. Quantum chemical calculations of the ^{1}H NMR spectra demonstrate the influence of POA/water cluster structure and dissociation of the PO-H bonds on the δ_H values [244].

Hydrophilic-hydrophobic characteristics of FMO and confined space effects

Interesting information on the interfacial and temperature behaviors of adsorbates bound to FMO can be obtained using the DSC method [53]. Comparison of the results of low-temperature ^{1}H NMR spectroscopy and DSC (Table 23) can allow one to attain a deeper insight into these phenomena. The differences in the values of the heat of immersion in water (Q_w) and free surface energy (γ_S) (Table 23) are due to the differences in the amounts of adsorbates and the approaches used to calculate these values. Note that Q_w deals with all water bound to FMO at $T \approx 293$ K, but γ_S deals with only a fraction of unfrozen water at $T < 273$ K [53].

The interaction of the silica surface with polar and non-polar molecules upon immersion in liquids is primarily determined by the nature and concentration of surface functional groups. The initial fumed silica surface contains hydrophilic silanol groups and siloxane bridges, which have rather hydrophobic properties [37,38], and the concentration of free silanol groups on the silica surface is 2.25–2.5 μmol/m^2. Therefore, fumed silica exhibits pronounced hydrophilic properties. Substitution of polar silanol groups for trimethylsilyl (TMS) groups leads to a change in the nature of the silica surface and the interaction with the polar and nonpolar molecules [53]. In the case of immersion of modified silica surface in polar liquids there is a significant reduction of the heat of immersion Q, normalized to 1 g of the sample, with increasing modification degree (Table 24). Immersion in nonpolar decane shows a decrease in Q with increasing degree of surface modification, but it is insignificant. Since the heat of immersion is proportional to changes in the Gibbs free energy of surface, the thermal effect is determined, respectively, not only by the nature of the surface, but also by the specific surface area. The modification of silica causes a decrease in the specific surface area of the samples (Table 24). Therefore, the heats of immersion reflect these changes. The average Q values normalized to 1 m^2 of the sample surface (Fig. 157) tend to decrease Q_w with increasing degree of surface modification. However, the values of Q_d (normalized to 1 m^2 of surface) are independent on modification degree.

Table 23. Adsorption characteristics determined from calorimetrical (Q_w, Q_d, K) and ^{1}H NMR spectroscopy (γ_S) measurements.

Sample	Q_w (J/m^2)	Q_d (J/m^2)	$K=Q_w/Q_d$	γ_S (J/m^2)
SA8	0.119	0.087	1.37	0.288
SA23	0.132	0.151	0.87	0.122
ST20	0.328	0.082	4.0	0.435
AST03	0.345			0.240
AST1	0.548	0.136	4.03	0.163
AST50	0.459	0.251	1.83	0.077
AST71	0.591	0.161	3.67	
AST82	0.493	0.148	3.33	0.479
Al_2O_3[a]	0.411	0.295	1.39	0.231
Al_2O_3[b]	0.400	0.160	2.50	
A-200[c]	0.183	0.149	1.23	0.124
A-50	0.231			0.177
TiO_2	0.262	0.083	3.16	

Note. S_{BET,N_2} = [a]133, [b]86, and [c]230 m^2/g; Q_d is the heat of immersion of FMO in n-decane.

Relatively high values of the heat of immersion in polar liquids (triethylamine, TEA, acetonitrile, 2-propanol and water) and small values of Q_d are caused by the differences in

intermolecular interactions between the liquids and the polar and nonpolar groups of the modified silica surface. Interactions of nonpolar liquid with surface functionalities (polar OH or nonpolar CH_3) are determined only by van der Waals forces. Therefore, the heats of immersion of silica in nonpolar decane are relatively small (due to low energy of the interactions) and they practically do not depend on the concentration of OH or CH_3 groups on the silica surface. The interaction of polar liquids (TEA, acetonitrile, water, 2-propanol) with the solid surface is more complex. There are additive effects of various components of polar interactions, whose energy is much higher than that of the dispersion forces. The heat of immersion for all polar liquids depends on the modification degree of the silica surface, because polar interactions occur only with the polar centers at the surface (OH groups). The heat of immersion in TEA, acetonitrile, and 2-propanol depends almost linearly on the concentration of silanol groups. The decrease in the heat of immersion of modified silica in water at a small degree of modification is insignificant, while for samples with high modification degree small values of the heat of immersion (0.23 – 0.24 J/m^2) were observed. Such dependency for water is probably explained by the high energy of interactions between the molecules of water (surface tension of water is in 3 – 4 times higher than for the rest of investigated liquids) and low ability to interact with nonpolar CH_3 groups.

Table 24. Heats of immersion modified silicas in polar and non-polar liquids.

Sample	□[a]	Q_{water} (J/g)	Q_{TEA} (J/g)	$Q_{2\text{-propanol}}$ (J/g)	$Q_{acetonitrile}$ (J/g)	Q_{decane} (J/g)	S_{BET} (m^2/g)	K_h
A-300 (initial)	0	41.0	63.8	49.4	48.4	17.9	291	2.41
Si1	0.07	40.4	64.0	44.5	44.3	16.8	282	2.41
Si2	0.14	36.1	60.2	41.6	44.9	15.6	275	2.35
Si3	0.30	31.8	53.0	39.5	40.5	15.6	270	2.20
Si4	0.43	30.1	50.3	22.1	38.1	13.7	274	2.12
Si5	0.53	26.0	44.2	33.3	33.6	13.5	250	1.88
Si6	0.62	22.0	45.5	29.8	29.4	15.2	245	1.61
Si7	0.89	4.9	33.4	23.3	23.6	15.3	250	0.43
Si8	1.0	5.5	29.5	23.0	24.6	12.2	246	0.42

Note. [a] Degree of OH group substitution with TMS groups determined by integral intensity of the band at 2966 cm^{-1}.

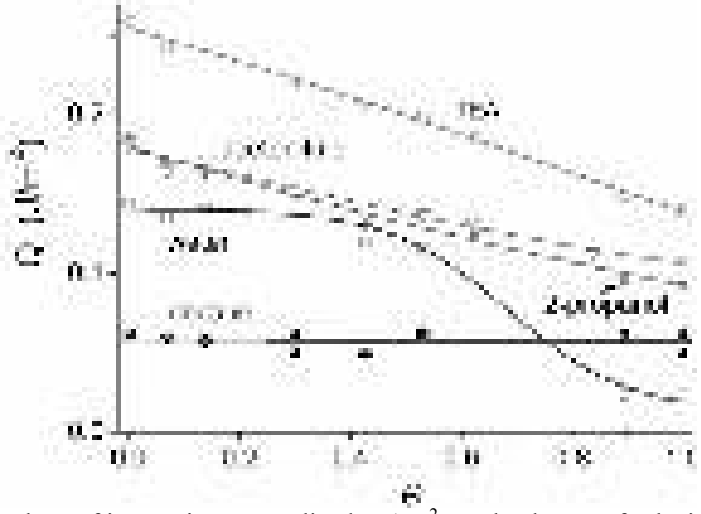

Fig. 157. Dependence of the heat of immersion, normalized to 1 m^2, on the degree of substitution of the silanol groups of the silica surface for TMS groups.

Adsorption of polar polymers onto silica surface occurs due to formation of the hydrogen bonds between polar groups of polymers and surface silanols. Therefore, if the amount of adsorbed polymer corresponds to monolayer, the surface properties are mainly determined by functional groups of the polymers. If the adsorbed polymer amount is less than the monolayer, the interactions of liquid occur with both silanols and functional groups of the polymers. Therefore, the heat of immersion in polar and nonpolar liquids is determined by the total surface area of the

composite, the accessibility of silanols and functional groups of the polymer for interactions with solvent molecules.

Figure 158 shows the heat of immersion in water (normalized to 1 g and 1 m^2) for oxide-polymer composites with various concentrations of PVP (12 000 Da), PVA (43 000 Da), and PEG (35 000 Da). The hydrophilicity of composites may decrease (PEG) or increase (PVP and PVA) depending on the polymer nature and the degree of surface coating. For PVP/silica composites (Fig. 158a) the heat of immersion in water decreases in the initial section due to reducing specific surface area of composites (Fig. 159a). However, at high content of PVP, the heat of immersion in water increases again almost to the initial level. Since the heat of immersion in decane decreases proportionally to the specific surface area, the hydrophilicity index (K_h=Q_w/Q_d) increases (Fig. 159b). Such behavior indicates higher hydrophilicity of surface covered with PVP compared to the initial silica, that confirmed by the values of the heat of immersion normalized per 1 m^2 (Fig. 158b). These data correlate with a high heat of dissolving PVP (J/g) (Table 25), which demonstrates the high solvation energy. For silicas modified with PVA, an increase in the heat of immersion in water normalized per 1 m^2 is also observed with increasing polymer concentration (Fig. 158b), but composites with PEG show a significant decrease in the heat of immersion in water with increasing polymer content (Fig. 158a,b). The heat of dissolution of PEG in water is negative (Table 25) that can argue that PEG reduces the surface hydrophilicity compared with the initial silica. The increase in the surface hydrophilicity of PVA/silica composites in comparison with the initial silica may be caused by the hydrophilic properties of PVA and silanols.

Table 25. The heat of dissolution of polymers in water.

	PVP	PEG	PVA
Heat of dissolution (J/g)	50	–10	soluble only at 80 ºC (n/m)

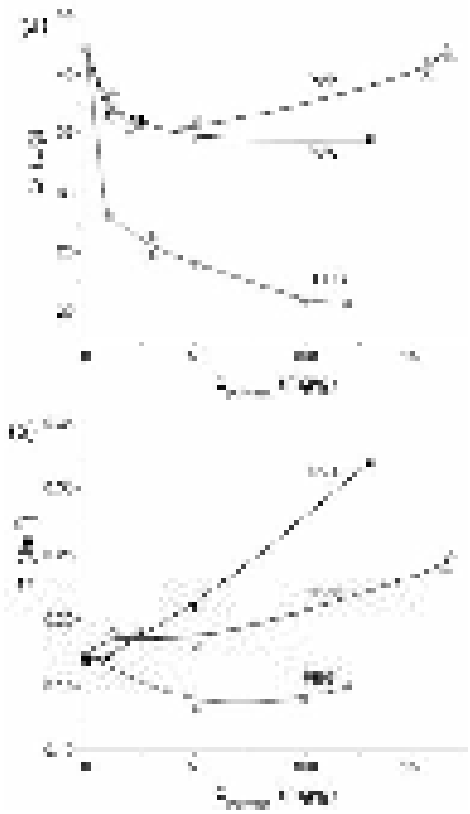

Fig. 158. The heat of immersion in water, normalized to 1 g (a) and 1 m^2 (b), for oxide-polymer composites with different concentrations of PVP, PVA and PEG.

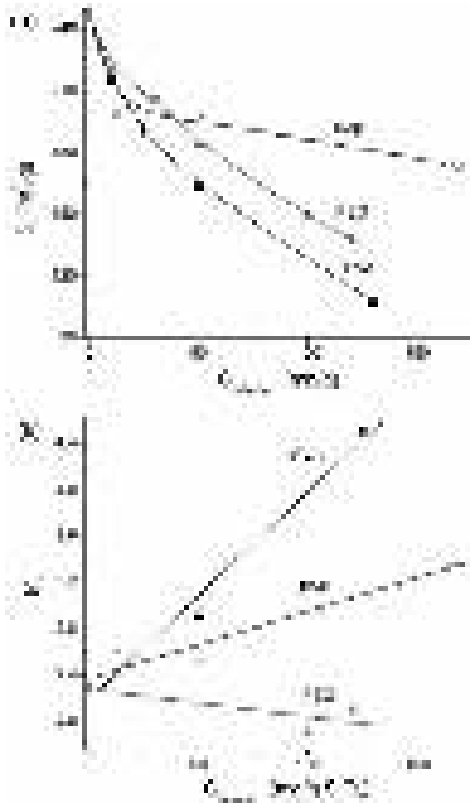

Fig. 159. Specific surface area S (a) and hydrophilicity index K_h (b) of oxide-polymer composites with different concentrations of PVP, PVA and PEG.

Changes in the surface composition for complex oxides are accompanied by changes in the amounts and types of surface sites that can affect the hydrophilicity of these oxides. Therefore, a question arises about regularities in the relationships between the surface composition and hydration properties of complex FMO. The heat of immersion of ST, SA and AST (Tables 26-28) calculated per 1 g of oxide differs over a wide range because of the large differences in the values of S_{BET}.

To avoid the influence of the S_{BET} value, the heat of immersion was also calculated per m^2 of oxide surface area. To estimate the hydrophilicity of oxides, the heat of immersion was measured for both hydrophilic (water) and hydrophobic (decane) liquids, and the hydrophilicity index K_h was calculated. According to the data (Tables 26 and 28), at small content of the second oxide (alumina in SA and titania in ST) the heat of immersion (per m^2) increases. However, a monotonic increase in this value is not observed since the hydrophilicity decreases and then increases at high content of the second phase. This difference can be caused by non-monotonic changes in the surface content of the second phase at the surface of the materials [53]. Additionally, the most acidic sites with bridging OH groups actively interacting with water are formed at the interfaces of SiO_2/Al_2O_3 and SiO_2/TiO_2. Contribution of the interfacial region depends on the surface content of the second phase, its crystallite sizes, and the amounts of sites with isomorphous substitution of Si for Ti or Al or *vice versa*. The use of the K_h values independent of the S_{BET} value but dependent on the ratio between polar and nonpolar sites allows one to observe certain correlations between the surface content of the Al or Ti atoms in the binary and ternary oxides, their surface content and the K_h values.

Notice that the hydrophilicity of fumed titania is much higher than that of silica and alumina, and, accordingly, the availability of surface structures with TiO_2 in binary and ternary oxides can promote the hydrophilicity of the surface in comparison with SiO_2/Al_2O_3. For ternary oxides, there is a synergetic effect since the values of the hydrophilicity index of ternary oxides is higher than that of individual SiO_2, Al_2O_3, and TiO_2.

Table 26. Heat of immersion of FMO with SiO_2/Al_2O_3 at different content of Al_2O_3.

Sample	S_{BET} (m^2/g)	C_{Al} (at.%)	Liquid	Q, J/g	Q, J/m^2	K_h
A300	230	0	water	42.2	0.18	1.2
			decane	34.4	0.15	
Al_2O_3	140	39	water	55. 3	0.39	1.41
			decane	39.5	0.28	
SA1	207	6.2	water	55.2	0.27	1.44
			decane	38.3	0.18	
SA3	188	27.7	water	62.8	0.31	1.42
			decane	44.2	0.23	
SA6	76		water	18.7	0.24	
SA8	308	29.5	water	36.7	0.12	1.36
			decane	26.9	0.09	
SA23	353	11.9	water	46.5	0.13	0.87
			decane	53.6	0.15	
SA75	85	34.1	water	39.7	0.47	1.38
			decane	28.7	0.34	
SA96	81		water	44.0	0.54	1.51
			decane	29.1	0.36	

Therefore, one can assume that the presence of TiO_2 (having high hydrophilicity) at the oxide surface (especially at high surface content of TiO_2) and the formation of bridge OH groups (having high Brønsted acidity at low surface content of Ti and Al) can result in increase of the AST hydrophilicity. The influence of bridge OH groups is especially noticeable for ternary oxides with high amounts and different nature of bridge OH groups leading to the increase in the hydrophilicity of the surface in comparison with SiO_2, Al_2O_3 and TiO_2 (Tables 26-28).

Table 27. Heat of immersion of FMO with SiO_2/TiO_2 at different content of TiO_2.

Sample	S_{BET} (m^2/g)	C_{Ti} (at. %)	Liquid	Q (J/g)	Q (J/m^2)	K_h
TiO_2	50	31.5	water	11.05	0.22	3.2
ST2	77	4.3	water	3.47	0.07	
			decane	27.97	0.36	2.5
ST9	188	7.1	water	11.3	0.15	
			decane	40.56	0.22	2.1
ST14	137	7.8	water	19.7	0.10	
			decane	35.85	0.26	1.6
ST20	86	6.5	water	22.3	0.16	
			decane	28.18	0.33	1.7
ST40	109	7.4	water	16.42	0.19	
			decane	26.54	0.24	1.4
ST65	34	14.4	water	18.9	0.17	
			decane	13.53	0.40	2.8
ST94	30	30.9	water	4.91	0.14	

The enthalpy of phase transitions of bound adsorbates was smaller by the modulus than that of bulk liquids (freezing) or solids (fusion) with the exception of *n*-decane (40% longer than *n*-hexane) bound to initial A-300/AST1 [90]. The decrease in the $|\Delta H|$ occurred due to (i) the small size of bound structures (clusters, nanodomains) located in voids between nanoparticles, and (ii) the disorder of bound liquids (being in amorphous state after freezing) which were frozen at temperatures lower than the freezing point of bulk liquids. Both factors caused smaller endotherms for melting, or exotherms for freezing per bound molecule of adsorbate [90].

Table 28. Heat of immersion of $SiO_2/Al_2O_3/TiO_2$ of different composition.

FMO	S_{BET} (m^2/g)	C_{Si} (at. %)	C_{Al} (at. %)	C_{Ti} (at. %)	Liquid	Q (J/g)	Q (J/m^2)	K_h
ATS0.3	125				water	43.2	0.35	
ATS0.6	97				water	49.3	0.51	3.7
					decane	13.2	0.14	
ATS1	99				water	54.3	0.55	3.0
					decane	17.94	0.18	
ATS50	38	32.1	0.7	11.1	water	17.4	0.46	1.8
					decane	9.52	0.25	
ATS71	74	10.2	2.7	24.9	water	43.7	0.59	3.7
					decane	11.93	0.16	
ATS82	39	0.3	5.8	31.9	water	19.2	0.49	3.3
					decane	5.77	0.15	
ATS87	42	3.8	5.4	30.8	water	30.3	0.72	5.0
					decane	6.08	0.14	
ATS88	39	5.3	4.8	27.7	water	24.8	0.63	2.1
						11.81	0.30	

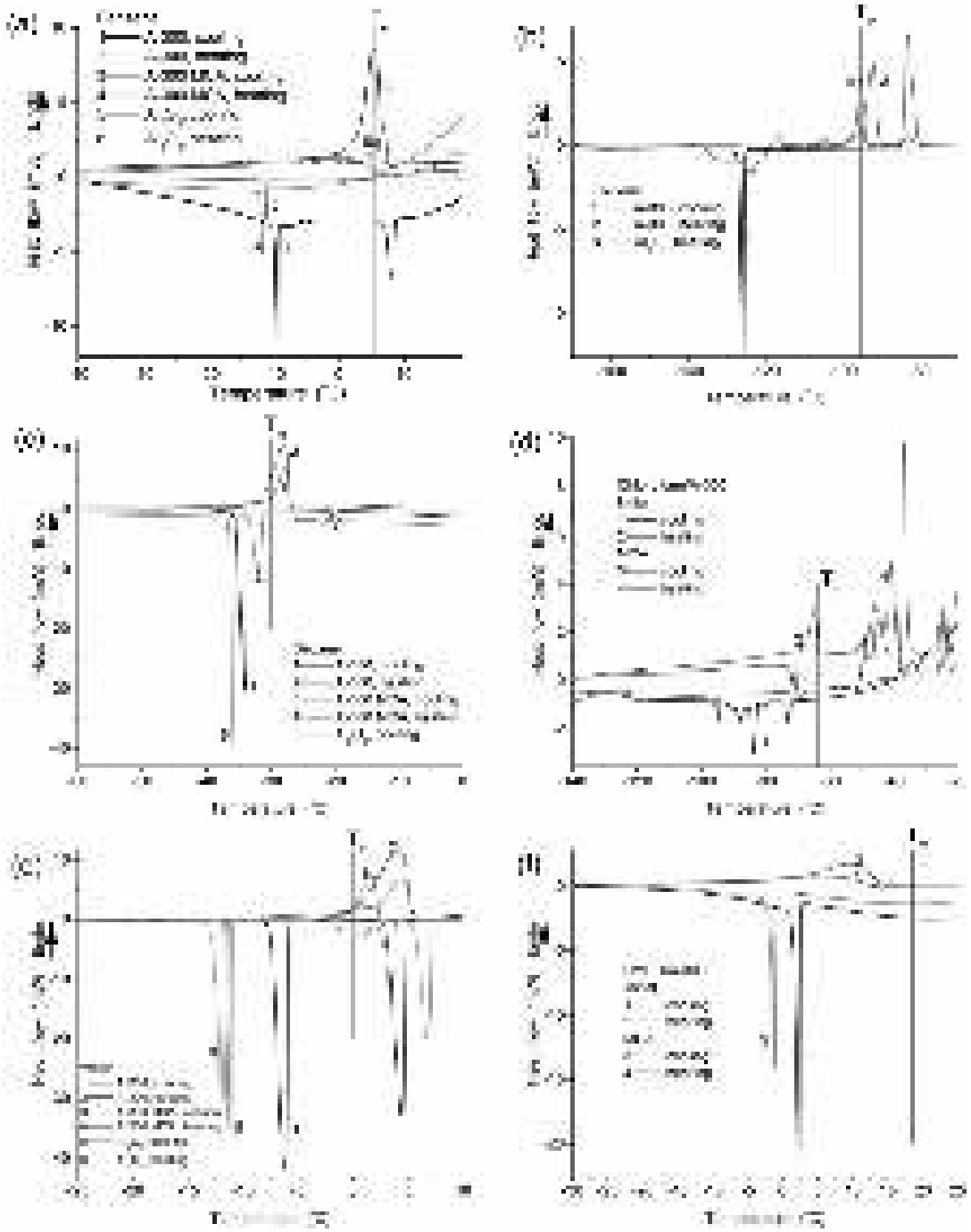

Fig. 160. Normalized (per mg of adsorbates with subtracted baseline) DSC thermograms of (a-c) nonpolar and (d-f) polar adsorbates bound to initial A-300 and alumina or MCA A-300: (a) benzene (melting point T_m = 5.53 °C, boiling point T_b = 80.1 °C), (b) toluene (T_m = −95 °C, T_b = 111 °C), (c) n-decane (T_m from −30.5 °C to −29.2 °C, T_b from 173.8 °C to 174.4 °C), (d) chloroform (T_m = −63.5 °C, T_b = 61.15 °C), (e) water (melting point T_m = 0 °C, boiling point T_b = 100 °C), and (f) DMSO (T_m = 18.5 °C, T_b = 189 °C). Cooling/heating rate was β = 10 °C/min for benzene, decane, water, and DMSO, and β = 20 °C/min for chloroform and toluene.

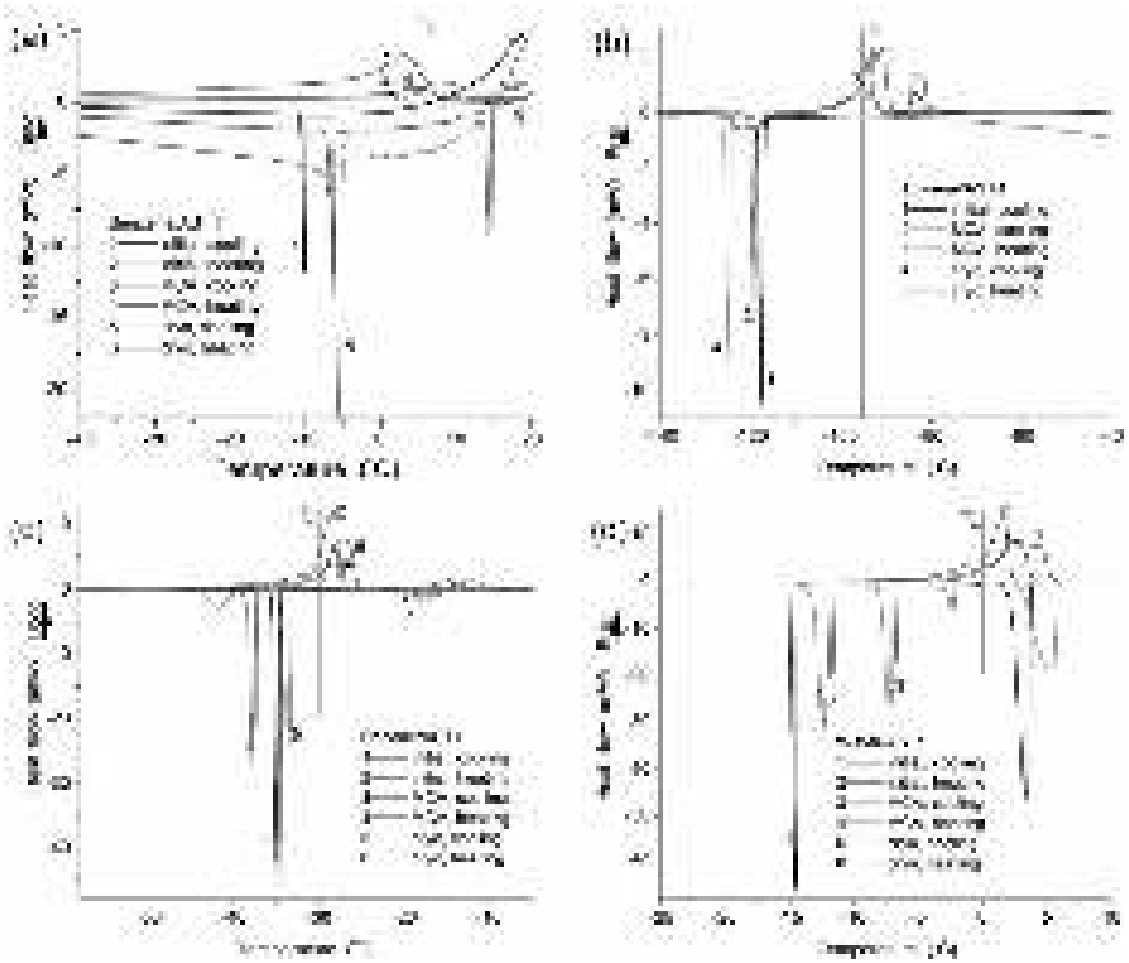

Fig. 161. Normalized (per mg of adsorbates with subtracted baseline) DSC thermograms of (a-c) nonpolar and (d) polar adsorbates bound to initial, MCA, and high-pressure cryogel of AST1: (a) benzene, (b) toluene, (c) decane, and (d) water. Cooling/heating rate was $\beta = 10\ ^{o}C/min$ for all samples.

The values of the exotherms (cooling → freezing) and endotherms (heating → melting) on the DSC thermograms depended on the amounts of adsorbates and adsorbents [90]. The adsorbate amounts have a greater influence on the exotherms/endotherms related to strongly (SBA) or weakly bound adsorbates (WBA). For the majority of the studied samples, the amounts of adsorbates were larger than that of adsorbents. Therefore, a significant portion of adsorbates was weakly bound. This gives rise to the sharp exotherms of freezing, and the main endotherms at temperatures close to the melting point of the bulk frozen compound. For a better view of the role the types of adsorbates and adsorbents play, DSC thermograms were normalized per mg of adsorbate with subtraction of the baseline (Figs. 160-162). Relatively large amounts of adsorbates interacting with FMO led to a low intensity of melting endotherms of SBA located at $T < T_m$ at $\Delta T = T - T_m > 10\ ^{o}C$, compared with the melting endotherms of weakly bound adsorbates located close to the melting point at $\Delta T < 10\ ^{o}C$ [90].

For aromatics (benzene, toluene), the freezing point depression was greater than for *n*-decane (Figs. 160-162) [90]. Melting delay (*i.e.* melting of frozen adsorbates at $T > T_m$) was observed for both nonpolar and polar adsorbates. However, it was absent for DMSO bound to initial or MCA A-300 (Fig. 160f). Note that DMSO possesses the largest donor number, DN = 125 kJ/mol, among the studied adsorbates (*e.g.,* for water DN = 75 kJ/mol) [208]. DN was a quantitative measure of Lewis basicity, *i.e.* the tendency to form strong hydrogen bonds with surface hydroxyls. Therefore, DMSO formed stronger hydrogen bonds with surface hydroxyls than the other adsorbates studied. This has a strong influence on the structure of interfacial DMSO layers in comparison with bulk liquid (and frozen DMSO) [90].

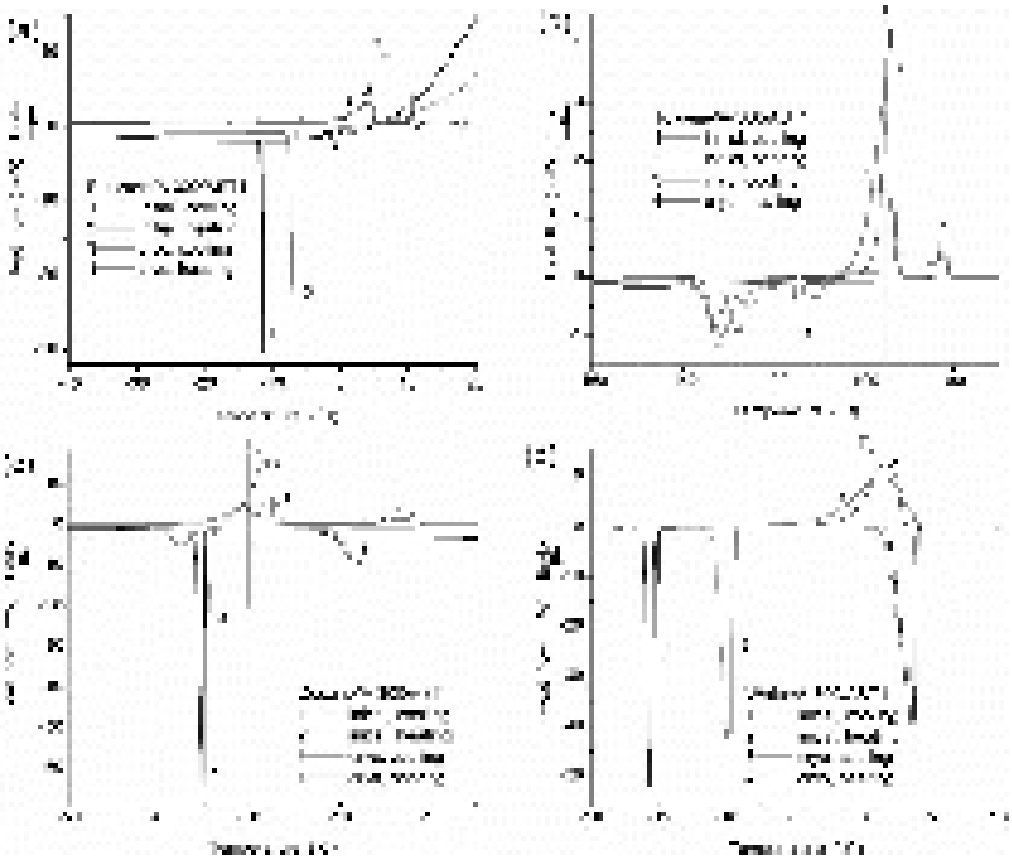

Fig. 162. Normalized (per mg of adsorbates with subtracted baseline) DSC thermograms of (a-c) nonpolar and (d) polar adsorbates bound to initial and high-pressure cryogel of A-300/AST1: (a) benzene, (b) toluene, (c) decane, and (d) water. Cooling/heating rate was $\beta = 10\ ^{o}C/min$ for all samples.

On the other hand, the acceptor number (AN) was higher for water than for DMSO. Therefore, in contrast to the other studied adsorbates, water tends to form adsorbed clusters in which water molecules act as both proton-acceptors and proton-donors [90]. Even at low water content, water formed cyclic clusters around surface hydroxyls. For the other studied adsorbates, the values of DN were much less than DMSO or water, *e.g.,* DN = 0 for chloroform. However, the AN of chloroform was larger (by 11 kJ/mol) than DMSO. These features of the electronic and molecular structures of adsorbates affected their behavior in pores (voids between nanoparticles) in different ways. For example, the freezing-melting point depression (or delay) *vs*. pore sizes and structures of adsorbates and pore surfaces could be a result of adsorbate electronic and molecular structure. The observed freezing point depression was greater for DMSO and water bound to MCA A-300 than that for initial A-300 (Figs. 160-162), because voids became narrower after MCA. This was due to the pure confined space effect. MCA did not appreciably change the surface structure of nanosilica, in contrast to AST1 which was more strongly affected by MCA (due to the destruction of large core-shell nanoparticles) evidenced by the change in sample color. The HPCG results in much larger changes to the melting thermograms of adsorbates bound to AST1 than MCA of AST1 (Fig. 161). In the A-300/AST1 blend, nanosilica plays an inhibiting role during HPCG. Therefore, the difference in the melting endotherms in comparison with the initial powder was smaller for this blend (Fig. 162) than for both initial and treated AST1 (Fig. 161) [90].

For some samples, the freezing point depression corresponded to relatively small shifts of the phase transition (melting) temperature at $|\Delta T| < 10\ ^{o}C$. This melting point shift range corresponded to WBA, since $|\Delta T| > 10\ ^{o}C$ corresponded to SBA [53,90]. Typically, larger structures of adsorbates (domains) located in broader voids (pores) mainly corresponded to WBA. Structures located in narrow voids (*i.e.* relatively small clusters of adsorbates), or adsorption layers located close to the pore walls, frequently represent SBA. The position of very narrow exotherms was related to freezing of WBA (due to excess of adsorbates much larger than the pore volume

V_p), and was dependent on the cooling rate (β); the greater the value of β the lower the freezing point. MCA results in shifts of the PSD peaks toward smaller pore sizes, and high-pressure or normal-pressure cryogelation led to compacting of the secondary particles. Therefore, these treatments could enhance the contributions of SBA. These treatment effects the texture of these powders could result in the appearance of open hysteresis loops for even non-polar compounds adsorbed onto treated FMO. The open shape of these isotherms could corresponded to activated desorption.

DFT quantum chemical calculations of the adsorption complexes of water and hexane showed that water molecules could form two strong hydrogen bonds with neighboring active surface sites or cyclic clusters [53,90,101,209,210]. This caused the adsorption energy values (Table 29), calculated taking into account the solvation effects for the free clusters and with adsorbed molecule, to be larger for water than for adsorbed hexane. Non-electrostatic components of the solvation energy (Table 29, E_{CDS} corresponding to cavitation (C), dispersion (D), and changes in the otherwise homogeneous solvent structure (S) induced by the solute) were destabilizing for the adsorbed water molecule ($E_{CDS} > 0$), but stabilizing for hexane ($E_{CDS} < 0$). For complex oxides, the interaction energy is greater for bound water, but it could be lower for a bound hexane molecule. The difference in the interaction energy with and without consideration of solvation effects was much smaller for bound hexane than for bound water (comp. $\Delta E_{t,l,cl+m}$ and $\Delta E_{t,g}$, Table 29). The values of $-\Delta E_{t,l,cl+m}$ for water interacting with oxide clusters were much larger than for hexane. These calculation results showed why hexane could be evaporated much faster than water from any FMO [101]. Clearly, the evaporation rate for liquids from pores differs from the rate of free liquids [254-256].

Table 29. Interaction energy of water and n-hexane (hex) molecules with silica, silica/alumina (SA), silica/titania (ST) and alumina/silica/titania (AST) clusters (DFT ωB97X-D calculations with the cc-pVDZ basis set) [90,101].

Parameter	H_2O/silica	H_2O/SA	H_2O/ST	H_2O/AST	hex/silica	hex/SA	hex/ST	hex/AST
$-E_{t,g}$ (Ha)	3902.69920591	3856.27283154	4539.17465345	4416.33144339	4063.30390686	4016.86762615	4699.77637712	4576.92397921
$-E_{t,l}$ (Ha)	3902.75652436	3856.33414420	4539.25412599	4416.42150981	4063.32657790	4016.88976195	4699.79978938	4576.94681724
$-\Delta E_{t,g}$ (kJ/mol)	66.9 (2H-bonds) 56.1 (cor. BSSE)	97.0 (2H-bonds)	75.6 (2H-bonds)	96.3 (2H-bonds)	28.3 25.3 (cor. BSSE)	32.3	29.2	25.7
$-\Delta E_{t,l,cl+m}$ (kJ/mol)	41.7	66.0	51.6	63.3	24.8	28.0	25.6	22.3
E_{CDS} (kJ/mol)	23.9	25.9	28.7	26.4	–35.4	–32.6	–36.4	–34.3
	silica	SA	ST	AST	silica	SA	ST	AST
$-E_{t,g}$ (Ha)	3826.27502792	3779.83720394	4462.74716547	4339.89607929	3826.27502792	3779.83720394	4462.74716547	4339.89607929
$-E_{t,l}$ (Ha)	3826.33089333	3779.89924168	4462.82470557	4339.98762667	3826.29289925	3779.85486709	4462.76580134	4339.91407967
$-\Delta E_{s,cl}$ (kJ/mol)	146.7	162.9	203.6	240.4	46.9	46.4	48.9	47.3

Note. The total energy of water molecule $E_{t,g}$ = –76.3986999307 Ha and $E_{t,l}$ = –76.4097574717 Ha (solvation energy ΔE_s = –29.0 kJ/mol); and hexane molecule $E_{t,g}$ = –237.018101921 Ha and $E_{t,l}$ = –237.024235496 Ha (ΔE_s = –16.1 kJ/mol). E_{CDS} corresponds to non-electrostatic components of the solvation energy. Subscripts 'g' and 'l' correspond to calculations in the gas or liquid phase, respectively. $\Delta E_{s,cl}$ is the energy of solvation of a pure cluster; $\Delta E_{t,l,cl+m} = E_{t,l,cl+m} - E_{t,l,cl} - E_{t,l,m}$ is the solvation energy of an adsorbed molecule (it takes into account the solvation effects and interaction of a molecules with a cluster). $\Delta E_{t,g}$ is the interaction energy of a molecule with a cluster in the gas phase. Structure of the clusters is shown in Figs. S53 (water) and S54 (hexane). $\Delta E_{t,g}$ = –71.4, –93.5, and –85.1 kJ/mol and $\Delta E_{t,l,cl+m}$ = –46.5, –67.2, and –58.2 kJ/mol per a water molecule for $9H_2O$, $3H_2O$, and $6H_2O$ interacting with the silica and SA clusters.

High-molecular weight adsorbates

Interactions of polymers with FMO

FMO are appropriate materials to be used in composites with polymers [32-45,257-266] because nanoparticles (especially modified silicas) could be easily distributed in the polymer matrices. The polymer-nanoparticle, polymer-polymer, and nanoparticle-nanoparticle interactions in the composites play a very important role in respect to the properties of whole materials. Composites could be nanoporous or macroporous [267].

The PSD functions and AFM images of the treated FMO and FMO/polymer systems revealed that the structure of secondary particles depended on oxide type, adsorbed polymers, and treatment conditions [53,107]. Monolayer coverage could cause a small loss of the specific surface area $\left|\frac{\Delta S_{BET}}{S_{BET}}\right| < 0.1$ if nanoparticles do not stick tightly together in aggregates, because of interactions with polymer molecules. More than monolayer coverage, or stronger particle-polymer interactions, could lead to a greater reduction of the specific surface area. For instance, for A-380/PEG $\left|\frac{\Delta S_{BET}}{S_{BET}}\right| > 0.3$ at C_{PEG} = 180 mg/g (monolayer coverage), a significant reduction of pore volume (from 1.56 to 0.59 cm^3/g) was observed. PEG is an adhesive for strongly aggregated nanoparticles of A-380, since this silica has a V_p value much greater than dry initial A-300 powder [107]. The increase in aggregate size of A-380/PEG was readily observed in the AFM images [53,107]. Smaller effects of monolayer adsorbed PEG (with respect to reduction of the S_{BET} and V_P values) were observed for A-300/PEG (C_{PEG} = 125 mg/g, $\left|\frac{\Delta S_{BET}}{S_{BET}}\right| < 0.3$ and $\left|\frac{\Delta V_p}{V_p}\right| < 0.2$) and A-50/PEG ($C_{PEG}$ = 25 mg/g, $\left|\frac{\Delta S_{BET}}{S_{BET}}\right| < 0.17$ and $\Delta V_p > 0$) because of the weakening of primary particle aggregates with increasing sizes of nanoparticles for a variety of FMO [53].

Despite the scatter in changes in the S_{BET} and V_p values for a large set of the A-300/polymer or A-300/protein systems [107], due to variations in the type of macromolecules and treatment techniques, there were several clearly visible trends. The adsorption capacity V_p for treated silica or silica/polymer powder samples was typically greater than that for the initial dry powder if the polymer content C_{pol} < 30 wt.%. However, this value decreased with increasing polymer concentration and the maximal V_p value (1.8 cm^3/g) was observed for suspended-sonicated-dried A-300 alone. Generally, the adsorption of polymers led to a reduction of the specific surface area; however, these changes could be relatively small if the polymer content C_{pol} < 20 wt.%; *i.e.*, at monolayer or lower coverage. Minimal loss of the S_{BET} value for polymer/nanooxide powders occurred under the following conditions: (i) relatively weak polymer-polymer intermolecular interactions (*e.g.*, dispersive without hydrogen bonding as in PEO, PEG, PVP, PDMS); (ii) maximal decomposition of secondary particles upon their coating by linear polymer molecules and minimal aggregation of coated particles (*i.e.* maximal number of segments should interact with the silica surface); (iii) decreased possibility for the interactions of adsorbed polymers with many primary particles simultaneously (*e.g.*, short polymer molecules); (iv) good correlation of the distances between active sites on particle surfaces and polar groups of polymer molecules; (v) relatively short distances between polar groups of polymer molecules; and (vi) high rotational mobility of side polar groups (*e.g.*, in PVP) forming hydrogen bonds with the silica surface.

The PSD functions for A-300/PEG (Fig. 163b) were narrower at pore radii R > 10 nm and have lower intensity at 1 < R < 10 nm than A-50/PEG (Fig. 163a) [107]. Additionally, the difference in the PSD functions for the initial A-300 powder (Fig. 163b, curve 1) and treated samples with A-300/PEG was much larger than that for A-50 and A-50/PEG (Fig. 163a).

However, differences in the effects of various ball-milling and other treatments were larger for A-50/PEG (Fig. 136a) and A-380/PEG (Fig. 164) than A-300/PEG (Fig. 163b).

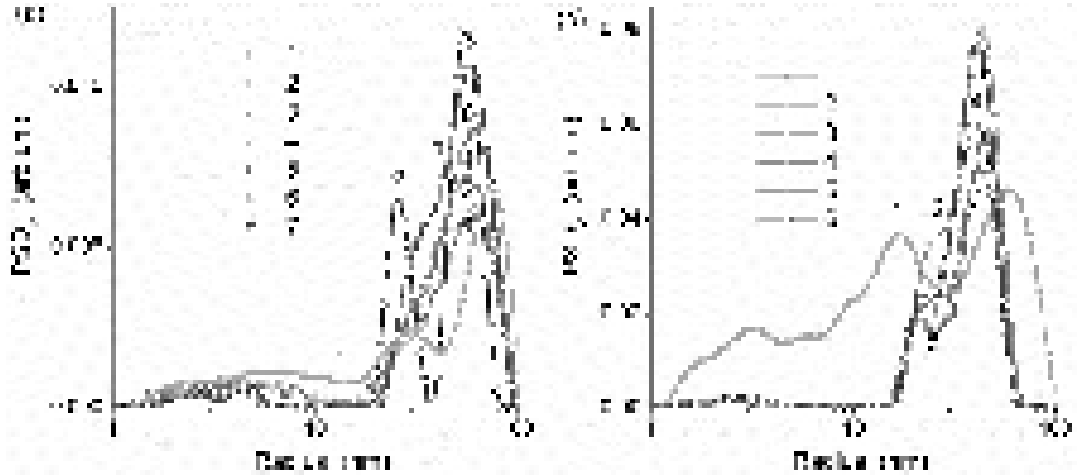

Fig. 163. $IPSD_V$ for dried (a) initial A-50 (curve 1), residual of aqueous suspension with A-50 (2), A-50/PEG (25 mg per gram of silica) impregnated (3), ball-milled for 5 min (4) then treated in (5) saturated water vapor or (6) ethanol for 24 h, and ball-milled A-50/PEG with addition 30 wt.% of water for 5 min (7); (b) initial A-300 (curve 1); dried A-300/PEG (125 mg per gram of silica) impregnated (2), ball-milled (3), then treated in saturated (4) water vapor or (5) ethanol for 24 h, ball-milled A-300/PEG with addition of 30 wt.% of water (6) (DFT with the model of voids between spherical particles in aggregates).

Significant changes in the amount of adsorbed PVA (≤ 1 monolayer) have a weak influence on the IPSD shape for the A-300/PVA and SA/PVA systems (Fig. 165). Similar results were observed for A-300/PEO (Fig. 166). However, the IPSD functions with respect to the specific surface area (Fig. 166b,d) demonstrate a reduced contribution of both narrow and broad pores. This could be explained by a relatively uniform distribution of the linear and long (molecular weight ~600 kDa) PEO molecules on the silica surface and the interaction of a PEO with many particles simultaneously. This affected the topology of voids in both aggregates of primary particles, and agglomerates of aggregates. The changes in total porosity as a function of PEO content was $\Delta V_p < 0$ at $C_{PEO} > 15$ wt.% (Fig. 167a). On the other hand ΔS_{BET} monotonically decreased with increased C_{PEO}, while macroporosity increased and mesoporosity decreased (Fig. 167b) [107].

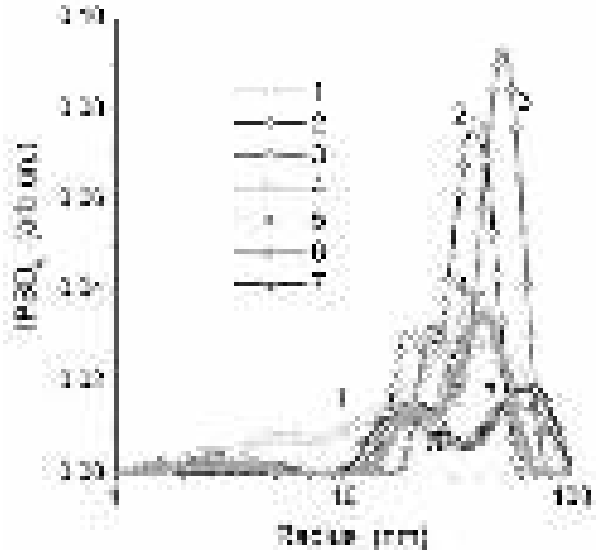

Fig. 164. $IPSD_V$ of initial dry A-380 powder (curve 1) and dried residual of aqueous suspension of A-380 (1 wt.%) (2), A-380/PEG (180 mg/g) (3) impregnated, (4) ball-milled dry mixture A-380/PEG (180 mg/g) and then treated in saturated (5) water or (6) ethanol vapor for 24 h, (7) ball-milled with addition of 30 wt.% of water (DFT with the model of voids between spherical particles in aggregates).

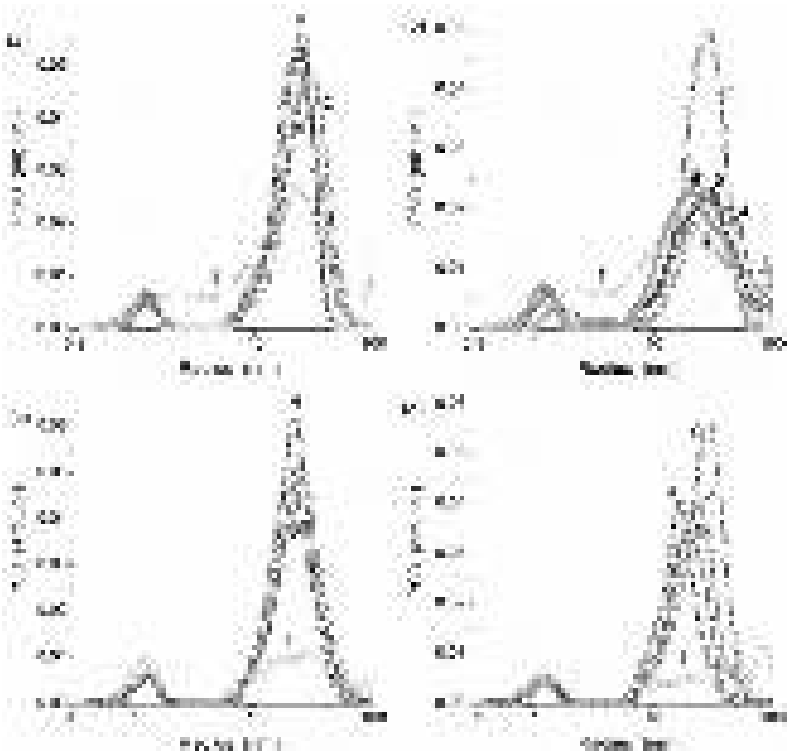

Fig. 165. $IPSD_V$ of (a) initial A-300 (1), dried solid residual of A-300 (2), A-300/PVA at C_{PVA} = 15 (3), 75 (4) and 150 (5) mg/g; (b) initial A-300 (1), dried solid residual of A-300 (2), and A-300/PVP at C_{PVP} = (3) 25, (4) 75, (5) 87.5 and (6) 175 mg/g; (c) initial SA8 (1), dried solid residual of SA8 (2), and SA8/PVA at C_{PVA} = (3) 10, (4) 50 and (5) 100 mg/g; (d) initial ST9 (1), dried solid residual of ST9 (2), and ST9/PVA at C_{PVA} = (3) 9, (4) 45 and (5) 90 mg/g (DFT calculations with the model of cylindrical pores).

Different effects of adsorbed PVA on the V_p and S_{BET} values were observed for A-300/PVA (both parameters decreased with C_{PVA}) and SA/PVA (V_p grows or remained nearly constant while S_{BET} slightly decreased or remained nearly constant) [107]. These differences, resulting from the structure of the PVA coating on the oxide nanoparticles, may be caused by differences in the acid-base properties of amphoteric silica and silica/alumina, the latter possessing a set of acid-base sites which could strongly interact with the PVA molecules.

Strong aggregation of ossein molecules with silica nanoparticles led to PSD_V functions [107] similar to A-300/PEO samples at pore radii $R < 10$ nm. However, for A-300/ossein samples the contribution of broad mesopores at $R > 15$ nm and macropores at $R > 25$ nm was much smaller than that for other nanooxide/polymer systems. This was due to stronger aggregation of particles and protein macromolecules indicated by a loss in S_{BET} and V_p with increasing C_{ossein} (S_{BET} = 221, 151 and 112 m^2/g and V_p = 0.72, 0.54 and 0.41 at C_{ossein} = 31.6, 158 and 316 (monolayer coverage) mg/g, respectively) [107]. Similar $IPSD_V$ functions were observed for A-300/gelatin (S_{BET} = 145 and 125 m^2/g and V_p = 1.0 and 0.88 cm^3/g, respectively) and A-300/BSA (S_{BET} = 178, 160 and 141 m^2/g and V_p = 1.17, 1.08 and 0.95 cm^3/g, respectively). However, the $IPSD_V$ peaks for A-300/BSA and A-300/gelatin were characterized by larger contributions of broad pores compared to A-300/ossein samples [107].

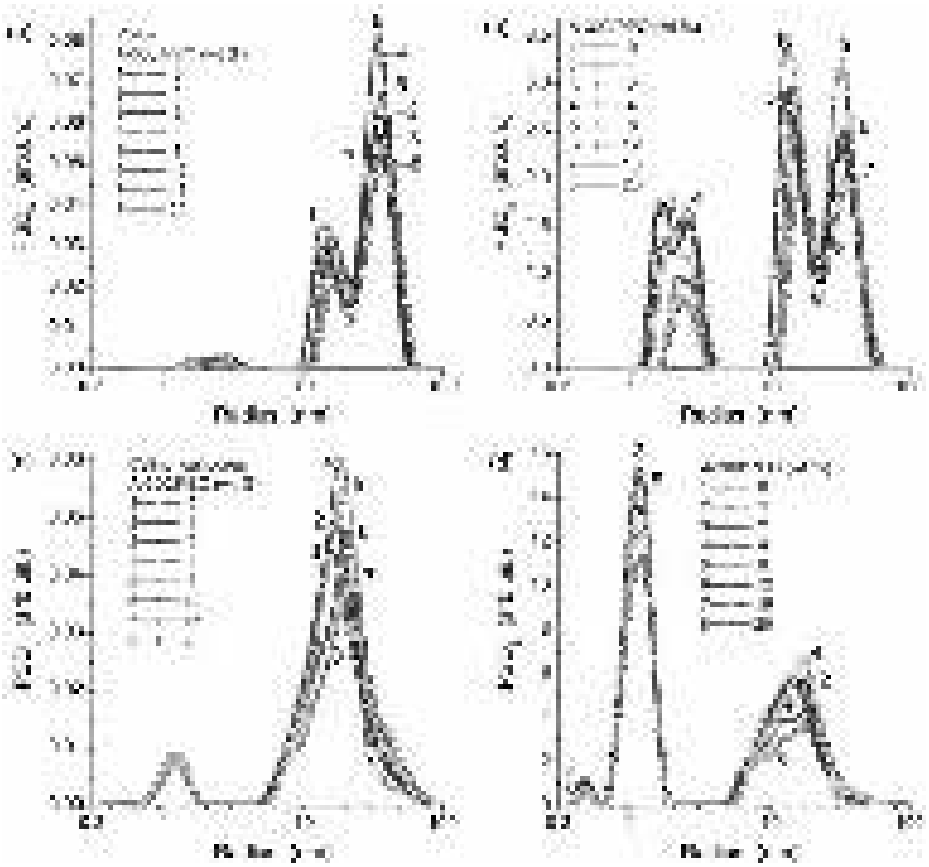

Fig. 166. (a, c) $IPSD_V$ and (b, d) IPSD for dried solid residual of A-300/PEO (adsorption from aqueous solution) at different content of PEO (DFT with the models of (a, b) voids between spherical particles in aggregates and (c, d) cylindrical pores).

Fig. 167. Relative changes in the specific surface area and the porosity (a) total and (b) meso- and macropores as a function of adsorbed PEO.

The adsorption of several types of polymers onto nanosilica A-300 gives different interfacial layer structures. PEG and PEO having the same structure of the segments were characterized by a close $\Phi(C_{pol})$ shape (Fig. 168a) [107]. Despite weak polymer-polymer interactions, PDMS gives the lowest $\Phi(C_{pol})$ values (as a function of C_{pol} in mg/g) because of (i) a large segment (m_{seg}) weight $-(CH_3)_2Si-O-Si(CH_3)_2-$, (ii) its weak interaction with silanols due to relatively poor electron-donor properties of oxygen atoms in the siloxane bonds, (iii) steric effects of the CH_3 groups, and (iv) the helical structure of the PDMS chain. PVA molecules could form strong hydrogen bonds with both silanols and OH groups of neighboring molecules, leading to low Φ values as a function of C_{pol} and the lowest Φ values as a function of C_{pol}/m_{seg} (Fig. 168c). PVP has a larger segment weight than PEG, PEO, and PVA by a factor of 2.4. Therefore, $\Phi(C_{pol})$ for PVP was lower than PEG or PEO, but close to that of PVA (Fig. 168a) [107].

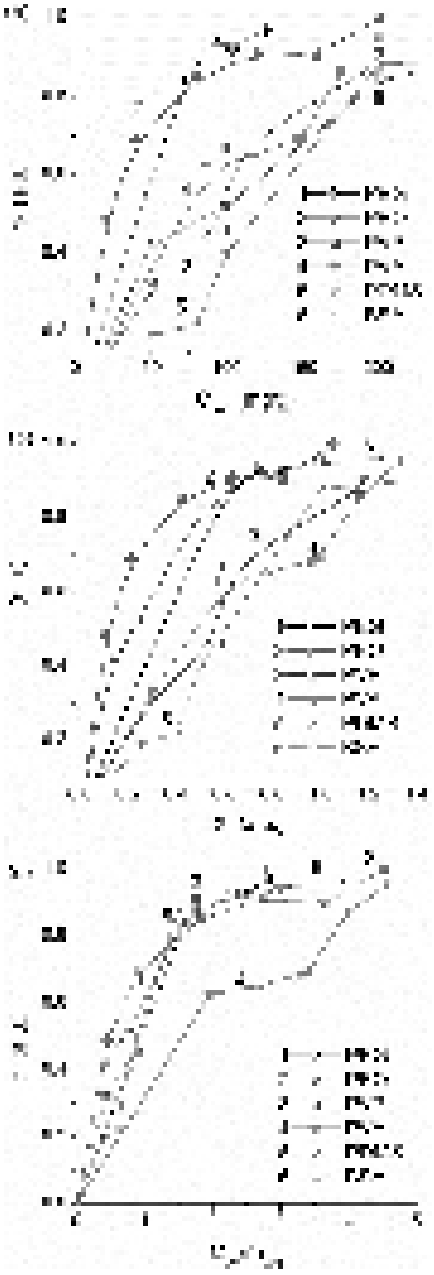

Fig. 168. Perturbation degree (Φ) of free surface silanols as a function of the polymer loading (a) C_{pol} in mg per gram of silica, (b) $\Theta = C_{pol}/C_{pol,monolayer}$ and (c) C_{pol} normalized by dividing by the molecular weight of a segment (m_{seg}) for PEG (35 kDa), POE (600 kDa), PVP (12.7 kDa), PVA (43 kDa), PDMS (8 kDa) and BSA (67 kDa) onto A-300.

PVP molecules could more effectively interact with surface silanols than other linear polymer molecules because of the rotational mobility of the side groups responsible for the formation of hydrogen bonds (Fig. 168c). BSA molecules demonstrate relatively low $\Phi(C_{pol})$ values because of the high average m_{seg} value, and the globular protein shape. Therefore, a significant portion of the molecules could not be in contact with the silica surface. However, protein molecules have several types of polar side groups in addition to the polypeptide chain which could form strong hydrogen bonds with silanols. That could partially compensate for the effect of the globular shape of the molecules on the $\Phi(C_{pol})$ values. Normalization of C_{pol} by dividing by the segment m_{seg} molecular weight (Fig. 168c) results in similar $\Phi(C_{pol}/m_{seg})$ graphs for all A-300/polymer systems except A-300/PVA, probably because of the effects of strong hydrogen bonds between PVA molecules. The globular structure of BSA molecules prevents strong lateral interactions, therefore $\Phi(C_{pol}/m_{seg})$ for BSA was similar to other systems characterized by relatively weak polymer-polymer interactions [107].

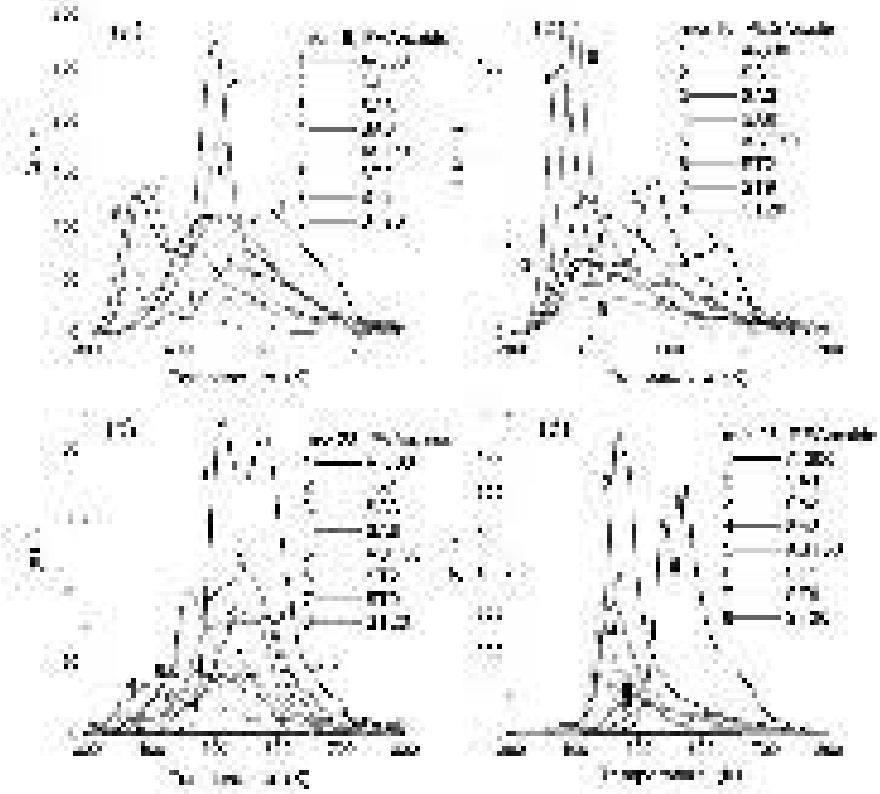

Fig. 169. TPD MS thermograms at m/z (a, b) 18 (water) and (c, d) 28 (CO) formed on decomposition of PVA (a, c) and PEG (b, d) adsorbed on silica A-300, silica/alumina SA1, SA3, SA8, silica/titania ST2, ST9, ST20 and alumina/silica/titania AST50.

The effects of residual interfacial water, which could disturb silanols and form hydrogen bond bridges between polar groups of polymer molecules and surface silanols, could provide a small difference in the $\Phi(C_{pol}/m_{seg})$ graphs for different polymers (especially at $C_{pol}/m_{seg} > 1$) (Fig. 168c). Thus a minimal loss of the specific surface area for the nanooxide/polymer powders results from a monolayer coating of nanoparticles by PEO or PEG, because of the formation of strong hydrogen bonds with silanols and weak polymer-polymer interactions, result in a dense coverage with more intensive interaction between polymer molecules and surface silanols. Notice that the shape of the $\Phi(\Theta)$ graphs (Fig. 168b) slightly differs from that of $\Phi(C_{pol})$ (Fig. 168a) due to certain differences in the monolayer capacity for the studied polymers: 125 (PEG), 150 (PVA), 170 (PVP), 190 (PEO), 200 (PDMS) and 400 mg/g (BSA) [107].

The strong interaction of adsorbed polymers with oxide surface caused changes during their thermal decomposition. Additionally, the catalytic effect of active surface sites on complex oxides on thermolysis of adsorbed PVA and PEG molecules (Fig. 169) caused displacement of the

TPD peaks toward lower temperatures in comparison with thermolysis on silica. There was a difference in the catalytic effects for PVA and PEO because of their structural differences and the type of surface interactions. Dehydration of PVA/silica was complete at 650 K, but the dehydration of fumed silica alone occurred at much higher temperatures (up to 1000 K and higher) [37-40,53]. The strong hydrogen bonding of OH groups of PVA and silica was the main reason for this difference [107].

The sample mass used in all of the TPD MS measurements was almost identical [107]. Therefore, differences in the TPD peak intensities of eliminated water and CO on decomposition of PVA and PEG (Fig. 169), could be caused by not only the differences in the catalytic effects of SA and ST samples or the reaction mechanisms, but also the differences in the specific surface area (by order of the value) of nanooxides and the amounts of polymers (monolayer coverage was used here).

Investigations of the morphological and structural characteristics of a set of powder nanocomposites with fumed oxides and different linear polar polymers (PEO, PEG, PVA, PVP, and PDMS) and proteins (ossein, gelatin, and BSA) showed that monolayer or lower coverage of nanoparticles by the macromolecules results in relatively small reductions of specific surface area and adsorption capacity in comparison with similarly treated fumed oxides alone [107]. Proteins result in larger reductions than linear polar polymers. Oxide/polymer powders have a more ordered pore structure than the initial oxide powders, evidenced by the narrower pore size distribution for the oxide/polymer systems. This structure and secondary particle morphology depended only slightly on the content and the type of polymers at coverage less than a monolayer. If polymer-polymer interactions were weaker than polymer-oxide interactions (PEO, PEG, PVP, and PDMS), the amounts of hydrogen bonds between silanols and polymers per segment depended weakly on the type and size of polymers [107].

Interfacial and temperature behaviors of low- and high-molecular weight compounds

Studied silica gels Si-60 and Si-100 and nanosilica A-400 could be assigned to mainly mesoporous materials since contributions of mesopores to the specific surface area and pore volume were predominant [268]. Silica gel Si-60 did not practically have nanopores and macropores with PSD in the range of R = 2-7 nm (Fig. 26). Silica gel Si-100 has mesopores at R = 3.5-15 nm at small contributions of nanopores and macropores [268]. Nanosilica A-400 was characterized by a broader PSD than silica gels with significant contributions of macropores. This was due to its texture and particle morphology, since nanoparticles (average diameter ~ 6.7 nm) form relatively rigid aggregates (< 1 μm in size) and soft agglomerates (> 1 μm) with empty volume in them $V_{em} \approx 16$ cm^3/g. The pore volume determined from low-temperature nitrogen adsorption was much lower than V_{em}. However, this volume could be filled by polymers. The adsorption of polymers onto A-400 could be accompanied by re-organization of the texture of aggregates and agglomerates [53] in contrast to silica gels with rigid microparticles. The absence of macropores in silica gels could cause slow diffusion of macromolecules in mesopores that could result in partial filling of pores by PDMS during the NMR measurements. A portion of narrow pores accessible for nitrogen molecules was inaccessible for much larger PDMS molecules. A helix shape of PDMS with six Si–O bonds in a cycle restricts the number of segments which could directly interact with a matrix surface to form the hydrogen bonds $SiO–H\cdots O(Si(CH_3)_2–)_2$. However, the PDMS conformation could be changed in the adsorption layer depending on the PDMS content [53,268].

At a low content of water (hydration h = 0.005 g/g) in dried silicas with adsorbed PDMS, single signal of water observed at 2.5-5 ppm depended weakly on temperature (Fig. 170) [268].

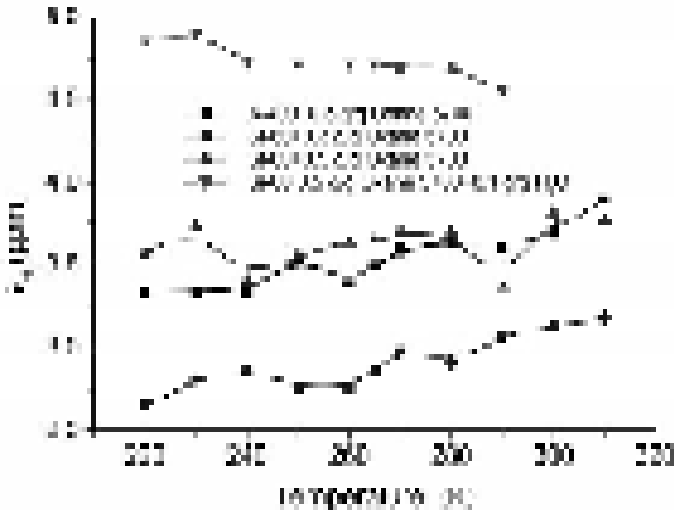

Fig. 170. Temperature dependence of the chemical shift δ_H of water at different hydration (h = 0.005 or 0.1 g/g) bound to A-400 or Si-60 with adsorbed Oxane 5700.

Assuming that δ_H = 0 ppm for PDMS, the δ_H values could be estimated for adsorbed water (Fig. 170). Minimal δ_H values were observed for residual water (h = 0.005 g/g) bound to Si-60 with adsorbed 0.3 g/g of Oxane 5700 corresponding to approximately one third of the pore volume. However, for a higher hydration at $h \approx 0.1$ g/g and at 0.5 g/g of adsorbed Oxane 5700, the δ_H values were close to that for bulk water; *i.e.* adsorbed water became strongly associated water (SAW). However, at the residual amounts of water ($h \approx 0.005$ g/g), an increase in the amounts of Oxane 5700 to 0.5 g/g, corresponding to 62-65 % of V_p for Si-60 and A-400, results in an increase in the δ_H values (3.2-3.5 ppm). The δ_H values for water adsorbed to A-400/Oxane 5700 were lower than that for Si-60/Oxane 5700 because of the difference in the texture of these silicas [268]. The increase in the δ_H values could be explained by an increase in the sizes of the water clusters and nanodomains since the associativity of bound water increased under action of PDMS. However, it was lower than that at h = 0.1 g/g. PDMS displaces water from pores or from the silica surface, and to decrease the surface area of contact of water with hydrophobic silicone oil, water formed larger structures [269]. However, water at low hydration at h = 0.005 g/g was not typical SAW characterized by δ_H = 4-5ppm [53] because of too low amounts of adsorbed water. However, 10-15% filling of pores by water (h = 0.1 g/g) results in the appearance of SAW [268].

The temperature dependences of ^{1}HNMR signals of the CH_3 groups of PDMS (Oxane 1000 or 5700) bound to silicas or bulk oils alone (Fig. 171a) were obtained for samples during their thawing [268]. The intensity was normalized to that of silicone oils before freezing. The PDMS adsorption onto silicas results in an increase in the melting temperature for a main fraction of adsorbed polymers (Fig. 171a). However, a certain fraction of adsorbed polymers could be melted at lower temperatures than the bulk polymer. This heterogenization of adsorbed polymers was due to their interactions with the silica surface and confined space effects affecting both crystallization and melting processes. These phenomena were typical for different polymers, which could be in crystalline, semicrystalline or amorphous states, under confined space effects [53].

Relative changes in the Gibbs free energy of adsorbate-adsorbent systems (ΔG) were proportional to changes in temperature (ΔT) of the corresponding phase transition (*e.g.*, freezing or melting of adsorbate crystallites in pores and in the bulk) and the difference in content of liquid phase ($\Delta C_{PDMS,liq}$) vs. temperature [268] $\Delta G \approx k \Delta T \Delta C_{PDMS,liq}$, where k was a constant. The data (Fig. 171a) could be transformed into the temperature dependences of relative changes in the Gibbs free energy of PDMS. The $\Delta C_{PDMS,liq}$ values were determined as the differences in the amounts of liquid fraction in bulk and adsorbed oils (Fig. 171b,c). These dependences have ranges with positive and negative values. Adsorption interactions should be accompanied by diminution of the Gibbs free energy of adsorbates. However, confined space effects could reduce density of

polymers adsorbed in relative narrow pores. Additionally, crystalline structures in pores could be more stable because of stronger interactions with the pore walls than with neighboring macromolecules of residual water molecules. Therefore, the segmental mobility of a fraction of PDMS could appear at higher temperatures than that for bulk polymers but for another fraction of the polymer loosely packed in pores the opposite effect could be observed [268].

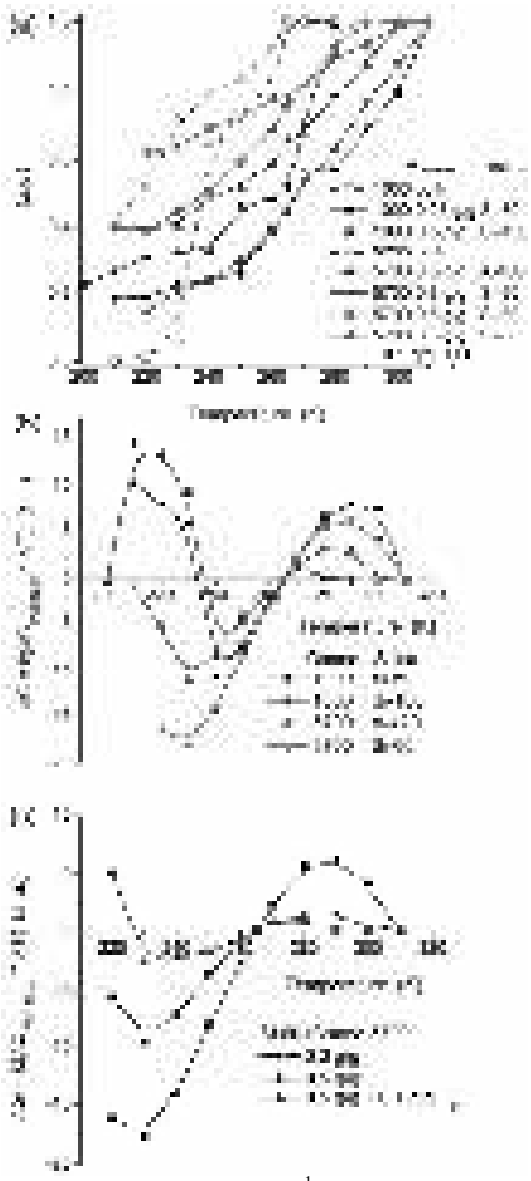

Fig. 171. Temperature dependences of (a) relative intensity of ^{1}H NMR signals of silicone oils alone (dashed lines) or bound to silicas (solid lines), and (b, c) relative changes in the Gibbs free energy of polymers bound to silicas.

A minimal stabilization of solid Oxane 1000 at $T < 260$ K was observed for Si-100 because it has broader pores than Si-60 and did not have narrow pores as A-400 [268]. Notice that the PSD calculated with the cryoporometry method based on the Gibbs-Thomson equation for freezing point depression for adsorbates confined in pores for Si-100/Oxane 1000 has a shape broader than PSD calculated from the nitrogen adsorption isotherm. This could be explained by location of a fraction of PDMS out of pores because the surface area of silica in contact with PDMS was equal to 47 m^2/g (~13% of S_{BET} of Si-100) but the PDMS amount corresponded to 37% of the pore volume of Si-100 [268].

A maximal stabilization of solid Oxane 1000 and Oxane 5700 was observed for Si-60 possessing narrow and rigid mesopores. A-400 was composed of soft agglomerates which could be re-organized during the adsorption of polymers [53,107,268,270]. Temperature of melting was

lower for Oxane 5700 than for Oxane 1000 (Fig. 144a). The stability of solid Oxane 5700 decreased (at $T < 260$ K) with increasing amounts of polymer and water (Fig. 171c).

The effects of both decreasing and increasing of the melting temperature were observed for silicone oils confined in pores of silica gel particles and voids between nanoparticles in nanosilica powder [268]. The broadening of the range of melting of PDMS depended on the pore size distribution and it was minimal for silica gel Si-100 with broader pores. An increase in the amounts of polymer and adsorbed water results in decreasing effects because of decreasing interactions of a fraction of the macromolecules with the silica surface and location of PDMS out of pores. The cryoporometry results showed that the surface area in contact with macromolecules (Oxane 1000) was about 13% of the S_{BET} value of silica gel Si-100. Consequently, PDMS fills only a portion of pores despite its volume corresponded to 37% of the pore volume of Si-100 [268].

Nanosilica dispersed in PDMS represents mainly agglomerates of 1-10 μm in size (Fig. 172) [271]. Stronger agglomeration of nanosilica in silicone oil in comparison with nanosilica suspended in aqueous media was due to a hydrophilic character of silica. Confined space effects could be expected for the PDMS molecules located between silica nanoparticles in agglomerates that differ for PDMS bound to silica gel.

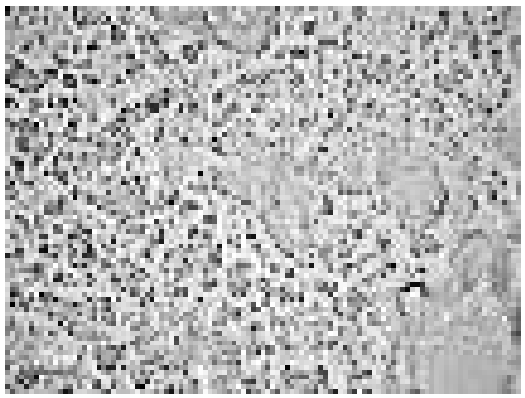

Fig. 172. Microphotograph (Primo Star optical microscope, Carl Zeiss) of PS400 (30 wt.%) in PDMS (scale bar 10 μm).

The temperature dependences of relative intensity of ^{1}H NMR signal differ for individual PDMS initial and preheated at 420 K for 20 min (Fig. 173b). The I/I_0 value corresponded to a weight fraction of liquid PDMS. The mentioned difference could be explained by additional disordering of PDMS supramolecular structures [267-271] during heating at 420 K that slows down the PDMS freezing during subsequent cooling; *i.e.* this disorder was partially irreversible.

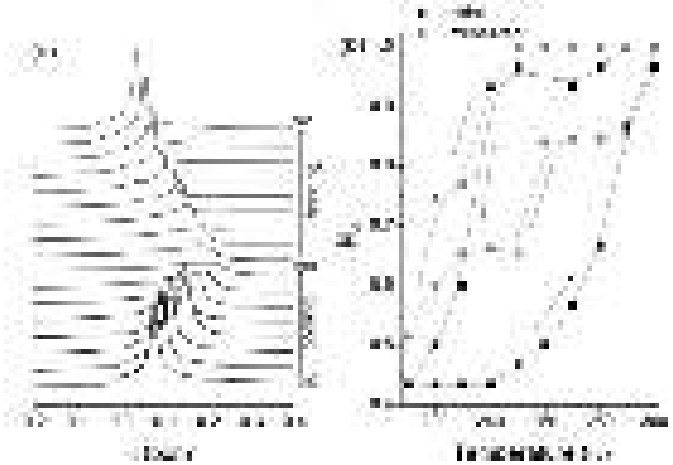

Fig. 173. (a) ^{1}H NMR spectra of individual Oxane 1000 recorded at different temperatures during cooling and subsequent heating (initial sample); and (b) relative intensity (normalized by dividing of current intensity by I_0 of signal recorded at 290 K) of ^{1}H NMR signals for PDMS initial and preheated at 420 K for 20 min.

The ^{1}H NMR signal width was narrow (Fig. 173a) that allows us to observe a small upfield shift of δ_H up to −0.1 ppm upon cooling from 280 K to 210 K. Subsequent heating gives a downfield shift toward practically the same δ_H values at the same temperatures. There was a hysteresis loop for signal intensity (Fig. 173b). A significant decrease in intensity of PDMS signal occurred during cooling from 240 K to 220 K (Fig. 173b), corresponding to the melting point of Oxane 1000 (≈231 K). However, complete freezing of PDMS was not observed even at 210 K. During heating, melting of a part of a frozen PDMS fraction occurred at T > 250 K. However according to DSC data, melting endotherm was at ~233 K. The hysteresis loop was narrower for preheated PDMS than for initial one due to disordering of supramolecular PDMS structures [271].

The temperature behavior of PDMS depended on the surroundings. Confined space effects could be analyzed for PDMS bound to silica gel Si-100 and nanosilica PS400. One could assume that both mesopores and macropores of silicas could be accessible of PDMS molecules [271].

In contrast to the upfield shift for PDMS alone with decreasing temperature (Fig. 173a), PDMS adsorbed onto silica gel demonstrates a downfield shift with decreasing temperature (Fig. 174a). The spectra of PDMS bound to nanosilica PS400 have a similar shape (not shown here). The ^{1}H NMR spectra were recorded for PDMS/silica samples equilibrated at 293 K for a week (labeled as "initial") and then these samples were heated at 420 K for 1 h (labeled as "preheated") and measured after preheating [271].

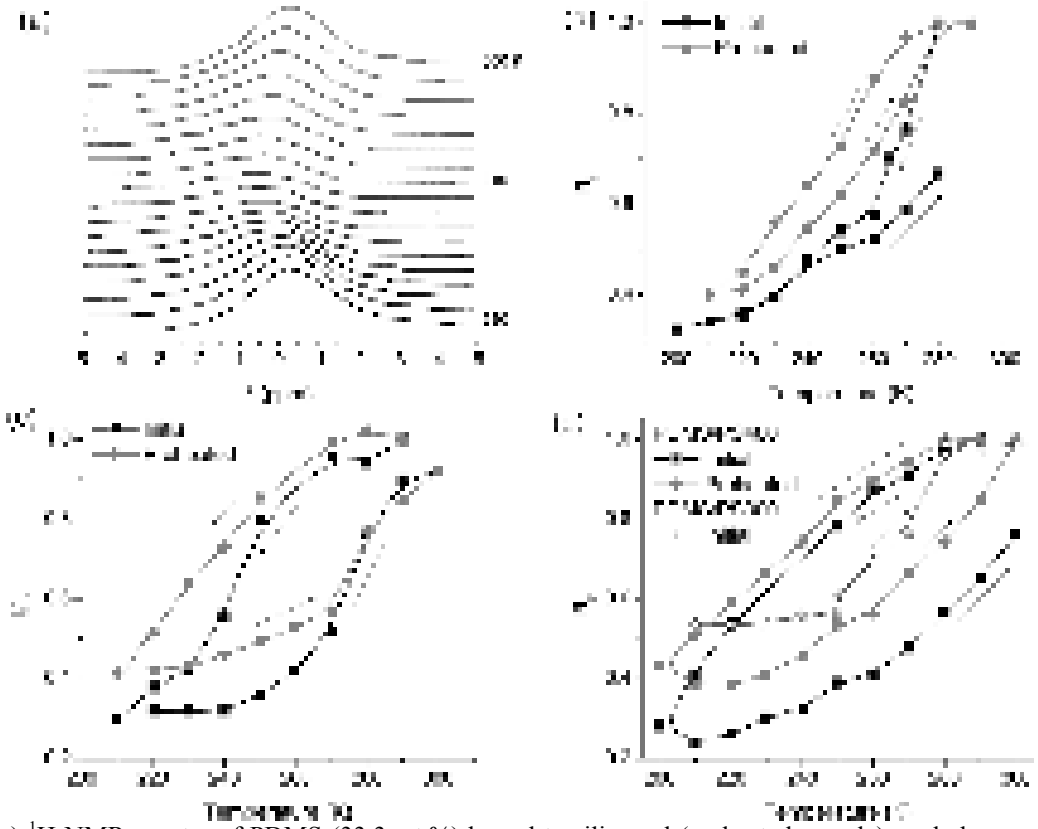

Fig. 174. (a) ^{1}H NMR spectra of PDMS (33.3 wt.%) bound to silica gel (preheated sample), and changes in relative intensity of ^{1}H NMR signal of CH_3 groups of PDMS adsorbed onto (b) silica gel (0.5 g PDMS per gram of Si-100), (c) 8 wt.% PS400 in PDMS, and (d) PS400 : PDMS or PS300 : PDMS = 1 : 1 for initial and preheated samples.

Comparison of relative intensity curves for PDMS alone (Fig. 173b) and adsorbed onto silicas (Fig. 174b-d) suggests that PDMS molecules became solid-like at temperatures higher than T_f (freezing point) for bulk PDMS [271]. Typically, the freezing point depression was observed for low-molecular weight adsorbates located in pores, and this effect increased with decreasing pore size [53]. For adsorbed polymers, this picture was more complex, since a polymer fraction remained liquid at $T < T_f$ but another fraction remained frozen at $T > T_m$ (melting point). It was

possible that freezing occurred for an interfacial layer of adsorbed polymer at $T > T_m$. The next layers of the polymer located in pores could be in unfrozen (mobile) state at $T < T_f$. Notice that the hysteresis loops of ^{1}H NMR signal intensity were observed for smaller adsorbates such as hydrophobic *n*-decane bound to silica gel and nanosilica [158,248,271].

To compare the effects of different sizes of nanoparticles and time of equilibration of PDMS/nanosilica, PDMS/PS300 was also studied (Fig. 174d) [271]. Nanosilica PS300 was composed of larger nanoparticles (average d = 9.2 nm) than PS400 (d = 6.7 nm). Therefore, the surface area of contact of the PDMS molecules with silica nanoparticles in PDMS/PS300 should be smaller than that in PDMS/PS400. This led to a curve which was closer to that for initial PDMS alone (Fig. 173b) than the curve for PDMS/PS400. Consequently, the relaxation of PDMS was deeper due to a smaller effect of PS300 than that of PS400. The heating rate was the same (5 K/min) for PDMS/PS300, but the equilibration time at a certain temperature was longer: 10 min (instead of 7 min used for PDMS/PS400) at 210 K < T < 250 K for each temperature point, then 30 min (an intensity step observed) and 10 min for subsequent points. Changes in the heating regime led to certain changes in the intensity curve due to deeper relaxation of the PDMS structure [271].

Theoretical calculations of the ^{1}H NMR spectra of PDMS fragments (7, 18 or 36 units) free and bound in a pore or out of a pore of silica nanoparticle (Fig. 175) showed the effects of both a silica surface (in pore or out of pore) and co-adsorbed water [271].

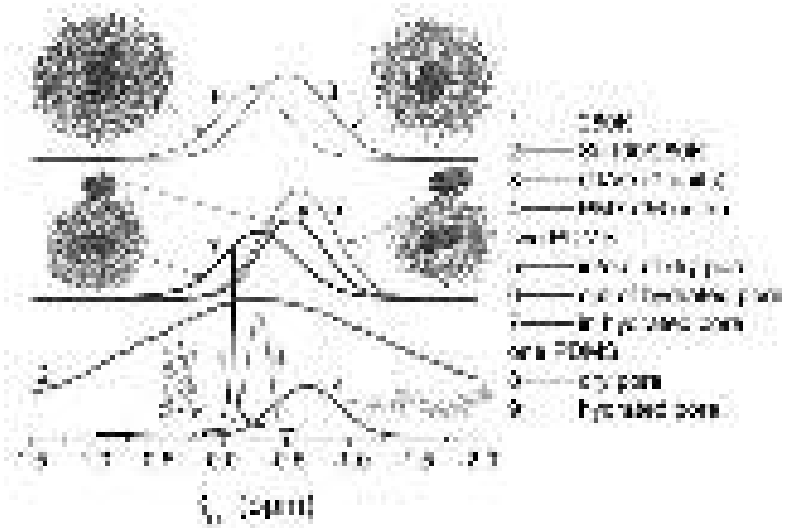

Fig. 175. Experimental ^{1}H NMR spectra of PDMS alone (curve 1) and adsorbed onto Si-100 (0.5 g/g PDMS) (curve 2) at 280 K, and theoretically calculated spectra of PDMS alone (7 units) by GIAO/B3LYP/6-31G(d,p) (curve 3), and PM7 (with full optimization of geometry) with the correlation function $\delta_H = -5.96214 + 33.7732q_H$ (q_H is the atom H charge) for PDMS alone (36 units) (curve 4), two PDMS molecules (each of 18 units) bound into pore and out of dry pore (curve 5), out of (curve 6) and in (curve 7) hydrated ($517H_2O$) pore of silica particle (1624 atoms), one PDMS molecule (18 units) in dry pore (curve 8) or hydrated pore (curve 9).

For PDMS located in the pore, the downfield shift was greater than that for PDMS placed out of the pore (Fig. 175, curves 6 and 7) [271]. For PDMS located in a dry pore, there was the upfield shift (curves 5 and 8) in comparison with PDMS located in a hydrated pore (curves 6, 7, and 9) due to enhanced van-der-Waals and electrostatic interactions with surroundings (both silica and water). PDMS in a liquid state (curve 1) was also characterized by the downfield shift in comparison with individual molecule without neighbors (curves 3 and 4) due to the effects of the surroundings. Notice that the interaction energy between two PDMS fragments (each with three units) calculated using the DFT wB97XD/6–31G(d,p) method (with HF/6-31G(d,p) geometry) was ΔE_t = –9.4 kJ/mol. However, according to calculation of these two fragments using the Morokuma method by HF/6–31G(d,p), contribution of electrostatic energy was 46.9% due to interactions of the H atoms of the CH_3 group of a molecule with the O atom in the Si-O-Si bridge of another molecule. This interaction caused a certain polarization of the bonds (H charge

increased in the complex from 0.132 a.u. to 0.145 a.u. and q_O = –0.634 and –0.636 a.u., respectively) and the shielding of protons decreased. This explains the downfield shift of PDMS in the liquid state in comparison with individual PDMS molecules [271].

Investigations performed by spectroscopic (NMR), relaxation (DRC, TSDC), scattering (SAXS, SANS), thermal (DSC) methods showed importance of the confined space effects on the interfacial behavior of polymers interacting with a solid surface in pores or at open surface of disperse but nonporous particles [53]. To estimate the effects of open silica surface and confined space in silica pores on the phase transition of adsorbed PDMS, the temperature dependences of the differences between the I/I_0 values for adsorbed ($(I/I_0)_a$) and individual ($(I/I_0)_i$) polymers as $\Delta(I/I_0) = (I/I_0)_a - (I/I_0)_i$ for initial and preheated samples were calculated (Fig. 176) [271].

The negative values of $\Delta(I/I_0)$; *i.e.* diminution of the relative intensity I/I_0 for adsorbed PDMS, corresponded to a relative increase in freezing temperature of a fraction of adsorbed PDMS [271]. For all samples, there was a significant difference in the temperature behavior of ^{1}H NMR signals of initial and preheated samples. The hysteresis loops of the $\Delta(I/I_0)(T)$ curves for preheated samples were much narrower than that for the initial samples. This difference could be interpreted as diminution of the surface and confined space effects on the temperature behavior of PDMS bound to silica due to enhanced disordering of the supramolecular structure of preheated PDMS and removal of adsorbed water. Notice that the DSC data showed the difference in the temperature behavior of PDMS adsorbed onto silicas in the first and second scans analogous to initial and preheated samples studied by the NMR method [53,271].

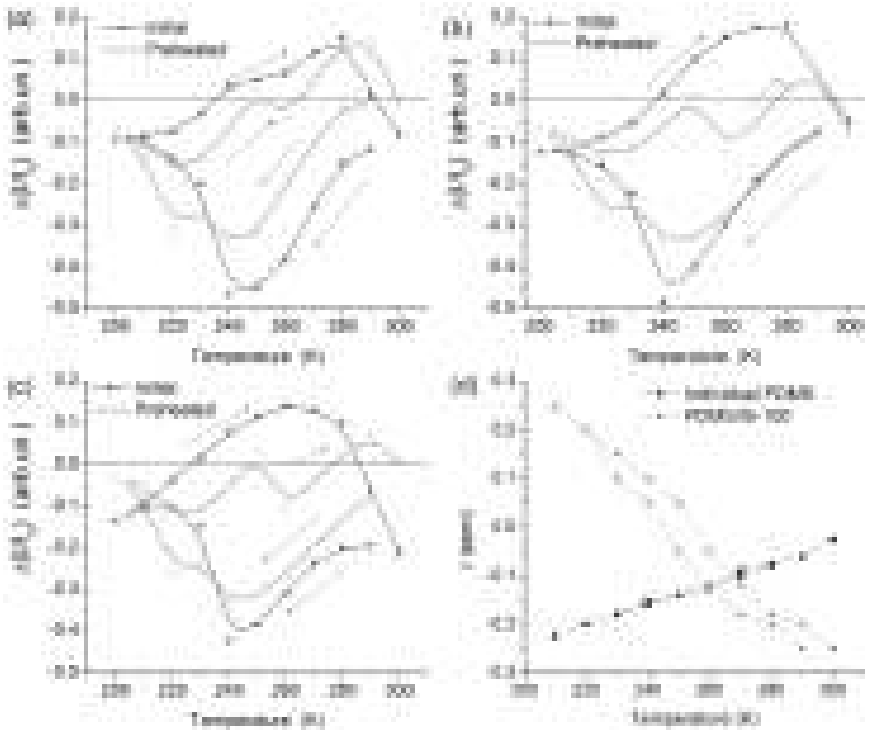

Fig. 176. Changes in relative intensity of ^{1}H NMR signals of bulk PDMS and PDMS bound to silicas for initial and preheated samples: (a) 33.3 wt.% PDMS bound to silica gel, (b) 8 wt.% PS400 in PDMS, (c) PS400 : PDMS = 1 : 1; and (d) temperature dependence of chemical shift of proton resonance for PDMS alone and bound (33.3 wt.%) to Si-100.

The positive values of $\Delta(I/I_0)$ (*i.e.* a decrease in the freezing temperature) was more characteristic for initial samples than for preheated ones (Fig. 176) [271]. For preheated samples, this effect was well observed for PDMS adsorbed onto silica gel (Fig. 176a) that was due to the confined space effects. During freezing of PDMS alone the upfield shift was observed with decreasing temperature in contrast to PDMS bound to silica gel (Fig. 176d). Thus, the PDMS-PDMS interactions result in an increase in proton shielding with lowering temperature. However, PDMS-silica surface interactions caused certain diminution in proton shielding with decreasing

temperature. This could be explained by stronger polarity of adsorption sites of the silica surface interacting with the macromolecules than that of PDMS molecules [271].

The low-temperature ^{1}H NMR spectroscopy used here gives information of the behavior of PDMS with respect to phase transition between liquid and solid-like fractions [271]. Additional information on the temperature behavior of PDMS interacting with different silicas could be obtained using the DSC method. According to the DSC data, the crystallization temperature (T_c) for the sample with 33.3 wt.% PDMS/silica gel was about 177 K during the first scan (Fig. 177a) that corresponded to published results [272]. During the second scan, T_c was about 188 K but this feature was much weaker than that during the first scan. This effect could be explained by disordering supramolecular structure [272,273] of PDMS macromolecules bound to silica that remained during the second scan [267-271].

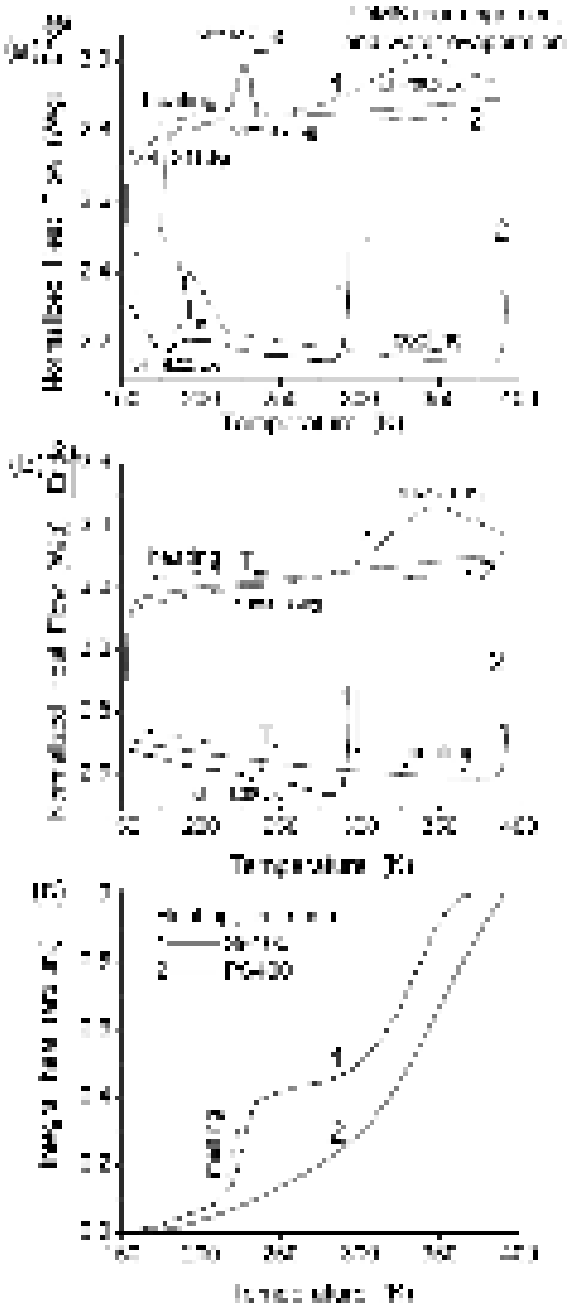

Fig. 177. Results of the first (1) second (2) DSC scans for PDMS (33.3 wt.%) bound to (a) silica gel Si-100 and (b) nanosilica PS400 at cooling-heating rate of 10 K/min; and (c) integral heat as a function of temperature $\Phi(T)$ (with subtraction of a nonlinear baseline and normalization to unit) for endo-effects (heating, melting) for PDMS (1) confined in pores of Si-100 or (2) bound to non-porous PS400 nanoparticles.

For PDMS adsorbed in pores of silica gel with the average diameter $d_p \approx 14$ nm similar to the size of typical lamellar structures of PDMS (~10 nm), the melting endotherm was well seen at 227 K for both scans (Fig. 177a) in contrast to that for the PDMS/PS400 system with a very small endotherm observed only upon the first scan (Fig. 177b) [271]. This effect could be due to much stronger disordering effect of small nanoparticles of PS400 onto PDMS supramolecular structure than that of silica gel with relatively broad mesopores, where the PDMS structure could be close to that in the bulk PDMS. These DSC results were in agreement with the NMR data showing the stronger effects of nanosilica than silica gel on the temperature behavior of PDMS. During the first cooling-heating scan, there was a broad endotherm at 273-393 K (Fig. 177) which could be due to several processes [53,274-279]. Water evaporation could contribute this endotherm but this effect could be small, since the water content in both systems was small < 0.5 wt.% [271].

For PDMS (33.3 wt.%) bound to nanosilica surface, the melting endotherm peak at 233 K was very small during the first scan (Fig. 177b), and it was practically absent during the second heating run [271]. Additionally, the crystallization exotherm (around 183 K) was absent. However, a small exotherm was observed at 233 K during the first cooling run. This could be due to freezing a small portion of PDMS and/or water bound in narrow nanopores of PS400 which were poorly accessible for PDMS macromolecules. Notice that the broad endotherm at 300-400 K observed during the first scan was larger for PDMS/PS400 (ΔH = 47 J/g) than that for PDMS/Si-100 (ΔH = 39 J/g). This difference could be caused by stronger interactions of the PDMS molecules with the open PS400 surface than that with the silica surface in pores of Si-100 [271]. Despite the PDMS amount was much lower (~0.35 cm^3 per gram of silica) than the pore volume of Si-100 (V_p = 1.23 cm^3/g), a film of PDMS was observed at a surface of Si-100 particles. The difference in the morphology of silicas caused a significant difference in the curves of integrated heat flow [134, 213, 271] $\Phi(T) = \int_{T_{min}}^{T} |F(T)|\,dT$ during heating (endo-effects due to melting) of PDMS bound to Si-100 and PS400 (Fig. 177c), since the PDMS/Si-100 curve has a significant step at 220-230 K in contrast to a smooth curve for PDMS/PS400 (Fig. 177c). This step for PDMS/Si-100 in not vertical because of certain nonuniformity of PDMS with respect to both molecular weight and supramolecular structure of PDMS located in pores of different sizes and out of pores.

The temperature behavior of PDMS (Oxane 1000) differs for polymers alone or bound to silica gel Si-100 and nanosilica PS400 [271]. The low-temperature ^{1}H NMR spectroscopy showed that two fractions of PDMS (liquid and solid-like, frozen) co-exist over a broad temperature range spreading toward both sides from the Oxane 1000 melting point. The transverse relaxation times of protons in methyl groups strongly differ for liquid and solid-like PDMS that allows quantitative estimation of contributions of both fractions *vs*. temperature.

The cooling-heating of PDMS and PDMS/silica samples gives the hysteresis loop for intensity of ^{1}H NMR signals. The loop width depended on the surrounding (bulk PDMS or PDMS adsorbed on a silica surface) and confined space effects (silica gel or nanosilica) [271]. It also strongly differs for initial and samples preheated at 420 K. The observed differences could be explained by different order or disorder of supramolecular structures of PDMS alone, adsorbed and preheated.

DSC measurements of polymers (33.3 wt.%) bound to silica gel and nanosilica showed that bound PDMS was characterized by different temperature behavior on the first and second cooling-heating scans and this behavior differs for silica gel and nanosilica. For PDMS/silica gel, supramolecular structures could be more ordered than that for PDMS/nanosilica. Both melting endotherm and crystallization exotherm were observed for PDMS/silica gel. However, both thermal features were much weaker for PDMS/nanosilica and observed only during the first temperature scan. This difference could be explained by stronger interactions of polymers with silica nanoparticles than with a surface in pores of silica gel because penetrating of macromolecules into relatively narrow and long pores (since silica gel beads have 0.2-0.5 mm in diameter) could be more difficult than mixing nanoparticles with PDMS molecules [271].

Oxide composite with SiO_2/ZrO_2 (labeled as AZr) at 2.4 wt.% of ZrO_2 was prepared by a wet impregnation method using zirconium acetylacetonate dissolved (0.4 wt.%) in CCl_4, and nanosilica A-300 as a substrate, calcined up to 823 K [149]. The amounts of unfrozen water (C_{uw}) at $T > 240$ K for AZr ($h = 50$ mg/g) in air was equal to the h value (Fig. 178a), *i.e.* all water was unfrozen at $240 < T < 273$ K and $\Delta G < -1.2$ kJ/mol; *i.e.* it was SBW [53,149]. The behavior of bound water changes in the chloroform medium or/and after the adsorption of PDMS (Fig. 178a). The amount of SBW (Table 30, C_{uw}^{s}) decreased and WBW appears (C_{uw}^{w}). This led to strong decrease in the γ_S value (Table 30); *i.e.* water more weakly interacts with the oxide surface. These changes could be caused by two factors. First, water and chloroform were immiscible liquids. Therefore, bound water tends to reduce the boundary area with weakly polar (hydrophobic) dispersion medium. This could occur by the formation of larger water domains (Fig. 179) [149].

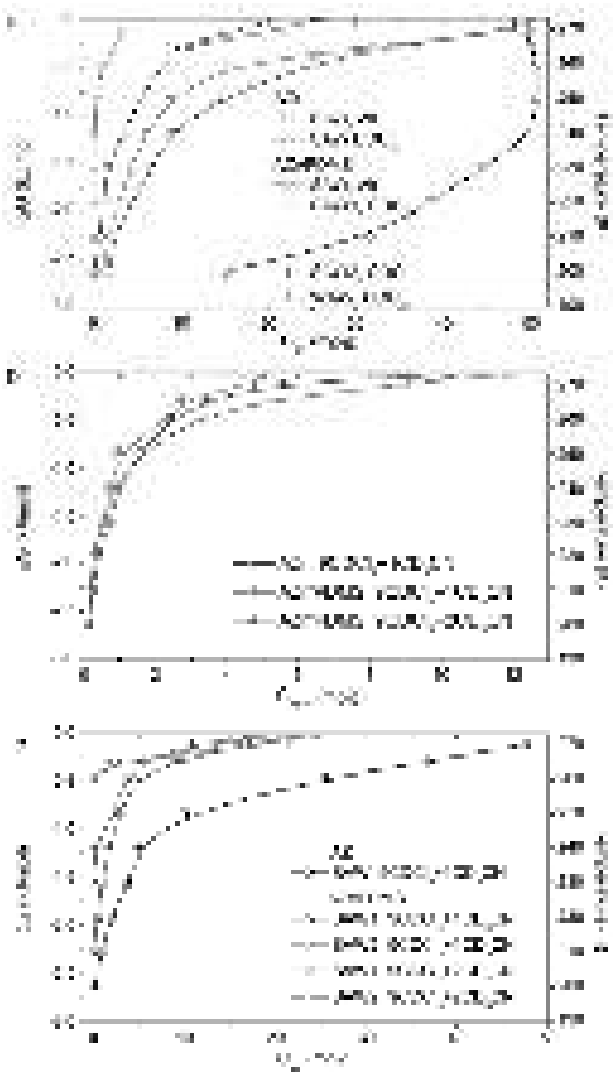

Fig. 178. Relationships between the amounts of unfrozen water (C_{uw}) and changes in the Gibbs free energy of bound water and temperature for AZr and AZr/PDMS in (a) air or $CDCl_3$ and (b, c) in mixture with $CDCl_3/CD_3CN$ at 9:1 or 9:2 for three types of bound water: SAW, WAW and ASW.

Table 30. Characteristics of water bound to AZr or AZr/PDMS samples in air or chloroform medium [149].

Sample	Medium	Water type	C_{uw}^{s} (mg/g)	C_{uw}^{w} (mg/g)	$-\Delta G_s$ (kJ/mol)	$-\Delta G_w$ (kJ/mol)	γ_S (J/g)	<*T*> (K)	S_{uw} (m^2/g)	S_{nano} (m^2/g)	S_{meso} (m^2/g)	V_{nano} (cm^3/g)	V_{meso} (cm^3/g)
AZr	Air	SAW	50	-	3.6	-	6.9	205.6	63.3	55.8	7.5	0.024	0.026
	$CDCl_3$	SAW	14	36	4.0	0.8	2.1	250.4	12.4	5.0	7.4	0.002	0.040
	$9CDCl_3/1CD_3CN$	SAW	10	40	3.2	0.8	1.9	254.0	8.2	1.3	6.9	0.001	0.045
AZr/PDMS	Air	SAW	10	40	3.9	0.6	1.7	254.4	10.5	3.5	7.1	0.001	0.038
	$CDCl_3$	SAW1	10	10	2.7	0.6	0.7	255.0	2.6	0.8	1.8	0	0.017
	$CDCl_3$	SAW2	0	26	-	0.4	0.4	266.9	2.9	0	2.8	0	0.021
	$CDCl_3$	WAW	1	3	2.6	0.5	0.1	257.4	0.7	0.03	0.6	0	0.003
	$9CDCl_3/1CD_3CN$	SAW1	5	17	2.3	0.5	0.5	260.6	1.7	0	1.6	0	0.020
	$9CDCl_3/1CD_3CN$	SAW2	0	21	-	0.5	0.3	267.0	2.8	0	2.7	0	0.020
	$9CDCl_3/2CD_3CN$	SAW1	4	13	1.6	0.5	0.3	263.3	1.1	0	1.0	0	0.016
	$9CDCl_3/2CD_3CN$	SAW2	0	17	-	0.5	0.2	266.7	2.0	0	2.0	0	0.015

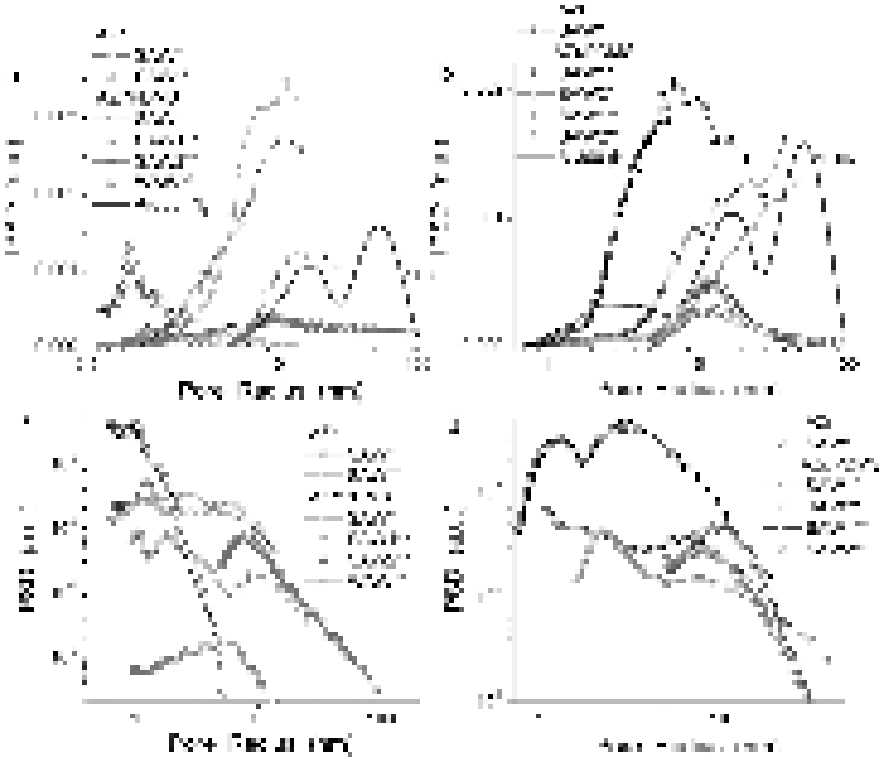

Fig. 179. Size distributions of pores filled by unfrozen water for AZr and AZr/PDMS in (a, c) air (*) or $CDCl_3$ (**) and (b, d) in mixture with $CDCl_3/CD_3CN$ at 9:1 (*) or 9:2 (**) shown as (a, b) incremental and (c, d) differential distributions. The PSD based on the N_2 adsorption isotherm [34] was multiplied by 0.06 since the water content corresponded to approximately 6% of the pore volume calculated from the nitrogen adsorption.

However, an increase in the water domain sizes led to diminution of the interaction of water with the oxide surface (Table 30, γ_S). Second, PDMS was hydrophobic polymer, which displaces a water portion from the AZr surface. Therefore, water bound to AZr/PDMS in air or chloroform tends to reduce the contact area with both hydrophobic PDMS and $CDCl_3$. This results in diminution of water interaction with the oxide surface and the γ_S value drops down and $<T>$ increased (Table 30). The effects of PDMS and organic solvents on bound water structure were well seen in the PSD (Figs. 179 and 180). The water domain size increased in comparison with water bound to AZr in air. The S_{uw}, S_{nano} and V_{nano} values strongly decreased (Table 30). Water structures in the mesopore range give the main contributions (Table 30, S_{meso}, V_{meso}). Therefore, $<T>$ (Table 30) increased by 45-60 K because the main fraction of water became WBW but it remained SAW. Contribution of WAW was small in all samples (Fig. 181, Table 30). The cryoporometry and thermoporometry give similar PSD for AZr in air (Fig. 180), despite significant difference in the used temperature ranges and related phenomena (melting and evaporation of water). The difference in the N_2, NMR and TG PSD shapes (Figs. 179 and 180), especially at $R < 2$ nm, could be caused by a strong influence of water on the organization of aggregates of nanoparticles. In contrast to nitrogen molecules, water molecules could penetrate between adjacent oxide nanoparticles bonded in aggregates by the hydrogen (electrostatic) and van-der-Waals bonds, therefore, individual silica nanoparticles could be observed in concentrated aqueous suspensions [53,149,238].

Water bound in weakly hydrated powders (h = 50 mg/g) with silica/zirconia (2.4 wt.%) alone or with immobilized PDMS was mainly strongly associated (δ_H = 4-5 ppm) but weakly bound to the oxide surface in the chloroform medium. Both PDMS and $CDCl_3$ stimulate an increase in size of water structures to reduce the contact area (S_{uw}) between water and hydrophobic polymer or organic solvent. Adsorbed water did not completely cover the oxide surface in air since S_{uw} = 63 m^2/g at the specific surface area of 290 m^2/g. The S_{uw} value decreased by 5-10 times for samples with or without PDMS in the chloroform medium. Thus, the used techniques allow

quantitative description of structures of water bound to complex surfaces in different dispersion media [149].

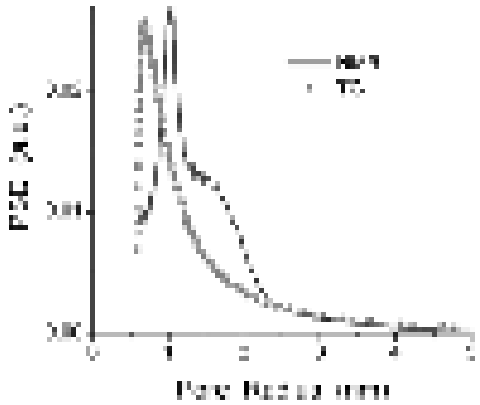

Fig. 180. Comparison of the size distributions of pores filled by unfrozen water at h = 50 mg/g (NMR) or evaporated water at $h \approx 60$ mg/g (TG) for AZr in air.

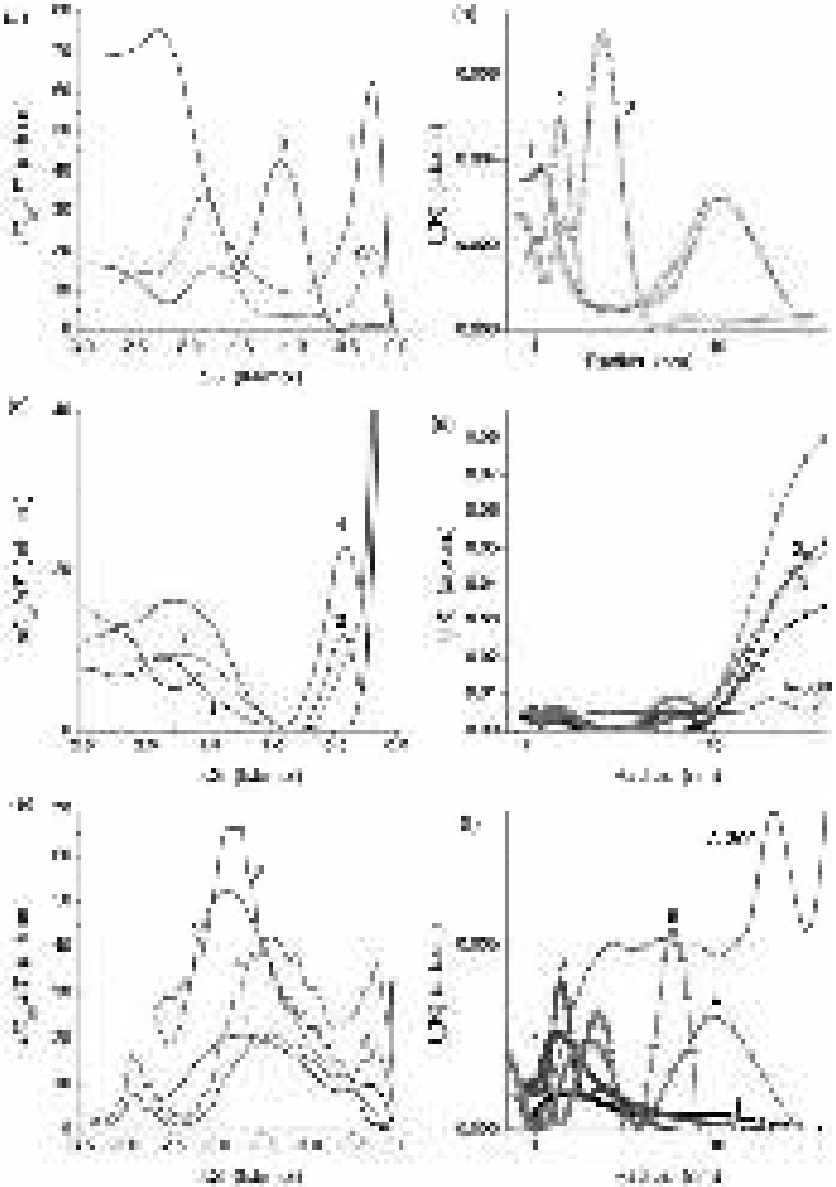

Fig. 181. Changes in (a, c, e) the amounts of unfrozen water dC_{uw}/dT as a function of changes in the Gibbs free energy, and (b, d, f) size of unfrozen water structures in starch at h = (a, b) 0.3 g/g, (c, d) 1 (curve 1), 1.5 (2, 3) and 2.3 g/g (4), (e, f) 0.1 (1), 0.2 (2-5) g/g; on addition of $CDCl_3$ at C_{CDCl3} = (a, b) 2 g/g (2, 3), (e, f) 2 g/g (3-5), and C_{DMSO} = (a, b) 1 g/g (3), (e, f) 0.5 (4) and 1 (5) g/g, C_{Qc} = 4.8 wt.% (c, d, curves 2-4) and (e, f, 1-5), $C_{A\text{-}300}$ = 4.8 wt.% (c, d, curve 4) and (e, f curves 1-5); PSD for A-300 calculated on the basis of the nitrogen adsorption was shown (d, f).

Comparison of changes in the dC_{uw}/dT and $f_V(R)$ functions for unfrozen water (Fig. 181) showed that SBW ($\Delta G < -(0.5 \div 0.8)$ kJ/mol) corresponded to mainly water structures at $R <$ 2-3 nm, and WBW (($\Delta G > -(0.5 \div 0.8)$ kJ/mol) was linked to structures at $R >$ 2-3 nm [280]. The boundary ΔG and R values between SBW and WBW depended on system composition. For more complex systems with starch/Qc/A-300/water this boundary was nonabrupt (Fig. 181e) in contrast to starch/water or starch/water/$CDCl_3$ (Fig. 181a) because There were the differences in the freezing point depression (*i.e.* the corresponding size (R) of pores where water was unfrozen at this temperature) and the ΔG values for water interacting with organics and silica nanoparticles [53,280]. Addition of DMSO to starch/water/$CDCl_3$ caused significant changes in the dC_{uw}/dT (Fig. 181a, curve 3) and $f_V(R)$ (Fig. 181b, curve 3) functions. Addition of Qc and A-300 (Fig. 181) to hydrated starch led to more complicated shapes of both dependences because of different tendencies in the DMSO, $CDCl_3$, Qc, starch, and A-300 effects on structure of interfacial water. For instance, the bound water displacement to both broader and narrower pores (in starch and/or silica) occurred due to its interactions with organic solvents [53,280].

The interfacial behavior, energetic characteristics and structure of both SBW and WBW depended strongly on the amounts of water and the type and amounts of co-adsorbates (organic solvents) in hydrated starch with addition of quercetin, nanosilica, and weakly polar ($CDCl_3$) and polar (DMSO) organic solvents [53,280]. The addition of these solvents to hydrated quercetin/starch/nanosilica caused the appearance of three additional water signals at δ_H = 1.3, 3 and 4 ppm differently dependent on temperature. Thus, the composite systems with hydrated starch/quercetin/nanosilica were characterized by structural and energetic nonuniformities which could be varied due to changes in the amounts of water and treatment temperature.

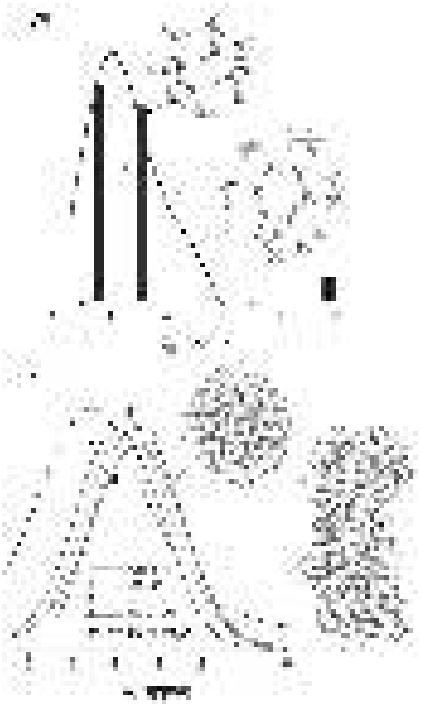

Fig. 182. Theoretically calculated ^{1}H NMR spectra for (a) water cluster with $12H_2O$ (1) and distribution function $f(\delta_H)$ for $12H_2O*6((CH_3)_2SO)$ (only for water) (2) (method GIAO/B3LYP/6-31G(d,p)//6-31G(d,p)), (b) distribution functions $f(\delta_H)$ for water nanodomain (1), hydrated two starch fragments (2), quercetin molecule in water nanodrop (3), and hydrated starch/Qc (4) calculated using correlation equation (geometry was optimized using PM6/MOZYME), curve 5 – experimental ^{1}H NMR spectrum of water (0.3 g/g) bound to starch recorded at 280 K.

In the presence of organics, the hydrogen bond network in water was disturbed that led to upfield shift in the ^{1}H NMR spectra [53,280]. This effect depended on the type of organics. The calculated ^{1}H NMR spectra were broadened for water interacting with small organic molecules, *e.g.*, DMSO (Fig. 182a). The presence of the quercetin molecule or two starch (amylose)

fragments in water nanodomain results in the upfield shift in the spectra (Fig. 182b). This suggests weakening of the hydrogen bonding or changes in orientation of the O–H bonds of water molecules with respect to lone-electron pairs of the O atoms of neighboring molecules.

For hyaluronic acid (HA), which could form strong hydrogen bonds, the upfield shift for bound water was slightly smaller (Fig. 183) than for water disturbed by quercetin or starch (Fig. 182). Appearance of a small number of chloroform molecules (ratio $CHCl_3/H_2O$ = 17 : 624) around hydrated HA (Fig. 183, curve 3) weakly affected the spectrum. Much stronger upfield shift of the ^1H NMR spectra was observed for water bound to DNA or DNA intercalated by doxorubicin (anticancer medicine) (Fig. 184) due to chemical structure of DNA. A water shell of DNA was more strongly clustered and tends to be weakly associated water (WAW) than water around polysaccharides (Figs. 182 and 183) [53,210].

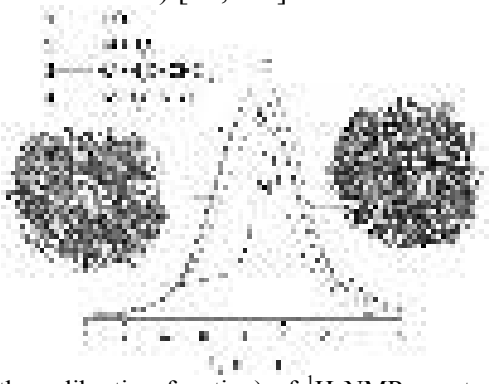

Fig. 183. PM6 calculations (using the calibration function) of ^1H NMR spectra of pure water (curve 1) and water bound to a fragment (773 atoms) of hyaluronic acid HA (curve 2) and with addition of $CHCl_3$ ($17CHCl_3/624H_2O$) (curve 3), experimental ^1H NMR spectrum of water/HA/A-300 (4 wt.% H_2O and 10 wt.% HA) recorded at 280 K (curve 4). [210]

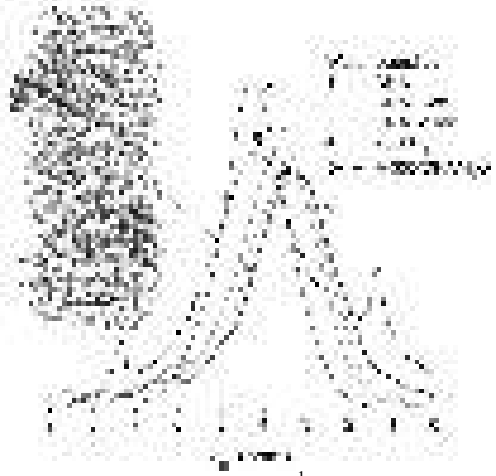

Fig. 184. PM6 calculations (using the calibration function) of ^1H NMR spectra of water bound to a DNA fragment without (curve 1) and with (2) one or (3) two molecules of doxorubicin (Dox) intercalating DNA, nanodomain of pure water with $2000H_2O$ (curve 4), experimental ^1H NMR spectrum of water/DNA/A-300 (50 wt.% H_2O and 6 wt.% DNA) recorded at 280 K (curve 5) [210].

To characterize interfacial interactions, the peculiarities of molecular dynamics and conformational state in PVP nanoshells compared with those in bulky PVP, far-IR spectra at 20-500 cm^{-1} were registered [277]. These spectra obtained for neat PVP and PVP shells with different thicknesses including monomolecular layers in the $20PVP/80SiO_2$ and $20PVP/80Al_2O_3$ samples (Fig. 185). Seven partly overlapping absorption bands with the maxima at 42, 83, 100, 169, 247, 355 and 446 cm^{-1} were present in the far-IR spectrum of neat PVP. The band assignment was given in Table 31. The relative values of absorption coefficients were calculated for the bands characterizing interfacial interactions and shell thicknesses (Table 32).

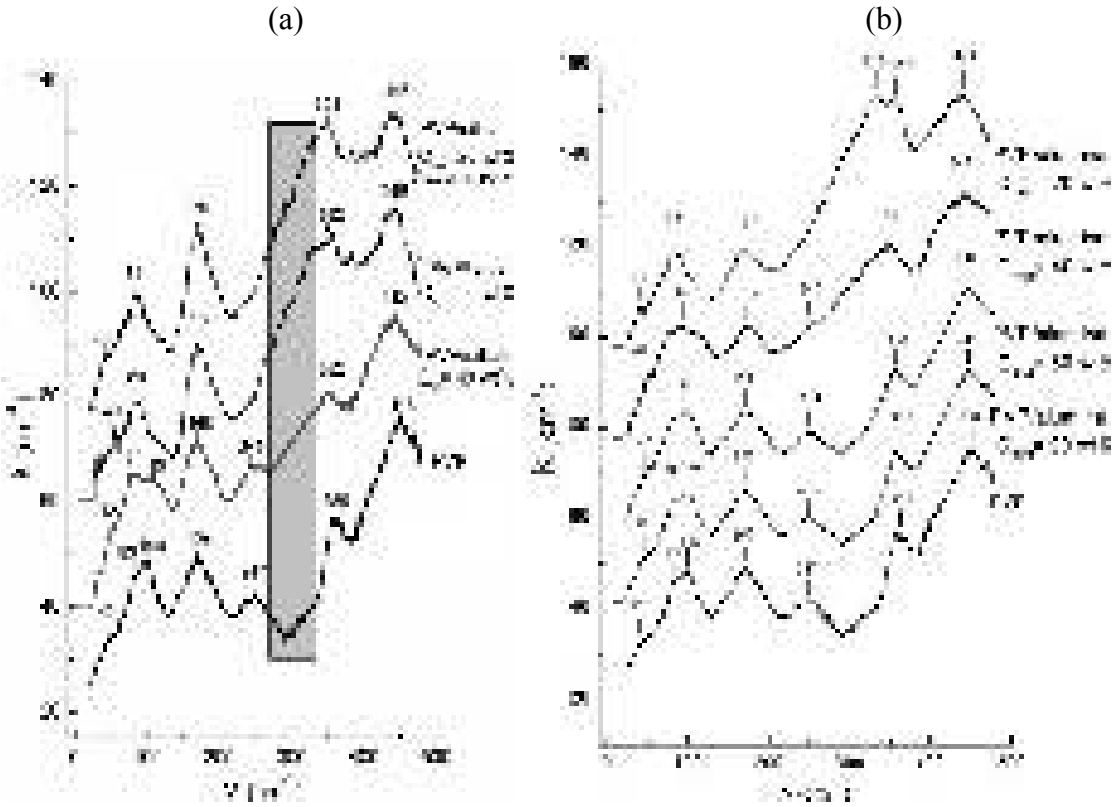

Fig. 185. Far-IR spectra of neat PVP and PVP shells in (a) PVP/SiO_2 and (b) PVP/Al_2O_3 at different content C_{PVP} and shell thickness. Monomolecular PVP coverage was at 20 wt.% of PVP. The spectra of PVP shells were shifted along the ordinate axis relative to the spectra of neat PVP. Shaded rectangle between ~260 and 350 cm^{-1} characterizes the region of Lewis/Brønsted interactions at polymer/oxide interfaces (tentatively, see text).

Table 31. Absorption bands in the far-IR spectra of PVP in bulky state and nanoshells [277].

Absorption band, cm^{-1}	Assignment
40-46	Hydrogen bonds, torsional vibrations [a]
78-104	Small-angle pyrrolidone ring vibrations (librations, Poley-type absorption)
167-172	Hydrogen bonds, stretching vibrations [a]
245-248	Torsional skeletal vibrations
~260 to 350	PVP/oxide Lewis/Brønsted interactions [b]
350-357	Deformation pyrrolidone ring vibrations
442-447	Ditto

Note. [a] The hydrogen bonds in neat PVP were assigned to PVP-residual tightly-bound water complexes. [b] Tentative assignment (see text).

The PVP far-IR spectrum substantially changes when PVP was transformed into nano-dispersive adsorbed state, *i.e.*, for monomolecular and thicker PVP nanoshells [277]. These changes relating to interactions, dynamics and conformational state of chains at interfaces were most pronounced for PVP monolayers (C_{PVP} = 20 wt.%). Additionally, somewhat different spectra of PVP nanolayers adsorbed on silica and alumina surfaces were also observed.

Generally, four peculiarities of the nanoshell spectra have to be noted [277]. First, the doublet 83/100 cm^{-1} librational band transforms into the single band at ~80 cm^{-1} for the monomolecular shell. Splitting of the librational bands into two bands with the difference in the maxima values of 10-20 cm^{-1} has earlier been observed for polymers and explained by the complicated conformation of molecules with the existence of two isomeric states. The disappearance of the doublet may indicate, therefore, "simplifying" conformational state of the majority of the PVP segments (flattened conformations, extending chains) in the adsorbed monolayer strongly interacting with the oxide substrate. Secondly, the absorption band at 245-247 cm^{-1} of torsional skeletal vibrations disappears at C_{PVP} = 20 wt.% indicating some suppression of

the chain dynamics in the PVP monolayer. At last, the changes in the spectra in the regions of ~170 and 260-350 cm^{-1} directly characterize strong physical interactions at the PVP-oxide interfaces (Table 32) [277].

Table 32. Far-IR characterization of PVP-oxide interfacial interactions [277].

Sample	Nanoshell thickness, Nm	Hydrogen bonding	PVP/oxide Lewis/Brønsted interactions (~ 260 to 350 cm^{-1} region)		
		k_{170}/k_{80}	k_{318}/k_{80}	k_{350}/k_{80}	k_{350}/k_{444}
Neat PVP		1.05	0.85	1.15	0.72
40PVP/60SiO_2	2-5	1.14	1.20	1.23	0.82
20PVP/80SiO_2	1-2	1.25	1.53	1.35	0.96
90PVP/10Al_2O_3	20-90	1.05	0.89	1.23	0.76
80PVP/20Al_2O_3	15-70	1.04	0.94	1.24	0.78
40PVP/60Al_2O_3	5-20	1.02	1.26	1.40	0.88
20PVP/80Al_2O_3	2-9	1.02	1.56	1.72	1.02

Note. The coefficients k_{80} and k_{444} and their ratio remained practically unchangeable and were used as internal standards.

Thus, if interfacial interactions between PVP and silica core were controlled basically by the hydrogen bonds and to some extent by the Lewis/Brønsted (LB) interactions, the latter mainly control the PVP-alumina interactions. Strong PVP/oxide interactions and peculiar conformational state of adsorbed polymer at the interfaces crucially affected the glass transition dynamics, especially for the monomolecular layer shells. This was confirmed by the DSC experiments presented below [277].

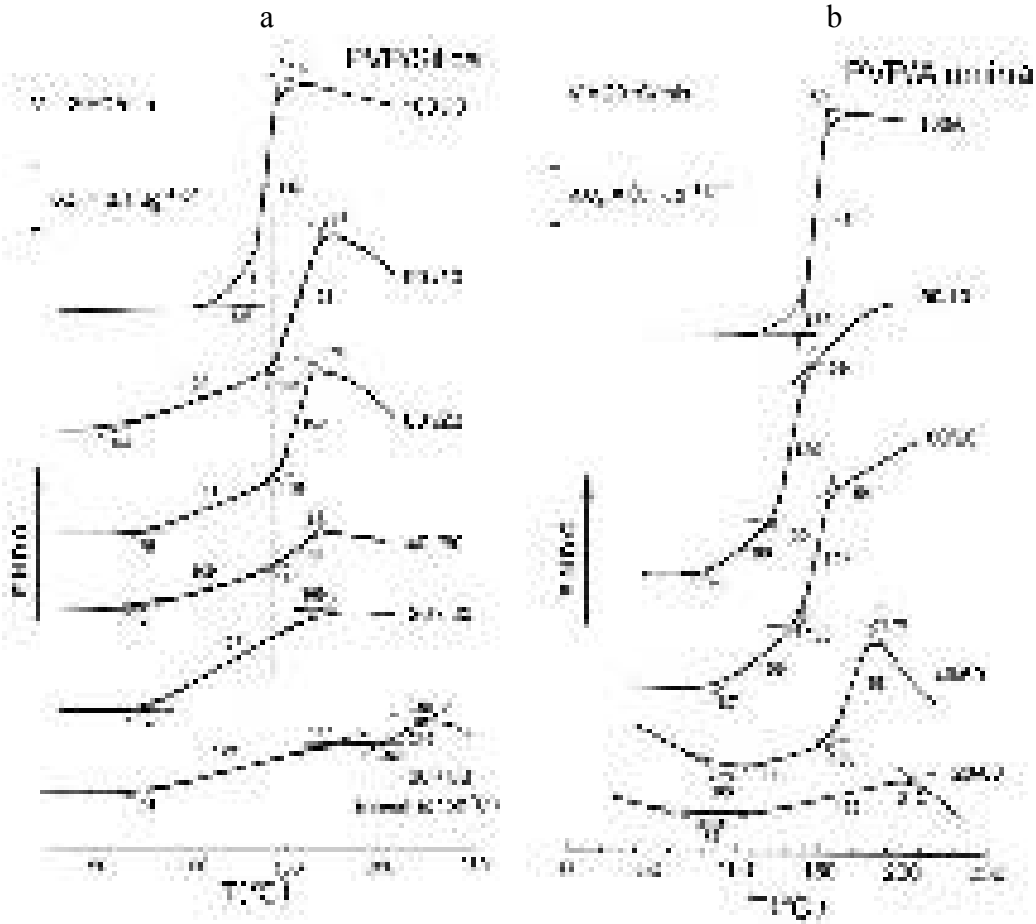

Fig. 186. DSC curves obtained in the temperature region of glass transition for neat PVP and PVP shells in PVP/oxide nanoparticles with (a) silica and (b) alumina. The second scans were taken after heating samples to 217°C at V = 20°C/min and subsequent cooling down to 20°C at V = 320°C/min. The curve obtained for 20PVP/80SiO_2 after annealing at 150°C for 1 h was also shown.

The DSC thermograms (Fig. 186) characterized PVP glass transition in waterless neat polymer and PVP/oxide nanoparticles [277]. Glass transition temperature T_g at the half-height of heat capacity step, and the transition breadth $\Delta T_g = T_g'' - T_g'$, where T_g' and T_g'' are the temperatures of the glass transition onset and completion, respectively, were shown. One could see a peculiar glass transition manifestation in core-shell samples depending on their composition (shell thickness) and oxide type. The main point here was that no simple dependence of T_g on the shell thickness was observed. The strongly broadened in both directions, at the limit from 63 to 230°C, and two-stage glass transition may be seen for the PVP shells unlike the transition range ΔT_g = 18°C for neat PVP. The glass transition width ΔT_g =100-150°C was typical of the monomolecular PVP shells at C_{pol} = 20 wt.% in the core-shell particles. For instance, Figure 186 showed that instead of T_g = 143°C for neat PVP one could see T_gs at 104 and 158°C for the 90PVP/10SiO_2 composition (h_{pol}=7-25 nm); at 109 and 157°C for the 40PVP/60SiO_2 composition (h_{pol}=2-5 nm) but at 127°C for the 20PVP/80SiO_2 composition (h_{pol} = 1-2 nm) or at 129 and 216°C for the latter shell after its annealing at 150°C for 1 h [277].

The shell transition characteristics differed for fillers with silica or alumina [277]. The basic difference was higher T_g' and T_g'' temperatures for 20PVP/80Al_2O_3 and 40PVP/60Al_2O_3. At the close PVP nanolayer thickness in the 40PVP/60SiO_2 and 20PVP/80Al_2O_3 (Table 32) stronger LB interactions in the latter result in higher T_g' and T_g'' values: 87 and 213°C instead of 76 and 169°C for the silica-containing particles, respectively (Fig. 186) [277].

It was found that "anomalous" dynamic modes contribute to the broad, complicated glass transition in the monomolecular PVP nanoshells [277]. This was corroborated in the experiments performed at different heating rates V, from 5 to 40°C/min, with the determination of apparent activation energy Q of segmental dynamics in transition as a function of temperature.

Combined far-IR/DSC study allowed us also to reveal the cardinal changes in the dynamic and structural characteristics of PEG nanolayers adsorbed on alumina and silica surfaces compared to those for neat bulky PEG [277]. DSC data were obtained for melting of neat PEG and PEG nanoshells (Figs. 187 and 188 and Table 33). One could see that the characteristics of this transition depended both on the type of oxide cores and the nanoshell thickness (*i.e.* PEG content in core-shell particles). Despite a high PEG ability to crystallization, the total amorphization of the PEG monolayer adsorbed on amorphous silica surface was observed. Some crystalline phase appeared for PEG-silica pairs only in the thicker PEG nanolayers (not shown therein). *Vice versa*, the PEG monolayer adsorbed on the alumina surface remained highly-crystalline (Table 33, 20PEG/80Al_2O_3). It was characterized with the anomalous, doublet melting endotherm consisting of the lower-temperature (I) and "normal" (II) peaks (Fig. 187). Crystallinity of the PEG nanoshell somewhat decreased with its thinning from χ = 93-95% for neat PEG and PEG shells at the thickness h_{pol} = 20-90 nm to χ = 70% for the PEG shells at h_{pol} = 2-9 nm (20PEG/80Al_2O_3) [277].

Table 33. Melting transition characteristics, crystallinity and crystallite sizes of neat PEG and PEG nanolayers in core-shell nanoparticles [277].

Sample	Melting point T_m at V = 20 °C/min, °C	True melting points, °C			Melting enthalpy ΔH_m, J/g PEG	Crystallinity χ %	Crystallite thickness l_c, nm
		T_m^{tr}'	T_m^{tr}	T_m^{tr}''			
PEG	75[a]	59	65	65	185±10	93±5	9-22
20PEG/80Al_2O_3		46[b]	58[b]		80±3[b]	70±5	3-8[b]
	66		59	59	58±3		9
40PEG/60Al_2O_3	68				155±7	79±5	
80PEG/20Al_2O_3	71[a]				162±8	82±5	
90PEG/10Al_2O_3	71[a]				187±10	95±5	
20PEG/80SiO_2					0	0	

Note. [a] These experimental melting points were higher than the equilibrium melting temperature of a perfect PEG crystal T^0_m = 69°C for methodical reasons (due to thermal delay). [b] These true melting temperatures, melting enthalpy and crystallite thickness values relate to anomalous low-temperature part I of PEG monolayer melting peak (see Fig. 187).

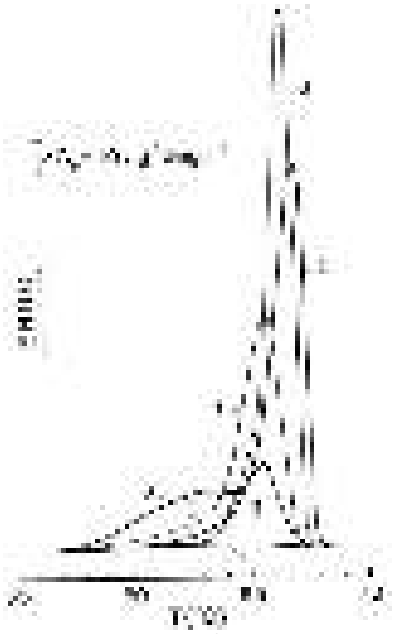

Fig. 187. DSC curves obtained at a heating rate V = 0.62°C/min in the temperature region of PEG melting for 20PEG/80SiO_2 nanoparticles (1, monolayer), neat PEG (2), 90PEG/10Al_2O_3 (3), 40PEG/60Al_2O_3 (4), and 20PVP/80Al_2O_3 nanoparticles (5, "monolayer").

True melting points were determined for neat PEG and PEG monolayers adsorbed on alumina cores, in particular for the correct calculation of lamellar crystallite thickness [277]. The characteristic melting temperatures vs. $V^{1/2}$ were obtained at the heating rate ranging from 0.62 to 20°C/min; temperature T_m^{anom} relates to the maximum of anomalous peak I (Fig. 188). Additionally, the equilibrium melting point T_m^o for PEG crystal was also indicated. One could see that only two plots for T_m and T_m" in neat PEG were linear over the whole range of heating rates, whereas the deviations from linearity toward higher temperatures were observed at low heating rates in other cases, especially considerable for PEG nanoshells. As known, this effect was associated with metastability and reorganization of lamellae during the experiment; however, extrapolation of the linear sections of these plots to V = 0 gives true melting points typical of the initial lamellae [277].

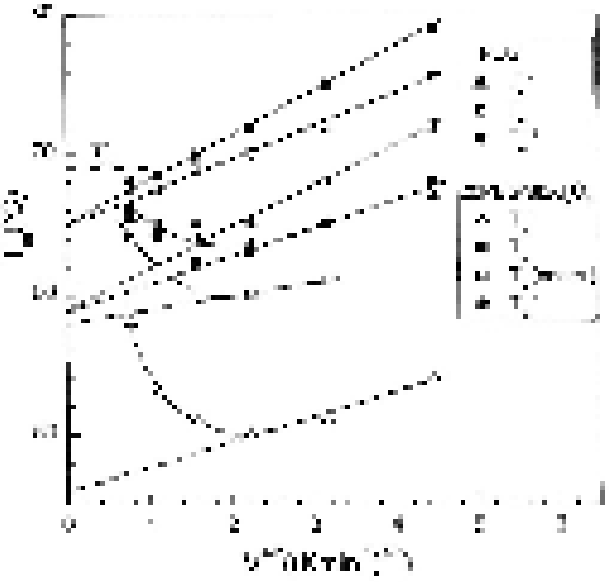

Fig. 188. Melting points *vs.* (heating rate $V)^{1/2}$ plots obtained for neat PEG and PEG nanolayer in 20PVP/80Al_2O_3. Temperatures of melting peak maxima (T_m, T_m^{anom}), onset (T_m') and completion (T_m"), and the equilibrium melting point T_m^o for PEG crystallites were indicated. True melting temperatures of these samples were obtained by extrapolating linear parts of these curves to V = 0.

Onset of true melting range (T^{tr}_m)' was at 59°C for neat PEG but at 46°C for the thinnest PEG shells (Fig. 188 and Table 33) [277]. The calculation of the crystalline lamellae thicknesses l_c showed that the anomalously thin (l_c = 3-8 nm) lamellae prevail in the monomolecular PEG shells adsorbed on the alumina surface. Of significance, this value coincides in fact with the shell thickness estimated (Table 32). It means that alumina surface was mainly covered with single lamellae forming these nanolayers.

PEG depicts a high affinity to the fumed silica surface in aqueous medium, and the hydrogen bonding ≡SiO–H···O(RR) between ether oxygen atoms and surface silanols was responsible for strong adsorption of PEG. The IR spectra showed that PEG molecules disturbed accessible surface silanols at the monolayer coverage (20PEG/80SiO_2). This resulted in disappearance of the majority of free silanols; however, only 20% of oxygen atoms of PEG molecules took part in the hydrogen bonding with the surface silanols, obviously, in the train segments [277].

Combined AFM/FTIR/fluorescence spectroscopy study of PEO films with 15-500 nm in thickness adsorbed on oxidized silicon substrate showed that lamellar growth rates, morphology, and the degree of crystallinity were functions of film thickness [277]. The degree of crystallinity decreased steadily when the film thickness became smaller than 200 nm; the lamellar growth rates decreased in the thinnest (15 nm) films to below 1% of their bulk value. In the experiments, correlation between polymer crystallization in thin films and the surface free energy of several substrates was observed. It was concluded, in particular, that the crystallization was strongly influenced by the interfacial hydrogen bonding (as in our PEG-silica pair); and it was suppressed on quartz surface due to constraining effect that influenced orientational and conformational changes of polymer chains at the interfaces. Especially strong suppression of the crystallization was observed for PEO chains (the same of PEG) after their grafting onto fumed silica particles that inhibited the chain mobility necessary for this process. As it follows from the NMR spectra, some train PEO segments with suppressed mobility were trapped near the silica surface in this case, alongside the presence of segments in the molecular loops and tails with anomalously high mobility. Therefore, totally amorphous PEG monolayer of ~1-2 nm in thickness adsorbed on amorphous fumed silica in our experiments was in fact the limiting case of structural disordering of this polymer caused by local hydrogen bonding of chains to the substrate hydroxyls [277].

Monte Carlo simulations [281] of polymer crystallization in thin films of thickness comparable to the polymer−coil sizes (radius of gyration R_g of a few nanometers) suppose nucleation on “sticky walls” (due to increased affinity to a substrate) with formation of preferentially flat-on lamellar crystals. When the PEO film of hundreds of nanometers in thickness anneals at Au substrate it changes from isotropic film to one with some degree of preferred chain orientation. The effect was more pronounced in the thinner films, suggesting that this phenomenon was caused by the presence of polymer-substrate interface. The PEO chains within the crystallites were oriented preferentially with their helical axes perpendicular to the substrate surface [282]. Really, the PEO chains crystallized in the layer of ~10 nm in thickness on the Au surface into the lamellae where chains were oriented perpendicular to the film plane [283]. Analogously, the PEO films of 300-400 nm in thickness were formed by spin coating onto aluminized glass substrate, *i.e.*, in fact on an alumina surface; on *in-situ* recrystallization, macromolecules oriented themselves to be normal to the substrate. Such recrystallization occurred in our work during preparing the samples for spectroscopic measurements.

Layer-multiplying co-extrusion of alternating polystyrene (or poly(ethylene-*co*-acrylic acid)) and PEO layers was used to study crystallization of PEO in a confined, two-dimensional space [284,285]. When the PEO layer thickness was equal to 20-25 nm these layers crystallized as single, high-aspect-ratio flat-on lamellae that resembled single crystals. The fold surfaces of lamellae were in the plane of the layer, and the chains were perpendicular to the film plane.

The alumina surface contains much less sites for the hydrogen bonding, such as free hydroxyls, than silica surface [53,277]. Nevertheless, strong polymer-alumina interfacial interactions were expected. For instance, a highly constrained relaxation, associated with these

interactions, was observed for a polymer in pores of ~20 nm in size [286]. Therefore, it may be supposed that the formation of the highly-crystalline PEG shells of 2-9 nm in thickness corresponding approximately to the main lamellar thickness on crystalline alumina substrate may be caused by both LB interfacial interactions and surface-induced heterogeneous nucleation process similar to heteroepitaxial crystallization.

Thus, as the thickness of the adsorbed PEO layer decreased from micro- to nanoscale the morphology changes from complicated 3D spherulite structure to lamellar stacks and then basically to single lamellae with a preferred flat-on orientation in films when the PEO helices were mainly perpendicular to the substrate surface. It was obvious that such structural changes have to result in the relevant changes in molecular dynamics, most sharply pronounced in the monomolecular crystalline PEG films when the substrate−polymer interface and free polymer surface dominate the dynamics of ultrathin films [287].

Such an assumption was confirmed by the far-IR spectra. PEO (or PEG) molecule has a 7/2 helix structure with the helix length (identity period) of 1.93 nm. In the frequency range between 80 and 300 cm^{-1} three spectral bands with the maxima around 110, 165-170, and 210-220 cm^{-1} have earlier been observed in the PEO spectra [277]. These bands were assigned to the symmetric and antisymmetric torsional and deformation vibrational modes in chains, viz., torsional vibrations around C-O bonds (τ_{COC}, ~110 cm^{-1}), or around C-O and C-C bonds (τ_{COC} + τ_{CC}, 165-170 cm^{-1}), and the complex motions in chains (210-220 cm^{-1}) including deformation (bending δ_{COC} and δ_{CC} modes), and torsional vibrations (τ_{CC}) (Table 34). The analysis allowed us also to assign the 110 cm^{-1} band to the limited torsional vibrations (libration) on the scale of a monomer unit $–CH_2–CH_2–O–$ in this polymer. The polarized spectra of oriented POE showed that (COC) torsion dipole transition moment (band at 107 cm^{-1}) was parallel to the PEO helix axis, whereas two other far-IR bands were associated with the vibrations perpendicular to macromolecular axis [277].

Table 34. Absorption bands in the far-IR spectra of PEG in bulky state and nanoshells [277].

Sample	Nanoshell thickness, nm	Absorption bands (cm^{-1})		
		Torsional vibrations τ_{COC}, or libration of a monomer unit[53]	Torsional vibrations τ_{CC} + τ_{COC}	Torsional-deformation vibrations (δ_{CC}, δ_{COC}, τ_{CC})
PEG		103, 110	169	218
80PEG/20Al_2O_3	15-70	109	166	214
40PEG/60Al_2O_3	5-20	109	165	213
20PEG/80Al_2O_3	2-9	100	160, 182	210, 223
20PEG/80SiO_2	1-2	110	170	217

Note. Enhancing absorption in the region of ~ 260-400 cm^{-1} with shell thinning in PEG/Al_2O_3 was observed that may be tentatively assigned to increasing contribution of LB interactions at the interfaces (see text).

The far-IR spectra were obtained in the region of 20-400 cm^{-1} for neat PEG and PEG shells with ~1-2 nm (monomolecular PEG layer) or 3-9 nm (thin PEG lamellae thickness, see Table 34) for 20PEG/80SiO_2 and 20PEG/80Al_2O_3, respectively, as well as for thicker PEG nanoshells (Fig. 189) [277]. These spectra allowed us to reveal peculiarities of the chain dynamics in the PEG nanoshells from 1-2 to 70 nm in thickness (Table 34) compared with that in neat PEG. Additionally, to lesser extent, information on interfacial interactions may be obtained from the spectra. The spectra manifest three features including the presence of three mentioned absorption bands; however, a considerable difference in the spectral contours of different samples, and arising of an additional absorption over the range between 300 and 400 cm^{-1} (for PEG nanolayers in PEG/Al_2O_3) were observed. Modifying of the spectrum of neat PEG in the nanolayers depended on the layer thickness and the type of oxide. The effects became more pronounced with thinning of films suggesting that This was caused by the presence of polymer-oxide interface and

free surface (more strictly, contacting with nonpolar LDPE matrix in our samples). The most cardinal changes in the PEG spectra were observed for the thinnest PEG layer adsorbed on alumina (spectrum 5) [277].

Far-IR spectrum 1 of neat PEG (Fig. 189) consists of broad intense bands at maxima ~110, 169 and 218 cm^{-1} [277]. A slight tendency to splitting into two modes (103 and 110 cm^{-1}) was observed for the first of these peaks. According to XRD analysis of PEO crystals, this effect was identified as a result of distortion of the normal helical structure of PEO chains. Nevertheless, splitting of this band could not be resolved in the spectra of PEG nanolayers. Spectrum 2 of the amorphous PEG monomolecular layer adsorbed on the silica surface differs from spectrum 1 mainly only by decreased band intensities and widths. This may be associated, apparently, with the impact of interfacial interactions resulting in some constraining effect. Unfortunately, the stretching vibrations of hydrogen bonds may manifest at the same frequencies as dynamic mode (τ_{COC} + τ_{CC}, 165-170 cm^{-1}) of PEG. Therefore, it was impossible to separate the compensating effects of decreasing the relevant band intensity and possible some increasing of the hydrogen bond band [277].

It was assumed [277] that substantial LB interactions between the ether oxygen atoms of PEG molecules and the silica surface were absent. Such interactions manifest themselves over the ~260-400 cm^{-1} range (see above). Therefore, the coincidence of spectra 1 and 2 in this region (Fig. 189) confirms such assumption. Far-IR spectra 3 and 4 of thicker PEG nanolayers in PEG/Al_2O_3 composites (Fig. 189) were also characterized by some decreasing intensities of three absorption bands. However, the absorption at ~260-400 cm^{-1} increased in this case, obviously, as a consequence of arising substantial LB interactions between PEG and alumina surface. Finally, the most pronounced changes in the far-IR spectrum were observed for 2-9 nm layer of PEG in the 20PEG/80Al_2O_3 composite (spectrum 5). This highly-crystalline layer consisted mainly from thin PEG flat-on lamellae. One could see three peculiarities in spectrum 5 compared to spectrum 1 of neat PEG (Fig. 189, Table 34). First, it was large decreasing and narrowing of 109 cm^{-1} band. Then, it was some tendency to splitting of 169 cm^{-1} band into the bands at 160 and 182 cm^{-1} and the distinct splitting of 218 cm^{-1} band into the bands at 210 and 223 cm^{-1}. At last, the maximal effect of absorption at ~ 260-400 cm^{-1}, with the maxima at 320 and 360 cm^{-1}, was observed for this PEG nanolayer adsorbed on alumina [277].

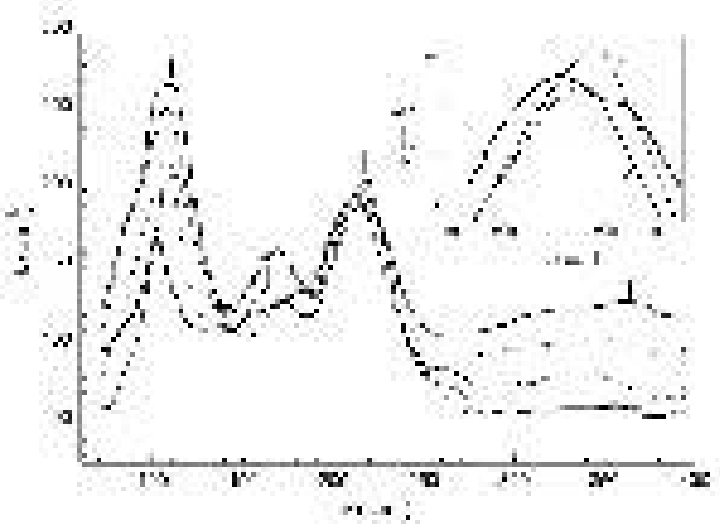

Fig. 189. Far-IR spectra of neat PEG (1) and PEG shells in the 20PEG/80SiO_2 (2), 80PEG/20Al_2O_3 (3), 40PEG/60Al_2O_3 (4), and 20PEG/80Al_2O_3 (5) nanoparticles with different shell thicknesses.

Thus, very specific chain dynamics was registered in the far-IR spectrum of the thinnest (2-9 nm) layer of PEG adsorbed on alumina. By analogy with the data obtained for adsorbed PVP monolayers, one could assume that arising of the absorption at ~ 260-400 cm^{-1} characterizes, really, LB interactions between PEG and alumina [277]. The prevailing feature of PEG nanolayer

structure in this case was the presence of thin (3-8 nm) lamellae located in the plane of the layer when the lamellar folds from one side were strongly interact with alumina substrate (interfacial forces) but remained undisturbed by surroundings (nonpolar PE matrix or air in our samples) from the opposite side of lamellae. The PEG chains between lamellar fold include only about 2-4 identity periods (or Kuhn segments). Therefore, different dynamics in chain segments, close to substrate or to the opposite lamellar surface, may be reflected in the observed splitting of two absorption bands in far-IR spectrum of this nanolayer. At last, a sharp decreasing of bandwidth at 109 cm^{-1} for nanoshell in the $20PEG/80Al_2O_3$ composite may be due to narrowing a dispersion of potential barriers to the smallest-scale torsional τ_{COC} motion within lamellae with chains oriented perpendicular to alumina surface.

The combined study of four series of oxide core - polymer shell nanoparticles (prepared in the pseudo-liquid state or using polymer adsorption onto oxides from the aqueous solution then dried) with different shell thicknesses (monomolecular and thicker nanolayers) and comprehensively characterized was performed. Fumed oxide cores, amorphous silica (5-18 nm in size) or crystalline alumina (12-47 nm in size) and water-soluble PVP and PEG shells were used [277]. IR spectroscopy in the far (20-500 cm^{-1}) and middle (400-4000 cm^{-1}) spectral regions was used to estimate the interfacial interactions and peculiarities of molecular dynamics in the polymer nanoshells. The peculiarities of the glass transition in the PVP nanolayers and melting transition/crystallites in the PEG nanolayers were characterized using DSC method. The obtained calorimetric data were in an accord with the spectral results.

The contributions of strong hydrogen bonding and, tentatively, LB forces to PVP/silica interfacial interactions but only of the enhanced LB ones to PVP/alumina interfaces were revealed, and the distinct impact of interfaces (interfacial interactions) on dynamics was observed. Some suppression of dynamics in chains and "simplifying" their conformational state in nanolayers were shown. All the effects observed were the functions of the nanoshell thickness and the type of substrate. The most pronounced peculiarities were found for the monomolecular PVP and PEG layers when the substrate-polymer interface and "free" polymer surface dominate the film dynamics [277].

Unlike bulky polymer, 1-2 nm thick PVP monomolecular layers were characterized with the dramatically high dynamic heterogeneity within the glass transition extending from 70 to 230^oC, while varying the activation energy from 80 to 560 kJ/mol. Three "abnormal" dynamic modes only constituted this transition including two decelerated, constrained motion modes and ultra-fast one caused by a collapse of intermolecular dynamic cooperativity [53,277].

Despite a high PEG ability to crystallization, total amorphization of PEG monolayer adsorbed on silica surface was observed that was due apparently to local hydrogen bonding of chains with substrate silanols. On the contrary, highly-crystalline PEG monolayer was formed on alumina surface. The single anomalously thin "flat-on" lamellae, of 3-8 nm thick, prevailed in this layer: this value coincided with the shell thickness estimated. As presumed, the latter effect was caused by the quasi-heteroepitaxial crystallization process of PEG on crystalline alumina surface. Such structure of the thinnest PEG layer manifested itself in the characteristic changes of the far-IR spectra [277].

Features of the interactions between water and solutes with silicas (Fig. 190) or macromolecules (such as starch gel, fibrinogen, etc.) and A-300 (Fig. 191) reflected in the dielectric spectra and TSDC thermograms [53,214,245,288]. Enhanced clusterization of water bound to silicas led to diminution of the value of permittivity (Fig. 190a). An increase in the degree of hydration or formation of larger structures in pores of silica gel resulted in increased values of ε'. Treatment in organic solvents for 24 h, drying at 473 K and wetting gave smaller clusters of water than that for initial A-300 or treated in CCl_4 (Fig. 190a). However, if the amount of water bound to treated A-300 was greater that this effect could be masked (Fig. 190b) because of stronger increase in the size of clusters.

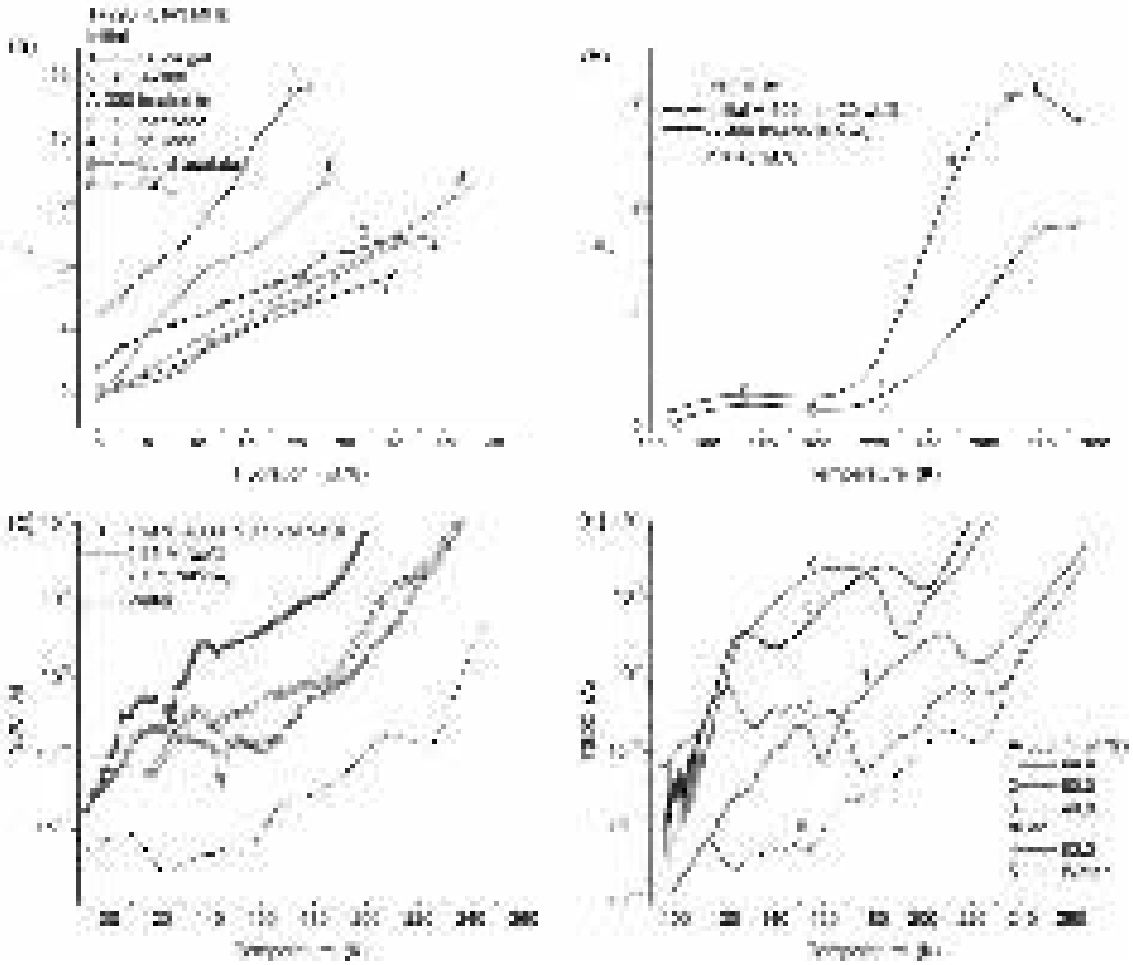

Fig. 190. Relaxational characteristics of water free, pure or with solutes or bound to silicas differently affected: (a) permittivity (at frequency 3 MHz) vs. hydration degree (h) of silicas initial or suspended in organic solvents at 298 K for 24 h, dried at 473 K (24 h) and wetted using a certain amount of water; (b) dielectric loss (at 3 MHz) vs. temperature for A-300 initial (h = 20 wt.%) and pretreated in CCl_4 (h = 40 wt.%). TSDC thermograms (sample thickness ~1 mm, polarization at 300 V) of (c) 1 wt.% suspension of A-300 in solution at 0.15 M NaCl, solutions of NaCl and $NaClO_4$ and pure water (polarized at F_p = 0.1 MV/m); and (d) wetted A-300 initial (h = 66.6 wt.%) and after MCA (6 h) at h = 50 and 40 wt.%, silica gel Si-60 at h = 83.3 wt.% and pure water [53,214].

Even relatively small content of A-300 in the solution of NaCl caused enhanced polarization of various structures because intensity of both dipolar relaxations at 90-190 K and dc relaxation at T > 190 K were greater in the A-300 suspension than that in pure NaCl solution (Fig. 190c). Note that the salinity led to enhanced relaxations in comparison with pure water. Changes in the content of water or MCA treatment of A-300 or changes in the texture of silicas (compare A-300 and Si-60) led to significant changes in the dipolar and dc relaxations of frozen and thawed structures of wetted silicas (Fig. 190d).

A low-temperature (LT) band (T < 170 K) shits toward higher temperatures and its intensity for water/starch/A-300 was smaller than that for water alone or A-300 suspension (Fig. 191a). A high-temperature (HT) band (T > 170 K) shifted toward lower temperatures and its intensity increased. The first effect was due to stronger hydrogen bonding of interfacial water molecules in composite than in starch. The second effect was due to enhancement of plasticizing of starch by water in the presence of A-300 because of transition of adsorbate (starch macromolecules) into nanostate (*i.e.* diminution of supramolecular interactions between macromolecules), and an increase in the amounts of more mobile relaxing dipoles in glycoside structures characterized by greater polarity due to interaction with neighboring water molecules or surface silanols of silica nanoparticles [53,288]. Note that relaxation of dipolar structures could

start at much lower temperatures than the relaxations appeared in the low-temperature ^{1}H NMR spectra and caused by local molecular mobility (Fig. 191b) [23,245].

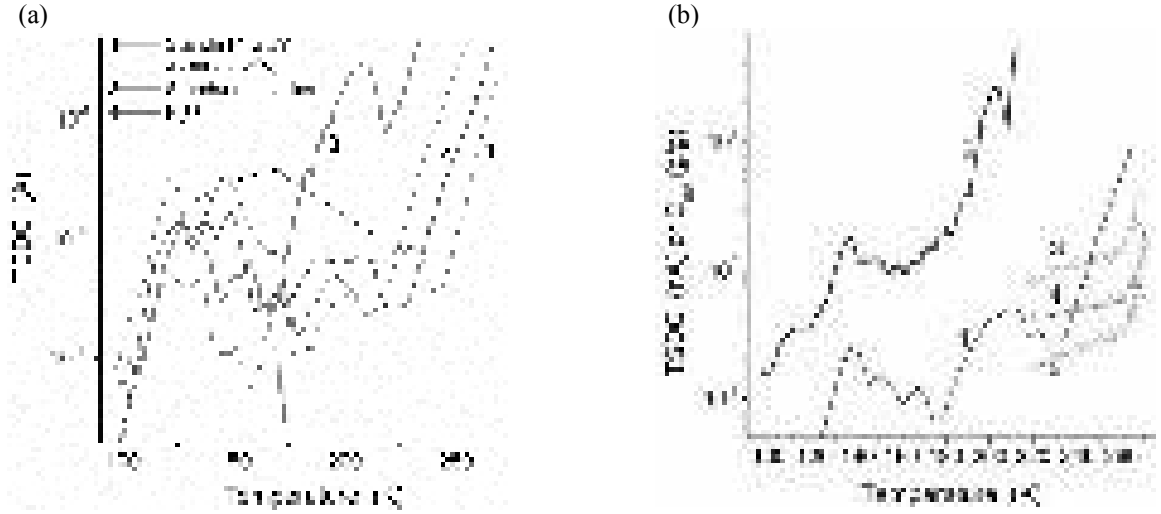

Fig. 191. (a) TSDC thermograms of hydrogel of gelatinized starch (14.2 wt.%) (1), aqueous suspension of A-300 (5 wt.%) (2), gelatinized starch/nanosilica (7.7: 1) at h = 16.9 g/g (3), and water (polarized at F_p = 0.35 MV/m) (4); arrows showed directions of the displacement of LT and HT bands on addition of silica and starch to water. (b) TSDC thermograms (curves 1 and 2) and C_{uw} (NMR, curves 3, 4 and 5) as functions of temperature for A-300 alone (1 and 5), solution of fibrinogen (2.5 wt.% HPF and 0.15 M NaCl, curve 3) and after addition of nanosilica A-300 (3.5 wt.%) (2 and 4).

The behavior of polymers or proteins interacting with FMO in the aqueous media depended on their concentration and salinity and pH of the solution [53,287,289,290]. An increase in concentration of PEG led to diminution of the PEG/A-300 aggregate sizes (Fig. 192a, $SPSD_I$ and $SPSD_V$ and Fig. 192b); however, an increase in the amount of PEG/A-300 in the suspension gives the opposite result (Fig. 192b). The broadest SPSD was observed at minimal content of PEG (Fig. 192a). The main factor determining these regularities was stronger PEG-A-300 interactions than PEG-PEG interactions. Increasing PEG content led to an increase in the number of PEG-PEG contacts which were less effective than PEG-silica ones. At C_{PEG} = 20 wt.% ($\Delta S_{BET}/S_{BET} \approx -0.3$) the amount of the macromolecules was not enough to bond all particles in large aggregates; therefore, the $SPSD_N$ peak shifts toward smaller D values (Fig. 192a). An increase in C_{PEG} led to tendencies: diminution of the sizes of large aggregates ($SPSD_V$ = 100-1000 nm), and increase (C_{PEG} = 40 wt.%) and then diminution (C_{PEG} = 80 and 90 wt.%) of the smallest aggregates sizes ($SPSD_N$ < 100 nm). Notice that the SPSD for PEG/AST samples were not measured because of fast sedimentation of particles [287].

The ζ potential for PEG/A-300 depended weakly on the presence and content of PEG (Fig. 192c). This could be explained by several factors: (i) sizes of aggregates with A-300 [53,287] and PEG/A-300 change in the same range; (ii) PEG macromolecules were uncharged; (iii) the surface charge density of silica nanoparticles was not practically changed on interactions with PEG; and (iv) charge distributions in the electrical double layer (EDL) and the shear plane [238,289,290] were not strongly changed. However, for PEG/AST the ζ potential dependence on C_{PEG} was stronger than that for PEG/A-300 (Fig. 192c). This difference could be explained by stronger interactions of PEG molecules with Brønsted acid sites (SiO(H)Al, SiO(H)Ti, AlO(H)Ti) and an increase in the amounts of PEG per surface square unit for PEG/AST in comparison with PEG/A-300 due to large difference (approximately by order in magnitude) in the S_{BET} values of these oxides [287].

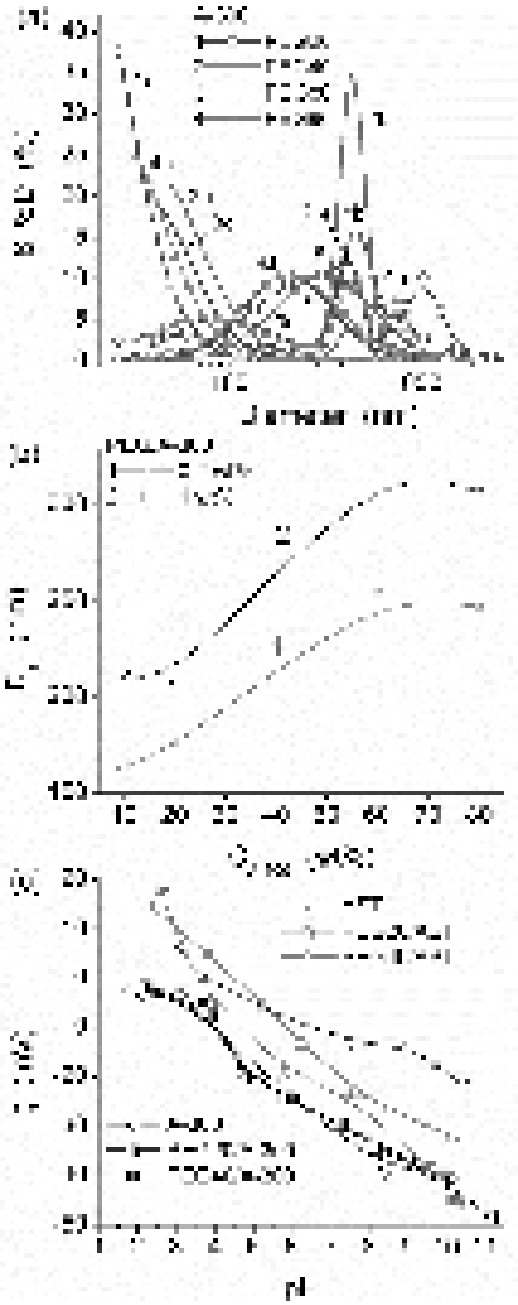

Fig. 192. Characteristics of the aqueous suspensions of PEG-oxides (1 wt.%): (a) particle size distributions for PEG/A-300 with respect to the light scattering ($SPSD_I$, curves 1a-4a), particle volume ($SPSD_V$, 1b-4b) and particle numbers ($SPSD_N$, 1c-4c); (b) effective diameter for PEG/A-300 (0.2 and 1 wt.%); and (c) ζ potential for the diluted suspensions (0.1 and 0.025 wt.% for PEG/A-300 and PEG/AST, respectively) as a function of pH.

In the first DSC scan, glass transition steps were observed only for two samples and no crystallization or melting peaks were observed. In order to delete any previous thermal history of the samples, as usually done in DSC [291-293], the measurements were performed in the second DSC scan. The results presented below (Fig. 193 and Table 35) refer to these second-scan measurements. The temperature dependences of structural changes (melting, crystallization, glass transition) of PEG in the PEG/nanooxide systems change with PEG content (Table 35, Fig. 193). The glass transition temperature (T_g) for PEG (–53 ^oC, Table 35) was in agreement with previous measurements of PEG and PEO at molecular weight ~ 0.1-1 MDa [294-296]. For all PEG/oxide systems, except for PEG20/AST, the T_g value was higher than that for individual PEG (Table 35) [287].

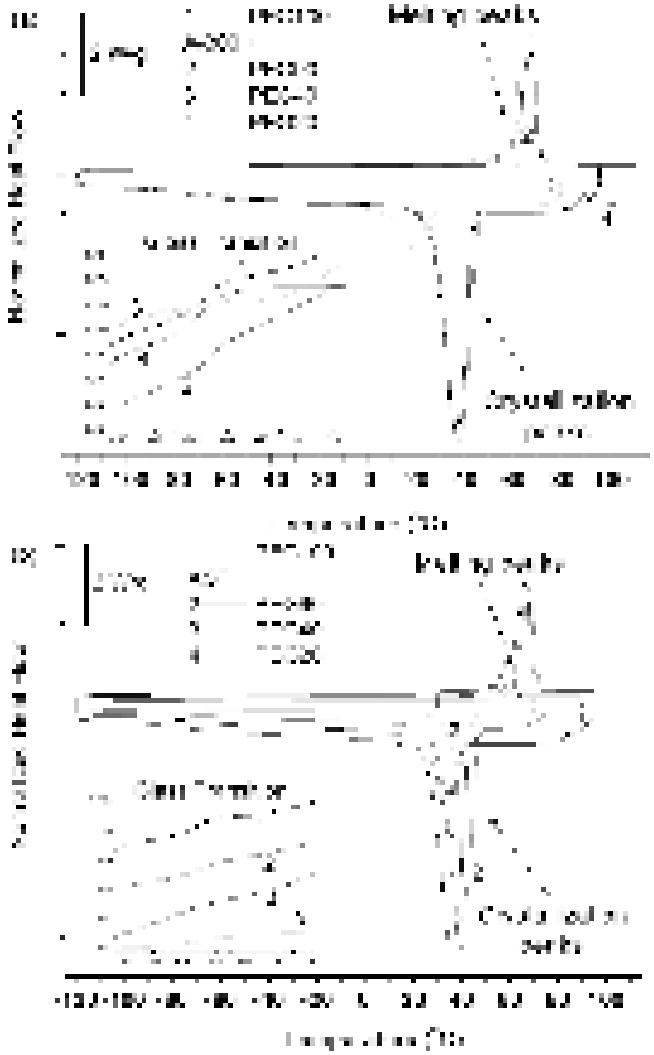

Fig. 193. Results of the second DSC scans for individual PEG (PEG100, curve 1) and (a) PEG-A-300 and (b) PEG-AST at heating rate =10 °C/min and cooling rate = 30 °C/min.

Table 35. Characteristics of PEG/oxide systems from the DSC measurements [287].

Sample	T_g (°C)	T_{cr} (°C)	T_m (°C)	$\Delta c_{p/am}$ (J/g °C)	$\Delta H_{cr/pol}$ (J/g)	$\Delta H_{m/pol}$ (J/g)	X_{cr}	X_{im}	h (wt.%)
PEG	–53	36	67	0.70	157	159	0.81	0	1.8
PEG90/A-300	–49	37	67	0.32	146	142	0.72	0.15	1.0
PEG40/A-300	-	17	54	0	85	90	0.46	0.54	3.2
PEG20/A-300	–46	-	-	0.66	0	0	0	0.06	
PEG90/AST	–46	39	68	0.34	154	151	0.77	0.12	0.3
PEG40/AST	–47	39	64	0.59	143	145	0.74	0.07	0.4
PEG20/AST	–66	35	59	0.52	125	145	0.74	0.07	

Note that the melting enthalpy of the 100% crystalline PEG corresponds to ΔH_0=197 J/g [297].

Somewhat higher T_g differences were between PEG - PEG/AST than PEG - PEG/A-300, due to stronger local interactions between PEG - AST than PEG - A-300 as observed in the FTIR and PCS results [287]. Glass transition was not observed for PEG40/A-300 (signal at T_g was weak, Fig. 193), whereas glass transition was observed for PEG20/A-300 (fully amorphous) with a smaller C_{PEG} value and for all PEG/AST samples. It was well established that in semicrystalline polymers glass transition could not be observed if a fraction of amorphous phase was smaller than a critical value because of the presence of a rigid amorphous phase [298]. However, glass transition was observed for PEG40/AST due to the interactions of a larger fraction of the polymer

with silica than with AST. In general, we may expect an increase in the T_g value due to constraints for PEG due to bonding to the oxide surfaces and a decrease in the T_g value because of an increase in the free volume due to loosened molecular packing of the chains confined in voids between adjacent primary particles [299-302]. It seems that the latter dominates only for PEG20/AST. The lower T_g values at lower polymer content for PEG/AST (Table 35) were reasonable in terms of constrains imposed to packing of the polymeric chains. Notice that in polyimide/silica hybrids glass transition was not observed at C_{pol} < 40 wt.% because of strong polymer-silica interactions [300]. Similar results were reported also for poly(2-hydroxyethyl acrylate)/silica [301] and poly(methyl methacrylate)/silica nanocomposites [302]. Water as an additional factor affected the T_g value, so that for PEG/A-300, where hydration levels (Table 35) were higher than for PEG/AST (Table 35), the T_g values were lower because of stronger plasticization. It should be mentioned that water content (Table 35) was calculated gravimetrically from the masses of hydrated and dried samples, $m_{amb.}$ and m_{dried} respectively, using simple equation [287]

$$h = \frac{m_{amb.} - m_{dried}}{m_{amb.}} (\cdot 100\%) = \frac{m_{water}}{m_{amb.}} (\cdot 100\%) . \quad (30)$$

In addition to the effects on the glass transition temperature discussed above, filler content strongly affected the heat capacity step on the glass transition. The heat capacity step (Table 35) has been normalized to the same amorphous polymer fraction ($\Delta c_{p,am}$). Compared with pure PEG the $\Delta c_{p,am}$ value decreased strongly at low filler contents and increased again on further particle addition (Table 35). Generally, filler addition reduces the polymer mobility, while a thin polymer layer (~nm) close to the nanoparticles (surface, porous) was almost immobilized [299-302]. Despite some uncertainty of the Δc_p calculation. This was a useful tool for estimation of a fraction of immobilized polymer, X_{im}. The latter may be defined as a fraction of amorphous polymer which did not contribute the glass transition [287]

$$X_{im} = (1 - \frac{\Delta c_{p,am}}{\Delta c_{p,am(PEG)}})(1 - X_{cr}) , \quad (31)$$

where $\Delta c_{p,am}$ refers to the nanocomposites

$$\Delta c_{p,am} = \frac{\Delta c_{p,DSC}}{(1 - X_{cr}) C_{PEG}} , \quad (32)$$

$\Delta c_{p,am(PEG)}$ is the corresponding quantity for the neat polymer sample, C_{PEG} is the weight fraction of the polymer in composite, and X_{cr} is the degree of crystallinity calculated through the melting enthalpy, ΔH_{DSC} [287]

$$X_{cr} = \frac{\Delta H_{DSC}}{\Delta H_0 \cdot C_{PEG}} . \quad (33)$$

Between 0.06 and 0.54 (Table 35) X_{im} is a non-monotonous function of C_{PEG}. This differs from polymer nanocomposites with dispersed oxide nanoparticles synthesized by the sol-gel method in the polymer matrix, where an approximately linear increase of X_{im} was observed at low filler content increased [299]. For fumed oxides the opposite behavior was observed. The higher the content of polymer in the systems, the less restricted mobility was observed in general. This phenomenon indicates layer-by-layer polymer shell growth on the oxide surface during material preparation, leading to diminution of both polymer-oxide interactions for subsequent polymer layers and the restriction of the polymer mobility. The PEG immobilization was more intensive for A-300 than AST50 (with smaller S_{BET}). Larger X_{im} values for PEG/silica were due to a larger fraction of PEG being in the interfacial layer at the silica surface (larger S_{BET} value). Nonlinear changes in $X_{im}(C_{PEG})$ (Table 35) could be due to nonlinear changes in particle aggregation, which differs for PEG/A-300 and PEG/AST in addition to the effects of different S_{BET} values [287].

There are FMO effects on crystallization and melting of PEG [287]. It is obvious that at low oxide content the crystallization temperature (T_{cr}) somewhat increased because the oxide particles could act as crystallization nuclei (facilitating crystallization) (Table 35 and Fig. 193).

However, at higher oxide content T_{cr} strongly decreased (crystallization was suppressed) probably due to spatial constrains imposed to the diffusion of polymer chains. The melting temperature T_m was not affected at low oxide contents but decreased at higher contents corresponding to lower quality or smaller polymer crystallites which melt (deform) easier with temperature [303]. Finally, the degree of crystallinity X_{cr} decreased in the nanocomposites (Table 35); *i.e.* oxide nanoparticles reduce the crystallization ability of PEG there. This was in agreement with results obtained for nanocomposites with particles dispersed in a polymeric matrix ($C_{PEG} > C_{ox}$), where, in general, reduction of polymer crystallization was observed with decreasing T_{cr}, T_m, and X_{cr} values with increasing filler content [304]. The effects were stronger for PEG/A-300 (smaller oxide nanoparticles), and no crystallinity was observed in PEG20/A-300. Moreover, a stronger T_m reduction for that series indicates that the quality of PEG crystallites was lower comparing to the PEG/AST series [287].

It should be mentioned that in semicrystalline polymers There was also a fraction of immobilized amorphous polymer at the interfaces with crystallites (*i.e.* rigid amorphous phase) [239]. Measured values depended on combined effects of both constrains caused by nanoparticles and polymer crystallites. Thus the differences in the DSC results were due to the differences in the S_{BET} values (*i.e.* primary particle sizes), relative amounts of PEG per surface area unit (at the same C_{PEG} values), and the numbers of different active surface sites at silica and AST surfaces strongly interacting with the macromolecules (Table 36) [287].

Table 36. Temperature of different relaxations maxima (T_{rel}) [287].

Sample	T_{rel} (°C)					
	β	β´	β_{JG}	A	MWS	CR
PEG	-	-	–57	–42	–27	–7
Dried PEG	–118	–87	–54	–22	1	-
Melted PEG	–115	–77	–60	–36	–20	–7
PEG90/A-300	–127	–92	–57	–39	–27	–3
PEG40/A-300	–124	–91	–76	–58	–48	–34
PEG90/AST	–124	–89	–64	–44	–28	–14
PEG40/AST	–122	–82	-	–43	–36	–18
Dried PEG90/A-300	–123	–85	-	–15	8	-
Dried PEG40/A-300	–107	-	-	–27	–20	-
Dried PEG90/AST	–112	–85	–58	–16	2	-
Dried PEG40/AST	–118	–79	-	–40	–20	–7

The TSDC measurements were performed for both initial composites (containing some amounts of water as they were hydrophilic) and dried samples to clarify the origin of the relaxation processes observed (Figs. 194 and 195) [287]. At temperatures below T_g (*i.e.* in the glassy state, where secondary relaxations were observed) three observed weak peaks (shoulders) could be attributed to the β, β´ and β_{JG} processes discussed below. The main process, α-relaxation (associated to the glass transition), follows as a shoulder on a stronger Maxwell-Wagner-Sillars (MWS) peak, which was related to the interfacial relaxation phenomena. At higher temperatures, the conductivity relaxation (CR) [305] was observed, followed by a strong current uptake, related to ionic dc-conductivity, which was characteristic for hydrophilic systems (Table 36). The γ-relaxation of PEG at about –160°C could not be fully seen in this particular temperature range. The identification and discussion of that and other secondary relaxations will be based on the DRS measurements [287].

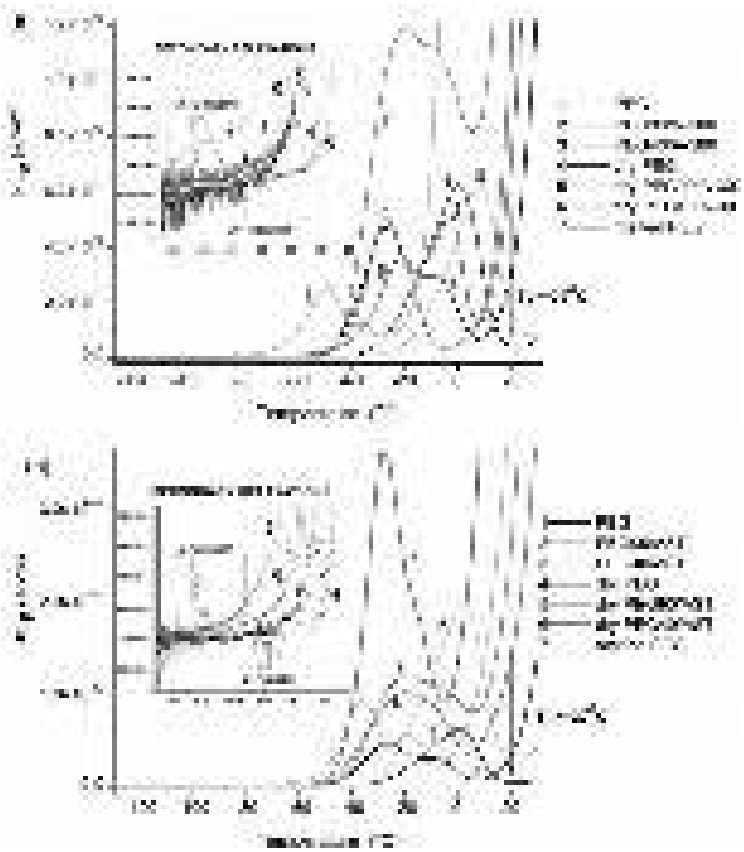

Fig. 194. TSDC thermograms for (a) PEG/A-300 and (b) PEG/AST initial and dried; inserts showed low-temperature ranges related to β-relaxations.

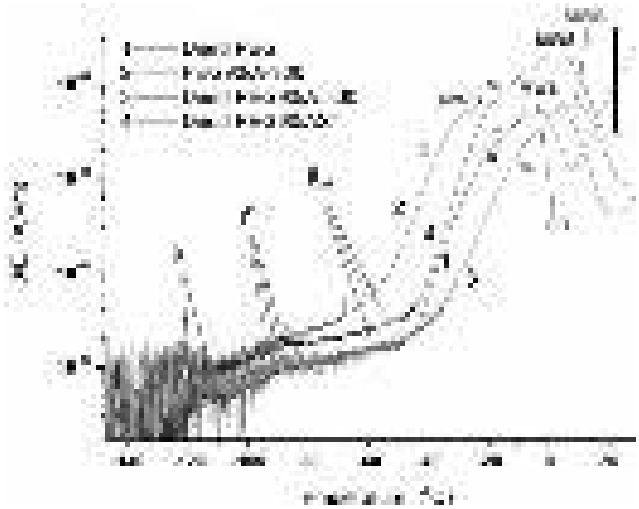

Fig. 195. TSDC thermograms for dried PEG, PEG/A-300 and PEG/AST.

Three relaxation processes at low temperatures (sub-glass relaxations) were characterized by relatively low values of current maxima (Figs. 194 and 195) corresponding to relatively small values of dielectric strength typical for dipolar processes in the glassy state [287]. Additionally, these systems include a small quantity of water (Table 35) which could affect relaxations at low temperatures because of plasticization of the polymer matrix. In particular, the following relaxations were observed: β-relaxation (between −127 and −107°C) affected (plasticized) by water; β′-relaxation (from −92 to −79°C); β_{JG}-relaxation (from −76 to −54°C) (Johari-Goldstein relaxation) (Table 36), which could be observed as a shoulder on the low-temperature side of the α-relaxation peak and located at 15-30 °C lower than the latter (Fig. 195 and Table 36) [287].

The PEG relaxation processes at higher temperatures exhibit higher values of current maxima (by about two orders in magnitude) and dielectric strength indicating significant contribution of charge carrier motion [287,306-309]. The α-relaxation (from −58 to −42°C) was

associated with the glass transition of PEG plasticized by water (Table 36). A small displacement of the α-relaxation toward higher temperatures was observed in PEG90/A-300 with respect to pure PEG, and a larger displacement but toward lower temperatures was observed for samples at 40 wt.% PEG, especially for PEG40/A-300 (Fig. 194). This led to the corresponding displacement of the distribution function of activation energy of depolarization (Fig. 196). This effect was more clearly observed for dried samples (Fig. 192). The results could be explained by two opposite effects: constrains due to PEG-oxide interactions and an increase in free volume in more loosely packed macromolecules in voids between adjacent primary oxide particles. Both effects increased with increasing C_{PEG} value. Relatively small amounts of bound water were in composites (Table 35); nevertheless, it caused essential plasticization effect resulting in the displacement of the TSDC response toward lower temperatures in comparison with dry samples. This displacement was larger for PEG/A-300 than PEG/AST because of higher water content in PEG/A-300 samples (Table 35) [287].

The MWS relaxation (from –48 to +2°C) (Table 36), typically located by 8-20 °C higher than the α-relaxation, was associated with interfacial polarization and space charges [287]. This relaxation could be also assigned to the α_{cr}-relaxation associated with the glass transition of some parts of polymers strongly restricted between condensed crystalline regions, and observed for PEG and PEO. However, this suggestion comes in contradiction with the high strength and the shape of the relaxation. Judging from the fact that the dielectric strength of the relaxation has a clear dependence on the degree of crystallinity, the most probable explanation of its origin could be based on release of charges trapped during the polarization step at the interfaces between crystalline and amorphous regions. It was affected by water and oxide nanoparticles similar to the α-relaxation. The CR relaxation observed at higher temperatures following the main relaxation by 15-20 °C higher refers to changes in conductivity related to dc (direct current in isothermal measurements at low effective frequencies) and ac (alternating current at higher frequencies). This relaxation was not observed for some samples that could be explained by deplasticization (water drying) of the main dielectric relaxation and the fixed polarization temperature (20°C). It was affiliated to space charges (conductivity effects), and also observed for PEO. Compared with the results of the DSC measurements, the T_α and T_{MWS} values showed similar trends to the T_g value (Table 28), providing further support that in the high polymer content samples polymer-filler interactions dominate over free volume effects, whereas the contrary was true for the low polymer content samples. We come back to these relaxations later in relation to the DRS data. It should be mentioned that the two peaks which follow the α-relaxation at higher temperatures (MWS and CR peaks, respectively) could be also MWS relaxation indicating the variety in phase separation surfaces (polymer-filler, amorphous-crystalline polymer, *etc.*) [287].

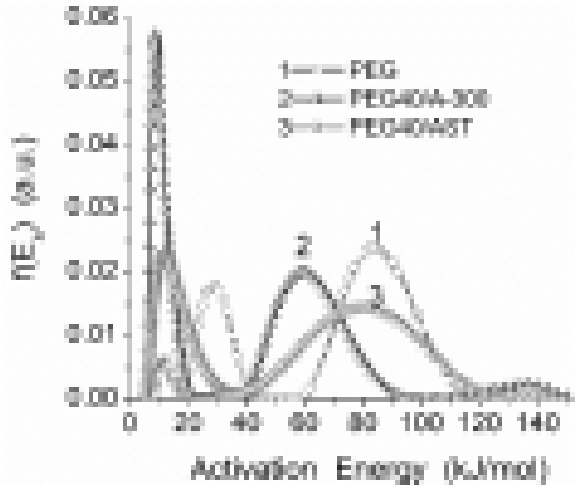

Fig. 196. Distribution functions of activation energy of dipolar relaxations for individual PEG and PEG (40 wt.%) - oxide systems (calculated from the TSDC data).

Typical DRS spectra (dielectric loss against frequency at different temperatures) were presented in Fig. 197. At low temperatures the secondary γ and β relaxations were well observed. As temperature increased, the response gets dominated by the segmental dynamics, space charge polarization/relaxation and conductivity effects, giving rise to high values of ε′′ and ε′ (Fig. 198), orders of magnitude higher than at low temperatures. A main DRS peak was well observed for all samples at higher temperatures (~30 °C) (Fig. 198). Judging from the TSDC and the DRS isochronal (constant frequency) plots [287], this peak was probably composed from more than one relaxations (at least MWS and CR).

An overall increase in the response was observed for nanocomposites with both oxides in comparison with individual PEG; however, There was no systematic variation with composition, but only in combination with the dehydration of the samples, which decreased the response and the γ-relaxation was better resolved for the dry samples (Fig. 197c,d). The response value increased for series pure PEG < 90 wt.% < 40 wt.% PEG in the region of the γ-relaxation [287].

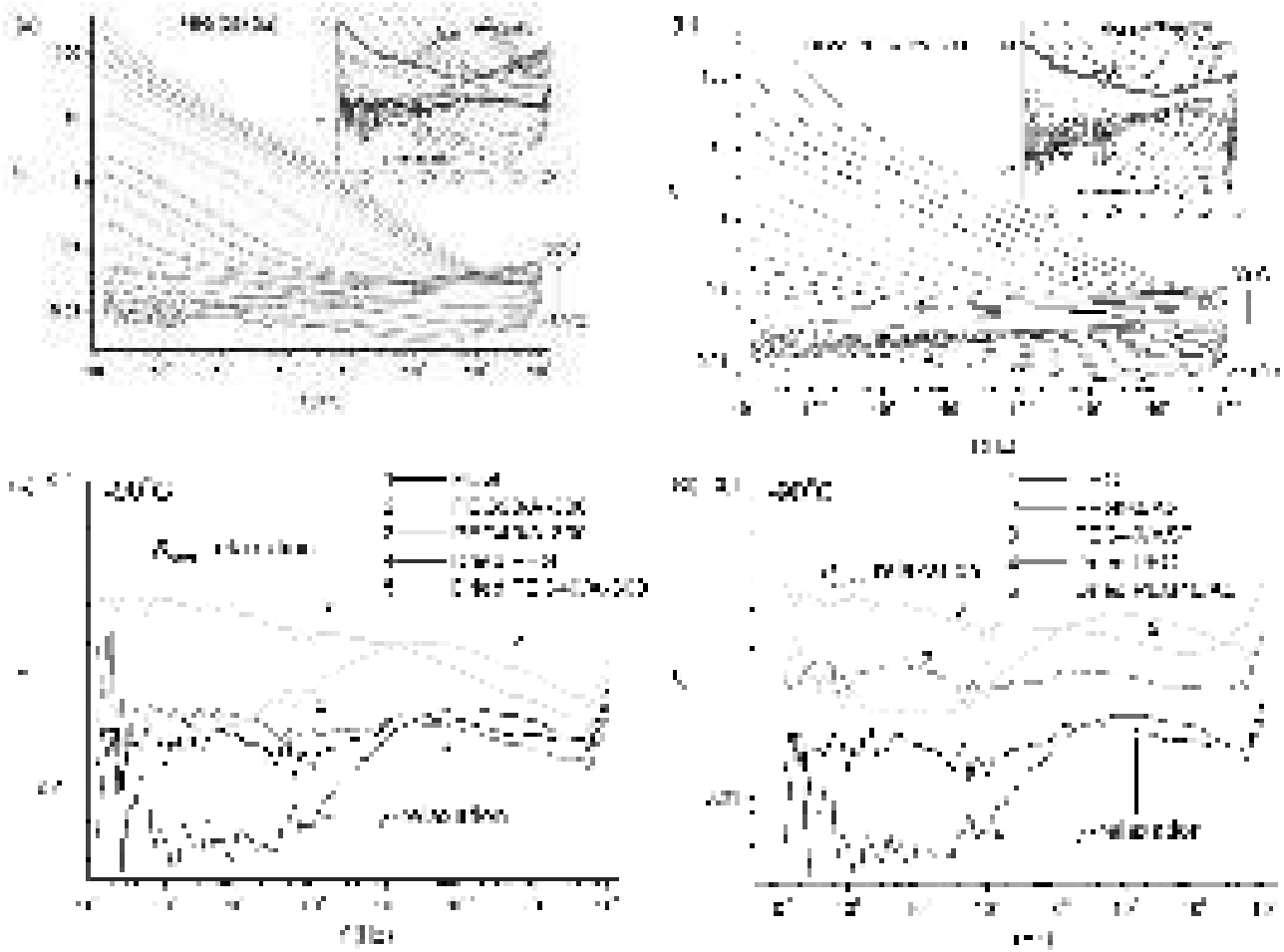

Fig. 197. DRS for (a) PEG and (b) dried PEG/A-300 at C_{PEG} = 40 wt.% over the range between –150 and +30 °C. Secondary relaxations at –90 °C for (c) PEG/A-300 and (d) PEG/AST.

The resolving power of the dielectric techniques gets higher as frequency decreased. That was the reason why in the TSDC measurements (10^{-4}–10^{-2} Hz) the α, MWS, and CR relaxations were better resolved in comparison with DRS, where one broad relaxation was observed. The data for PEG were included that was melted between the plates of the capacitor (melted PEG). We may expect better resolution in that case because of the better contact of the sample with the electrodes and a smaller sample thickness (~50 μm) [287].

Based on the isothermal (Fig. 197) and the isochronal plots and by recording the frequency and temperature maxima, respectively, for all the relaxations observed, the Arrhenius plots were constructed (Figs. 199 and 200) [287]. The TSDC data (peak temperatures) at the equivalent

frequency of 1.6 mHz corresponding to a relaxation time of ~100 s and the DSC data (T_g) at the equivalent frequency of 10 mHz have been included in the plots to facilitate comparison of the results obtained using three techniques. The Arrhenius equation

$$f_{\max} = f_0 \exp\left(-\frac{E_a}{kT}\right) \tag{34}$$

was well fitted to the data for the secondary relaxations and the activation energy (E_a) values were determined.

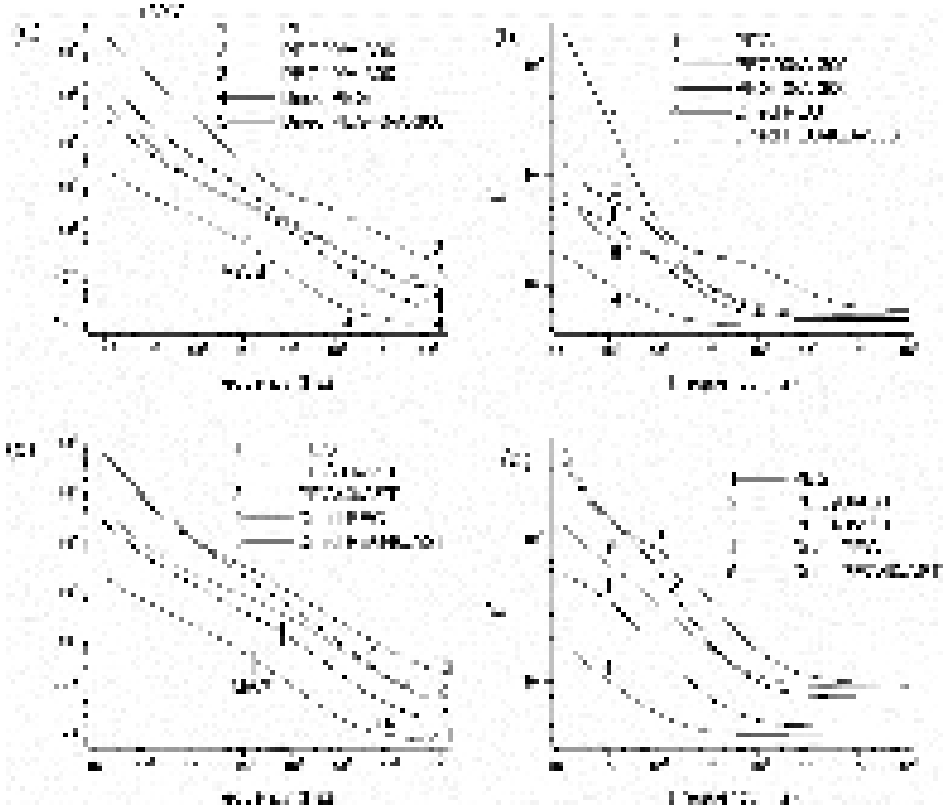

Fig. 198. The dielectric loss ε'' (a, c) and permittivity ε' (b, d) as a function of frequency at 30 °C for individual PEG (initial and dried), PEG/A-300 (a, b) and PEG/AST (c, d) at C_{PEG} = 90 and 40 wt.%.

The γ-relaxation was followed only by DRS since extrapolation to low frequencies showed that the corresponding TSDC peak (~ −160 °C) was out of the temperature range of the TSDC measurements. The activation energy of the γ-relaxation for individual PEG was equal to 38 kJ/mol which was in agreement with the literature data. This relaxation was attributed to 'crankshaft motions' of methylene sequences [287].

The situation was more complex with the β-relaxation, *e.g.*, for individual PEG two strained lines could be found in the Arrhenius plot (trends (1) and (2) in Fig. 199) [287]. A change in slope was observed at about −45 °C for pure PEG to higher activation energy from E_a = 63 to 146 kJ/mol. This behavior may suggest that the relaxation was of the Goldstein-Johari type [310,311], and for this sample the change in slope occurred close to T_g determined with DSC and TSDC. However, the single behavior was observed for several composites (Fig. 200) with straight lines (by Arrhenius equation). For PEG40/AST a similar behavior was observed at low activation energy (56 kJ/mol). Close activation energy (60-63 kJ/mol) was observed for initial PEG90/oxide and PEG40/AST samples. High activation energy (183 kJ/mol) was observed for dried PEG40/AST sample which was higher than that for dried PEG40/A-300 (95 kJ/mol). Trend (1) (Figs. 199 and 200) for β_{DRS} relaxation observed for initial samples (hydration 0.3-3.2 wt.%) was alike to a water relaxation [53,214], on mixtures of ethylene glycol oligomers and PEG600 with 35 wt.% of water. The activation energies of the trends (1), (3) and (4) were close. The observed horizontal displacement was possibly related to the larger amounts of respective groups (water

molecules). Notice that the activation energies calculated from the DRS data and shown above were in the same range as the E_a values based on the TSDC measurements (Fig. 199) because the mechanisms of the relaxations observed here by both methods were linked to the mobility of polar structures in PEG and bound water molecules in composites [287].

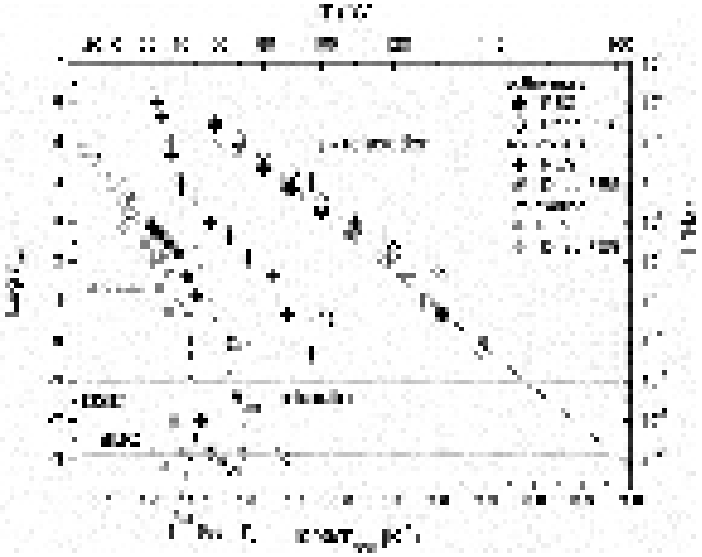

Fig 199. Comparative Arrhenius plots for pure PEG: points from isothermal and isochronal plots; and respective TSDC and DSC (1st and 2nd scans) data were added.

At higher temperatures (mainly at $T > -20$ °C, Figs. 197-200) a broad relaxation could be identified as a superposition of the α-relaxation, MWS and CR by comparing with each other results for ε′, tanδ, ε′′ and TSD current. The dielectric T_g value was estimated as temperature, where ε′′ values start to increase significantly, by almost one order of magnitude, at the lowest frequency. This procedure provided the data for the α-relaxation included in the Arrhenius plots. Figs. 172 and 173 showed the VTF behavior of the α-relaxation and plasticization by water. As a whole the overall complex trends of the β-relaxations in relation to the Johari-Goldstein relaxation and the 'α-β' temperature range were of interest and need additional investigations [287].

It should be stressed that within this work the glass transition temperature values were recorded for the various compositions by using three different methods, DSC, TSDC and DRS [53,214,245,287]. The results by these three techniques showed in general the same trends with changes in PEG/oxide composition and close T_g values for the systems with similar thermal treatments and equivalent frequencies.

In the aqueous media PEG macromolecules form stronger hydrogen bonds with surface hydroxyls of oxide nanoparticles (silica, alumina/silica/titania) than with macromolecules or water molecules that result in the formation of hydride aggregates (50-1000 nm in size) with well distributed PEG molecules and allow to form relatively uniform composites on drying of the systems [53,287]. The weakly hydrated (0.3-3 wt.% of water) PEG (20-90 wt.%)/oxide powders were characterized by full coverage of nanoparticles by macromolecules. Therefore, relaxational characteristics of individual PEG and PEG in composites differ and depended on polymer content, temperature and treatments (*e.g.*, drying or melting). Addition of nanoparticles suppresses hydrophilicity, crystallinity and mobility of the amorphous polymer fraction, the effects becoming in general stronger with increasing filler fraction. However, some of the characteristics do not demonstrate a linear dependence on the C_{PEG} value because changes in the interfacial layer structure, confined effects, number of nanoparticles interacting with a macromolecule (which was several times longer than the size of nanoparticles, especially for A-300 at 8 nm in diameter) with C_{PEG} value. Drying and melting of PEG in the PEG/oxide systems, despite low amounts of residual water ($h \leq 3.2$ wt.%), results in significant inhibition of polymer motion and the activation energy of the β_{DRS}-relaxation increased in 1.5-3 times. Consequently, appropriate changes in hydration of hydrophilic PEG/nanooxide composites allow one to strongly change their characteristics even at

the same content of polymer. The influence of the nanooxides on the thermal transitions and the dielectric relaxation mechanisms was stronger for silica than AST, although the local interaction between polymer and AST was found to be stronger. Combining with the fact that silica particles were much smaller, the overall conclusion was that the polymer was better distributed for silica rather than AST [287].

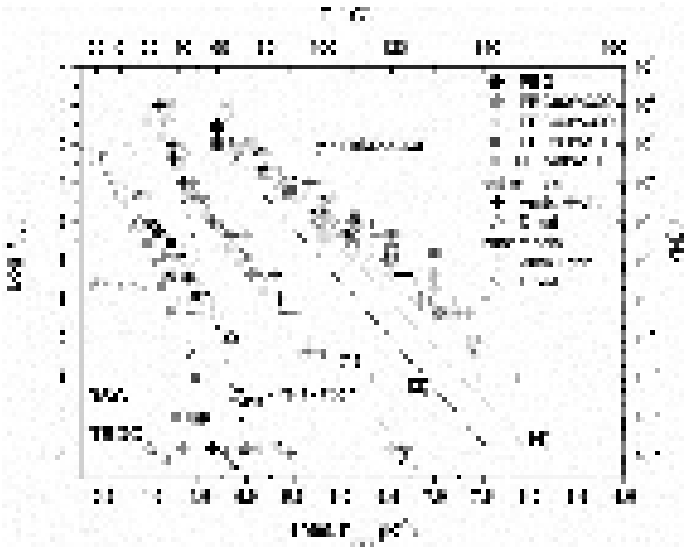

Fig. 200. Comparative Arrhenius plots for PEG and PEG/oxide composites: points from isothermal and isochronal plots; respective TSDC and DSC (1st and 2nd scans) data were added. Two relaxation lines were also added for mixture of ethylene glycol oligomers and PEG600 with 35 wt.% of water (trends (3) and (4) respectively).

The interfacial behavior of water located in narrow pores [312-315] could affect interactions of macromolecules with FMO [39,40,53,69,107,174-183,214,230,248, 268,271,280, 287, 288,290, 316-322] and other materials [103,216,217,245,323-326]. These effects appear as changes in the relaxation characteristics of adsorbates. During controlled preparation of nanomaterials [327] and filled polymeric composites [328] these effects should be considered, as well as in the cases of catalytically active FMO such as titania [329-331] or to control the toxicity of nanomaterials [332]. Note that many of aspects of the interfacial and temperature behaviors of various adsorbates bound to FMO were analyzed in several monographs [53,333,334] and recent research papers [335-368]. It should be noted several additional aspects in changes in the characteristics and properties of FMO due to hydrocompaction [369-372].

Hydrocompartion, surface modification and confined space effects

SEM (Fig. 201a,b) and TEM (Fig. 201c,d) images of initial (a, c) and hydro-compacted (b, d) nanosilicas (Table 38) demonstrates that the particulate morphology does not practically change with respect to primary NPNP [369].

The secondary structures (NPNP aggregates), as well ternary structures with agglomerates, become denser after hydro-compaction of nanosilica [369].

The differential pore size distribution functions $f(r)$ based on the small-angle X-ray scattering (SAXS) data were calculated using Fredholm integral equation of the first kind for scattering intensity $I(q)$ [373]

$$I(q) = C \int_{r_{\min}}^{r_{\max}} \frac{\left(\sin qr - qr\cos qr\right)^2}{(qr)^2} V(r) f(r) dr \,, \tag{35}$$

where C is a constant, $q = 4\pi\sin(\theta)/\lambda$ the scattering vector value, 2θ is the scattering angle, λ is the wavelength of incident X-ray, $V(r)$ is the volume of a pore with radius r (proportional to r^3), and $f(r)\mathrm{d}r$ represents the probability of having pores with radius r to $r + dr$. The values of $r_{\min}$ (= $\pi/q_{\max}$) and $r_{\max}$ (= $\pi/q_{\min}$) correspond to lower and upper limits of the resolvable real space due to instrument resolution. This equation was solved using the CONTIN algorithm [195]. The $f(r)$

function could be converted into incremental PSD (IPSD) $\Phi(r_i) = (f(r_{i+1}) + f_V(r_i))(r_{i+1} - r_i)/2$ for better view of the PSD at larger r values.

Table 38. Textural characteristics of unmodified and hydro-compacted A-300 (SCV/SCR method)

Sample	h_{cp} (g/g)	S_{BET} (m^2/g)	V_p (cm^3/g)	$<R_V>$ (nm)	$<R_S>$ (nm)	S_{nano} (m^2/g)	S_{meso} (m^2/g)	S_{macro} (m^2/g)	V_{nano} (cm^3/g)	V_{meso} (cm^3/g)	V_{macro} (cm^3/g)
A-300	0	294	0.850	21.13	6.22	45	233	17	0.023	0.560	0.266
cA-300	0.5	305	0.918	34.62	6.86	57	224	24	0.027	0.388	0.503
cA-300	1.0	303	1.109	31.49	8.10	52	219	32	0.025	0.484	0.600
cA-300	1.5	228	1.116	41.98	11.25	34	156	39	0.017	0.297	0.802
cA-300	2.0	227	1.447	26.90	13.79	23	164	40	0.012	0.819	0.616
cA-300	2.5	232	1.540	23.25	13.12	31	163	38	0.018	0.977	0.545
cA-300	3.0	228	1.492	19.82	12.14	34	163	31	0.020	1.082	0.389
cA-300	4.5	234	1.488	18.13	11.00	47	167	21	0.027	1.177	0.284
cA-300	5.0	231	1.515	21.64	12.34	41	157	34	0.023	1.024	0.468

Note. The values of V_{nano} and S_{nano} were calculated by integration of the $f_V(R)$ and $f_S(R)$ functions, respectively, at 0.35 nm < R < 1 nm, V_{meso} and S_{meso} at 1 nm < R < 25 nm, and V_{macro} and S_{macro} at 25 nm < R < 100 nm. The values of $<R_V>$ and $<R_S>$ as the average pore radii were calculated as a ratio of the first moment of $f_V(R)$ or $f_S(R)$ to the zero moment (integration over the 0.35-100 nm range) $<R> = \int f(R)RdR/\int f(R)dR$.

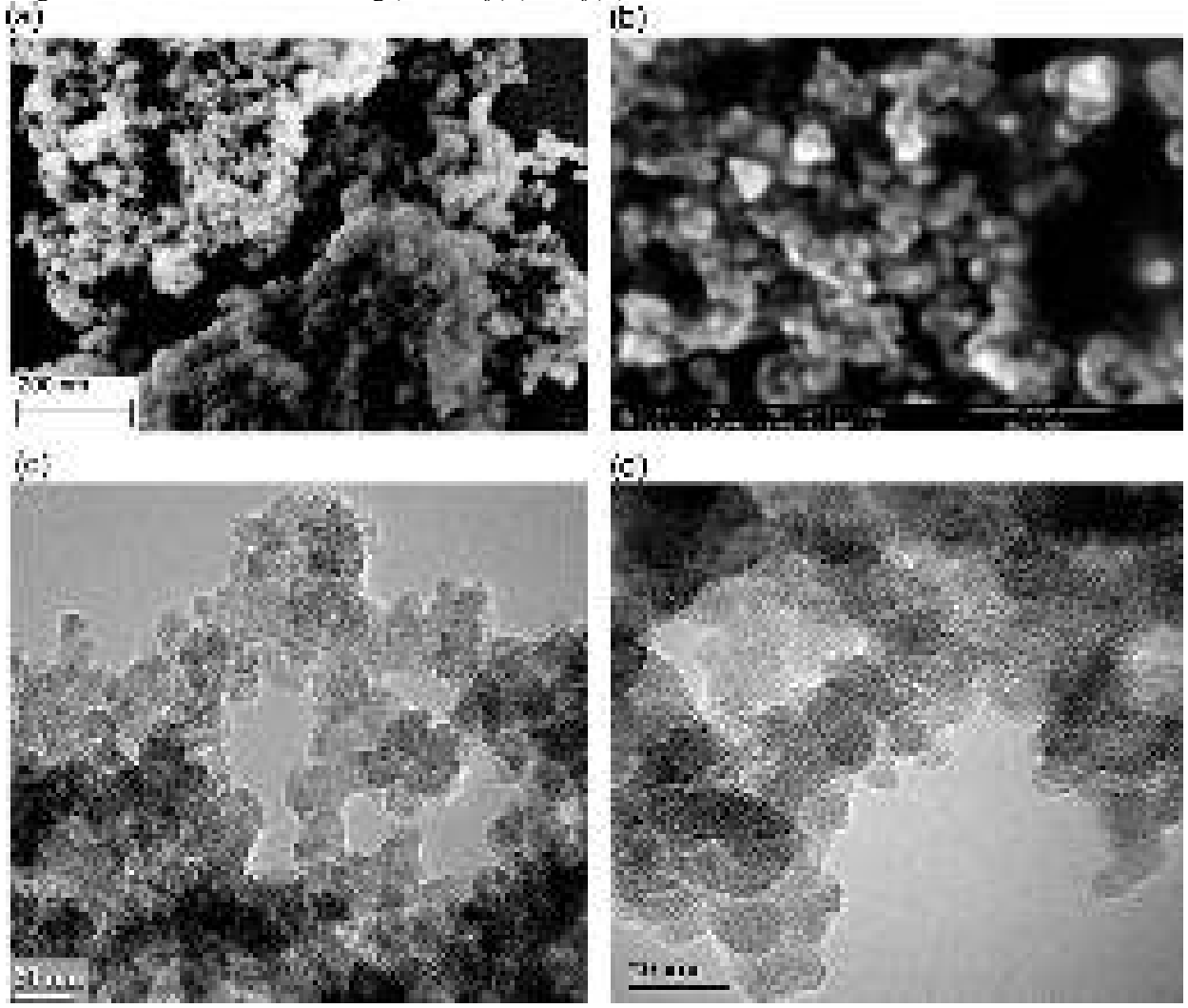

Fig. 201. (a, b) SEM and (c, d) TEM images of A-300 (a, c) initial and hydro-compacted at water content h_{cp} = (b) 3 g/g and (d) 4 g/g (scale bars are (a) 200 nm, (b) 100 nm, and (c, d) 20 nm).

To calculate the particle size distribution (PaSD) functions, several models of particles (e.g. spherical, cylindrical, lamellar ones and various blends of them) could be used. For spherical particles, integral equation similar to Eq. (35) could be written as follows

$$I(q) = C \int_{R_{min}}^{R_{max}} P(q,R) f(R) dR \,, \tag{36}$$

where C is a constant, R is the radius of particles, $f(R)$ is the distribution function (differential PaSD), and $P(R)$ is the form factor for spherical particles [374] (the kernel of the integral equation S7): $P(q,R) = (4\pi R^3/3)^2[\Phi(q)]^2$ and $\Phi(q,R) = (3/(qR)^3)[\sin(qR) - qR\cos(qR)]$.

The PaSD with respect to the volume of particles (as abundance in vol%) could be calculated as follows

$$\text{abundance(vol\%)} = R^3 f(R) / \int R^3 f(R) dR \,. \tag{37}$$

For cylindrical particles, there are two variable parameters, such as the radius (R) and length (H) of cylinders

$$I(q) = C \int_{H_{min}}^{H_{max}} \int_{R_{min}}^{R_{max}} f(H) f(R) P(q,H,R) dH dR \,, \tag{38}$$

where $P(q,H,R) = CV \int_0^{\pi/2} \frac{2J_1(qR\sin\theta)}{qR\sin\theta} \frac{\sin(0.5qH\cos\theta)}{0.5qH\cos\theta} \sin\theta d\theta$, $J_1(x)$ is the first-order Bessel function, $V = \pi R^2 H$ is the cylinder volume, and C is a constant [374].

For lamellar particles [374]

$$I(q) = C \int_{L_{min}}^{L_{max}} P(q,L) f(L) dL \,, \tag{39}$$

where $P(q,L) = (L/q)^2 \left[\frac{\sin(qL/2)}{(qL/2)} \right]^2$, L is the lamellar thickness, and the prefactor ($1/q^2$) is the so-called Lorentz factor required to randomize the orientation of the lamellar particle [374]. In the case of complex systems, several models with various blends of spherical, cylindrical and lamellar particles could be used with certain weight coefficients.

For a complex model of particles, the integral equation includes three terms

$$\begin{aligned} I(q) = {} & c_{sph} \int_{R_{min}}^{R_{max}} \left(\frac{4\pi R^3}{3} \right)^2 \left[\frac{3}{(qR)^3} (\sin(qR) - qr\cos(qR)) \right]^2 f(R) dR + \\ & + c_{lam} \int_{L_{min}}^{L_{max}} (L/q)^2 \left[\frac{\sin(qL/2)}{(qL/2)} \right]^2 f(L) dL + \\ & + c_{cyl} \int_{H_{min}}^{H_{max}} f(H) \int_{R_{min}}^{R_{max}} \frac{\pi R^2}{H} f(R) \int_0^{\pi/2} \sin\theta \frac{2J_1(qR\sin\theta)}{qR\sin\theta} \frac{\sin(0.5qH\cos\theta)}{0.5qH\cos\theta} d\theta dR dH \end{aligned} \tag{40}$$

where $I(q)$ is the X-ray scattering intensity, $q = 4\pi\sin(\theta)/\lambda$ is the scattering vector value, 2θ is the scattering angle, λ is the wavelength of incident X-ray, R is the radius of particles, H and R are the length and radius of cylinders, L is the lamellar thickness, $f(R)$, $f(L)$, and $f(H)$ are the distribution functions, $J_1(x)$ is the first-order Bessel function, c_x are the weight coefficients calculated, as well $f(x)$ functions, using a self-consistent regularization procedure. Equation (40) could be solved using a self-consistent regularization procedure [86].

The chord size distribution, $G(r)$ as a geometrical statistic description of a multiphase medium, was calculated from the SAXS data [375,376]

$$G(r) = C \int_0^{\infty} \left[K - q^4 I(q) \right] \frac{d^2}{dr^2} \left(-4 \frac{\sin qr}{qr} \right) dq \,, \tag{41}$$

where K is the Porod constant (corresponding to scattering intensity $I(q) \sim Kq^{-4}$ in the Porod range).

The specific surface area from the SAXS data was calculated (in m^2/g) using equation

$$S_{\mathrm{SAXS}} = 10^4 \pi\phi(1-\phi)\frac{K}{Q\rho_a}, \tag{42}$$

where $\phi = \rho_a/\rho_0$ is the solid fraction of adsorbent, and Q is the invariant

$$Q = \int_0^\infty q^2 I(q)dq\,. \tag{43}$$

The Q value is sensitive to the range used on integration of Eq. (43) (since experimental q values are measured between the $q_{\min}$ and $q_{\max}$ values different from 0 and ∞). Therefore, the invariant value Q was calculated using equation [377]

$$Q = \sum_{q_{\min}}^{q_{\max}} (I(q_i) - b)q_i^2 \Delta q_i + K / q_{\max} \tag{44}$$

where b is a constant determined using equation

$$I(q)q^4 = K + bq^4 \tag{45}$$

valid in the Porod range.

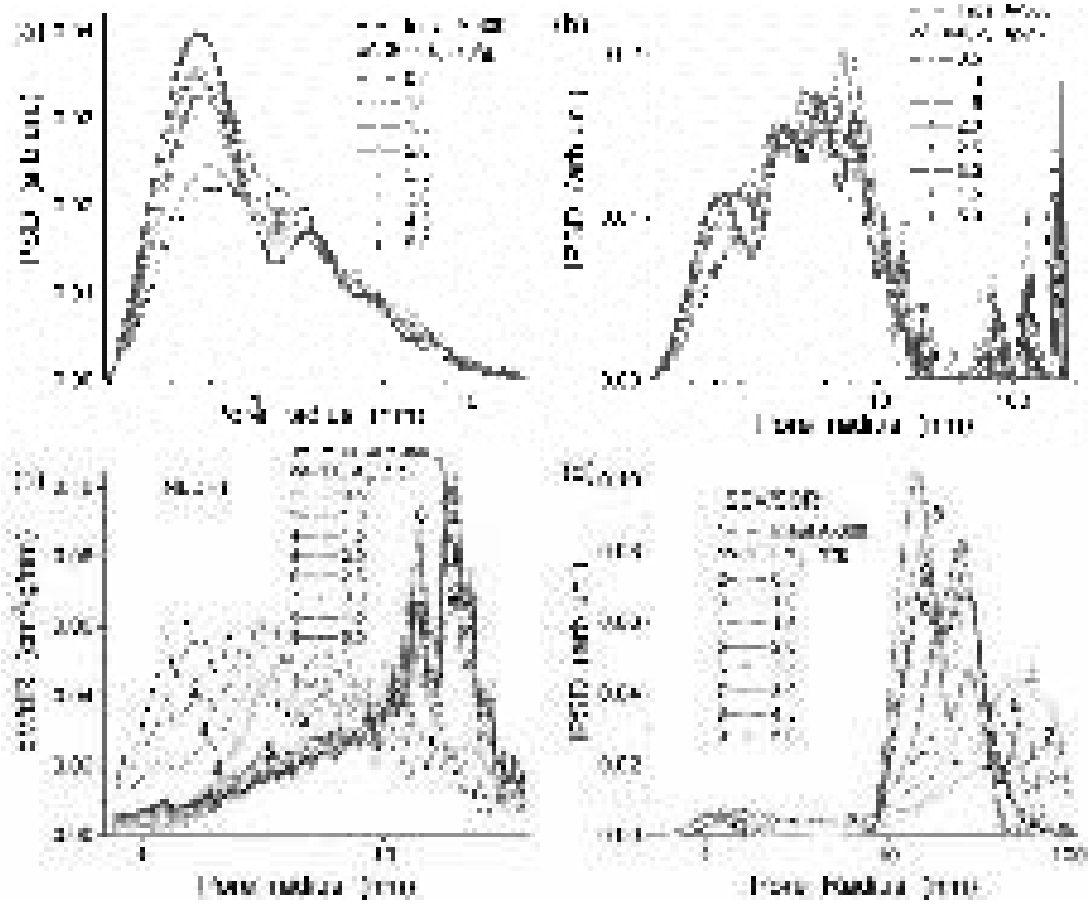

Fig. 202. Pore size distributions (a, c) differential (PSD) and (b, d) incremental (IPSD) calculated using (a, b) SAXS and (c, d) nitrogen adsorption-desorption isotherms with (c) NLDFT (dV/dR) and (d) SCV/SCR (IPSD) methods for initial and hydro-compacted A-300 samples prepared at different content of water (h_{cp} = 0.5 – 5.0 g/g).

The analyses of the SAXS and nitrogen adsorption-desorption isotherms (Table 38, Figs. 202 and 203) are in agreement with microscopic images. However, there are some additional factors, which should be considered upon the analysis of the textural characteristics of nanosilicas. First, the empty volume in the nanosilica powder ($V_{\mathrm{em}} = 1/\rho_b - 1/\rho_0$, where ρ_b and ρ_0 are the bulk and true densities of samples) is much greater than the V_p value of adsorbed nitrogen even at p/p_0 = 0.999. For example, V_{em} = 21.8 cm^3/g for initial A-300 at ρ_b = 0.045 g/cm^3, but the value of V_p is much smaller (Table 38). This underestimation of the value of V_p calculated from the nitrogen

adsorption is due to very weak influence of the pore walls (nanoparticle surface) on the nitrogen molecules located in macropores far from the solid surface in loose silica agglomerates. After hydro-compaction of A-300, the difference between the values of V_{em} and V_p strongly decreases, *e.g.* V_{em} = 3.45 cm^3/g and V_p = 1.49 cm^3/g for cA-300 treated at h_{cp} = 4.5 g/g. Therefore, the various PSD (Fig. 2) describe only a part of voids between NPNP in secondary/ternary structures, and these parts differ for PSD based on the data of the SAXS, NLDFT, and SCV/SCR methods due to features of these methods.

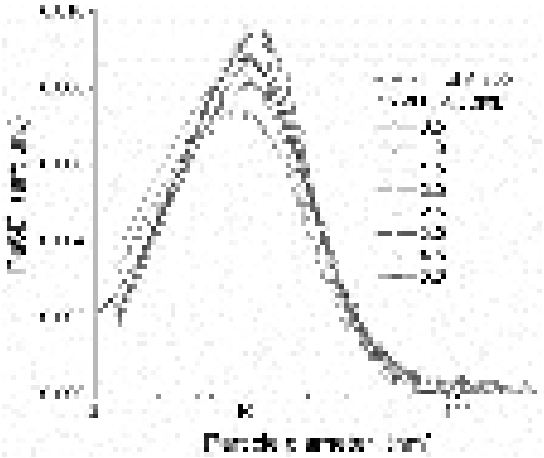

Fig. 203. Particle size distributions (PaSD) for initial and hydro-compacted nanosilica calculated using the SAXS patterns analyzed as described in ESM file.

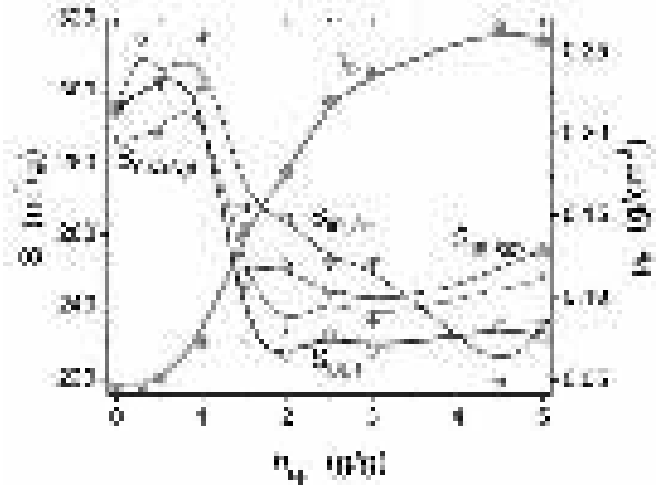

Fig. 204. The specific surface area estimated from nitrogen adsorption (S_{BET}), SAXS data for maximum of PaSD at d_m ($S_{SAXS,d}$ = 6/($d_m\rho_0$), where ρ_0 = 2.2 g/cm^3 is the true density of fumed silica), IR spectra from integral intensity of surface TO modes (Si-O) at 1200 cm^{-1} ($S_{IR,SiO}$), and a ratio of the integral intensity of bands of silanols at 3745 cm^{-1} and Si-O overtone at 1870-1860 cm^{-1} ($S_{IR,OH}$) and bulk density (ρ_b) *vs*. the water amount used on silica compaction.

According to SAXS PSD and IPSD (Fig. 202a,b), contributions of nanopores at radius R < 1 nm increases with increasing h_{cp} value. However, contribution of narrow mesopores at 1 nm < R < 10 nm decreases upon nanosilica compaction. Note that SAXS can give information on pores inaccessible for nitrogen molecules. Therefore, contribution of narrow nanopores in the SAXS PSD is much greater than that in the NLDFT PSD (Fig. 202c) or SCV/SCR IPSD (Fig. 202d). However, the tendency in a decrease in contribution of narrow mesopores with increasing h value is similar to that in the SAXS PSD. Both NLDFT PSD and SCV/SCR IPSD demonstrate an increased contribution of broad mesopores at 10 nm < R < 25 nm with increasing h_{cp} value. A more complex picture is observed for the SAXS PSD in the range of broad mesopores, as well for macropores at R > 25 nm, *vs*. the h_{cp} value. The SCV/SCR method shows that the maximal contribution of macropores (Table 38, V_{macro}, S_{macro}) is observed in a middle range of h_{cp} = 1-2 g/g

with a maximum of the SCV/SCR IPSD for macropores at h_{cp} = 1.5 g/g. Sample cA-300 at h_{cp} =1.5 g/g corresponds to the first sample with the water amount greater than V_p and this sample is the first one with partially collapsed secondary structure since a significant decrease in the value of S_{BET} (Table 38, Fig. 204) is observed. However, the value of ρ_b is middle at h_{cp} = 1.5 g/g and it continue grows with increasing h_{cp} to 4.5 g/g [369].

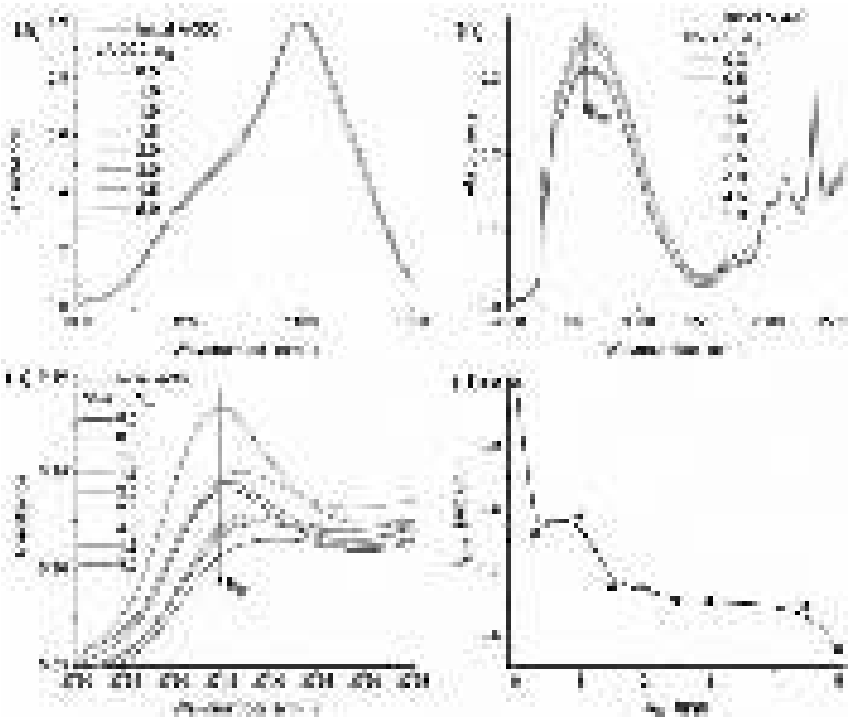

Fig. 205. IR spectra of nanosilicas in the range of (a) the Si-O stretching vibrations, (b) 4000-1350 cm^{-1}, and (c, d) the SiO-H stretching vibrations depending on the amount of water used upon silica compaction.

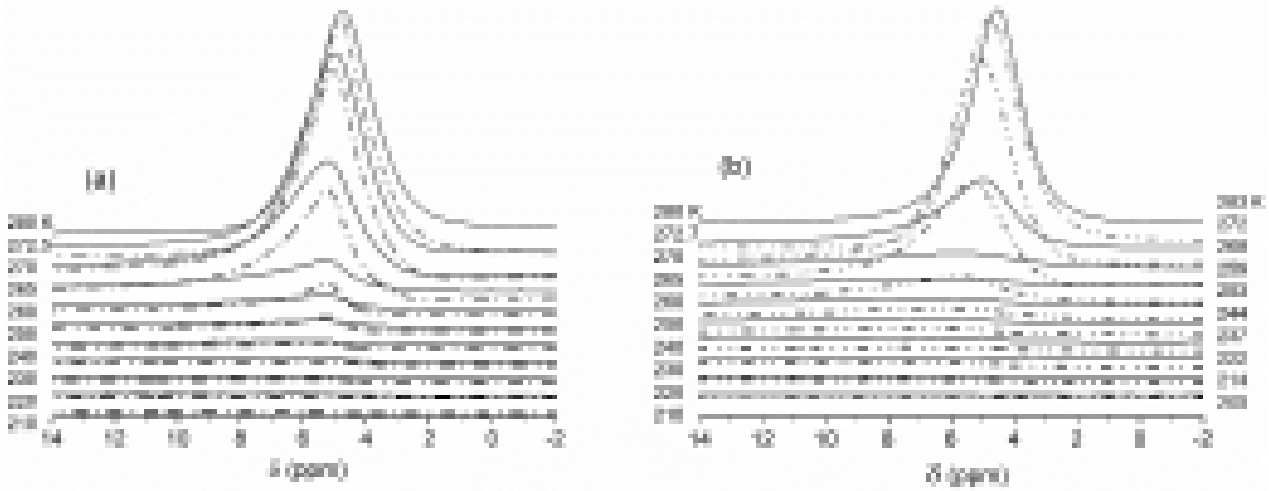

Fig. 206. ^{1}H NMR spectra (recorded at different temperatures upon heating from minimal one used) of water (1.1 g/g) adsorbed on a surface of nanosilica A-300 (a) initial (dot-dashed lines) and hydro-compacted at h_{cp} = (a) 1.5 g/g (solid lines) and (b) 2.0 g/g (dot-dot-dashed lines) and 3.0 g/g (solid lines).

The estimations of the specific surface area (Fig. 204) using a peak value in the SAXS PaSD (Fig. 203) or the use of the IR spectra (Fig. 205) confirm that the value of h_{cp} = 1.5 g/g is critical for reorganization of the NPNP in secondary and ternary structures. Note that the estimation of the specific surface area gives S_{SAXS} = 332 and 251 m^2/g for initial A-300 and cA-300 treated at h_{cp} = 5 g/g, respectively. The S_{SAXS} values are larger than $S_{SAXS,d}$ or S_{BET} because the former corresponds to total surface area, a part of which is inaccessible for N_2 molecules, and upon calculation of the $S_{SAXS,d}$ value, only the peak PaSD value (Fig. 203) is used. Certain structural

changes in cA-300 are already observed at lower h_{cp} values (Fig. 205c,d), even at h_{cp} = 0.3 g/g. It is possible that these changes at small h_{cp} values (0.3-0.5 g/g) are due to complex treatment with wetting-stirring-aging-drying. These textural changes features can be explained by the clustered adsorption of water, *i.e.* it can be located in contact zones between adjacent NPNP. In this case, the amount of water at h_{cp} = 0.3 g/g is greater than contribution of nanopores (Table 38, V_{nano}). Therefore, it can stimulate reorganization of contacts between neighboring NPNP in their aggregates. This reorganization leads to an increase in the accessibility of the NPNP surface for nitrogen molecules and the S_{BET} value increases at h_{cp} = 0.5 and 1.0 g/g (Table 38), but this effect is stronger at h_{cp} =0.5 g/g [369].

Additional information on the reorganization of NPNP in secondary/ternary structures of the cA-300 samples in comparison with A-300 could be obtained using low-temperature ^{1}H NMR spectroscopy and NMR cryoporometry. The ^{1}H NMR spectra of water (h = 1.1 g/g) bound to A-300 and cA-300 (Fig. 6) demonstrate single, slightly asymmetrical signal at the chemical shift of proton resonance $\delta_H \approx 5$ ppm close to that of liquid bulk water. Intensity of this signal decreases with decreasing temperature due to freezing of a part of bound water. A fraction of water frozen at $T < 260$ K can be attributed to strongly bound water (SBW) (Fig. 207). Water frozen at 260 K < T < 273 K is weakly bound water (WBW). The amounts of unfrozen water (C_{uw}) *vs*. T (Fig. 207a) could be used to estimate the size distribution of pores filled by unfrozen water (Fig. 208) using the Gibbs-Thomson relation for the freezing/melting point depression of water (or other liquids confined in pores) depending on the pore sizes. These distributions could be used to estimate a part of pores (in different size ranges) containing unfrozen water (Table 39).

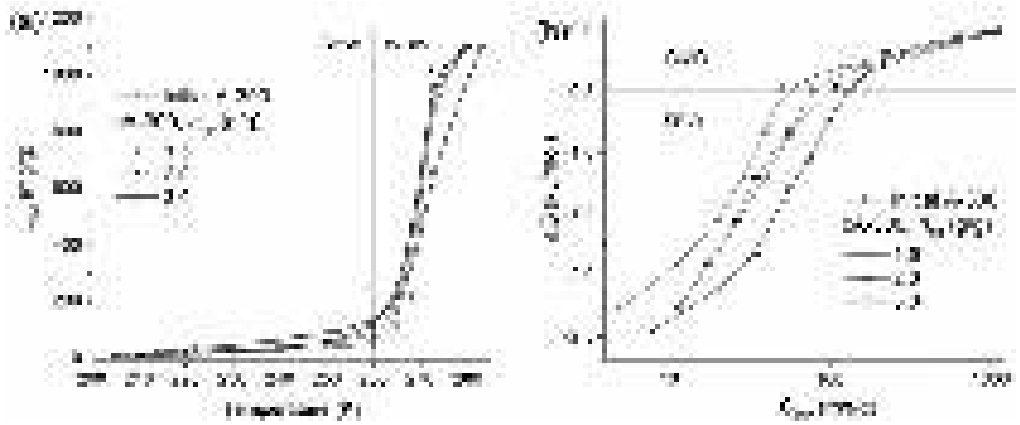

Fig. 207. (a) Temperature dependences of the content of unfrozen water (C_{uw}) estimated from integral intensity of the ^{1}H NMR spectra recorded at different temperatures, and (b) changes in the Gibbs free energy ΔG *vs*. C_{uw} (for A-300 and cA-300 samples with constant hydration upon NMR measurements h = 1.1 g/g).

The amount of adsorbed water in samples studied using the ^{1}H NMR spectroscopy was constant at h = 1.1 g/g that is smaller than V_p of cA-300 but it is greater than V_p of A-300 and close to the critical value of water strongly affecting the reorganization of NPNP in the secondary/ternary structures (Table 38). The amount of SBW increases with increasing h_{cp} (Table 39, C_{uw}^s); therefore, the average melting temperature $\langle T_m \rangle$ decreases. There is a tendency in increasing of the values of $-\Delta G_s$ (related to SBW) and γ_S (related to all bound water) with h_{cp} (Table 39). This is due to an increase in contribution of nanopores (Table 39, $S_{nano,uw}$, $V_{nano,uw}$) filled by unfrozen water with increasing h_{cp} used on the silica compaction treatment [369].

Table 39. Characteristics of water bound to unmodified and hydro-compacted A-300 (h = 1.1 g/g)

Sample	h_{cp} (g/g)	C_{uw}^{s} (mg/g)	C_{uw}^{w} (mg/g)	$-\Delta G_s$ (kJ/mol)	γ_S (J/g)	γ_S (mJ/m^2)	$<T_m>$ (K)	$S_{nano,uw}$ (m^2/g)	$S_{meso,uw}$ (m^2/g)	$S_{macro,uw}$ (m^2/g)	$V_{nano,uw}$ (cm^3/g)	$V_{meso,uw}$ (cm^3/g)	$V_{macro,uw}$ (cm^3/g)
A-300	0	50	1050	2.58	11.55	114.5	266.1	32	63	6	0.014	0.790	0.085
cA-300	1.5	75	1025	2.74	14.17	115.5	264.8	48	68	6	0.020	0.796	0.084
cA-300	2.0	110	1090	2.88	15.39	121.2	264.4	48	71	8	0.020	0.819	0.105
cA-300	3.0	170	1030	2.66	14.10	102.6	261.9	82	53	2	0.035	0.578	0.030

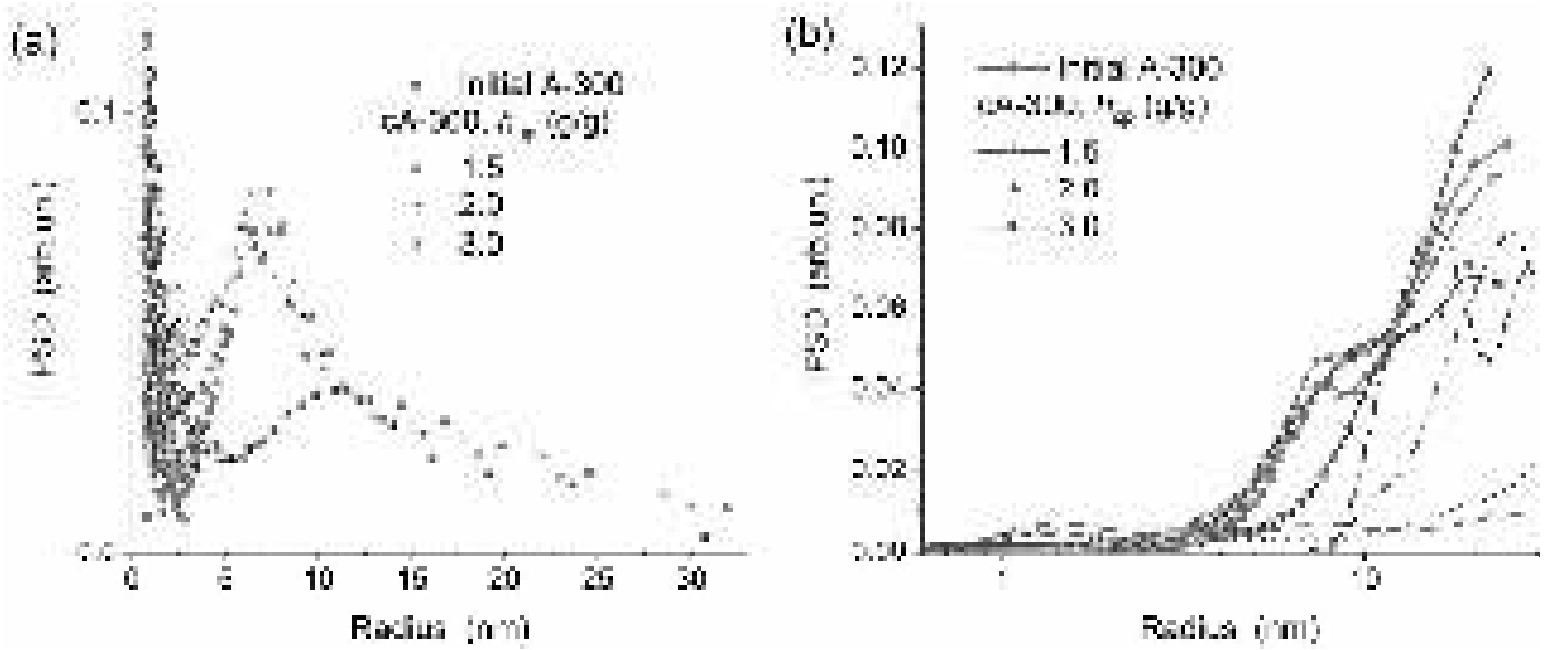

Fig. 208. Size distributions of unfrozen water structures filling voids between NPNP (a) differential (PSD) and (b) incremental (IPSD) calculated using NMR cryoporometry method (at constant h = 1.1 g/g) applied to initial A-300 and cA-300 at different h_{cp} values.

This is matching with TEM images (Fig. 209) of A-300 and related modified fumed silicas with no strong compaction of the secondary structures (note that stronger compaction results in greater ρ_b values).

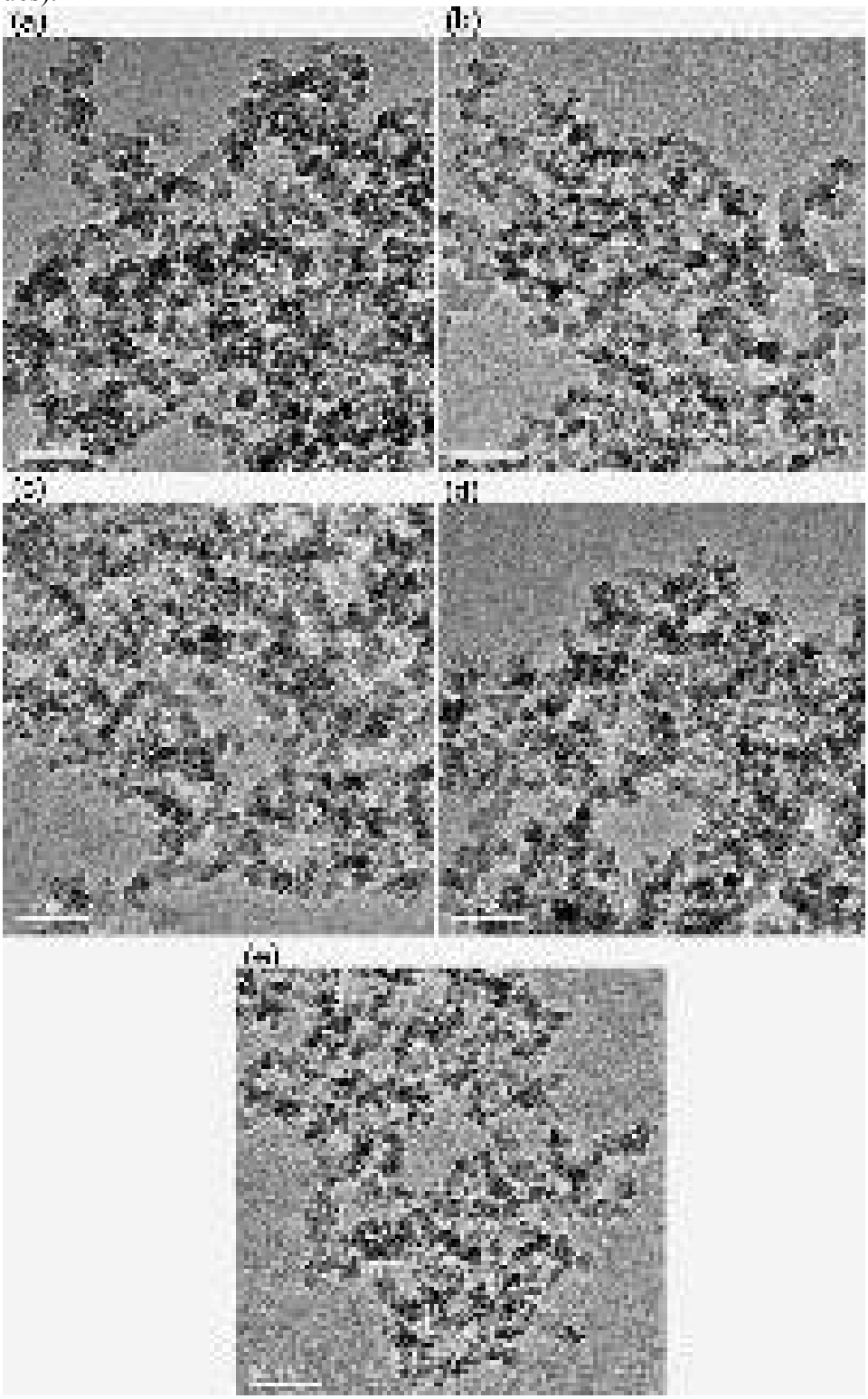

Fig. 209. TEM images of A-300 (a) unmodified and (b-e) modified (b) AP1, (c) AP2D, (d) AP4D, and (e) AP5D (scale bar 50 nm).

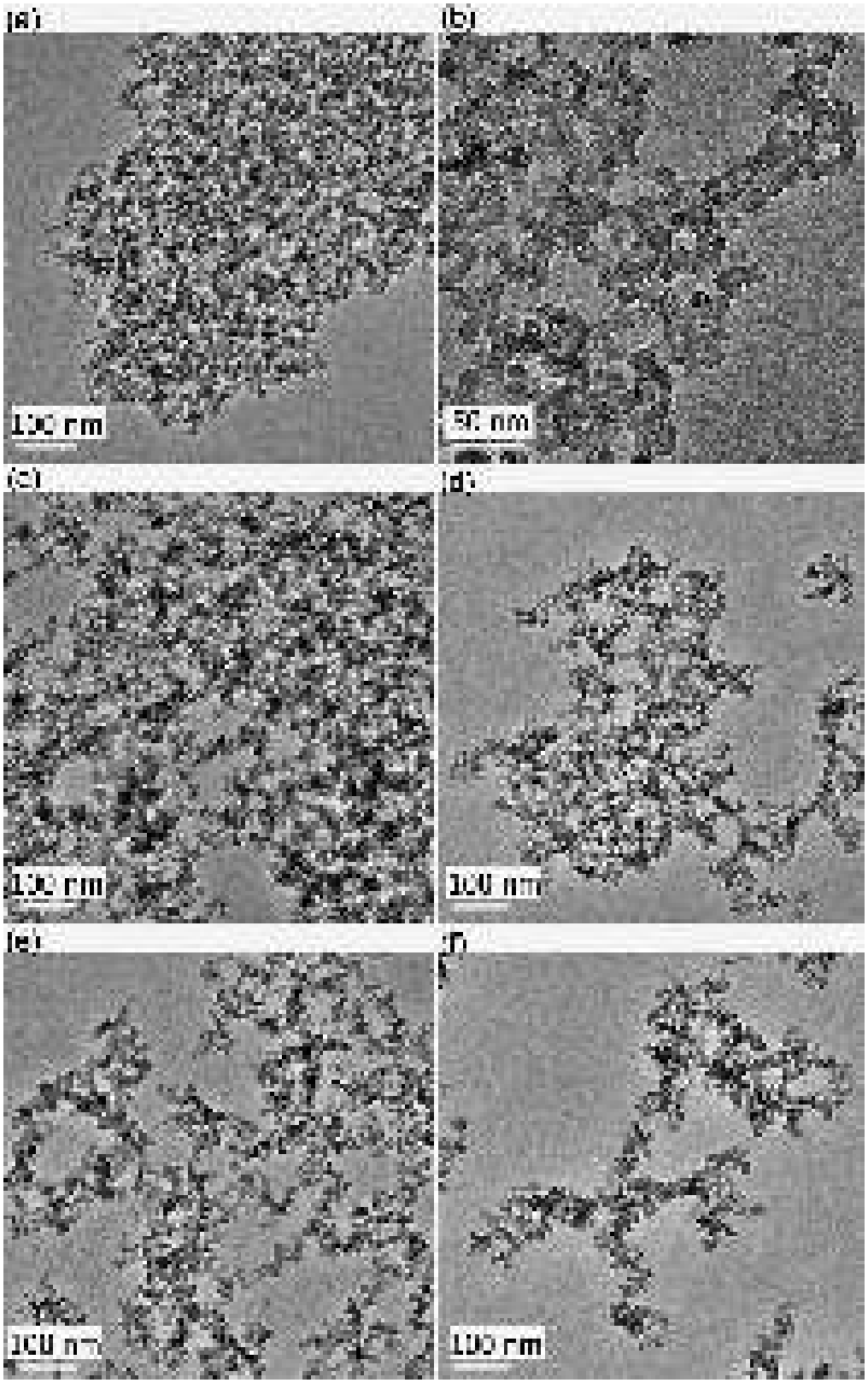

Fig. 210. TEM images of (a) cA-300, (b) cAP3D, (c) A300, (d) AEP1, (e) AEP2D, and (f) AEP4D.

For other silicas, the modification does not result in great changes in the compaction of the secondary structures (Fig. 210), despite a certain increase in the *r* values (Table 40). These results are of importance for the application of these composites as fillers for various nonpolar media (e.g.

polymers), since strong compaction of ANPNP can lead to a worsened and nonuniform distribution of filler particles in the polymer matrices. This can lead to impairment of the mechanical and other characteristics of the final materials. Note that the secondary structures of Syloid 244 (precipitated silica) look like more strongly compacted than for other silicas such as cA-300 or TS 100 undergoing compaction treatments at low and high temperatures. However, Syloid 244 has a maximal S_{BET} value and a minimal r value (Table 40) among the silicas studied. Therefore, the contents of attached hydrophobic functionalities (Table 40, C_C+C_H) for samples SP3D and cAP3D are similar. It is worth mentioning that nanopores (voids between adjacent NPNP in ANPNP at R < 1 nm in pore radius) are practically absent (Table 40, V_{nano}, S_{nano}, Fig. 212) in the unmodified and modified silicas. This is of importance for effective silica modification as nanopores are poorly accessible for relatively large PMDS molecules or their fragments [345].

The values of $<R_V>$ > 25 nm and V_{macro} > V_{meso} (Table 40), as well the PSD (Fig. 212, PSD maxima at R > 25 nm), suggest that the organization of ANPNP corresponds to meso/macroporous materials rather than to mesoporous ones. This could be of importance for SiO_2 surface modification by the polymer fragments (formed as a result of interactions with DMC), since the surfaces of NPNP are better accessible in broad mesopores and macropores than in narrow mesopores or nanopores (voids between NPNP in ANPNP), while for TS 100 and Syloid 244, V_{macro} < V_{meso}, but $<R_V>$ > 25 nm. Thus, both these compacted silicas are characterized by significant macroporosity [345].

The modification of NAS by short PDMS (PMS5 at an average degree of polymerization of *ca*. 11); long PDMS (but with DMC addition used to cleave the Si-O bonds in PDMS); or HMDS typically leads to reduction of the values of V_p and S_{BET} (Table 40); and an increase in the average radius (r) of nanoparticles. However, changes in the values of the textural characteristics of mesopores and macropores are different for modified A-300 (A and AE series) and other silicas (cA, T, and S series) due to the differences in the PSD of the unmodified silicas reflecting the organization of ANPNP. However, changes in the NPNP *per se* after additional treatment of nanosilicas (*e.g.* hydro-compaction A-300 → cA-300 and A-300(AE) → TS 100) are not significant. For example, SAXS analysis of the particle size distributions (PaSD) for A-300 and cA-300 shows similar curves with the same position for the PaSD maximum (Fig. 211), which shifts toward larger values due to cA-300 functionalization (cAP3D). This is in agreement with the changes in the r values (Table 40) computed from the nitrogen adsorption isotherms. It should be noted that hydro-compaction (cA-300) or PDMS/DMC modification (cAP3D) of A-300 results in a diminishing ANPNP contribution (Fig. 211, r > 10 nm), in comparison to unmodified A-300. In other words, both processes cause a certain amount of decomposition of ANPNP (see *e.g.* Fig. 210a,b) [345].

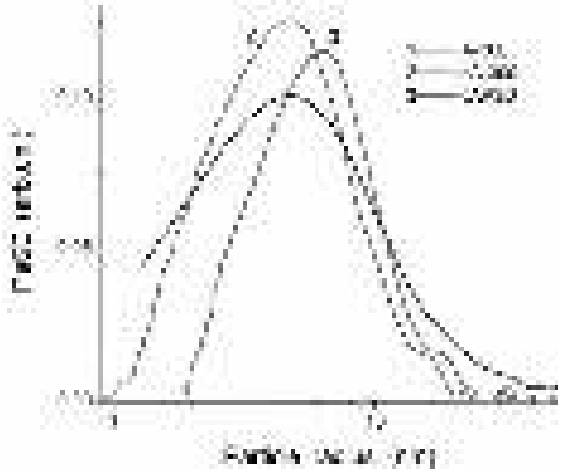

Fig. 211. Nanoparticle size distributions (SAXS data treated assuming that particles are spherical) for unmodified A-300, hydro-compacted cA-300, and cA-300 modified by P3D.

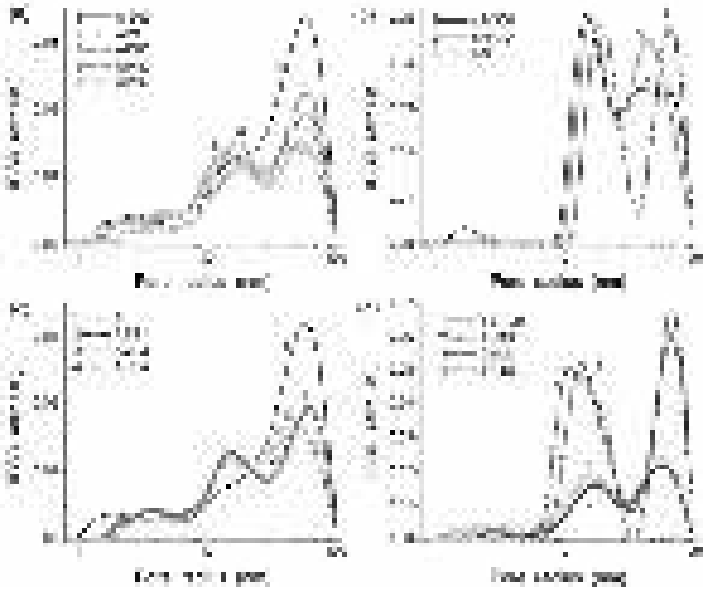

Fig. 212. Incremental pore size distribution calculated using the nitrogen ads-des isotherms treated with the DFT method (with a model of voids between spherical NPNP in silica) for (a) A-300 unmodified and modified, (b) cA-300 unmodified and modified, (c) A300 (AE) unmodified and modified, (d) TS 100 and Syloid 244 unmodified and modified samples.

The difference in the organization of secondary structures ANPNP causes certain changes in the characteristics of silicas (Figs. 209-215), e.g. in the adsorption of water from air (Fig. 215, a broad IR band at 3500-3250 cm^{-1}). Adsorbed water partially remains after pre-heating. This effect depends also on the structure of the silica surface hydroxyl layer. This appears in variations in intensity of ^{1}H MAS and ^{29}Si CP/MAS (Q_3 – SiOH, Q_2 – $Si(OH)_2$) NMR spectra of unmodified silicas (Figs. 213 and 214), and also in the values of zeta potential (Table 40, ζ), which becomes less negative due to surface hydrophobization upon substitution of silanols, responsible for the surface charging *vs*. pH, e.g. negative charging at pH > pH at point of zero charge, by nonpolar functionalities. For example, samples A-300 (hydrophilic) and A-300/PMS5 (hydrophobic) are characterized by the ζ potential of –4.2 mV and –0.9 mV, respectively. However, there is no a linear dependence of the ζ potential on the C_C value as a certain measure of the hydrophobicity of modified surfaces (see Table 40) due to the structural features of a modifier layer depending on a type of PDMS and reaction conditions, as well structural features of silicas studied [345].

Thus, features in the organization of NPNP in ANPNP (Figs. 209-211) and changes in the porosity and specific surface area in the ranges of mesopores and macropores (Table 40, Fig. 212), as well changes in the concentrations of surface silanols (single ≡SiOH and twin $=Si(OH)_2$) can affect the hydrophobization of NAS by various silicones [345]. This appears first in the different content of the attached hydrophobic functionalities (Table 40, C_C and C_H). Second, the length of PDMS plays a very important role in the degree of hydrophobization (Table 40). As a whole, the effects of PDMS length on the degree of hydrophobization can be explained by several factors such as: (i) longer molecules are characterized by lower molecular mobility due to stronger molecule-molecule or molecule-nanoparticle interactions (the η value increases for a polymer alone); (ii) penetration of longer molecules into narrower pores is stronger restricted because longer linear molecules tend to form clews; (iii) longer molecules generate greater steric barriers for interaction of DMC with a silica surface and neighboring PDMS; (iv) surface-attached longer PDMS fragments produce greater negative effects (umbrella screening) on the possibility of other fragments becoming attached to neighboring active surface sites.

The barriers generated by longer PDMS molecules or their fragments are well seen in the incomplete substitution of surface silanols (the θ values decreased by 14-50% in comparison to the reaction of silica with short PMS5 or HMDS) [345]. In addition, these factors result in a diminution of intensity of the D_2 ($Si(CH_3)_2$) line in the ^{29}Si CP/MAS NMR spectra, and also the incomplete disappearance of the Q_2 ($Si(OH)_2$) line at −91 ppm (Fig. 213) or ^1H MAS NMR at δ_H = 4-5 ppm (related to silanols and bound water) (Fig. 214). For AP1 and AEP1, the intensity of the D_2 line is maximal and the Q_2 line at −91 ppm is not observed (Fig. 213), as well the line of silanols/water at δ_H = 4-5 ppm (Fig. 214). The IR and NMR spectral features correspond to complete substitution of surface silanols by hydrophobic functionalities generated by PMS5 reacted with a silica surface with no DMC (but it is optimal at slightly higher temperatures). These results are close to the ones obtained upon modification of cA-300 by HMDS (Figs. 213 and 214) at lower temperature. However, the total weight of the attached trimethylsilyl (TMS) groups (upon reaction of HMDS with cA-300) is much smaller than that after the reaction of PMS5 with A-300 (Table 40, C_C+C_H). Therefore, from a practical point of view, PMS5 could be preferable to HMDS for nanosilica hydrophobization in spite of the higher temperatures of the reaction [345].

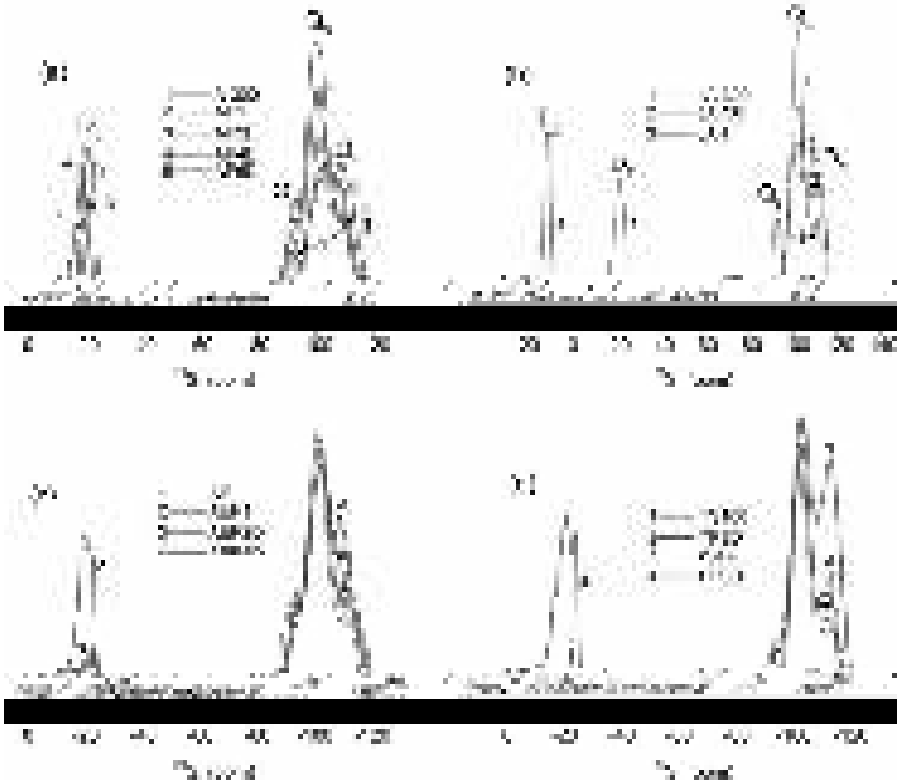

Fig. 213. ^{29}Si CP/MAS NMR spectra of unmodified and modified silicas based on (a) A-300, (b) cA-300, (c) A300 (AE), and (d) TS 100 and Syloid 244 (lines Q_n correspond to $Si(OH)_{4-n}(OSi\equiv)_n$ at n = 2, 3, and 4; line D_2 corresponds to $(-O)_2Si(CH_3)_2$; line T_3 corresponds to $OSi(CH_3)_3$).

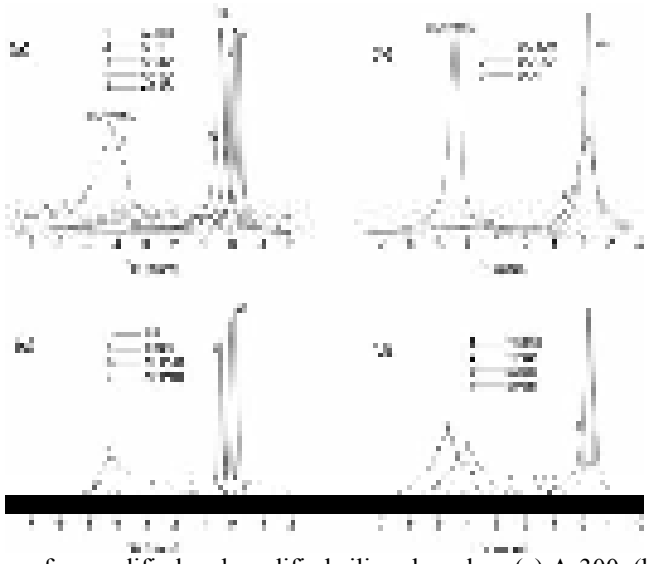

Fig. 214. [1]H MAS NMR spectra of unmodified and modified silicas based on (a) A-300, (b) cA-300, (c) A300 (AE), and (d) TS 100 and Syloid 244.

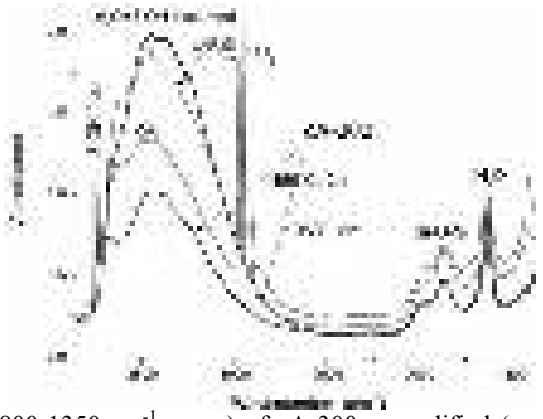

Fig. 215. The IR spectra (in the 3800-1350 cm^{-1} range) of cA-300 unmodified (preheated at 105 ^{o}C and 450 ^{o}C) and modified by P3D (cAP3D) and HMDS (cAH).

There is a general tendency for an increasing θ value (corresponding to better hydrophobization [345]) with an increase in the reaction temperature from 100 °C to 250 °C. However, this effect could be lessened with increasing length of PDMS, e.g., for AP2D, θ = 0.67 and 0.86, and for AP5D, θ = 0.60 and 0.63 at the reaction temperature of 100 °C and 200 °C, respectively.

Thus, various nanostructured silicas (fumed silicas such as initial (A-300, A300) and hydro-compacted (cA-300, TS 100), and precipitated silica Syloid 244) were modified by different PDMS using DMC as an initiator of the Si-O bond splitting. HMDS was used to modify cA-300. Investigation of the materials using microscopy, infrared spectroscopy, thermo-desorption, nitrogen adsorption-desorption, solid state NMR, SAXS, and zeta-potential methods show that the morphological, textural, and structural characteristics of modified silicas depend greatly on the type and content of the modifiers employed and on the organization of nonporous nanoparticles in secondary structures, as well on the reaction temperature. The results reveal that functionalization with PMS5 alone (T_r = 250 °C) leads to a higher degree (Θ > 0.95) of silanol substitution [345]. The S_{BET} reduction is larger; and silanol groups, that remained at the silica surface after its modification, are mainly absent as compared with the results for longer PDMS/DMC reactions occurring at 200-220 °C, giving Θ = 0.50-0.86, and a larger S_{BET} value. For nonporous particles of fumed silica, better modification by shorter PDMS is not trivial because the material is rather macroporous with only the

textural porosity caused by voids between nonporous nanoparticles in soft secondary structures. The texture of crude NAS studied is favorable for effective surface modification both by short organosiloxane (e.g. PMS5 giving C_C = 8.2 wt.% (A300) or 9.1 wt.% (A-300) at 250 °C) alone or for longer polymers with the presence of DMC. Silicas TS 100 and Syloid 244 modified by PMS200/DMC demonstrate similar C_C values (~5 wt.%) but smaller than that (5.4 wt.%) for hydrocompacted cA-300 modified by PMS200/DMC. Overall, the PDMS/DMC modified nanostructured silicas could be of interest from a practical point of view, as they remain in a dispersed state with no strong compaction of the secondary structures after the functionalization that is appropriate for better distribution of the modified nanoparticles in various polymer matrices or other nonpolar media [345].

Interactions of polymethylsiloxane (PMS) with nanosilica was studied under forced hydrocompaction to elucidate changes in confined space effects upon mechanical treatments [344]. PMS hydrogel, synthesized using methyltrichlorosilane as a precursor, at ~7-8 wt.% of PMS and 93-92 wt.% of water (Enterosgel, Kreoma-Pharm, Ukraine) was used as the initial material. After drying at room temperature for a week, the amount of water bound in PMS was small (0.7 wt.%). Dried and stirred PMS was rehydrated (h = 1 g/g) and stirred again. The bulk density of hydro-compacted wetted PMS powder is $\rho_b \approx 0.5$ g/cm^3 at $V_{em} \approx 1.5$ cm^3/g; i.e., it remains as a disperse material, as well the blends with nanosilica [344]. Dry PMS and dry fumed silica (nanosilica) A-300 were mixed in a porcelain mortar, and then distilled water (h = 1 g/g) was added. If the system was stirred without any strong mechanical loading (simple mixing) that $\rho_b \approx 0.5$ g/cm^3 (PMS/A-300). If the system was stirred under strong mechanical loading (careful grinding in a porcelain mortar with strong hand-loading giving ~20 atm, estimated from the geometry of the mortar and a pestle used and a loading weight, for 15 min) that $\rho_b \approx 0.6$ g/cm^3. This is a hydro-compacted sample labeled as cPMS/A-300 [344].

The IR spectrum of cPMS/A-300 (Fig. 216a, a broad band of the O-H stretching vibrations at 3700-2700 cm^{-1} and a band of the bending vibrations of water molecules at 1630 cm^{-1}) shows that water is strongly bound in the cPMS/A-300 blend (dried at room temperature) despite the presence of a hydrophobic component (PMS). In contrast to cPMS/A-300, hydrophobic PMS, as well PDMS, is practically free of water (Fig. 216a, curves 2 and 3, 1630 cm^{-1} is absent for both samples, as well a band at 3700-2700 cm^{-1} for PDMS). A band at 3700-3200 cm^{-1} in the PMS spectrum (Fig. 216a, curve 2) is due to silanols, both residual and formed during grinding of the dried PMS sample. The bending vibrations at 1630 cm^{-1} characteristic for water molecules are practically absent for PMS similarly to PDMS in contrast to cPMS/A-300 (Fig. 216a) [344]. Note that a band of free silanols of nanosilica (as well residual SiOH in PMS) is observed as a shoulder at 3740 cm^{-1}. Silanols disturbed due to interactions with adsorbed water molecules or adjacent nanoparticles contribute the broad band at 3700-2700 cm^{-1} also characteristic for water. PMS has intensive bands of the C–H (Fig. 216a, at 2972 and 2916 cm^{-1}), Si–C (Fig. 216b, asymmetrical at 1272 cm^{-1} and symmetrical at 780 cm^{-1}), and Si–O (asymmetrical at 1128 cm^{-1} and symmetrical at 1032 cm^{-1}) stretching vibrations. In contrast to PDMS (linear polymer), intensity of two main asymmetrical and symmetrical bands of the Si–O stretching vibrations in PMS (cross-linked 2D-3D polymer) differs, as well the bands of the Si–C stretching vibrations because the amount of CH_3 groups is twice larger in PDMS than in PMS. The additional cross-linking bonds in PMS change the ratio of the mentioned bands in comparison to that for linear PDMS.

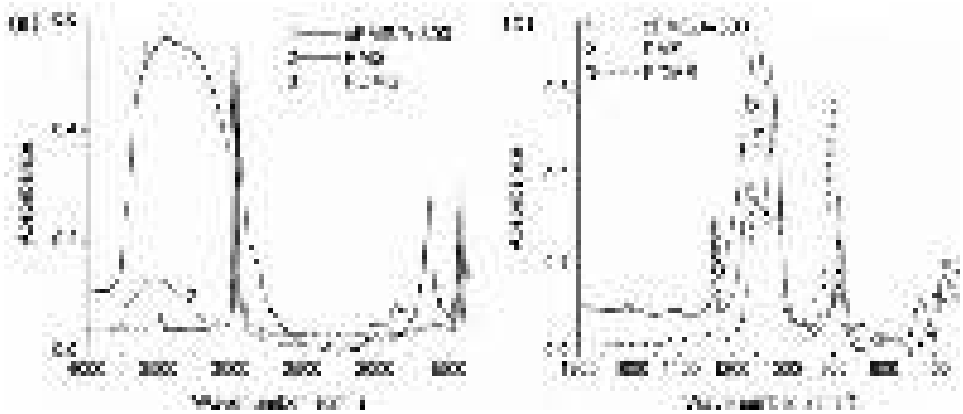

Fig. 216. Infrared spectra of air-dried cPMS/A-300, PMS, and PDMS alone in the range of (a) 4000-1300 cm^{-1} (pure samples) and (b) 1800-300 cm^{-1} (samples with KBr at 1 : 400 w/w ratio).

If all intact water is desorbed from the initial PMS hydrogel upon heating at $T < 200$ °C (Fig. 217, curve 1) that the amount of this water is *ca*. 92.7 wt.%. Note that this value corresponds to firm information on Enterosgel. The DTG minimum at 107.4 °C (curve 4) corresponds to 51.2% of removed water. Thus, 48.8% of water (evaporated at $T > 107.4$ °C) could be assigned to bound water, which really interacts with PMS. The main portion of water in Enterosgel corresponds to weakly bound water (WBW). In the case of rehydrated dried PMS [344] at a much smaller amount of water ($h = 1$ g/g), all water is bound, and 72% of this water is weakly associated water (WAW). Thus, PMS rather weakly interacts with water due to the abundance of hydrophobic CH_3 groups and a very small contribution of nanopores (Table 41, S_{nano}, V_{nano}).

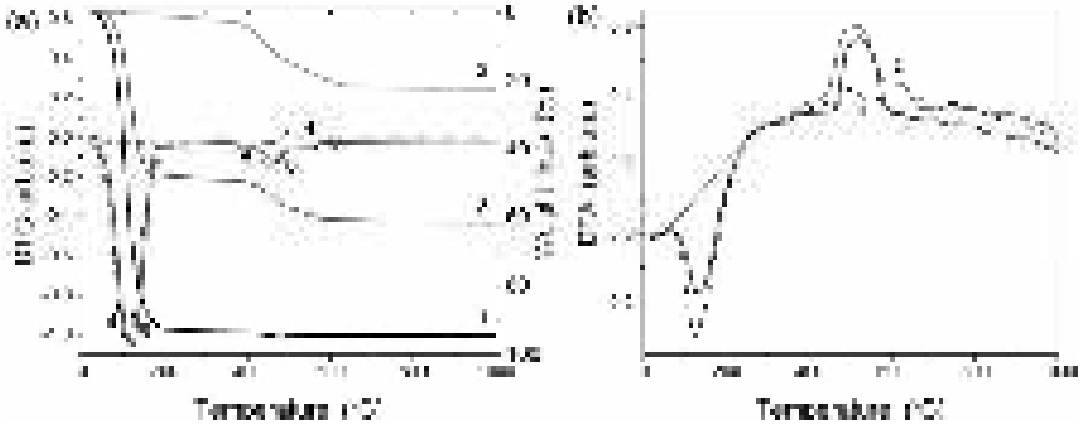

Fig. 217. (a) Thermogravimetry (TG) curves (1-3), differential TG (DTG, curves 4-6) and (b) differential thermal analysis (DTA, curves 1-3) of initial PMS hydrogel (Enterosgel) (a1, a4, b1), PMS dried at room temperature (a2, a5, b2) and hydro-compacted wetted PMS (a3, a6, b3).

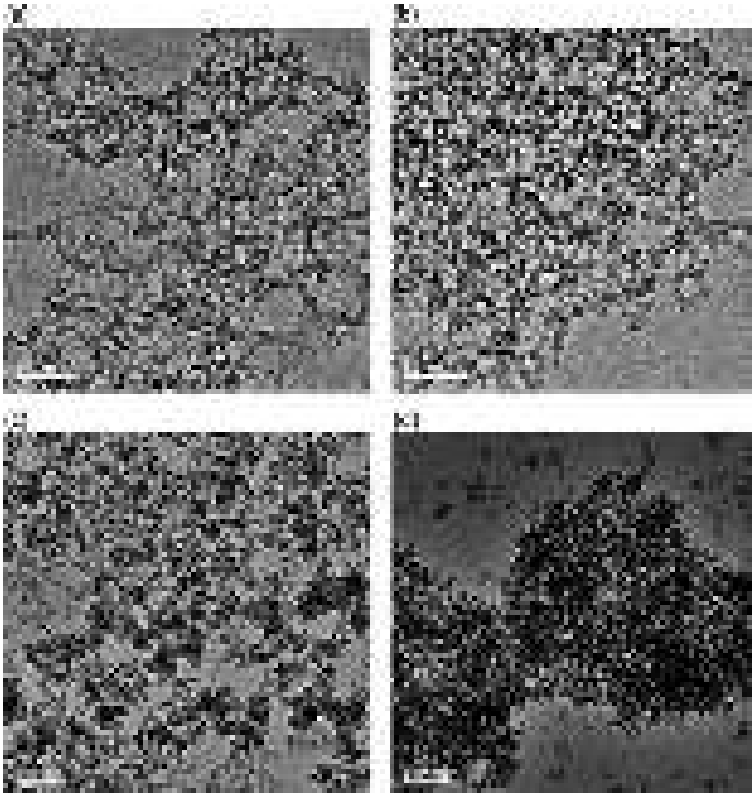

Fig. 218. TEM images of degassed (a) initial PMS (Enterosgel); (b) PMS dried at room temperature and stirred; (c) PMS/A-300 (1:1); and (d) cPMS/A-300 (1:1).

Desorption of water from the PMS hydrogel is an endothermic process, and a DTA minimum is at 123.6 ^{o}C (Fig. 217b, curve 1). For dried PMS (Fig. 218b), the residual amount of water is small as 0.7 wt.% (Fig. 217a, curve 2, T = 200 ^{o}C), and it is hydrophobic as it remains at the top of water [344]. For wetted (h = 1 g/g), stirred, and hydro-compacted PMS (which could be considered as rather non-hydrophobic since it forms a suspension), the amount of water is *ca*. 47.5 wt.% (curve 3) that is slightly smaller than the added amount of water due to its certain loss during sample preparation for the measurements [344].

The second weight loss for PMS at T > 400 ^{o}C (Fig. 217a) is due to oxidizing of CH_3 groups. Note that the main DTA maximum related to this exothermic (oxidizing) peak for hydro-compacted PMS shifts toward higher temperatures (Fig. 217b, curve 3, ~521 ^{o}C) than that for hydrogel (Fig. 217b, curve 1, ~502 ^{o}C) or dried PMS (Fig. 217b, curve 2, ~516.5 ^{o}C). However, for the latter, there is a DTA shoulder at 590-627 ^{o}C. Thus, both drying of the hydrogel and hydro-compaction of PMS affect not only the amounts of water, intact and differently bound to PMS, but also the temperature course of the desorption of water (both intact and formed upon condensation of silanols) and oxidizing of the CH_3 groups. These effects could be caused by changes in the morphology and texture of the materials, *e.g*. in the organization of nanoparticles in their aggregates (Figs. 218-221), with decomposition of a part of interparticle bonds and reduced sizes of interparticle voids. The reaction rate of oxidation kinetics of CH_3 functionalities in pores depends on the PSD because there are flows with oxygen (air) into and reaction products out of pores. Additionally, the samples were heated at a heating rate of 10 ^{o}C/min that also affect reaction features in pores. Thus, the compaction of the secondary structures can affect the gas flows and, therefore, the reaction rate of oxidation (or associative desorption of water with condensation of hydroxyls) [344].

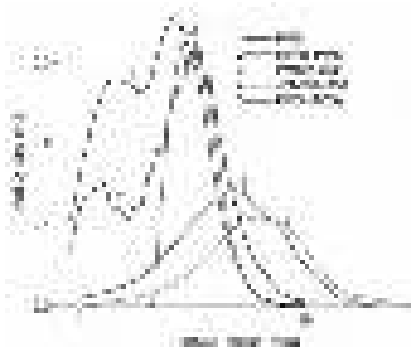

Fig. 219. Nanoparticle (*i.e*. with no secondary structures) size distributions (PaSD, curves 1-4) of calculated from TEM images shown in Fig. 218 (using ImageJ, version 1.52w with granulometry plugin, https://imagej.nih.gov/ij/download.html, accessed on November 13, 2018.), and (curve 5) PaSD for aqueous suspension of Enterosgel (0.0078 wt.%, pH 3.1) measured using photon correlation spectroscopy (Zetasizer 3000, Malvern Ins., λ = 633 nm, scattering angle 90^o).

Microscopic images (TEM, Fig. 218, and SEM, Fig. 219) show that PMS nanoparticles are mainly of 2-4 nm in radius (Fig. 220) form secondary structures of various sizes. These small sizes of PMS nanoparticles correspond to relatively high value of S_{BET} (Table 41). The secondary particles are responsible for the textural porosity of the PMS, A-300, and PMS/A-300 powders (Fig. 221, Table 41). The pores determined from the nitrogen adsorption-desorption isotherms are mainly in the range of mesopores (Fig. 221). However, the PSD correspond only to a part of pores because nitrogen can only partially fill broad macropores. Therefore, the PSD (Fig. 221, Table 41) cannot give a complete picture on textural features in the range of macropores. Additionally, practically always there is an inequality $V_{em} > V_p$ for highly disperse materials such as fumed oxides or dried PMS that is caused by a larger contribution of macropores to V_{em} than to V_p. However, features in the organization of bound water (or other liquids) depend more strongly on the textural characteristics of nanopores (R < 1 nm) and mesopores (1 nm < R < 25 nm) than on macropores. In the latter, the water characteristics are similar to those of bulk water.

Table 41. Textural characteristics of PMS alone and PMS/A-300 [344].

Sample	S_{BET} (m^2/g)	S_{DFT} (m^2/g)	S_{nano} (m^2/g)	S_{meso} (m^2/g)	S_{macro} (m^2/g)	V_p (cm^3/g)	V_{nano} (cm^3/g)	V_{meso} (cm^3/g)	V_{macro} (cm^3/g)	$<R_V>$ (nm)	$<R_S>$ (nm)
PMS	507	471	2	504	1	1.320	0.002	1.304	0.014	6.08	5.28
Stirred PMS	572	581	1	558	13	2.604	0.001	2.248	0.355	16.86	9.42
PMS/A-300	354	322	35	306	13	1.265	0.019	1.084	0.163	15.25	7.64
cPMS/A-300	407	357	8	399	1	1.021	0.006	1.005	0.011	6.56	5.17
A-300	294	289	44	229	16	0.850	0.023	0.567	0.259	20.41	6.14

Note. The values of V_{nano} and S_{nano}, V_{meso} and S_{meso}, and V_{macro} and S_{macro} were calculated by integration of the $f_V(R)$ and $f_S(R)$ functions at 0.35 nm < R < 1 nm, 1 nm < R < 25 nm, and 25 nm < R < 100 nm, respectively. The values of $<R_V>$ and $<R_S>$ as the average pore radii were calculated as a ratio of the first moment of $f_V(R)$ or $f_S(R)$ to the zero moment (integration over the 0.35-100 nm range) $<R> = \int f(R)RdR/\int f(R)dR$.

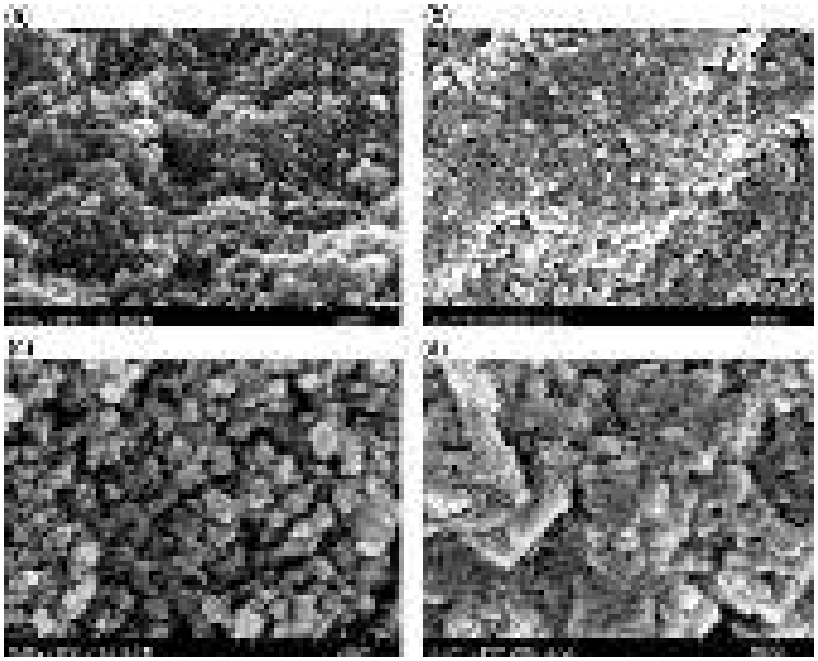

Fig. 220. SEM images (giving secondary structures with aggregates and agglomerates) of degassed (a) Enterosgel; (b) PMS dried at room temperature; (c) PMS/A-300 (1:1); and (d) cPMS/A-300 (1:1) (scale bar 500 nm).

Dried (and degassed) PMS hydrogel (with no stirring) possesses a smaller (by 12.8%) surface area than dried, stirred, and degassed PMS (Table 41, S_{BET}) due to certain decomposition of the secondary particles in the latter. The drying/stirring treatment results in an increased pore volume of PMS (Table 41, V_p), however, the V_{em} value decreases because the value of ρ_b increases. There are also changes in the PSD (Fig. 221) and other textural characteristics (Table 41, S_{nano}, V_{nano}, S_{meso}, V_{meso}, S_{macro}, V_{macro}, $<R_V>$ and $<R_S>$) of PMS, A-300, and PMS/A-300 differently treated [344]. These results can be explained by decomposition of the bonds (both chemical and physical cross-linkages) between adjacent polymer and silica nanoparticles, reorganization of their aggregates and agglomerates. This is accompanied by changes in voids between nanoparticles, and contribution of mesopores can increase, but contribution of macropores can decrease. The character of these changes for treated PMS differs from that of the PMS/A-300 blend or nanosilica alone (Figs. 216-221, Table 41) because rigid silica nanoparticles can provide abrasive effects on the soft polymer structures. Thus, for wetted PMS/A-300 stirred without and with strong mechanical loading and then dried, the textural and morphological characteristics differ due to the reorganization of the secondary particles formed by nanoparticles with practically the same sizes and structure [344].

The value of S_{BET} increases (similar to PMS alone) only by 15% (Table 41) upon strong stirring, but the value of V_p decreases in contrast to PMS alone due stronger compaction of the secondary structures. Therefore, the average value of $<R>$ (Table 41) decreases upon hydro-compaction of cPMS/A-300, but it increases during stirring of PMS alone. Note that the maximal $<R_V>$ value is observed for the initial loose A-300 powder characterized by minimal $\rho_b = 0.05$ g/cm^3. Thus, A-300 addition to PMS provides enhanced compaction of macro/meso-structures and additional decomposition of the secondary particles both of PMS and A-300. This is due to the abrasive effects (appearing upon mechanical treatments of the slurry) of A-300 on PMS nanoparticles and their secondary structures, and *vice versa* due to the polymer effects on the A-300 aggregates and agglomerates. Therefore, nanopores and narrow mesopores practically disappear in the composite (Fig. 221, curves 4 and 5 at $R < 2$ nm, Table 41, S and V). These pores could be assigned to nanosilica aggregates because the PSD of weakly treated PMS/A-300 (Fig. 221, curve 4) and A-300 (curve 5) are similar at $R < 2$ nm. During strong stirring of wetted PMS/A-300 ($h = 1$ g/g)

with subsequent drying, the nanosilica aggregates were strongly destroyed (Fig. 218), and A-300 nanoparticles were covered by nonuniform shells with smaller PMS nanoparticles. The changes in the organization of PMS/A-300 aggregates and agglomerates upon weak and strong stirring of the slurry are well seen in SEM images (Fig. 220c,d) since for the latter, they are much denser. Note that the systems were dehydrated and degassed before the nitrogen adsorption, TEM and SEM studies. These treatments can affect the organization of the nanoparticles in the aggregates and agglomerates of aggregates. However, low-temperature ^{1}H NMR spectroscopy and NMR cryoporometry allow one to study hydrated PMS and PMS/A-300 for a deeper insight into the structure of the secondary particles and the behavior of bound water. This gives information on the organization of hydrated nanoparticles depending on pretreatment conditions and dispersion media [344].

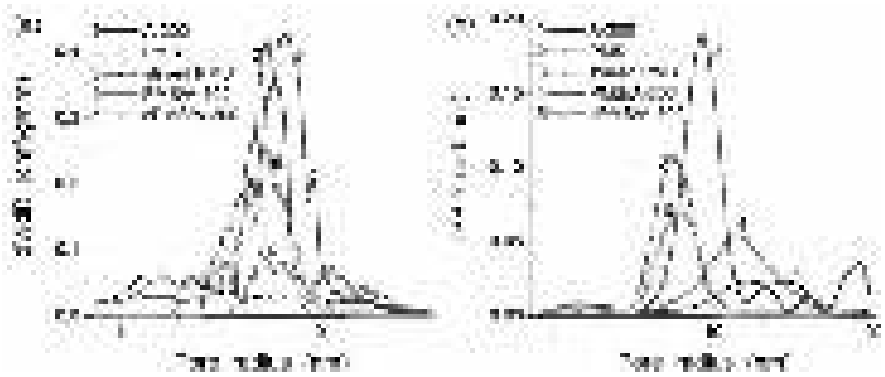

Fig. 221. (a) Differential (dV/dR) NLDFT PSD and (b) incremental SCV/SCR PSD ($\Phi_V(R_i) = (f_V(R_{i+1}) + f_V(R_i))(R_{i+1} - R_i)/2$ at $\sum\Phi_V(R_i) = V_p$) for A-300 (curve 1), dried PMS hydrogel (2), dried, rehydrated, hydro-compacted, and dried PMS (3), stirred wetted PMS/A-300 without (curve 4) and with (curve 5) strong mechanical loading (the difference in the NLDFT and SCV/SCR PSD shapes is due to the difference in the PSD and IPSD and a smaller value of the regularization parameter upon the NLDFT calculations).

To avoid the effects of different amounts of water in various hydrated systems studied using low-temperature ^{1}H NMR spectroscopy and cryoporometry, all of them were investigated at a constant hydration degree at 1 g of water per gram of dry solid matters [344].

Water bound to dried, rehydrated, and stirred PMS (h = 1 g/g) located in air gives ^{1}H NMR signal at the chemical shift of the proton resonance at δ_H = 4.0-6.5 ppm (similar to that of bulk water) dependent on temperature (Fig. 222a). Its intensity decreases with decreasing temperature due to partial freezing of bound water (Fig. 222) [344]. The δ_H value increases with lowering temperature due to several effects such as (i) ordering water structure with decreasing contribution of interstitial water; (ii) decreasing mobility of the molecules tending to spatial positions corresponding to them in ice (for ice Ih $\delta_H \approx 7$ ppm); and (iii) decreasing vibrational and rotational mobility of the bonds and functional groups [344]. A relatively large width of signals is due to the presence of various water clusters in interparticle voids of different sizes and decreased molecular mobility of bound water. The ^{1}H NMR spectra of water bound in the PMS hydrogel [344], similar to those of dried and rehydrated PMS (Fig. 222a, h = 1 g/g), but slightly narrower, show that a significant fraction of water is unfrozen at $T < 273$ K. However, it is practically all frozen at $T \le 257$ K in contrast to that in hydrated PMS at a smaller h value because the relative content of strongly bound water (SBW) frozen at $T < 260$ K increases with decreasing total amount water in the system [344].

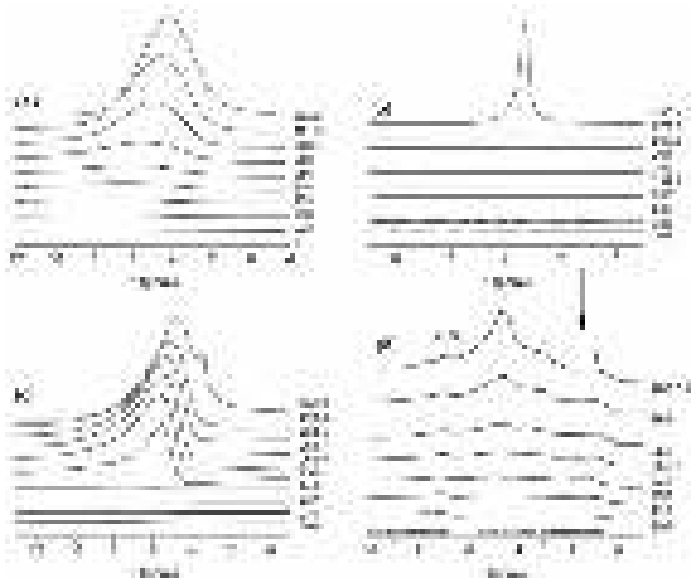

Fig. 222. ^{1}H NMR spectra recorded at different temperatures of hydrated (h = 1 g/g) samples of dried, rehydrated, stirred PMS located in (a) air and (b, c) chloroform dispersion medium and (d) with addition of TFAA ($6CDCl_3$+1TFAA); (c) a part of the spectra (b) at low temperatures shown SBW.

If the hydrated PMS is located in the chloroform-d medium (Fig. 222b,d) that signals become narrower. This, as well changes in the temperature behavior of bound water, is due to changes in the water organization. At low temperatures (Fig. 222d), several signals are observed. They can be attributed to structures with different associativity of the water molecules in various clusters located in different voids (pores). Note that frozen water (ice) structures can effectively change the pore (void) size distribution that can also affect the behavior of remained unfrozen water located in these narrower pores. Water with δ_H = 4.5-5.0 ppm (Fig. 222d, signal 1) can be assigned to strongly associated water (SAW) similar to bulk water with the molecules having 3-4 hydrogen bonds per a molecule. Water with δ_H = 1-2 ppm (Fig. 222d, signal 3) could be considered as weakly associated water (WAW) forming 1D or 2D clusters of LDW (with smaller average numbers of the hydrogen bonds per a molecule than that in bulk water) with hydrophobic surroundings affecting the organization of water clusters. Water at $\delta_H \approx 3$ ppm (Fig. 222d, signal 2) is intermediate between SAW and WAW with respect to the sizes and shapes of the clusters [53,344].

Addition of trifluoroacetic acid (TFAA) to chloroform leads to certain broadening of signals and to a downfield shift of signals of unfrozen water. Intensity of signal demonstrates a smaller decrease with lowering temperature due to dissolution of the acid in bound water and the colligative properties of the solution (Fig. 222c) that enhances the SBW amount. As a whole, interfacial bound water is rather a poor solvent even for TFAA. Therefore, only a weak shoulder is observed at high δ_H values (8-10 ppm) corresponding to the acidic solution, and there is a signal (at 280 K) of water with no dissolved acid [344].

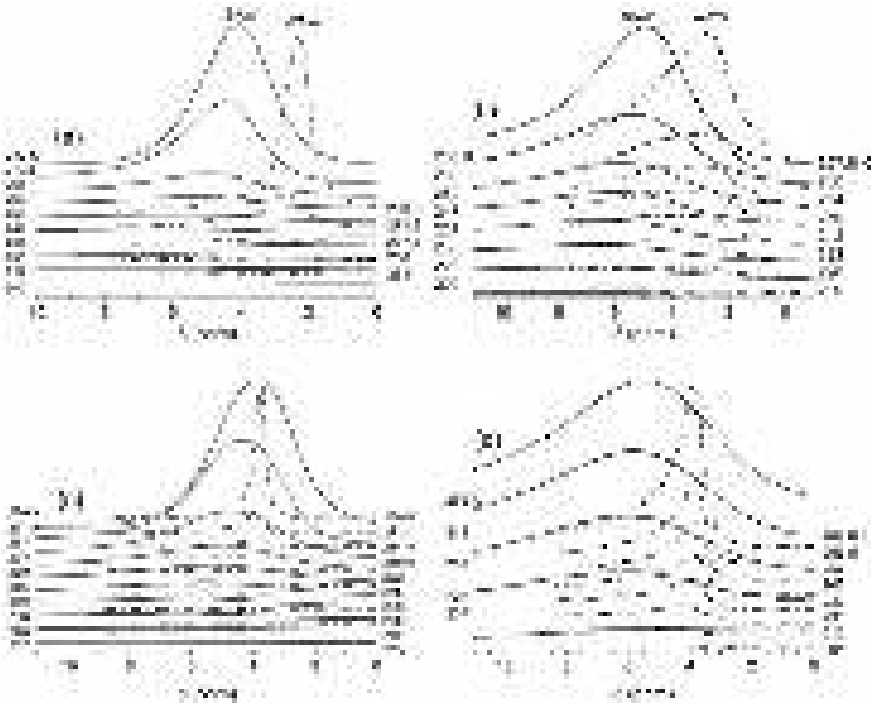

Fig. 223. ^{1}H NMR spectra recorded at different temperatures of hydrated (h = 1 g/g) PMS/A-300 in air (solid lines) and chloroform (dotted-dashed lines) stirred without (a, b) and with (c, d) strong mechanical loading; (c, d) correspond to a part of the spectra recoded at low temperatures.

For hydrated PMS/A-300 (Fig. 223a,b, solid lines) and cPMS/A-300 (Fig. 223c,d, solid lines) located in air, the spectra shapes are similar to those of hydrated PMS (Fig. 222a). In the chloroform dispersion media, the spectra shapes depend on the mechanical treatment of the samples (Fig. 223, dotted-dashed lines). Upon weak mechanical loading, signals of SAW and WAW are observed (Fig. 223a,b). WAW signal is greater in the total temperature range. For the blend after strong mechanical loading, practically only SAW signal is observed (Fig. 223c,d). These results suggest that the organization of bound water depends on the textural and morphological rearrangement of the secondary structures of hydrated PMS/A-300 (h = 1 g/g) under the strong mechanical loading. For example, contribution of nanopores and narrow mesopores decreases (Table 41, Fig. 221). Therefore, chloroform can displace water only into broad mesopores and macropores, in which, all bound water corresponds to SAW only [344]. Besides SAW and WAW, it is possible to differentiate unfrozen (at T < 273 K) water into strongly (SBW) and weakly (WBW) bound waters [53]. It is assumed that SBW corresponds to a fraction frozen at T < 260 K (changes in Gibbs free energy ΔG < –0.5 kJ/mol) and WBW is frozen at 260 K < T < 273 K (ΔG > –0.5 kJ/mol) (Fig. 224a). This assumption is based on the difference in the temperature behavior of unfrozen SBW and WBW. As a whole, freezing of SBW occurs in broad temperature and ΔG value ranges, but in a narrow C_{uw} value range in contrast to WBW. This is due to a fast decrease of the effects of solid surface fields on distant interfacial water layers. This decay of the surface fields is stronger for hydrophobic (*i.e*. nonpolar or weakly polar) surfaces than for polar ones due to different dependences of the electrostatic fields (caused by charges and dipoles) and van der Waals forces on distance. However, there is an additional factor caused by the confined space because the opposite walls in pores can enhance the influence of the surface fields on the temperature behavior of bound water. Additionally, the hydrophobic media (*e.g*. chloroform) can change the organization of bound water. Water tends to locate in narrow nanopores (inaccessible for larger chloroform molecules) or in broad mesopores and macropores to reduce the surface area of contacts between immiscible liquids. Both in PMS and PMS/A-300, nanopores at R < 1 nm are practically absent (Fig. 221). Therefore, water is mainly displaced by chloroform into larger

mesopores. SBW transforms into WBW (mainly SAW) for all systems (Fig. 224a and Table 42, compare the systems located in air and chloroform), but with one exception with the chloroform/TFAA medium.

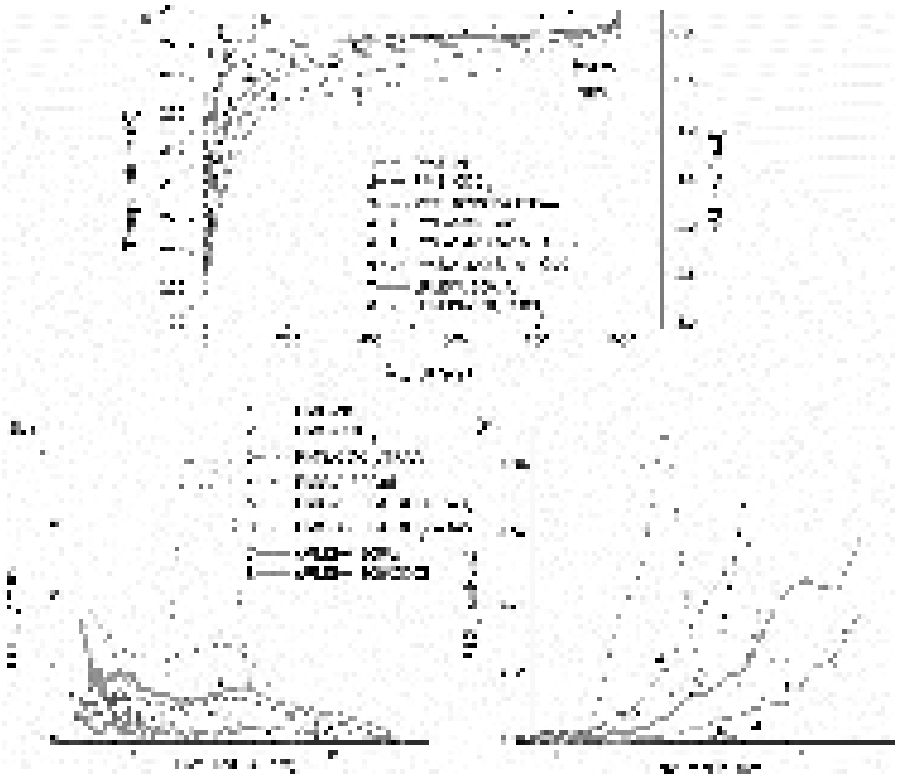

Fig. 224. (a) Relationships between the amounts of unfrozen water (C_{uw}) and changes in the Gibbs free energy (ΔG) depending on temperature; (b, c) size distributions of pores filled by unfrozen water (PSD_{uw}) for PMS alone in (1) air, (2) chloroform and (3) $6CDCl_3$+1TFAA; and PMS/A-300 stirred without (4-6) and with (7, 8) strong mechanical loading in air (4, 7) and chloroform (5, 6, 8); (b) differential PSD_{uw} and (c) incremental $IPSD_{uw}$.

The latter is due to the colligative properties of the acidic solution that result in the freezing temperature depression. Note that a fraction of water located in macropores (R > 25 nm) could be assigned to non-bound water with the properties similar to those of bulk water. Therefore, NMR cryoporometry with water as a probe cannot appropriately describe total contribution of macropores (Table 42, Fig. 224b,c). The effects of chloroform on bound water are well seen in a decrease in the γ_S values giving the sum of total changes in the modulus of ΔG for all interfacial water (due to diminution of interaction of water with solid surfaces) and an increase in the average melting temperature $<T_m>$ (due to transformation SBW → WBW) (Table 42). This is due to a decrease in the confined space effects on bound water displaced into larger pores.

There is a certain difference in contribution of nanopores to the total porosity and specific surface area calculated on the basis of nitrogen adsorption data (Table 41, Fig. 221) and NMR cryoporometry (Table 42, Fig. 224b,c). This difference could be explained by the effects of frozen water (ice) located in mesopores that can result in transformation of mesopores into nanopores upon the use of the NMR cryoporometry. Additionally, dried (nitrogen adsorption) and wetted (NMR study) PMS samples could have different structures of nanoparticles, as well different secondary structures, due to a certain swelling effect, and the amount of water is smaller than V_{em} in the powders.

Table 42. Characteristics of water bound to non-compacted and compacted PMS alone and with A-300 (1 : 1) in air, chloroform medium alone or with addition of TFAA (h = 1.0 g/g) [344].

Sample	Medium	C_{uw}^{s} (mg/g)	C_{uw}^{w} (mg/g)	$-\Delta G_s$ (kJ/mol)	γ_S (J/g)	$<T_m>$ (K)	$S_{nano,uw}$ (m^2/g)	$S_{meso,uw}$ (m^2/g)	$V_{nano,uw}$ (cm^3/g)	$V_{meso,uw}$ (cm^3/g)
PMS	Air	280	720	2.48	25.13	258.63	138	98	0.056	0.758
PMS	$CDCl_3$	10	990	2.44	0.69	262.36	3	1	0.001	0.007
PMS	$CDCl_3$/TFAA	475	525	2.45	27.73	257.39	15	226	0.006	0.796
PMS/A-300	Air	115	885	2.85	12.06	257.04	64	86	0.026	0.297
PMS/A-300 (SAW)	$CDCl_3$	95	25	3.04	2.88	251.26	20	14	0.008	0.041
PMS/A-300 (WAW)	$CDCl_3$	795	95	2.77	9.91	257.88	52	54	0.021	0.202
cPMS/A-300	Air	225	775	2.68	17.45	261.78	110	70	0.044	0.675
cPMS/A-300	$CDCl_3$	30	970	2.90	5.01	263.69	31	20	0.012	0.207

Note. C_{uw}^{s} and C_{uw}^{w} are the amounts of weakly and strongly bound waters; ΔG_s is the changes in the Gibbs free energy of water layer closely located to a surface; γ_S is the modulus of the total changes in the Gibbs energy of bound water unfrozen at $T < 273.15$ K; $<T_m>$ is the average melting temperature; $S_{nano,uw}$ and $V_{nano,uw}$, $S_{meso,uw}$ and $V_{meso,uw}$ are the specific surface area and pore volume of nanopores at $R < 1$ nm and mesopores at 1 nm < R < 25 nm, respectively, in contact with unfrozen water.

The PSD_{uw} curves (Fig. 224b,c) well show the effects of chloroform (*i.e.*, the displacement of water into larger pores) and hydro-compaction (*i.e.*, the diminution of a contribution of narrow pores and an increase in contribution of broader mesopores) because both ones result in the shifts of the PSD_{uw} toward larger pores. These effects appear in changes in the δ_H values and entropy of bound water *vs*. temperature (Fig. 225).

The secondary structures of PMS and PMS/A-300, treatment features, and a medium type affect the temperature dependence of the δ_H values of bound water (Fig. 225a,b). The mentioned effects influence the changes in the entropy of bound unfrozen (melted ice) water *vs*. temperature (Fig. 225c,d). The maximal peak of the $s(T)$ function for PMS alone (Fig. 225c) corresponds to increased entropy both of SBW and WBW that appears due to melting of ice (with decreasing structural order) with increasing temperature to 255-265 K. However, for intermediate clusters of water (Fig. 222d, signal 2) bound to PMS located in chloroform, this peak becomes larger (Fig. 225c, curve 3) than that in the air medium (curve 1) or for SAW (curve 2, signal 1 in Fig. 222d). For the chloroform/TFAA medium (curve 4), the $s(T)$ curve strongly differs from others due to the colligative properties of the acidic solution with strongly shifted freezing/melting points toward lower temperatures [53,344].

For both PMS/A-300 samples located in air (Fig. 225d, curves 1 and 4), the $s(T)$ peaks at 263.5 K slightly shift toward higher temperature in comparison to that for PMS alone (Fig. 225c). This is rather unexpected result because addition of hydrophilic nanosilica results in the effect, which could be expected upon addition of a hydrophobic component. However, the appearance of the hydrophobic surroundings (chloroform) results in the shift of the $s(T)$ maximum toward lower temperature both for SAW (Fig. 225d, curve 2) and WAW (curve 3). For compacted cPMS/A-300 (Fig. 225d, curve 5), a strong decrease in the $s(T)$ values is observed at temperatures corresponding to melting of WBW (which is mainly SAW, Fig. 223c,d). This effect could be explained by diminution of the porosity of the compacted blend that leads to increased effects of hydrophobic functionalities on unfrozen water, which, therefore, becomes more ordered [53].

Interaction energy (ΔE_t) in the system with dehydrated PMS particle (119 structural units with residual 9 OH groups) surrounded by a water shell clustered is $\Delta E_t = -19.1$ kJ/mol per a water molecule [344]. The interaction between the water shell and PMS particle (per a water molecule) gives $\Delta E_t = -7.1$ kJ/mol, but in the water shell per se, it is stronger $\Delta E_t = -12.0$ kJ/mol. This result corresponds to a tendency of the formation of larger water structures (clusters, domains) upon interaction with hydrophobic surroundings. However, for the water shell around a non-dehydrated PMS particle (119 structural units with 60 OH groups), the ^{1}H NMR spectrum is similar to that for

the shell around the dehydrated PMS particle (with residual 9 OH groups). This effect is due to the clusterization of the water shells for both particles [344].

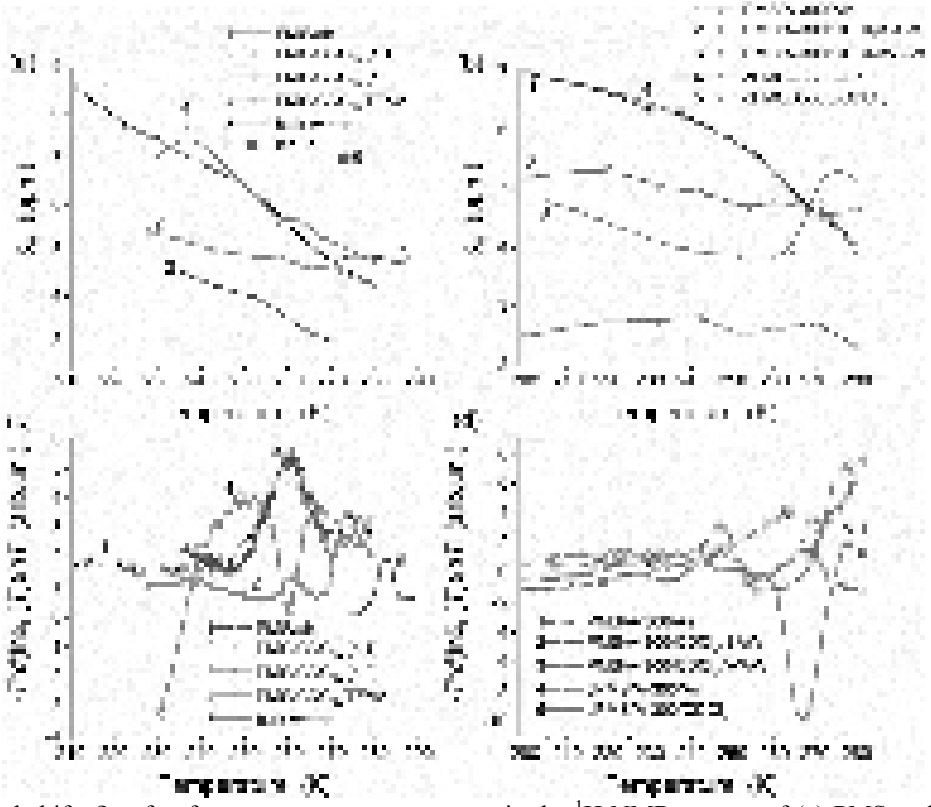

Fig. 225. Chemical shifts δ_H of unfrozen water *vs*. temperature in the ^{1}H NMR spectra of (a) PMS and (b) PMS/A-300 differently treated and in different media (air and chloroform or $CDCl_3$/TFAA), and (c, d) corresponding functions $s(T) = -T(\partial(\ln\delta(T))/\partial T)_P$ *vs*. *T*.

Thus, the powders of dried disperse hydrophobic PMS alone and in the blends with hydrophilic nanosilica can be easily rehydrated upon stirring with water [344]. The properties of the slurry depend on the mechanical treatment due to stronger compaction of the PMS/A-300 secondary structures with increasing mechanical loading. Note that a similar behavior of the blends with hydrophobic and hydrophilic nanostructured materials was observed for several compositions that reflects the general regularities appearing at appropriate amounts of added water and certain mechanical loading onto the blends of hydrophilic and hydrophobic nanostructured materials. These conditions result in the reorganization of the secondary structures and removal of micro-scaled air bubbles bound to hydrophobic components in the initial mixtures. Note that after drying of the slurry, the powder can demonstrate the hydrophobic properties since it can remain at the top of liquid water [344].

A fraction of water (h = 1 g/g) bound to PMS or PMS/A-300 located in air corresponds to strongly bound water frozen at T < 260 K, but practically all water is strongly associated and characterized by the chemical shift at δ_H = 4.5-5.0 ppm. If these systems are located in the hydrophobic chloroform dispersion medium that the organization of bound water strongly changes to reduce the contact area between immiscible liquids. Typically, chloroform can displace adsorbed water into narrow nanopores (inaccessible for larger chloroform molecules) or/and into larger pores (to reduce the contact area between them). In the system studied, narrow nanopores are practically absent; therefore, chloroform displaces water mainly into larger pores. This results in a decrease in the amounts of SBW. A fraction of weakly associated water (δ_H = 1-2 ppm), *i.e*., strongly clustered water with 1D and 2D structures, appears in the systems undergoing low mechanical loading. After

stronger mechanical loading, only strongly associated water is observed due to changes in the confined space effects in more strongly compacted secondary particles [344]. If trifluoroacetic acid is added to the chloroform medium that the colligative and confined space effects overlap and the amount of SBW increases. Note that in this case, the changes in the porosity caused by the appearance of the ice clusters in interparticle voids can be smaller than that in the systems with a main fraction of SAW/WBW [344]. The PMS/nanosilica blends can be of interest from a practical point of view for applications as medical sorbents. The blends are with improved or better controlled textural and adsorption characteristics, which can be easily varied in a broader range due to changes in composition and pretreatment conditions. Note that tests of these systems in various applications were started, and some promised results were obtained [344].

Conclusion

Complex FMO such as silica/alumina, silica/titania, and alumina/silica/titania could consist of core-sell nanoparticles including crystalline or polycrystalline cores with an amorphous shell. In contrast to simple and small silica or titania nanoparticles in individual FMO, complex core-shell nanoparticles (50-200 nm in size) with titania or alumina cores and silica or alumina shells in binary and ternary FMO could be destroyed under mechanochemical activation in a ball mill or a microbreaker. Both can affect the structure of aggregates of nanoparticles and agglomerates of aggregates, resulting in more compaction. This could be accompanied by changes in color from white to beige of different tints, with resulting changes in the UV-vis spectra in the 300-600 nm, as well as changes in the crystalline structure of alumina. This study showed that complex nanooxides could be more sensitive to external actions than simple nanooxides such as fumed silica. This aspect is of importance for practical applications of FMO.

The results of the hydrocompaction of nanosilica A-300 depend strongly on the amounts of water (in the range of 0.3-5.0 g/g) used in the process. A selection of a certain amount of water allows the appropriate reorganization of the secondary and ternary structures of nanoparticles that is accompanied by changes in the textural characteristics (*S*, *V*, PSD) of the powder. However, according to TEM and SAXS data, the nanoparticles *per se* are practically not affected by this treatment, i.e., only the rearrangement of their secondary formations occurs. At a low amount of water ($h_{cp} \leq 1$ g/g), the reorganization of secondary/ternary structures does not lead to reduction of the specific surface area (it even slightly increases). However, at $h_{cp} \geq 1.5$ g/g, the specific surface area decreases, but the pore volume (nitrogen adsorption at $p/p_0 \approx 0.99$) increases despite the empty volume of the powder decreases from 21.8 cm^3/g for initial A-300 ($\rho_b = 0.045$ g/cm^3) to 3.45 cm^3/g after compaction at $h_{cp} = 4.5$ g/g ($\rho_b = 0.256$ g/cm^3). Note that the structural reorganization of the hydro-compacted powders is possible due to addition of new amounts of water. This suggests that the chemical bonds between adjacent NPNP do not practically form upon the hydro-compaction under soft conditions. Thus, hydro-compacted nanosilica loses the dust-forming property but remains active with respect to the NPNP activity and mobility in the secondary structures. This is of importance for practical applications of nanosilicas, especially in aqueous suspensions, drug delivery systems, and upon filling of polymers.

Any treatment of nanooxides affected the interfacial and temperature behaviors of polar and nonpolar adsorbates those depend on concentrations, treatment history and other conditions. For some adsorbates, open hysteresis loops result in adsorption-desorption isotherms. Rearrangement of secondary FMO particles can strongly affect the freezing-melting point depression of bound adsorbates such as water and low-molecular weight organics. Clustering of adsorbates in pores caused reduced enthalpy changes during phase transition (freezing, fusion). Freezing point depression and increasing melting point caused significant hysteresis effects for some adsorbates,

both low- and high-molecular weight compounds, bound to oxide nanoparticles in textural pores as voids between nanoparticles in secondary structures of FMO.

Confined space effects for various adsorbates bound to initial or treated FMO lead to reduction of the activity of solvents in the interfacial layers depending on the pore sizes and temperature. This results in differentiation of aqueous solutions of acids, salts and other compounds in different structures located in pores of different sizes that are characterized by decreased amounts of solutes in pores of smaller sizes. This differentiation enhances with decreasing temperature and partial freezing of adsorbates because of, at least, two effects related to freezing a portion of adsorbates in pores (that results in changes in the effective porosity and pore sizes) and cryoconcentrating of the solution because frozen fractions tend to be with much lower content of solutes than that dissolved in the liquid solvent.

Glossary of abbreviations		Units
A	constant	
a	adsorption	cm^3/g
a_m	BET monolayer adsorption	cm^3/g
b_{ij}	collision rate	s^{-1}
C_d	concentration of decane	(g/g)
C_{SiO2}	concentration of silica	wt%
C_{uw}	amount of unfrozen water (g) per gram of adsorbent	g/g
C^s_{uw}	concentration of unfrozen water strongly bound to surface	wt%
C^w_{uw}	concentration of unfrozen water weakly bound to surface	wt%
dC_{uw}/dR	derivative	g/g/nm
dC_{uw}/dT	derivative	g/g/K
d_p	diameter of pores	nm
$dV_{uw}(R)/dR$	derivative	$cm^3/g/nm$
E	adsorption energy	kJ/mol
E_k	kinetics energy	kJ/mol
E_p	potential energy	kJ/mol
F_p	intensity of the electrostatic field	kV/m
$f(k)$	distribution function of rate constant	arb.un.
$f(R_p)$	differential pore size distribution	arb.un.
$f_S(R)$	distribution function of pore size with respect to surface area	arb.un.
$f_V(R)$	distribution function of pore size with respect to pore volume	arb.un.
h	hydration	g/g
I	intensity of ^{1}H NMR signal	-
$I_{0,i}$	intensity of the temperature distribution curve of phase i	arb.un.
I_c	intensity of ^{1}H NMR signal of water adsorbed from the gas phase	-
I_{uw}	intensity of ^{1}H NMR signal of unfrozen water at $T < 273$ K	-
k	rate constant	(s^{-1})
k_B	Boltzmann constant	$(1.3806488\times10^{-23}$ J/K)
K_h	coefficient of hydrophilicity	-
k_{GT}	constant in Gibbs-Thomson equation	K nm
L_p	pore length	nm
p	equilibrium pressure	Pa
p_0	saturation pressure	Pa
Q	heat of adsorption	kJ/mol
Q_d	heat of immersion in n-decane	kJ/mol

Q_w	heat of immersion in water	kJ/mol
q_H	charge on H-atom	a.u.
R	radius of pores	nm
R_g	gas constant	kJ/K/mol
R_p	pore radius	nm
R_{max}	maximal pore radius on integration	nm
R_{min}	minimal pore radius on integration	nm
S_{BET}	specific surface area by the Brunauer-Emmett-Teller method	m^2/g
$S_{BET,X}$	specific surface area determined from adsorption of compound X	m^2/g
S_{IR}	specific surface area determined using IR spectra	m^2/g
S_{macro}	specific surface area of macropores	m^2/g
S_{meso}	specific surface area of mesopores	m^2/g
S_{nano}	specific surface area of nanopores	m^2/g
S_{sum}	corrected total specific surface area	m^2/g
S_{uw}	specific surface area determined using NMR cryoporometry	m^2/g
T	absolute temperature	K
T_1	longitudinal relaxation time	s
T_2	transverse relaxation time	s
T_b	boiling temperature	K
T_c	critical temperature	K
T_{cr}	crystallization temperature	K
T_g	glass-transition temperature	K
T_m	melting temperature	K
$T_{m,\infty}$	bulk melting temperature	K
$T_m(R)$	melting temperature of a frozen liquid in pores of radius R	K
$<T_m>$	average melting temperature	K
t	time	s
t	thickness of an adsorbed nitrogen layer	nm
$t(p,R_p)$	statistical thickness of an adsorbed layer	nm
t_m	statistical thickness of a monolayer	nm
t_{MCA}	time of MCA	hour
t_T	heating time	min
V_{em}	empty volume	cm^3/g
V_p	pore volume	cm^3/g
V_{macro}	volume of macropores	cm^3/g
V_{meso}	volume of mesopores	cm^3/g
V_{nano}	volume of nanopores	cm^3/g
$V_{uw}(R)$	volume of unfrozen water in pores of radius R	cm^3/g
w	parameter in Kelvin equation	arb.un.
w_{ef}	effective parameter in Kelvin equation	arb.un.
X	normalized inverse transition temperature	1/K
X_{ci}	normalized inverse transition temperature of phase i,	1/K
α	regularization parameter	-
β	heating rate	K/s
Γ	Gibbs adsorption	
γ	surface tension	N/m
γ_p	surface tension in pores	N/m

γ_S	module of total changes in the Gibbs free energy of interfacial water	mJ/m^2
ΔE_H	energy of the hydrogen bonds	kJ/mol
ΔG	changes in Gibbs free energy of the interfacial water	kJ/mol
ΔG^s	changes in Gibbs free energy of the strongly bound water	kJ/mol
ΔG^w	changes in Gibbs free energy of the weakly bound water	kJ/mol
ΔH_f	bulk enthalpy of fusion	kJ/mol
ΔH_{im}	immersion enthalpy	kJ/mol
ΔT_m	melting point depression	degr.
$\Delta\sigma$	changes in the surface tension	mJ/m^2
Δw	relative deviation from the pore model	arb.un.
δ	chemical shift	ppm
δ_H	chemical shift of protons	ppm
$\Phi(T)$	integrated heat flow in DSC	arb.un.
ρ	density	g/cm^3
ρ_b	bulk density	g/cm^3
$\varphi(a)$	primary particle size distribution	arb.un.
Θ	reduced (a/a_m) adsorption	-
ζ	ζ-potential	mV

200DF	silica gel;
A-50	fumed silica;
A-100	fumed silica;
A-150	fumed silica;
A-200	fumed silica;
A-300	fumed silica;
A-380	fumed silica;
A-400	fumed silica;
A-500	fumed silica;
AFM	Atom Force Microscopy;
APMS	AminoPropylMethylSilyl groups;
ASTxx	Alumina/Silica/Titania nanooxide; xx = titania content (wt.%)
ASW	water in associates HO-H…A (A– electron donor center);
B3LYP	Exchange-correlation functional in DFT
BW	Bound Water;
Cab-O-Sil HS-5	fumed silica;
CNO	CryoNanoOxides;
CSNP	Core-Shell NanoParticles;
DEA	DiEthylAmine;
DFT	Density Functional Theory;
DLS	Dynamic Light Scattering;
DMAAB	(DiMethylAmino)AzoBenzene;
DMSO	DiMethylSulfOxide;
DON	DiOxiNaphthalene;
DRS	Dielectric Relaxation Spectroscopy;
DRS	Diffuse Reflectance Spectra;
DSC	Differential Scanning Calorimetry;
DTG	Differential TG;

EDL Electric Double Layer;
FMO Fumed Metal or Metalloid Oxides;
FT Fourier Transformation;
FTIR Fourier Transform Infrared Spectroscopy;
HMDS HexaMethylDiSilazane;
HOMO Highest Occupied Molecular Orbital;
HPCG High-Pressure CryoGelation;
HRTEM High Resolution Transmission Electron Microscopy;
HTT HydroThermal Treatment;
IEP IsoElectric Point;
IGT Integral Gibbs-Thomson equation;
Ih hexagonal ice;
IPSD Incremental Pore Size Distribution;
LTNA Low-Temperature Nitrogen Adsorption;
MAS Magic Angle Spinning;
MB Methylene Blue
MCA MechanoChemical Activation;
MCM-41 ordered mesoporous silica;
MCM-48 ordered mesoporous silica;
MND Modified Nguyen-Do method;
MS Methylated Silica;
MW Molecular Weight;
NMR Nuclear Magnetic Resonance;
OX-50 fumed silica;
PaSD Particle Size Distributions;
PC-100 photocatalyst with titania;
PC-105 photocatalyst with titania;
PC-500 photocatalyst with titania;
PDMS Poly(DiMethyl Siloxane);
PEG Poly(Ethylene Glycol);
PM6 and PM7 Semiempirical methods
PMS Poly(Methyl Siloxane);
POA Phosphorus OxyAcids;
POE Poly(Oxy Ethylene);
PPA PolyPhosphoric Acid;
PPSD Primary Particle Size Distribution;
PS300 pyrogenic silica analogues of A-300;
PSD Pore Size Distribution;
PSD_{uw} Pore Size Distribution determined from the C_{uw} values;
PVA Poly(Vinyl Alcohol);
PVP Poly(Vinyl Pyrrolidone);
QC Quantum Chemistry;
Qc quercetin;
SAxx Silica/Alumina nanooxides; xx = alumina content (wt.%)
SAW Strongly Associated Water;
SAXS Small-Angle X-ray Scattering;
SBA-15 ordered mesoporous silica;
SBA Strongly Bound Adsorbate;

SBW	Strongly Bound Water;
SCR	Self-Consistent Regularization;
SCV	model of a pore mixture with Slitshaped and Cylindrical pores and Voids between spherical nanoparticles packed in random aggregates;
SEM	Scanning Electron Microscopy;
SI	Supplementary Information;
Si-40	silica gel;
Si-60	silica gel;
Si-100	silica gel;
SMD	Solvation Model
STxx	Silica/Titania nanooxides; xx = titania content (wt.%)
TEA	TriEthylAmine;
TEM	Transmission Electron Microscopy;
TEOS	TetraEthOxySilane; TetraEthyl OrthoSilicate
TG	ThermoGravimetry;
TMS	TetraMethylSilane;
TMS	TriMethylSilyl groups
TPD-MS	Temperature-Programmed Desorption with Mass-Spectrometry control;
TSDC	Thermally Stimulated Depolarization Current;
UV–Vis	Ultra-Violet–Visible (spectroscopy);
WAW	Weakly Associated Water;
WBA	Weakly Bound Adsorbate;
WBW	Weakly Bound Water;
wB97XD	DFT functional;
XPS	X-ray Photoelectron Spectroscopy;
XRD	X-Ray Diffraction

References

[1] Bergna H.E., Roberts W.O. (editors). *Colloidal Silica: Fundamentals and Applications*. (CRC Press, Boca Raton, 2006).

[2] Hastie J.W. (editor). *Materials Chemistry at High Temperatures. Vol. 1, Characterization. Vol. 2, Processing and Performance*. (NJ: Clifton, Humana Press, 1990).

[3] Ullmann's Encyclopedia of Industrial Chemistry. Wiley-VCH, Weinheim. 2008.

[4] Basic Characteristics of Aerosil. Technical Bulletin Pigments, No 11, Degussa AG, Hanau. 1997.

[5] Shchukin E.D., Zelenev A.S. *Physical-Chemical Mechanics of Disperse Systems and Materials*. (CRC Press, Boca Raton, 2015).

[6] Cabot Corporation. http://www.cabotcorp.com/solutions/products-plus/fumed-metal-oxides/.

[7] DuPont. http://www.dupont.com/.

[8] Evonik Ind. http://corporate.evonik.com/en/Pages/default.aspx; http://www.aerosil.com/product/aerosil/en/services/downloads/Pages/test-methods.aspx.

[9] Kulkarni P., Baron P.A., Willeke K. (editors). *Aerosol Measurement: Principles, Techniques, and Applications. Third Edition.* (New York : John Wiley & Sons, 2011).

[10] Büchel K.H., Moretto H.-H., Woditsch P. *Industrial inorganic chemistry*. (Weinheim: Wiley-VCH Verlag GmbH, 2000).

[11] Auner N., Weis J. (editors). *Oganosilicon Chemistry VI*. (Weinheim: Wiley-VCH Verlag GmbH, 2005).

[12] Piemonte V., De Falco M., Basile A. (editors). *Sustainable Development in Chemical Engineering – Innovative Technologies. First Edition*. (UK: Chichester , John Wiley & Sons, 2013).

[13] Kriechbaum G.W., Kleinschmit P. Superfine oxide powders- flame hydrolysis and hydrothermal synthesis. *Adv. Mater*. 1989.**10**:330.

[14] Gutsch A., Mühlenweg H., Krämer M. Tailor-made nanoparticles via gas-phase synthesis. *Small* . 2005.**1**:30.
[15] Jacobsen H., Kleinschmit P. Flame Hydrolysis. In: Ertl G, Knozinger H, Weitkamp J (editors), *Preparation of Solid Catalysts*. (Weinheim: Wiley-VCH Verlag GmbH, 1999, pp. 99-109).
[16] Afyon S., Hagemann M., Somer M., Isfort C.S. Thermal and hydrothermal stability of flame hydrolytically synthesized SiO_2/TiO_2 mixed oxides. *Solid State Sci*. 2013.**18:** 91.
[17] Albers P., Maier M., Reisinger M., Hannebauer B., Weinand R. Physical boundaries within aggregates – differences between amorphous, para-crystalline, and crystalline structures. *Cryst. Res. Technol*. 2015.**1:** 20. DOI: 10.1002/crat.201500040
[18] Schaefer D.W., Hurd A.J. Growth and structure of combustion aerosols: fumed silica. *Aerosol Sci. Technol*. 1990. **12**(4): 876.
[19] Roth P. Particle synthesis in flames. *Proceedings of the Combustion Institute*. 2007. **31**: 1773.
[20] Pratsinis S.E. Flame aerosol synthesis of ceramic powders. *Prog. Energy Combust. Sci*. 1998. **24**: 197.
[21] Mueller R., Madler L., Pratsinis S.E. Nanoparticle synthesis at high production rates by flame spray pyrolysis. *Chem. Eng. Sci*. 2003. **58**: 1969.
[22] Camenzind A., Caseri W.R., Pratsinis S.E. Flame-made nanoparticles for nanocomposites. *Nano Today*. 2010. **5**: 48.
[23] Teoh W.Y., Lutz M. Flame spray pyrolysis: An enabling technology for nanoparticles design and fabrication. *Nanoscale*. 2010.**2**: 1324.
[24] Weston J.S., Venkataramani D., Aichele C.P., Grady B.P., Harwell J., Resasco D. Pseudosolid, shear-thinning gel formation in binary dispersions of metal oxide nanoparticles at low volume fractions. *Langmuir*. 2014. **30**: 14982.
[25] Gun'ko V.M., Mironyuk I.F., Zarko V.I., Voronin E.F., Turov V.V., Pakhlov E.M., Goncharuk E.V., Nychiporuk Yu.M., Kulik T.V., Palyanytsya B.B., Pakhovchishin S.V., Vlasova N.N., Gorbik P.P., Mishchuk O.A., Chuiko A.A., Skubiszewska-Zięba J., Janusz W., Turov A.V., Leboda R. Morphology and surface properties of fumed silicas. *J. Colloid. Interface Sci.* 2005. **289**: 427.
[26] Gun'ko V.M., Nychiporuk Yu.M., Zarko V.I., Goncharuk E.V., Mishchuk O.A., Leboda R., Skubiszewska-Zięba J., Skwarek E., Janusz W., Yurchenko G.R., Osovskii V.D., Ptushinskii Y.G., Turov V.V., Gorbik P.P., Blitz J.P., Gude K. Relationships between surface compositions and properties of surfaces of mixed fumed oxides. *Appl. Surf. Sci.* 2007. **253**: 3215.
[27] Gun'ko V.M., Blitz J.P., Gude K., Zarko V.I., Goncharuk E.V., Nychiporuk Yu.M., Leboda R., Skubiszewska-Zięba J., Osovskii V.D., Ptushinskii Y.G., Mishchuk O.A., Pakhovchishin S.V., Gorbik P.P. Surface structure and properties of mixed fumed oxides. *J. Colloid. Interface. Sci*. 2007. **314**: 119.
[28] Gun'ko V.M., Zarko V.I., Turov V.V., Oranska O.I., Goncharuk E.V., Nychiporuk Yu.M., Pakhlov E.M., Yurchenko G.R., Leboda R., Skubiszewska-Zięba J., Osovskii V.D., Ptushinskii Y.G., Derzhypolskyi A.G., Melenevsky D.A., Blitz J.P. Morphological and structural features of individual and composite nanooxides with alumina, silica, and titania in powders and aqueous suspensions. *Powder Technology*. 2009. **195**: 245.
[29] Gun'ko V.M., Bogatyrev V.M., Borysenko M.V., Galaburda M.V., Sulim I.Y., Petrus L.V., Korduban O.M., Polshin E.V., Zaulychnyy Ya.V., Karpets M.V., Foya O.O., Myronyuk I.F., Chelyadyn V.L., Dzhura U.Ya., Leboda R., Skubiszewska-Zięba J., Blitz J.P. Morphological, structural and adsorptional features of oxide composites of different origin. *Applied Surface Science*. 2010. **256**: 5263.
[30] Gun'ko V.M., Yurchenko G.R., Turov V.V., Goncharuk E.V., Zarko V.I., Zabuga A.G., Matkovsky A.K., Leboda R., Skubiszewska-Zięba J., Janusz W., Phillips G.J., Mikhalovsky S.V. Adsorption of polar and nonpolar compounds onto complex nanooxides with silica, alumina, and titania. *J. Colloid Interface Sci*. 2010. **348**: 546.
[31] Park H.K., Park K.Y., Jung K.Y. Alumina-precursor nanoparticles prepared by partial hydrolysis of $AlCl_3$ vapor in tubular flow reactor: Effect of hydrolysis conditions on particle size distribution. *Ind. Eng. Chem. Res.* 2014. **53**: 10372.
[32] Dorigato A., Pegoretti A. The role of alumina nanoparticles in epoxy adhesives. *J. Nanopart. Res.* 2011. **13**: 2429.

[33] Sabzi M., Mirabedini S.M., Zohuriaan-Mehr J., Atai M. Surface modification of TiO_2 nano-particles with silane coupling agent and investigation of its effect on the properties of polyurethane composite coating. *Prog. Org. Coating.* 2009. **65**: 222.
[34] Rodríguez-Castellón E., Jiménez-López A., Maireles-Torres P., Jones D.J., Rozière J., Trombetta M., et al. Textural and structural properties and surface acidity characterization of mesoporous silica-zirconia molecular sieves. *J. Solid. State Chem.* 2003. **175**: 159.
[35] Liang S., Neisius N.M., Gaan S. Progress in organic coatings recent developments in flame retardant polymeric coatings. *Prog. Org. Coating.* 2013. **76**: 1642.
[36] Allahverdi A., Ehsani M., Janpour H., Ahmadi Sh. The effect of nanosilica on mechanical, thermal and morphological properties of epoxy coating. *Prog. Org. Coating.* 2012. **75**: 543.
[37] Iler R.K. *The Chemistry of Silica.* (Chichester: Wiley, 1979).
[38] Legrand A.P. (editor). *The Surface Properties of Silicas.* (New York: Wiley, 1998).
[39] Blitz J.P., Gun'ko V.M. (editors). *Surface Chemistry in Biomedical and Environmental Science. NATO Science Series II: Mathematics, Physics and Chemistry. Springer, Vol. 228*. (Dordrecht: Springer, 2006).
[40] Chuiko A.A. (editor). *Chemistry of Silica Surface.* (Kiev: UkrINTEI, 2001). [in Russian].
[41] Nicolais L., Borzacchiello A., Lee S.M. (editors). *Wiley Encyclopedia of Composite. Materials, 5-Volume set, 2nd ed.* (NJ: Wiley, Hoboken, 2012).
[42] Dodiuk H., Goodman S. (editors). *Handbook of Thermoset Plastics. Third Edition*. (UK: Oxford, Elsevier, 2014).
[43] Wicks Z.W., Jr, Jones F.N., Pappas S.P., Wicks D.A. *Organic Coatings: Science and Technology. Third Edition*. (New York: John Wiley & Sons, 2007).
[44] Ghosh S.K. (editor). *Functional Coatings.* (Weinheim: Wiley-VCH Verlag GmbH, 2006).
[45] Wu L., Baghdachi J. (editors). *Functional Polymer Coatings: Principles, Methods, and Applications. First Edition.* (New York: John Wiley & Sons, 2015).
[46] Gun'ko V.M., Turov V.V., Zarko V.I., Pakhlov E.M., Matkovsky A.K., Oranska O.I., Palyanytsya B.B., Remez O.S., Nychiporuk Yu.M., Ptushinskii Y.G., Leboda R., Skubiszewska-Zięba J. Cryogelation of individual and complex nanooxides under different conditions. *Colloids Surf. A: Physicochem. Eng. Aspects.* 2014. **456**: 261.
[47] Gun'ko V.M., Zarko V.I., Pakhlov E.M., Matkovsky A.K., Remez O.S., Charmas B., Skubiszewska-Zięba J. Low-temperature high-pressure cryogelation of nanooxides. *Journal of Sol-Gel Science and Technology.* 2015. **74**: 45.
[48] Gun'ko V.M., Ilkiv V.Ya., Zaulychnyy Ya.V., Zarko V.I., Pakhlov E.M., Karpetz MV. Structural features of fumed silica and alumina alone, blend powders and fumed binary systems. *J. Non-Crystal Solid.* 2014: **403**: 30.
[49] Gun'ko V.M., Zaulychnyy Ya.V., Ilkiv BI, Zarko V.I., Nychiporuk Yu.M., Ptushinskii Yu.G., Pakhlov E.M., Leboda R., Skubiszewska-Zięba J. Textural and electronic characteristics of mechanochemically activated composites with nanosilica and activated carbon. *Appl. Surf. Sci.* 2011: **258**: 1115.
[50] Ertl G., Knozinger H., Weitkamp J. (editors). *Handbook of Heterogeneous Catalysis.* (Weinheim: VCH Verlagsgesellschaft mbH, 1997).
[51] Busca G. *Heterogeneous Catalytic Materials: Solid State Chemistry, Surface Chemistry and Catalytic Behaviour.* (Amsterdam: Elsevier, 2014).
[52] Regalbuto J. (editor). *Catalyst Preparation: Science and Engineering.* (Boca Raton: CRC Press, 2007).
[53] Gun'ko V.M., Turov V.V. *Nuclear Magnetic Resonance Studies of Interfacial Phenomena.* (Boca Raton: CRC Press, 2013).
[54] Pietsch W. *Agglomeration in Industry.* (Weinheim: Wiley-VCH Verlag GmbH, 2005).
[55] Sandkühler P., Lattuada M., Wu H., Sefcik J., Morbidelli M. Further insights into the universality of colloidal aggregation. *Adv. Colloid Interface Sci.* 2005. **113**: 65.
[56] Schießl K., Babick F., Stintz M. Calculation of double layer interaction between colloidal aggregates. *Advanced Powder Technology.* 2012. **23**: 139.
[57] Karlsson H.L., Toprak M.S., Fadeel B. Toxicity of metal and metal oxide nanoparticles. In: Nordberg G.F., Fowler B.A., Nordberg M. (editors). *Handbook on the Toxicology of Metals. Fourth Edition*. (Amsterdam: Elsevier, 2015, pp. 75-112).

[58] Bolis V., Busco C., Ciarletta M., Distasi C., Erriquez J., Fenoglio I., Livraghi S., Morel S. Hydrophilic/hydrophobic features of TiO_2 nanoparticles as a function of crystal phase, surface area and coating, in relation to their potential toxicity in peripheral nervous system. *J. Colloid Interface Sci*. 2012. **369**: 28.
[59] Theodore L., Kunz R.G. *Nanotechnology: Environmental Implications and Solutions.* (NJ: Hoboken, John Wiley & Sons, 2005).
[60] Theodore L. *Nanotechnology: Basic Calculations for Engineers and Scientists.* (NJ: Hoboken, John Wiley & Sons, 2006).
[61] Mills A. The freezing bomb. *Phys. Education.* 2010. **45**: 153.
[62] Vidovskii A.L. Experimental determination of pressure during ice expansion. *Hydrotechnical Construction.* 1972. **6**: 791.
[63] Gun'ko V.M., Turov V.V., Zarko V.I., Pakhlov E.M., Prykhod'ko G.P., Remez O.S., Leboda R., Skubiszewska-Zięba J., Blitz J.P. High-pressure cryogelation of nanosilica and surface properties of cryosilicas. *Colloids Surf. A: Physicochem. Eng. Aspects.* 2013. **436**: 618.
[64] Gun'ko V.M., Zarko V.I., Turov V.V., Leboda R., Chibowski E. The effect of second phase distribution in disperse X/silica (X= Al_2O_3, TiO_2, and GeO_2) on its surface properties. *Langmuir.* 1999. **15**: 5694.
[65] Gun'ko V.M., Turov V.V., Zarko V.I., Voronin E.F., Tischenko V.A., Dudnik V.V., Pakhlov E.M., Chuiko A.A. Active site nature of pyrogenic alumina/silica and water bound to surfaces. *Langmuir.* 1997. **13**: 1529.
[66] Gun'ko V.M., Zarko V.I., Turov V.V., Voronin E.F., Tischenko V.A., Chuiko A.A. Dielectric properties and dynamic simulation of water bound to titania/silica surfaces. *Langmuir.* 1995. **11**: 2115.
[67] Gun'ko V.M., Zarko V.I., Chibowski E., Dudnik V.V., Leboda R., Zaets V.A. Structure of fumed titania and silica/titania and influence of the nature of surface sites on interaction with water. *J. Colloid Interface Sci.* 1997. **188**: 39.
[68] Gun'ko V.M., Mironyuk I.F., Zarko V.I., Turov V.V., Voronin E.F., Pakhlov E.M., Goncharuk E.V., Leboda R., Skubiszewska-Zięba J., Janusz W., Chibowski S., Levchuk Yu.N., Klyueva A.V. Fumed silicas possessing different morphology and hydrophilicity. *J. Colloid Interface Sci.* 2001. **242**: 90.
[69] Gun'ko V.M., Turov V.V., Zarko V.I., Goncharuk E.V., Gerashchenko I.I., Turova A.A., Mironyuk I.F., Leboda R., Skubiszewska-Zięba J., Janusz W. Comparative characterization of polymethylsiloxane hydrogel and silylated fumed silica and silica gel. *J Colloid Interface Sci*. 2007. **308**: 142.
[70] Blitz J.P., Christensen J.M., Gun'ko V.M. Silica surface modification reactions with aluminum and boron alkyls and (alkyl) chlorides: reactivities and surface nanostructures. *J. Nanoscience & Nanotechnology.* 2008. **8**: 660.
[71] Frei R., Blitz J.P., Gun'ko V.M., Frost B.E., Sergeev V.S. Kinetics and computational studies of an aminosilane reaction with a silsesquioxane silanol. *J. Phys. Chem. A*. 2009. **113**: 6612.
[72] Gun'ko V.M., Turov V.V., Myronyuk I.F., Goncharuk O.V., Pakhlov E.M., Bezruka N.A., , Skwarek E., Janusz W., Blitz J.P. Interfacial phenomena at a surface of partially silylated nanosilica. *J. Colloid Interface Sci.* 2014. **434**(15): 28.
[73] Blitz J.P., Gun'ko V.M., Samala R., Lawrence B.A. Mixed bifunctional surface-modified silicas using tethered aminofunctional silane catalysts. *Colloids Surf. A: Physicochem. Eng. Aspects.* 2014. **462**: 1.
[74] Terpilowski K., Rymuszka D., Goncharuk O.V., Sulym I.Y., Gun'ko V.M. Wettability of modified silica layers deposited on glass support activated by plasma. *Appl. Surf. Sci.* 2015. **353**: 843.
[75] Gun'ko V.M., Voronin E.F., Nosach L.V., Turov V.V., Wang Z., Vasilenko A.P., Leboda R., Skubiszewska-Zięba J., Janusz W., Mikhalovsky S.V. Structural, textural and adsorption characteristics of nanosilica mechanochemically activated in different media. *J. Colloid. Interface Sci.* 2011. **355**: 300.
[76] Zaulychnyy Ya.V., Gun'ko V.M., Yavorskyi Y.V., Zarko V.I., Petrovska S.S., Mischenko V.N. Effect of mechanical activation of highly disperse SiO_2/α-Fe_2O_3 mixtures on distribution of valence electrons. *Metallofizika i Noveishie Tekhnologii.* 2015. **37**: 1063.
[77] Sulim I.Y., Borysenko M.V., Korduban O.M., Gun'ko V.M. Influence of silica matrix morphology on characteristics of grafted nanozirconia. *Appl. Surf. Sci.* 2009. **255**: 7818.
[78] Boratyrev V.M., Gun'ko V.M., Galaburda M.V., Borysenko M.V., Pokrovsky V.A., Oranska O.I., Polshin E.V., Korduban O.M., Leboda R., Skubiszewska-Zięba J. Synthesis and characterization of Fe_2O_3/SiO_2 nanocomposites. J. Colloid Interface Sci. 2009. **338**: 376.

[79] Gun'ko V.M., Bogatyrev V.M., Leboda R., Skubiszewska-Zięba J., Petrus L.V., Nychiporuk Yu.M., Oranska O.I., Dudarko O.A., Osovskii V.D., Ptushinskii Y.G. Titania deposits on nanosilicas. *Annales Universitatis Marie Curie-Sklodowska Sectio Chemia.* 2009. **64**: 21.
[80] Gun'ko V.M., Bogatyrov V.M., Oranska O.I., Borysenko LI, Skubiszewska-Zięba J., Książek A., Leboda R. **S**tructural features of Zn_xO_y/nanosilica composites. *Appl. Surf. Sci.* 2013. **276**: 802.
[81] Nazarkovsky M.A., Gun'ko V.M., Zarko V.I., Skwarek E., Skubiszewska-Zięba J., Leboda R., Janusz W. Textural characteristics of SnO_2-doped titania/nanosilica and transition of phase of bound water. *Journal of Chemical Technology and Metallurgy (Sofia, Bulgaria).* 2013. **48**: 373.
[82] Sulym I., Goncharuk O., Skwarek E., Sternik D., Borysenko M.V., Derylo-Marczewska A., Janusz W., Gun'ko V.M. Silica-supported ceria–zirconia and titania–zirconia nanocomposites: Structural characteristics and electrosurface properties. *Colloids Surf. A: Physicochem. Eng. Aspects.* 2015. **482**: 631.
[83] Myronyuk L.I., Myronyuk I.F., Chelyadyn V.L., Sachko V.M., Nazarkovsky M.A., Leboda R., Skubiszewska-Zięba J., Gun'ko V.M. Structural and morphological features of crystalline nanotitania synthesized in different aqueous media. *Chem. Phys. Lett.* 2013. **583**: 103
[84] Adamson A.W., Gast A.P. *Physical Chemistry of Surface. Sixth edition.* (New York: Wiley, 1997).
[85] Gregg S.J., Sing K.S.W. *Adsorption, Surface Area and Porosity.* (London: Academic Press, 1982).
[86] Gun'ko V.M. Composite materials: textural characteristics. *Applied Surface Sci.* 2014. **307**: 444.
[87] Schmidt M.W., Baldridge K.K., Boatz J.A., Elbert S.T., Gordon M.S., Jensen J.H., Koseki S., Matsunaga N., Nguyen K.A., Su S.J., Windus T.L., Dupuis M., Montgomery J.A. General atomic and molecular electronic structure system. *J. Comput. Chem.* 1993. **14**: 1347.
[88] Gun'ko V.M., Leboda R., Skubiszewska-Zięba J. Heating effects on morphological and textural characteristics of individual and composite nanooxides. *Adsorption.* 2009. **15**: 89.
[89] Gun'ko V.M., Skubiszewska-Zięba J., Leboda R., Khomenko K.N., Kazakova O.A., Povazhnyak M.O., Mironyuk I.F. Influence of morphology and composition of fumed oxides on changes in their structural and adsorptive characteristics on hydrothermal treatment at different temperatures. *J. Colloid Interface Sci.* 2004. **269**: 403.
[90] Gun'ko V.M., Zarko V.I., Goncharuk O.V., Matkovsky A.K., Remez O.S., Skubiszewska-Zięba J., Wojcik G., Walusiak B., Blitz J.P. Nature and morphology of fumed oxides and features of interfacial phenomena. *Appl. Surf. Sci.* 2016. **366**: 410.
[91] Gun'ko V.M., Turov V.V., Zarko V.I., Pakhlov E.M., Charmas B., Skubiszewska-Zięba J. Influence of structural organization of silicas on interfacial phenomena. *Colloids Surf. A: Physicochem. Eng. Aspects.* 2016. **492**: 230.
[92] Nishihara H., Mukai S.R., Fujii Y., Tago T., Masuda T., Tamon H. Preparation of monolithic SiO_2–Al_2O_3 cryogels with inter-connected macropores through ice template. *J. Mater. Chem.* 2006. **16**: 3231.
[93] Nishihara H., Iwamura S., Kyotani T. Synthesis of silica-based porous monoliths with straight nanochannels using an ice-rod nanoarray as a template. *J. Mater. Chem.* 2008. **18**: 3662.
[94] Mukai S.R., Nishihara H., Tamon H. Porous microfibers and microhoneycombs synthesized by ice templating. *Catal. Surv. Asia.* 2006. **10**: 161.
[95] Nishihara H., Mukai S.R., Shichi S., Tamon H. Preparation of titania–silica cryogels with controlled shapes and photocatalysis through unidirectional freezing. *Materials Letters.* 2010. **64**: 959.
[96] Mukai S.R., Nishihara H., Shichi S., Tamon H. Preparation of porous TiO_2 cryogel fibers through unidirectional freezing of hydrogel followed by freeze-drying. *Chem. Mater.* 2004. **16**: 4987.
[97] Shlyakhtin OA, Oh Y-J. Inorganic cryogels for energy saving and conversion. *J. Electroceram.* 2009. **23**: 452.
[98] Pons A., Casas Ll., Estop E., Molins E., Harris K.D.M., Xu M. A new route to aerogels: Monolithic silica cryogels. *J. Non-Crystal Solid.* 2012. **358**: 461.
[99] Tamon H., Akatsuka T., Mori H., Sano N. Synthesis of zeolite monolith with hierarchical micro/macropores by ice-templating and steam-assisted crystallization. *Chem. Eng. Trans.* 2013. 32: 2059.
[100] Chen L., Ye G., Xu D., Zhu L., Lu Z., Dong L., Liu Y. Chemical bond change of gibbsite and fumed silica mixture during mechanic al activation. Materials Letters. 2012. **85**: 91.

[101] Gun'ko V.M., Goncharuk O.V., Goworek J. Evaporation of polar and nonpolar liquids from silica gels and fumed silica. Colloids Surf. A: Physicochem. Eng. Aspects. 2015. **474**: 52.
[102] Voronin E.F., Gun'ko V.M., Guzenko N.V., Pakhlov E.M., Nosach L.V., Malysheva M.L., Skubiszewska-Zięba J., Leboda R., Borysenko M.V., Chuiko A.A. Interaction of poly(ethylene oxide) with fumed silica. *J. Colloid Interface Sci.* 2004. **279**: 326.
[103] Gun'ko V.M., Turov V.V., Leboda R., Zarko V.I., Skubiszewska-Zięba J., Charmas B. Adsorption, NMR and thermally stimulated depolarization current methods for comparative analysis of heterogeneous solid and soft materials. *Langmuir.* 2007. **23**: 3184.
[104] Gun'ko V.M., Turov V.V., Bogatyrev V.M., Petin A.Y., Turov A.V., Trachevskyi V.V., Blitz J.P. The influence of pre-adsorbed water on adsorption of methane on fumed and nanoporous silicas. *Appl. Surf. Sci.* 2011. **258**: 1306.
[105] Kiselev A.V., Lygin V.I. *Infrared Spectra of Surface Compounds.* (New York: Wiley, 1975).
[106] McCool B., Murphy L., Tripp C.P. A simple FTIR technique for estimating the surface area of silica powders and films. *J. Colloid Interface Sci.* 2006. **295**: 294.
[107] Gun'ko V.M., Leboda R., Skubiszewska-Zięba J., Goncharuk E.V., Nychiporuk Yu.M., Zarko V.I., Blitz J.P. Influence of different treatments on characteristics of nanooxide powders alone or with adsorbed polar polymers or proteins. *Powder Technology.* 2008. **187**: 146.
[108] Gude K., Gun'ko V.M., Blitz J.P. Adsorption and photocatalytic decomposition of methylene blue on surface modified silica and silica-titania. *Colloids Surf. A: Physicochem. Eng. Aspects.* 2008. **325**: 17.
[109] Gun'ko V.M., Blitz J.P., Zarko V.I., Turov V.V., Pakhlov E.M., Oranska O.I., Goncharuk E.V., Gornikov Y.I., Sergeev V.S., Kulik T.V., Palyanytsya B.B., Samala R.K. Structural and adsorption characteristics and catalytic activity of titania and titania-containing nanomaterials. *J. Colloid Interface Sci.* 2009. **330**: 125.
[110] Silberberg M.A. *Chemistry – The Molecular Nature of Matter and Change. Fourth edition*. (New York: McGraw-Hill, 2006).
[111] Ashgriz V. (editor). *Handbook of Atomization and Sprays*. (Heidelberg: Springer, 2011).
[112] Fujikawa S., Yano T., Watanabe M. *Vapor-Liquid Interfaces, Bubbles and Droplets.* (Heidelberg: Springer, 2011).
[113] McElroy M.B. *The Atmospheric Environment.* (Princeton: Princeton University Press, 2002).
[114] Ahsan A. (editor), *Evaporation, Condensation and Heat Transfer.* (Rijeka: InTech, Croatia, 2010).
[115] Sazhin S.S. *Droplets and Sprays.* (London: Springer, 2014).
[116] Chapman S., Cowling T.G. *The Mathematical Theory of Nonuniform Gases.* (Cambridge: Cambridge University Press, 1970).
[117] Tamim J., Hallett W.L.H. A continuous thermodynamics model for multicomponent droplet vaporization. *Chem. Eng. Sci.* 1995. **50**: 2933.
[118] Lippert A.M., Reitz R.D. Modeling of multicomponent fuels using continuous distributions with application to droplet evaporation and sprays. SAE Technical Paper 1997, 972882.
[119] Hallett W.L.H. A simple model for the vaporization of droplets with large numbers of components. *Combustion and Flame.* 2000. **121**: 334.
[120] Zhu G.-S., Reitz R..D. A model for high-pressure vaporization of droplets of complex liquid mixtures using continuous thermodynamics. *Int. J. Heat Mass Transf.* 2002. **45**: 495.
[121] Derkachov G., Kolwas K., Jakubczyk D., Zientara M., Kolwas M. Drying of a microdroplet of water suspension of nanoparticles: from surface aggregates to microcrystal. *J. Phys. Chem. C.* 2008. **112**: 16919.
[122] Sefiane K., Ward C.A. Recent advances on thermocapillary flows and interfacial conditions during the evaporation of liquids. *Adv. Colloid Interface Sci.* 2007. **134–135**: 201.
[123] Erbil H.Y. Evaporation of pure liquid sessile and spherical suspended drops: a review. *Adv. Colloid Interface Sci.* 2012. **170**: 67.
[124] Erbil H.Y. Control of stain geometry by drop evaporation of surfactant containing dispersions. *Adv. Colloid Interface Sci.* 2015. **222**: 275.
[125] Sokolowski S., Fischer J. Liquid-vapour' density profiles for fluids in pores from density functional theory. *J. Chem. Soc. Faraday Trans.* 1993. **89**: 789.

[126] Bucior K., Yelash L., Binder K. Molecular-dynamics simulation of evaporation processes of fluid bridges confined in slitlike pores. Phys. Rev. E. 2009. **79**: 031604 (1-12).
[127] Morishige K., Shikimi M. Adsorption hysteresis and pore critical temperature in a single cylindrical pore. *J. Chem. Phys.* 1998. **108**: 7821.
[128] Paulik F., Paulik J. Investigations under quasi-isothermal and quasi-isobaric conditions by means of the Derivatograph. *J. Thermal Anal.* 1973. **5**: 253.
[129] Meyers R.A. (editor). *Encyclopedia of Analytical Chemistry.* (Chichester: John Wiley & Sons Ltd., 2000).
[130] Haines P.J. (editor). *Principles of Thermal Analysis & Calorimetry. Ch. 4.* (Cambridge: Royal Society of Chemistry, 2002).
[131] Semenov S., Trybala A., Rubio R.G., Kovalchuk N., Starov V., Velarde M.G. Simultaneous spreading and evaporation: recent developments. Adv. Colloid Interface Sci. 2014. **206**: 382.
[132] Frisch M.J., Trucks G.W., Schlegel H.B., Scuseria G.E., Robb M.A., Cheeseman J.R, Scalmani G, Barone V, Mennucci B, Petersson GA, Nakatsuji H, Caricato M, Li X, Hratchian HP, Izmaylov AF, Bloino J, Zheng G, Sonnenberg JL, Hada M, Ehara M, Toyota K, Fukuda R, Hasegawa J, Ishida M, Nakajima T, Honda Y, Kitao O, Nakai H, Vreven T, Montgomery JA Jr, Peralta JE, Ogliaro F, Bearpark M, Heyd JJ, Brothers E, Kudin KN, Staroverov VN, Kobayashi R, Normand J, Raghavachari K, Rendell A, Burant J C, Iyengar SS, Tomasi J, Cossi M, Rega N, Millam JM, Klene M, Knox JE, Cross JB, Bakken V, Adamo C, Jaramillo J, Gomperts R, Stratmann RE, Yazyev O, Austin AJ, Cammi R, Pomelli C, Ochterski JW, Martin RL, Morokuma K, Zakrzewski VG, Voth GA, Salvador P, Dannenberg JJ, Dapprich S, Daniels AD, Farkas Ö, Foresman JB, Ortiz JV, Cioslowski J, Fox DJ. Gaussian, Inc., Wallingford CT, 2009., Gaussian 09, Revision D.01, Gaussian, Inc., Wallingford CT; 2013.
[133] Chai J.-D., Head-Gordon M. Long-range corrected hybrid density functionals with damped atom-atom dispersion corrections. *Phys. Chem. Chem. Phys.* 2008. **10**: 6615.
[134] Yang K., Zheng J., Zhao Y., Truhlar D.G. Tests of the RPBE, revPBE, τ-HCTHhyb, ωB97X-D, and MOHLYP density functional approximations and 29 others against representative databases for diverse bond energies and barrier heights in catalysis. *J. Chem. Phys.* 2010. **132**: 164117.
[135] Marenich A.V., Cramer C.J., Truhlar D.G. Universal solvation model based on solute electron density and on a continuum model of the solvent defined by the bulk dielectric constant and atomic surface tensions. *J. Phys. Chem. B.* 2009. **113**: 6378.
[136] Becke A.D. Perspective: Fifty years of density-functional theory in chemical physics. *J. Chem. Phys.* 2014. **140**: 18A301.
[137] Ho J., Coote M.L., Cramer C.J., Truhlar D.G. Theoretical calculations of reduction potentials. In : Hammerich O., Speiser B (editors). *Organic Electrochemistry. Fifth Edition*. (Boca Raton: CRC Press, 2016, pp. 229-59).
[138] Gun'ko V.M., Nasiri R., Sazhin S.S., Lemoine F., Grisch F. A quantum chemical study of the processes during the evaporation of real-life Diesel fuel droplets. *Fluid Phase Equilibria.* 2013. **356**: 146.
[139] Gun'ko V.M., Nasiri R., Sazhin S.S. A study of the evaporation and condensation of n-alkane clusters and nanodroplets using quantum chemical methods. *Fluid Phase Equilibria.* 2014. **366**: 99.
[140] Ortega I.K., Kupiainen O., Kurtén T., Olenius T., Wilkman O., McGrath M.J., Loukonen V., Vehkamäki H. From quantum chemical formation free energies to evaporation rates. *Atmos. Chem. Phys.* 2012. **12**: 225.
[141] Kupiainen O., Ortega I.K., Kurtén T., Vehkamäki H. Amine substitution into sulfuric acid – ammonia clusters. *Atmos. Chem. Phys.* 2012. **12**: 3591.
[142] Beverley K.J., Clint J.H., Fletcher P.D.I., Thubron S. Evaporation rates of water contained within porous silica particles. *Phys. Chem. Chem. Phys.* 1999. **1**: 909.
[143] Yaws C.L. (editor). *Thermophysical Properties of Chemicals and Hydrocarbons.* (NY: William Andrew Inc., Norwich, 2008).
[144] Gun'ko V.M., Nasiri R., Sazhin S.S. Effects of the surroundings and conformerisation of n-dodecane molecules on evaporation/condensation processes. *J. Chem. Phys.* 2015. **142**: 034502.

[145] Goworek J., Stefaniak W., Prudaczuk M. The influence of polarity of liquids on the parameters characterizing the porosity of silica gels estimated by thermogravimetric analysis. *Thermochimica Acta.* 2001. **379**: 117.
[146] Singh M.P., Singh R.K., Chandra S. Ionic liquids confined in porous matrices: Physicochemical properties and applications. *Prog. Mater. Sci.* 2014. **64**: 73.
[147] Gubbins K.E., Long Y., Sliwinska-Bartkowiak M. Thermodynamics of confined nano-phases. *J. Chem. Thermodynamics.* 2014. **74**: 169.
[148] Wang L., Yu Q. Methane adsorption on porous nano-silica in the presence of water: An experimental and ab initio study. J. Colloid Interface Sci. 2016. **467**: 60.
[149] Gun'ko V.M., Sulym I.Y., Borysenko M.V., Turov V.V. Interfacial behavior of water bound to zirconia/nanosilica with adsorbed poly(dimethylsiloxane). *Colloids Surf. A: Physicochem. Eng. Aspects.* 2013. **426**: 47.
[150] Stewart J.J.P. MOPAC 2016, Stewart Computational Chemistry, Colorado Springs, CO, USA, http://openmopac.net/, 2019.
[151] Stewart J.J.P. Optimization of parameters for semiempirical methods VI: more modifications to the NDDO approximations and re-optimization of parameters. *J. Mol. Mod.* 2013. **19**: 1.
[152] Maia J.D.C., Carvalho G.A.U., Mangueira C.P. Jr., Santana S.R., Cabral L.A.F., Rocha G.B. GPU linear algebra libraries and GPGPU programming for accelerating MOPAC semiempirical quantum chemistry calculations. *J. Chem. Theory Comput.* 2012. **8**: 3072.
[153] Cheeseright T., Mackey M., Rose S., Vinter J.G. Molecular field technology applied to virtual screening and finding the bioactive conformation. *Expert. Opin. Drug. Discov.* 2007. **2**: 131.
[154] Cheeseright T., Mackey M., Rose S., Vinter J.G. Molecular field extrema as descriptors of biological activity: definition and validation. *J. Chem. Inf. Model.* 2006. **46**: 665.
[155] Dennington R., Keith T., Millam J. GaussView, Version 5.0.9, Semichem Inc., Shawnee Mission KS; 2009.
[156] Zhurko G.A, Zhurko D.A. Chemcraft (version 1.8), 2019, http://www.chemcraftprog.com.
[157] Pettersen E.F., Goddard T.D., Huang C.C., Couch G.S., Greenblatt D.M., Meng E.C., Ferrin T.E. UCSF Chimera--a visualization system for exploratory research and analysis. *J. Comput. Chem.* 2004. **25**: 1605.
[158] Turov V.V., Gun'ko V.M., Zarko V.I., Goncharuk O.V., Krupska T.V., Turov A.V., Leboda R., Skubiszewska-Zięba J. Interfacial behavior of n-decane bound to weakly hydrated silica gel and nanosilica over a broad temperature range. *Langmuir.* 2013. **29**: 4303.
[159] Takei T., Mukasa K., Kofuji M., Fuji M., Watanabe T., Chikazawa M., Kanazawa T. Changes in density and surface tension of water in silica pores. *Colloid Polym. Sci.* 2000. **278**: 475.
[160] Petch H.E. The hydrogen positions in portlandite, $Ca(OH)_2$, as indicated by the electron distribution. *Acta Crystallogr.* 1961. **14**: 950.
[161] Desgranges L., Grebille D., Calvarin G., Chevrier G., Floquet N., Niepce J.C. Hydrogen thermal motion in calcium hydroxide: $Ca(OH)_2$. *Acta Crystallogr. Sect. B: Struct. Sci.* 1993. **49**: 812.
[162] Jennings H. Refinements to colloidal model of C–S–H in cement: CM-II. *Cem. Concr. Res.* 2008. **38**: 275.
[163] Famy C., Scrivener K.L., Atkinson A. Effects of an early or a late heat treatment on the microstructure and composition of inner C–S–H products of Portland cement mortars. *Cem. Concr. Res.* 2002. **32**: 269.
[164] Nonat A. The structure and stoichiometry of C–S–H. *Cem. Concr. Res.* 2004. **34**: 1521.
[165] Gallucci E., Zhang X., Scrivener K.L. Effect of temperature on the microstructure of calcium silicate hydrate (C–S–H). *Cem. Concr. Res.* 2013. **53**: 185.
[166] Muller A.C.A., Scrivener K.L., J. Skibsted J., Gajewicz A.M., McDonald P.J. Influence of silica fume on the microstructure of cement pastes: New insights from ^{1}H NMR relaxometry. *Cement and Concrete Research.* 2015. **74**: 116.
[167] Zhu W., Zhou Y., Ma W., Li M., Yu J., Xie K. Using silica fume as silica source for synthesizing spherical ordered mesoporous silica. *Materials Letters.* 2013. 92129.
[168] Gun'ko V.M., Zarko V.I., Mironyuk I.F., Goncharuk E.V., Guzenko N.V., Borysenko M.V., Gorbik P.P., Mishchuk O.A., Janusz W., Leboda R., Skubiszewska-Zięba J., Grzegorczyk W., Matysek M.,

Chibowski S. Surface electric and titration behaviour of fumed oxides. *Colloids Surf. A: Physicochem. Eng. Aspects.* 2004. **240**: 9.
[169] Gun'ko V.M., Zarko V.I., Turov V.V., Goncharuk E.V., Nychiporuk Yu.M., Turova A.A., Gorbik P.P., Leboda R., Skubiszewska-Zięba J., Pissis P., Blitz J.P. Regularities in the behaviour of nanooxides in different media affected by surface structure and morphology of particles. In: Shpak A.P., Gorbyk P.P. (editors). *Nanomaterials and Supramolecular Structures.* (Dordrecht: Springer, 2010, pp. 93-118).
[170] Gun'ko V.M., Andriyko L.S., Zarko V.I., Marynin A.I., Olishevskiy V.V., Janusz W. Effects of chlorides of alkaline metals on the behavior of nanosilica in aqueous media. *Central Eur. J. Chem.* 2014. **12**(4): 480.
[171] Andriyko L.S., Zarko V.I., Gun'ko V.M., Marynin A.I., Olishevskiy V.V., Skwarek E., Janusz W. Electrical and physical characteristics of silica nanoparticles in aqueous media affected by cations Na^{+}, Ba^{2+} and Al^{3+}. *Adsorption Science & Technology.* 2015. **33**: 601.
[172] Janusz W., Skwarek E., Zarko V.I., Gun'ko VM. Structure of electrical double layer at the Al_2O_3-SiO_2/electrolyte solution interface. *Physicochemical Problems of Mineral Processing.* 2007. **41**: 215.
[173] Skwarek E., Matysek-Nawrocka M., Janusz W., Zarko V.I., Gun'ko V.M. Adsorption of heavy metal ions at the Al_2O_3-SiO_2/$NaClO_4$ electrolyte interface. *Physicochemical Problems of Mineral Processing.*2008. **42**: 153.
[174] Wiśniewska M., Terpiłowski K., Chibowski S., Chibowski E., Urban T., Zarko V.I., Gun'ko V.M. Effect of polyacrylic acid (PAA) adsorption on stability of mixed alumina ‑ silica oxide suspension. Powder Technology. 2013. **233**: 190.
[175] Wiśniewska M., Terpiłowski K., Chibowski S., Urban T., Zarko V.I., Gun'ko V.M. Effect of solution pH on the stability of mixed silica -alumina suspension in the presence of polyacrylic acid (PAA) with different molecular weights. *Central Eur. J. Chem.* 2013. **11**: 101.
[176] Wiśniewska M., Terpiłowski K., Chibowski S., Chibowski E., Urban T., Zarko V.I., Gun'ko V.M. Stability of colloidal silica modified by macromolecular polyacrylic acid (PAA) – application of turbidymetry method. *J. Macromol. Sci. Part A: Pure Appl. Chem.* 2013. **50**: 639.
[177] Wiśniewska M., Urban T., Grządka E., Zarko V.I., Gun'ko V.M. Comparison of adsorption affinity of polyacrylic acid for surfaces of mixed silica–alumina. Colloid Polym. Sci. 2014. **292**: 699.
[178] Wiśniewska M., Urban T., Nosal-Wiercińska A., Zarko V.I., Gun'ko V.M. Comparison of stability properties of poly(acrylic acid) adsorbed on the surface of silica, alumina and mixed silica-alumina nanoparticles - Application of turbidimetry method. *Central Eur. J. Chem.* 2014. **12**: 476.
[179] Wiśniewska M., Terpiłowski K., Chibowski S., Urban T., Zarko V.I., Gun'ko V.M. Investigation of stabilization and destabilization possibilities of water alumina suspension in polyelectrolyte presence. *International Journal of Mineral Processing.* 2014. **132**: 34.
[180] Wiśniewska M., Ostolska I., Szewczuk-Karpisz K., Chibowski S., Terpiłowski K., Gun'ko V.M., Zarko V.I. Investigation of the polyvinyl alcohol stabilization mechanism and adsorption properties on the surface of ternary mixed nanooxide AST 50 (Al_2O_3–SiO_2–TiO_2). *Journal of Nanoparticle Research.* 2015. **17**: 14.
[181] Wiśniewska M., Szewczuk-Karpisz K., Ostolska I., Urban T., Terpiłowski K., Zarko V.I., Gun'ko V.M. Effect of polyvinyl alcohol adsorption on the mixed alumina–silica–titania suspension stability. *Journal of Industrial and Engineering Chemistry.* 2015. **23**: 265. http://dx.doi.org/10.1016/j.jiec.2014.08.027.
[182] Wawrzkiewicz M., Wiśniewska M., Gun'ko V., Zarko V. Adsorptive removal of acid, reactive and direct dyes from aqueous solutions and wastewater using mixed silica-alumina oxide. *Powder Technology.* 2015. **278**: 306.
[183] Grządka E., Wiśniewska M., Gun'ko V.M., Zarko V.I. Adsorption, electrokinetic and stabilizing properties of the system: guar gum/surfactant/alumina. *Journal of Sufractants and Detergents.* 2015. **18**: 445.
[184] Blitz I.P., Blitz J.P., Gun'ko V.M., Sheeran D.J. Functionalized silicas: structural characteristics and adsorption of Cu(II) and Pb(II). *Colloids Surf. A: Physicochem Eng Aspects.* 2007. **307**: 83.
[185] Kothalawala N., Blitz J.P., Gun'ko V.M., Jaroniec M., Grabicka B., Semeniuc R.F. Post-synthesis surface modified silicas as adsorbents for heavy metal ion contaminants Cd(II), Cu(II), Cr(III), and Sr(II) in aqueous solutions. *J. Colloid Interface Sci.* 2013. **392**: 57.

[186] Gun'ko V.M., Blitz J.P., Bandaranayake B., Pakhlov E.M., Zarko V.I., Sulym I.Ya., Kulyk K.S., Galaburda M.V., Bogatyrev V.M., Oranska O.I., Borysenko M.V., Leboda R., Skubiszewska-Zięba J., Janusz W. Structural characteristics of mixed oxides MO_x/SiO_2 affecting photocatalytic decomposition of methylene blue. *Appl. Surf. Sci.* 2012. **258**: 6288.
[187] Rahni M.T., Karbaschi M., Miller R. (editors). *Computational Methods for Complex Liquid-Fluid Interfaces*. (CRC Press, Boca Raton; 2015).
[188] Zhan C., Chen F., Yang J., Dai D., Cao X., Zhong M. Visible light responsive sulfated rare earth doped TiO_2/fumed SiO_2 composites with mesoporosity: Enhanced photocatalytic activity for methyl orange degradation. *J. Hazard Mater.* 2014. **267**: 88–97.
[189] Yu Y., Wang J., Parr J.F. Preparation and properties of TiO_2/fumed silica composite photocatalytic materials. *Procedia Eng.* 2012. **27**: 448.
[190] Diamanti M.V., Ormellese M., Marin E., Lanzutti A., Mele A., Pedeferri M.P. Anodic titanium oxide as immobilized photocatalyst in UV or visible light devices. *J. Hazard Mater.* 2011. **186**: 2103.
[191] Bokare A., Pai M., Athawale A.A. Surface modified Nd doped TiO_2 nanoparticles as photocatalysts in UV and solar light irradiation. *Solar Energy.* 2013. **91**: 111.
[192] Zhan C.C., Chen F., Dai H.H., Yang J.T., Zhong M.Q. Photocatalytic activity of sulfated Mo-doped TiO_2/fumed SiO_2 composite: a mesoporous structure for methyl orange degradation. *Chem. Eng. J.* 2013. **225**: 695.
[193] Goncharuk E.V., Mishchenko V.N., Zarko V.I., Gun'ko V.M. Effect of the composition and structure of titanosilicas on their photocatalytic activity in the decomposition of methylene blue. *Theor. Experim. Chem.* 2006. **42**: 26.
[194] Jaroenworaluck A., Pijarn N., Kosachan N., Stevens R. Nanocomposite TiO_2–SiO_2 gel for UV absorption. *Chem. Eng. J.* 2012. **181–182**: 45.
[195] Provencher SW. A constrained regularization method for inverting data represented by linear algebraic or integral equations. *Comp. Phys. Comm.* 1982. **27**: 213.
[196] Laidler K.J., Meiser J.H. *Physical Chemistry.* (Menlo Park CA: Benjamin/Cummings, 1982).
[197] Fujishima A., Hashimoto K., Wanable H. *TiO_2 Photocatalysis: Fundamentals and Applications.* (Tokyo, Japan: BKC Inc., 1997).
[198] Thompson T.L., Yates J.T. Jr. Surface Science studies of the photoactivation of TiO_2 - new photochemical processes. *Chem. Rev.* 2006. **106**: 4428.
[199] Glushko V.P. (editor). *Handbook of thermodynamic properties of individual substances.* (Moscow: Nauka, 1978). [in Russian].
[200] Mitchell J., Webber J.B.W., Strange J.H. Nuclear magnetic resonance cryoporometry. *Phys. Rep.* 2008. **461**(1): 1.
[201] Petrov O.V., Furó I. NMR cryoporometry: Principles, application and potential. *Progr. NMR Spectroscopy.* 2009. **54**: 97.
[202] Aksnes D.W., Forl K., Kimtys L. Pore size distribution in mesoporous materials as studied by ^{1}H NMR. *Phys. Chem. Chem. Phys.* 2001. **3**: 3203.
[203] Webber J.B.W., Anderson R., Strange J.H., Tohidi B. Clathrate formation and dissociation in vapor/water/ice/hydrate systems in SBA-15, sol–gel and CPG porous media, as probed by NMR relaxation, novel protocol NMR cryoporometry, neutron scattering and ab initio quantum–mechanical molecular dynamics simulation. *Magnet Reson. Imag.* 2007. **25**: 533.
[204] Gun'ko V.M., Savina I.N., Mikhalovsky S.V. Cryogels: Morphological, structural and adsorption characterization. *Adv. Colloid Interface Sci.* 2013. **187–188**: 1.
[205] Petrov O.V., Furó I. A joint use of melting and freezing data in NMR cryoporometry. *Micropor. Mesopor. Mater.* 2010. **136**(1-3): 83.
[206] Schulz P.S. Ionic liquids as solvent probes for NMR cryoporometry. *Chem.Phys.Chem.* 2010. **11**: 87. doi:10.1002/cphc.200900804.
[207] Shiko E., Edler K.J., Lowe J.P., Rigby S.P. Probing hysteresis during sorption of cyclohexane within mesoporous silica using NMR cryoporometry and relaxometry. *J. Colloid Interface Sci.* 2013. **398**: 168.
[208] Mitchell J., Gladden L.F., Chandrasekera T.C., Fordham E.J. Low-field permanent magnets for industrial process and quality control. *Prog. Nucl. Magn. Reson. Spectrosc*. 2014. **76**: 1.

[209] Gun'ko V.M. Interfacial phenomena: effects of confined space and structure of adsorbents on the behavior of polar and nonpolar adsorbates at low temperatures. *Current Physical Chemistry*. 2015. **5**: 137.
[210] Gun'ko V.M. Modeling of interfacial behavior of water and organics. *J. Theor. Comp. Chem.* 2013. **12**(7):1350059.
[211] Mallamace F., Corsaro C., Broccio M., Branca C., González-Segredo N., Spooren J., Chen S.-H., Stanley H.E. NMR evidence of a sharp change in a measure of local order in deeply supercooled confined water. *Proc. Natl. Acad. Sci. USA*. 2008. **105**(35): 12725.
[212] Landry M.R. Thermoporometry by differential scanning calorimetry: experimental considerations and applications. *Thermochim. Acta* 2005. **433**(1-2): 27.
[213] Gun'ko V.M., Turov V.V., Bogatyrev V.M., Zarko V.I., Leboda R., Goncharuk E.V., Novza A.A., Turov A.V., Chuiko A.A. Unusual properties of water at hydrophilic/hydrophobic interfaces. *Adv. Colloid Interface Sci.* 2005. **118**(1-3): 125.
[214] Gun'ko V.M., Zarko V.I., Goncharuk E.V., Andriyko L.S., Turov V.V., Nychiporuk Y.M, Leboda R., Skubiszewska-Zieba J., Gabchak A.L., Osovskii V.D., Ptushinskii Y.G., Yurchenko G.R., Mishchuk O.A., Gorbik P.P., Pissis P., Blitz J.P. TSDC spectroscopy of relaxational and interfacial phenomena. *Adv. Colloid Interface Sci.* 2007. **131**(1-2): 1.
[215] Turov V.V., Gun'ko V.M., Turova A.A., Morozova L.P., Voronin E.F. Interfacial behavior of concentrated HCl solution and water clustered at a surface of nanosilica in weakly polar solvents media. *Colloids Surf. A: Physicochem. Eng. Aspects* 2011. **390**(1-3): 48. doi: 10.1016/j.colsurfa.2011.08.053.
[216] Gun'ko V.M., Turov V.V., Skubiszewska-Zięba J., Leboda R., Tsapko M.D., Palijczuk D. Structural characteristics of a carbon adsorbent and influence of organic solvents on interfacial water. *Appl. Surf. Sci.* 2003. **214**(1-4): 178.
[217] Turov V.V., Gun'ko V.M., Zarko V.I., Leboda R., Jabłoński M., Gorzelak M., Jagiello-Wojtowicz E. Weakly and strongly associated nonfreezable water bound in bones. *Colloids Surf. B: Biointerfaces* 2006. **48**(2): 167.
[218] Kinney D.R., Chuang I.-S., Maciel G.E. Water and the silica surface as studied by variable temperature high resolution ^{1}H NMR. *J. Am. Chem. Soc.* 1993. **115**(15): 6786.
[219] Chuang I.-S., Maciel G.E. Probing hydrogen bonding and the local environment of silanols on silica surfaces via nuclear spin cross polarization dynamics. *J. Am. Chem. Soc.* 1996. **118**(2): 401.
[220] Liu C.C., Maciel G.E. The fumed silica surface: a study by NMR. *J. Am. Chem. Soc.* 1996. **118**(21): 5103.
[221] Humbert H. Estimation of hydroxyl density at the surface of pyrogenic silicas by complementary NMR and Raman experiments. *J. Non-Crystal Solid* 1995. **191**(1-2): 29.
[222] Hu J.Z., Kwak J.H., Herrera J.E., Wang Y., Peden Ch.H.F. Line narrowing in ^{1}H MAS spectrum of mesoporous silica by removing adsorbed H_2O using N_2. *Solid State Nuclear Magnetic Resonance* 2005. **27**(3): 200.
[223] Fonseca I., Matos J., Gonçalves M.C., Carvalho A., Sebasti P.J. Silica and silica organically modified nanoparticles: Water dynamics in complex systems. *Microporous and Mesoporous Materials* 2015. **217**: 102.
[224] Jimura K., Hayashi S. Proton diffusion in hybrid materials of $CsHSO_4$ and silica nanoparticles as studied by ^{1}H solid-state NMR. *Solid State Sci.* 2012. **14**(1): 171.
[225] Walia J., Crone J., Liang J., Niknam M., Lemaire C., Thompson R.T., Peemoeller H. Temperature and hydration dependence of proton MAS NMR spectra in MCM-41: Model based on motion induced chemical shift averaging. *Solid State Nucl. Magn. Reson.* 2013. **49-50**: 26.
[226] Brinker C.J., Scherer G.W. *Sol-Gel Science: The Physics and Chemistry of Sol-Gel Processing*. (NY: Academic Press, 1990).
[227] Pierre A.C. *Introduction to Sol-Gel Processing*. (Boston: Kluwer, 1998).
[228] Vansant E.F., Van Der Voort P., Vrancken K.C. *Characterization and Chemical Modification of the Silica Surface. Studies in Surface Science and Catalysis*. Vol. **93** (Amsterdam: Elsevier, 1995).
[229] Gun'ko V.M., Zarko V.I., Voronin E.F., Turov V.V., Mironyuk I.F., Gerashchenko I.I., Goncharuk E.V., Pakhlov E.M., Guzenko N.V., Leboda R., Skubiszewska-Zięba J., Janusz W., Chibowski S.,

Levchuk Yu.N., Klyueva A.V. Impact of some organics on structural and adsorptive characteristics of fumed silica in different media. *Langmuir.* 2002. **18**(3): 581.
[230] Mironyuk I.F., Gun'ko V.M., Turov V.V., Zarko V.I., Leboda R., Skubiszewska-Zięba J. Characterization of fumed silicas and their interaction with water and dissolved proteins. *Colloids Surf. A: Physicochem. Eng. Aspects* 2001. **180**(1-2): 87.
[231] Gun'ko V.M., Voronin E.F., Mironyuk I.F., Leboda R., Skubiszewska-Zięba J., Pakhlov E.M., Guzenko N.V., Chuiko A.A. The effect of heat, adsorption and mechanochemical treatments on stuck structure and adsorption properties of fumed silicas. *Colloids Surf. A: Physicochem. Eng. Aspects* 2003. **218**(1-3): 125.
[232] Turov V.V., Voronin E.F., Morozova L.P., Gun'ko V.M., Nosach L.V. The effect of mechanical activation on the hydration properties of nanodispersed silica. *Russian Journal of Applied Chemistry* 2011. **84**: 1304.
[233] Gupta S., Pel L., Kopinga K. Crystallization behavior of NaCl droplet during repeated crystallization and dissolution cycles: An NMR study. *Journal of Crystal Growth* 2014. **391**: 64.
[234] Xu J.-A., Huang E., Lin J.-F., Xu L.Y. Raman study at high pressure and the thermodynamic properties of corundum: Application of Kieffer's model. *Am. Mineral.* 1995. **80**(11-12): 1157.
[235] Hair M.L. *Infrared Spectroscopy in Surface Chemistry*. (NY: Dekker, 1967).
[236] Gun'ko V.M., Turov V.V., Bogatyrev V.M., Charmas B., Skubiszewska-Zięba J., Leboda R., Pakhovchishin S.V., Zarko V.I., Petrus L.V., Stebelska O.V., Tsapko M.D. Influence of partial hydrophobization of fumed silica by hexamethyldisilazane on interaction with water. *Langmuir* 2003. **19**(26): 10816.
[237] Gun'ko V.M., Sheeran D.J., Augustine S.M., Blitz J.P. Structural and energetic characteristics of silicas modified by organosilicon compounds. *J. Colloid Interface Sci.* 2002. **249**(1): 123.
[238] Gun'ko V.M., Zarko V.I., Leboda R., Chibowski E. Aqueous suspensions of fumed oxides: particle size distribution and zeta potential. *Adv. Colloid Interface Sci.* 2001. **91**: 1.
[239] Karraker K.A., Radke C.J. Disjoining pressures, zeta potentials and surface tensions of aqueous non-ionic surfactant/electrolyte solutions: theory and comparison to experiment. *Adv. Colloid Interface Sci.* 2002. **96**: 231.
[240] Bourikas K., Kordulis C., Lycourghiotis A. The mechanism of the protonation of metal (hydr)oxides in aqueous solutions studied for various interfacial/surface ionization models and physicochemical parameters: A critical review and a novel approach. *Adv. Colloid Interface Sci.* 2006. **121**: 111. doi: 10.1016/j.cis.2006.06.002.
[241] Kovalchuk N.M., Starov V.M. Aggregation in colloidal suspensions: Effect of colloidal forces and hydrodynamic interactions. *Adv. Colloid Interface Sci.* 2012. **179-182**: 99. doi: 10.1016/j.cis.2011.05.009.
[242] Chaplin M. Water Structure and Science. http://www.lsbu.ac.uk/water/, 23 October, 2015.
[243] Pople J.A., Schneider W.G., Bernstein H.J. *High-Resolution Nuclear Magnetic Resonance*. (NY: McGraw-Hill Book Company, 1959).
[244] Gun'ko V.M., Morozova L.P., Turova A.A., Turov A.V., Gaishun V.E., Bogatyrev V.M., Turov V.V. Hydrated phosphorus oxyacids alone and adsorbed on nanosilica. *J. Colloid Interface Sci.* 2012. **368**(1): 263.
[245] Gun'ko V.M., Turov V.V., Zarko V.I., Goncharuk E.V., Turova A.A. Regularities in the behaviour of water confined in adsorbents and bioobjects studied by ^{1}H NMR spectroscopy and TSDC methods at low temperatures. *Colloids Surf. A: Physicochem. Eng. Aspects.* 2009. **336**(1-3): 147.
[246] Petin A.Yu., Gun'ko V.M., Turov A.V., Turov V.V., Leboda R. Clusterization of water at a surface of nanosilica A-380. *Annales Universitatis Marie Curie-Sklodowska Sectio Chemia* 2009. **64**(1): 184.
[247] Gun'ko V.M., Turov V.V., Turov A.V. Hydrogen peroxide – water mixture bound to nanostructured silica. *Chem. Phys. Lett.* 2012. **531**: 132.
[248] Turov V.V., Krupska T.V., Tsapko M.D., Gun'ko V.M. Temperature behavior of water and n-decane bound to nanosilica or poly(methylsiloxane). *Chemistry, Physics and Technology of Surface* 2015. **6**(2): 244.
[249] Murakhtina T., Heuft J., Meijer E.J, Sebastiani D. First principles and experimental ^{1}H NMR signatures of solvated ions: the case of HCl(aq). *Chem. Phys. Chem.* 2006. **7**(12): 2578.

[250] Wypych G. (editor), *Handbook of Solvents*. (Toronto: ChemTec Publishing, 2001).
[251] Gun'ko V.M. Modelling of evaporation of clusters and nanodroplets of organic molecules using quantum chemical and the kinetic gas theory methods. *Chemistry, Physics and Technology of Surface* 2015. **6**(1): 5.
[252] Liboff R.L. *Kinetic Theory*. (NY: Prentice-Hall, Englewood Cliffs, 1990).
[253] Laurendeau N.M. *Statistical Thermodynamics: Fundamentals and Applications*. (Cambridge: Cambridge University Press, 2005).
[254] Sefiane K. Patterns from drying drops. *Adv. Colloid Interface Sci.* 2014. **206**: 372. doi: 10.1016/j.cis.2013.05.002.
[255] Peng C.-C., Cerretani C., Braun R.J., Radke C.J. Evaporation-driven instability of the precorneal tear film. *Adv. Colloid Interface Sci.* 2014. **206**: 250. doi: 10.1016/j.cis.2013.06.001.
[256] Askounis A., Sefiane K., Koutsos V., Shanahan M.E.R. Effect of particle geometry on triple line motion of nanofluid drops and deposit nano-structuring. *Adv. Colloid Interface Sci.* 2015. **222**: 44. doi: 10.1016/j.cis.2014.05.003.
[257] Thomas S., Shanks R., Chandrasekharakurup S. (editors), *Design and Applications of Nanostructured Polymer Blends and Nanocomposite Systems*. (Amsterdam: Elsevier, 2016).
[258] Ahmed W., Jackson M.J. (editors) *Emerging Nanotechnologies for Manufacturing*. Second Edition, (Amsterdam: Elsevier, 2015).
[259] Piemonte V., De Falco M., Basile A. (editors), *Sustainable Development in Chemical Engineering – Innovative Technologies*. First Edition. (Hoboken, NJ: John Wiley & Sons, 2013).
[260] Demir M.M., Wegner G. Challenges in the preparation of optical polymer composites with nanosized pigment particles: a review on recent efforts. *Macromol. Mater. Eng.* 2012. **297**(9): 838.
[261] Kim D.J., Jo M.J., Nam S.Y. A review of polymer-nanocomposite electrolyte membranes for fuel cell application. *J. Ind. Eng. Chem.* 2015. **21**: 36.
[262] Wang Y., He J., Liu C., Chong W.H., Chen H. Thermodynamics versus kinetics in nanosynthesis. *Angew. Chem. Int. Ed.* 2015. **54**(7): 2022.
[263] Martinez L.J., Sanchez M.L., Kikot P., Candal R., Grasselli M. Preparation of functional currant-bun-like fumed silica/polymethacrylate nanoparticles by radiation-induced polymerization. *Colloids Surf. A: Physicochem. Eng. Asp.* 2014. **463**: 110.
[264] Shadjou N., Hasanzadeh M. Bone tissue engineering using silica-based mesoporous nanobiomaterials: Recent progress. *Mater. Sci. Eng.* C 2015. **55**: 401.
[265] Yoosuk B., Wongsanga T., Prasassarakich P. CO_2 and H_2S binary sorption on polyamine modified fumed silica. *Fuel.* 2016. 168: 47.
[266] Ramesh S., Liew C.-W. Exploration on nano-composite fumed silica-based composite polymer electrolytes with doping of ionic liquid. *J. Non-Crystal Solid* 2012. **358**(2): 931.
[267] Damouny C.W., Silverstein M.S. Hydrogel-filled, semi-crystalline, nanoparticle crosslinked, porous polymers from emulsion templating: Structure, properties, and shape memory. *Polymer*. 2016. **82**:262.
[268] Gun'ko V.M., Turov V.V., Krupska T.V., Ruban AN, Kazanets A.I., Leboda R., Skubiszewska-Zięba J. Interfacial behavior of silicone oils interacting with nanosilica and silica gels. *J. Colloid Interface Sci.* 2013. **394**: 467.
[269] Kawaguchi M. Silicone oil emulsions stabilized by polymers and solid particles. *Adv. Colloid Interface Sci.* 2016. **233**: 186.
[270] Klonos P., Kyritsis A., Pissis P. Interfacial dynamics of polydimethylsiloxane adsorbed on fumed metal oxide particles of a wide range of specific surface area. *Polymer*. 2015. **77**: 10.
[271] Gun'ko V.M., Turov V.V., Turova A.A., Krupska T.V., Pissis P., Leboda R., Skubiszewska-Zięba J. Interactions of poly(dimethylsiloxane) with nanosilica and silica gel upon cooling-heating. *J. Colloid Interface Sci.* 2014. **426**: 48.
[272] Dollase T., Wilhelm M., Spiess H.W., Yagen Y., Yerushalmi-Rozen R., Gottlieb M. Effect of interfaces on the crystallization behavior of PDMS. *Interface Sci.* 2003. **11**(2): 199.
[273] Lehn J.-M., *Supramolecular Chemistry*. (Weinheim: VCH Verlagsgesellschaft mbH, 1995).
[274] Bershtein V.A., Egorov V.M. *Differential Scanning Calorimetry of Polymers. Physics, Chemistry, Analysis, Technology*. (NY: Ellis Horwood, 1994).

[275] Bershtein V., Gun'ko V., Egorova L., Guzenko N., Pakhlov E., Ryzhov V., Zarko V. I. Well-defined silica core – poly(vinyl pyrrolidone) shell nanoparticles: interactions and multi-modal glass transition dynamics at interfaces. *Polymer.* 2009. **50**(3): 860.
[276] Bershtein V.A., Gun'ko V.M., Karabanova L.V., Sukhanova T.E., Yakushev P.N., Egorova L.M., Glievyy O.B., Lutsyk E.D., Pakhlov E.M., Turova A.A., Zarko V.I., Vylegzhanina M.E. Hybrid polyurethane-poly(2-hydroxyethyl methacrylate) semi-ipn-silica nanocomposites: interfacial interactions and glass transition dynamics. *J. Macromol. Sc.i Part B: Phys.* 2010. **49**(1): 18.
[277] Bershtein V.A., Gun'ko V.M., Egorova L.M., Guzenko N.V., Pakhlov E.M., Ryzhov V.A., Zarko V. I. Well-defined oxide core-polymer shell nanoparticles: interfacial interactions, peculiar dynamics and transitions in polymer nanolayers. *Langmuir* 2010. **26**(13): 10968.
[278] Bershtein V.A., Gun'ko V.M., Egorova L.M., Wang Z., Illsley M., Voronin E.F., Prikhod'ko G.P., Yakushev P.N., Leboda R., Skubiszewska-Zięba J., Mikhalovsky S.V. Dynamics, thermal behaviour and elastic properties of thin films of poly(vinyl alcohol) nanocomposites. *RSC Advances* 2012. **2**(4): 1424.
[279] Bershtein V.A., Gun'ko V.M., Karabanova L.V., Sukhanova T.E., Yakushev P.N., Egorova L.M., Turova A., Zarko V.I., Pakhlov E.M., Vylegzhanina M.E., Mikhalovsky S.V. Polyurethane–poly(2-hydroxyethyl methacrylate) semi-IPN–nanooxide composites. *RSC Advances* 2013. **3**(34): 14560.
[280] Gun'ko V.M., Turov V.V., Barvinchenko V.N., Turova A.A., Rugal A.A., Zarko V.I., Leboda R. Nonuniformity of starch/nanosilica composites and interfacial behaviour of water and organic compounds. *Appl. Surf. Sci.* 2010. **256**(17): 5275.
[281] Ma Y., Hu W., Reiter G. Lamellar crystal orientations biased by crystallization kinetics in polymer thin films. *Macromolecules* 2006. **39**(15): 5159.
[282] Hoffman, C. L. Rabolt, J. F. Self-assembled thin-film blends by polymer codeposition - poly(ethylene oxide) and poly(methyl methacrylate). *Macromolecules* 1996. **29**(7): 2543.
[283] Zhu J., Wang M. Phase ordering and crystallization kinetics in ultrathin poly(ethylene oxide)/poly(methyl methacrylate) blend films. *J. Macromol. Sci. Part B: Phys.* 2008. **47**(5): 1008.
[284] Wang H., Keum J.K., Hiltner A., Baer E. Confined crystallization of PEO in nanolayered films impacting structure and oxygen permeability. *Macromolecules* 2009. **42**(18): 7055.
[285] Wang H., Keum J.K., Hiltner A., Baer E., Freeman B., Rozanski A., Galeski A. Confined crystallization of polyethylene oxide in nanolayer assemblies. *Science* 2009. **323**(5915): 757.
[286] Martin J., Mijangos C.,Sanz A., Ezquerra T.A., Nogales A. Segmental dynamics of semicrystalline poly(vinylidene fluoride) nanorods. *Macromolecules* 2009. **42**: 5395.
[287] Klonos P., Pissis P., Gun'ko V.M., Kyritsis A., Guzenko N.V., Pakhlov E.M., Zarko V.I., Janusz W., Skubiszewska-Zięba J., Leboda R. Interaction of poly(ethylene glycol) with fumed silica and alumina/silica/titania. *Colloids Surf. A: Physicochem. Eng. Aspects* 2010. **360**(1-3): 220.
[288] Gun'ko V.M., Pissis P., Spanoudaki A., Turova A., Turov V.V., Zarko V.I., Goncharuk E.V. Interfacial phenomena in starch/fumed silicaat varied hydration levels. *Colloids Surf. A: Physicochem. Eng. Aspects* 2008. **320**(1-3): 247.
[289] Hunter R.J. *Zeta Potential in Colloid Sciences* (London: Academic Press, 1981).
[290] Gun'ko V.M., Turov V.V., Zarko V.I., Dudnik V.V., Tischenko V.A., Voronin E.F., Siltchenko S.S., Barvinchenko V.N., Chuiko A.A. Aqueous suspensions of fumed silica and adsorption of proteins. *J. Colloid Interface Sci.* 1997. **192**(1): 166.
[291] Sorai M (editor), *Comprehensive Handbook of Calorimetry and Thermal Analysis* (West Sussex, England: Wiley, 2004).
[292] Beaumont R.H., Clegg B., Gee G., Herbert J.B.M., Marks D.J., Roberts R.C., et al. Heat capacities of propylene oxide and of some polymers of ethylene and propylene oxides. *Polymer.* 1966. **7**(8): 401.
[293] Donth E. (editor), *The Glass Transition: Relaxation Dynamics in Liquids and Disordered Materials. Springer Series in Materials Science*. vol **48** (Berlin: Springer, 2001).
[294] Fontanella J.J., Wintersgill M.C., Calame J.P., Andeen C.G. Electrical relaxation in pure and alkali metal thiocyanate complexed poly(ethylene oxide). *Solid State Ionics* 1983. **8**(4): 333.
[295] Kyritsis A., Pissis P., Tsonos C., Laudat J., Ren J. Dielectric and conductivity relaxation in dry and humid solid PEO electrolytes. *J. Non-Crystal Solid* 1994. **172-174**(2): 1431.

[296] Kripotou S., Pissis P., Sysel P., Sindelar V., Bershtein V.A. Structure-property relationships in novel poly(imide-amide)-poly(ethylene glycol)hybrid networks. *Polymer.* 2006. **47**(1): 357.
[297] Jia Z., Zhang K., Tan J., Han C., Dong L., Yang Y. Crystallization behavior and mechanical properties of crosslinked plasticized poly(L-lactic acid). *J. Appl. Polymer. Sci.* 2009. **111**(3): 1530.
[298] Dobbertin J., Hensel A., Schick C. Dielectric spectroscopy and calorimetry in the glass transition region of semi-crystalline poly(ethylene terephthalate). *J. Thermal Analys Calorimetry* 1996. **47**(4): 1027.
[299] Fragiadakis D., Pissis P. Glass transition and segmental dynamics in poly (dimethylsiloxane)/silica nanocomposites studied by various techniques. *J. Non-Crystal Solid* 2007. **353**(47-51): 4344.
[300] Bershtein V.A., Egorova L.M., Yakushev P.N., Pissis P., Sysel P., Brozova L. Molecular dynamics in nanostructured polyimide–silica hybrid materials and their thermal stability. *J. Polymer. Sci. B: Polymer. Phys.* 2002. **40**(10): 1056.
[301] Gómez Tejedor J.A., Rodriguez Hernández J.C., Gómez Ribelles J.L., Monleón Pradas M. Dynamic mechanical relaxation of poly(2- hydroxyethyl acrylate)-silica nanocomposites obtained by the sol– gel method. *J. Macromol. Sci. B: Phys.* 2007. **46**(1): 43.
[302] Sargsyan A., Tonoyan A., Davtyan S., Schick Ch. The amount of immobilized polymer in PMMA SiO_2 nanocomposites determined from calorimetric data. *Europ. Polymer. J*. 2007. **43**(8): 3113.
[303] Aranguren M.I. Crystallization of polydimethylsiloxane: effect of silica filler and curing. *Polymer.* 1998. **39**(20): 4897.
[304] Fragiadakis D., Pissis P., Bokobza L. Glass transition and molecular dynamics in poly (dimethylsiloxane)/silica nanocomposites. *Polymer.* 2005. **46**(16): 6001.
[305] Kalogeras I.M., Roussos M., Christakis I., Spanoudaki A., Pietkiewicz D., Brostow W., Vassilikou-Dova A. Dielectric properties of cured epoxy resin + poly(ethylene oxide) blends. *J. Non-Crystal Solid* 2005. **351**: 2728.
[306] Hedvig P. *Dielectric Spectroscopy of polymers*. (Bristol: Adam Hilger, 1977).
[307] Brauenlich P. (editor), *Thermally stimulated currents in solids. Topics in applied physics*. vol. **37** (Berlin: Springer, 1979).
[308] Kremer F., Schönhals A. (eds), *Broadband Dielectric Spectroscopy*. (Berlin: Springer-Verlag, 2003).
[309] Donth E. (editor), *The Glass Transition: Relaxation Dynamics in Liquids and Disordered Materials. Springer Series in Materials Science.* Vol **48** (Berlin: Springer, 2001).
[310] Capaccioli S., Ngai K.L., Shinyashiki N. The Johari-Goldstein-relaxation of water. *J. Phys. Chem. B* 2007. **111**(28): 8197.
[311] Shinyashiki N., Sudo S., Yagihara S., Spanoudaki A., Kyritsis A., Pissis P. Relaxation processes of water in the liquid to glassy states of water mixtures studied by broadband dielectric spectroscopy. *J. Phys.: Condens. Matter.* 2007. **19**(20): 205113.
[312] Osti N.C., Coté A., Mamontov E., Ramirez-cuesta A., Wesolowski D.J., Diallo S.O. Characteristic features of water dynamics in restricted geometries investigated with quasi-elastic neutron scattering. *Chem. Phys.* 2016. **465-466**: 1.
[313] Tan S.P., Piri M. Equation-of-state modeling of confined fluid phase equilibria in nanopores. *Fluid Phase Equilibria.* 2015. **393**: 48.
[314] Nouri-Khorasani A., Malek K., Malek A., Mashio T., Wilkinson D.P., Eikerling M.H. Molecular modeling of the proton density distribution in a water-filled slab-like nanopore bounded by Pt oxide and ionomer. *Catalysis Today* 2016. **262**: 133.
[315] Weiland E., Springuel-Huet M., Nossov A., Gédéon A. Xenon NMR: Review of recent insights into porous materials. *Micropor. Mesopor. Mater.* 2016. **225**: 41.
[316] Klonos P., Kaprinis S., Zarko V.I., Peoglos V., Pakhlov E.M., Pissis P., Gun'ko V.M. Thermal and dielectric studies of PEG/C/AST nanocomposites. *J. Appl. Polymer. Sci.* 2013. **128**(3): 1601.
[317] Stamatopoulou C., Klonos P., Bondaruk O., Koutsoumpis S., Gun'ko V., Pissis P., Karabanova L. Hydrophilic nanocomposites based on polyurethane/poly(2-hydroxyethyl methacrylate) semi-IPNs and modified/unmodified nanosilica for biomedical applications. *J. Polymer Sci. Part B: Polymer Phys.* 2014. **52**(5): 397.
[318] Galaburda M.V., Klonos P., Gun'ko V.M., Bogatyrov V.M., Borysenko M.V., Pissis P. Dielectric properties and thermal destruction of poly(dimethylsiloxane)/Fe_2O_3/SiO_2 nanocomposites. *Appl. Surf. Sci.* 2014. **305**: 67.

[319] Sulym I.Ya., Klonos P., Borysenko M.V., Pissis P., Gun'ko V.M. Dielectric and thermal studies of segmental dynamic in silica/PDMS and silica/titania/PDMS nanocomposites. *J. Appl. Polymer. Sci.* 2014. **131**(23): 41154.
[320] Klonos P., Sulym I.Ya., Borysenko M.V., Gun'ko V.M., Kripotou S., Kyritsis A., Pissis P. Interfacial interactions and complex segmental dynamics in systems based on silica-polydimethylsiloxane core-shell nanoparticles: Dielectric and thermal study. *Polymer.* 2015. **58**: 9.
[321] Klonos P., Sulym I.Ya., Kyriakos K., Vangelidis I., Zidropoulos S., Sternik D., Borysenko M.V., Kyritsis A., Deryło-Marczewska A., Gun'ko V.M., Pissis P. Interfacial phenomena in core–shell nanocomposites of PDMS adsorbed onto low specific surface area fumed silica nanooxides: Effects of surface modifications. *Polymer.* 2015. **68**: 158.
[322] Klonos P., Dapei G., Sulym I.Ya., Zidropoulos S., Sternik D., Deryło-Marczewska A., Borysenko M.V., Gun'ko V.M., Kyritsis A., Pissis P. Morphology and molecular dynamics investigation of PDMS adsorbed on titania nanoparticles: effects of polymer molecular weight. *Eur. Polymer. J.* 2016. **74**: 64.
[323] Leboda R., Turov V.V., Charmas B., Skubiszewska-Zięba J., Gun'ko V.M. Surface properties of mesoporous carbon-silica gel adsorbents. *J. Colloid Interface Sci.* 2000. **223**(1): 112.
[324] Gun'ko V.M., Leboda R., Skubiszewska-Zięba J., Turov V.V., Kowalczyk P. Structure of silica gel Si-60 and pyrocarbon/silica gel adsorbents thermally and hydrothermally treated. *Langmuir.* 2001. **17**(11): 3148.
[325] Melillo M., Gun'ko V.M., Mikhalovska L.I, Phillips G.J., Davies J.D., Lloyd A.W., Kozynchenko O.P., Malik D.J., Streat M., Mikhalovsky S.V. Structural characteristics of activated carbons and ibuprofen adsorption affected by bovine serum albumin. *Langmuir.* 2004. **20**(7): 2837.
[326] Tomaszewski W., Gun'ko V.M., Leboda R., Skubiszewska-Zięba J. Structural characteristics of modified activated carbons and adsorption of explosives. *J. Colloid Interface Sci.* 2003. **266**: 388.
[327] Ahmed W., Jackson M.J. (eds) *Emerging Nanotechnologies for Manufacturing*. Second Edition (Amsterdam: Elsevier, 2015).
[328] Thomas S., Shanks R., Chandrasekharakurup S. (eds) *Design and Applications of Nanostructured Polymer Blends and Nanocomposite Systems*. (Amsterdam: Elsevier, 2016).
[329] Zaleska A. Doped-TiO_2: a review. *Recent Patents on Engineering.* 2008. **2**(3): 157.
[330] Bagheri S., Shameli K., Hamid S.B.A. Synthesis and characterization of anatase titanium dioxide nanoparticles using egg white solution via sol-gel method. *J. Chem*. 2013. **2013**: 848205.
[331] Safaei-Naeini Y., Aminzare M., Golestani-Fard F., Khorasanizadeh F., Salahi E. Suspension stability of titania nanoparticles studied by UV-vis spectroscopy method. *Iranian Journal of Materials Science & Engineering.* 2012. **9**(1): 62.
[332] Buzea C., Blandino I.I.P., Robbie K. Nanomaterials and nanoparticles: sources and toxicity. *J. Biointerphases.* 2007. **2**(4): 17.
[333] Gun'ko V.M., Turov V.V., Gorbik P.P. *Water at the Interfaces*. (Kiev: Naukova Dumka, 2009). [in Russian].
[334] Turov V.V., Gun'ko V.M. *Clustered Water and Ways of Its Applications*. (Kiev: Naukova Dumka, 2011). [in Russian].
[335] Gun'ko V.M., Turov V.V., Zarko V.I., Goncharuk O.V., Pakhlov E.M., Skubiszewska-Zięba J., Blitz J.P. Interfacial phenomena at a surface of individual and complex fumed nanooxides. *Adv. Colloid Interface Sci.* 2016. **235**: 108.
[336] Gun'ko V.M., Turov V.V., Zarko V.I., Pakhlov E.M., Charmas B., Skubiszewska-Zięba J. Influence of structural organization of silicas on interfacial phenomena. *Colloids and Surfaces A: Physicochem. Eng. Aspects.* 2016. **492**: 230.
[337] Gun'ko V.M., Zarko V.I., Goncharuk O.V., Matkovsky A.K., Remez O.S., Skubiszewska-Zięba J., Wojcik G., Walusiak B., Blitz J.P. Nature and morphology of fumed oxides and features of interfacial phenomena. *Appl. Surf. Sci.* 2016. **366**: 410.
[338] Gun'ko V.M., Turov V.V., Zarko V.I., Goncharuk O.V., Matkovsky A.K., Prykhod'ko G.P., Nychiporuk Yu.M., Pakhlov E.M., Krupska T.V., Balakin D.Yu., Charmas B., Andriyko L.S., Skubiszewska-Zięba J., Marynin A.I., Ukrainets A.I., Kartel M.T. Multi-layer graphene oxide alone and in a composite with nanosilica: preparation and interactions with polar and nonpolar adsorbates. *Appl. Surf. Sci.* 2016. **387**: 736.

[339] Gun'ko V.M., Turov V.V., Pakhlov E.M., Matkovsky A.K., Krupska T.V., Kartel M.T., Charmas B. Blends of amorphous/crystalline nanoalumina and hydrophobic amorphous nanosilica. *Journal of Non-Crystalline Solids.* 2018. **500:** 351.
[340] Gun'ko V.M., Pakhlov E.M., Skubiszewska-Zięba J., Blitz J.P. Infrared spectroscopy as a tool for textural and structural characterization of individual and complex fumed oxides. *Vibrational Spectroscopy.* 2017. **88:** 56.
[341] Zaulychnyy Ya.V., Gun'ko V.M., Yavorskyi Y.V., Gasyuk I.M., Wanderka N., Dudka O.I. Effect of mechanical treatment on the distribution of valence electrons and characteristics of nanocomposite $(SiO_2)_x(Al_2O_3)_{1-x}$ (x = 0.8, x= 0.7) electrodes in lithium power sources. *Applied Surface Sci.* 2019. **494**: 1013.https://doi.org/10.1016/j.apsusc.2019.07.206
[342] Gun'ko V.M., Pakhlov E.M., Goncharuk O.V., Andriyko L.S., Marynin A.I., Ukrainets A.I., Charmas B., Skubiszewska-Zięba J., Blitz J.P. Influence of hydrophobization of fumed oxides on interactions with polar and nonpolar adsorbates. *Appl. Surf. Sci.* 2017. **423**: 855.
[343] Mironyuk I.F., Gun'ko V.M., Vasylyeva H.V., Goncharuk O.V., Tatarchuk H.V., Mandzyuk V.I., Bezruka N.A., Dmytrotsa T.V. Effects of enhanced clusterization of water at a surface of partially silylated nanosilica on adsorption of cations and anions from aqueous media. *Microporous and Mesoporous Materials.* 2019. **277**: 95.https://doi.org/10.1016/j.micromeso.2018.10.016
[344] Gun'ko V.M., Turov V.V., Krupska T.V., Protsak I.S., Borysenko M.V., Pakhlov E.M. Polymethylsiloxane alone and in composition with nanosilica under various conditions, *J. Colloid Interface Sci.* 2019. **541**: 213.
[345] Protsak I., Gun'ko V.M., Henderson I.M., Pakhlov E.M., Sternik D., Le Z. Nanostructured amorphous silicas hydrophobized by various pathways. *ACS Omega.* 2019**. 4**(9): 13863.
[346] Skwarek E., Janusz W., Gun'ko V.M., Pakhlov E.M., Zarko V.I., Gdula K. Characteristics of surface and electrochemical properties of composites with fumed metal oxides and hydroxyapatite. *Adsorption.* 2016. **22**(4-6): 725.
[347] Skwarek E., Goncharuk O.V., Janusz W., Pakhlov E.M., Gun'ko V.M. Heats of immersion of hydroxyapatite and hydroxyapatite/fumed oxides composites in water and n-decane. *Materials Chemistry and Physics* 2018. **215**: 99.
[348] Wawrzkiewicz M., Wiśniewska M., Gun'ko V.M. Application of silica–alumina oxides of different compositions for removal of C.I. Reactive Black 5 dye from wastewaters. *Adsorption Science & Technology.* 2017. **35**(5–6): 448.
[349] Wawrzkiewicz M., Wiśniewska M., WołowiczA., Gun'ko V.M., Zarko V.I. Mixed silica-alumina oxide as sorbent for dyes and metal ions removal from aqueous solutions and wastewaters. *Microporous and Mesoporous Materials.* 2017. **250**: 128.
[350] Klonos P., Dapei G., Sulym I.Ya., Zidropoulos S., Sternik D., Deryło-Marczewska A., Borysenko M.V., Gun'ko V.M., Kyritsis A., Pissis P. Morphology and molecular dynamics investigation of PDMS adsorbed on titania nanoparticles: effects of polymer molecular weight. *European Polymer Journal.* 2016. **74**: 64.
[351] Klonos P., Kulyk K., Borysenko M., Gun'ko V., Kyritsis A., Pissis P. Effects of molecular weight below the entanglement threshold on interfacial nanoparticles/polymer dynamics. *Macromolecules.* 2016. **49**(24): 9457.
[352] Klonos P., KyritsisA., BokobzaL., Gun'ko V.M., Pissis P. Interfacial effects in PDMS/titania nanocomposites studied by thermal and dielectric techniques. *Colloids and Surfaces A: Physicochem. Eng. Aspects.* 2017. **519**: 212.
[353] Klonos P., Goncharuk O., PakhlovE., Sternik D., Derylo-Marczewska A., Kyritsis A., Gun'ko V., Pissis P. Morphology, Molecular Dynamics, and Interfacial Phenomena in Systems Based on Silica Modified by Grafting Polydimethylsiloxane Chains and Physically Adsorbed Polydimethylsiloxane. *Macromolecules.* 2019. **52**(7): 2863.
[354] Gun'ko V.M., Lupascu T., Krupska T.V., Golovan A.P., Pakhlov E.M., Turov V.V. Influence of tannin on aqueous layers at a surface of hydrophilic and hydrophobic nanosilicas. *Colloids and Surfaces A: Physicochem. Eng. Aspects.* 2017. **531**: 9.
[355] Nosach L.V., Voronin E.F., Pakhlov E.M., Charmas B., Skubiszewska-Zięba J., Skwarek E., Janusz W., Gun'ko V.M. Nano-particulate structures with glucose-derived char and compacted fumed silica in

gaseous and aqueous media. 2017. **195:** 729. In: *Nanophysics, Nanomaterials, Interface Studies, and Applications. NANO 2016. Springer Proceedings in Physics.* Fesenko O., Yatsenko L. (eds) (Springer, Cham).

[356] Gun'ko V.M., Turov V.V., Krupska T.V., Pakhlov E.M. Behavior of water and methane bound to hydrophilic and hydrophobic nanosilicas and their mixture. *Chem. Phys. Lett.* 2017. **690**: 25.

[357] Goncharuk O.V., Andriyko L.S., Malysheva M.L., Korotych O.I., Marynin A.I., Zarko V.I., Ukrainets A.I., Gun'ko V.M. Influence of indifferent electrolytes on the coagulative structure formation in aqueous silica dispersions. *French-Ukrainian Journal of Chemistry.* 2017. **5**(2): 40.

[358] Goncharuk O.V., Gun'ko V.M., Ugnivenko A.P., Terpilowski K., Skwarek E., Janusz W. Effect of ethonium adsorption on structure formation in nanosilica dispersions. *Nano Research & Applications.* 2017. **29**(3): 1.

[359] Voronina O.E., Malysheva M.L., Nosach L.V., Voronin E.F., Gun'ko V.M., Charmas B., Skubiszewska-Zięba J. A role of free silanol groups of nanosilica surface in interaction with poly(vinyl pyrrolidone). *Annales Universitatis Mariae Curie-Sklodowska, Sectio AA Chemia* 2017. **LXXII**(2): 51.

[360] Gun'ko V.M., Krupska T.V., Andriyko L.S., Klymenko N.Yu., Siora I.V., Novikova O.A., Marynin A.I., Ukrainets A.I., Charmas B., Shekhunova S.B., Turov V.V. Bonding of doxorubicin to nanosilica and human serum albumin in various media. *J. Colloid Interface Sci.* 2018. **513**: 809.

[361] Gun'ko V.M., Turov V.V., Krupska T.V. Interfacial behavior of methane and organic solvents with low freezing points upon interaction with hydrophilic and hydrophobic nanosilicas. *Chemistry, Physics and Technology of Surface* 2018. **9**(2): 107.

[362] Turov V.V., Gun'ko V.M., Pakhlov E.M., Krupska T.V., Tsapko M.D., Charmas B., Kartel M.T. Influence of hydrophobic nanosilica and hydrophobic medium on water bound in hydrophilic components of complex systems. *Colloids and Surfaces A: Physicochem. Eng. Aspects.* 2018. **552**: 39.

[363] Gun'ko V.M., Pakhlov E.M., Goncharuk O.V., Andriyko L.S., Nychiporuk Yu.M., Balakin D.Yu., Sternik D., Derylo-Marczewska A. Nanosilica modified by polydimethylsiloxane depolymerized and chemically bound to nanoparticles or physically bound to unmodified or modified surfaces: Structure and interfacial phenomena. *J. Colloid Interface Sci.* 2018. **529**: 273.

[364] Goncharuk O., Bogatyrov V., Kazakova O., Galaburda M., Oranska O., Skwarek E., Waniak-Nowicka H., Janusz W., Gun'ko V. Silica-supported Ni_xO_y, Zn_xO_y and Mn_xO_y nanocomposites: physicochemical characteristics and interactions with water and n-decane. *Bulletin of Materials Science.* 2019. **42**: 243.

[365] Nosach L.V., Voronin E.F., Pakhlov E.M., Guzenko N.V., Gun'ko V.M. Polymer modified nanosilica as a sorbent for medical applications, chapter 7. In: *Biocompatible Hybrid Oxide Nanoparticles for Human Health, From Synthesis to Applications, Micro and Nano Technologies*. Melnyk I.V., Vaclavikova M., Seisenbaeva G.A., Kessler V.G. (Eds.) (Amsterdam: Elsevier, 2019)

[366] Gun'ko V.M., Polymer composites with functionalized silica. In: *Polymer Composites with Functionalized Nanoparticles. Synthesis, Interactions, Properties and Applications*. Majka T., Pielichowski K. (Eds.) (Amsterdam: Elsevier, 2019).

[367] Protsak I., Gun'ko V.M., Turov V.V., Krupska T.V., Pakhlov E.M., Zhang D., Dong W., Le Z. Nanostructured polymethylsilosane/fumed silica blends. *Materials* 2019. **2409**(12): 1.

[368] Turov V.V., Gun'ko V.M., Krupska T.V., Protsak I.S., Pakhlov E.M., Structural and adsorption features of amorphous nanosilica modified by various addition of polymethylsiloxane. *Chemistry, Physics and Technology of Surface.* 2019. **10**(3): 203.

[369] Gun'ko V.M., Turov V.V., Pakhlov E.M., Krupska T.V., Charmas B. Effect of water content on the characteristics of hydro-compacted nanosilica. *Appl. Surf. Sci*. 2018. **459**: 171.

[370] Gun'ko V.M., Turov V.V., Pakhlov E.M., Krupska T.V., Borysenko M.V., Kartel M.T., Charmas B. Water interactions with hydrophobic versus hydrophilic nanosilica. *Langmuir.* 2018. **34**(40): 12145.

[371] Turov V.V., Gun'ko V.M., Krupska T.V., Kartel M.T. Influence of solid and liquid hydrophobic compounds on characteristics of water located in an adsorption layer of a hydrophilic component of the system. *Chemistry, Physics and Technology of Surface.* 2018. **9**(4): 341.

[372] Gun'ko V.M., Turov V.V., Protsak I.S., Krupska T.V., Pakhlov E.M., Tsapko M.D. Effects of pre-adsorbed water on methane adsorption onto blends with hydrophobic and hydrophilic nanosilicas. *Colloids and Surfaces A: Physicochem. Eng. Aspects.* 2019. **570**: 471.

[373] Pujari, P.K., Sen, D., Amarendra, G., Abhaya S., Pandey A.K., Dutta D., Mazumder S. Study of pore structure in grafted polymer membranes using slow positron beam and small-angle X-ray scattering techniques. *Nuclear. Instr. Method Phys. Res. B*. 2007. **254**: 278.
[374] Sakurai S., SAXS evaluation of size distribution for nanoparticles. Chapter 5. In: A.E. Ares (ed.), *X-ray Scattering*, InTech, Croatia, 2017, pp. 107-134.
[375] Brumberger H. (Ed.) *Small Angle X-ray Scattering*. Gordon & Breach, New York, Syracuse, 1965.
[376] Dieudonné Ph., Hafidi A.A., Delord P., Phalippou J. Transformation of nanostructure of silica gels during drying. *J. Non-Crystal. Solid.* 2000. **262**: 155.
[377] Fairén-Jiménez D., Carrasco-Marín F., Djurado D., Bley F., Ehrburger-Dolle F., Moreno-Castilla C. Surface area and microporosity of carbon aerogels from gas adsorption and small- and wide-angle X-ray scattering measurements. *J. Phys. Chem. B* 2006. **110**: 8681.

ЯВИЩА НА МЕЖАХ ПОДІЛУ БІЛЯ ПОВЕРХНІ ІНДИВІДУАЛЬНИХ ТА СКЛАДНИХ ПІРОГЕННИХ НАНООКСИДІВ

В.М. Гунько, В.В. Туров, О.В. Гончарук, Є.М. Пахлов, О.К. Матковський

Інститут хімії поверхні ім. О.О. Чуйка Національної академії наук України
вул. Генерала Наумова, 17, Київ, 03164, Україна, e-mail:vlad_gunko@ukr.net

Мета цього огляду проаналізувати дослідження поведінки на границях поділу та в залежності від температури неполярних та полярних адсорбатів, що взаємодіють з індивідуальними та складними пірогенними оксидами металів та металоїдів (ПОМ), вихідними та тренованими чи хімічно модифікованими, у порівнянні з пористими силікагелями, осадженими кремнеземами, композитами тощо. Комплексні ПОМ можуть представляти собою частинки ядро-оболонка (ЧЯО, розміром 50-200 нм) з ядром з TiO_2 чи Al_2O_3 та оболонкою з SiO_2 чи Al_2O_3 на відміну від простих та менших наночастинок індивідуальних ПОМ. ЧЯО можуть бути зруйнованими при кріожелюванні при високому тиску чи при механохімічній обробці. Ці тренування, як і гідроущільнення (контрольоване змочування та сушка) впливають на будову агрегатів наночастинок та агломератів з агрегатів, які стають більш компактними. Аналіз вказує на те, що складні ПОМ можуть бути більш чутливими до різних зовнішніх впливів, ніж прості ПОМ, як нанокремнезем. Любе тренування «м'яких» ПОМ впливає на міжфазну та температурну поведінку полярних та неполярних адсорбатів. Перебудова вторинних частинок та поверхнева функціоналізація впливають на зсув точки замерзання-розморожування адсорбатів, локалізованих у порах. Для деяких адсорбатів спостерігається відкрита петля гістерезису адсорбції-десорбції. Кластеризація адсорбатів, локалізовиних у порах, призводить до зменшення змін ентальпії при фазових переходах (замерзання, плавлення). Зсув точки замерзання та плавлення призводить до суттєвих гістерезисних ефектів при замерзанні-розмерзанні адсорбатів, що локалізовани у текстурних порах вихідних та тренованих ПОМ. Релаксаційні явища як для низькомолекулярних, так і високомолекулярних адсорбатів чи полімерних композитів залежать від морфології первинних частинок, структурної організації вторинних частинок ПОМ, тренованих чи модифікованих різним чином, вмісту адсорбатів, порядку ко-адсорбції, температури тощо.

Ключові слова: *нанокремнезем, складні нанооксиди, міжфазні явища, адсорбція, випаровування, ефекти замкнутого простору.*

ЯВИЛЕНИЯ НА ГРАНИЦАХ РАЗДЕЛА У ПОВЕРХНОСТИ ИНДИВИДУАЛЬНЫХ И СЛОЖНЫХ ПИРОГЕННЫХ НАНООКСИДОВ

В.М. Гунько, В.В. Туров, Е.В. Гончарук, Е.М. Пахлов, А.К. Матковский

Институт химии поверхности им. А.А. Чуйко Национальной академии наук Украины
ул. Генерала Наумова, 17, Киев, 03164, Украина, e-mail: vlad_gunko@ukr.net

Цель этого обзора проанализировать исследования поведения на границах раздела и в зависимости от температуры неполярных и полярных адсорбатов, которые взаимодействуют с индивидуальными и сложными пирогенными оксидами металлов и металлоидов (ПОМ), исходными и тренированными или химически модифицированными, по сравнению с пористыми силикагелями, осажденными кремнеземами, композитами и др. Комплексные ПОМ могут представлять собою частицы ядро-оболочка (ЧЯО, размерами 50-200 нм) с ядром из TiO_2 или Al_2O_3 и оболочкой из SiO_2 или Al_2O_3 в отличии от простых и меньших наночастиц индивидуальных ПОМ. ЧЯО могут быть разрушены при криожелировании при высоком давлении или при механохимической обработке. Такая подготовка, как и гидроуплотнение (контролируемое смачивание и сушка) влияют на строение агрегатов наночастиц и агломератов из агрегатов, которые становятся более компактными. Анализ показывает, что сложные ПОМ могут быть более чувствительными к различным внешним воздействия, чем простые ПОМ, как нанокремнезем. Любая подготовка «мягких» ПОМ влияет на межфазное и температурное поведение полярных и неполярных адсорбатов. Перестройка вторичных частиц и поверхностное модифицирование влияют на сдвиг точки замерзания-плавления адсорбатов, локализованных в порах. Для некоторых адсорбатов наблюдается открытая петля гистерезиса адсорбции-десорбции. Кластеризация адсорбатов, локализованных в порах, приводит к уменьшению изменений энтальпии при фазовых переходах (замерзание, плавление). Сдвиг точки замерзания и плавления приводит к существенным гистерезисным эффектам при замерзании-плавлении адсорбатов, локализованных в текстурных порах исходных и тренированных ПОМ. Релаксационные явления как для низкомолекулярных, так и высокомолекулярных адсорбатов или полимерных композитов зависят от морфологии первичных частиц, структурной организации вторичных частиц ПОМ, тренированных или модифицированных различным образом, концентрации адсорбатов, порядка ко-адсорбции, температуры и т.д.

Ключевые слова: *нанокремнезем, сложные нанооксиды, межфазные явления, адсорбция, испарение, эффекты замкнутого пространства.*